Storage of Energy in Chemical Bonds Utilizing Earth-Abundant Molecular Electrocatalysts: Improving Catalyst Design Through an Understanding of Mechanism

Asa Wesley Nichols
Saint Marys, West Virginia

B.S. Chemistry, West Virginia Wesleyan College, 2012

Dissertation presented to the Graduate Faculty of the
University of Virginia in Candidacy for the Degree of
Doctor of Philosophy

Department of Chemistry

University of Virginia

April, 2021

Abstract

Storage of Energy in Chemical Bonds Utilizing Earth-Abundant Molecular Electrocatalysts: Improving Catalyst Design Through Understanding Mechanism

The studies described in this dissertation focus on the use of N_2O_2 ligands in the CO_2 reduction reaction and the oxygen reduction reaction. The use of Fe and Co metal centers in these ligand frameworks leads to different reactivity profiles. Chapter 2 of this dissertation focuses on the synthesis, characterization, and reactivity of an $Fe(N_2O_2)$ compound towards CO_2 under electrochemically reducing conditions in the presence of phenol for the production of formate. These studies are continued in Chapter 3 with a focus on studying how secondary-sphere moieties oriented towards the protonation-sensitive Fe-bound phenolate ligands affect catalytic reactivity towards CO_2. Chapter 4 focuses on synthesis, characterization, and reactivity of a $Co(N_2O_2)$ compound towards the oxygen reduction reaction. These oxygen reduction studies are continued in Chapter 5 with a focus on studying how secondary-sphere moieties oriented towards the catalytically active Co metal center affect catalytic reactivity towards O_2. Finally, Chapter 6 summarizes the previous chapters and outlines preliminary results and future directions for new projects.

Thesis Advisor: Professor Charles W. Machan

Acknowledgements

Without the knowledge and encouragement of others, the work here would not be achievable. Here, I will attempt to thank the people who have stood by me throughout my studies, without whom I wouldn’t be where I stand today.

First, I’m deeply indebted to my advisor, Charles W. Machan, for bringing me into his research group as one of the original members. Charlie’s hands-on approach to my initial training in the lab led me to develop a repertoire of skills, which would be difficult to come by elsewhere. I am extremely grateful for having the opportunity to work and learn alongside him; the ability to learn mentoring skills by observing how he supports myself and others will be irreplaceable in my future career. His balanced mentorship style has allowed me to work as an independent researcher, with guidance when it is needed. This has allowed me to learn skills needed to be successful in the future including confidently proposing research questions, thinking critically about research results, and knowing when to look to others for help. I would also like to thank my committee members Professors Brent Gunnoe and Ian Harrison for helping me to remember that sometimes you just need to take a day to fish.

My parents, Matt and Tammi Nichols, have been an invaluable place to look for support in my entire life. Their love, kindness, and support have molded me into a person who can persevere through the toughest of challenges, and I know I can count on them any time it is needed. My sister, Alice, has always been there to support me whenever I text or call. I wish her luck as she finishes her studies and moves into her new career, and know I will soon learn about her successes. My grandparents, Darrel and Cindy

Gooden & Paul and Sandra Nichols, have nurtured my intellectual growth for many years. They have been a rock for me to rely on whenever needed, and I wouldn't be in the position I am in today without them.

The Machan Group has been a wonderful place to grow and learn as a scientist. Shelby Hooe and I started in the group at nearly the same time, and have learned a lot about both what to do and what not to do during many hours spent in the lab. We have had great conversations and collaborations which have attributed to my growth. I thank Dr. CC Jiang and Dr. Juanjo Moreno who made the group a thriving place to learn, with a great breadth of knowledge, skills, and interesting non-scientific interests, they made the group exponentially better. I also would like to thank other students throughout the department who have contributed greatly to my mental health. I'd like to specifically thank Spencer Simpson, Philip Hahn, Robert Dyer, and Dr. Katy Wilson in this regard.

Outside of the department I've made a plethora of friends, and I couldn't have completed this journey without their support. The Wesley Foundation at UVA has been an amazing place to go for worship and gather in fellowship with kind friends who will listen to any problem you have been having. The climbing community at UVA taught me that sometimes to get your head right you just need to pull or even fall from a height of 10 feet to get your head back in the right place. Anne, Tim, Henry, George, and Martha: I can't thank you enough for being a pandemic pod with myself, Lauren, and Sully; it was the highlight of our year, and we wouldn't want it to be any different.

Finally, Lauren, the last 9 years have been the best I could ask for. I'm so happy that I have you in my life to eat full lines of cookies, force me to sleep-in on some weekends, and go on countless adventures. I’m excited for 70 more years of all that we have together. I’m incredibly happy we found Sully one late night before the pandemic began. His love and affection keep the both of us going, and I can’t wait to watch him continue to mature. Our best days are ahead, and I’m excited to see our careers blossom as we move forward into the next adventure in our life.

Table of Contents

Chapter 1 Motivation and Precedence for Studying Electrochemical Transformations of Carbon Dioxide and Oxygen 1

1.1 Problems and solutions in the production and utilization of electrical energy 2

1.2 Secondary-Sphere Effects in the CO_2 Reduction Reaction (CO_2RR): Introduction ... 3

1.3 Biological inspiration for development of CO_2RR catalysts 5

1.3.1 Cu,Mo-Containing Carbon Monoxide Dehydrogenase (Cu,Mo-CODH) 5

1.3.2 Monofunctional Ni,Fe-containing CODHs 6

1.3.3 Formic Acid Dehydrogenase (FADH) 7

1.4 Benchmarking Molecular Electrocatalysts for CO_2RR 8

1.5 Secondary-Sphere Effects in Molecular Electrocatalysts for CO_2RR 11

1.5.1 Secondary-Sphere Effects in $[Fe(TPP)]^+$ 11

1.5.2 Secondary-Sphere Effects in $Re(bpy)(CO)_3X$ 18

1.5.3 Secondary-Sphere Effects in $Mn(bpy)(CO)_3X$ 24

1.5.4 Secondary-Sphere Effects in $Ni(cyclam)]^{2+}$ 28

1.5.5 Secondary-Sphere Effects in Multimetallic Systems 30

1.5.6 Secondary-Sphere Effects in Emerging Systems 34

1.6 Conclusions and Future Directions of Secondary-Sphere Effects with Molecular CO_2RR Electrocatalysts. 35

1.7 Alternate Approaches: O_2 Reduction 37

1.8 Benchmarking Catalysts for the O_2 Reduction Reaction 37

1.9 Mononuclear Molecular Electrocatalysts for O_2 Reduction 40

1.9.1 Co(porphyrin) derivatives as ORR catalysts 40

1.9.2 Co(corroles) as ORR catalysts 44

1.9.3 Co(chlorins) as ORR catalysts 45

1.9.4 Co(phthalocyanines) as ORR catalysts 45

1.9.5 $[Co(cyclam)]^{3+}$ derivatives as ORR catalysts 46

1.9.6 $Co(N_2O_2)$ derivatives as ORR catalysts 48

1.10 An N_2O_2 ligand with a bipyridine backbone for development of catalysts for CO_2RR and ORR 49

Chapter 2 Electrocatalytic Reduction of CO_2 to Formate by an Iron Schiff Base Complex 51

2.1 Abstract 52

2.2 Introduction 52

2.3 Materials and Methods 55
2.3.1 General 55
2.3.2 Synthesis of 2-Bromo-4,6-di-tert-butyl Phenol 55
2.3.3 Synthesis of 6,6′-di(3,5-di-tert-butyl-2-hydroxybenzene)-2,2′-bipyridine ^{tbu}dhbpy(H)$_2$ 56
2.3.4 Synthesis of Fe(^{tbu}dhbpy)Cl **1** 57
2.3.5 Synthesis of [Fe(^{tbu}dhbpy)][OTf] **1[OTf]** 58
2.3.6 Synthesis of Zn(^{tbu}dhbpy) 58
2.3.7 Electrochemistry 59
2.3.8 IR Spectroelectrochemistry 60
2.3.9 Computational Methods 60
2.4 Results 61
2.4.1 Characterization of Fe(^{tbu}dhbpy)Cl 61
2.4.2 Electrochemistry 62
    2.4.2.1 Electrochemical Response under Ar Saturation 62
    2.4.2.2 Electrochemical Response under Ar Saturation with added PhOH 65
    2.4.2.3 Electrochemical Response in the Presence of CO$_2$ 68
    2.4.2.4 Electrochemical Response with CO$_2$ and added PhOH 71
2.4.3 Product Analysis by Controlled Potential Electrolysis 72
2.4.4 Mechanistic Experiments with Infrared-Spectroelectrochemistry 73
2.4.5 DFT Calculations 76
2.4.6 Foot-of-the-Wave Analysis 77
2.5 Discussion 78
2.6 Conclusions 81
2.7 Supporting Information for Chapter 2 82
2.7.1 Evans method 82
2.7.2 Determination of Proton and CO Binding Constants 83
2.7.3 Determination of Theoretical Isotopic CO$_2$ Shift 83
2.7.4 Product Analysis 84
2.7.5 Synthesis of d_1-PhOD 85
2.7.6 Foot-of-the-Wave Analysis 85
2.7.7 Determination of KIE from FOWA 86
2.7.8 Figures 87

Chapter 3 Electrocatalytic CO_2 Reduction to Formate with Molecular Fe(III) Complexes Containing Pendent Proton Relays 141

3.1 Abstract 142

3.2 Introduction 143

3.3 Results 146

3.3.1 Synthesis and Characterization of Complexes **2** and **3** 146

3.3.2 Electrochemistry 148

  3.3.2.1 Electrochemical Response under Ar Saturation 148

  3.3.2.1 Electrochemical Response under CO_2 Saturation 150

  3.3.2.3 Comparative Analysis 151

3.3.3 Product Analysis 154

3.3.4 Electrochemistry with a Sterically Hindered Proton Donor 156

3.4 Discussion 157

3.5 Conclusions 160

3.6 Experimental and Methods 161

3.6.1 General. 161

3.6.2 Electrochemistry. 162

3.6.3 Synthesis of 2-methoxy-4-methyl-6-(4,4,5,5-tetramethyl-1,3,2-dioxaborolan-2-yl)phenol, II. 164

3.6.4 Synthesis of ^{me}crebpy[H]$_2$, III. 165

3.6.5 Synthesis of Fe(^{me}crebpy)Cl, 2, IV. 165

3.6.6 Synthesis of Zn(^{me}crebpy). 166

3.6.7 Synthesis of 3-bromo-5-tert-butyl-benzene-1,2-diol, VI. 167

3.6.8 Synthesis of 1-bromo-5-tert-butyl-2,3-bis(methoxymethoxy)benzene, VII. 168

3.6.9 Synthesis of bis(MOM)catbpy, IX. 169

3.6.10 Synthesis of ^{tbu}catbpy[H]$_4$, X. 170

3.6.11 Synthesis of Fe(^{tbu}catbpy), **3**. 171

3.6.12 Synthesis of Zn(^{tbu}catbpy). 172

3.7 Supporting Information for Chapter 3 173

Chapter 4 Reduction of dioxygen to water by a Co(N_2O_2) complex with a 2,2′-bipyridine backbone 218

4.1 Abstract 219

4.2 Introduction 219

4.3 Results and Discussion 221

4.3.1 Synthesis and Characterization of Co[(^{tbu}dhbpy)(py)$_2$][PF$_6$] (**1)** 221

4.3.2 Electrochemistry 222

4.3.3 Spectrochemical Kinetic Studies 223

4.3.4 Proposed Mechanism 226

4.4 Conclusions 227

4.5 Supporting Information for Chapter 4 229

4.5.1 Experimental and Methods 229

  4.5.1.1 General 229

  4.5.1.2 Electrochemistry 229

  4.5.1.3 Synthesis of ^{tbu}dhbpy[H]$_2$ 230

  4.5.1.4 Synthesis of [Co(^{tbu}dhbpy)(py)$_2$][PF$_6$] (**1**) 230

  4.5.1.5 Synthesis of Co(^{tbu}dhbpy) 231

4.5.2 Figures 231

  4.5.2.1 Electrochemical Experiments 237

  4.5.2.2 Iodometric Titration for Determination of Product Selectivity for ORR. 239

  4.5.2.3 Mechanistic Studies of the 2+2 Mechanism 242

  4.5.2.4 Determination of the Catalytic Rate Law for **1** 243

  4.5.2.5 Determination of rate constant, k_{cat}. 249

  4.5.2.6 Py Controls for Selectivity Testing with Co(salen) and Co(^{tbu}dhbpy) 250

Chapter 5 Reduction of Dioxygen by bpy-based Co-N$_2$O$_2$ Complexes: Optimizing Efficiency for Water and H$_2$O$_2$ 252

5.1 Abstract 253

5.2 Introduction 253

5.3 Results 256

5.3.1 Synthesis and Characterization 256

5.3.2 Initial Reactivity Screening 257

5.3.2 Electrochemistry 258

5.3.3 Selectivity 259

5.3.4 Spectrochemical Kinetic Studies 260

5.3.5 Determination of Kinetic Isotope Effect 261

5.4 Discussion 262

5.5 Conclusions 265

Supporting Information for Chapter 5 266

5.6 Experimental and Methods 266

5.6.1 General 266

5.6.2 Electrochemistry 266

5.6.3 Synthesis of ^{tbu}dhbpy[H]$_2$ and [Co(^{tbu}dhbpy)(py)$_2$][PF$_6$] (**1**) 267

5.6.4 Synthesis of 2-methoxy-4-propyl-6-(4,4,5,5-tetramethyl-1,3,2-dioxaborolan-2-yl)phenol 267

5.6.5 Synthesis of ^{pro}bpy[H]$_2$ 268

5.6.6 Synthesis of [Co(^{pro}bpy)py)$_2$][PF$_6$] 269

5.6.7 Figures and Tables 270

- 5.6.7.1 Electrochemical Experiments 273
- 5.6.7.2 Determination of product selectivity for ORR. 279
- 5.6.7.3 Determination of the Catalytic Rate Law for **1** with all acids and **2** with benzoic acid and 2-chlorobenzoic acid. 288
- 5.6.7.4 Determination of the Catalytic Rate Law for **2** with 2,4-dichlorobenzoic acid and 2,6-dichlorobenzoic acid. 302
- Determination of turnover frequency (TOF). 309
- 5.6.7.5 Determination of Overpotential: 310
- 5.6.7.6 Determination of KIE 311

Chapter 6 Conclusions and Future Work 316

6.1 Introduction 317

6.2 Summary and Conclusions 317

6.3 Preliminary Results and Future Directions 319

6.3.1 CO_2 Reduction with Fe Compounds in the presence of Lewis Acids 319

6.3.2 CO_2 Reduction with Co(^{tbu}dhbpy) and [Co(^{tbu}dhbpy)(py)$_2$][PF$_6$] 324

6.3.3 Application of N_2O_2 Ligands with Non-innocent Secondary-Sphere Moieties to Mn and Cr Electrocatalyst systems 326

6.4 Perspective 327

Chapter 1 References 328

Chapter 2 References 344

Chapter 2 SI References 349

Chapter 3 References 350

Chapter 3 SI References 354

Chapter 4 References 354

Chapter 4 SI References 358

Chapter 5 References 358
Chapter 5 SI References 361
Chapter 6 References 362
Vita 365

List of Figures

Figure 1.1. Typical electrical load without variable generation (solar and wind), dark blue, load when corrected for added variable generation (light blue), solar generation (green), and wind generation (red) for a spring day in California. Adapted from Overgeneration from solar energy in California. a field guide to the duck chart; National Renewable Energy Lab.(NREL), Golden, CO (United States): 2015. 2

Figure 1.2. (A) Active site of Cu,Mo-CODH. (B) Proposed catalytic cycle for oxidation of CO by Cu,Mo-CODH.[79-80] 5

Figure 1.3. (A) Proposed mechanism for CO oxidation Ni,Fe CODH.[83] (B) Active site of FADH in *E. coli* with bound formate substrate.[84] 7

Figure 1.4. Example of a catalytic Tafel plot of a generic molecular species with regions where better and worse catalysts are located explicitly labeled, along with the position of important benchmarking parameters. 10

Figure 1.5. Catalytic Tafel plot showing enhancements from the inclusion of a secondary coordination sphere in the $[Fe(TPP)]^+$ system.[11] Adapted from *Proc. Natl. Acad. Sci.* **2014**, *111*, 14990-14994. 11

Figure 1.6. Plot of log(TOF_{max}) vs E^0_{cat} for hangman porphyrins used to study positional dependence of catalytic enhancement for this system. Circles are $[Fe(TPP)]^+$ derivatives which utilize electronic substitution of the phenyl rings for modulation of the redox potential of the $Fe^{I/0}$ couple. Upwards purple triangle is [Fe(*p*-1-amide-TPP)]$^+$, downwards orange triangle is [Fe(*p*-2-amide-TPP)]$^+$, blue diamond is [Fe(*o*-1-amide-TPP)]$^+$, red square is [Fe(*o*-2-amide-TPP)]$^+$. Reprinted with permission from *Chem. Sci.*, **2018**, *9*, 2952 –published by the Royal Society of Chemistry. 14

Figure 1.7. Figure showing effect of pK_a of hanging group on CO_2RR activity in hangman $[Fe(TPP)]^+$. Reprinted with permission from *Organometallics*, **2019**, *38*, 1219-1223. Copyright 2018 American Chemical Society. 15

Figure 1.8. Faradaic reduction of $Re(bpy)(CO)_3X$. Adapted with permission from *Organometallics*, **2014**, *33*, 4550–4559. Copyright 2014 American Chemical Society.. 19

Figure 1.9. $2e^-/2H^+$ dependent catalytic cycle for $Re(bpy)(CO)_3X$ in the reduction of CO_2 to CO. Adapted with permission from *Organometallics*, **2014**, *33*, 4550–4559. Copyright 2014 American Chemical Society. 20

Figure 1.10. Faradaic reduction mechanism of $Mn(bpy)(CO)_3X$. Adapted with permission from *Organometallics*, **2014**, *33*, 4550–4559. Copyright 2014 American Chemical Society. 25

Figure 1.11. ‘Protonation-First’ and ‘Reduction-First’ Pathways for CO_2RR by $Mn(bpy)(CO)_3X$.[65] 26

Figure 1.12. Figure showing proposed transition state which occurs to turn on a low overpotential, secondary-sphere promoted mechanism for CO_2RR with $Mn((OMe)_2bpy)(CO)_3X$. Adapted with permission from *J. Am. Chem. Soc.*, **2017**, *139* , 2604–2618. Copyright American Chemical Society 2017. 28

Figure 1.13. Space filling models of *trans-I* $[Ni(cyclam)(CO_2)]^+$ (A), *trans-III* $[Ni(cyclam)(CO_2)]^+$ (B), and $[Ni(DMC)(CO_2)]^+$ (C). Structures indicate that enhanced CO_2RR in the case of *trans-I* $[Ni(cyclam)(CO_2)]^+$ may be due to increased stabilization of the CO_2 adduct through increased hydrogen bond donors oriented towards the hydrogen bond accepting O atoms on the CO_2 adduct. Used with permission from *Inorg. Chem.*, **2014**, *53*, 7500–7507. Copyright American Chemical Society 2014. 29

Figure 1.14. Catalytic Tafel plot showing overpotential tuning in co-facial Fe(TTP) through the introduction of electron with drawing substituents on the phenyl groups of the porphyrin system. Adapted from *Scientific Reports,* **2016**, *6*, 24553. 31

Figure 1.15. (A) $Co(Cp)(P_2N_2)$ utilizing pendent tertiary amines for reduction of CO_2 to formate. (B) $Fe(^{tbu}dhbpy)Cl$ is protonated at the Fe-coordinating O atoms upon reduction and reduces CO_2 to formate. (C) Macrocyclic-aminopyridyl complex which reduces CO_2 to CO. 35

Figure 1.16. Scaling relationships for Fe(TPP) ORR catalysis predicted (lines) and measured (points) upon changing the acid concentration (black), partial pressure of O_2 (green), pK_a of the acid (purple) and $E_{1/2}$ of the catalyst. The intersection point is Fe(TPP) with 100 mM $H\text{-}DMF^+$ under 1 atm O_2. Reproduced with permission from *J. Am. Chem. Soc.* **2017**, *139*, 11000–11003, DOI: 10.1021/jacs.7b05642, Copyright 2017 American Chemical Society. Further permissions should be directed to the ACS. 38

Figure 1.17. Structure of Co(TMPyP) utilized for ORR in both aqueous and non-aqueous conditions. Co(TMPyP) was studied as either a ClO_4^- or Cl^- salt.[157-159] 41

Figure 1.18. Structures of non-planar $Co(TMPyPBr_8)$[161] and $Co(TSPPBr_8)$[160] utilized for ORR in aqueous conditions studied as Cl^- and Na^+ salts, respectively. 42

Figure 1.19. Structure of Co(TRuPyP) utilized for ORR in aqueous conditions.[165] 43

Figure 1.20. Co(corroles) studied for the ORR.[170] 44

Figure 1.22. Co(chlorin) complexes utilized for ORR.[44, 171] 45

Figure 1.23. Co(phthalocyanines) tested for ORR.[164, 169, 174, 203] 46

Figure 1.24. Co(cyclam) derivatives studied for O_2 reduction.[162-163, 166] 48

Figure 1.25. N_2O_2 complexes with their reduction potentials and Faradaic efficiencies for production of hydrogen peroxide and their Log(TOF) vs $E_{1/2}$ relationship. Adapted with permission from *J. Am. Chem. Soc.* **2017**, *139*, 16458–16461 Copyright 2017 American Chemical Society. 49

Figure 1.26. N_2O_2 ligands for study in this thesis. 50

Figure 2.1. ORTEP plot of Fe(^{tbu}dhbpy)Cl. Thermal ellipsoids set to 50%. Occluded acetonitrile molecule and hydrogen atoms omitted for clarity. C = grey, O = red, N = blue, Cl = green, Fe = orange. 61

Figure 2.2. Cyclic voltammogram of 0.5 mM Fe(^{tbu}dhbpy)Cl 1 in *N*,*N*-DMF with 0.1 M TBAPF$_6$ supporting electrolyte under an atmosphere of Ar. Conditions: scan rate 100 mV/s; working electrode glassy carbon (3 mm), counter electrode Pt wire, and pseudo-reference Ag/AgCl wire behind a PTFE tip with ferrocene (Fc) added as internal reference. 62

Figure 2.3. Nernstian shift of 0.5 mM Fe(^{tbu}dhbpy)Cl first reduction (E^0 = –0.89 V) upon addition of PhOH as a proton source under in *N*,*N*-DMF with 0.1 M TBAPF$_6$ supporting electrolyte under Ar saturation; scan rate is 100 mV/s. Working electrode is glassy carbon, counter electrode is Pt wire, and pseudoreference is Ag/AgCl wire with ferrocene (Fc) added as internal reference. Arrow shows direction of shift with increasing PhOH concentration. 67

Figure 2.4. (A) Second reduction (E^0 = –2.09 V vs Fc/Fc$^+$) of 0.5 mM Fe(^{tbu}dhbpy)Cl in *N*,*N*-DMF with 0.1 M TBAPF$_6$ supporting electrolyte under Ar (black and blue) and CO$_2$ (red and green) saturation; scan rate is 100 mV/s. Working electrode is glassy carbon, counter electrode is Pt wire, and pseudo-reference is Ag/AgCl wire with ferrocene (Fc) added as internal reference. Red arrow shows direction of potential sweep. (B) Highlight of oxidative features on the return sweep corresponding to CO$_2$ reaction products at –1.9 V vs Fc/Fc$^+$. 67

Figure 2.5. Second reduction (E^0 = –2.65 V vs Fc$^+$/Fc) of 0.5 mM Fe(^{tbu}dhbpy)Cl in *N*,*N*-DMF 0.1 M TBAPF$_6$ supporting electrolyte under Ar (black and blue) and CO$_2$ (red and green) saturation; scan rate is 100 mV/s. Working electrode is glassy carbon, counter electrode is Pt wire, and pseudo-reference is Ag/AgCl wire with ferrocene (Fc) added as internal reference. Arrow shows direction of potential sweep. 69

Figure 2.6. IR-SEC experiment with 3 mM Fe(^{tbu}dhbpy)Cl in 0.1 M TBAPF$_6$/*N,N*-DMF supporting electrolyte with CO$_2$. CO$_2$ was sparged through the solution for approximately 20 s. Glassy carbon working electrode, Ag metal pseudoreference electrode, glassy carbon counter electrode; referenced to Fc standard. 75

Figure S2.1. Infrared Spectroelectrochemistry cell. The three-electrode set-up consists of an inner glassy carbon working electrode disc (10 mm diameter), a central circular silver metal pseudoreference electrode, and an outer circular glassy carbon counter electrode embedded within a PEEK block. 87

Figure S2.2. Characteristic UV-Vis Spectrum of 0.046 mM Fe(^{tbu}dhbpy)Cl **1** and the predicted DFT UV-Vis spectrum in *N*,*N*-DMF. 87

Figure S2.3. Cyclic voltammograms of 0.5 mM Fe(^{tbu}dhbpy)Cl **1** in *N*,*N*-DMF with 0.1 M TBAPF$_6$ solution under Ar saturation, showing response to variable scan rate. Working electrode is glassy carbon (3 mm diameter), counter electrode is Pt wire, and pseudo-reference is Ag/AgCl wire with ferrocene (Fc) added as internal reference. 88

Figure S2.4. Variable scan rate plots of Fe(^{tbu}dhbpy)Cl **1** A) First reduction potential ($E^0 = –0.89$ V vs Fc/Fc$^+$) B) Second reduction potential ($E^0= –2.09$ V vs Fc/Fc$^+$) C) Third reduction potential ($E^0= –2.65$ V vs Fc/Fc$^+$). Working electrode is glassy carbon (3 mm diameter), counter electrode is Pt wire, and pseudo-reference is Ag/AgCl wire with ferrocene (Fc) added as internal reference. 89

Figure S2.5. Cyclic voltammograms of 0.5 mM Fe(^{tbu}dhbpy)Cl **1** in *N*,*N*-DMF with 0.1 M TBAPF$_6$ supporting electrolyte under an atmosphere of Ar, showing chemical reaction of diradical species on the CV timescale. Scan rate is 100 mV/s. Working electrode is glassy carbon (3 mm diameter), counter electrode is Pt wire, and pseudo-reference is Ag/AgCl wire with ferrocene (Fc) added as internal reference. 90

Figure S2.6. Cyclic voltammograms of 0.5 mM Fe(^{tbu}dhbpy)Cl **1** in *N*,*N*-DMF 0.1 M TBAPF$_6$ supporting electrolyte under an atmosphere of Ar, showing loss of chloride at first reduction feature. Scan rate is 1000 mV/s. Working electrode is glassy carbon (3 mm diameter), counter electrode is Pt wire, and pseudo-reference is Ag/AgCl wire with ferrocene (Fc) added as internal reference. 90

Figure S2.7. Cyclic voltammogram of 0.5 mM and Fe(^{tbu}dhbpy)Cl **1** or Zn(^{tbu}dhbpy) and in *N*,*N*-DMF 0.1 M TBAPF$_6$ supporting electrolyte under an atmosphere of Ar. Scan rate is 100 mV/s. Working electrode is glassy carbon (3 mm diameter), counter electrode is glassy carbon rod, and pseudo-reference is Ag/AgCl wire with ferrocene (Fc) added as internal reference. 91

Figure S2.8. Cyclic voltammogram of 0.5 mM [Fe(^{tbu}dhbpy)][OTf] **1[OTf]** or Fe(^{tbu}dhbpy)Cl **1** in *N*,*N*-DMF 0.1 M TBAPF$_6$ supporting electrolyte under an atmosphere of Ar. Scan rate is 100 mV/s. Working electrode is glassy carbon (3 mm diameter), counter electrode is glassy carbon rod, and pseudo-reference is Ag/AgCl wire with ferrocene (Fc) added as internal reference.. 91

Figure S2.9. Cyclic voltammogram of 0.5 mM Fe(^{tbu}dhbpy)Cl **1** or [Fe(^{tbu}dhbpy)][OTf] **1[OTf]** in *N*,*N*-DMF 0.1 M TBAPF$_6$ supporting electrolyte under an atmosphere of Ar. Scan rate is 100 mV/s. Working electrode is glassy carbon (3 mm diameter), counter electrode is glassy carbon rod, and pseudo-reference is Ag/AgCl wire with ferrocene (Fc) added as internal reference.. 92

Figure S2.10. Nernst plot for Fe(^{tbu}dhbpy)Cl **1** under Ar atmosphere. At concentrations of PhOH < 0.76 M, a slope of 37±1 mV/decade is observed. At concentrations of PhOH > 0.76 M, a slope of 27±3 mV/decade is observed. 92

Figure S2.11. Nernst plot for 0.5 mM [Fe(^{tbu}dhbpy)][OTf] **1[OTf]** in *N*,*N*-DMF 0.1 M with TBAPF$_6$ under Ar atmosphere. At all concentrations studied a consistent slope of 25±2 mV/decade is observed.. 93

Figure S2.12. Nernstian shift of 0.5 mM [Fe(^{tbu}dhbpy)][OTf] **1[OTf]** first reduction ($E^0 = –0.89$ V) towards oxidizing potentials upon addition of PhOH as a proton source under in *N*,*N*-DMF 0.1 M with TBAPF$_6$ supporting electrolyte under an atmosphere of CO_2. Scan rate is 100 mV/s. Working electrode is glassy carbon (3 mm diameter), counter electrode is glassy carbon, and pseudo-reference is Ag/AgCl wire with ferrocene (Fc) added as internal reference. Red arrow shows direction of potential sweep. Black arrow shows direction of shift with increasing PhOH concentration. 93

Figure S2.13. Cyclic voltammograms of 0.5 mM Fe(^{tbu}dhbpy)Cl **1** in *N*,*N*-DMF with 0.1 M TBAPF$_6$ supporting electrolyte under an atmosphere of Ar (black) and varying CO_2 concentrations (red, blue, green, and purple). Scan rate is 100 mV/s. Working electrode is glassy carbon (3 mm diameter), counter electrode is Pt wire, and pseudo-reference is Ag/AgCl wire with ferrocene (Fc) added as internal reference. 94

Figure S2.14. Log-Log plot of current density and [CO_2] under aprotic conditions. Slope of 0.16 consistent with rate-limiting kinetics with respect to [CO_2] for catalytic current.[8] 94

Figure S2.15. Log-log of current density and [Fe(^{tbu}dhbpy)Cl] **1** [mM] under saturated CO_2 conditions. Slope of 0.93 is indicative of 1st order kinetics with respect to Fe(^{tbu}dhbpy)Cl. 95

Figure S2.16. Cyclic voltammograms of 0.5 mM Fe(^{tbu}dhbpy)Cl **1** in *N*,*N*-DMF with 0.1 M TBAPF$_6$ supporting electrolyte under an atmosphere of Ar (black) and CO (red). Scan rate is 100 mV/s. Working electrode is glassy carbon (3 mm diameter), counter electrode is glassy carbon, and pseudo-reference is Ag/AgCl wire with ferrocene (Fc) added as internal reference. 95

Figure S2.17. Nernstian shift of 0.5 mM Fe(^{tbu}dhbpy)Cl **1** first reduction (E^0 = –0.89 V) towards oxidizing potentials upon addition of PhOH as a proton source under in *N*,*N*-DMF 0.1 M with TBAPF$_6$ supporting electrolyte under an atmosphere of CO_2. Scan rate is 100 mV/s. Working electrode is glassy carbon (3 mm diameter), counter electrode is Pt wire, and pseudo-reference is Ag/AgCl wire with ferrocene (Fc) added as internal reference. Red arrow shows direction of potential sweep. Black arrow shows direction of shift with increasing PhOH concentration. 96

Figure S2.18. Nernst plot for 0.5 mM [Fe(^{tbu}dhbpy)][OTf] **1[OTf]** in *N*,*N*-DMF 0.1 M with TBAPF$_6$ under saturated CO_2 atmosphere. At concentrations of PhOH < 0.76 M, a slope of 39±2 mV/decade is observed. At concentrations of PhOH > 0.76 M, a slope of 18±2 mV/decade is observed. 96

Figure S2.19. Response of 0.5 mM [Fe(^{tbu}dhbpy)][OTf] **1[OTf]** in *N*,*N*-DMF 0.1 M with TBAPF$_6$ at third reduction when varying concentrations of CO_2 are added with 0.509 M PhOH. Scan rate is 100 mV/s. Working electrode is glassy carbon (3 mm diameter), counter electrode is Pt wire, and pseudo-reference is Ag/AgCl wire with ferrocene (Fc) added as internal reference. 97

Figure S2.20. Log-log of current density and [Fe(^{tbu}dhbpy)Cl] **1** [mM] under saturated CO_2 conditions with 0.5 M PhOH. Slope of 0.83 is indicative of 1st order kinetics with respect to Fe(^{tbu}dhbpy)Cl. 97

Figure S2.21. IR-SEC experiment with 3 mM Fe(^{tbu}dhbpy)Cl **1** in 0.1 M TBAPF$_6$/*N,N*-DMF supporting electrolyte. CO_2 was sparged through the solution for ~20 s. Arrows show growth of intermediate CO_2 bound species when potential is held at –2.0 V and reversible loss of this feature when potentials are returned to –1.5 V. Glassy carbon working electrode, Ag metal pseudoreference electrode, glassy carbon counter electrode; referenced to Fc standard. 98

Figure S2.22. IR-SEC experiment with 3 mM Fe(^{tbu}dhbpy)Cl **1** in 0.1 M TBAPF$_6$/*N,N*-DMF supporting electrolyte. ^{13}CO$_2$ was sparged through the solution for ~10 s. Glassy carbon working electrode, Ag metal pseudoreference electrode, glassy carbon counter electrode; referenced to Fc standard. 98

Figure S2.23. (A) IR-SEC spectra of Fe(^{tbu}dhbpy)Cl **1** with CO$_2$ and 0.5 M PhOH at the Fe(II)/Fe(I) redox wave. Growth of bands at 2nd reduction feature. (B) IR-SEC spectra at the bpy/bpy$^{•-}$ redox wave. Experiments conducted with 3 mM Fe(^{tbu}dhbpy)Cl **1** in 0.1 M TBAPF$_6$/*N,N*-DMF supporting electrolyte. CO$_2$ was sparged through the solution for approximately 20 s. Glassy carbon working electrode, Ag metal pseudoreference electrode, glassy carbon counter electrode; referenced to Fc standard. 99

Figure S2.24. IR-SEC experiment with 3 mM Fe(^{tbu}dhbpy)Cl **1** and 0.5 M PhOH in 0.1 M TBAPF$_6$/*N,N*-DMF supporting electrolyte. ^{13}CO$_2$ was sparged through the solution for ~10 s. Glassy carbon working electrode, Ag metal pseudoreference electrode, glassy carbon counter electrode; referenced to Fc standard. 99

Figure S2.25. IR-SEC experiment with 3 mM Fe(^{tbu}dhbpy)Cl in 0.1 M TBAPF$_6$/*N,N*-DMF supporting electrolyte. (A) CO was sparged through the solution for ~20 s (B) Identical conditions with 0.51 M PhOH added. Arrows show growth of two bands which are consistent to those seen after a CO$_2$ sparge. 100

Figure S2.26. (A) Charge passed vs time for bulk electrolysis experiments (B) Current time trace (C) UV-Vis spectrum of Pre (black) and Post (Red) bulk electrolysis solutions after dilution. Conditions were 0.5 mM Fe(^{tbu}dhbpy)Cl **1**, 0.5 M PhOH, and under a CO$_2$ atmosphere at –2.5 V vs Fc/Fc$^+$ in 0.1 M TBAPF$_6$/*N,N*-DMF supporting electrolyte; 2.7 turnovers for the total system were achieved. Working and counter electrodes were glassy carbon rods. 0.05 M Fc was used as sacrificial oxidant. Reference was non-aqueous Ag/AgCl pseudoreference electrode. Control trace represents identical conditions with no Fe(^{tbu}dhbpy)Cl added. 101

Figure S2.27. (A) Charge passed vs time for bulk electrolysis experiments (B) Current time trace (C) UV-Vis spectrum of Pre (black) and Post (Red) bulk electrolysis solutions after dilution. Conditions were 0.5 mM Fe(^{tbu}dhbpy)Cl **1**, 0.5 M PhOH, and under an Ar atmosphere at –2.5 V vs Fc/Fc$^+$ in 0.1 M TBAPF$_6$/*N,N*-DMF supporting electrolyte; 2.7 turnovers for the total system were achieved. Working and counter electrodes were glassy carbon rods. 0.05 M Fc was used as sacrificial oxidant. Reference was non-aqueous Ag/AgCl pseudoreference electrode. Control trace represents identical conditions with no Fe(^{tbu}dhbpy)Cl added. 102

Figure S2.28. Kohn-Sham representations of HOMO (B) and LUMO (C) for model complex Fe(dhbpy)Cl (A); spin density is shown in (D). Used the B3LYP/G[9-13] functional and def2-TZVP[14-15] basis set with the RIJCOSX approximation[16], D3BJ dispersion correction[17-18], and CPCM[19] to model the *N,N*-DMF solvent; 2S + 1 = 6. 103

Figure S2.29. Kohn-Sham representations of HOMO (B) and LUMO (C) for model complex $[Fe(dhbpy)Cl]^{-}$ (A); spin density is shown in (D). Used the B3LYP/G[9-13] functional and def2-TZVP[14-15] basis set with the RIJCOSX approximation[16], D3BJ dispersion correction[17-18], and CPCM[19] to model the *N,N*-DMF solvent; 2S + 1 = 5. 103

Figure S2.30. Kohn-Sham representations of HOMO (B) and LUMO (C) for model complex $[Fe(dhbpy)]^{0}$ (A); spin density is shown in (D). Used the B3LYP/G[9-13] functional and def2-TZVP[14-15] basis set with the RIJCOSX approximation[16], D3BJ dispersion correction[17-18], and CPCM[19] to model the *N,N*-DMF solvent; 2S + 1 = 5. 104

Figure S.31. Kohn-Sham representations of HOMO (B) and LUMO (C) for model complex $[Fe(dhbpy)]^{-}$ (A); spin density is shown in (D). Used the B3LYP/G[9-13] functional and def2-TZVP[14-15] basis set with the RIJCOSX approximation[16], D3BJ dispersion correction[17-18], and CPCM[19] to model the *N,N*-DMF solvent; 2S + 1 = 4. 104

Figure S2.32. Kohn-Sham representations of HOMO (B) and LUMO (C) for model complex $[Fe(dhbpy)]^{2-}$ (A); spin density is shown in (D). Used the B3LYP/G[9-13] functional and def2-TZVP[14-15] basis set with the RIJCOSX approximation[16], D3BJ dispersion correction[17-18], and CPCM[19] to model the *N,N*-DMF solvent; 2S + 1 = 4. 105

Figure S2.33. Difference densities predicting LMCT in the Visible Region. Used the B3LYP/G[9-13] functional and def2-TZVP[14-15] basis set with CPCM[19] to model the *N,N*-DMF solvent; 2S + 1 = 6. 105

Figure S2.34. (A) CV trace overlays of Ar saturation (black) and CO_2 saturation (red). (B) Full plot of i_c/i_p vs $(1+\exp(FR^{-1}T^{-1}(E-E^0cat))^{-1}$ (C) Linear region from FOWA analysis which gives a slope of 11.8. Conditions are 0.5 mM Fe(^{tbu}dhbpy)Cl in 0.1 M $TBAPF_6$/*N,N*-DMF supporting electrolyte. Working and counter electrodes are glassy carbon. Pseudoreference electrode is Ag/AgCl. All data is referenced to a ferrocene internal standard. 106

Figure S2.35. (A) CV trace overlays of Ar saturation (grey) and CO_2 saturation (red). (B) Full plot of i_c/i_p vs $(1+\exp(FR^{-1}T^{-1}(E-E^0cat))^{-1}$ (C) Linear region from FOWA analysis which gives slopes of 18.2, 20.8, and 26.0 for 0.122, 0.182, and 0.252 M PhOH, respectively. Conditions are 0.5 mM Fe(^{tbu}dhbpy)Cl in 0.1 M $TBAPF_6$/*N,N*-DMF supporting electrolyte. Working and counter electrodes are glassy carbon. Pseudoreference electrode is Ag/AgCl. All data is referenced to a ferrocene internal standard. 107

Figure S2.36. (A) CV trace overlays of Ar saturation (grey) and CO_2 saturation (red). (B) Full plot of i_c/i_p vs $(1+\exp(FR^{-1}T^{-1}(E-E^0cat))^{-1}$ (C) Linear region from FOWA analysis which gives slopes of 14.5, 15.8, and 17.2 for 0.045, 0.101, and 0.155 M PhOD, respectively. Conditions are 0.5 mM Fe(^{tbu}dhbpy)Cl in 0.1 M $TBAPF_6$/*N,N*-DMF supporting electrolyte. Working and counter electrodes are glassy carbon. Pseudoreference electrode is Ag/AgCl. All data is referenced to a ferrocene internal standard. 108

Figure S2.37. Plots of TOF_{max} vs [PhOH(D)]. A ratio of the slopes of linear fits can be used to determine KIE (k_H/k_D). In this case a KIE of 4.8±0.9 was found. 109

Figure S2.38. ^{1}H NMR of d_1-PhOD in $CDCl_3$. Two sets of aromatic protons not infringed upon by solvent (δ 6.82, 6.92 ppm) integrate to 1 H and 2 H respectively. Phenolic proton

(δ 4.67) integrates to 0.107, indicating 89% deuteration. ^{1}H NMR taken in $CDCl_3$ dried on 4 Å molecular sieves for 3 days. 110

Figure S2.39. Control (black) and 0.5 mM Fe(^{tbu}dhbpy)Cl (Red) upon addition of 0.5 M PhOH as a proton source under a saturated Ar atmosphere in *N*,*N*-DMF 0.1 M with $TBAPF_6$ supporting electrolyte. Scan rate is 100 mV/s. Working electrode is glassy carbon (3 mm diameter), counter electrode is glassy carbon rod, and pseudo-reference is Ag/AgCl wire with ferrocene (Fc) added as internal reference. 111

Figure S2.40. X-band EPR spectrum of Fe(^{tbu}dhbpy)Cl in dichloromethane and acetonitrile (1:1) glass mixture. (Experimental parameters: temperature = 77 K, microwave frequency = 9.13 GHz, microwave power = 0.998 mW, modulation frequency = 100 kHz, modulation width = 1 mT, time constant = 0.03 s). 111

Figure S2.41. Plots of (A) i_c/i_p vs $1/(\upsilon)^{1/2}$ under CO_2 saturation, (B) i_c/i_p vs $1/(\upsilon)^{1/2}$ under CO_2 saturation with 0.526 M PhOH, and (C) TOF vs υ for Fe(^{tbu}dhbpy)Cl **1** under a CO_2 atmosphere (black) and under a CO_2 atmosphere with 0.526 M PhOH. Working electrode is glassy carbon (3 mm diameter), counter electrode is glassy carbon, and pseudo-reference is Ag/AgCl wire with ferrocene (Fc) added as internal reference. These data indicate that this catalyst is not under kinetically controlled steady-state conditions for all non-Faradaic conditions.[20] 112

Figure S2.42. $^{13}C\{^1H\}$ NMR of $TBAHCO_3$ in D_2O with a single drop of *N,N*-DMF added for internal reference. Peak at δ 158.48 assigned to HCO_3^-. 151 MHz, Varian 113

Figure S2.43. $^{13}C\{^1H\}$NMR of extract from controlled potential electrolysis in D_2O. Peak at δ 158.04 assigned to HCO_3^-. Referenced to residual *N-N*-DMF in extract. 151 MHz, Varian 114

Figure S2.44. $^{13}C\{^1H\}$ NMR overlay of $TBAHCO_3$ in D_2O with a single drop of *N,N*-DMF added for reference (Red), and extract from controlled potential electrolysis in D_2O (Green). 151 MHz, Varian. 115

Figure 3.1. Molecular electrocatalysts for CO_2 reduction to formate (HCO_2^-) studied previously (**1**; Fe(^{tbu}dhbpy)Cl)[9] and in this work (**2**; Fe(^{me}crebpy)Cl and **3**; Fe(^{tbu}catbpy). 144

Figure 3.2. (A) Unit cell and (B) overall dimer structure for Fe(^{me}crebpy)Cl **2**; each equivalent of **2** is generated by symmetry and not crystallographically distinct. C = grey, O = red, N= blue, Fe = orange, Cl = green. Thermal ellipsoids set to 50%. Occluded acetonitrile molecules and hydrogen atoms omitted for clarity. 147

Figure 3.3. Cyclic Voltammograms of 0.5 mM Fe(^{me}crebpy)Cl **2** (black) and Fe(^{tbu}catbpy) **3** (red) under an Ar atmosphere in 0.1 M $TBAPF_6$/*N,N*-DMF supporting electrolyte. Working electrode is glassy carbon, counter electrode is a glassy carbon rod, AgCl/Ag pseudoreference electrode. Referenced to Fc^+/Fc from internal decamethylferrocene (Cp_2*Fe) standard; 100 mV/s scan rate. 149

Figure 3.4. CVs of (A) Fe(^{me}crebpy)Cl **2** and (B) Fe(^{tbu}catbpy) **3** under Ar (black) and CO_2 (red, blue, and green) saturation conditions. Blue and green traces are in the presence of

PhOH added as a proton source. Working electrode is glassy carbon, counter electrode is a glassy carbon rod, AgCl/Ag pseudoreference electrode. Referenced to Fc^+/Fc from internal Cp_2*Fe standard. 100 mV/s scan rate. 150

Figure 3.5. Diagram of select possible equilibria involving complexes **2** (A) and **3** (B and C) in the reduced state. In previous studies, formal proton transfer to the O atom of the ligand was implicated for **1**; the effect of multipoint hydrogen-bonding interactions for **2** and **3** with PhOH is observed in their concentration-dependent electrochemical responses. Where **n** = 0 or -1 and **m** = 0, -2, or -2. 153

Figure 3.6. Summary of the basic relay mechanism of the exogenous proton donor. For boosting effects to be observable in an electrocatalytic response, the forward reaction rate constants of the relay need to be competitive with the rate of direct protonation.[31] AH and A^- are PhOH and its conjugate base PhO^-. 158

Figure S3.1. (A) Representative monomer structure (one of two structurally inequivalent units crystallographically) from (B) overall dimeric structure of Fe(^{tbu}catbpy) **3**. C = grey, O = red, N= blue, Fe = orange, H = white. Thermal ellipsoids set to 30%. Non-catecholate H-atoms, occluded MeCN and second set of coordinates for disordered *tert*-butyl groups and bpy ring omitted for clarity. All hydrogen atoms in Fe(^{tbu}catbpy) **3**, including the O–H hydrogens, were placed in calculated positions. 173

Figure S3.2. (A) UV-Vis absorbance spectra of serial dilutions of Fe(^{me}crebpy)Cl **2** in *N,N*-DMF showing absence of equillibrium processes. Quartz call with 1 cm pathlength. (B) Plot of absorbance versus concentration for complex **2** in *N,N*-DMF at 354 nm (28000 $M^{-1}cm^{-1}$). 173

Figure S3.3. (A)UV-Vis absorbance spectra of serial dilutions of Fe(^{tbu}catbpy) **3** in *N,N*-DMF showing absence of equillibrium processes. Quartz call with 1 cm pathlength. (B) Plot of absorbance versus concentration for complex **3** in *N,N*-DMF at 345 nm (20000 $M^{-1}cm^{-1}$). 174

Figure S3.4. (A) Linear Sweep Voltammograms of RRDE experiment Fe(^{tbu}dhbpy)Cl **1** (0.25 mM) at various rotation rates under Ar saturation conditions. (B) Levich plot from data obtained from linear sweep voltammograms of Fe(^{tbu}dhbpy)Cl **1** (0.25 mM) at various rotation rates under Ar saturation conditions. Conditions: 0.25 mM analyte in 0.1 M $TBAPF_6$/*N,N*-DMF; glassy carbon working electrode, glassy carbon rod counter electrode, Ag/AgCl pseudoreference electrode; scan rate 0.01 V/s. 174

Figure S3.5. (A) Linear Sweep Voltammograms of RRDE experiment Fe(^{me}crebpy)Cl **2** (0.25 mM) at various rotation rates under Ar saturation conditions. (B) Levich plot from data obtained from linear sweep voltammograms of Fe(^{me}crebpy)Cl **2** (0.25 mM) at various rotation rates under Ar saturation conditions. Conditions: 0.25 mM analyte in 0.1 M $TBAPF_6$/*N,N*-DMF; glassy carbon working electrode, glassy carbon rod counter electrode, Ag/AgCl pseudoreference electrode; scan rate 0.01 V/s. 175

Figure S3.6. (A) Linear Sweep Voltammograms of RRDE experiment Fe(^{tbu}catbpy) **3** (0.25 mM) at various rotation rates under Ar saturation conditions. (B) Levich plot from data obtained from linear sweep voltammograms of Fe(^{tbu}catbpy) **3** (0.25 mM) at various rotation rates under Ar saturation conditions. Conditions: 0.25 mM analyte in 0.1 M

TBAPF$_6$/*N,N*-DMF; glassy carbon working electrode, glassy carbon rod counter electrode, Ag/AgCl pseudoreference electrode; scan rate 0.01 V/s. 175

Figure S3.7. CVs of Fe(^{me}crebpy)Cl **2** at various scan rates under Ar saturation conditions. Conditions: 0.5 mM analyte in 0.1 M TBAPF$_6$/*N,N*-DMF; glassy carbon working and counter electrodes, Ag/AgCl pseudoreference electrode, referenced to Fc$^+$/Fc from internal decamethylferrocene (Cp$_2$*Fe) standard. 176

Figure S3.8. CVs of Fe(^{me}crebpy)Cl **2** upon addition of TBACl under Ar saturation conditions at 100 mV/s (A) and at 1000 mV/s (B) illustrating that at fast scan rates, the reduction at –1.45 V vs Fc$^+$/Fc dissapears. Conditions: 0.5 mM analyte in 0.1 M TBAPF$_6$/*N,N*-DMF; glassy carbon working and counter electrodes, Ag/AgCl pseudoreference electrode, referenced to Fc$^+$/Fc from internal decamethylferrocene (Cp$_2$*Fe) standard. 176

Figure S3.9. CVs of Fe(^{tbu}catbpy) **3** at various scan rates under Ar saturation conditions. Conditions: 0.5 mM analyte in 0.1 M TBAPF$_6$/*N,N*-DMF; glassy carbon working and counter electrodes, Ag/AgCl pseudoreference electrode, referenced to Fc$^+$/Fc from internal decamethylferrocene (Cp$_2$*Fe) standard. 177

Figure S3.10. (A) Plots of CVs of 3rd and 4th reductions of Fe(^{tbu}catbpy) **3** at variable scan rates under Ar saturation conditions showing scan rate dependence of the relative current response of these two features. (B) Plot of the ratio of the peak current of the 3rd and 4th reductions of Fe(^{tbu}catbpy) **3** vs. scan rate. Conditions: 0.5 mM analyte in 0.1 M TBAPF$_6$/*N,N*-DMF; glassy carbon working and counter electrodes, Ag/AgCl pseudoreference electrode, referenced to Fc$^+$/Fc from internal decamethylferrocene (Cp$_2$*Fe) standard. 177

Figure S3.11. Plots of current density vs $\upsilon^{1/2}$ for the reductions with $E_{1/2}$ = –0.84 V (A) and –1.93 V (B) vs Fc$^+$/Fc for Fe(^{me}crebpy)Cl **2**. Linearity indicates Fe(^{me}crebpy)Cl **2** is operating in a diffusion limited regime. Conditions: 0.5 mM analyte in 0.1 M TBAPF$_6$/*N,N*-DMF; glassy carbon working and counter electrodes, Ag/AgCl pseudoreference electrode, referenced to Fc$^+$/Fc from internal decamethylferrocene (Cp$_2$*Fe) standard. 178

Figure S3.12. Plots of current density vs $\upsilon^{1/2}$ for the reductions with $E_{1/2}$ = –1.01 V (A) and –1.65 V (B) vs Fc$^+$/Fc for Fe(^{tbu}catbpy) **3**. Linearity indicates Fe(^{tbu}catbpy) **3** is operating in a diffusion limited regime. Conditions: 0.5 mM analyte in 0.1 M TBAPF$_6$/*N,N*-DMF; glassy carbon working and counter electrodes, Ag/AgCl pseudoreference electrode, referenced to Fc$^+$/Fc from internal decamethylferrocene (Cp$_2$*Fe) standard. 179

Figure S3.13. Cyclic voltammogram of 0.5 mM Fe(^{me}crebpy)Cl **2** (black) or Zn(^{me}crebpy) (red) under Ar saturation conditions. Conditions: 0.5 mM analyte in 0.1 M TBAPF$_6$/ *N,N*-DMF; glassy carbon working and counter electrodes, Ag/AgCl pseudoreference electrode, referenced to Fc$^+$/Fc from internal decamethylferrocene (Cp$_2$*Fe) standard, 100 mV/s scan rate. 180

Figure S3.14. Cyclic voltammogram of 0.5 mM Fe(^{tbu}catbpy) **3** (black) or Zn(^{tbu}catbpy) (red) under Ar saturation conditions. Conditions: 0.5 mM analyte in 0.1 M TBAPF$_6$/*N,N*-DMF; glassy carbon working and counter electrodes, Ag/AgCl pseudoreference electrode, referenced to Fc$^+$/Fc from eitherinternal Cp$_2$*Fe or Cp$_2$Co standard, 100 mV/s scan rate. 180

Figure S3.15. Cyclic voltammograms of 0.5 mM Fe(^{me}crebpy)Cl **2** under Ar saturation conditions with varied amounts of PhOH showing a shift in the first two reduction features. Conditions: 0.5 mM analyte in 0.1 M TBAPF$_6$/*N,N*-DMF; glassy carbon working and counter electrodes, Ag/AgCl pseudoreference electrode, referenced to Fc$^+$/Fc from internal decamethylferrocene (Cp$_2$*Fe) standard, 100 mV/s scan rate.......... 181

Figure S3.16. Cyclic voltammograms of 0.5 mM Fe(^{tbu}catbpy) **3** under Ar saturation conditions with varied amounts of PhOH showing a shift in the first two reduction features. Conditions: 0.5 mM analyte in 0.1 M TBAPF$_6$/*N,N*-DMF; glassy carbon working and counter electrodes, Ag/AgCl pseudoreference electrode, referenced to Fc$^+$/Fc from internal decamethylferrocene (Cp$_2$*Fe) standard, 100 mV/s scan rate.......... 181

Figure S3.17. (A) UV-Vis titration of PhOH into a solution of Fe(^{me}crebpy)Cl **2** in *N,N*-DMF. Quartz cell of 1 cm pathlength. (B) Plot of absorbance at 347 nm versus PhOH equivalents. 182

Figure S3.18. (A) UV-Vis titration of PhOH into a solution of Fe(^{tbu}catbpy) **3** in *N,N*-DMF. Quartz cell of 1 cm pathlength. (B) Plot of absorbance at 335 nm versus PhOH equivalents. (C) Plot of absorbance at 463 nm versus PhOH equivalents. 183

Figure S3.19. Cyclic voltammograms of 0.5 mM Fe(^{me}crebpy)Cl **2** under labeled conditions. Conditions: 0.5 mM analyte in 0.1 M TBAPF$_6$/*N,N*-DMF; glassy carbon working and counter electrodes, Ag/AgCl pseudoreference electrode, referenced to Fc$^+$/Fc from internal decamethylferrocene (Cp$_2$*Fe) standard, 100 mV/s scan rate. ... 184

Figure S3.20. Cyclic voltammograms of 0.5 mM Fe(^{tbu}catbpy) **3** under labeled conditions. Conditions: 0.5 mM analyte in 0.1 M TBAPF$_6$/*N,N*-DMF; glassy carbon working and counter electrodes, Ag/AgCl pseudoreference electrode, referenced to Fc$^+$/Fc from internal decamethylferrocene (Cp$_2$*Fe) standard, 100 mV/s scan rate.......... 184

Figure S3.21. Cyclic Voltammograms of 0.5 mM Fe(^{me}crebpy)Cl **2** under CO$_2$ saturation conditions with scans to the catalytic wave showing current saturation occurs at ~0.9 M PhOH. Conditions: 0.5 mM analyte in 0.1 M TBAPF$_6$/*N,N*-DMF; glassy carbon working and counter electrodes, Ag/AgCl pseudoreference electrode, referenced to Fc$^+$/Fc from internal decamethylferrocene (Cp$_2$*Fe) standard, 100 mV/s scan rate.......... 185

Figure S3.22. Cyclic Voltammograms of 0.5 mM Fe(^{tbu}catbpy) **3** under CO$_2$ saturation conditions with scans to the catalytic wave showing current saturation occurs at 0.5 M PhOH. Conditions: 0.5 mM analyte in 0.1 M TBAPF$_6$/*N,N*-DMF; glassy carbon working and counter electrodes, Ag/AgCl pseudoreference electrode, referenced to Fc$^+$/Fc from internal decamethylferrocene (Cp$_2$*Fe) standard, 100 mV/s scan rate.......... 185

Figure S3.23. Log-log plot of peak current density versus [CO$_2$] for 0.5 mM Fe(^{me}crebpy)Cl **2** with 1.0 M PhOH. Kinetic current saturation is observed above 0.04 M

CO_2. Conditions: 0.5 mM analyte in 0.1 M $TBAPF_6$/*N,N*-DMF; glassy carbon working and counter electrodes, Ag/AgCl pseudoreference electrode, referenced to Fc^+/Fc from internal decamethylferrocene (Cp_2*Fe) standard, 100 mV/s scan rate....................... 186

Figure S3.24. Log-log plot of peak current density versus [PhOH] for 0.5 mM Fe(^{me}crebpy)Cl **2** under CO_2 saturation conditions. Slope of 0.5 is indicative of 1st order kinetics with respect to [PhOH].[1] Conditions: 0.5 mM analyte in 0.1 M $TBAPF_6$/*N,N*-DMF; glassy carbon working and counter electrodes, Ag/AgCl pseudoreference electrode, referenced to Fc^+/Fc from internal decamethylferrocene (Cp_2*Fe) standard, 100 mV/s scan rate. 186

Figure S3.25. Log-log plot of peak current density versus [CO_2] for 0.5 mM Fe(^{tbu}catbpy) **3** with 0.5 M PhOH. Kinetic current saturation is observed above 0.04 M CO_2. Conditions: 0.5 mM analyte in 0.1 M $TBAPF_6$/*N,N*-DMF; glassy carbon working and counter electrodes, Ag/AgCl pseudoreference electrode, referenced to Fc^+/Fc from internal decamethylferrocene (Cp_2*Fe) standard, 100 mV/s scan rate. 187

Figure S3.26. Log-log plot of peak current density versus [PhOH] for 0.5 mM Fe(^{tbu}catbpy) **3** under CO_2 saturation conditions. Conditions: 0.5 mM analyte in 0.1 M $TBAPF_6$/*N,N*-DMF; glassy carbon working and counter electrodes, Ag/AgCl pseudoreference electrode, referenced to Fc^+/Fc from internal decamethylferrocene (Cp_2*Fe) standard, 100 mV/s scan rate.. 187

Figure S3.27. Plot of peak current density versus [**2**], Fe(^{me}crebpy)Cl under CO_2 saturation conditions with 1.0 M PhOH. Linearity is consistent with 1st order kinetics with respect to [**2**].[1] Conditions: 0.5 mM analyte in 0.1 M $TBAPF_6$/*N,N*-DMF; glassy carbon working and counter electrodes, Ag/AgCl pseudoreference electrode, referenced to Fc^+/Fc from internal decamethylferrocene (Cp_2*Fe) standard, 100 mV/s scan rate. ... 188

Figure S3.28. Plot of peak current density and [**3**], Fe(^{tbu}catbpy) under CO_2 saturation conditions with 0.5 M PhOH. Linearity is consistent with 1st order kinetics with respect to [**3**].[1] Conditions: 0.5 mM analyte in 0.1 M $TBAPF_6$/*N,N*-DMF; glassy carbon working and counter electrodes, Ag/AgCl pseudoreference electrode, referenced to Fc^+/Fc from internal decamethylferrocene (Cp_2*Fe) standard, 100 mV/s scan rate....................... 188

Figure S3.29. Current vs. Time and (A) Charge Passed vs. Time (B) plots for CPE experiments at –2.50 V vs Fc^+/Fc Conditions: Black: 0.5 mM Fe(^{me}crebpy)Cl **2**, 0.9 M PhOH, and CO_2 atmosphere; Blue: Ethanol rinsed working electrode from black experiment, 0.5 M PhOH and CO_2 atmosphere; Red: 0.5 M PhOH and CO_2 atmosphere. 0.1 M $TBAPF_6$/*N,N*-DMF electrolyte; graphite working and counter electrodes were used; reference electrode nonaqueous Ag/AgCl pseudoreference electrode which was referenced to Fc^+/Fc before each run; 0.05 M Fc was used as sacrificial oxidant....... 189

Figure S3.30. Current vs. Time (A) and Charge Passed vs. Time (B) plots for CPE experiments at –2.60 V vs Fc^+/Fc with Black: 0.5 mM Fe(^{tbu}catbpy) **3**, 0.5 M PhOH, and CO_2 atmosphere; Blue: Ethanol rinsed working electrode from black experiment, 0.5 M PhOH and CO_2 atmosphere; Red: 0.5 M PhOH and CO_2 atmosphere. 0.1 M $TBAPF_6$/*N,N*-DMF electrolyte; graphite working and counter electrodes were used; reference electrode nonaqueous Ag/AgCl pseudoreference electrode which was referenced to Fc^+/Fc before each run; 0.05 M Fc was used as sacrificial oxidant 190

Figure S3.31. ^1H NMR spectra showing (green) HCO_2^- generated during CPE experiments under a CO_2 atmosphere with Fe(^{me}crebpy)Cl **2** and (red) $H^{13}CO_2^-$ generated under a $^{13}CO_2$ atmosphere under identical conditions (inset) after extraction with D_2O and washing with CH_2Cl_2 (600 MHz). 191

Figure S3.32. ^1H NMR spectra showing (green) HCO_2^- generated during CPE experiments under a CO_2 atmosphere with Fe(^{tbu}catbpy) **3** and (red) $H^{13}CO_2^-$ generated under a $^{13}CO_2$ atmosphere under identical conditions (inset) after extraction with D_2O and washing with CH_2Cl_2 (600 MHz). 192

Figure S3.33. Current vs. Time (A) and Charge Passed vs. Time plots (B) for CPE experiments at –2.50 V vs Fc^+/Fc with 0.5 mM Fe(^{me}crebpy)Cl **2,** 0.5 M PhOH and $^{13}CO_2$ atmosphere. 0.1 M $TBAPF_6$/*N,N*-DMF electrolyte; graphite working and counter electrodes were used; reference electrode nonaqueous Ag/AgCl pseudoreference electrode which was referenced to Fc^+/Fc before each run; 0.05 M Fc was used as sacrificial oxidant 193

Figure S3.34. Current vs. Time (A) and Charge Passed vs. Time plots (B) for CPE experiments at –2.60 V vs Fc^+/Fc with 0.5 mM Fe(^{tbu}catbpy) **3,** 0.5 M PhOH and $^{13}CO_2$ atmosphere. 0.1 M $TBAPF_6$/*N,N*-DMF electrolyte; graphite working and counter electrodes were used; reference electrode nonaqueous Ag/AgCl pseudoreference electrode which was referenced to Fc^+/Fc before each run; 0.05 M Fc was used as sacrificial oxidant 194

Figure S3.35. Current vs. Time (A) and Charge Passed vs. Time (B) Plots for CPE experiments at –2.50 V vs Fc^+/Fc with 0.5 mM Fe(^{me}crebpy)Cl **2** and CO_2 atmosphere. 0.1 M $TBAPF_6$/*N,N*-DMF electrolyte; graphite working and counter electrodes were used; reference electrode nonaqueous Ag/AgCl pseudoreference electrode which was referenced to Fc^+/Fc before each run; 0.05 M Fc was used as sacrificial oxidant 195

Figure S3.36. Current vs. Time (A) and Charge Passed vs. Time plots (B) for CPE experiments at –2.60 V vs Fc^+/Fc with 0.5 mM Fe(^{tbu}catbpy) **3** and CO_2 atmosphere. 0.1 M $TBAPF_6$/*N,N*-DMF electrolyte; graphite working and counter electrodes were used; reference electrode nonaqueous Ag/AgCl pseudoreference electrode which was referenced to Fc^+/Fc before each run; 0.05 M Fc was used as sacrificial oxidant 196

Figure S3.37. Current vs. Time (A) and Charge Passed vs. Time plots (B) for CPE experiments at –2.60 V vs Fc^+/Fc with 0.5 mM Fe(^{me}crebpy)Cl **2**, 0.9 M PhOH, and Ar atmosphere. 0.1 M $TBAPF_6$/*N,N*-DMF electrolyte; graphite working and counter electrodes were used; reference electrode nonaqueous Ag/AgCl pseudoreference electrode which was referenced to Fc^+/Fc before each run; 0.05 M Fc was used as sacrificial oxidant 197

Figure S3.38. Current vs. Time (A) and Charge Passed vs. Time plots (B) for CPE experiments at –2.60 V vs Fc^+/Fc with 0.5 mM Fe(^{tbu}catbpy) **3**, 0.5 M PhOH, and Ar atmosphere. 0.1 M $TBAPF_6$/*N,N*-DMF electrolyte; graphite working and counter electrodes were used; reference electrode nonaqueous Ag/AgCl pseudoreference electrode which was referenced to Fc^+/Fc before each run; 0.05 M Fc was used as sacrificial oxidant 198

Figure S3.39. Current vs. Time (A) and Charge Passed vs. Time plots (B) for CPE experiments at –2.60 V vs Fc^+/Fc with 0.5 mM Fe(^{tbu}catbpy) **3** and Ar atmosphere. 0.1 M $TBAPF_6$/*N,N*-DMF electrolyte; graphite working and counter electrodes were used; reference electrode nonaqueous Ag/AgCl pseudoreference electrode which was referenced to Fc^+/Fc before each run; 0.05 M Fc was used as sacrificial oxidant 199

Figure S3.40. Cyclic Voltammograms of 0.5 mM Fe(^{tbu}dhbpy)Cl **1** (red), Fe(^{me}crebpy)Cl **2** (green), and Fe(^{tbu}catbpy) **3** (blue) with 0.5 M 2,4,6-tri-*tert*-butyl-phenol (^{tbu3}PhOH) under CO_2 saturation conditions. Control experiment is under identical conditions with no catalyst material added. Conditions: 0.5 mM analyte in 0.1 M $TBAPF_6$/ *N,N*-DMF; glassy carbon working and counter electrodes, Ag/AgCl pseudoreference electrode, referenced to Fc^+/Fc from internal decamethylferrocene (Cp_2*Fe) standard, 100 mV/s scan rate. 200

Figure S3.41. Crystal structure of 3-bromo-5-*tert*-butyl-benzene-diol. Grown by sublimation. Thermal ellipsoids set to 50%. C = carbon, Br = orange, O = red, H = white. CCDC: 1940614 200

Figure S3.42. ^1H–^{13}C HSQC NMR of **^{me}crebpy** (DMSO-*d$_6$*, ^1H 600 MHz; ^{13}C 151 MHz). 201

Figure S3.43. ^1H NMR of **^{me}crebpy** (DMSO-*d$_6$*, 600 MHz). 202

Figure S3.44. $^{13}C\{^1H\}$ NMR of **^{me}crebpy** (DMSO-*d$_6$*, 151 MHz) 203

Figure S3.45. ^1H–^{13}C HSQC NMR of **VI** ($CDCl_3$, ^1H 600 MHz; ^{13}C 151 MHz). 204

Figure S3.46. ^1H NMR of **VI** ($CDCl_3$, 600 MHz). 205

Figure S3.47. $^{13}C\{^1H\}$ NMR of **VI** ($CDCl_3$, 151 MHz) 206

Figure S3.48. ^1H–^{13}C HSQC NMR of **VII** ($CDCl_3$, ^1H 600 MHz; ^{13}C 151 MHz). 207

Figure S3.49. ^1H NMR of **VII** ($CDCl_3$, 600 MHz). 208

Figure S3.50. $^{13}C\{^1H\}$ NMR of **VII** ($CDCl_3$, 151 MHz) 209

Figure S3.51. ^1H–^{13}C HSQC NMR of **IX** ($CDCl_3$, ^1H 600 MHz; ^{13}C 151 MHz). 210

Figure S3.52. ^1H NMR of **IX** ($CDCl_3$, 600 MHz). 211

Figure S3.53. $^{13}C\{^1H\}$ NMR of **IX** ($CDCl_3$, 151 MHz) 212

Figure S3.54. ^1H–^{13}C HSQC NMR of **^{tbu}catbpy** (DMSO-*d$_6$*, ^1H 600 MHz; ^{13}C 151 MHz). 213

Figure S3.55. ^1H NMR of **^{tbu}catbpy**(DMSO-d$_6$, 600 MHz). 214

Figure S3.56. $^{13}C\{^1H\}$ NMR of **^{tbu}catbpy** (DMSO-*d$_6$*, 151 MHz) 215

Figure 4.1. X-ray crystal structure of **1**. C = gray; N = blue; O = red; Co = green. Thermal ellipsoids set to 50%, H atoms and $PF_6^–$ omitted for clarity, CCDC: 2035029 222

Figure 4.2. Representative UV-Vis changes under catalytic conditions in MeOH over a timeframe of 15 min. Concentrations: 40 μM **1**, 25 mM AcOH, 0.9 mM Cp^*_2Fe, 9 mM

O_2.[31, 38-40] Inset: absorbance changes at 780 nm are due to the formation of Cp*$_2$Fe$^+$. 224

Figure S4.1. (A) UV-Vis spectra of **1** in MeOH. (B) determination of ε for **1**. 231

Figure S4.2. ^{1}H NMR spectra of **1** in CD_2Cl_2. (600 MHz, Varian) 233

Figure S4.3. ^{13}C NMR of **1** in CD_2Cl_2. (151 MHz, Varian). Inset is region from 110-170 ppm. 234

Figure S4.4. ^{1}H-^{13}C HSQC NMR of **1** in CD_2Cl_2. (^{1}H 600 MHz; ^{13}C 151 MHz, Bruker). 235

Figure S4.5. Stacked ^{1}H NMR spectra of 1 and py in *d$_4$*-MeOH. (600 MHz, Varian). Grey boxes indicate free py; asterisks indicate [Co(^{tbu}dhbpy)(py)$_2$]$^+$. 236

Figure S4.6. DPV of 1 mM **1** under Ar. Conditions: 0.1 M TBAPF$_6$/MeOH, glassy carbon working electrode, glassy carbon counter electrode, Ag/AgCl pseudoreference electrode, ΔE = 0.025 V, modulation time 0.01 s, interval time 0.1 s, scan rate 50.354 mV/s. Referenced to external Cp*$_2$Fe solution under the same conditions. 237

Figure S4.7. CVs of **1** under Ar (black), with added 25 mM AcOH (red), and with an added buffer comprised of 25 mM AcOH and 25 mM TBAOAc (blue). Conditions: 1 mM **1**, 0.1 M TBAPF$_6$/MeOH; glassy carbon working electrode, glassy carbon counter electrode, Ag/AgCl pseudoreference electrode, scan rate 100 mV/s; referenced to external decamethylferrocene standard. 238

Figure S4.8. DPVs of **1** under Ar (black), and with 10 mM py under aprotic conditions. Conditions: 1 mM **1**, 0.1 M TBAPF$_6$/MeOH; glassy carbon working electrode, glassy carbon counter electrode, Ag/AgCl pseudoreference electrode, ΔE = 0.025 V, modulation time 0.01 s, interval time 0.1 s, scan rate 50.354 mV/s. Referenced to external Cp*$_2$Fe solution under the same conditions. 238

Figure S4.9. Iodometric titration calibration curve. (A) Serial dilution of urea•H_2O_2 in methanol treated using the above method for iodometric titration. (B) Calibration curve made utilizing a serial dilution of urea•H_2O_2 in MeOH, the observed slope of 290±10 is consistent with reported molar absorptivity of 2.8×10^4 M^{-1} cm^{-1}. 239

Figure S4.10. H_2O_2 disproportionation test. Iodometric titrations of MeOH solutions of 0 (A) or 40 μM (B) of **1** in the presence of 25 mM AcOH/TBAOAc and 0.5 mM urea•H_2O_2 to determine if the 1 interacted with I_3^- or urea•H_2O_2. 240

Figure S4.11. Iodometric titration of **1**. Black trace is prior to the addition of NaI. Red trace is after the addition of NaI. 241

Figure S4.12. Iodometric titration of **1** in the presence of 20 equivalents of py. Black trace is prior to the addition of NaI. Red trace is after the addition of NaI. 241

Figure S4.13. Iodometric titration of 40 μM **1** in MeOH. (A) Effect of NaI addition after 30 min reaction time in the presence of 0.9 mM Cp*2Fe, 0.2 mM urea•H_2O_2, and 25 mM AcOH under anaerobic conditions. (B) Monitoring of the growth of [Cp*$_2$Fe]$^+$ at 780 nm, which indicates that a negligible amount of catalytic reduction of H_2O_2 occurs. 242

Figure S4.14. Determination of ORR reaction dependence upon [**1**]. (A) Uncorrected for background O_2 reduction. (B) Corrected for background O_2 reduction. 243

Figure S4.15. Determination of ORR reaction dependence upon [AcOH]. (A) Uncorrected for background O_2 reduction. (B) Corrected for background O_2 reduction, note that the background reaction is assumed to have minimal initial ORR rate dependence on [AcOH] relative to the reaction catalyzed by **1**. 244

Figure S4.17. Determination of ORR reaction dependence upon [O_2]. Horizontal line represents the global average rate observed across all experiments described for variable [O_2]. 247

Figure S4.18. Determination of ORR reaction dependence upon [py]. Horizontal line represents the global average rate observed across all experiments described for variable [py]. 248

Figure S4.19. Iodometric titration of Co(salen) in the presence of two equivalents of py under conditions identical to testing of **1**. 250

Figure S4.20. Iodometric titration of 20 μM **Co(^{tbu}dhbpy)** in the presence of 25 mM AcOH and O_2 saturation. 251

Figure 5.1. Summary of complexes studied in this work and their ORR selectivity. 256

Figure 5.2. Observed changes in UV-Vis absorbance at 780 nm resulting from catalytic ORR utilizing 40 uM **2**, 25 mM AH, 1.5 mM Cp^*_2Fe, and 8.1 mM O_2. 257

Figure 5.3. Kinetic isotope effect determination for complex **2**. Black line is with naturally abundant 2,6-dichlorobenzoic acid (O-H). Red line is with isotopically enriched (92%) d_1-2,6-dichlorobenzoic acid (O-D). 262

Figure 5.4. (A) General proposed ORR mechanism for complex **1**. (B) General proposed ORR mechanism for complex **2**. 263

Figure 5.5. Proposed pendent relay interaction relevant to the ORR mechanism for complex **2**. 264

Figure S5.1. (A) UV-vis spectra of **2** in MeCN. (B) determination of ε for **2**. 270

Figure S5.2. ^{1}H NMR spectra of **2** in CD_2Cl_2. (600 MHz, Varian) 271

Figure S5.3. ^{13}C NMR of **2** in CD_2Cl_2. (201 MHz, Bruker). 272

Figure S5.4. DPV of 0.5 mM **1** under Ar (black) and O_2 (red) saturation. Conditions: 0.1 M $TBAPF_6$/MeCN, glassy carbon working electrode, glassy carbon counter electrode, Ag/AgCl pseudoreference electrode, ΔE = 0.025 V, modulation time 0.01 s, interval time 0.1 s, scan rate 50.354 mV/s. Referenced to internal ferrocene standard. 273

Figure S5.5. DPVs of **1** under Ar (black), with added 25 mM benzoic acid (red), and with an added buffer comprised of 25 mM benzoic acid and 25 mM tetra-n-butylammonium benzoate (green). Conditions: 0.5 mM **1**, 0.1 M $TBAPF_6$/MeCN; glassy carbon working electrode, glassy carbon counter electrode, Ag/AgCl pseudoreference electrode, ΔE = 0.025 V, modulation time 0.01 s, interval time 0.1 s, scan rate 50.354 mV/s. Referenced to internal ferrocene standard. 274

Figure S5.6. DPVs of **1** under Ar (black), with added 25 mM 2-chlorobenzoic acid (red), and with an added buffer comprised of 25 mM 2-chlorobenzoic acid and 25 mM tetra-n-butylammonium 2-chlorobenzoate (green). Conditions: 0.5 mM **1**, 0.1 M TBAPF$_6$/MeCN; glassy carbon working electrode, glassy carbon counter electrode, Ag/AgCl pseudoreference electrode, ΔE = 0.025 V, modulation time 0.01 s, interval time 0.1 s, scan rate 50.354 mV/s. Referenced to internal ferrocene internal standard................ 274

Figure S5.7. DPVs of **1** under Ar (black), with added 25 mM 2,4-dichlorobenzoic acid (red), and with an added buffer comprised of 25 mM 2,4-dichlorobenzoic acid and 25 mM tetra-n-butylammonium 2,4-dichlorobenzoate (green). Conditions: 0.5 mM **1**, 0.1 M TBAPF$_6$/MeCN; glassy carbon working electrode, glassy carbon counter electrode, Ag/AgCl pseudoreference electrode, ΔE = 0.025 V, modulation time 0.01 s, interval time 0.1 s, scan rate 50.354 mV/s. Referenced to internal ferrocene standard.................. 275

Figure S5.8. DPVs of **1** under Ar (black), with added 25 mM 2,6-dichlorobenzoic acid (red), and with an added buffer comprised of 25 mM 2,6-dichlorobenzoic acid and 25 mM tetra-n-butylammonium 2,6-dichlorobenzoate (green). Conditions: 0.5 mM **1**, 0.1 M TBAPF$_6$/MeCN; glassy carbon working electrode, glassy carbon counter electrode, Ag/AgCl pseudoreference electrode, ΔE = 0.025 V, modulation time 0.01 s, interval time 0.1 s, scan rate 50.354 mV/s. Referenced to internal ferrocene standard.................. 275

Figure S5.9. DPV of 0.5 mM **2** under Ar (black) and O$_2$ (red) saturation. Conditions: 0.1 M TBAPF$_6$/MeCN, glassy carbon working electrode, glassy carbon counter electrode, Ag/AgCl pseudoreference electrode, ΔE = 0.025 V, modulation time 0.01 s, interval time 0.1 s, scan rate 50.354 mV/s. Referenced to internal ferrocene standard.................. 276

Figure S5.10. DPVs of **2** under Ar (black), with added 25 mM benzoic acid (red), and with an added buffer comprised of 25 mM benzoic acid and 25 mM tetra-n-butylammonium benzoate (green). Conditions: 0.5 mM **2**, 0.1 M TBAPF$_6$/MeCN; glassy carbon working electrode, glassy carbon counter electrode, Ag/AgCl pseudoreference electrode, ΔE = 0.025 V, modulation time 0.01 s, interval time 0.1 s, scan rate 50.354 mV/s. Referenced to internal ferrocene internal standard... 276

Figure S5.11. DPVs of **2** under Ar (black), with added 25 mM 2-chlorobenzoic acid (red), and with an added buffer comprised of 25 mM 2-chlorobenzoic acid and 25 mM tetra-n-butylammonium 2-chlorobenzoate (green). Conditions: 0.5 mM **2**, 0.1 M TBAPF$_6$/MeCN; glassy carbon working electrode, glassy carbon counter electrode, Ag/AgCl pseudoreference electrode, ΔE = 0.025 V, modulation time 0.01 s, interval time 0.1 s, scan rate 50.354 mV/s. Referenced to internal ferrocene standard. 277

Figure S5.12. DPVs of **2** under Ar (black), with added 25 mM 2,4-dichlorobenzoic acid (red), and with an added buffer comprised of 25 mM 2,4-dichlorobenzoic acid and 25 mM tetra-n-butylammonium 2,4-dichlorobenzoate (green). Conditions: 0.5 mM **2**, 0.1 M TBAPF$_6$/MeCN; glassy carbon working electrode, glassy carbon counter electrode, Ag/AgCl pseudoreference electrode, ΔE = 0.025 V, modulation time 0.01 s, interval time 0.1 s, scan rate 50.354 mV/s. Referenced to internal ferrocene standard.................. 277

Figure S5.13. DPVs of **2** under Ar (black), with added 25 mM 2,6-dichlorobenzoic acid (red), and with an added buffer comprised of 25 mM 2,4-dichlorobenzoic acid and 25 mM tetra-n-butylammonium 2,6-dichlorobenzoate (green). Conditions: 0.5 mM **2**, 0.1 M TBAPF6/MeCN; glassy carbon working electrode, glassy carbon counter electrode, Ag/AgCl pseudoreference electrode, ΔE = 0.025 V, modulation time 0.01 s, interval time 0.1 s, scan rate 50.354 mV/s. Referenced to internal ferrocene standard.................. 278

Figure S5.14. Calibration curve for H_2O_2 quantification utilizing $TiO(SO_4)$ addition. (A) Serial dilution of urea•H_2O_2 in 2 mL of MeCN diluted by 5 mL of H_2O. (B) Calibration curve made utilizing a serial dilution of urea•H_2O_2 in MeCN. 279

Figure S5.15. $Ti(O)SO_4$ titration of **1** with benzoic acid. Black trace is prior to the addition of $Ti(O)SO_4$. Red trace is after the addition of $Ti(O)SO_4$. 280

Figure S5.16. $Ti(O)SO_4$ titration of **1** with 2-chlorobenzoic acid. Black trace is prior to the addition of $Ti(O)SO_4$. Red trace is after the addition of $Ti(O)SO_4$.............................. 280

Figure S5.17. $Ti(O)SO_4$ titration of **1** with 2,4-dichlorobenzoic acid. Black trace is prior to the addition of $Ti(O)SO_4$. Red trace is after the addition of $Ti(O)SO_4$......................... 281

Figure S5.18. $Ti(O)SO_4$ titration of **1** with 2,6-dichlorobenzoic acid. Black trace is prior to the addition of $Ti(O)SO_4$. Red trace is after the addition of $Ti(O)SO_4$......................... 281

Figure S5.19. $Ti(O)SO_4$ titration of **2** with benzoic acid. Black trace is prior to the addition of $Ti(O)SO_4$. Red trace is after the addition of $Ti(O)SO_4$. 282

Figure S5.20. $Ti(O)SO_4$ titration of **2** with 2-chlorobenzoic acid. Black trace is prior to the addition of $Ti(O)SO_4$. Red trace is after the addition of $Ti(O)SO_4$.............................. 282

Figure S5.21. $Ti(O)SO_4$ titration of **2** with 2,4-dichlorobenzoic acid. Black trace is prior to the addition of $Ti(O)SO_4$. Red trace is after the addition of $Ti(O)SO_4$......................... 283

Figure S5.22. $Ti(O)SO_4$ titration of **2** with 2,6-dichlorobenzoic acid. Black trace is prior to the addition of $Ti(O)SO_4$. Red trace is after the addition of $Ti(O)SO_4$......................... 283

Figure S5.23. H_2O_2 disproportionation test. $Ti(O)SO_4$ titrations of **1** in the presence of 25 mM benzoic acid and 0.60 mM urea•H_2O_2. Black trace is prior to the addition of $Ti(O)SO_4$. Red trace is after the addition of $Ti(O)SO_4$. 98±2% H_2O_2 recovered.......................... 284

Figure S5.24. H_2O_2 disproportionation test. $Ti(O)SO_4$ titrations of **1** in the presence of 25 mM 2-chlorobenzoic acid and 0.60 mM urea•H_2O_2. Black trace is prior to the addition of $Ti(O)SO_4$. Red trace is after the addition of $Ti(O)SO_4$. 96±2% H_2O_2 recovered......... 284

Figure S5.25. H_2O_2 disproportionation test. $Ti(O)SO_4$ titrations of **1** in the presence of 25 mM 2,4-dichlorobenzoic acid and 0.60 mM urea•H_2O_2. Black trace is prior to the addition of $Ti(O)SO_4$. Red trace is after the addition of $Ti(O)SO_4$. 104±2% H_2O_2 recovered. ... 285

Figure S5.26. H_2O_2 disproportionation test. $Ti(O)SO_4$ titrations of **1** in the presence of 25 mM 2,6-dichlorobenzoic acid and 0.60 mM urea•H_2O_2. Black trace is prior to the addition of $Ti(O)SO_4$. Red trace is after the addition of $Ti(O)SO_4$. 102±2% H_2O_2 recovered. ... 285

Figure S27. H_2O_2 disproportionation test. $Ti(O)SO_4$ titrations of **2** in the presence of 25 mM benzoic acid and 0.45 mM urea•H_2O_2. Black trace is prior to the addition of $Ti(O)SO_4$. Red trace is after the addition of $Ti(O)SO_4$. 103±4% H_2O_2 recovered....................... 286

Figure S5.28. H_2O_2 disproportionation test. $Ti(O)SO_4$ titrations of **2** in the presence of 25 mM 2-chlorobenzoic acid and 0.45 mM urea•H_2O_2. Black trace is prior to the addition of $Ti(O)SO_4$. Red trace is after the addition of $Ti(O)SO_4$. 95±4% H_2O_2 recovered.......... 286

Figure S5.29. H_2O_2 disproportionation test. $Ti(O)SO_4$ titrations of **2** in the presence of 25 mM 2,4-dichlorobenzoic acid and 0.45 mM urea•H_2O_2. Black trace is prior to the addition of $Ti(O)SO_4$. Red trace is after the addition of $Ti(O)SO_4$. 101±3% H_2O_2 recovered. ... 287

Figure S5.30. H_2O_2 disproportionation test. $Ti(O)SO_4$ titrations of **2** in the presence of 25 mM 2,6-dichlorobenzoic acid and 0.45 mM urea•H_2O_2. Black trace is prior to the addition of $Ti(O)SO_4$. Red trace is after the addition of $Ti(O)SO_4$. 93±4% H_2O_2 recovered..... 287

Figure S5.31. Determination of ORR reaction dependence upon [**1**] with benzoic acid. (A) Uncorrected for background O_2 reduction. (B) Corrected for background O_2 reduction. 288

Figure S5.32. Determination of ORR reaction dependence upon [**1**] with 2-chlorobenzoic acid. (**A**) Uncorrected for background O_2 reduction. (B) Corrected for background O_2 reduction. 289

Figure S5.33. Determination of ORR reaction dependence upon [**1**] with 2,4-dichlorobenzoic acid. (A) Uncorrected for background O2 reduction. (B) Corrected for background O2 reduction. 289

Figure S5.34. Determination of ORR reaction dependence upon [**1**] with 2,6-dichlorobenzoic acid. (A) Uncorrected for background O_2 reduction. (B) Corrected for background O_2 reduction.. 290

Figure S5.35. Determination of ORR reaction dependence upon [**2**] with benzoic acid. (A) Uncorrected for background O_2 reduction. (B) Corrected for background O_2 reduction. 290

Figure S5.36. Determination of ORR reaction dependence upon [**2**] with 2-chlorobenzoic acid. (A) Uncorrected for background O_2 reduction. (B) Corrected for background O_2 reduction. 291

Figure S5.37. Determination of ORR reaction dependence upon [Benzoic Acid] with **1**. (A) Uncorrected for background O_2 reduction. (B**)** Corrected for background O_2 reduction, note that the background reaction is assumed to have minimal initial ORR rate dependence on [Benzoic Acid] relative to the reaction catalyzed by **1**...................... 292

Figure S5.38. Determination of ORR reaction dependence upon [2-chlorobenzoic Acid] with **1**. (A) Uncorrected for background O_2 reduction. (B) Corrected for background O_2 reduction, note that the background reaction is assumed to have minimal initial ORR rate dependence on [2-chlorobenzoic Acid] relative to the reaction catalyzed by **1**. 292

Figure S5.39. Determination of ORR reaction dependence upon [2,4-chlorobenzoic Acid] with **1**. (A) Uncorrected for background O_2 reduction. (B) Corrected for background O_2 reduction, note that the background reaction is assumed to have minimal initial ORR rate dependence on [2,4-dichlorobenzoic Acid] relative to the reaction catalyzed by **1**...... 293

Figure S5.40. Determination of ORR reaction dependence upon [2,6-chlorobenzoic Acid] with **1**. (A) Uncorrected for background O_2 reduction. (B) Corrected for background O_2 reduction, note that the background reaction is assumed to have minimal initial ORR rate dependence on [2,6-dichlorobenzoic Acid] relative to the reaction catalyzed by **1**...... 293

Figure S5.41. Determination of ORR reaction dependence upon [benzoic acid] with **2**. (A) Uncorrected for background O_2 reduction. (B) Corrected for background O_2 reduction, note that the background reaction is assumed to have minimal initial ORR rate dependence on [Benzoic Acid] relative to the reaction catalyzed by **2**. 294

Figure S5.42. Determination of ORR reaction dependence upon [2-chlorobenzoic Acid] with **2**. (A) Uncorrected for background O_2 reduction. (B) Corrected for background O_2 reduction, note that the background reaction is assumed to have minimal initial ORR rate dependence on [2-chlorobenzoic Acid] relative to the reaction catalyzed by **2**. 294

Figure S5.43. Determination of ORR reaction dependence upon [Cp^*_2Fe] with **1** and benzoic acid. Horizontal line represents the global average rate observed across all experiments described for variable [Cp^*_2Fe]. 295

Figure S5.44. Determination of ORR reaction dependence upon [Cp^*_2Fe] with **1** and 2-chlorobenzoic acid. Horizontal line represents the global average rate observed across all experiments described for variable [Cp^*_2Fe]... 295

Figure S5.45. Determination of ORR reaction dependence upon [Cp^*_2Fe] with **1** and 2,4-dichlorobenzoic acid. Horizontal line represents the global average rate observed across all experiments described for variable [Cp^*_2Fe]... 296

Figure S5.46. Determination of ORR reaction dependence upon [Cp^*_2Fe] with **1** and 2,6-dichlorobenzoic acid. Horizontal line represents the global average rate observed across all experiments described for variable [Cp^*_2Fe]... 296

Figure S5.47. Determination of ORR reaction dependence upon [Cp^*_2Fe] with **2** and benzoic acid. Horizontal line represents the global average rate observed across all experiments described for variable [Cp^*_2Fe]. 297

Figure S5.48. Determination of ORR reaction dependence upon [Cp^*_2Fe] with **2** and 2-chlorobenzoic acid. Horizontal line represents the global average rate observed across all experiments described for variable [Cp^*_2Fe]... 297

Figure S5.49. Determination of ORR reaction dependence upon [O_2] with **1** and benzoic acid. Horizontal line represents the global average rate observed across all experiments described for variable [O_2]. 299

Figure S5.50. Determination of ORR reaction dependence upon [O_2] with **1** and 2-chlorobenzoic acid. Horizontal line represents the global average rate observed across all experiments described for variable [O_2]. 299

Figure S5.51. Determination of ORR reaction dependence upon [O_2] with **1** and 2,4-dichlorobenzoic acid. Horizontal line represents the global average rate observed across all experiments described for variable [O_2]. 300

Figure S5.52. Determination of ORR reaction dependence upon [O_2] with **1** and 2,6-dichlorobenzoic acid. Horizontal line represents the global average rate observed across all experiments described for variable [O_2]. 300

Figure S5.53. Determination of ORR reaction dependence upon [O_2] with **2** and benzoic acid. Horizontal line represents the global average rate observed across all experiments described for variable [O_2]. 301

Figure S5.54. Determination of ORR reaction dependence upon [O_2] with **2** and 2-chlorobenzoic acid. Horizontal line represents the global average rate observed across all experiments described for variable [O_2]. 301

Figure S5.55. Determination of ORR reaction dependence upon [**2**] with 2,4-dichlorobenzoic acid. (A) Uncorrected for background O_2 reduction. (B) Corrected for background O_2 reduction. 303

Figure S5.56. Determination of ORR reaction dependence upon [**2**] with 2,6-dichlorobenzoic acid. (A) Uncorrected for background O_2 reduction. (B) Corrected for background O_2 reduction. 303

Figure S5.57. Determination of ORR reaction dependence upon [2,4-dichlorobenzoic acid] with **2**. (A) Uncorrected for background O_2 reduction. (B) Corrected for background O_2 reduction, note that the background reaction is assumed to have minimal initial ORR rate dependence on [2,4-dichlorobenzoic Acid] relative to the reaction catalyzed by **2**. 304

Figure S5.58. Determination of ORR reaction dependence upon [2,6-dichlorobenzoic Acid] with **2**. (A) Uncorrected for background O_2 reduction. (B) Corrected for background O_2 reduction, note that the background reaction is assumed to have minimal initial ORR rate dependence on [2,6-dichlorobenzoic Acid] relative to the reaction catalyzed by **2**. 304

Figure S5.59. Determination of ORR reaction dependence upon [Cp^*_2Fe] with **2** and 2,4-dichlorobenzoic acid. Horizontal line represents the global average rate observed across all experiments described for variable [Cp^*_2Fe]. 305

Figure S5.60. Determination of ORR reaction dependence upon [Cp^*_2Fe] with **2** and 2,6-dichlorobenzoic acid. Horizontal line represents the global average rate observed across all experiments described for variable [Cp^*_2Fe]. 306

Figure S5.61. Determination of ORR reaction dependence upon [O_2] with **2** and 2,4-dichlorobenzoic acid. Horizontal line represents the global average rate observed across experiments from 4.1-8.1 mM O_2 described for variable [O_2]. 308

Figure S5.62. Determination of ORR reaction dependence upon [O_2] with **2** and 2,6-dichlorobenzoic acid. (**A**) Uncorrected for background O_2 reduction. (**B**) Corrected for background O_2 reduction, note that the background reaction is assumed to have minimal initial ORR rate dependence on [O_2] relative to the reaction catalyzed by 2. 308

Figure S5.63. Iodometric titration of a catalytic reaction of **2** with 0.9 mM Cp^*_2Fe, 25 mM AcOH, and O_2 saturation in MeOH to determine ORR selectivity by our previously reported method.[3] 309

Figure S5.64. ^1H NMR of 2,6-dichlorobenzoic acid (O-H) in dry CD_2Cl_2....... 313

Figure S5.65. ^1H NMR of d_1-2,6-dichlorobenzoic acid (O-D) in dry CD_2Cl_2. 314

Figure S5.66. Determination of KIE with **1**. Corrected ratio of slopes gives a KIE of 1.2±0.1. 315

Figure 6.1. Proposed structures of secondary-sphere supported Lewis-acid additives for CO_2 reduction 319

Figure 6.2. Cyclic voltammograms of 0.5 mMFe(^{me}crebpy)Cl in 0.1 M $TBAPF_6$/*N,N*-DMF supporting electrolyte with no added Lewis acid under Ar (black) or CO_2 (red) atmospheres and upon the addition of equimolar (0.5 mM) $Mg(OTf)_2$ or $Zn(OTf)_2$ under Ar (green) or CO_2 (blue) atmospheres. Working electrode: 3 mM diameter glassy carbon; counter electrode: glassy carbon; reference electrode Ag/AgCl pseudoreference. Potentials referenced to internal ferrocene standard. 321

Figure 6.3. Cyclic voltammograms of 0.5 mM $Mg(OTf)_2$ or $Zn(OTf)_2$ in 0.1 M $TBAPF_6$/*N,N*-DMF supporting electrolyte with no added Fe(^{me}crebpy)Cl under Ar (black) or CO_2 (red) atmospheres and upon the addition of equimolar Fe(^{me}crebpy)Cl under Ar (green) or CO_2 (blue) atmospheres. Working electrode: 3 mM diameter glassy carbon; counter electrode: glassy carbon; reference electrode Ag/AgCl pseudoreference. Potentials referenced to internal ferrocene standard. 323

Figure 6.4. CVs of (A) Co(^{tbu}dhbpy) and (B) [Co(^{tbu}dhbpy)$(py)_2$][PF_6] under an Ar atmosphere, under a CO_2 atmosphere with optimized PhOH concentrations. 325

Figure 6.5. Proposed structures of Cr and Mn catalysts with secondary-sphere –OMe groups for CO_2 and O_2 reduction, respectively. 327

List of Schemes

Scheme 2.1. Proposed reduction mechanism for Fe(^{tbu}dhbpy)Cl with no substrate added; **R** = ^{t}Bu. 63

Scheme 2.2. Proposed reactivity of Fe(^{tbu}dhbpy)Cl **1** in the presence of CO_2 at reducing potentials. **R** = ^{t}Bu 70

Scheme 2.3. Proposed catalytic mechanism of Fe(^{tbu}dhbpy)Cl **1** in the presence of PhOH and CO_2. **R** = ^{t}Bu 80

Scheme 3.1. Synthesis of Fe(^{me}crebpy)Cl. 164

Scheme 3.2. Synthesis of Fe(^{tbu}catbpy). 167

Scheme 4.1. General summary of known $Co(N_2O_2)$ catalysts for homogeneous ORR, emphasizing the known diversity of the diimine ligand backbone (top). The

[Co(^{tbu}dhbpy)(py)$_2$][PF$_6$] **(1)** catalyst reported here shows selectivity for H_2O (bottom). 220

Scheme 4.2. Proposed catalytic mechanism for ORR mediated by **1** in MeOH with AcOH as a proton donor and Cp*$_2$Fe as a chemical reductant. L = [^{tbu}dhbpy]$^{2-}$. 227

List of Tables

Table 2.1. Summary of Controlled Potential Electrolysis Data. Conditions were 0.1 M TBAPF$_6$/N,N-DMF supporting electrolyte with 0.05 M Fc as sacrificial oxidant. Working electrode was glassy carbon, counter electrode was glassy carbon, pseudoreference was Ag/AgCl. a Faradaic Efficiency. b 0.5 mM Fe(^{tbu}dhbpy)Cl. c 0.5 M PhOH. d –2.5 V vs Fc/Fc+. e –2.1 V vs Fc/Fc$^+$ 73

Table 2.2. Summary of kinetic data extracted from CVs using FOWA. Trial 1 is under CO_2 saturation conditions. Trials 2-6 are under CO_2 saturation conditions with added ^{a}PhOH or ^{b}*d*$_1$-PhOD. 78

Table S2.1. ΔE_p for variable scan rate experiments under Faradaic conditions and upon the addition of 10.8 mM TBACl. 0.5 mM Fe(^{tbu}dhbpy)Cl in *N*,*N*-DMF with 0.1 M TBAPF$_6$ supporting electrolyte under an atmosphere of Ar. Working electrode is glassy carbon (3 mm diameter), counter electrode is Pt wire, and pseudo-reference is Ag/AgCl wire with ferrocene (Fc) added as internal reference. ^{a}0.5 M Fe(^{tbu}dhbpy)Cl ^{b}10.8 mM TBACl ^{c}Value for Fc internal standard for the same scan. 116

Table S2.2. $E_{1/2}$ and ΔE_p for variable PhOH concentrations under Ar atmosphere. 0.5 mM Fe(^{tbu}dhbpy)Cl in *N*,*N*-DMF with 0.1 M TBAPF$_6$ supporting electrolyte. Working electrode is glassy carbon (3 mm diameter), counter electrode is Pt wire, and pseudo-reference is Ag/AgCl wire with ferrocene (Fc) added as internal reference. ^{a}First reduction wave of Fe^{tbu}dhbpy. ^{b}Fc for the corresponding scan. 117

Table S2.3. $E_{1/2}$ and ΔE_p for variable PhOH concentrations under CO_2 atmosphere. 0.5 mM Fe(^{tbu}dhbpy)Cl in *N*,*N*-DMF with 0.1 M TBAPF$_6$ supporting electrolyte. Working electrode is glassy carbon (3 mm diameter), counter electrode is Pt wire, and pseudo-reference is Ag/AgCl wire with ferrocene (Fc) added as internal reference. 118

Table S2.5. Crystal data and structure refinement for $C_{40}H_{49}N_3O_2ClFe$. 119

Table 3.1. Summary of Controlled Potential Electrolysis Data.^{a} 156

Table S3.1. Average diffusion coefficient for the first reduction feature for each of the Fe complexes 216

Table S3.2. ΔE_p and $i_{p,c}/i_{p,a}$ for **2** at the first reduction feature under various scan rates. 216

Table S3.3. ΔE_p and $i_{p,c}/i_{p,a}$ for **2** at the second reduction feature under various scan rates. 216

Table S3.4. ΔE_p and $i_{p,c}/i_{p,a}$ for **2** at the third reduction feature under various scan rates. 216

Table S3.5. ΔE_p and $i_{p,c}/i_{p,a}$ for **3** at the first reduction feature under various scan rates. 217

Table S3.6. ΔE_p and $i_{p,c}/i_{p,a}$ for **3** at the second reduction feature under various scan rates. 217

Table 5.1. Summary of selectivity for different acids with complexes **1** and **2**. 259

Table 5.2. Summary of turnover frequencies (TOF) for different acids with complexes **1** and **2**. 261

Table S5.1. Summary of redox potentials of each complex under conditions studied. 278

Chapter One

Motivation and Precedence for Studying Electrochemical Transformations of Carbon Dioxide and Oxygen

Portions of this chapter published as Nichols, A. W., Machan, C. W. *Front. Chem*. **2019**, *7* (397).

1.1 Problems and solutions in the production and utilization of electrical energy

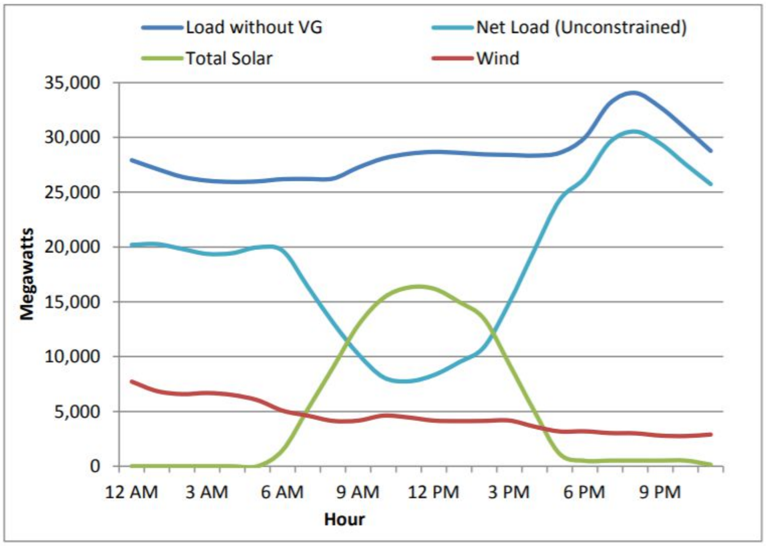

Figure 1.1. Typical electrical load without variable generation (solar and wind), dark blue, load when corrected for added variable generation (light blue), solar generation (green), and wind generation (red) for a spring day in California. Adapted from Denholm, P; O'Connel, M.; Brinkman, G.; Jorgenson, J. *Overgeneration from Solar Energy in California. A Field Guide to the Duck Chart*; Technical Report for National Renewable Energy Lab. (NREL), Golden, CO **2015**.

Since the industrial revolution, a dramatic increase in the consumption of fossil fuels and unsustainable emissions of CO_2 have led to one of the greatest challenges we face today: development of renewable, carbon-neutral fuels and more efficient ways to utilize them.[1] The development of renewable energy technologies which harvest energy from sources like the sun, wind, and tide has begun to bridge the gap into a new era of energy production; however, inherent problems with the intermittency and portability of the produced energy have led to the need for the development of efficient energy storage solutions, with a need to displace energy from peak generation to peak use (**Figure 1.1**). A few energy storage solutions include mechanical storage, Li^+ ion batteries, and redox-flow batteries, which all have inherent issues when utilized with our current infrastructure for liquid fuels. This thesis focuses on catalyst development of molecular electrocatalysts for the redcution of carbon dioxide and dioxygen for applications related to these issues.

1.2 Secondary-Sphere Effects in the CO_2 Reduction Reaction (CO_2RR): Introduction

One alternative solution to this problem is the development of scalable and cost-effective processes to store electrical energy in chemical bonds using CO_2 as a primary feedstock remains a significant challenge for energy research.[1-2] Of particular interest are homogeneous catalysts for CO_2RR, as their well-defined structures give chemists an opportunity to effectively characterize intermediates relevant to the operating mechanism and further optimize active catalyst families through iterative ligand design.[3-4] While the influence of different ligand types in the primary coordination sphere can be observed in the catalytic activity and selectivity of transition metals across the *d*-block towards CO_2RR, more subtle effects—including rate enhancement and lowered overpotentials—can be obtained by modulation of the secondary coordination sphere within specific classes of metal complexes.[5] This has been particularly successful in the design of highly active and selective catalysts for CO_2RR, directing a paradigmatic shift in the general understanding of 'design principles'.[6-11]

While this section focuses on molecular catalysts which were specifically examined for electrochemical CO_2RR, secondary-sphere effects have been successfully harnessed in related catalytic processes, including thermal CO_2 hydrogenation,[12-21] hydrogen evolution,[22-33] hydrogen oxidation,[25, 27-35] formate oxidation,[36-38] and oxygen reduction [39-50] reactions. Here, the focus is on how the mechanism of CO_2RR relates to the type of secondary-sphere effects employed in molecular systems. Strategies discussed here which have been shown to increase catalytic activity and selectivity include: pendent proton donors/shuttles in the form of Brønsted sites, charged moieties, sterically demanding functional groups, bimetallic active species, and stoichiometric participation of alkali and alkaline earth metal cations.

To contextualize the motivation and principles, examples of secondary-sphere effects in enzymes which catalyze the interconversion of CO_2 with either CO or formic acid as products are discussed. This overview is followed by a careful examination of secondary-sphere effects in several abiotic molecular electrocatalyst examples, beginning with the $[Fe(tetraphenylporphyrin)]^+$ $[Fe(TPP)]^+$ systems pioneered by Savéant, Robert, and Costentin, including a discussion of the effects of pendent proton source placement and the distance dependence of through-space effects induced by charged residues.[9-11, 51-56] Next, $M(bpy)(CO)_3X$ catalysts (M=Mn or Re; X=solvent molecule or halide)[8, 50, 56-70] in which steric parameters, pendent Lewis acid effects, and charged residues have been shown to be effective will be discussed. Finally, $[Ni(cyclam)]^{2+}$ (cyclam = 1,4,8,11-tetraazacyclotetradecane), which contains pendent proton donors on the coordinating N atoms of the macrocycle, is discussed.[71-77] These systems are among the most highly studied in the field and representative of the progress that has been made in understanding how secondary-sphere coordination effects enhance molecular electrocatalysis. Additional discussion on emerging systems for CO_2RR which utilize secondary-sphere effects are included to summarize some of the current work in the field.

1.3 Biological inspiration for development of CO_2RR catalysts

1.3.1 Cu,Mo-Containing Carbon Monoxide Dehydrogenase (Cu,Mo-CODH)

The structure and function of Cu,Mo-CODH enzymes have been previously reviewed in great detail.[78-79] Of this class of enzyme, the Cu,Mo-CODH in *O. carboxydovorans* has been the most extensively studied (**Figure 1.2A**).[80-82] The active site of this enzyme contains Mo and Cu ions which are bridged by a μ_2-sulfido ligand. Mo is coordinated in a distorted square pyramidal fashion by an enedithiolate moiety (from the pyran ring found in the pyranopterin cofactor), a μ_2-sulfido ligand and an oxo/hydroxo ligand in the equatorial plane. The apical ligand is an oxo, with a glutamine residue within hydrogen-bonding distance and a glutamate residue in a *trans* position. A unique structural feature of Cu,Mo-CODH in comparison to other Mo–containing hydrogenases is its covalent linkage through a cysteine residue to the Cu ion, connecting the heterobimetallic active site to the large subunit of the CODH enzyme.

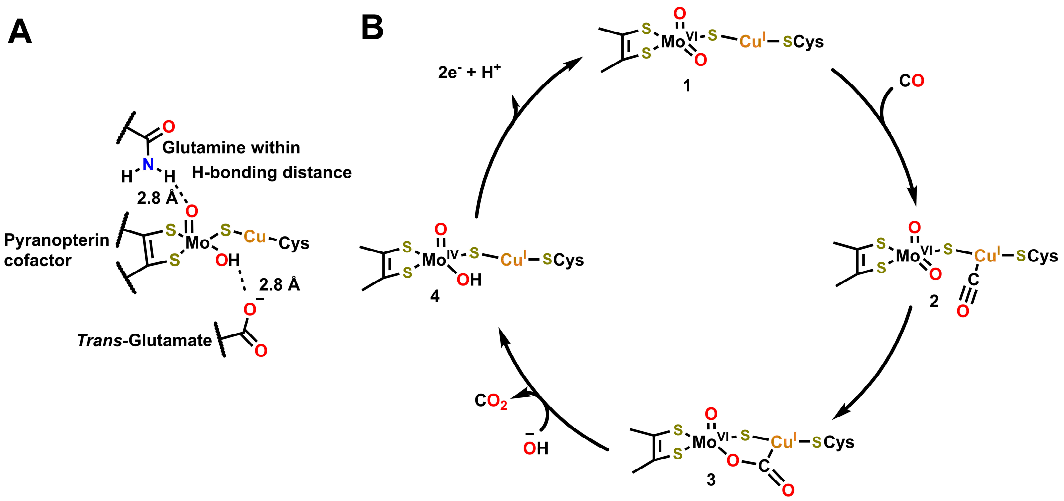

Figure 1.2. (A) Active site of Cu,Mo-CODH. (B) Proposed catalytic cycle for oxidation of CO by Cu,Mo-CODH.[79-80]

In the catalytic cycle for transformation of CO to CO_2 by Cu,Mo-CODH, CO is proposed to initially bind to the Cu(I) ion **2**, followed by nucleophilic attack by the equatorial oxo ligand to generate the bridging μ_2-η^2-CO_2 adduct **3** (**Figure 1.2B**).[80] The five-membered metallacycle **3** results from a redox-neutral reaction which maintains the Mo(VI) state (**Figure 1.2B**). Following rearrangement and net oxidation of CO, CO_2 release occurs with hydroxide binding to produce the Mo(IV) species **4**. Subsequent $2e^-$ oxidation returns the Mo active site to the initial Mo(VI) oxidation state. Notably, the glutamine residue which is in contact with the equatorial oxo ligand (**Figure 1.2B**) can act as a Brønsted base (proton acceptor) to regenerate the more nucleophilic oxo ligand when transitioning from **4** to **1**. If the reverse of this catalytic cycle is imagined, it is clear that a proton-donating residue would be beneficial for CO_2RR and C–O bond cleavage to produce CO.

1.3.2 Monofunctional Ni,Fe-containing CODHs

The active site of Ni,Fe-containing CODHs, known as Cluster C, is proposed to cycle between three separate redox states during catalytic CO oxidation (C_{red1}, C_{int}, and C_{red2}; **Figure 1.3**).[83] The behavior and activity of cluster C from *Carboxydothermus hydrogenoformans* has been experimentally interrogated in these three different redox states utilizing chemical reducing agents.[83] The cofactor contains an Fe_4Ni cluster bridged by sulfide ligands with a single Fe and Ni atom in the active site, which also contains histidine and lysine residues in close proximity to interact with active site-bound substrate molecules. In C_{red1} the active site contains Fe^{2+} and Ni^{2+} ions with an Fe-bound hydroxo ligand that is within hydrogen bonding distance of the proximal lysine residue. Upon exposure to CO, the Fe-bound hydroxide is deprotonated and the resultant oxo species can form a new C–O bond to generate the μ_2-η^2-CO_2 adduct C_{red2}-CO_2, where CO_2 is bound through C by Ni and O by Fe (**Figure 1.3**).[83] This μ_2-η^2-CO_2 binding mode is stabilized by hydrogen-bonding interactions with the pendent histidine and lysine residues.[83] A 2e⁻ oxidation with concomitant binding of an aquo ligand reduces the Ni^{2+} to Ni^0 in C_{red1}, triggering release of CO_2. Oxidation of the reduced cofactor by 2e⁻ regenerates the C_{red1} catalytic resting state.

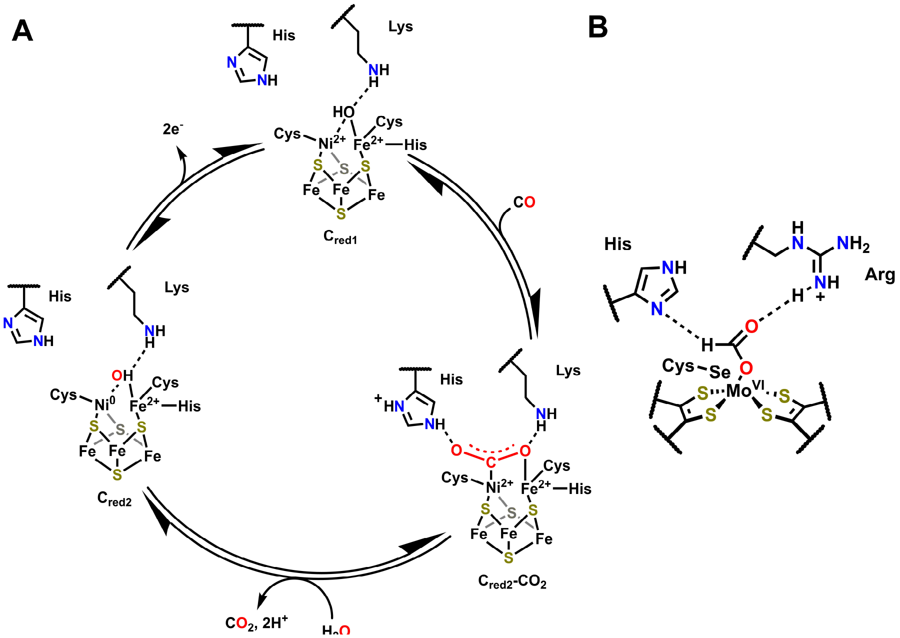

Figure 1.3. (A) Proposed mechanism for CO oxidation Ni,Fe CODH.[83] (B) Active site of FADH in *E. coli* with bound formate substrate.[84]

1.3.3 Formic Acid Dehydrogenase (FADH)

FADH enzymes catalyze the reversible 2e⁻/1H⁺ interconversion of CO_2 and formate, another reaction of interest to CO_2 utilization.[85] The active site of the FADH enzyme in *E. coli* contains a single Mo(VI) atom coordinated to four S atoms from two *cis*-dithiolene moieties originating from the bis(molybdopterin guanine dinucleotide) cofactor, a hydroxyl ligand, and a SeCystine.[84] The active site also contains histidine and arginine residues in a position to interact with activated Mo-bound intermediates (**Figure 1.3B**). The catalytic oxidation of formate begins by displacement of the hydroxyl ligand with an equivalent of formate, which binds as an *η¹*-OCHO ligand; the *η¹-O* binding mode is stabilized through hydrogen bonding interactions between the arginine and histidine residues and the unbound H and O atoms of formate (**Figure 1.3B**). Subsequent oxidation and transfer of 2e⁻ from formate to the Mo center occurs with release of CO_2 and proton transfer to the to the SeCysteine residue. The Mo(IV) center can then be returned to the resting state through the loss of 2e⁻ as the histidine deprotonates the Mo-bound SeCysteine. Abiotic structural motifs similar to these three examples are discussed in the subsequent sections where either a) bimetallic active sites or b) secondary-sphere moieties are used to mediate electrochemical CO_2RR.

1.4 Benchmarking Molecular Electrocatalysts for CO_2RR

Electrochemical techniques can facilitate the determination of kinetic and thermodynamic parameters for both Faradaic and catalytic reactions. Cyclic voltammetry (CV), a non-destructive potentiostatic technique, is particularly informative. Indeed, the breadth and importance of rigorous CV analysis has been reviewed in great detail.[4, 86-90] Experimental determination of fundamental reaction parameters is essential for comparing the effects of pendent functional groups on the activity of electrocatalysts.

The effective catalytic overpotential (η) is the difference between the standard potential of CO_2RR ($E^0_{CO2/CO}$) and the potential at half catalytic current height ($E_{cat/2}$) as described in **Eq (1.1)** and describes a thermodynamic quantity: the electrochemical energy beyond the standard potential which is required to drive a reaction of interest at an appreciable rate. We note that some prefer to define the overpotential term as $E_{CO2} - E_{1/2}$. We distinguish between these through the use of 'effective catalytic overpotential' to describe the overpotential calculated utilizing $E_{cat/2}$.[91]

$$\eta = E^0_{CO2/CO} - E_{cat/2} \quad (1.1)$$

Another reaction parameter commonly measured through cyclic voltammetry (CV) is the maximal turnover frequency (TOF_{max}), which can also be described as the observed catalytic rate constant (k_{obs}) with units of s^{-1}.[87] In a Nernstian electrocatalytic reaction, TOF is related to overpotential by the catalytic Tafel equation, **Eq (1.2)**. TOF is the turnover frequency at the applied potential, F is Faraday's constant, R is the ideal gas constant, T is temperature, $E_{1/2}$ is the catalyst standard reduction potential, and η_{app} is the difference between $E^0_{CO2/CO}$ and the applied potential. It is worth noting however, that the limitations of the molecular catalytic reactions, including diffusion and side phenomena, can cause 'peaks' in catalytic CV waves and truncate the region where the Tafel relationship results in increased activity as the applied potential becomes more negative.

$$TOF = \frac{TOF_{max}}{1 + \exp\,[\frac{F}{RT}\left(E^0_{CO2/CO} - E_{1/2} - \eta_{app}\right)]} \qquad (1.2)$$

To benchmark the kinetic and thermodynamic parameters of different electrocatalysts, **Eq (1.2)** can be used to generate catalytic Tafel plots (*nota bene*, these explicitly include the limitations imposed on molecular Tafel behavior mentioned above and enable comparison across different experimental conditions). **Figure 1.4** shows an example of a catalytic Tafel plot for a generic molecular catalyst: 'better' catalysts are located to the top left of catalytic Tafel plots, where overpotential is low and TOF_{max} is large and 'worse' catalysts are located in the bottom right of a catalytic Tafel plot where the trends in overpotential and TOF_{max} are reversed. **Figure 1.5** shows a Tafel plot comparing reported catalysts.

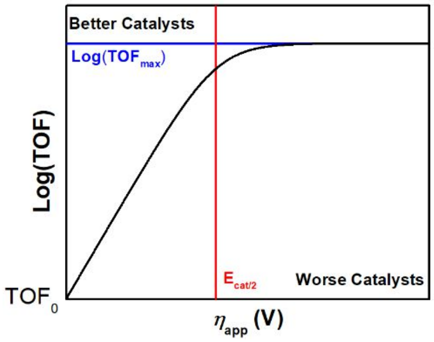

Figure 1.4. Example of a catalytic Tafel plot of a generic molecular species with regions where better and worse catalysts are located explicitly labeled, along with the position of important benchmarking parameters.

Finally, simple plots of log(TOF$_{max}$) vs E$_{cat/2}$ can be used to compare catalysts in the same family to look for secondary-sphere effects.[54, 92-93] If there is no secondary-sphere effect, then a linear scaling relationship based on electrochemical driving force should occur; however, if a secondary-sphere effect is present, a deviation from the linearity achieved by comparing inductive substitution effects can be observed. One should utilize caution using this method for comparing catalysts, however, as changes to the reaction mechanism that alter co-substrate identity, concentration dependence, solvent and co-solvent effects can greatly impact the catalytic activity of a series of complexes through scaling relationships that are unrelated to the secondary-sphere interactions of interest. Likewise, the effects of Nernstian changes in the experimentally observed potential based on changes in the reaction equilibrium, K_{eq}, can obscure details if not properly accounted for.[92]

It should also be noted that there are instances where benchmarking in a quantitative fashion not possible for a system due to missing thermodynamic parameters for a reaction which make determination of the standard reduction potential impossible. Other issues which can arise include the difficulty of determining kinetic parameters due to the inherent properties of the catalyst of interest under electrochemically reducing conditions which disallow the utilization of either foot of the wave analysis and variable scan rate techniques for determination of TOF.

1.5 Secondary-Sphere Effects in Molecular Electrocatalysts for CO_2RR

1.5.1 Secondary-Sphere Effects in $[Fe(TPP)]^+$

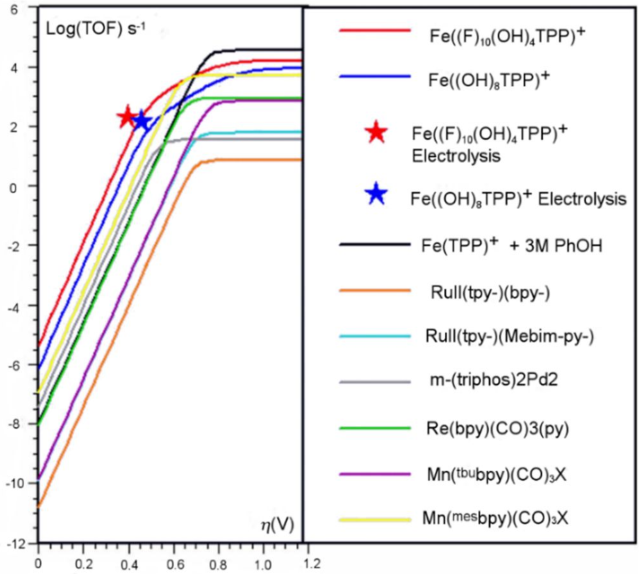

Figure 1.5. Catalytic Tafel plot showing enhancements from the inclusion of a secondary coordination sphere in the $[Fe(TPP)]^+$ system.[11] Adapted from *Proc. Natl. Acad. Sci.* **2014**, *111*, 14990-14994.

For $[Fe(TPP)]^+$ complexes, increased activity for the electrocatalytic reduction of CO_2 to CO is observed with the addition of both Lewis and Brønsted acids.[94-96] As a result, $[Fe(TPP)]^+$ complexes bearing secondary-sphere functionalities exploiting classical Brønsted acid/base push-pull reactions have been the subject of extensive studies.[6, 9, 11, 55] In particular, iron 5, 10, 15, 20-*tetrakis*-(2,6-dihydroxyphenyl)-porphyrin ($[Fe((OH)_8TPP)]^+$) was identified as a promising candidate for electrochemical CO_2RR because it positioned proton donors oriented towards the active site in close enough proximity to interact with bound substrate. Experimentally, the pendent –OH moieties were observed to cause a large catalytic current enhancement and a decrease in overpotential.[6] Control experiments using $[Fe((OMe)_8TPP)]^+$, where the –OH groups were converted to –OMe ether moieties, also showed an increased TOF_{max} relative to $[Fe(TPP)]^+$, however, the overpotential was much larger than both $[Fe(TPP)]^+$ and $[Fe((OH)_8TPP)]^+$. These differences relate to the mechanism of CO_2RR by $[Fe(TPP)]^+$ and how key steps are affected by the presence of the pendent –OH moieties.[97]

The proposed mechanism for the reduction of CO_2 by $[Fe(TPP)]^+$ requires the electrochemical generation of $[Fe(0)TPP]^{2-}$ at the electrode surface, followed by CO_2 binding and activation to generate $[Fe(I)(TPP)(\eta^1\text{-}CO_2^{\bullet-})]^{2-}$. The sacrificial proton donor, AH, stabilizes the binding of the $CO_2^{\bullet-}$ radical anion through hydrogen bonding. Concerted protonation and electron transfer from the metal center causes C–O bond cleavage, leading to the formation of $[Fe(II)(TPP)(CO)]^0$. Release of CO is facilitated by a comproportionation reaction with a second equivalent of $[Fe(0)TPP]^{2-}$ to generate two equivalents of $[Fe(I)TPP]^-$ and one equivalent of CO. We note that a second mechanism has been proposed for $[Fe(TPP)]^+$ wherein upon CO_2 binding the metal center is oxidized by $2e^-$ from Fe(0) to Fe(II) in the $\eta^1\text{-}CO_2$ adduct before interaction with the proton donor, rather than generating an Fe(I) species.[98]

The introduction of a pendent proton source minimally alters the mechanism for CO_2RR, but causes catalytic rate increases by favoring several steps of the reaction. Upon the generation of $[Fe(0)((OH)_8TPP)]^{2-}$, CO_2 also binds in η^1-fashion and is activated to the $CO_2^{\bullet-}$ radical anion, but stabilization occurs through hydrogen bonding interactions with the pendent proton donors.[6] Experimentally this is observed as a pre-wave to the catalytic feature in CV experiments, which can be more easily examined through additional modulation of electron density at the metal center with the related partially fluorinated derivative $[Fe((F)_{10}(OH)_8TPP)]^+$.[9, 11] Subsequent intramolecular protonation balanced by the exogenous proton source can occur, generating η^1-$^{\bullet}CO_2H$ at an Fe(I) center.[9] The cleavage of the C–OH bond is induced upon further reduction and a concerted intramolecular protonation reaction (again balanced by proton transfer from the sacrificial donor) to regenerate the resting state, Fe(I), of the electrocatalytic cycle and CO product. The enhanced catalytic activity at more negative potentials of the ether-containing control complex may also be explained through an enhancement of this mechanism (the ether groups function as a Brønsted base to orient and enhance the proton activity of the exogeneous proton donor), but this has a relatively lower enhancement effect on the CO_2RR reaction. A comparison of the catalytic activity increases from these effects can be seen through the catalytic Tafel analysis shown in **Figure 1.5**.

Another area of study for secondary-sphere effects focuses on ‘hangman-type’ porphyrins, which also orient functional groups towards the metal active site. Both the positioning of these functional groups relative to the active site and the pK_a of the pendent proton source are of importance to the electrocatalytic activity for CO_2RR. In a study by Chang *et al.*, the positional effects of pendent amide groups were investigated. It was found that orientation towards the active site and positioning above the active site were both important for catalytic enhancement, as these stabilized catalytic intermediates through hydrogen bonding and facilitated efficient proton transfer.[54] This was quantified experimentally through equilibrium binding constants for CO_2 determined by rapid-scan CV techniques. When a pendent amide group was attached to the *meso*-phenyl of the porphyrin in the ortho position, [(Fe(*o*-2-amide-TPP)]$^+$, the highest catalytic activity was observed. In comparison with the other reported derivatives, a ‘Goldilocks’ relationship was observed, where positioning the amide group either closer or farther did not result in comparable catalytic current enhancement (**Figure 1.6**).

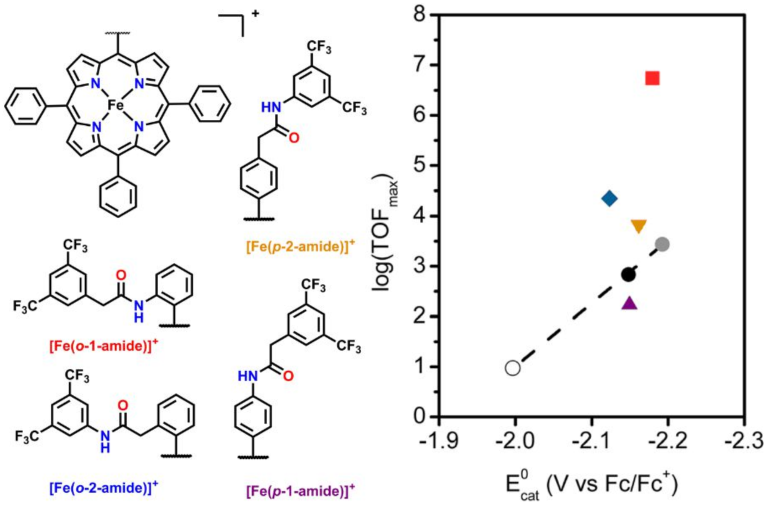

Figure 1.6. Plot of log(TOF$_{max}$) vs E$^0_{cat}$ for hangman porphyrins used to study positional dependence of catalytic enhancement for this system. Circles are [Fe(TPP)]$^+$ derivatives which utilize electronic substitution of the phenyl rings for modulation of the redox potential of the Fe$^{I/0}$ couple. Upwards purple triangle is [Fe(*p*-1-amide-TPP)]$^+$, downwards orange triangle is [Fe(*p*-2-amide-TPP)]$^+$, blue diamond is [Fe(*o*-1-amide-TPP)]$^+$, red square is [Fe(*o*-2-amide-TPP)]$^+$. Reprinted with permission from *Chem. Sci.*, **2018**, *9*, 2952 –published by the Royal Society of Chemistry.

Nocera and co-workers found that the pK_a of the pendent proton source was important for the stabilization of CO_2 binding in the active site of related ‘hangman-type’ porphyrin architectures (**Figure 1.7**).[52] Pendent phenol- and guanidinium-based hangman functional groups were predicted by DFT to cause a 2.1-6.6 kcal/mol stabilization of bound CO_2 within the hangman pocket. Conversely, a sulfonic acid derivative was found to function as a proton donor under the experimental conditions in the absence of applied potential, which was attributed to an estimated pK_a of ~3 under experimental conditions. The resultant anionic sulfonate derivative showed diminished catalytic activity relative to the porphyrins functionalized with phenol and guanidinium. The anionic charge of the conjugate base, combined with the overall steric bulk of the sulfonate, was proposed to prevent CO_2 binding within the hangman cleft and contribute minimally to the stabilization of the CO_2 adduct.[52] The pendent phenol-based 'hangman-type' architecture was predicted to have the greatest stabilization of CO_2 binding by DFT calculations and was observed to have the fastest catalytic rate constant by CV methods.

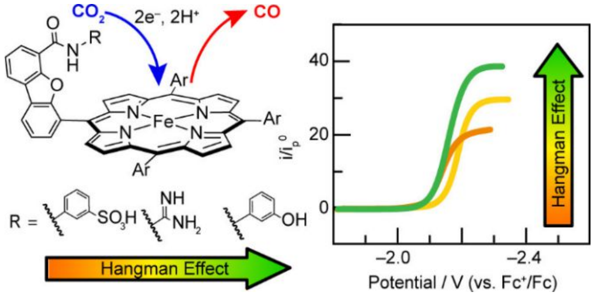

Figure 1.7. Figure showing effect of pK_a of hanging group on CO_2RR activity in hangman $[Fe(TPP)]^+$. Reprinted with permission from *Organometallics*, **2019**, *38*, 1219-1223. Copyright 2018 American Chemical Society.

Others have examined the relationship between electrocatalytic activity and the H-bonding ability of pendent residues on triazole-based picket-fence-type $[Fe(TPP)]^+$ derivatives with pendent amide functional groups.[99] In this report, a correlation between log(TOF_{max}) and the pK_a of the pendent proton donors was established for a picket fence-amide with an encapsulated water molecule by a comparison to previously reported $[Fe(TPP)]^+$ derivatives. The pendent groups are proposed to contribute to the stabilization of the Fe-bound CO_2 molecule through hydrogen-bonding interactions and facilitate proton transfer to mediate the rate-determining C–O bond cleavage step.

The studies discussed above and others[100-101] have shown that pendent protons can be beneficial for $[Fe(TPP)]^+$-based electrocatalysts, but also that careful consideration of steric constraints and the pK_a of the chosen pendent proton donor under experimental conditions is necessary. Installation of pendent proton groups in porphyrin ligands can have a detrimental effect if their pK_a and spatial orientation is not chosen carefully (e.g.

sulfonic acid, *vide supra*). A recent study has also shown that choice of solvent can largely alter the catalytic response of $[Fe(TPP)]^+$ with an asymmetrically substituted pendent proton moiety.[55] Using a porphyrin containing a single pendent hydroxy functionality in the 2-position of a single *meso*-phenyl ring it was demonstrated that the electrocatalytic activity of this system can be greatly hindered by utilizing solvents with strong hydrogen bonding properties through a comparison of activity in MeCN, DMF, and DMSO. Strong hydrogen bond acceptor solvents like DMF and DMSO lead to a decrease in activity of the catalyst, while in MeCN, the activity approached that reported for [Fe((*ortho*-TMA)TPP)]$^{5+}$, which is the fastest molecular electrocatalyst for CO_2RR reported to date. The authors postulated that the interference of competitive hydrogen bonding between solvent molecules leads to slowed electrochemical kinetics.[55] This suggests that more rigorous interrogations of functional group cooperativity (specifically the number and type of functional groups) and the interactions of functional groups with solvent and proton donors will offer additional insight into these mechanisms. Indeed, Savéant recently described the origin of catalytic enhancement by pendent proton relays.[92] Boosting of electrocatalytic activity by pendent proton donors occurs when the forward rate constant of proton transfer from the pendent group to the active site is competitive with that of exogeneous proton donor directly to the active site (under the assumption that re-protonation of the pendent donor is extremely rapid). Should these forward rate constants not be well-matched, inefficiency in the proton relay mechanism will limit the ultimate catalytic current enhancement.

Further studies on this class of catalysts have modulated the potential of the $Fe^{I/0}$ reduction where the catalytic response occurs by examining electron-withdrawing perfluorophenyl-substituted tetraphenylporphyrins ($[Fe(F_5TPP)]^+$, $[Fe(F_{10}TPP)]^+$, and $[Fe(F_{20}TPP)]^+$, where F_5 corresponds to a single perfluorinated phenyl ring, etc.).[10] This is a purely electronic effect, perturbing the continuum of electronic distribution in the ligand-metal manifold. The inclusion of proximal ionic charges has also been explored with trimethylanilinium- ([Fe(-*ortho*-TMA-TPP)]$^{5+}$ and [Fe(-*para*-TMA-TPP)]$^{5+}$) and sulfonato-functionalized porphyrins ([Fe(-*para*-sulfonato-TPP)]$^{3-}$) to understand the role of through-space electrostatic interactions.[10] The perfluorinated derivatives demonstrated a relationship between the catalytic response and the $Fe^{I/0}$ potential; as the potential of that redox couple becomes more positive, log(TOF_{max}) decreases in a linear fashion, corresponding to a relative decrease in added electron density at the metal center upon electrochemical reduction.[10, 102] However, for $[Fe(TPP)]^+$-substituted with a charged functional group (*para*–SO_3^{2-}, para– and *ortho*–NMe_3^+), log(TOF_{max}) increases linearly as the redox potential of the $Fe^{I/0}$ couple shifts to more positive potentials. [Fe-*ortho*-TMA-TPP]$^{5+}$ has the most positive $Fe^{I/0}$ redox potential of any $[Fe(TPP)]^+$-based electrocatalyst reported to date, while also having the largest log(TOF_{max}) value. To understand this, one can once again imagine the CO_2 binding mode wherein a single electron generates radical $CO_2^{\bullet-}$ anion which is stabilized by the charged groups close to the active site. It is compelling that such dramatic enhancements should be observed, but this could suggest that the reaction pathway might also be significantly altered from other $[Fe(TPP)]^+$ derivatives, as the effect is an inverse scaling relationship to that predicted for purely inductive reasons.[10]

The data points from charge-based functionalization are relatively limited, and proposal of design principles for new systems for molecular CO_2RR systems requires additional information on these effects. For instance, the synthesis of further positional isomers of charged systems could give more evidence that a scaling relationship exists based on the distance between the charged moiety and the active site. Ultimately, it is clear that the inclusion of charge should seek to explore deliberate manipulation of the known mechanism to achieve the greatest enhancement effect.

1.5.2 Secondary-Sphere Effects in Re(bpy)(CO)$_3$X

Re(bpy)(CO)$_3$X (where bpy is a 2,2′-bipyridine, often additionally functionalized in a symmetric fashion, and X is a Cl$^-$ or Br$^-$ anion or solvent molecule) is active for the electrocatalytic reduction of CO$_2$ to CO in near quantitative fashion.[103-104] Under Faradaic conditions, this complex is proposed to undergo reduction according to **Figure 1.8**. Initial reduction is localized at the bpy ligand, followed by loss of Cl$^-$ from [Re(bpy)(CO)$_3$Cl]$^-$ via an overall *EC* mechanism to generate the neutral five-coordinate species [Re(bpy)(CO)$_3$]^0. At this stage, two separate mechanisms for reduction can occur: 1) a single reduction assigned to the ligand framework can occur, generating the catalytically active monoanionic species [Re(bpy)(CO)$_3$]$^-$. Commonly, the [Re(bpy)(CO)$_3$Cl]$^-$ species is stable long-enough on the CV timescale that [Re(bpy)(CO)$_3$]$^-$ forms instead at the second reduction with Cl$^-$ loss. 2) following initial single-electron reduction and Cl$^-$ loss, a Re–Re bond between two equivalents of [Re(bpy)(CO)$_3$]^0 can form to generate Re(bpy)(CO)$_3$]$_2$. Dimer formation requires two, sequential reductions to cleave the Re–Re bond and form the [Re(bpy)(CO)$_3$]$^-$ active species. The formation of the metal-metal bond is slow under most conditions because of the persistence of [Re(bpy)(CO)$_3$Cl]$^-$ on the CV timescale and is most often outcompeted by the unimolecular pathway to [Re(bpy)(CO)$_3$]$^-$.[105]

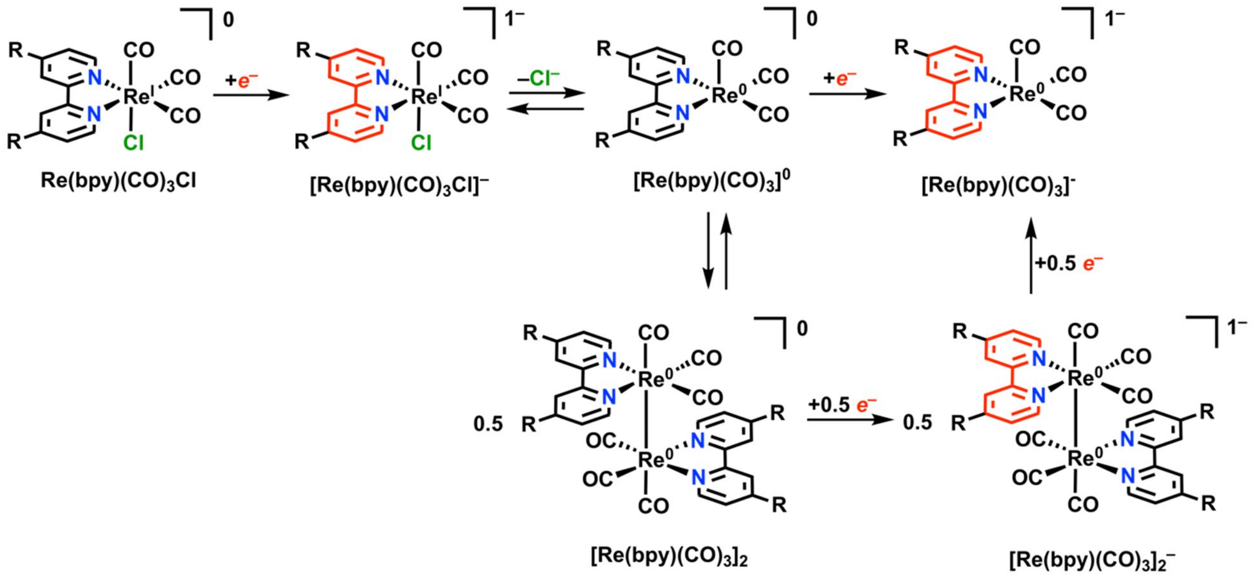

Figure 1.8. Faradaic reduction of Re(bpy)(CO)$_3$X. Adapted with permission from *Organometallics*, **2014**, *33*, 4550–4559. Copyright 2014 American Chemical Society.

There are also two possible mechanisms for CO$_2$RR under electrocatalytic conditions. First, a relatively slower bimolecular process involving two equivalents of [Re(bpy)(CO)$_3$]^0 can occur, resulting in a net reductive disproportionation of two equivalents of CO$_2$ into one each of CO and CO$_3^{2-}$.[106] Second, a unimolecular catalytic process with [Re(bpy)(CO)$_3$]$^–$ as the resting state, where the two-electron reduction of CO$_2$ occurs at a single Re center.[106-107] As is observed with the [Fe(TPP)]$^+$-based electrocatalysts above, there are observable enhancements in TOF$_{max}$ and catalyst stability for CO$_2$RR upon the addition of a sacrificial proton donor.[62]

As stated above, in the proposed mechanism for electrocatalytic CO$_2$RR, a monoanionic five-coordinate species [Re(bpy)(CO)$_3$]$^–$ is invoked as the active species which binds CO$_2$ **Figure 1.9**.[107] This has been validated experimentally through direct synthesis of [Re(bpy)(CO)$_3$]$^–$ using chemical reducing agents, with subsequent spectrochemical studies demonstrating a kinetic preference for CO$_2$ over H$^+$.[108-109] Re(bpy)(CO)$_3$(η^1-CO$_2$H) is initially formed upon the binding and activation of CO$_2$ by

$[Re(bpy)(CO)_3]^-$ with a proton donor present. Further reduction generates an anionic species, $[Re(bpy)(CO)_3(\eta^1\text{-}CO_2H)]^-$ at which point C–O bond cleavage is facilitated by an exogenous proton source to generate water and the neutral species, $[Re(bpy)(CO)_4]^0$. CO release from the 19e⁻ complex $[Re(bpy)(CO)_4]^0$ is facile and additional reduction regenerates the resting $[Re(bpy)(CO)_3]^-$ state. In the $Re(bpy)(CO)_3X$ catalyst family, most work has focused on modulating the steric and electronic properties of the bipyridine ligand in attempts to modulate the reducing power and activity of Re. Generally, the use of electron-rich bpy ligands like 4,4′-di-*tert*-butylbpy enhances the activity of the catalyst by creating a more nucleophilic Re center upon reduction, albeit at larger overpotentials.[110]

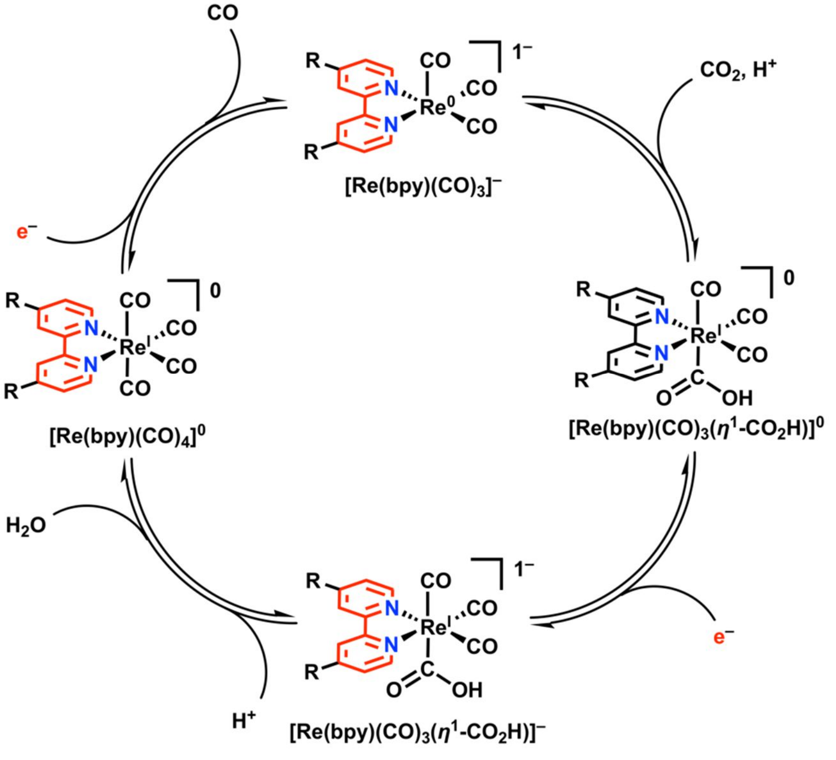

Figure 1.9. $2e^-/2H^+$ dependent catalytic cycle for $Re(bpy)(CO)_3X$ in the reduction of CO_2 to CO. Adapted with permission from *Organometallics*, **2014**, *33*, 4550–4559. Copyright 2014 American Chemical Society.

Kubiak and co-workers have demonstrated, however, that steric considerations can supersede electronic effects in this class of catalysts. Re(bpy)$(CO)_3$X-type complexes were synthesized with 3,3′-and 5,5′-dimethyl bpy.[61, 109] The methyl groups in those ring positions have the same Hammett parameters, so for purely electronic reasons, their respective electrocatalytic activities with a $[Re(CO)_3]^+$ core would be expected to be similar. When compared to the unsubstituted parent compound, however, the 5,5′-dimethyl bpy complex shows increased catalytic current at slightly more negative potentials, while the 3,3′-dimethyl bpy shows decreased catalytic current at nearly the same potential. This is rationalized through the steric hindrance from the methyl groups at the 3,3′-positions, which is observed in the non-planarity of the bpy ligand in the crystal structure of the pre-catalyst. Previous experimental and computational studies have postulated that a key mechanistic component is the participation of π^* orbitals in the bpy ligand in the redox mechanism, suggesting that an inability to achieve a higher degree of planarity upon reduction diminishes catalytic activity for 3,3′-dimethyl bpy-based Re catalysts.[61, 107, 109, 111] Since the distribution of added electron density between the bpy ligand and Re metal center has been identified as important to the selectivity for CO_2 over H^+ as the electrophile of choice; it is noteworthy that an essentially steric perturbation of the HOMO of the active species should have this effect.

The effect of secondary-sphere modifications on the Re(bpy)CO_3X system was directly explored through the incorporation of –OH groups at the 4,4′- and 6,6′-positions of the bpy, with the goal of using them both as a pendent proton source and to contribute electron density to the bpy ligand.[56] In this case, the authors found atypical behavior in the during electrocatalysis: the O–H bonds of the bipyridine ligand are cleaved by stepwise electrochemical reduction, which they propose leads to dearomatization of the doubly reduced bpy ligand. By isolating the deprotonated species in a chemical fashion, the authors were able to give both UV-Vis and IR spectroscopic evidence—which aligned well with IR-SEC, UV-Vis-SEC, and DFT calculations—supporting this hypothesis. Interestingly, only the 4,4′-dihydroxybpy complex is active as an electrocatalyst for CO_2RR, while the 6,6′-dihydroxybpy complex completes only ~1 TON for CO, despite having nearly identical electrochemical properties under Faradaic conditions by CV. This result suggests slow CO release and decomposition of intermediates at applied potentials limits activity for the 6,6′-dihydroxybpy derivative.

Further work with monomeric Re(bpy)$(CO)_3$X electrocatalysts showed promising results with the incorporation of peptide linkages of varying lengths containing proton relays and hydrogen bonding groups on the bpy backbone.[60] Through electrochemical experiments, 2D NMR spectroscopy, and molecular dynamics modeling, the study showed that an optimal chain length of five amino acids allows for the peptide backbone to adopt conformations which allow for intramolecular interactions on the NMR timescale. Importantly, this study showed the Re(bpy)$(CO)_3$X system to be stable to peptide synthesis conditions, allowing for insertion of the complex into peptide linkages at any desired point.[60]

The asymmetric incorporation of a thiourea tether into Re(bpy)$(CO)_3$X systems has been shown to be a successful technique for enhancing the CO_2RR activity.[112] Interestingly, the sulfur atom of the thiourea tether was shown to bind CO_2 *prior* to reduction of the Re catalyst, which is expected to lower the reorganization energy penalty expected for the reduction of the linear CO_2 molecule. This interaction was shown to work synergistically with the reduced Re state, as the thiourea moiety also enhanced the catalytic response by acting as a pendent proton donor capable of beneficial hydrogen bonding interactions and facilitating C–O bond cleavage. Added Brønsted acids inhibited catalytic activity, likely the result of competitive interactions with the pendent thiourea tether. In a separate study on the asymmetric incorporation of phenolic pendent proton sources to Re(bpy)$(CO)_3X$, catalysis was ‘turned on’ at lower overpotentials, specifically the first reduction potential by CV in the two complexes studied.[113] These complexes did, however, suffer from low Faradaic efficiencies for CO when no external proton source was present. Each of these catalysts also had issues with electrode absorption phenomena, a deleterious reaction with inhibitory consequences for nominally molecular electrocatalysts.

A Re(bpy)-based CO_2RR catalyst which features an imidazolium group as a charged residue in the secondary-sphere reported by Nippe and co-workers was observed to cause changes in redox properties and mechanism compared to unfunctionalized Re(bpy)$(CO)_3X$.[114] It was proposed that the C_2-H carbon of the imidazole moiety was important for the catalytic enhancement through an alteration of mechanism: theoretical methods suggested that hydrogen bond-like or electrostatic C_2-H---X (X= $Cl^–$, $CO_2^–$, or H_2O) interactions change the ground state energies of intermediates relevant to the catalytic cycle. These assignments were supported experimentally through testing of a control complex where the imidazolium C_2-H was replaced by C_2-CH_3 and the non-linear dependence of the catalytic activity of each complex on [H_2O], which is anomalous to the archetypal electrocatalytic response of Re(bpy)$(CO)_3X$. It was postulated that a reduction-first mechanism for CO_2RR was occurring, where reduction of the Re(I)(η^1-

CO_2H) adduct preceded protonation and C–O bond cleavage, as is classically seen in the unfunctionalized complex (**Figure 1.9**).

The effects of charge on the electrocatalytic activity of Re(bpy)$(CO)_3$X were studied in a series of polymeric frameworks using a series of charged monomers.[66] Three norbornenyl-based polymers containing either positively charge quaternary ammonium, neutral phenyl, or negatively charged trifluoroborate moieties were generated through ROMP and covalently end-labelled with a Re(bpy)$(CO)_3$X-based terminating reagent. Electrochemical studies in acetonitrile indicated that the polymers containing quaternary ammonium salts exhibited catalytic behavior at a significantly more positive potential (~300 mV) than the neutral polymer, which behaved consistently with unfunctionalized Re(bpy)$(CO)_3$X. The incorporation of negatively charged groups caused a shift to more reducing potentials and catalytic activity was not observed in the solvent window. The incorporation of known catalysts onto a polymeric framework with the ability to tune reduction potential is a possible precursor to highly ordered structures such as thin films, abiotic metalloproteins, porous catalytic membranes, and cationic nanoparticles for use in devices.

1.5.3 Secondary-Sphere Effects in Mn(bpy)$(CO)_3$X

Unpublished results referenced by Johnson *et al.* in 1996 stated that Mn(bpy)$(CO)_3$X, unlike its third row congener Re, was inactive for electrocatalytic CO_2RR under aprotic conditions.[115] A more recent examination by Deronzier and co-workers in 2011 repeated this result, but also showed that the addition of a weak proton donor facilitated a significant and selective electrocatalytic response for CO_2RR to CO.[59] One important mechanistic detail about the Mn(bpy)$(CO)_3$Br system is that upon reduction by a single electron and subsequent loss of Br^-, a Mn–Mn dimer $[Mn(bpy)(CO)_3]_2$ can rapidly form with rates approaching the diffusion limit **Figure 1.10**.[105] The formation of this dimer has two detrimental effects: 1) it increases the electrochemical driving force required to generate the catalytically active monoanionic five-coordinate $[Mn(bpy)(CO)_3]^-$ species required for CO_2RR (the Mn–Mn bond requires more reducing potentials to cleave) 2) it reduces the activity of the complex towards CO_2RR as a non-catalytic competing pathway.[64, 103]

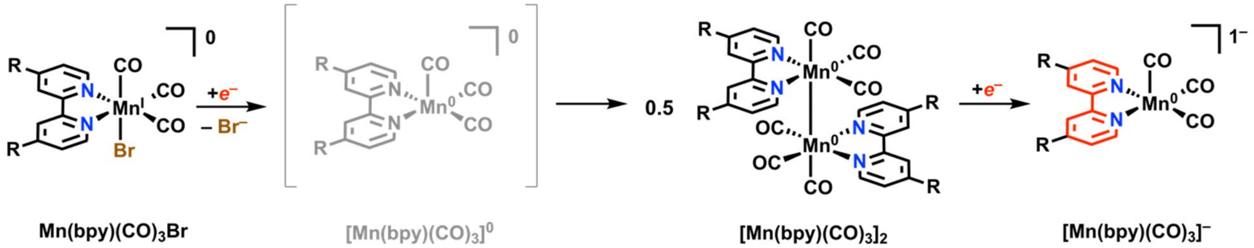

Figure 1.10. Faradaic reduction mechanism of $Mn(bpy)(CO)_3X$. Adapted with permission from *Organometallics*, **2014**, *33*, 4550–4559. Copyright 2014 American Chemical Society.

In attempts to combat these detrimental effects from dimerization, a bulky bpy analog was designed (6,6′-dimesitylbpy = mesbpy).[7, 116] This ligand framework proved to be effective in eliminating the dimerization reaction. Rather than two irreversible $1e^-$ waves on the reductive sweep as seen in $Mn(bpy)(CO)_3X$, a single reversible $2e^-$ wave was observed.[7] This leads to the formation of monomeric, anionic $[Mn(mesbpy)(CO)_3]^-$ at 300 mV more positive potentials than in the case of the original $Mn(bpy)(CO)_3X$ complexes.[7] In the presence of CO_2 and a proton source, the $2e^-$ reversible feature becomes irreversible and shifts towards positive potentials, which is indicative of CO_2 binding.[7] This mechanistic difference was confirmed through control experiments, infrared spectroelectrochemistry,[117-121] and the direct synthesis of the active species. A significant catalytic response does not occur in the presence of Brønsted acids until potentials similar to those which are catalytic for the un-functionalized parent complex, however.[7] Rapid C–O bond cleavage in the hydroxycarbonyl intermediate [Mn(mesbpy)(CO)$_3$(η^1-CO$_2$H)] does not occur until 'over-reduction' to generate [Mn(mesbpy)(CO)$_3$(η^1-CO$_2$H)]$^-$ at potentials 400 mV more negative than the 2e$^-$ reversible feature (**Figure 1.11**).[65] To take advantage of the initial CO$_2$ binding event by [Mn(mesbpy)(CO)$_3$]$^-$ at more positive potentials, a subsequent report used Lewis acid additives.[116] This strategy proved successful, as addition of Mg^{2+} ions as co-substrate to solution aided in C–O bond cleavage at the potential where CO$_2$ binding occurs, greatly reducing the overpotential required for the generation of CO from CO$_2$.[116]

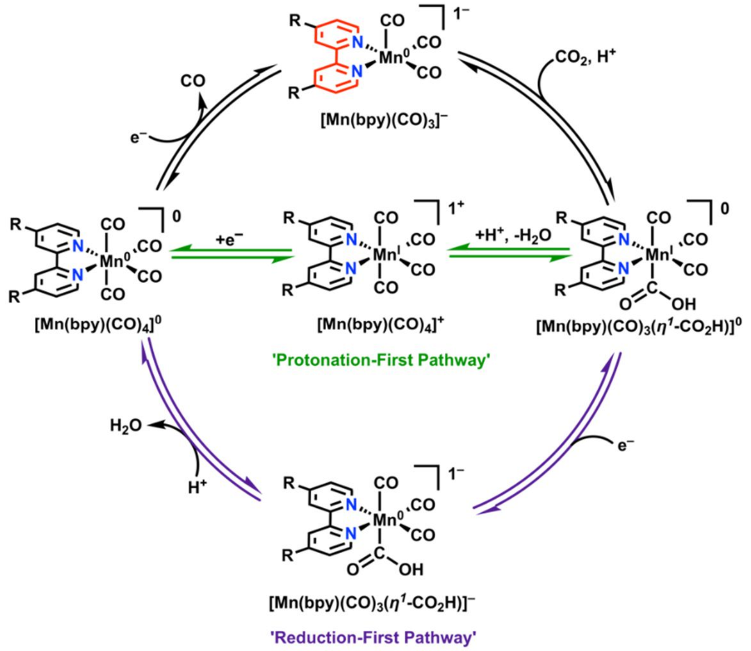

Figure 1.11. 'Protonation-First' and 'Reduction-First' Pathways for CO$_2$RR by Mn(bpy)(CO)$_3$X.[65]

Initial attempts to incorporate pendent proton relays into the Mn(bpy)(CO)$_3$X framework involved asymmetric attachment of phenol moieties onto the bpy ligand.[57-58] This led to enhanced activity in comparison to the parent Mn(bpy)(CO)$_3$X complex, including activity in the absence of a proton source; however, the competitive dimerization reaction was still apparent in each case.[57-58] Converting the pendent –OH groups to ethers with methoxy groups showed insignificant or no catalytic activity in control studies for these derivatives.

To extend these studies to symmetrically functionalized systems, Rochford and co-workers synthesized a methoxy ether-containing analogue of the bulky bpy ligand, 6,6′-(2,6-dimethoxyphenyl)bpy $[(MeO)_2Ph]_2$bpy.[8, 63] A combined experimental and theoretical analysis showed that through the introduction of sufficiently acidic exogeneous proton sources, the slower ‘protonation-first’ pathway seen in the original bulky bpy study could be ‘turned on’ at lower overpotentials in comparison to the ‘reduction-first’ pathway at more negative potentials.[8] In the protonation-first pathway, a bound hydroxycarbonyl is formed and further protonation by a sufficiently strong acid can lead to the facilitation of C–O bond cleavage prior to reduction and release of CO at more positive potentials than the reduction-first pathway (**Figure 1.11**). In the reduction-first pathway, a bound hydroxycarbonyl is again formed; however, without a sufficiently strong acid present, reduction of the hydroxycarbonyl must occur at more negative potentials prior to protonation and C–O bond cleavage.

The acid-dependence of the ‘protonation-first’ and ‘reduction-first’ pathways for Mn($[(MeO)_2Ph]_2$bpy)$(CO)_3$X was rationalized through a hydrogen-bonding interaction between the Mn-bound η^1-CO_2H hydroxycarbonyl species and the pendent Lewis base groups located on the ligand (**Figure 1.12**). This hydrogen bond donor-acceptor interaction was also proposed to facilitate the subsequent transfer of a second equivalent of a sufficiently strong Brønsted acid additive to protonate and assist in concerted reduction and C–O bond cleavage, ultimately producing H_2O and Mn-bound CO.[8] In the presence of a proton source of insufficient acidity, the reduction of the bound η^1-CO_2H hydroxycarbonyl species is instead required before protonation and C–O bond cleavage can occur, as is observed with the 'over-reduction' of the Mn catalyst with the 'bulky' bpy ligand.[8] Importantly, no metal-metal dimerization reaction was observed for this ligand.

Recently, a charged imidazolium functionality was also introduced asymmetrically into the $Mn(bpy)(CO)_3X$ system.[122] A series of derivatives examining hydrogen bonding effects showed activity for CO_2RR at potentials of only –1.4 V vs Fc^+/Fc in the presence of water. This was postulated to originate from a synergistic effect between the pendent imidazolium functionality and a network of water molecules in the solvation shell that facilitated CO_2RR. The combined use of charge and hydrogen-bonding donors shows promise for lowering the catalytic overpotential, but further work is needed to enhance Faradaic efficiencies to match other catalyst platforms in this family.

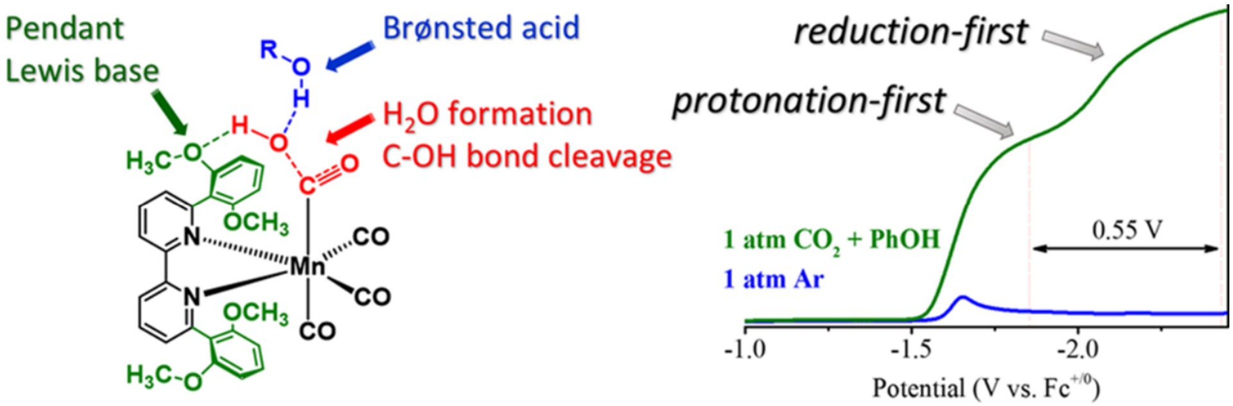

Figure 1.12. Figure showing proposed transition state which occurs to turn on a low overpotential, secondary-sphere promoted mechanism for CO_2RR with $Mn((OMe)_2bpy)(CO)_3X$. Adapted with permission from *J. Am. Chem. Soc.*, **2017**, *139* , 2604–2618. Copyright American Chemical Society 2017.

1.5.4 Secondary-Sphere Effects in $Ni(cyclam)]^{2+}$

The electrocatalytic activity of a $[Ni(cyclam)]^{2+}$ (cyclam = 1,4,8,11-tetraazacyclotetradecane) derivative was first reported in 1980 by Fisher and

Eisenberg.[123] It has been the subject of continuous study because of its tolerance for a wide range of acid strengths and solvent systems without a loss of catalytic activity.[71-74, 124] The activity of Ni(cyclam)]$^{2+}$ for electrocatalytic reduction of CO_2 to CO in the presence of water as a Brønsted acid source was attributed specifically to the *Trans I* isomer (one of six possible isomers based on the orientation of the H atoms on the four metal-coordinated secondary amines in the macrocycle; all four H atoms are cofacial). This isomer is the most favorable for high CO_2RR activity due to the hydrogen bond donor-acceptor interactions between the ligand NH groups and a Ni-bound CO_2 molecule.[75] Furthermore, DFT calculations have indicated that the *trans-I* isomer has a more stable CO_2 adduct than the *trans-III* isomer (two H atoms are cofacial) by approximately 3 kcal/mol.[76]

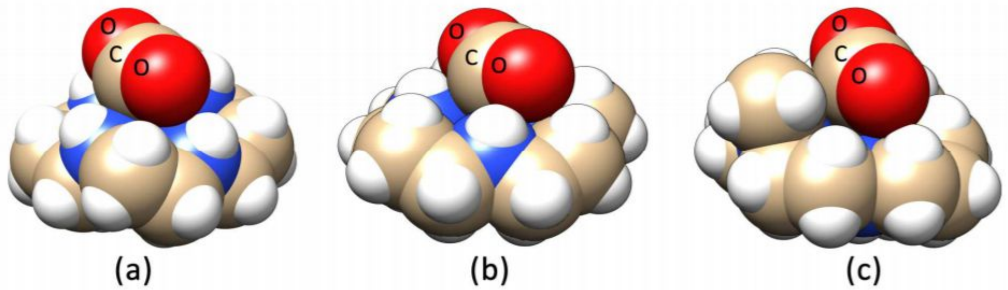

Figure 1.13. Space filling models of *trans-I* [Ni(cyclam)(CO_2)]$^+$ (a), *trans-III* [Ni(cyclam)(CO_2)]$^+$ (b), and [Ni(DMC)(CO_2)]$^+$ (c). Structures indicate that enhanced CO_2RR in the case of *trans-I* [Ni(cyclam)(CO_2)]$^+$ may be due to increased stabilization of the CO_2 adduct through increased hydrogen bond donors oriented towards the hydrogen bond accepting O atoms on the CO_2 adduct. Used with permission from *Inorg. Chem.*, **2014**, *53*, 7500–7507. Copyright American Chemical Society 2014.

Further evidence for the importance of the amine protons and these hydrogen bonding interactions is evident in a comparison with the *N*-alkylated derivatives [Ni(dimethylcyclam)]$^{2+}$ and [Ni(tetramethylcyclam)]$^{2+}$, where greatly diminished activity for electrocatalytic CO_2RR is observed.[75] The absence of hydrogen bond-induced stabilization effects and increased steric parameters make CO_2 binding less facile in the *N*-alkylated derivatives (**Figure 1.13**). Pendent proton donor effects have been shown with other functional groups as well: the introduction of a carboxylic acid on the carbon backbone of Ni(cyclam)]$^{2+}$ improves its activity by making it stable and selective for CO_2RR down to pH = 2 at similar overpotentials to other reported water-soluble CO_2RR catalysts.[125]

The use of an exogenous urea additive with Ni(cyclam)]$^{2+}$ was shown to improve catalytic activity for CO_2RR for similar reasons.[77] This study demonstrated that the urea additive acted as a co-catalyst for the system, and it was proposed that its unique structure allows for it to promote CO_2RR through the formation of multipoint hydrogen bonds with the bound CO_2 adduct [Ni(cyclam)(η^1-CO_2)]$^+$.[77] This conclusion was supported through the introduction of multiple cationic and neutral additives with similar pK_as. In each case the co-catalytic response observed with urea was not present.[77] Although the urea additive was not tethered to cyclam, it is conspicuous that it should have a co-catalytic role with both Ni(cyclam)]$^{2+}$ and Re(bpy)-based catalysts for CO_2RR, *vide supra*.

1.5.5 Secondary-Sphere Effects in Multimetallic Systems

Multimetallic systems are important examples of secondary-sphere interactions, because they are common to the enzymes which catalyze CO_2RR chemistry.[80, 126] In many cases, these multimetallic systems work cooperatively to both store excess charge and to activate the molecule of interest using ‘push-pull’ donor-acceptor effects. Homobimetallic co-facial [Fe(TPP)]$^+$ systems connected by a phenylene bridge were synthesized to generate a bimetallic species from the well-known [Fe(TPP)]$^+$ system discussed above.[53] By tuning the Fe-Fe distance through synthetic modification, CO_2

binding could be induced at the $Fe^{3+/2+}$ wave rather than the $Fe^{1+/0}$ as observed for most $[Fe(TPP)]^+$ systems.[53, 97] This was rationalized through the expected Fe-Fe distance of 3.2-4.0 Å in the *ortho*-bridged system, which would be suitable for binding the linear CO_2 molecule. In contrast, the *meta*-bridged system was expected to have a significantly shorter separation and showed diminished activity similar to monomeric $[Fe(TPP)]^+$.[53] The *ortho*-bridged system has significant catalytic activity (TOF_{max} = 4300 s^{-1}) and high Faradaic efficiency for CO (95%) at an overpotential of ~0.7 V in the presence of 10% H_2O in DMF, which is a significant improvement over monomeric $[Fe(TPP)]^+$. The overpotential for this class of homobimetallic catalyst could be further tuned using electron-withdrawing and -donating substituents on the phenyl rings of each $[Fe(TPP)]^+$ unit (**Figure 1.14**).[51] When the overpotential was synthetically tuned to ~0.4 V with electron-withdrawing groups, a ~3 fold decrease in activity in comparison to the parent phenyl-functionalized dimer was observed.[51] Chang and co-workers have recently demonstrated that these beneficial multimetallic effects extend beyond bimetallic systems using a porous organic cage containing six $[Fe(TPP)]^+$ units which was active for CO_2RR in aqueous solutions.[127]

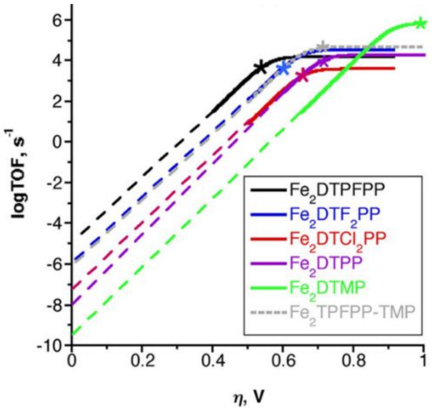

Figure 1.14. Catalytic Tafel plot showing overpotential tuning in co-facial Fe(TTP) through the introduction of electron with drawing substituents on the phenyl groups of the porphyrin system. Adapted from *Scientific Reports,* **2016**, *6*, 24553.

A multimetallic Fe carbonyl cluster system with an interstitial main group element $[Fe_4X(CO)_{12-n}L_n]^-$ (X=N or C, L = another ligand, n = 1 or O) has been developed by the Berben group for the reduction of CO_2 to formate under both aqueous and non-aqueous conditions.[128-131] This cluster is proposed to generate formate *via* an intermediate bridging hydride. The bridging hydride on the cluster motif has the ideal hydricity to selectively generate formate in the presence of CO_2, preventing the competitive formation of H_2.[131] Pendent proton groups in this system alter the selectivity of this catalyst family from nearly quantitative generation of formate to the generation of H_2, which highlights the importance of controlling the kinetics of substrate delivery in determining selectivity for competitive CO_2 and H^+ reduction reactions.[132]

The development of bimetallic Re complexes based on $Re(bpy)(CO)_3X$ and its derivatives has been of recent interest for both photocatalytic[133-134] and electrocatalytic processes due to the concentration dependent formation of binuclear intermediates as part of the catalytic cycle.[67, 70, 135-136] In electrocatalytic systems, the first bimolecular Re system studied utilized acetoamidomethyl modified bpy to generate a supramolecular catalyst system *in situ*. This system operated at more positive potentials (~250 mV) in MeCN than the 4,4′-dimethylbpy-based control complex as the result of a hydrogen-bonded dimer active state, albeit with a lower TOF and FE than the unimolecular process.[70] To further probe this hydrogen bond-based dimer system, a subsequent report focused on a heterobimetallic Re-Mn construct using a 1:1 mixture of acetoamidomethyl modified $Re(bpy)(CO)_3X$ with acetoamidomethyl modified $Mn(bpy)(CO)_3X$.[68] Results from this study indicated a cooperative heterobimetallic pathway was operative, and it was proposed that the Mn center was activating CO_2 followed by protonation to generate a

Mn-bound hydroxycarbonyl species within the heterobimetallic dimer. Enhanced reduction-first pathway kinetics were initiated in this case by electron transfer from the reduced Re species present in the dimer.

Further modifications to this supramolecular system replaced the acetoamidomethyl unit with an amide-linked PhOH-containing tyrosine functional group.[67] This modification lead to an increased TOF_{max} in comparison to the initial complex and near quantitative Faradaic efficiency; mechanistic studies where the PhOH unit was substituted for a phenyl ring showed the pendent –OH functionality was essential for improving catalytic activity in the bimetallic mechanism.[67] The 'soft' non-covalent linkages used in this strategy are reminiscent of biological active sites: the catalytic system can adopt a variety of conformations on the potential energy surface facilitated by weaker interactions, instead of more rigid systems reliant on distance or conformational tuning through purely synthetic means. The success of this approach is dependent on how well the weak interactions overcome the added diffusional component of the bimolecular reaction mechanism.

Work to generate rigid homobimetallic $Re(bpy)(CO)_3X$ systems where the metal centers are in close proximity has been achieved using an anthracene linker by Jurss and co-workers.[135] This complex can be isolated as *cis* or *trans* isomers through chromatography, which alters the relative positioning of the Re centers.[135] The *cis* isomer, in which the Re centers are in close proximity to one another, outperformed both a monometallic anthracene control complex and the *trans* isomer of the homobimetallic species. Another covalently linked homobimetallic system with an imidazole-pyridine bridge was examined Siewert and co-workers.[136] The observed catalytic activity of the homobimetallic species outperformed the mononuclear control complex which was inactive for CO_2RR.[137] The introduction of phenol linker between the two imidazole-pyridine arms to generate a proton relay in close proximity to the active site of the two metal centers was also examined.[136] The pendent proton source enhanced the activity of the bimetallic Re complex, with Faradaic efficiencies for CO of ~60%.[136]

1.5.6 Secondary-Sphere Effects in Emerging Systems

Several relatively new systems have also been reported where pendent functional group interactions are essential to the overall mechanism (**Figure 1.15**). A recent report on a series of cobalt(cyclopentadienyl)(P_2N_2) complexes by Artero and co-workers showed that pendent tertiary amines enabled selective formate generation from CO_2.[138] DFT calculations suggest that a reaction-defining transition state occurs where one of the pendent amines forms a hydrogen-bonding interaction with water to align it with CO_2 as simultaneous hydride transfer occurs from the Co center, lowering the overall transition state energy and enhancing activity.[138]. Work in our own group discussed in later chapters has identified a Schiff base-type ligand based on bpy as promising new direction: the Fe(III) derivative is active for the reduction of CO_2 to formate with PhOH as a proton source. Mechanistic investigations suggest the Fe-bound oxygen atoms act as a site for protonation upon initial reduction of the complex, generating a pendent proton source for the reaction at applied potential.[139] Further study of derivatives of these Fe- complexes indicated utilization of hydrogen bonding moieties for preconcentration of Brønsted acids is a promising strategy for enhancing activity and lowering overpotential in this family will be discussed in another chapter of this thesis.[140] A macrocyclic, aminopolypyridyl Co complex from Marinescu and co-workers generated CO in a near quantitative fashion in the presence of MeOH as a proton source.[141-142] Upon alkylation of the pendent amine functionalities, a two-fold decrease in activity occurred, suggesting that the pendent protons on the amines linking the pyridyl groups play an important role as hydrogen-bond donors during CO_2RR.[141-142] The activity and selectivity of all these platforms are promising for future studies on optimizing secondary-sphere effects.

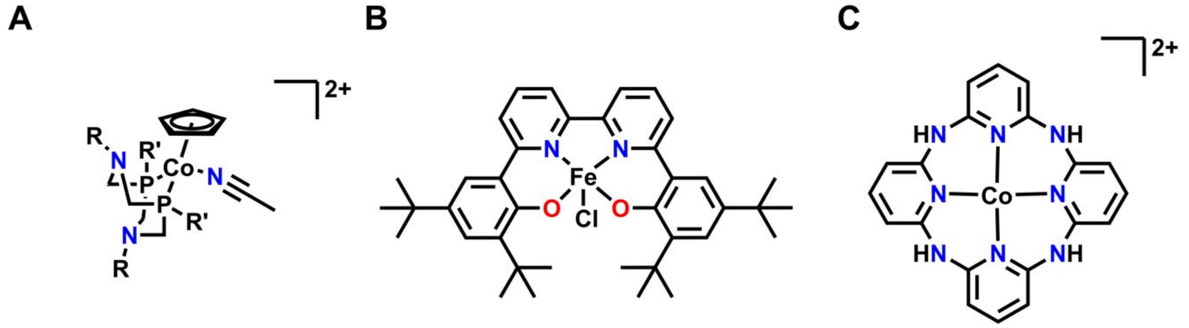

Figure 1.15. (A) Co(Cp)(P_2N_2) utilizing pendent tertiary amines for reduction of CO_2 to formate. (B) Fe(^{tbu}dhbpy)Cl is protonated at the Fe-coordinating O atoms upon reduction and reduces CO_2 to formate. (C) Macrocyclic-aminopyridyl complex which reduces CO_2 to CO.

1.6 Conclusions and Future Directions of Secondary-Sphere Effects with Molecular CO_2RR Electrocatalysts.

Molecular electrocatalysts for CO_2RR are of continuing interest for their possible utility in storage of renewable energy in chemical bonds. Through careful mechanistic observations and design principles inspired by nature, researchers have managed to improve many of the known catalyst systems for CO_2RR. This iterative optimization of catalysts has demonstrated that the incorporation of pendent Brønsted acids/bases, charged groups, sterically bulky groups, Lewis basic sites, and the use of multimetallic sites with careful solvent choice can lead to improved catalytic activity and even new mechanisms through secondary-sphere effects reminiscent of biological systems.

With these successes in mind, it is useful to acknowledge that there is still much work to do: CODH's can *reversibly* interconvert CO_2/CO in aqueous systems with a TOF_{max} of 0.5 s^{-1} (CO_2 to CO) and 31,000 s^{-1} (CO to CO_2) with minimal overpotentials.[143] However, the use of secondary-sphere effects in abiotic molecular electrocatalysts has already been shown to be important for enhancing selectivity and activity. Further development in this area may lead to development of catalysts capable of reduction products beyond CO and HCO_2H, which are a burgeoning area for molecular electrocatalysts. Incorporation of molecular Cu, which can generate hydrocarbons from CO_2 in aqueous solutions as a heterogenous catalyst,[144] into a TPP-based system has been shown to be a successful strategy for generating methane and ethylene in an electrocatalytic fashion.[145] Bringing molecular design principles to materials seems to be another viable strategy for using secondary-sphere effects in electrocatalysis: Gong *et al.* immobilized porphyrin cages on Cu electrodes to tune activity and selectivity for carbon-carbon coupling products from CO_2RR through supramolecular effects.[146] Recent reports have also described photocatalysts which convert CO_2 to methane from molecular catalysts related to those described here, which is promising for developing eventual electrocatalytic behavior.[147-148]

Running CO_2RR reactions reversibly with abiotic systems could close the 'loop' on the energy cycle, enabling the development of new fuel cell technologies beyond H_2.[149-151] New catalyst systems which approach these biological efficiencies are unlikely to be rapidly found through purely synthetic routes due to the inherent depth and synthetic difficulty of the parameter space. Rather, the most efficient approach to future catalyst development should utilize a multidisciplinary approach which combines statistical, computational, and experimental methods to assist in the search for new CO_2RR catalysts unique from the current catalytic systems by improving predictive power.

1.7 Alternate Approaches: O_2 Reduction

While the reduction of CO_2 is a promising avenue for optimization of reaction parameters with the eventual goal of developing industrially relevant materials, a multi-faceted approach towards discovery of systems with unique reactivity in energy relevant transformations is important. To this end, study of the oxygen reduction reaction (ORR) has special interest because it is an ideal reaction for the cathodic half of fuel cells when the $4e^-/4H^+$ product, water, is selectively formed rather than the $2e^-/2H^+$ product, hydrogen peroxide. This is, however, challenging because large overpotentials are often required to run the more kinetically challenging production of water. The current state-of-the-art cathode material for ORR in fuel cells is expensive and rare platinum metal. Development of new catalysts which can supplant platinum as the industry standard material for ORR is important to the electrochemistry field as a whole.

1.8 Benchmarking Catalysts for the O_2 Reduction Reaction

Benchmarking catalysts for O_2 reduction is similar to the benchmarking for CO_2 reduction discussed above. There are two possible pathways: the $4e^-/4H^+$ reduction to water and the $2e^-/2H^+$ reduction to hydrogen peroxide.[152] The standard potential for these two reduction events are located at 1.229 V vs SHE and 0.695 V vs SHE for the production of H_2O and H_2O_2, respectively.[153] This corresponds to a separation in standard potential of 0.534 V. If a catalyst can be designed such that its reduction potential is more positive than the standard reduction potential for H_2O_2 production in a given system, it will thermodynamically only allow for the production of H_2O.[154]

After catalyst selectivity is determined, comparison between catalysts can be performed in a very similar fashion to those for the CO_2RR reaction. Both Tafel plots and comparison between log(TOF) and η are utilized for this capacity. Scaling relationships depending upon acid strength, O_2 concentration, and reduction potential of the catalyst are often observed within catalyst families, which give us insight into the reaction mechanism and the key parameters to focus upon for catalyst design within a family.[93, 154-156] An example of this can be seen in **Figure 1.16**.[93]

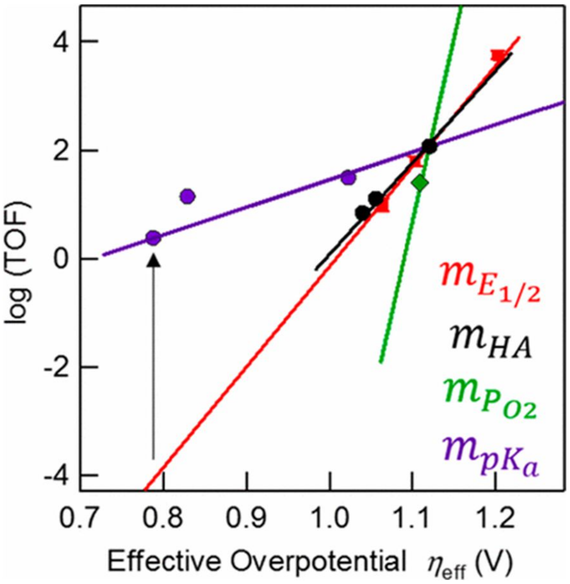

Figure 1.16. Scaling relationships for Fe(TPP) ORR catalysis predicted (lines) and measured (points) upon changing the acid concentration (black), partial pressure of O_2 (green), pK_a of the acid (purple) and $E_{1/2}$ of the catalyst. The intersection point is Fe(TPP) with 100 mM H-DMF$^+$ under 1 atm O_2. Reproduced with permission from *J. Am. Chem. Soc.* **2017**, *139*, 11000–11003, DOI: 10.1021/jacs.7b05642, Copyright 2017 American Chemical Society. Further permissions should be directed to the ACS.

One caveat which much be discussed for ORR catalysts is the replacement of the electrode with a soluble reductant like ferrocene (Fc) or decamethylferrocene (Cp^*_2Fe) due to inherent background reactivity of O_2 with electrode materials in the presence of added acid at reducing potentials.[152] This replacement leads to a few new considerations, namely that the added chemical reductant must be reducing enough such that electron transfer to the catalyst system is favorable. This does not, however, mean the standard reduction potential for the chemical reductant needs to be more negative than the catalyst of interest, because the solution potential (E_{soln}) will follow the Nernst equation, **Eq (1.3)**. This tells us that the very large (initially infinite) excess of reduced form of the chemical reductant (R) in comparison to the oxidized form (O) causes large shift towards negative potentials of the solution such that electron transfer to a catalyst species whose redox potential is more negative than the standard reduction potential reductant is possible.

$$E_{soln} = E^{0}_{ox/red} - \frac{RT}{nF}\log\left(\frac{[R]}{[O]}\right) \qquad (1.3)$$

For example, in a system utilizing 40 μM catalyst and 0.9 mM reductant with water as the sole product, the redox potential of the reductant, R, in solution is >100 mV more negative than its standard potential for the first 0.1 TON of the system according to **Eq (1.3)**. In addition to this shift of the reductant, the other components of the reactants in large excess also cause the system to shift more towards favorable electron transfer. This does not preclude the need to carefully select a reductant, as a reductant with a standard potential too positive will be unable to successfully transfer electrons, while a reductant which is too negative may have its own significant background reactivity with O_2. When sacrificial chemical reductants are utilized for the ORR, the most common potential used for benchmarking is either the catalyst standard reduction potential or its half-wave potential as determined by electrochemical techniques. Due to rapid changes in E_{soln} over the course of the reaction, it is imperative that the method of initial rates be used when the catalyst’s reduction potential is more negative than that of the chemical reductant. “Buffered” (both reduced and oxidized form of electron donor are present) systems can also be utilized as a complementary approach to minimize effects from solution redox change.

1.9 Mononuclear Molecular Electrocatalysts for O_2 Reduction

The majority of the known mononuclear earth-abundant molecular catalysts for the ORR have a Co-[44, 157-173] or Fe-[159, 164, 174-190] based active site, with a few examples of Mn-[159, 166-167, 191-194] or Cu-[159, 195-201] based active sites. Here, we will focus on Co- based systems, as they are the focus of ORR studies conducted in later chapters. While Fe-based systems generally generate H_2O as a primary product for ORR, mononuclear cobalt N_4 macrocycles including derivatives of porphyrins,[154, 157-161, 166-168, 172-173] corroles[170, 202], phthalocyanines[164, 169, 174, 203-204], chlorins,[44, 171] and cyclam[162-163, 166, 205-207] have been studied in great detail for ORR, with the majority demonstrating selectivity for H_2O_2. However, Brønsted-acid scaling relationships can be used to alter product selectivity through thermodynamic bracketing.[152, 154] Cobalt complexes containing non-macrocyclic N_2O_2 salen, salophen, and acen derivatives have been known to bind dioxygen since the late 1930s, but relatively few studies have been performed on their activity towards ORR and these systems will be the target of further study in this thesis.[154, 208-213]

1.9.1 Co(porphyrin) derivatives as ORR catalysts

Mononuclear Co(porphyrin) derivatives are the most highly studied group of compounds for the ORR based on Co. All of the tested Co(porphyrin) derivatives to date have generated H_2O_2 selectivity with the exception of a single study, which utilized thermodynamic bracketing to selectively access H_2O production.[152, 154] The most studied derivative of Co(porphyrin) for the ORR reaction is Co(TMPyP) shown in **Figure 1.17.**

Initial studies in aqueous solution showed it is readily absorbed to a glassy carbon electrode, which lead to studies comparing its solution and heterogeneous activity. On the glassy carbon electrode, the Co complex catalyzed the production of H_2O_2 from O_2 in aqueous solution at the Co(III)/(II) reduction potential in the presence of either H_2SO_4[157] or triflic acid[159]; however, in *N,N*-DMF solution it electrocatalytically produced 15 TON of $O_2^{\bullet-}$ at the Co(II)/(I) couple, which was indirectly quantified with benzoic acid anhydride.[158] The authors describe the difference in reactivity between adsorbed and homogeneous Co(TMPyP) as a pK_a shift in the adsorbed species.

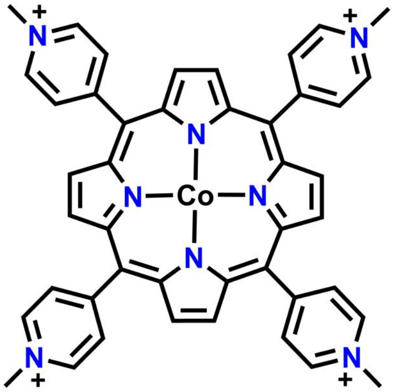

Co(TMPyP)

Figure 1.17. Structure of Co(TMPyP) utilized for ORR in both aqueous and non-aqueous conditions. Co(TMPyP) was studied as either a ClO_4^- or Cl^- salt.[157-159]

Two other charged, water-soluble porphyrins were also tested for ORR (Co(TMPyPBr$_8$) and Co(TSPPBr$_8$), **Figure 1.18**), and were shown to not absorb to the electrode due to non-planarity of the metal complex.[160-161] In each case, H_2O_2 was observed as the major product under all reported conditions, and the Co(II)/(I) reduction potential for Co(TMPyPBr$_8$) was 0.32 V more positive than Co(TSPPBr$_8$), consistent with expected inductive effects. Interestingly, this difference in reduction potential was proposed to have an effect on the catalytic mechanism: with Co(TMPyPBr$_8$) the catalytic onset was near the Co(II)/(I) potential, while the onset was more positive than the Co(II)/(I) potential of Co(TSPPBr$_8$), suggesting O_2 binding prior to reduction in Co(TSPPBr$_8$) had occurred.

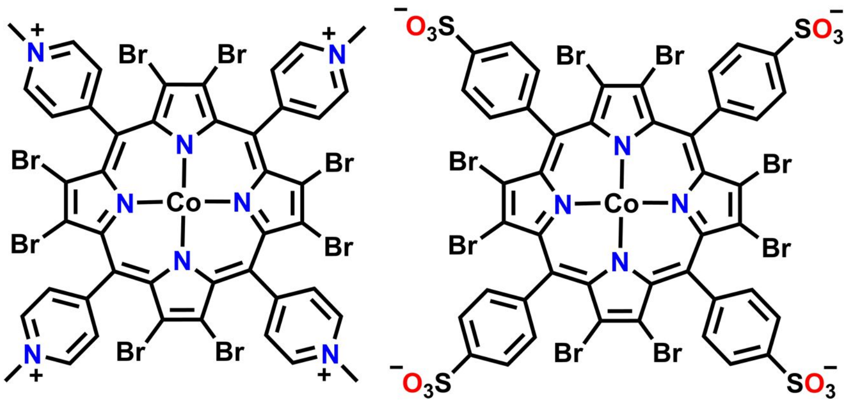

Co(TMPyPBr$_8$) Co(TSPPBr$_8$)

Figure 1.18. Structures of non-planar Co(TMPyPBr$_8$)[161] and Co(TSPPBr$_8$)[160] utilized for ORR in aqueous conditions studied as Cl^- and Na^+ salts, respectively.

Further reports of ruthenium moieties appended to Co(porphyrin) which was grafted to an electrode surface showed activity for O_2 reduction to H_2O_2 in aqueous acidic media containing $[Ru(NH_3)_6]^{2+}$ as chemical reductant (**Figure 1.19**).[165] In the absence of $[Ru(NH_3)_6]^{2+}$, no activity was observed, which was contrary to the authors' initial hypothesis that appended ruthenium sites act as an electron reservoir in the absence of outside chemical reductant to allow for dioxygen reduction. The authors hypothesized that production of H_2O_2 was kinetically favored by fast dissociation of H_2O_2 relative to the delivery of an extra $2H^+/2e^-$ for the production of two equivalents of H_2O.

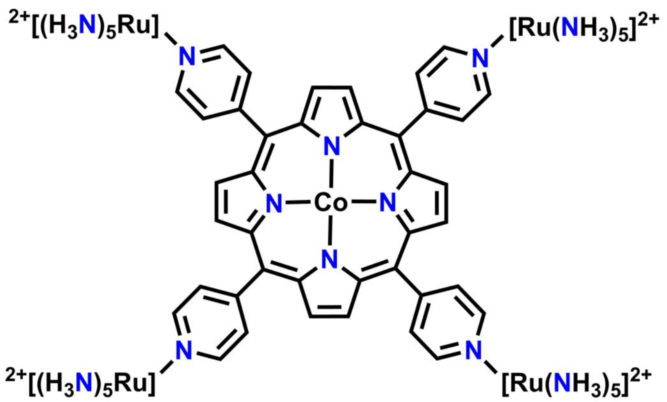

Co(TRuPyP)

Figure 1.19. Structure of Co(TRuPyP) utilized for ORR in aqueous conditions.[165]

Co(II)(TPP) was studied under a few different non-aqueous conditions with different chemical reductants. In MeCN, this complex catalyzes the production of H_2O_2 in the presence of $HClO_4$ with several different derivatives of Fc, with a slower reduction of H_2O_2 to H_2O observed as background reactivity from Fc and $HClO_4$.[166] In this study, the rate-determining step (RDS) was proposed to be electron transfer from the external reductant to Co(TPP)$^+$. However, when studied in dichloroethane utilizing stronger acids (HBAr$^F_4$) and Fc as a chemical reductant, first-order concentration dependencies upon HBAr$^F_4$ and Co(II)(TPP) were observed, indicating that a proton assisted coordination of O_2 to the Co(II) center was the likely RDS.[167] Addition of water to this system was inhibitory towards catalysis, indicating that coordination of water could prevent O_2 from binding to the Co center to initiate the catalytic cycle.

More recent studies of Co(T^{OMe}PP) (T^{OMe}PP = *meso*-tetra(4-methoxyphenyl)porphyrin) in *N,N*-DMF have shown that an understanding of the thermodynamics of the system can enable selective product generation by choosing an appropriate proton donor.[154] When weaker acids are used, Co(T^{OMe}PP) generates H_2O selectively. However; utilization of stronger acids makes H_2O_2 production thermodynamically allowed, and it observed as the major product. Interestingly, under the two conditions different rate laws are observed. In the production of H_2O, a first order dependence upon [Co], [Acid], and [$Cp^*{}_2Fe$] is observed. This suggests a PCET step after O_2 binding is rate determining. In the production of H_2O_2, the reaction shows first order dependence upon [Co], [Acid], and [O_2]. This suggests that in the presence of a strong acid leads to a shift in the redox potential of the process, which enables facile reduction of the system, with proton-assisted O_2 binding being rate determining and the release of H_2O_2 being kinetically favored over a further $2e^-/2H^+$ reduction to water.

1.9.2 Co(corroles) as ORR catalysts

Three derivatives of Co(corroles) have been utilized for the ORR (**Figure 1.20**).[170] Reduction of O_2 to H_2O_2 was indirectly observed through the measurement of electrons transferred under both heterogenous RDE in aqueous $HClO_4$ and chemically reducing conditions utilizing dimethylferrocene in the presence of $HClO_4$ in benzonitrile. The Co(III)(corrole$^{\bullet+}$)/Co(III)(corrole) is the redox couple proposed to be responsible for this reactivity based on EPR spectroscopic evidence.

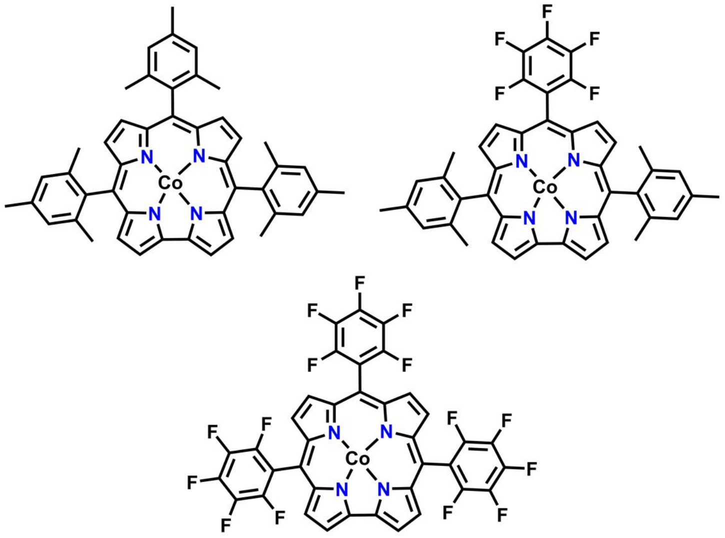

Figure 1.20. Co(corroles) studied for the ORR.[170]

1.9.3 Co(chlorins) as ORR catalysts

Co(chlorins) have been shown to be active for catalytic ORR in similar conditions to Co(corroles) with high stability for the production of H_2O_2 with TON >6 x 10^4 (**Figure 1.21**).[44, 171] Kinetic studies of these complexes revealed that in the presence of dimethylferrocene and $HClO_4$ in benzonitrile that the RDS was proposed to be the net addition of O_2 and H^+ to yield the protonated superoxo adduct [{Co(chlorin)(a)($HO_2^{\bullet}$][H^+]} [Co(II)(chlorin)(a)][H^+]]. Upon addition of $HClO_4$, a positive shift in the Co(III)/(II) reduction potential was observed for Co(chlorin)(a). In Co(chlorin)(b-c), no positive shifts are observed in the redox potential upon addition of $HClO_4$, due to the lower ligand pK_a induced by electron withdrawing effects from ligand modifications. As a result, higher rates were observed with Co(chlorin)(b-c) in relation to Co(chlorin)(a) due to the higher overpotential at which Co(chlorin)(a) operates.

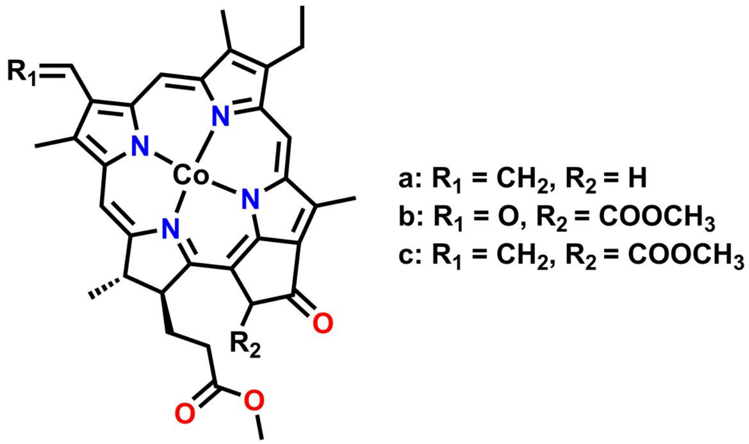

Co(chlorin)(a-c)

Figure 1.22. Co(chlorin) complexes utilized for ORR.[44, 171]

1.9.4 Co(phthalocyanines) as ORR catalysts

The Co(phthalocyanines) (phthalocyanine = pc) shown in **Figure 1.23** have been examined for ORR reactivity.[164, 169, 174, 203] Interestingly, Co(Pc) and Co(TCPc) only bound

O_2 upon the formation of Co(I), with an EC′ reaction leading to O_2 production of H_2O_2 with further reduction to H_2O at more negative potentials.[164, 174, 203] With few exceptions, the Co complexes discussed here bind O_2 in the Co(II) oxidation state. Further studies with Co(Ph_8Pc) showed that ORR reactivity was dependent upon reductant strength with formic acid as a proton donor in benzonitrile.[169] Using dimethylferrocene, the RDS was found to be a PCET reaction between Co(Ph_8Pc), O_2, and H^+ to form a bound hydroperoxyl radical. With more reducing Cp^*_2Fe present as a chemical reductant, the rate-limiting step did not involve O_2, but rather a multiple-site PCET reaction with reduction of the cobalt center and protonation of an outward-pointing *meso*-nitrogen, forming Co(I)(Ph_8PcH) or $[Co(I)(Ph_8PcH_2)]^+$ depending upon the acid strength. Both of these species react rapidly with O_2 with high selectivity for H_2O_2 (>74%), with faster reaction rates observed with Cp^*_2Fe.

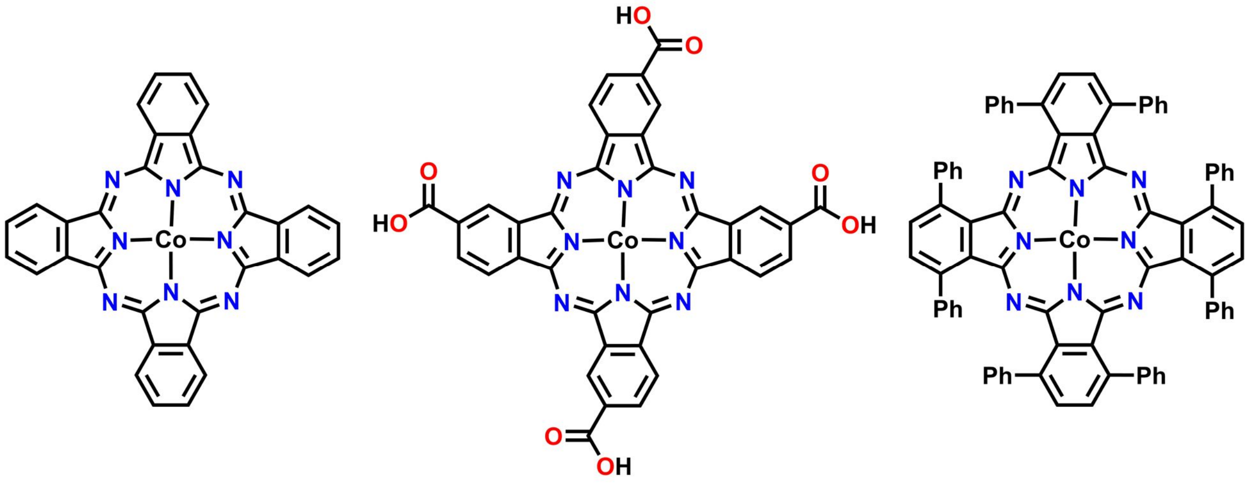

CoPc **CoTCPc** **$CoPh_8Pc$**

Figure 1.23. Co(phthalocyanines) tested for ORR.[164, 169, 174, 203]

1.9.5 $[Co(cyclam)]^{3+}$ derivatives as ORR catalysts

$[Co(cyclam)]^{3+}$ and its derivatives have also been tested for ORR.[162-163, 166, 205-207] Initial studies on $[Co(cyclam)]^{3+}$ (**Figure 1.24**) indicated it reacted in a two-step equilibrium with O_2 upon reduction to theCo(II) oxidation state. Initial formation of a 1:1 Co/O_2 adduct was followed by a reaction with another equivalent of $[Co(cyclam)]^{2+}$ to generate the μ-peroxo bridged species, $[LCo(III)–O–O–Co(III)L]^{4+}$.[205] Subsequent studies on this system investigated the decomposition of the $[LCo(III)–O–O–Co(III)L]^{4+}$ by both oxidizing and reducing agents in acidic aqueous media suggested the dimer could be cleaved through the upon oxidation of the Co- center to Co(III).[206] Finally, the monomeric superoxide complex of $[Co(cyclam)]^{3+}$ was accessed in the presence of excess oxygen, and both inner-sphere and outer-sphere reductants were examined.[207]

After these reports, Anson and co-workers set out to examine $[Co(cyclam)]^{3+}$ and $[Co(hmc)]^{3+}$ (**Figure 1.24**) for ORR.[162-163] Reduction in the presence of O_2 again formed the μ-peroxo bridged dimer $[(L)Co–O–O–Co(L)]^{4+}$, and, at more reducing potentials, a reduction by $2H^+/2e^-$ was observed to give rise to H_2O_2 as the major product of ORR. The more sterically hindered derivative, $[Co(hmc)]^{3+}$, had a smaller equilibrium constant for formation of the μ-peroxo bridged species, and also generated H_2O_2 as the major product.[163] RRDE of $Co(hmc)^{3+}$ indicated that a relatively stable Co–hydroperoxyl, Co(III)(hmc)(OOH) adduct was formed at potentials more positive than those required for production of H_2O_2.[163] The structurally similar $[Co(TIM)]^{3+}$ (**Figure 1.24**) was examined for ORR in the presence of $HClO_4$ with ferrocene derivatives in MeCN.[166] Catalysis was found to have a first-order dependence on all reactants, and H_2O was the proposed product based on the observation of $4e^-$ consumed per O_2 equivalent.

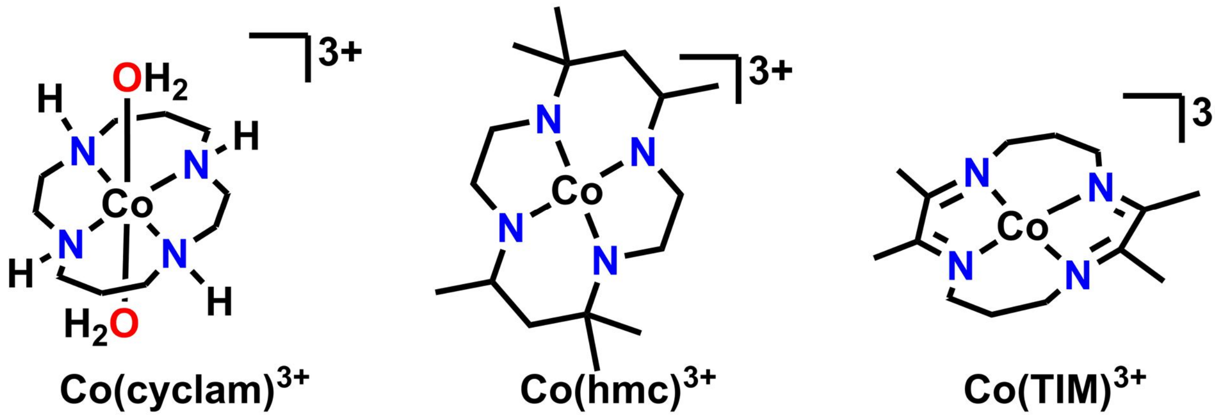

Figure 1.24. Co(cyclam) derivatives studied for O_2 reduction.[162-163, 166]

1.9.6 Co(N_2O_2) derivatives as ORR catalysts

Co(N_2O_2) complexes derived from salens (condensation of salicylaldehyde and ethylenediamine), salophens (condensation of salicylaldehyde and *o*-phenylenediamine), and acen (condensation of acetoacetic acid and ethylenediamine) have recently become of interest. Early work on these complexes indicated their ability to bind and act as oxygen transporters[208]; however, more recent literature reports have indicated their utility as catalysts for the production of H_2O_2 from O_2 in the presence of acetic acid (AcOH) and Cp^*_2Fe in methanol.[210] An initial publication from Stahl and co-workers indicated the reaction exhibited a first-order rate dependence on the concentration of the Co(N_2O_2) complex and AcOH, with a log(TOF) vs overpotential slope of 6.1 log(TOF)/V across a study of eight compounds (**Figure 1.25**). This is consistent with a protonation step after O_2 binding being the rate-determining step for catalysis and a resting state with bound O_2. A subsequent study which combined computational and experimental approaches indicated the rate-determining step of catalysis was protonation of a hydroperoxo species prior to release of hydrogen peroxide.[213] Overall, the complexes have been overwhelmingly selective for H_2O_2.[210, 213]

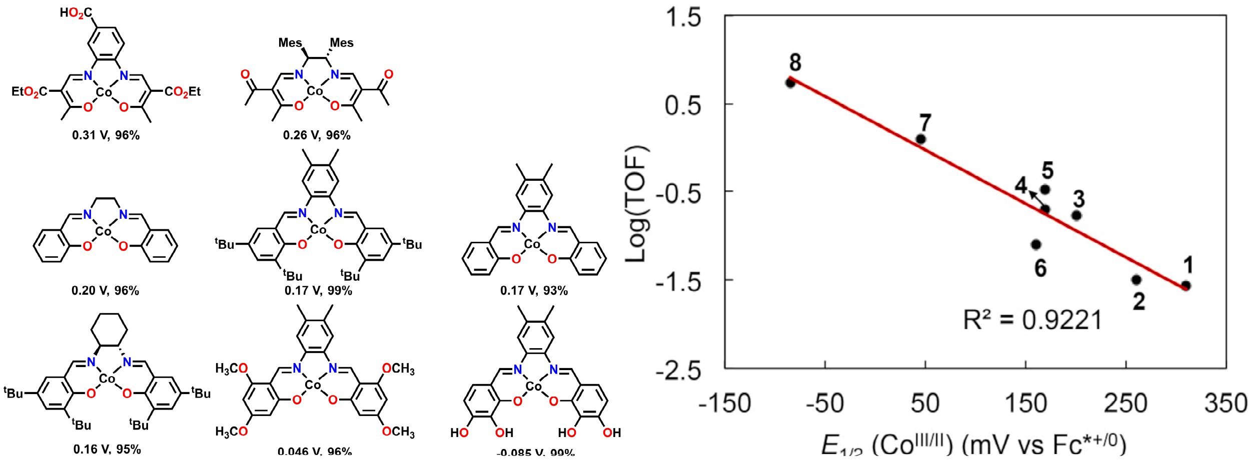

Figure 1.25. N_2O_2 complexes with their reduction potentials and Faradaic efficiencies for production of hydrogen peroxide and their Log(TOF) vs $E_{1/2}$ relationship. Adapted with permission from *J. Am. Chem. Soc.* **2017**, *139*, 16458–16461 Copyright 2017 American Chemical Society.

1.10 An N_2O_2 ligand with a bipyridine backbone for development of catalysts for CO_2RR and ORR

As can be seen in the introduction above, a great deal of ligand frameworks have been studied in great detail for both the CO_2RR and ORR. These ligands are almost exclusively multidentate ligands with synthetically modifiable motifs which allow for modulation of both electron donor-ability and secondary coordination spheres within the system itself. Within this dissertation, an examination of a family of Fe[140, 214] and Co[215] N_2O_2 complexes based on a bipyridine core with phenolic arms will be examined for activity towards both reactions (**Figure 1.26**). These ligands are expected to be stable relative to classical salen, salophen, and acen ligands discussed above due to the stability of bpy relative to imine functionalities under typical electrocatalytic conditions.[216-219] Further, the components of the ligand framework are aromatic, and a convergent synthetic approach lends itself to a large number of derivatives with different electronic and secondary-sphere properties. To this end, four derivatives of this ligand framework have been synthesized and metalated with either Fe or Co and studied for CO_2RR or ORR, respectively. In each series of metal complexes, successful studies are detailed in the future chapters: Chapter 2 describes Fe complexes generating HCO_2^- from CO_2 in the presence of phenol; Chapter 3 focuses on enhancing reactivity of these Fe complexes upon the addition of pendent hydrogen-bonding moieties; chapter 4 describes a Co(N_2O_2) complexes generating H_2O from O_2 under chemically reducing conditions with acetic acid as the added acid and Cp^*_2Fe as chemical reductant; chapter 5 describes the utilization of pendent hydrogen-bonding moieties with a Co(N_2O_2) complex for the ORR in MeCN utilizing various benzoic acid derivatives and Cp^*_2Fe as a chemical reductant.

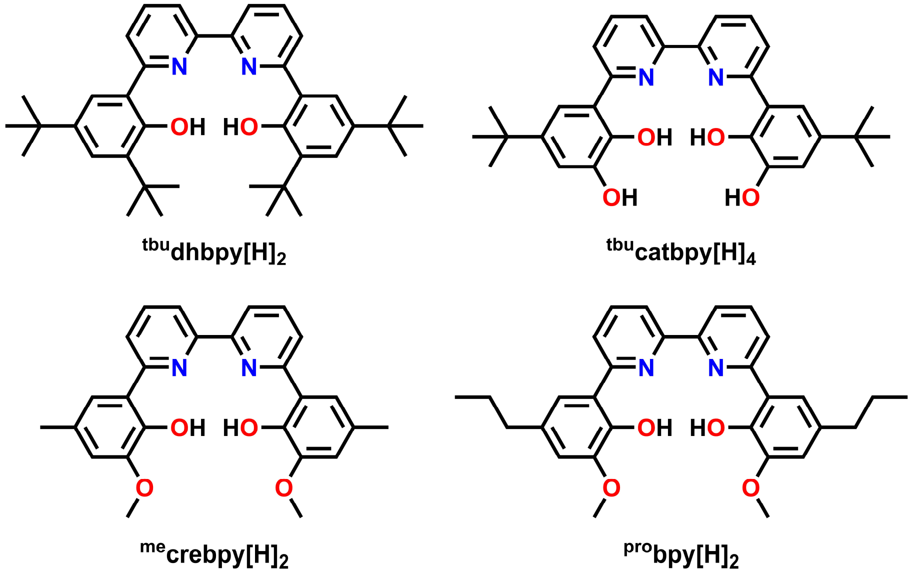

^{tbu}dhbpy[H]$_2$ **^{tbu}catbpy[H]$_4$**

^{me}crebpy[H]$_2$ **^{pro}bpy[H]$_2$**

Figure 1.26. N_2O_2 ligands for study in this thesis.

Chapter Two

Electrocatalytic Reduction of CO_2 to Formate by an Iron Schiff Base Complex

Published as: Nichols, A.W., Chatterjee, S., Sabat, M., Machan, C. W. *Inorg. Chem.* **2018**¸ *57*, 2111-2121.

2.1 Abstract

The synthesis, structural characterization, and reactivity of an iron (III) chloride compound of 6,6′-di(3,5-di-*tert*-butyl-2-hydroxybenzene)-2,2′-bipyridine (Fe(^{tbu}dhbpy)Cl), under electrochemically reducing conditions is reported. In the presence of carbon dioxide (CO_2) under anhydrous conditions in *N,N*-dimethylformamide (DMF), this complex mediates the 2e^{-} reductive disproportionation of two equivalents of CO_2 to carbon monoxide (CO) and carbonate (CO_3^{2-}). Upon addition of phenol (PhOH) as a proton source under CO_2 saturation, catalytic current is observed; product analysis from controlled potential electrolysis experiments shows the majority product is formate (68±4% Faradaic efficiency), with H_2 as a minor product (30±10% Faradaic efficiency) and minimal CO (1.1±0.3% Faradaic efficiency). Based on data obtained from cyclic voltammetry and infrared spectroelectrochemistry (IR-SEC), the release of CO from intermediate Fe carbonyl species is extremely slow and undergoes competitive degradation, limiting the activity and lifetime of this catalyst. Mechanistic studies also indicate the phenolate moieties coordinated to Fe are sensitive to protonation in the reduced state, suggesting the possibility of cooperative pendent proton interactions being involved in CO_2 reduction.

2.2 Introduction

The continual rise of atmospheric carbon dioxide (CO_2) concentrations related to anthropogenic emissions sustains interest in utilizing CO_2 as a chemical feedstock to generate fuels and commodity chemicals while potentially mitigating negative environmental effects.[1-2] To address this problem, a variety of molecular electrocatalysts have been developed for the reduction of CO_2, many of which are based on rare and precious metals like rhodium, rhenium, iridium, and ruthenium.[1, 3] However, the development of efficient and active molecular catalysts that incorporate Earth-abundant transition metals is essential for feasible extension to industrial scales.[4]

The two most readily obtained products from CO_2 reduction are formic acid and CO, which are net $2e^–/2H^+$ transformations.[1, 3] Formic acid is an attractive product because it can be used as a source of molecular hydrogen,[5] as an organic hydride reagent,[6-7] and directly as a fuel source in fuel cells.[1] Examples of highly active and selective catalysts for the reduction of CO_2 to CO (commonly with H_2O as a byproduct) have been reported with Earth-abundant transition metal complexes based on Fe, Co, Ni, and Mn systems.[1, 8-13] Less ubiquitous are catalysts capable of selectively producing formic acid, likely due to the difficulty of outcompeting thermodynamically favored H_2 production from presumptive metal hydride intermediates.[14-20] Electrocatalysts for CO_2 reduction often have multidentate ligand frameworks which provide high stability through their rigidity and conjugation.[3] For instance, in the Fe κ^4-*N*,*N'*,*N''*,*N'''*-tetraphenyl-porphyrin system reported by Savéant *et al*, the framework can be stable for at least 3.5 days with high activity.[10-13] The incorporation of active-site oriented hydroxy moieties as pendent relays for protons and alkyl ammonium groups to harness through-space electrostatic interactions have both been shown as effective strategies to enhance turnover frequency and reduce the overpotential of these porphyrin systems.[10-13]

In electrocatalytic transformations mediated by first-row transition metals, redox-active ligands are often employed.[21-24] The use of redox-active ligands presents an additional challenge, however, as radical character on the ligand framework can often lead to deleterious reactions or decomposition.[25-27] With judicious ligand design, cooperative metal-ligand interactions can lead to exceptional reactivity.[21-24] With this desirable property in mind, we were interested in modified ligand frameworks containing Schiff base-type functionality, specifically those with tetradentate κ^4-N_2O_2 coordination environments. Indeed, salens and salophens are commonly used as catalyst platforms because they are electron-rich, synthetically accessible, exhibit redox-activity, and are amenable to chirality at the metal center.[28-30] Cobalt derivatives of salen have been explored for CO_2 reduction, exhibiting selectivity for CO, but these frameworks contain a reactive imine bond within the ligand framework, which can cause dimers to form between metal complexes upon reduction.[25, 31-32] More broadly, the imine bond is generally formed through a condensation reaction, rendering the ligand sensitive to hydrolyzation in the presence of water.[29] A more robust Schiff base framework based upon a polypyridyl bis-hydroxyphenyl backbone has been previously examined as the ligand for a chiral catalyst for asymmetric cyclopropanation,[33] a phosphorescent Pt complex,[34] a dioxygen reduction electrocatalyst,[35] and a mimic for the active site of galactose oxidase.[36] A phenanthroline-bridged analogue has been examined as an electrocatalyst for CO_2 reduction with moderate selectivity for formate and CO.[20] Although these qualities make this ligand promising as a robust alternative to salens/salophens, the lack of a straightforward synthesis until recently has precluded rigorous exploration.[35-39] Here, we present a synthetic route to Fe complexes utilizing the 6,6′-di(3,5-di-*tert*-butyl-2-hydroxybenzene)-2,2′-bipyridine (^{tbu}dhbpy[H]$_2$) ligand framework, along with its electrocatalytic activity for the reduction of CO_2 to formate.[36-39]

2.3 Materials and Methods

2.3.1 General

All chemicals and solvents (ACS or HPLC grade) were commercially available and used as received unless otherwise indicated. For all air-sensitive reactions and electrochemical experiments, solvents were obtained as anhydrous and air-free from a PPT Glass Contour Solvent Purification System. Gas cylinders were obtained from Praxair (Ar as 5.0; CO_2 as 4.0; CO as 2.5) and passed through molecular sieves prior to use. Gas mixing for variable concentration experiments was accomplished using a gas proportioning rotameter from Omega Engineering. NMR spectra were obtained on either a Varian 600 MHz or 500 MHz instrument and referenced to the residual solvent signal. IR absorbance spectra were obtained on a Vertex V80 IR instrument from Bruker and UV-vis absorbance spectra on a Cary 60 from Agilent. GC experiments were performed using an Agilent 7890B Gas Chromatograph with an Agilent J&W Select Permanent Gases/CO_2 column; eluent retention times and product characterization were determined by standard injections. HRMS data were obtained by the Mass Spectrometry Lab at the University of Illinois at Urbana-Champaign and elemental analyses were performed by Midwest Microlab. X-band EPR measurements were performed on a JEOL JES-FA 200 instrument at Indian Association for the Cultivation of Science, Kolkata, India.

2.3.2 Synthesis of 2-Bromo-4,6-di-tert-butyl Phenol

2,4-di-*tert*-butylphenol (20.0 g, 96.9 mmol) was dissolved in CH_2Cl_2 (100 mL) and chilled to 0°C for 10 minutes under N_2. Bromine (Br_2, 16.0 g, 5.12 mL) was added dropwise via syringe over the course of 20 minutes. The reaction was stirred for 2 h at room temperature under nitrogen. Afterwards, the reaction was quenched with saturated $NaHCO_3$ (aq., 50 mL) in aliquots (10 mL) over the course of 1 h with vigorous stirring. The layers were separated, and the aqueous layer was extracted with CH_2Cl_2 (3x50 mL). The desired product was isolated as an orange solid in 98.0% yield, 27.1 g. ^{1}H NMR (d_2-CD_2Cl_2, 600 MHz): δ 7.35 (d, 1H, Ar*H*), 7.27 (d, 1H, Ar*H*), 1.41 (s, 9H, $-C(CH_3)_3$) 1.29 (s, 9H, $-C(CH_3)_3$). Elemental Analysis for $C_{14}H_{21}BrO$ Calc'd: C, 58.95; H, 7.42; N, 0.00. Found: C, 58.24; H, 7.23; N 0.00. ESI-MS (m/z) $[M]^+$: Calc'd. 284.07758 Found: 284.07723.

2.3.3 Synthesis of 6,6′-di(3,5-di-tert-butyl-2-hydroxybenzene)-2,2′-bipyridine ^{tbu}dhbpy(H)$_2$[36-39]

A Schlenk flask (500 mL) with stir bar was charged with 2-bromo-4,6-di-*tert*-butyl-phenol (5.0 g, 0.0175 mol) and dry diethyl ether (200 mL). The resulting solution was cooled to -78 °C under N_2 using a dry ice/acetone ice bath. After ten minutes, n-butyllithium (2.5 M in hexanes) was added slowly via syringe (16.0 mL, 0.040 mol), after which the solution was allowed to warm to room temperature with vigorous stirring for 2 hours. The solution was again chilled to -78 °C and trimethyl borate was added rapidly by syringe (3.15 mL, 0.0283 mol) with vigorous stirring and left for 10 minutes. The cooling bath was then removed and the mixture stirred overnight at room temperature under N_2 (16 h). After this time, the flask was cooled to 0°C before quenching with HCl (25 mL, 2 M) and opened to air. The resulting suspension was separated into organic and aqueous layers, and the aqueous layer was extracted with CH_2Cl_2 (3x50 mL). A yellow oil was isolated and used without further purification.

To a round-bottom flask (500 mL) with a stir bar, 6,6′-dibromobipyridine (1.78 g, 5.67 mmol), and toluene (250 mL) were added. To this suspension the crude (3,5-di-*tert*-butyl-2-hydroxy-phenyl) boronic acid, MeOH (30 mL), a 2 M Na_2CO_3 solution (60 mL), and $Pd(PPh_3)_4$ (5.0 mol. % cat., 340 mg) were also added. This mixture was then brought to reflux for 72 h (ca. 110 °C) under an N_2 atmosphere. Afterwards, the suspension was allowed to cool and the layers were separated. The organic layer was washed with brine (1x50 mL) and the aqueous layer with CH_2Cl_2 (3x50 mL). The organic fractions were combined and dried with $MgSO_4$ for 10 minutes. After this time, the suspension was filtered and concentrated under reduced pressure. Product was isolated in multiple portions by recrystallization first from toluene (10 mL) then from hexanes (10 mL) as a pale-yellow powder. Total yield: 2.46 g, 76.8%. ^{1}H NMR (d_2-CD_2Cl_2, 600 MHz): δ 8.10 (m, 6H, Ar*H*), 7.76 (d, 2H, Ar*H*), 7.45 (d, 2H, Ar*H*), 1.51 (s, 18H, $-C(CH_3)_3$), 1.38 (s, 18H, $-C(CH_3)_3$), $^{13}C\{^1H\}$ (d_2-CD_2Cl_2, 151 MHz) NMR δ 159.52 (Ar*C*), 157.09 (Ar*C*), 152.41 (Ar*C*), 140.85 (Ar*C*), 139.69 (Ar*C*), 138.05 (Ar*C*), 127.11 (Ar*C*), 121.90 (Ar*C*), 121.17 (Ar*C*), 119.30 (Ar*C*), 118.52 (Ar*C*), 35.81 (tbu*C)*, 34.88 (tbu*C)*, 31.91 (tbu*C)*, 29.92 (tbu*C)*. Elemental analysis for $C_{38}H_{48}N_2O_2$ Calc'd: C, 80.81; H, 8.57; N, 4.96. Found: C, 81.01; H, 9.11; N: 5.10. ESI-MS (m/z): calc'd $[M + H]^+$: 565.3789 found: 565.3789. These characterization data are in agreement with previous syntheses.[36-39]

2.3.4 Synthesis of Fe(^{tbu}dhbpy)Cl 1

6,6′-di(3,5-di-*tert*-butyl-2-hydroxybenzene)-2,2′-bipyridine (0.100 g, 0.177 mmol), sodium acetate (0.029 g, 0.35 mmol), and iron (III) chloride hexahydrate (0.048 g, 0.18 mmol) were combined in methanol (25 mL) in a round bottom flask (50 mL) equipped with stir bar and reflux condenser. The mixture was brought to reflux for 3.5 h and then allowed to cool to room temperature. The resultant dark purple solid was collected in a frit via vacuum filtration before being washed with water (3x5 mL) and hexanes (3x5 mL), 85 mg isolated, 73% yield. X-ray quality single crystals were grown by slow cooling a 50 °C saturated solution of Fe(^{tbu}dhbpy)Cl in acetonitrile. ^{1}H NMR spectra suggest the complex is a paramagnetic species. ^{1}H NMR (d_2-CD_2Cl_2, 600 MHz): δ 8.0-12.0 (broad resonance), 4.71 (broad resonance). Elemental analysis for $C_{38}H_{46}ClFeN_2O_2$: Calc'd: C, 69.78; H, 7.09; N: 4.28 Found: C, 69.87; H, 7.04; N: 4.27. ESI-MS: (m/z) Calc'd $[M - Cl]^+$: 618.2909 found: 618.2915.

2.3.5 Synthesis of [Fe(^{tbu}dhbpy)][OTf] 1[OTf]

A 100 mL Schlenk flask was charged with nitrogen and a stir bar. Fe(^{tbu}dhbpy)Cl **1** (0.040 g, 0.062 mmol) was added and suspended in *N,N*-DMF (10 mL). Thallium(I) trifluoromethanesulfonate Tl[OTf] (0.022 g, 0.062 mmol) was added under inert atmosphere, after which a white precipitate formed almost immediately. The reaction was left stirring under nitrogen atmosphere for 1 h in the dark. Solvent was removed under reduced pressure and the obtained solid was suspended in CH_2Cl_2 before being filtered through 1/2 inch of Celite^{TM} using a vacuum frit. The solvent was removed under reduced atmosphere, 29 mg isolated, 60% yield. An upfield shift in ^{1}H NMR resonances is observed, consistent with abstraction of Cl^- as reported by Mayer *et al.*[40] ^{1}H NMR (d_2-CD_2Cl_2, 600 MHz): δ 7.52 (broad resonance), 5.01 (broad resonance), 4.71 (broad resonance), 3.12 (broad resonance), 2.82 (broad resonance), 1.70 (broad resonance). Elemental analysis for $C_{38}H_{46}FeN_2O_2 \bullet [C_3H_7NO]_2 \bullet CH_2Cl_2$: Calc'd C, 55.32; H, 6.26; N, 5.61. Found: C, 56.95; H, 6.26; N, 5.28. ESI-MS: (m/z) Calc'd $[M–OTf]^+$: 618.2909 found: 618.2905.

2.3.6 Synthesis of Zn(^{tbu}dhbpy)

The synthetic procedure for Zn(^{tbu}dhbpy) was modified from previous reports.[36] Ligand (^{tbu}dhbpy$[H]_2$) (0.150 g, 0.266 mmol) was brought to reflux in methanol (45 mL) in a round-bottom flask equipped with a stir bar and reflux condenser. Zinc(II) chloride $ZnCl_2$

(0.038 g, 0.288 mmol) and triethylamine (94 μL, 0.66 mmol) were dissolved in methanol (5 mL) and added dropwise to the refluxing suspension. The resulting suspension was refluxed for 16 h, after which time the solution was allowed to cool to room temperature. An orange solid was collected via vacuum filtration. Upon washing with DI H_2O (3x50 mL), a microcrystalline yellow solid was obtained (120 mg, 72%). ^{1}H NMR (600 MHz, Varian) δ 7.81-8.15 (m, 6H, Ar*H*), 7.76 (d, 1H, Ar*H*), 7.36-7.50 (m, 3H, Ar*H*), 1.51 (s, 18H, -$C(CH_3)_3$), 1.38 (s, 9H, -$C(CH_3)_3$), 1.35 (s, 9H, -$C(CH_3)_3$) CHN Analysis: Theoretical (Zn(^{tbu}dhbpy) + 2 CH_3OH): C: 69.40 H: 7.86 N: 4.05 Found: C: 69.87 H: 7.17 N: 4.30 ESI-MS: (m/z) Calc'd $[M + H]^+$: 627.2929 Found: 627.2933.

2.3.7 Electrochemistry

All electroanalytical experiments were performed using a Metrohm Autolab PGSTAT302N potentiostat. Glassy carbon working (3 mm) and non-aqueous silver wire pseudoreference electrodes separated by PTFE tips were obtained from CH Instruments. Ag/AgCl pseudoreference electrodes were generated by depositing chloride on the bare silver wire in 10% HCl at oxidizing potentials and were stored in a 0.1 M tetrabutylammonium hexafluorophosphate/*N,N*-dimethylformamide solution prior to use. The counter electrode was Pt wire (Alfa Aesar, 99.95%, 0.5 mm diameter) or glassy carbon, as denoted. All cyclic voltammetry (CV) experiments were performed in a modified scintillation vial (20 mL volume) as a single-chamber cell with a cap modified with ports for all electrodes and a sparging needle. Controlled potential electrolysis experiments were performed in a five-port 120 mL European-style flask from Ace Glass with a glassy carbon rod working electrode (Alfa Aesar, type 1, 7 mm diameter), glassy carbon rod counter electrode (Alfa Aesar, type 2, 2 mm diameter) behind a glass frit, a custom silver/silver chloride pseudoreference electrode (Alfa Aesar, 99.9%, 1.0 mm diameter) behind a glass frit, and ports for head-space sampling and gas sparging via needles through septa. Tetrabutylammonium hexafluorophosphate ($TBAPF_6$) was purified by recrystallization from ethanol and dried in a vacuum oven overnight at 100 °C before being stored in a desiccator. All data were referenced to an internal ferrocene standard (ferricinium/ferrocene (Fc/Fc^+) redox potential under stated conditions) unless otherwise specified.

2.3.8 IR Spectroelectrochemistry

All IR-SEC experiments were conducted using a custom cell based on a previously published design (**Figure S1**).[41-42] The three-electrode set-up consists of an inner glassy carbon working electrode disc (10 mm diameter), a central circular silver bare metal pseudoreference electrode, and an outer circular glassy carbon counter electrode embedded within a PEEK block. All data were referenced to an internal ferrocene standard (ferricinium/ferrocene reduction potential under stated conditions); obtained by taking a CV with the cell prior to injecting analyte for IR-SEC experiments) unless otherwise specified. All spectra were processed by subtraction of a non-reactive/non-catalytic potential from those at which reactivity occurred.

2.3.9 Computational Methods

DFT calculations were performed on the Rivanna High-Performance Computing Cluster at the University of Virginia using ORCA 4.0.0.[43] Geometry optimizations were performed spin unrestricted with the B3LYP/G[44-48] functional and def2-TZVP[49-50] basis set with the RIJCOSX approximation[51], D3BJ dispersion correction[52-53], and CPCM[54] to model the *N,N*-DMF solvent. Numerical frequency calculations at the same level of theory were performed to validate the optimized geometries as minima on the potential energy surface and to generate thermochemical data. TD-DFT calculations on the verified minimum were performed with def2-QZ2P basis sets[50] with nroots = 50, and maxdim = 10. Molecular graphics and analyses were performed with the UCSF Chimera package. Chimera is developed by the Resource for Biocomputing, Visualization, and Informatics at the University of California, San Francisco (supported by NIGMS P41-GM103311).

2.4 Results

2.4.1 Characterization of Fe($^{\text{tbu}}$dhbpy)Cl

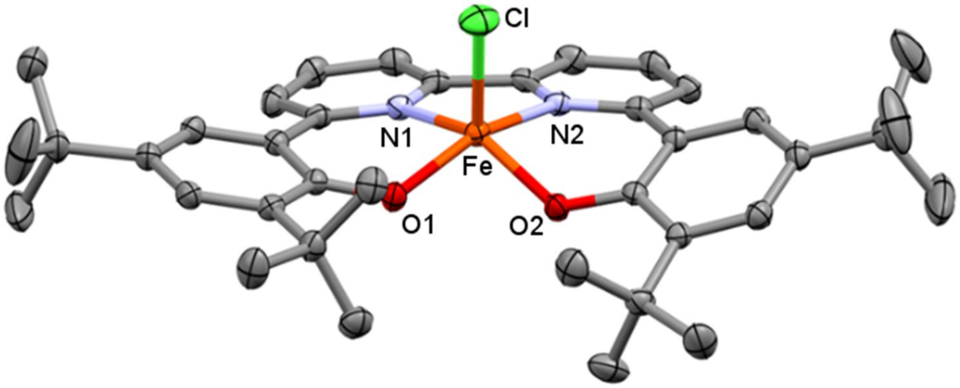

Figure 2.1. ORTEP plot of Fe($^{\text{tbu}}$dhbpy)Cl. Thermal ellipsoids set to 50%. Occluded acetonitrile molecule and hydrogen atoms omitted for clarity. C = grey, O = red, N = blue, Cl = green, Fe = orange.

Single crystals suitable for diffraction studies were obtained by slow cooling of a concentrated solution of **1** in hot acetonitrile (MeCN). The structure of Fe($^{\text{tbu}}$dhbpy)Cl **1** determined by X-ray crystallography is a discrete molecular Fe(III) complex in a distorted square pyramidal coordination environment, fully chelated by the deprotonated ligand, $^{\text{tbu}}$dhbpy^{2-}, in the equatorial plane with an open coordination site trans to an axial Cl^{-} ligand (**Figure 2.1**). By ^{1}H NMR, Fe($^{\text{tbu}}$dhbpy)Cl exhibits paramagnetic broadening and shifts in *N*,*N*-DMF-d_7. A μ_{eff} value of 5.90(7) Bohr magnetons is obtained in *N*,*N*-DMF-d_7, using the Evans' method for determining paramagnetic susceptibility, consistent with high spin Fe(III) (S=5/2).[55-56] An X-band EPR spectrum also gives a rhombic signal at g = 4.2 with no low spin impurities, consistent with results from Evans' method.[57-58] Three characteristic absorbances with λ_{max} at 320, 446, and 542 nm are observed by UV-vis in *N*,*N*-DMF (**Figure S2.2**). These absorbances are assigned to a single ligand π-π^* and two phenolate to Fe(III) ligand-to-metal charge transfers with molar absorptivities of 17200, 3120, and 2330 M^{-1} s^{-1}, respectively. These assignments are consistent with prior reports and TD-DFT results, *vide infra*.[59-62]

2.4.2 Electrochemistry

2.4.2.1 Electrochemical Response under Ar Saturation

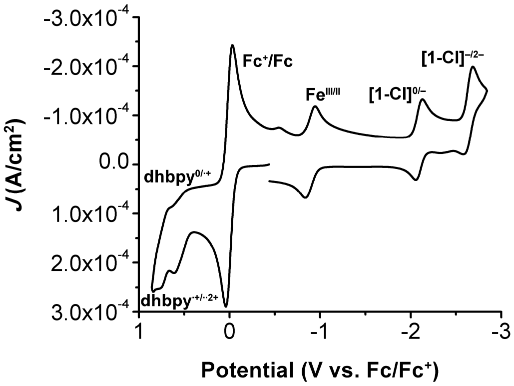

Figure 2.2. Cyclic voltammogram of 0.5 mM Fe(^{tbu}dhbpy)Cl **1** in *N*,*N*-DMF with 0.1 M TBAPF$_6$ supporting electrolyte under an atmosphere of Ar. Conditions: scan rate 100 mV/s; working electrode glassy carbon (3 mm), counter electrode Pt wire, and pseudo-reference Ag/AgCl wire behind a PTFE tip with ferrocene (Fc) added as internal reference.

Figure 2.2 shows the Faradaic cyclic voltammogram of Fe(^{tbu}dhbpy)Cl, and **Scheme 2.1** summarizes the proposed redox process that occurs at each feature. Beginning from **1**, two single electron oxidations with E_{pa} of 0.60 V and 0.75 V vs Fc/Fc$^+$ are observed. These two features are assigned to sequential oxidations of the phenolate moieties on the ligand framework to form [Fe^{III}(^{tbu}dhbpy$^{\cdot+}$)Cl]$^+$ and [Fe^{III}(^{tbu}dhbpy$^{\cdot\cdot2+}$)Cl]$^{2+}$, respectively.[36] Upon the return sweep to reducing potentials from ~+1.0 V vs Fc/Fc$^+$, a feature at –0.53 V is seen that can be attributed to a non-degradative chemical reaction on the CV timescale after the diradical species is formed. This is supported by the presence of this feature only when the scan switching potential is >+0.66 V vs Fc/Fc$^+$ (**Figure S2.5**). No deposition on the electrode was observed in subsequent CVs.

Scheme 2.1. Proposed reduction mechanism for Fe(^{tbu}dhbpy)Cl with no substrate added; **R** = ^{t}Bu.

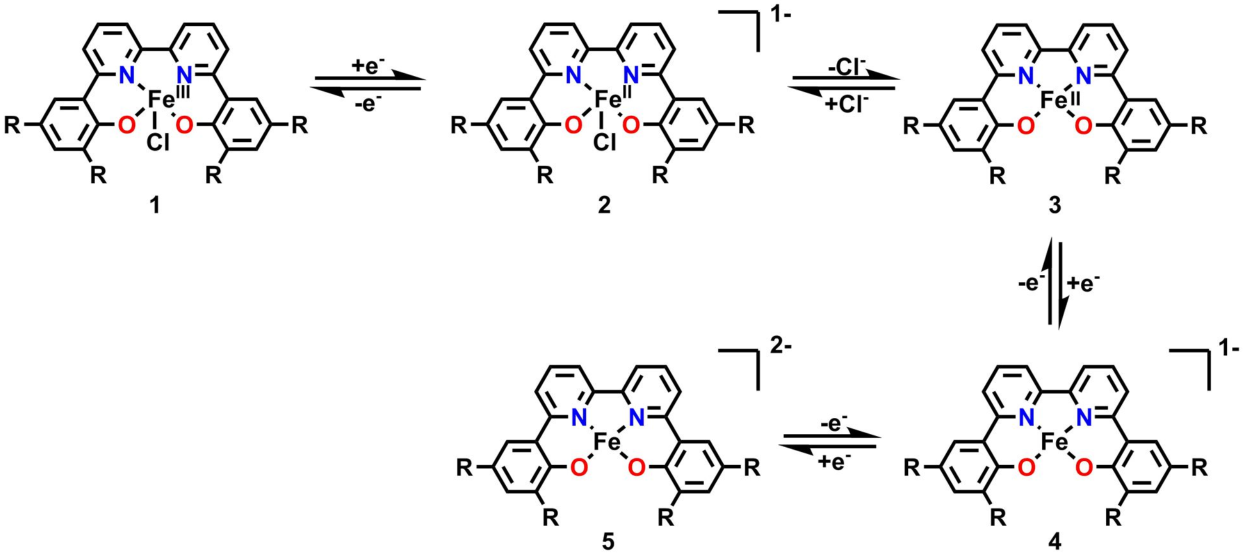

The first true reduction feature is a single electron, electrochemically quasi-reversible feature with an E^0 of –0.89 V vs Fc/Fc$^+$ (first reduction) and a peak-to-peak separation (ΔE$_p$) of approximately 104 mV at 100 mV/s scan rate, assigned to the Fe$^{III/II}$ couple. This feature meets the criteria for a first order reversible chemical reaction following a reversible electron transfer: the forward wave shifts to more negative potentials with increasing scan rate by 30/*n* (where *n* is the number of electrons involved in the redox event, one in this case) per 10-fold increase in scan rate, the current of the forward wave increases with increasing scan rate, and the magnitude of the anodic and cathodic currents is equal at scan rates less than 500 mV/s, but smaller than 1 with increasing ν (**Table S2.1**).[63] This reversible reaction was determined to be chloride loss, as discussed below. This assignment is consistent with literature reports on analogous salen compounds and the DFT results discussed below.[62, 64]

The observed chloride loss occurs at this feature to balance the overall charge of the complex upon reduction. This assignment is supported by a shift in the observed ΔE_p to approximately 150 mV at a scan rate of 1000 mV/s from 104 mV at 100 mV/s (**Figure S2.6, Table S2.1**) and a ΔE_p of approximately 76 mV (ΔE_p(Fc) = 81 mV for each scan rate) at all scan rates upon the addition of 10.8 mM tetrabutylammonium chloride (TBACl) as a Cl^- source (**Figure S2.6, Table S2.1**). The addition of TBACl also causes a corresponding shift towards more reducing potentials, suggesting a Nernstian shift in the reaction quotient has also occurred such that the forward reaction, the loss of Cl^-, is now less favorable (**Figure S2.6**).[65] This reversible 1e$^-$ reduction of **1** to the monoanionic species, $[Fe^{II}(^{tbu}dhbpy)Cl]^-$ **2** is followed by chloride loss to form the neutral species, $[Fe^{II}(^{tbu}dhbpy)]^0$ **3** (**Scheme 2.1**). Next, a reversible feature with E^0 of –2.09 vs Fc/Fc$^+$ (second reduction) is observed, followed by quasi-reversible feature with $\alpha > 0.5$ and E^0 of –2.65 V vs Fc/Fc$^+$ (third reduction).[63] Each of these features has a linear response when current density is plotted against the square root of scan rate, indicating $Fe(^{tbu}dhbpy)Cl$ **1** is behaving as a molecular species within a diffusion-limited regime (**Figure S2.3, Figure S2.4**).[65] It is clear the second and third reductions produce species with added electron density distributed across both the metal center and ligand. The second reduction observed at –2.09 V vs Fc/Fc$^+$ is not an exact overlay with the first reduction of $[Zn^{II}(^{tbu}dhbpy)]$ model compound (**Figure S2.7**) and DFT results suggest slight spin contamination on the ligand, *vide infra*, rendering the best description of this feature ambiguous, $[Fe(^{tbu}dhbpy)]^{–}$ **4**. Likewise, although the third reduction at E^0 = –2.65 V vs Fc/Fc^+ shows better overlay with electrochemical response of the model compound, $[Zn^{II}(^{tbu}dhbpy)]$ (**Figure S2.7**), we hesitate to make an assignment more exact than $[Fe(^{tbu}dhbpy)]^{2–}$ **5** for the reduction product for similar reasons.

To further probe the $Cl^–$ loss equilibrium, chloride was abstracted from $Fe(^{tbu}dhbpy)Cl$ **1** using thallium(I) trifluoromethanesulfonate Tl[OTf] to yield $[Fe(^{tbu}dhbpy)][OTf]$ **1**[OTf]. CV experiments under Ar saturation conditions exhibited an irreversible first reduction (E_p = –0.92 V), which is 30 mV positive of the forward reduction wave of $Fe(^{tbu}dhbpy)Cl$ **1** (**Figure S2.8**). The second and third reductions maintain consistent potentials and redox reversibility to the parent complex **1** (**Figure S2.9)**.

2.4.2.2 Electrochemical Response under Ar Saturation with added PhOH

Upon the addition of PhOH as a proton source, a shift to positive potentials is observed at the first reduction feature (**Figure 2.3**) and an increase in current is observed at the second (**Figure 2.4**) and third reduction features (**Figure 2.5**). The shift at the first reduction potential is assigned to the protonation of a phenolate oxygen on $Fe(^{tbu}dhbpy)Cl$ (**1**) to form $Fe(^{tbu}dhbpy[H])Cl$ (**6**). When the data at the first reduction is analyzed by a comparison of $E_{1/2}$ to the log of PhOH concentration, and to determine PhOH equilibrium binding constants[8, 66-69], two distinct regimes are observed under the conditions reported here. First, at concentrations of PhOH less than 0.76 M, a Nernstian relation of 37±1 mV/log of PhOH concentration (**Figure S2.10**), which is suggestive of PhOH acting as a proton donor during the reduction of **1**, allowing us to also calculate a PhOH equilibrium binding constant of 9.3±0.8 M^{-1}.[8, 66-69] At concentrations of PhOH higher than 0.76 M, the slope of this Nernstian relationship decreases to 27±3 mV/log of PhOH concentration; a diminished proton binding constant of 5±1 M^{-1} is also observed (**Figure S2.10**); statistical treatments validate the existence of two regimes, see **Supporting Information**. It should be noted that we are unaware of a homoconjugation equilibrium constant for PhOH in *N,N*-DMF (K_{AHA}), which would enable a more rigorous treatment than presented here.

Interestingly, the ΔE_p and PhOH concentration are inversely related: ΔE_p approaches the approximately 72 mV separation observed for Fc/Fc^+ at concentrations > 0.257 M PhOH (**Table S2.2**) and does not come within error of a $2e^-$ separation, suggesting this reduction remains a single-electron event at all PhOH concentrations. This can be rationalized by a shift in equilibrium towards protonation of an O atom on the ligand framework by PhOH acting as a proton donor prior to reduction, and thus a more positive overall charge on the complex at high concentrations of PhOH. Conversely, the addition of TBACl to a solution **1** containing 1.5 M PhOH diminishes the proton donor-induced shift towards positive potentials (**Figure S2.6**), indicating the equilibrium at this reduction event involves both proton binding and chloride loss, albeit at different timescales. Overall, the observed behavior at this reduction feature suggests a proton and electron have been added to the parent Fe(^{tbu}dhbpy)Cl species without disrupting the open Fe coordination site on the complex. The second regime corresponds to the appearance of a distinct second reduction with E_p at –1.10 V vs Fc/Fc^+, suggesting at high PhOH concentrations, Cl^- dissociation is appreciable enough to observe by CV.

Upon repeating these experiments with [Fe(^{tbu}dhbpy)][OTf], the results are supportive of the proton binding equilibrium discussed above; the Nernst concentration plot suggests a single regime, with a slope of 25±2 mV/log of PhOH concentration (**Figure S2.11**). The observed slope is within error of that obtained for Fe(^{tbu}dhbpy)Cl at PhOH concentrations greater than 0.76 M, consistent with the interpretation that at higher concentrations, Cl⁻ loss appreciably occurs for **1**.

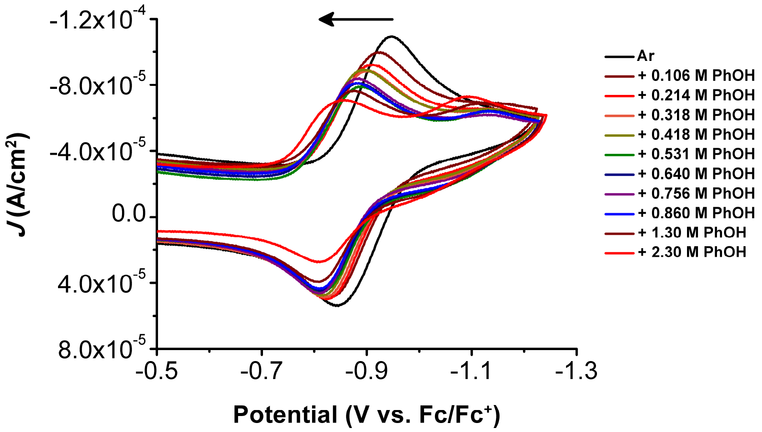

Figure 2.3. Nernstian shift of 0.5 mM Fe(^{tbu}dhbpy)Cl first reduction (E^0 = –0.89 V) upon addition of PhOH as a proton source under in *N*,*N*-DMF with 0.1 M $TBAPF_6$ supporting electrolyte under Ar saturation; scan rate is 100 mV/s. Working electrode is glassy carbon, counter electrode is Pt wire, and pseudoreference is Ag/AgCl wire with ferrocene (Fc) added as internal reference. Arrow shows direction of shift with increasing PhOH concentration.

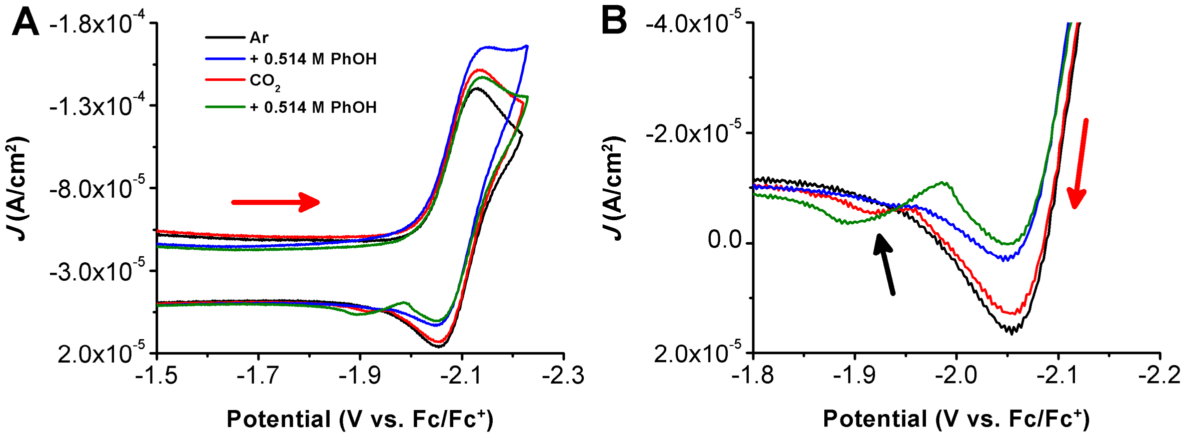

Figure 2.4. (A) Second reduction (E^0 = –2.09 V vs Fc/Fc$^+$) of 0.5 mM Fe(^{tbu}dhbpy)Cl in *N*,*N*-DMF with 0.1 M $TBAPF_6$ supporting electrolyte under Ar (black and blue) and CO_2 (red and green) saturation; scan rate is 100 mV/s. Working electrode is glassy carbon, counter electrode is Pt wire, and pseudo-reference is Ag/AgCl wire with ferrocene (Fc) added as internal reference. Red arrow shows direction of potential sweep. (B) Highlight of oxidative features on the return sweep corresponding to CO_2 reaction products at –1.9 V vs Fc/Fc$^+$.

At the second reduction there is an increase in current by a factor of 1.35 (i_{PhOH}/i_{Ar}) upon the addition of 0.509 M PhOH. This suggests a second protonation at the Fe center has occurred to form a species similar to [Fe(H)(^{tbu}dhbpy[H])]$^+$ **8** (**Figure 2.5**). After this step, further reduction of a presumably Fe(III) center at this potential would be expected to occur, generating a more hydridic complex where protonation of the hydride to release H_2 was favorable. Indeed, electrolysis experiments at –2.1 V vs Fc/Fc$^+$ with 0.5 M PhOH show H_2 is generated with 51±7% Faradaic efficiency with a TON of 2.9. This low efficiency suggests the feature is not completely catalytic, indeed, the electrode generates H_2 with comparable efficiency in control experiments at more negative potentials **(Table 1**, **Figure S2.24**). If the direction of the CV sweep is reversed at -2.23 V vs Fc/Fc$^+$, just negative of the second reduction feature, a new irreversible oxidation feature is observed at –1.07 V vs Fc/Fc$^+$, suggestive of a chemical reaction on this timescale. At applied potentials more negative than the second reduction, there is an increase in current by a factor of 22.6 (i_{PhOH}/i_{Ar}) with 0.526 M PhOH (**Figure 2.4**); however, control CVs with 0.517 M PhOH indicate the glassy carbon electrode produces a similar current response (**Figure S2.39**).

2.4.2.3 Electrochemical Response in the Presence of CO_2

Under CO_2 saturation conditions in the absence of an external proton source, no change is observed at the first reduction feature. A shift to chemical irreversibility is observed at the second reduction, however, as well as a new oxidative feature on the return sweep at –1.93 V vs Fc/Fc$^+$. These two observations suggest an intermediate species is formed during the experiment (**Figure 2.4**). This species is presumed to be an

Fe–CO_2 adduct (**12**), which is a necessary intermediate in the reductive disproportionation of two equivalents of CO_2 to one each of CO and CO_3^{2-} (**Scheme 2.2**).

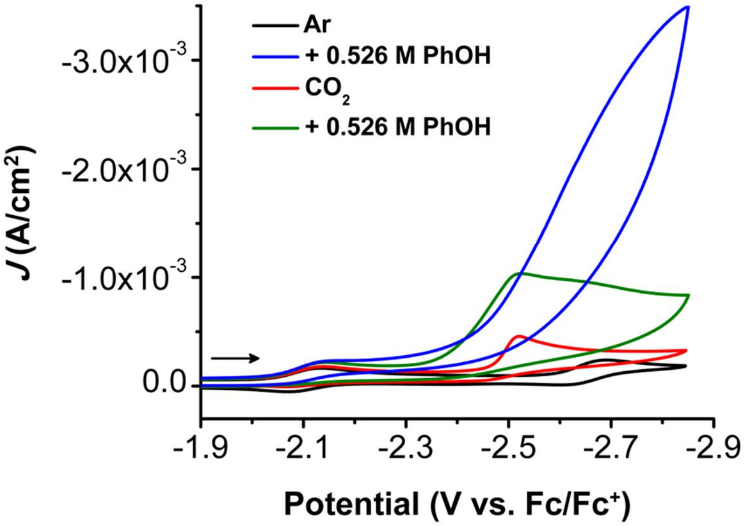

Figure 2.5. Second reduction (E^0 = –2.65 V vs Fc^+/Fc) of 0.5 mM Fe(^{tbu}dhbpy)Cl in *N*,*N*-DMF 0.1 M $TBAPF_6$ supporting electrolyte under Ar (black and blue) and CO_2 (red and green) saturation; scan rate is 100 mV/s. Working electrode is glassy carbon, counter electrode is Pt wire, and pseudo-reference is Ag/AgCl wire with ferrocene (Fc) added as internal reference. Arrow shows direction of potential sweep.

Consistent with this interpretation, both an intermediate Fe–CO_2 adduct (**12**) and an Fe(I) carbonyl species (**13**) were observed by IR-SEC (**Figure 2.6, Figure S2.21**), *vide infra*. Finally, an increase in current by a factor of 2.3 (i_{CO2}/i_{Ar}) and shift to more oxidizing potentials from the third reduction (E^0 = –2.65 V) to E_p = –2.51 V suggest that at this feature a more activated CO_2 adduct capable of an increased reaction rate is generated (**Figure 2.5**). A log-log plot comparing peak current density and concentration of Fe(^{tbu}dhbpy)Cl gives a slope of approximately 1, consistent with first-order dependence with respect to catalyst concentration (**Figure S2.15**).[70] Controlled potential electrolysis experiments at –2.5 V vs Fc/Fc^+ show CO is generated with 1.1±0.3% Faradaic efficiency when current corresponding to six reducing equivalents under aprotic conditions is passed, suggesting possible decomposition of the parent Fe species. The presence of HCO_3^- and therefore the overall reductive disproportionation of CO_2, was confirmed from the same controlled potential electrolysis experiments by $^{13}C\{^1H\}$ NMR (**Figures S2.42-2.44**). Consistent with this, CVs taken under a CO atmosphere show a shift in the second reduction feature from reversible to irreversible at more positive potentials (E_p = –2.00 V vs Fc/Fc$^+$, **Figure S2.16**). On the return sweep from –2.27 V vs Fc/Fc$^+$, a new oxidation feature is observed (E_p = –0.40 V, **Figure S2.16**), indicative of CO binding to the Fe(I) center. Using the potential at the half peak height for the shifted Fe$^{II/I}$ wave, an equilibrium binding constant of 3.8×10^4 M^{-1} for CO was calculated.[8, 66-69] This favorable binding event is likely the reason only trace CO is detected under electrolysis conditions: Fe–CO species are unlikely to release CO at applied potential and further degradation is implied by the bulk electrolysis results under aprotic conditions.

Scheme 2.2. Proposed reactivity of Fe(^{tbu}dhbpy)Cl **1** in the presence of CO_2 at reducing potentials. **R** = ^{t}Bu

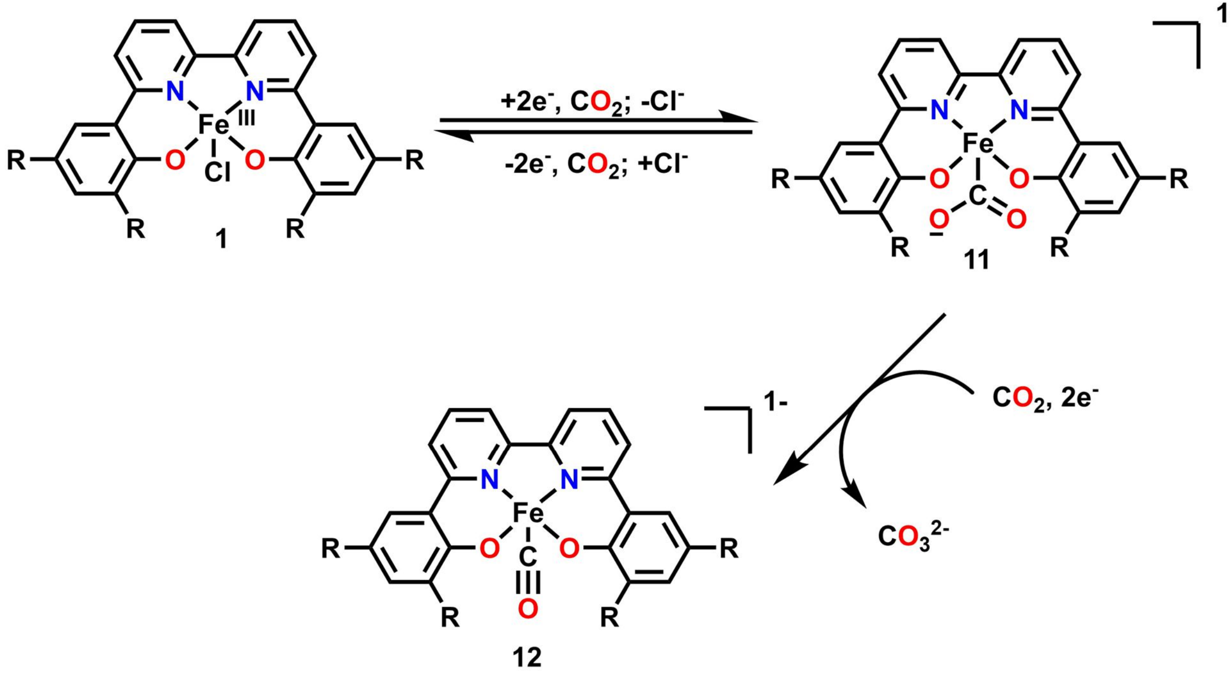

2.4.2.4 Electrochemical Response with CO_2 and added PhOH

Upon the addition of PhOH as a proton source under CO_2 atmosphere, a reversible binding interaction with the proton donor in two distinct regimes is again observed: one at less than 0.76 M PhOH with a Nernst relationship of 39±2 mV/log PhOH concentration, consistent with a protonation reaction and an estimated PhOH equilibrium binding constant of 10.3±0.5 M^{-1}.[8, 66-69] As was observed in the absence of CO_2, at concentrations of PhOH higher than 0.76 M, the Nernst relationship shifts to 18±2 mV/log PhOH concentration consistent with enhanced electron transfer kinetics and a PhOH equilibrium binding constant of 6±2 M^{-1} (**Figure S2.18**). As noted previously, these data suggest this Nernstian behavior is perturbed by a $Cl^–$ binding equilibrium that has its own PhOH concentration dependence. Chemical irreversibility is observed at the second reduction feature under saturated CO_2 conditions, as well as a new irreversible oxidation feature on the return sweep at –1.89 V vs Fc/Fc^+ under CO_2 saturation with added PhOH (0.514 M), however, this feature shifts to more oxidizing potentials (–1.89 V vs Fc/Fc^+) than under CO_2 saturation conditions with no added PhOH (–1.93 V vs Fc/Fc^+). The difference between these two oxidation features suggests added PhOH has a stabilizing effect on an activated CO_2 intermediate. With 0.526 M PhOH and CO_2 saturation conditions, a greater increase in current at the third reduction feature ($i_{CO2PhOH}/i_{Ar}$ =6.0) is observed than in the presence of CO_2 only ($i_{CO2PhOH}/i_{Ar}$ = 2.3, E_p = –2.53 V vs Fc/Fc^+; **Figure 2.5**). Based on PhOH titration studies, catalytic current becomes saturated in the presence of 0.2 M PhOH; however, 0.5 M PhOH was chosen to reflect the solubility of CO_2 in *N,N*-DMF (0.23 M under saturation) so more than two proton donors were present for every equivalent of CO_2. With fixed PhOH concentration (0.509 M), CV studies demonstrate an inverse relationship at the third reduction between catalytic current and CO_2 concentration; indicating suppression of the HER activity and thus kinetic selectivity for CO_2 reduction over thermodynamically favored proton reduction (**Figure S2.19**). With CO_2 saturation and 0.508 M PhOH, a log-log plot of peak current vs [Fe(^{tbu}dhbpy)Cl] gives a first-order dependence upon catalyst concentration (**Figure S2.20**).

2.4.3 Product Analysis by Controlled Potential Electrolysis

Fe(^{tbu}dhbpy)Cl **1** maintains modest selectivity (68±4% Faradaic efficiency) for with up to 10 hours of electrolysis (2.7 catalyst turnovers; 5.4 electron equivalents per catalyst) in the presence of 0.5 M PhOH and CO_2 at –2.5 V vs Fc/Fc$^+$ (**Table 2.1, Figure S2.26**). *Nota bene*, quantification by NMR methods is done at pH conditions low enough to protonate formate to simplify the product mixture (see Supporting Information). Under these conditions the remainder of the current went to H_2 production (30±10% Faradaic efficiency) with only trace CO detected (1.1±0.3% Faradaic efficiency). Based on this experiment and the controls discussed below, **1** is producing formate in addition to the background heterogeneous production of H_2 by the glassy carbon electrode. Control electrolysis experiments in the absence of catalyst under CO_2 saturation conditions with 0.5 M PhOH gives H_2 (58±6% Faradaic efficiency) and trace CO as the sole products by GC, with no formate detected by NMR methods (**Figure S2.26, Table 2.1**). Electrolysis at –2.5 V vs Fc/Fc$^+$ in the presence of 0.5 M PhOH under Ar saturation shows H_2 (57±7% Faradaic efficiency) evolution (3.8 catalyst turnovers; 7.6 electron equivalents per catalyst); a control experiment without catalyst under these conditions shows a comparable response: H_2 (56±10% Faradaic efficiency) with no CO or formate detected (**Table 2.1**), suggesting a non-catalytic response by **1**. In each case with catalyst present, a linear charge passage with respect to time is observed, consistent with a catalytic reduction response (**Figure S2.26A, S2.27A)**. UV-vis taken before and after electrolysis experiments indicate minimal change in solution composition over the course of the experiment (**Figure S2.26C, S2.27C**).

Table 2.1. Summary of Controlled Potential Electrolysis Data. Conditions were 0.1 M TBAPF6/N,N-DMF supporting electrolyte with 0.05 M Fc as sacrificial oxidant. Working electrode was glassy carbon, counter electrode was glassy carbon, pseudoreference was Ag/AgCl. a Faradaic Efficiency. b 0.5 mM Fe(^{tbu}dhbpy)Cl. c 0.5 M PhOH. d –2.5 V vs Fc/Fc+. e –2.1 V vs Fc/Fc$^+$

Trial	Atmosphere	Catalyst Turnovers	CO[a]	Formate[a]	H_2[a]
1[b,c,d]	CO_2	2.7 (10 h)	Trace	68(4)	30(10)
2[b,c,e]	CO_2	2.0(4.0 h)	Trace	-	51(6)
3[b,d]	CO_2	3.0 (15.0 h)	1.1(0.3)	-	-
4[c,d]	CO_2	N/A(3.0 h)	Trace	-	58(6)
5[b,c,d]	Ar	3.8(5.3 h)	-	-	57(7)
6[b,c,e]	Ar	2.9(4.3 h)	-	-	51(7)
7[b,c,d]	Ar	N/A(5.0 h)	-	-	56(10)

2.4.4 Mechanistic Experiments with Infrared-Spectroelectrochemistry

Infrared-spectroelectrochemistry (IR-SEC) is a technique where IR active modes are monitored with respect to changes in electrochemical potential as a function of time.[42, 71-73] This technique has previously been used to successfully identify catalytic mechanisms related to CO_2 reduction, where the substrate and products often have features with strong IR absorption.[41-42] After sparging a 3 mM solution of Fe(^{tbu}dhbpy)Cl **1** in 0.1 M TBAPF$_6$/*N,N*-DMF with CO_2 for 20 s, and setting the cell to resting potential, the strongest apparent IR absorption band appears at 2358 cm^{-1}, corresponding to CO_2. If the cell potential is brought to –2.0 V (vs Fc/Fc$^+$) from resting potential under these conditions, an absorption band at 1804 cm^{-1} appears and grows in intensity over the course of 5 minutes. We assign this feature at 1804 cm^{-1} to a Fe–CO_2 adduct

($[Fe(^{tbu}dhbpy)(\eta^1\text{-}CO_2)]^-$ **11**). The relatively high wavenumber value of the CO_2 adduct $[Fe(^{tbu}dhbpy)(\eta^1\text{-}CO_2)]^-$ **11** at 1804 cm^{-1} suggests a formal two electron reduction of bound CO_2 has not taken place and this adduct is possibly best described as an Fe-bound CO_2 radical anion. This band continues to grow in intensity if the cell is brought to –2.3 V vs Fc/Fc^+, until a steady state is reached after 30 s. At both –2.0 V and –2.3 V vs Fc/Fc^+, there is also growth of lower intensity IR modes at 1847, 1880, 1911, and 1941 cm^{-1} assigned to Fe carbonyl species, *vide infra* (**Figure 2.6**).[20] If the cell potential is increased again from –2.3 V to –2.5 V (vs Fc/Fc^+), a more rapid growth in the intensity of the carbonyl bands at 1847, 1880, 1911, and 1941 cm^{-1} occurs with concomitant disappearance of the Fe–CO_2 adduct band at 1804 cm^{-1}, suggesting complete consumption of the available Fe complex (**Figure 2.6**); electrochemical reversibility is not observed if the cell is again set to more positive potentials.

Interestingly, the Fe–CO_2 adduct band at 1804 cm^{-1} shows electrochemical reversibility; if these experiments are repeated with a freshly prepared sample to a cell potential of –2.0 V vs Fc/Fc^+ the absorption band at 1804 cm^{-1} disappears completely when the applied potential is lowered to –1.5 V vs Fc/Fc^+. (**Figure S2.21**). Based on these data, we believe the Fe–CO_2 adduct observed by IR-SEC corresponds to the feature observed by CV on the return sweep under CO_2 saturation conditions at –1.92 V vs Fc/Fc^+ (**Figure 2.4**), *vide supra.* When $^{13}CO_2$ was substituted for CO_2, an isotopically shifted band was not observed for this species at 1804 cm^{-1}, due to saturation in the IR spectra from solvent absorbance below 1778 cm^{-1}. However, isotopic shifts in the IR spectra were observed for the four carbonyl bands at 1847, 1880, 1911, and 1941 cm^{-1}. These shifts are consistent with $\Delta\nu_{CO}$ of 43, 43, 33, and 42 cm^{-1}, respectively (**Figure S2.22**). Using the harmonic oscillator solution to Schrodinger's equation and assuming only the C–O bond is involved in the IR modes, $\Delta\nu_{CO}$ of 41, 42, 42, and 43 cm^{-1} were calculated for each respective stretch. Based on these data and IR-SEC results with CO discussed below, these four bands can be initially assigned to mono- or di-carbonyl Fe species (e.g. [Fe(^{tbu}dhbpy)(CO)]$^{-}$ **12**).

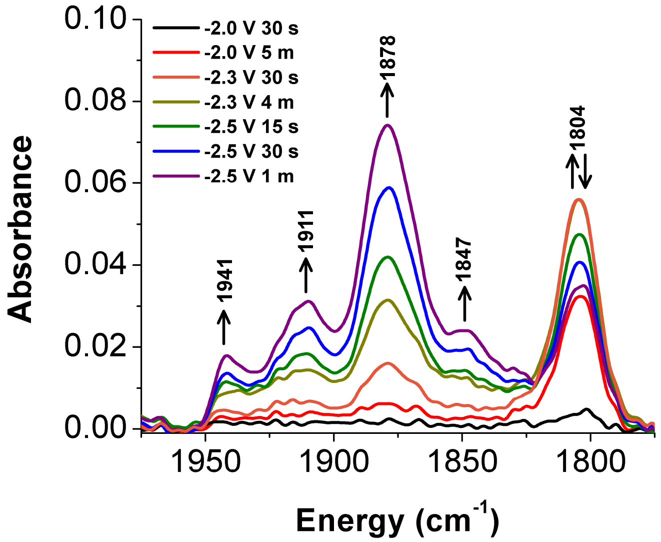

Figure 2.6. IR-SEC experiment with 3 mM Fe(^{tbu}dhbpy)Cl in 0.1 M TBAPF$_6$/*N,N*-DMF supporting electrolyte with CO$_2$. CO$_2$ was sparged through the solution for approximately 20 s. Glassy carbon working electrode, Ag metal pseudoreference electrode, glassy carbon counter electrode; referenced to Fc standard.

When these IR-SEC experiments are repeated under CO$_2$ saturation with added 0.5 M PhOH as a proton source and the cell is set to –2.5 V vs Fc/Fc^{+}, absorbance bands at 1830, 1880, 1911, and 1941 cm^{-1} are observed (**Figure S2.23B**). When ^{13}CO$_2$ was substituted for CO$_2$, isotopic shifts for the bands located at 1806, 1835, 1878, and 1898 cm^{-1} and were observed to have $\Delta\nu_{CO}$ of 24, 45, 33, and 43 cm^{-1} , respectively (**Figure S2.24**). The bands at 1880, 1911, and 1941 cm^{-1} can therefore be assigned to similar Fe–CO species to those obtained under nominally aprotic CO$_2$ atmosphere.

To corroborate the assignment of the bands between 1810 and 1975 cm^{-1} as Fe–CO stretching modes as discussed above, IR-SEC experiments were also conducted in the presence of CO without a proton source. At cell potentials of –2.5 V vs Fc/Fc^+, two bands at 1880 and 1911 cm^{-1} appear, which are consistent with the IR modes observed with added CO_2 experiments (**Figure S2.25A)**. Repeating this experiment with the addition of 0.5 M PhOH showed growth of bands at 1808, 1828, 1880, and 1911 cm^{-1}, which were also observed under CO_2 with added PhOH (**Figure S2.25B**). The absence of the bands observed at 1847 and 1941 cm^{-1} could be the result of the low solubility of CO in *N,N*-DMF (estimated to be 5.0 mM in DMF at STP, from the reported Bunsen coefficient; less than two equivalents CO per Fe),[74] however, carbonato or carboxylato complexes with CO ligands, or multiple CO ligands per Fe, cannot be excluded.

2.4.5 DFT Calculations

As a supplement to the experiments described above, DFT calculations were performed to examine the electronic structure of a model compound for **1**, where the tert-butyl groups had been replaced with H atoms, Fe(dhbpy)Cl. Kohn-Sham representations of the HOMO of model complex Fe(dhbpy)Cl show a primarily ligand-based orbital, consistent with our mechanistic hypothesis of phenoxy-based oxidation features at potentials positive of the Fc/Fc^+ redox couple (**Figure S2.28**).[36] In the presumptive reduction product, $[Fe(dhbpy)Cl]^-$, the HOMO is qualitatively assessed as more metal-based, relative to the ground state (**Figure S2.29**). The presumptive Cl^--loss product $[Fe(dhbpy)Cl]^0$ shows general agreement with this, suggesting the electronic structure is relatively unchanged by this chemical reaction (**Figure S2.30**). Consistent with the mixed-character of the second and third reductions discussed above, the HOMO of $[Fe(dhbpy)]^-$

shows an increase in the amide character of the bpy fragment, as well as a slight spin density contamination on the N atoms (**Figure S2.31**). In the model of the presumed catalytically active state $[Fe(dhbpy)]^{2-}$ the HOMO shifts to an almost exclusively bpy-based composition, although the spin distribution remains relatively unchanged from $[Fe(dhbpy)]^{-}$ (**Figure S2.32**). These results are in qualitative agreement with the assessment that the localization of added charge following the formation of the first reduction product becomes difficult to assign confidently.

TD-DFT calculations were used to compare the suitability of this electronic structure calculation through comparison to the experimental UV-Vis data described above (**Figure S2.1**). A normalized UV-Vis spectrum generated from this calculation shows qualitative agreement with experimental data, with a consistent red shift in absorbance maxima by about 20 nm. Difference densities for the predicted transitions are consistent with our assignment of the two bands at 446 and 552 nm as phenolate π to Fe(III) δ LMCT (**Figure S2.33**).

2.4.6 Foot-of-the-Wave Analysis

Following a previously reported method, variable-scan rate experiments were first performed to verify steady state conditions are not achieved under all of the conditions described (**Figure S2.41**).[24] Foot-of-the-wave analysis was used to determine apparent catalytic rates (k_{cat}) and maximal turnover frequencies (TOF_{max}) for aprotic conditions and separate titrations of PhOH and d_1-PhOD to a point where maximum current density is obtained with CO_2 saturation (**Figures S2.34-S2.36)**.[75] For all cases, E^0_{cat} assumed to be equivalent to $E_{1/2}$, and in all cases, $E_{1/2}$ = –2.45 V vs Fc/Fc$^+$. Kinetic data obtained from this method is summarized in **Table 2.2**. By plotting the TOF_{max} vs [PhOH], the slope obtained gives $k_H[CO_2]$, where k_H is k_{cat} for PhOH of normal isotopic abundance. If this is repeated with d_1-PhOD, then the ratio of these slope values directly provides k_H/k_D = 4.8±0.9 (**Figure S2.37**), where k_D is k_{cat} for deuterium-enriched d_1-PhOD. This kinetic isotope effect (KIE) is consistent with an intermediate hydride species and insertion of CO_2 into the Fe–H bond as the rate determining step, as has been reported previously.[17, 76]

Table 2.2. Summary of kinetic data extracted from CVs using FOWA. Trial 1 is under CO_2 saturation conditions. Trials 2-6 are under CO_2 saturation conditions with added [a]PhOH or [b]d_1-PhOD.

Trial	[PhOH(D)]	TOF_{max} (s^{-1})	k_{cat} ($M^{-2}s^{-1}$)
1	-	2.69E+01	5.08E+02
2	0.122[a]	6.43E+01	2.29E+03
3	0.182[a]	8.40E+01	2.01E+03
4	0.252[a]	1.31E+02	2.26E+03
5	0.0431[b]	4.08E+01	4.11E+03
6	0.101[b]	4.86E+01	2.09E+03
7	0.155[b]	5.76E+01	1.62E+03

2.5 Discussion

These data enable us to propose a mechanism for the behavior of Fe(^{tbu}dhbpy)Cl (**1**) under electrochemically reducing conditions. The first reduction feature of Fe(^{tbu}dhbpy)Cl (**1**) is an electrochemically quasi-reversible wave (E^0= –0.89 V vs Fc/Fc$^+$; $Fe^{III/II}$) which exhibits a Nernstian PhOH-dependent electrochemical response (**Figure 2.3, Figure S2.6-2.12, Table S2.2**). This Nernstian dependence is assigned to a proton transfer event involving the protonation of a bound phenolate moiety of the ligand framework by a PhOH proton donor, which leaves a vacant coordination site for further reactions, **7**. At the second reduction potential (E^0= –2.09 V vs Fc/Fc$^+$), a second protonation event occurs at the metal center in the presence of PhOH. Under conditions with saturated CO_2 only, an electrochemically reversible binding of CO_2 is observed by CV with a new oxidative wave (E_{pa} = –1.92 V vs Fc/Fc$^+$, **Figure 2.4**). IR-SEC studies confirm these observations are the result of an electrochemically reversible CO_2 binding event under aprotic conditions, with a corresponding IR stretching frequency for Fe–CO_2 of 1804 cm^{-1} (**Figure 2.6**). Upon reaching the third reduction (E^0= –2.65 V vs Fc/Fc$^+$), catalytic activity is observed in the presence of PhOH as a sacrificial proton donor (**Figure 2.5**). While good selectivity for CO_2 is observed by controlled potential electrolysis (HER activity is reduced to ~30% Faradaic efficiency, likely due to heterogeneous reduction performed by the glassy carbon electrode), it is clear from IR-SEC experiments bound CO species are observed to be significant products under both protic and aprotic conditions (**Figure 2.6-2.8**). The formation of Fe–CO species greatly limits the activity of Fe(^{tbu}dhbpy)Cl as a CO_2 reduction catalyst, as product analysis under aprotic conditions with CO_2 shows no catalytic turnover.

Scheme 2.3. Proposed catalytic mechanism of Fe(^{tbu}dhbpy)Cl **1** in the presence of PhOH and CO$_2$. **R** = ^{t}Bu

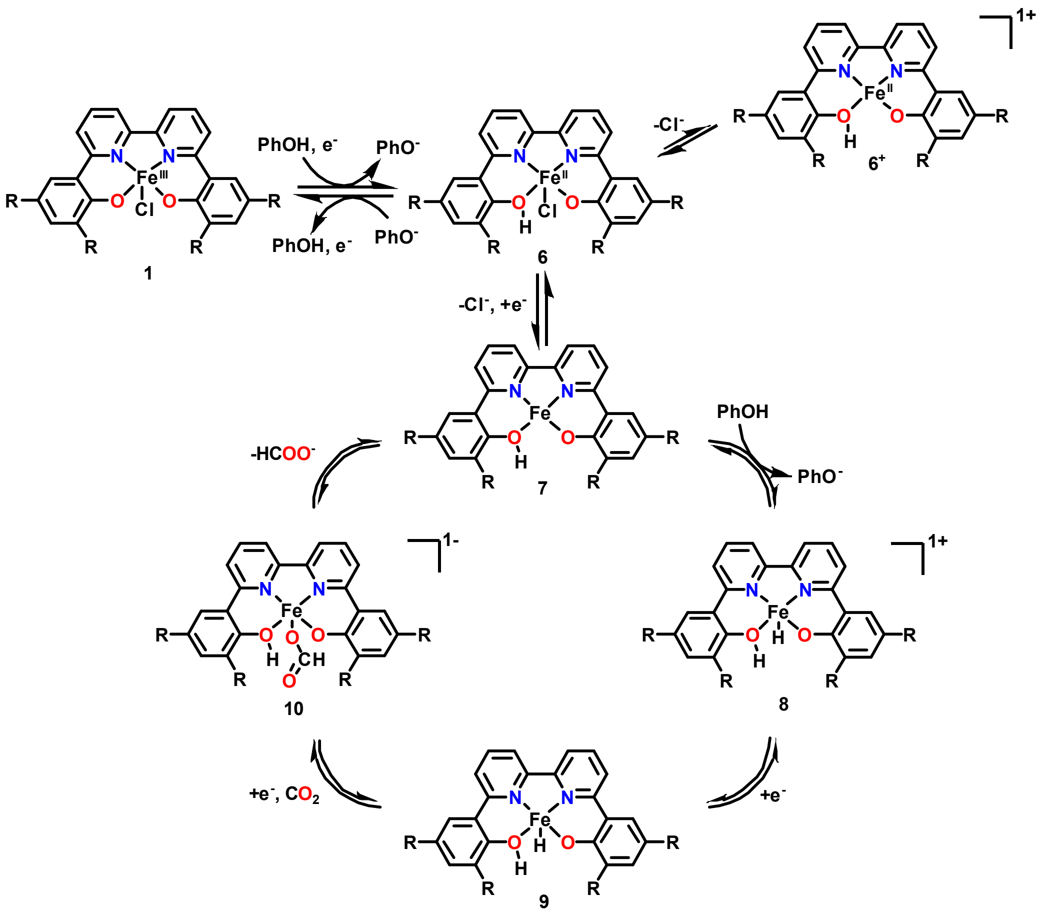

In the CO$_2$ reduction cycle for formate, protonation at the second reduction wave is proposed to generate an Fe hydride (**Scheme 2.2**). Following the reductive activation of CO$_2$, a formato adduct similar to **10** could be further reduced to regenerate the resting state of the catalytic cycle **7** (**Scheme 2.3**). Consistent with these assignments, kinetic isotope effect studies show a KIE of 4.8±0.9 when PhOD is used instead of PhOH. This KIE is consistent with insertion of CO$_2$ into an Fe–H bond as the rate determining step for this reaction (**Figure S2.37**).[17, 76] For comparison, KIE of ~2 have been found for systems which selectively generate CO.[77-78]

2.6 Conclusions

In summary, we have described the synthesis and electrocatalytic behavior of Fe(^{tbu}dhbpy)Cl **1** for CO_2 reduction. Through cyclic voltammetry, UV-vis Spectroscopy, IR-SEC, controlled potential electrolysis and DFT calculations, we have shown **1** exhibits Nernstian behavior with respect to added PhOH in the presence of Ar and CO_2, and reduces CO_2 and protons to formate, hydrogen, and CO with a kinetic preference for formate. The mechanistic studies detailed here suggest it is possible to protonate and reduce the overall complex without losing an active site at the Fe center through cooperative metal-ligand behavior.[35] However, these studies also suggest CO loss from stable Fe–CO species is a limiting factor in catalytic turnover number, as these accumulate under applied potential and appear to result in decomposition. This Fe-based system shows modest selectivity for formate as the primary reduction product of CO_2, but further studies to modify this ligand framework and improve catalytic selectivity and activity are currently underway.

2.7 Supporting Information for Chapter 2

2.7.1 Evans' method

The Evans' method for determining paramagnetic susceptibility was performed by first making a known concentration of ***Fe(^{tbu}dhbpy)Cl* 1** in *N*,*N*-DMF. A capillary insert was then made with a 50% v/v mixture of *N*,*N*-DMF and *N*,*N* -DMF-d_7. The insert was flame sealed, and then placed in an NMR tube loaded with the Fe(^{tbu}dhbpy)Cl solution. ^{1}H NMR spectra with 64 scans were then taken using a 600 MHz Varian NMR Spectrometer.

Paramagnetic moment was then determined using the following equations[1-2]:

χ_D(dhbpy) = 1χ_D(bpy) + 12χD(C_{ring}) + 16χ_D(C) + 42χ_D(H) + 2χ_D(O) + 2 λ(Ar-Ar) + 2 λ(Ar-OR) + 2 λ(benzene)

χ_D(dhbpy) = [(-105) + 16(-6.24) + 12(-6.00) + 42(-2.93) + 2(-4.6) + 2(-0.5) + 2(-1)+ 2(-1.4)] x 10^{-6} emu mol^{-1} =-405.30 x 10^{-6} emu mol^{-1}

$\chi_{dia} = \chi_{ligand} + \chi_{Fe3+} + \chi_{Cl-}$

χ^{dia} = [-380.34 + (-10) + (-23.4)] x 10^{-6} emu mol^{-1} =

-438.70 x 10^{-6} emu mol^{-1}

δv^p = (5.34-4.64)*600 Hz$\chi^{para} = \dfrac{(420\text{ Hz})*(656.07\text{ g/mol})}{(600\text{E}6\text{ Hz})*(1.33\pi)*(7.2 \times 10^{-3}\text{ g/mL})} - \chi_{dia}$

=1.47 x 10^{-2} emu mol^{-1}

2.7.2 Determination of Proton and CO Binding Constants

Binding constants were determined by using **Eq (2.1)** as originally reported.[3] Proton binding constants were calculated using M PhOH concentration. Different binding constant regimes were determined by using Student's t-test after using an F-test to determine equal or unequal variance. P-value under Ar was 9 x 10^{-7}. P value under CO_2 atmosphere was 2 x 10^{-8}.[4] CO binding constant was using the CO saturation concentration estimated to be 5.0 mM from the reported Bunsen coefficient.[5]

$$E = E^0 - \frac{0.059}{n} \ln\left(1 + K_q[Substrate]\right) \qquad (2.1)$$

2.7.3 Determination of Theoretical Isotopic CO_2 Shift

Using the harmonic oscillator approximation for a diatomic molecule in Schrodinger's equation, one can derive **Eq (2.2)** which describes the energy in cm^{-1} of radiation ($\bar{\upsilon}$) required to vibronically excite the molecule by one energy level, where k is the force constant of the bond, and μ is the effective mass ($\mu = \frac{m_1 \times m_2}{m_1 + m_2}$).[6]

$$\bar{\upsilon} = \frac{1}{2\pi c}\sqrt{\frac{k}{\mu}} \qquad (2.2)$$

By solving for k and substituting the IR-spectral energies from the naturally abundant sample (m_1 = 12; m_2 = 16 for ^{12}C and ^{16}O, respectively) for $\bar{\upsilon}$, one can obtain a value for k, which remains constant upon isotopic substitution. By using this value for k derived from empirical data, one can approximate the isotopic shift expected for experiments using $^{13}CO_2$ (m_1 = 13; m_2 = 16).

2.7.4 Product Analysis

Analysis of gas phase products was done by sampling electrolysis headspace through syringe injections into an Agilent 7890B GC equipped with a specialty gas split column 5 Å mol sieve/Porabond Q column and thermal conductivity detector. Quantification was done by calibration curve made by injections of known volumes of H_2 and CO into a flask containing *N,N*-DMF which was degassed and sparged for 15 min with CO_2 while stirring at all times. Manual injections were made using an SGE air-tight 1 mL syringe into a split inlet with a split ratio of 11.7:1. GC oven conditions were 50 °C for 10 minutes, followed by a 20 °C/min to 250 °C, with a final hold at 250 °C for 5 minutes. Column flow rate was set to 1.8 mL/min. The electrolysis cell was calibrated using $Re(bpy)(CO)_3Cl$, with 1 mM catalyst, 0.5 M PhOH, and CO_2 saturation in 0.1 M $TBAPF_6$/*N*,*N*-DMF, Faradaic efficiencies of 88% for CO and 9% for H_2 were observed. Quantitation limit for CO for this method was determined by taking 7 consecutive measurements from the calibration flask at a value estimated to be 5x the detection limit. The standard deviation of these measurements was found according to standard methods.[4]

Solution phase products were analyzed by diluting electrolysis solution to 50% v/v with D_2O and obtaining a ^1H NMR on a Varian 600 MHz NMR Spectrometer. After acidification of this solution with HCl (aq.), a shift from 8.46 ppm to 8.23 ppm, referenced to residual D_2O signal, was observed, which is consistent with the protonation of formate to formic acid. Formic acid was then quantified by extracting 2 mL of bulk electrolysis solution with 2 mL of D_2O, and then washing the aqueous layer one time with 2 mL of

CH_2Cl_2. A known amount of maleic acid was then added to the aqueous layer as an internal standard, and quantification was achieved by integration of ^1H NMR spectra.

Carbonate was analyzed using the same workup procedure as above using ^{13}C NMR. It was compared to an authentic standard of $TBAHCO_3$ synthesized according to a previously reported procedure[7] using a D_2O as solvent with a single drop of *N,N*-DMF as an internal reference.

2.7.5 Synthesis of d_1-PhOD

d_1-PhOD was synthesized by stirring PhOH in D_2O overnight in a 100 mL Schlenk flask under inert atmosphere, followed by solvent removal by reduced pressure. *d_1*-PhOD was stored in the glovebox at -40 °C until use. ^1H NMR were taken in $CDCl_3$ (dried on 4 Å molecular sieves for 3 days) the day of use to determine % deuteration (89%, **Figure S2.38**). To account for sub-stoichiometric deuteration, the final values were corrected following equation (6) where $\chi_{H/D}$ is the mol fraction of the given isotope.

2.7.6 Foot-of-the-Wave Analysis

Foot of the wave (FOWA) analysis was performed based on previously described methods. In brief, catalytic CVs were overlayed with the Faradaic CV to give the best overlay possible. Next i_c/i_p and $(1+\exp(RT/nF(E-E^0_{cat}))^{-1}$ plotted for the full overlay. E^0_{cat} was adjusted from the $E_{1/2}$ of the third reduction to be the potential at half current height (E^0_{cat} = –2.45 V vs Fc/Fc^+) for all cases. Finally, the region starting at $i_c/i_p=1$ was fit with a linear regression to give $r^2 \geq 0.975$ in all cases. TOF_{max} was computed using the slopes from these linear regressions and the equation, where $slope = 2.24 n_{cat}^{\sigma}\sqrt{\frac{RT}{Fv}TOF_{max}}$. n_{cat}

was considered to be 2 and σ was considered to be 1; k_{cat} can then be determined using the equation $TOF_{max} = k_{cat}[substrate]^m$. For aprotic conditions the reaction order for CO_2 was considered to be 2. For conditions with phenol added, reaction orders for both CO_2 and PhOH were considered to be 1.

2.7.7 Determination of KIE from FOWA

To determine a KIE from FOWA, TOF_{max} were plotted vs [PhOH] and [PhOD]. A KIE can then be directly determined from the slopes of these lines as demonstrated below.

$$TOF_{max} = k_{cat}[PhOH][CO_2] \qquad (2.3)$$

Starting from **Eq (2.3)**, by plotting TOF_{max} vs PhOH(D) the slope of the line is proportional to k_{cat} by equation (3).

$$Slope = k_{cat}[CO_2] \qquad (2.4)$$

When TOF_{max} vs [PhOH] is plotted, a slope of $k_{cat}[CO_2]$ is obtained **Eq (2.4)**.

Since $[CO_2]$ is constant under CO_2 saturation conditions, it follows that by taking a direct ratio of the slopes obtained with PhOH and d_1-PhOD, a KIE can be obtained **Eq (2.5)**. k_H is k_{cat} for PhOH of normal isotopic abundance; k_D is k_{cat} for D-enriched d_1-PhOH. To correct for non-stoichiometric deuteration, consider **Eq (2.6)**, which gives the observed slope for deuteration as a function of the mol fraction (χ_H/χ_D) and the known slope for naturally abundant PhOH. This leads to **Eq (2.7)** to give the corrected KIE. The uncorrected value for k_h/k_d is 3.4±0.7, the corrected value obtained using **Eq (2.7)** to correct for incomplete deuteration is 4.8±0.9.

$$\frac{Slope_H}{Slope_D} = \frac{k_H[CO_2]}{k_D[CO_2]} = \frac{k_H}{k_D} \qquad (2.5)$$

$$Slope_D = \frac{(Slope_{obs} - (\chi_H \times slope_H)}{\chi_D} \qquad (2.6)$$

$$\frac{\mathrm{k_H}}{\mathrm{k_D}} = \frac{\chi_\mathrm{D}\times\mathrm{Slope_H}}{\mathrm{Slope_{obs}}\text{- }(\chi_\mathrm{H}\times\mathrm{Slope_H})} \qquad (2.7)$$

2.7.8 Figures

Figure S2.1. Infrared Spectroelectrochemistry cell. The three-electrode set-up consists of an inner glassy carbon working electrode disc (10 mm diameter), a central circular silver metal pseudoreference electrode, and an outer circular glassy carbon counter electrode embedded within a PEEK block.

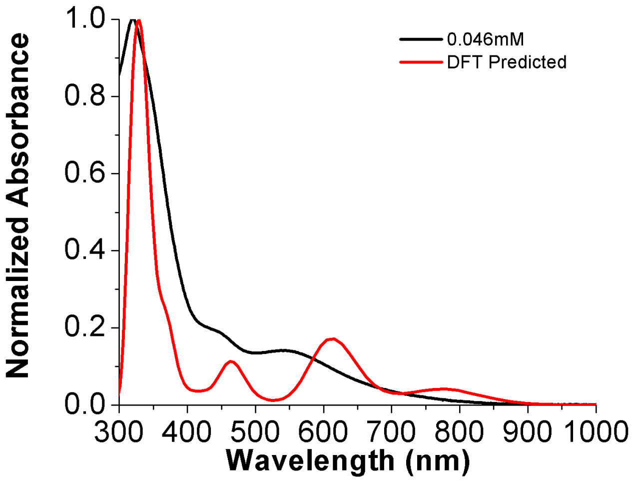

Figure S2.2. Characteristic UV-Vis Spectrum of 0.046 mM Fe($^{\mathrm{tbu}}$dhbpy)Cl **1** and the predicted DFT UV-Vis spectrum in *N*,*N*-DMF.

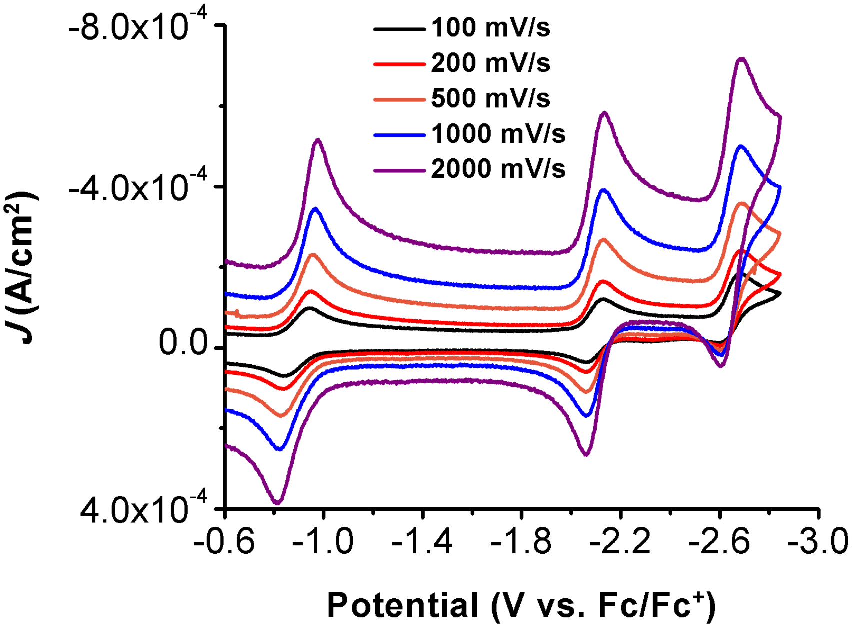

Figure S2.3. Cyclic voltammograms of 0.5 mM Fe(^{tbu}dhbpy)Cl **1** in *N*,*N*-DMF with 0.1 M TBAPF$_6$ solution under Ar saturation, showing response to variable scan rate. Working electrode is glassy carbon (3 mm diameter), counter electrode is Pt wire, and pseudo-reference is Ag/AgCl wire with ferrocene (Fc) added as internal reference.

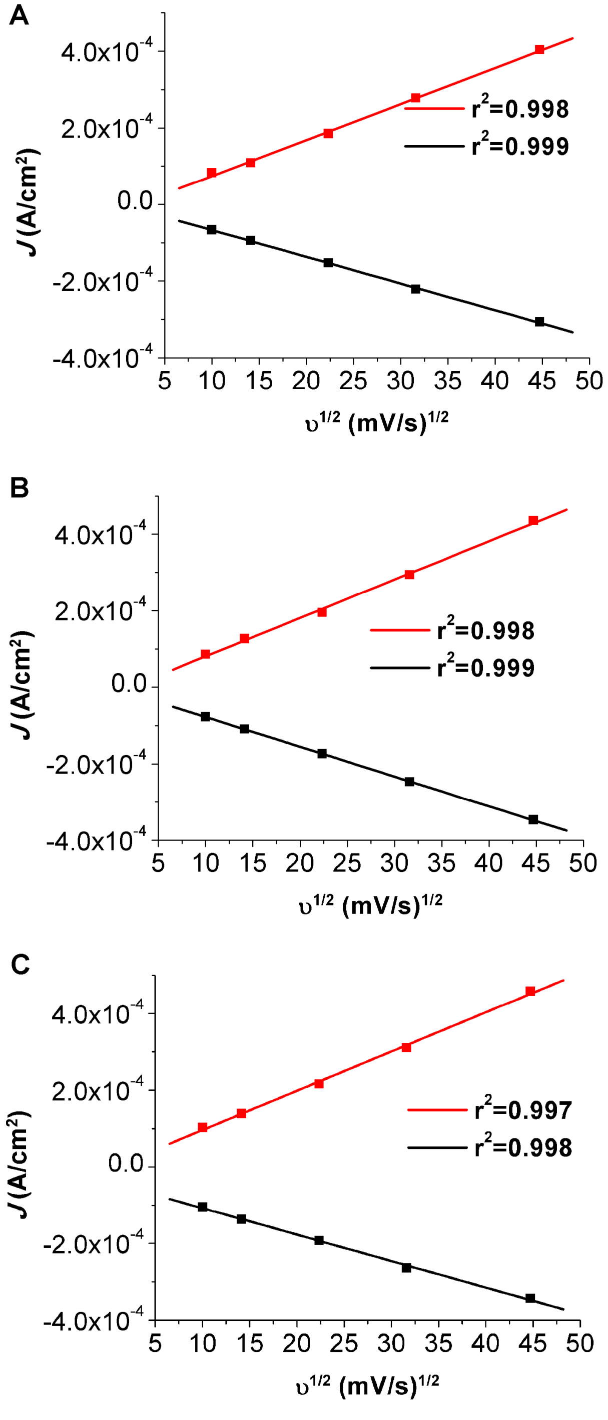

Figure S2.4. Variable scan rate plots of Fe(^{tbu}dhbpy)Cl **1** A) First reduction potential (E^0 = –0.89 V vs Fc/Fc$^+$) B) Second reduction potential (E^0 = –2.09 V vs Fc/Fc$^+$) C) Third reduction potential (E^0 = –2.65 V vs Fc/Fc$^+$). Working electrode is glassy carbon (3 mm diameter), counter electrode is Pt wire, and pseudo-reference is Ag/AgCl wire with ferrocene (Fc) added as internal reference.

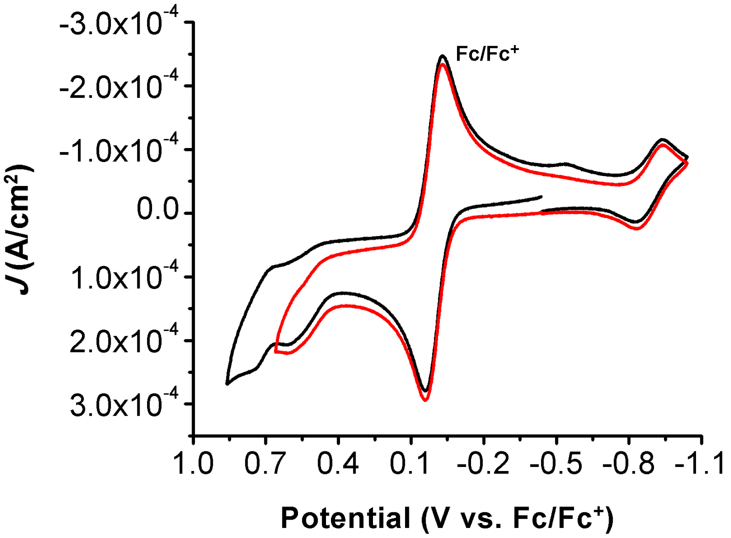

Figure S2.5. Cyclic voltammograms of 0.5 mM Fe(^{tbu}dhbpy)Cl **1** in *N*,*N*-DMF with 0.1 M $TBAPF_6$ supporting electrolyte under an atmosphere of Ar, showing chemical reaction of diradical species on the CV timescale. Scan rate is 100 mV/s. Working electrode is glassy carbon (3 mm diameter), counter electrode is Pt wire, and pseudo-reference is Ag/AgCl wire with ferrocene (Fc) added as internal reference.

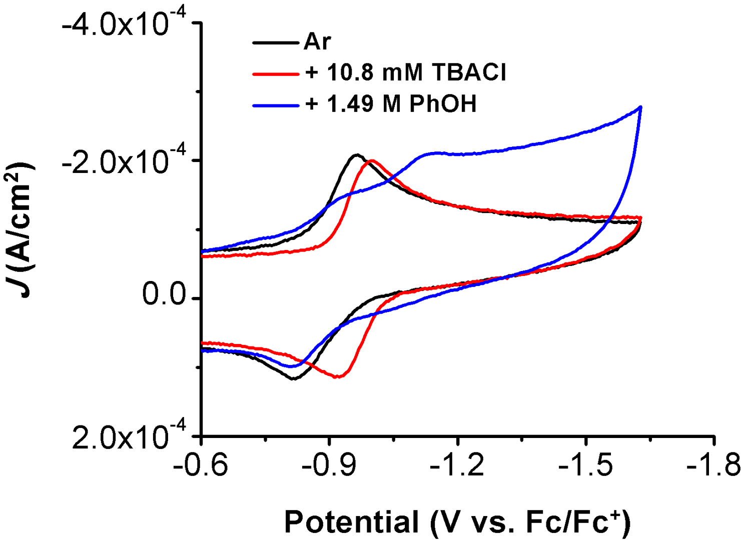

Figure S2.6. Cyclic voltammograms of 0.5 mM Fe(^{tbu}dhbpy)Cl **1** in *N*,*N*-DMF 0.1 M $TBAPF_6$ supporting electrolyte under an atmosphere of Ar, showing loss of chloride at first reduction feature. Scan rate is 1000 mV/s. Working electrode is glassy carbon (3 mm diameter), counter electrode is Pt wire, and pseudo-reference is Ag/AgCl wire with ferrocene (Fc) added as internal reference.

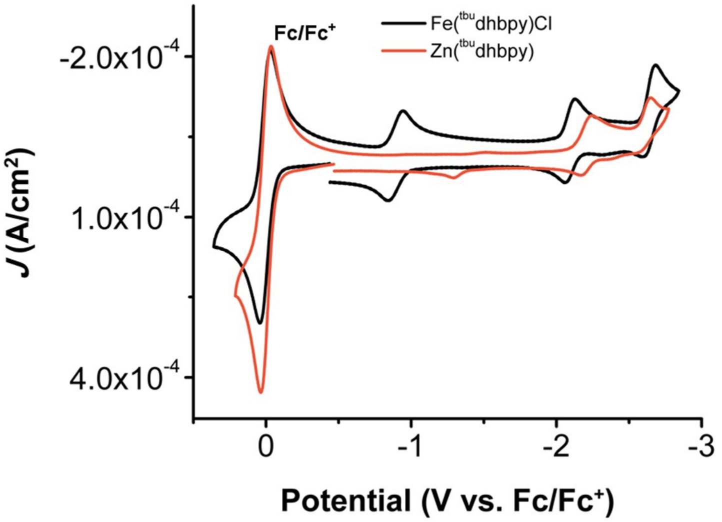

Figure S2.7. Cyclic voltammogram of 0.5 mM and Fe(^{tbu}dhbpy)Cl **1** or Zn(^{tbu}dhbpy) and in *N*,*N*-DMF 0.1 M TBAPF$_6$ supporting electrolyte under an atmosphere of Ar. Scan rate is 100 mV/s. Working electrode is glassy carbon (3 mm diameter), counter electrode is glassy carbon rod, and pseudo-reference is Ag/AgCl wire with ferrocene (Fc) added as internal reference.

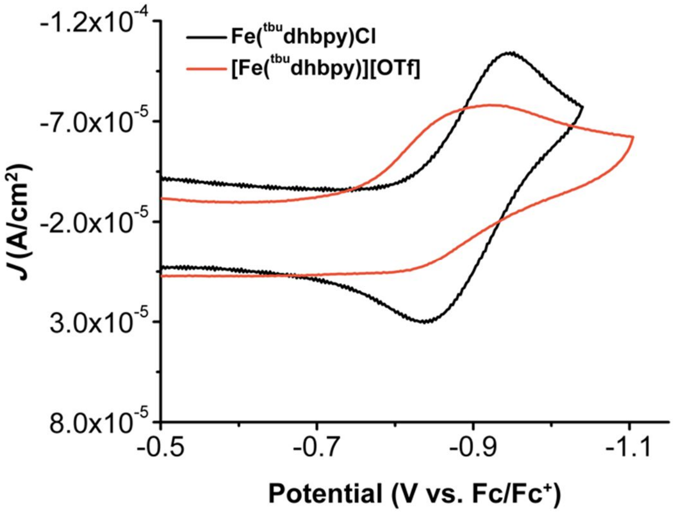

Figure S2.8. Cyclic voltammogram of 0.5 mM [Fe(^{tbu}dhbpy)][OTf] **1[OTf]** or Fe(^{tbu}dhbpy)Cl **1** in *N*,*N*-DMF 0.1 M TBAPF$_6$ supporting electrolyte under an atmosphere of Ar. Scan rate is 100 mV/s. Working electrode is glassy carbon (3 mm diameter), counter electrode is glassy carbon rod, and pseudo-reference is Ag/AgCl wire with ferrocene (Fc) added as internal reference.

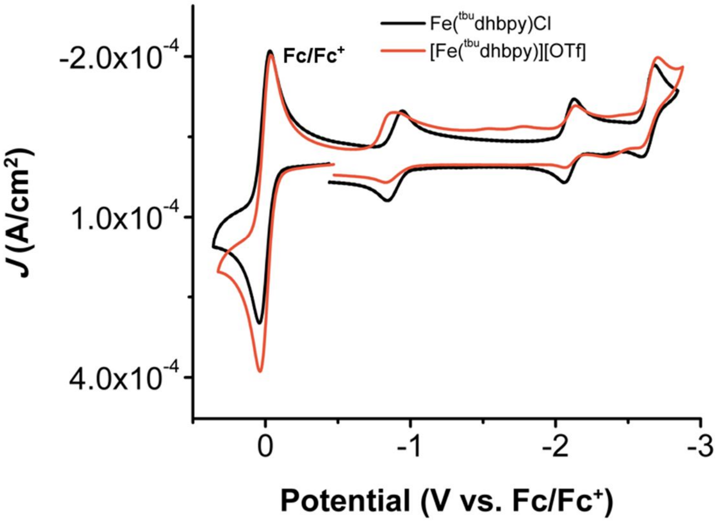

Figure S2.9. Cyclic voltammogram of 0.5 mM Fe(^{tbu}dhbpy)Cl **1** or [Fe(^{tbu}dhbpy)][OTf] **1[OTf]** in *N*,*N*-DMF 0.1 M TBAPF$_6$ supporting electrolyte under an atmosphere of Ar. Scan rate is 100 mV/s. Working electrode is glassy carbon (3 mm diameter), counter electrode is glassy carbon rod, and pseudo-reference is Ag/AgCl wire with ferrocene (Fc) added as internal reference.

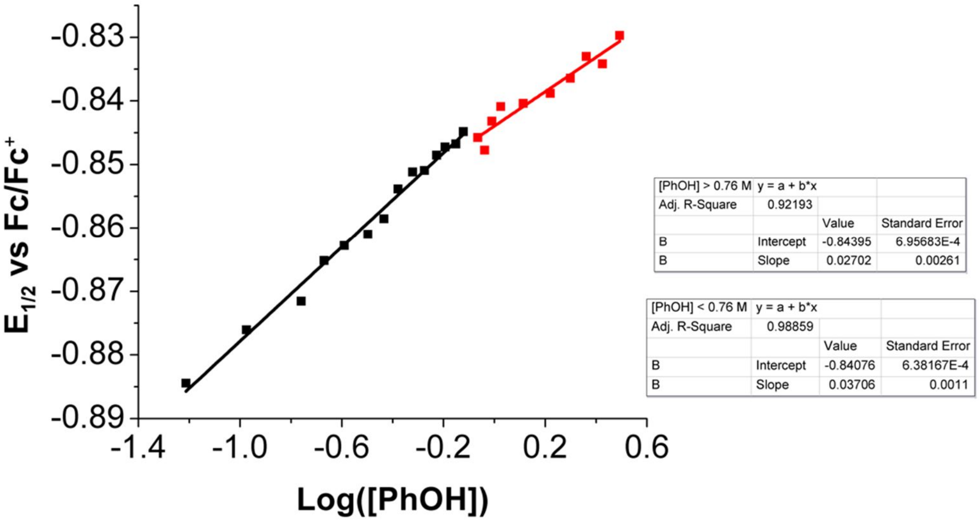

[PhOH] > 0.76 M	y = a + b*x		
Adj. R-Square	0.92193		
		Value	Standard Error
B	Intercept	-0.84395	6.95683E-4
B	Slope	0.02702	0.00261

[PhOH] < 0.76 M	y = a + b*x		
Adj. R-Square	0.98859		
		Value	Standard Error
B	Intercept	-0.84076	6.38167E-4
B	Slope	0.03706	0.0011

Figure S2.10. Nernst plot for Fe(^{tbu}dhbpy)Cl **1** under Ar atmosphere. At concentrations of PhOH < 0.76 M, a slope of 37±1 mV/decade is observed. At concentrations of PhOH > 0.76 M, a slope of 27±3 mV/decade is observed.

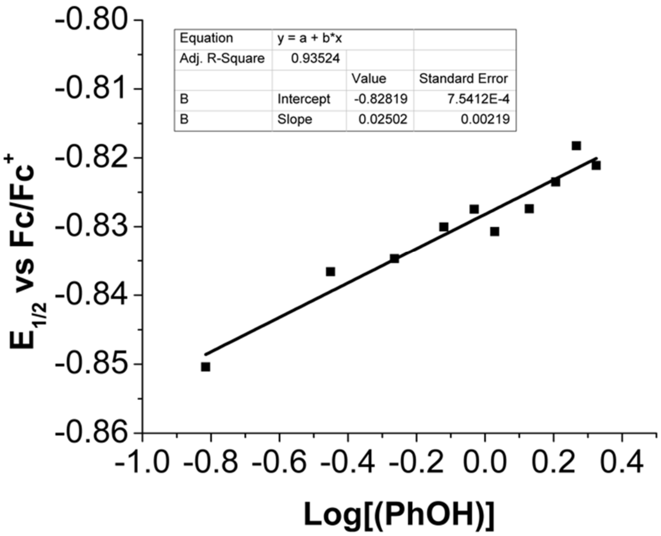

Figure S2.11. Nernst plot for 0.5 mM [Fe(^{tbu}dhbpy)][OTf] **1[OTf]** in *N*,*N*-DMF 0.1 M with $TBAPF_6$ under Ar atmosphere. At all concentrations studied a consistent slope of 25±2 mV/decade is observed.

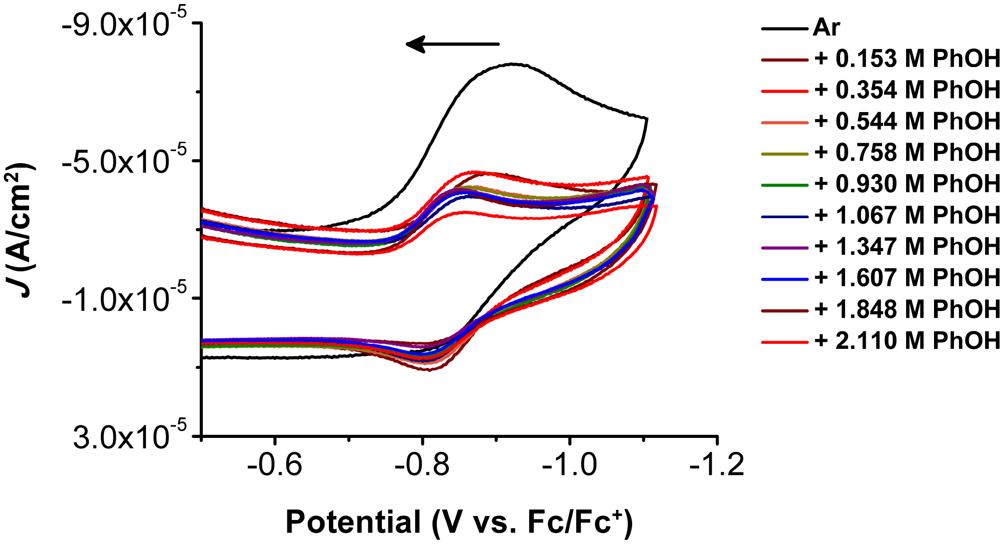

Figure S2.12. Nernstian shift of 0.5 mM [Fe(^{tbu}dhbpy)][OTf] **1[OTf]** first reduction (E^0 = –0.89 V) towards oxidizing potentials upon addition of PhOH as a proton source under in *N*,*N*-DMF 0.1 M with $TBAPF_6$ supporting electrolyte under an atmosphere of CO_2. Scan rate is 100 mV/s. Working electrode is glassy carbon (3 mm diameter), counter electrode is glassy carbon, and pseudo-reference is Ag/AgCl wire with ferrocene (Fc) added as internal reference. Red arrow shows direction of potential sweep. Black arrow shows direction of shift with increasing PhOH concentration.

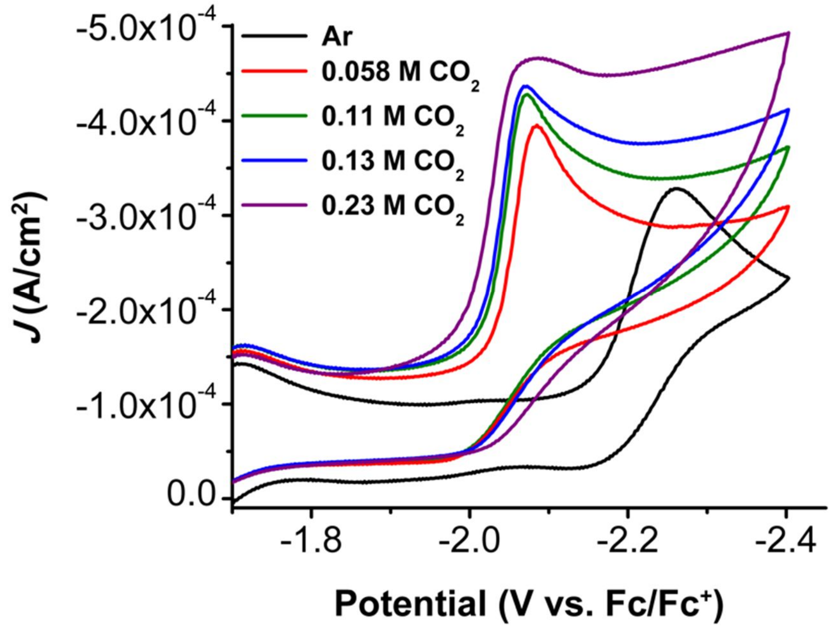

Figure S2.13. Cyclic voltammograms of 0.5 mM Fe(^{tbu}dhbpy)Cl **1** in *N*,*N*-DMF with 0.1 M $TBAPF_6$ supporting electrolyte under an atmosphere of Ar (black) and varying CO_2 concentrations (red, blue, green, and purple). Scan rate is 100 mV/s. Working electrode is glassy carbon (3 mm diameter), counter electrode is Pt wire, and pseudo-reference is Ag/AgCl wire with ferrocene (Fc) added as internal reference.

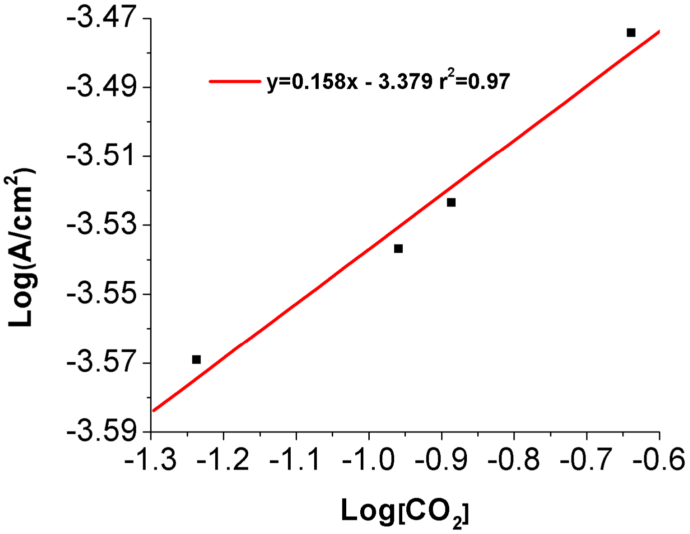

Figure S2.14. Log-Log plot of current density and [CO_2] under aprotic conditions. Slope of 0.16 consistent with rate-limiting kinetics with respect to [CO_2] for catalytic current.[8]

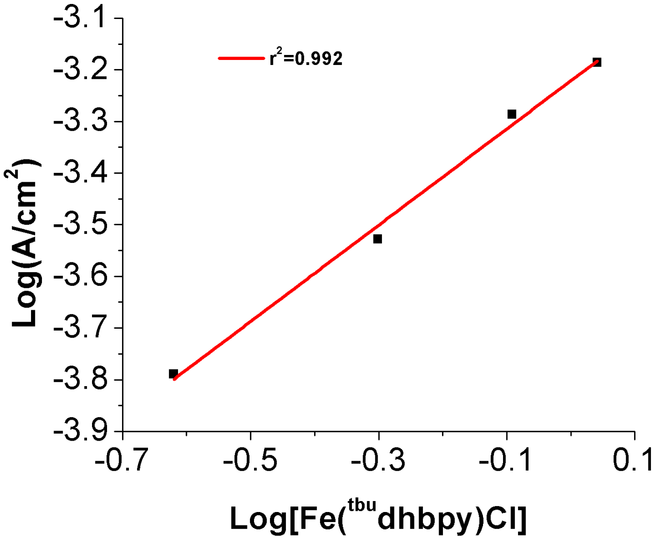

Figure S2.15. Log-log of current density and [Fe(^{tbu}dhbpy)Cl] **1** [mM] under saturated CO$_2$ conditions. Slope of 0.93 is indicative of 1st order kinetics with respect to Fe(^{tbu}dhbpy)Cl.

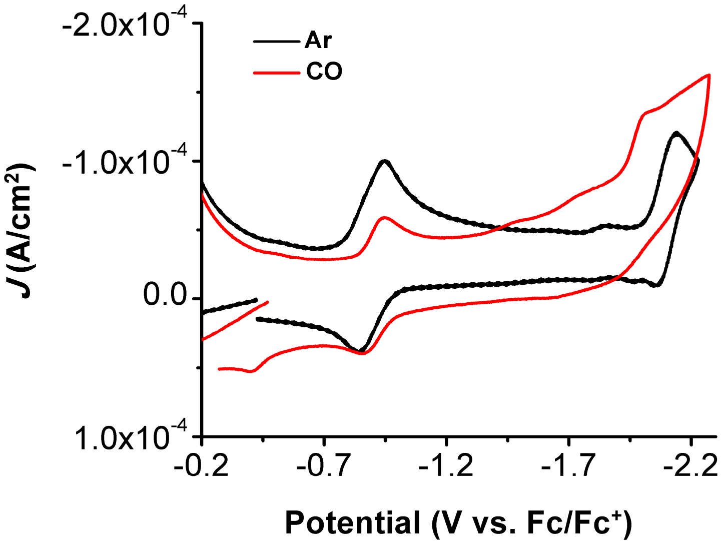

Figure S2.16. Cyclic voltammograms of 0.5 mM Fe(^{tbu}dhbpy)Cl **1** in *N*,*N*-DMF with 0.1 M TBAPF$_6$ supporting electrolyte under an atmosphere of Ar (black) and CO (red). Scan rate is 100 mV/s. Working electrode is glassy carbon (3 mm diameter), counter electrode is glassy carbon, and pseudo-reference is Ag/AgCl wire with ferrocene (Fc) added as internal reference.

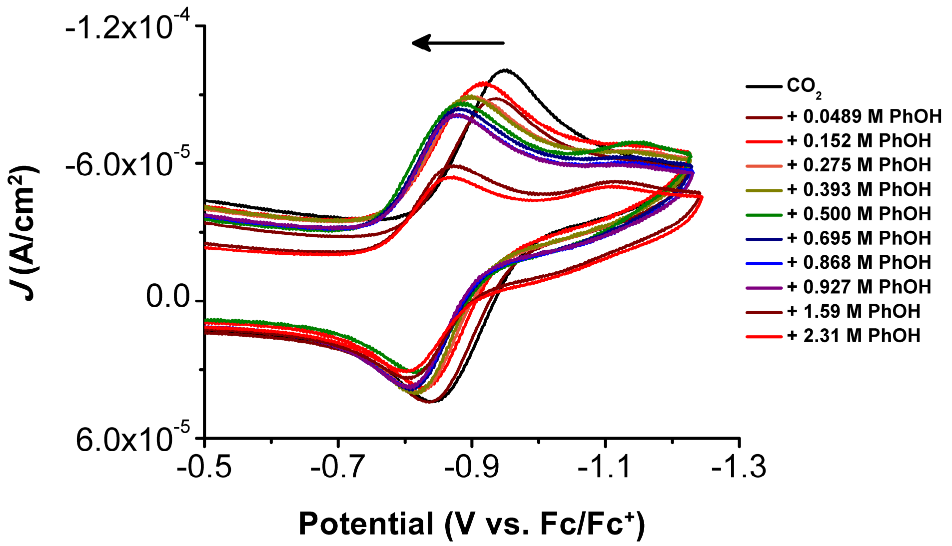

Figure S2.17. Nernstian shift of 0.5 mM Fe(^{tbu}dhbpy)Cl **1** first reduction (E^0 = –0.89 V) towards oxidizing potentials upon addition of PhOH as a proton source under in *N*,*N*-DMF 0.1 M with TBAPF$_6$ supporting electrolyte under an atmosphere of CO_2. Scan rate is 100 mV/s. Working electrode is glassy carbon (3 mm diameter), counter electrode is Pt wire, and pseudo-reference is Ag/AgCl wire with ferrocene (Fc) added as internal reference. Red arrow shows direction of potential sweep. Black arrow shows direction of shift with increasing PhOH concentration.

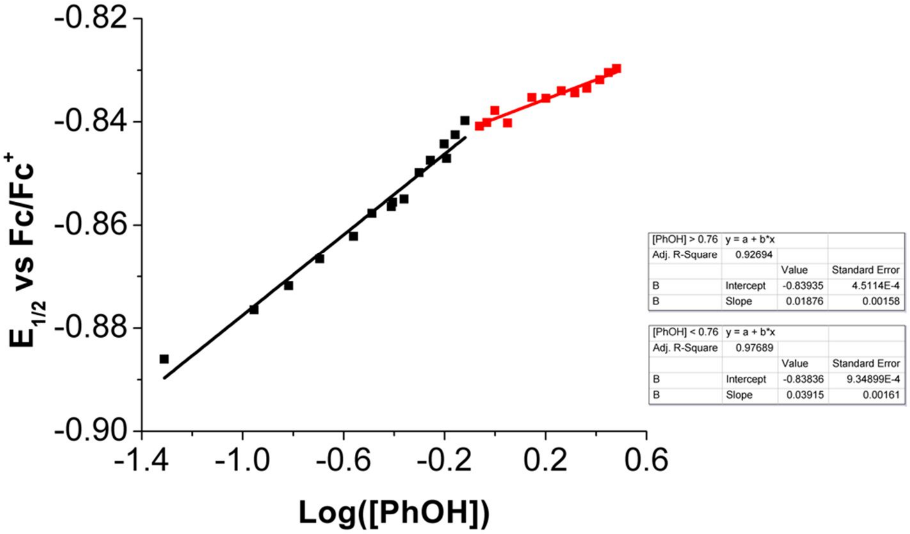

[PhOH] > 0.76	y = a + b*x		
Adj. R-Square	0.92694		
		Value	Standard Error
B	Intercept	-0.83935	4.5114E-4
B	Slope	0.01876	0.00158

[PhOH] < 0.76	y = a + b*x		
Adj. R-Square	0.97689		
		Value	Standard Error
B	Intercept	-0.83836	9.34899E-4
B	Slope	0.03915	0.00161

Figure S2.18. Nernst plot for 0.5 mM [Fe(^{tbu}dhbpy)][OTf] **1[OTf]** in *N*,*N*-DMF 0.1 M with TBAPF$_6$ under saturated CO_2 atmosphere. At concentrations of PhOH < 0.76 M, a slope of 39±2 mV/decade is observed. At concentrations of PhOH > 0.76 M, a slope of 18±2 mV/decade is observed.

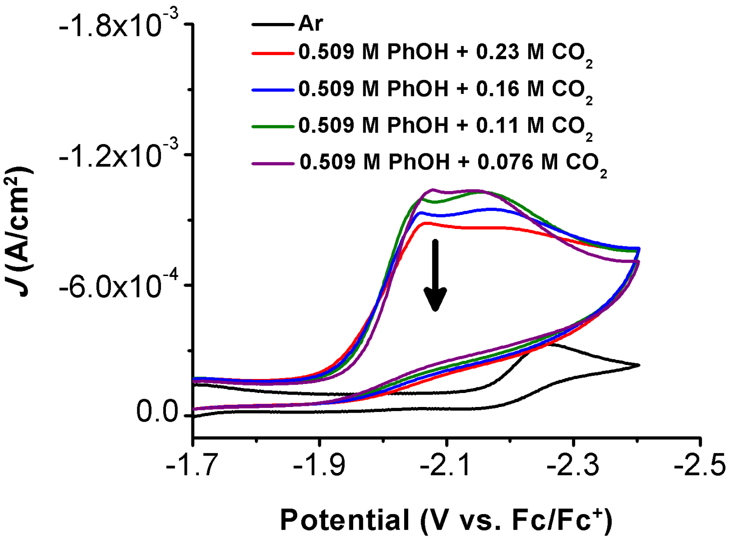

Figure S2.19. Response of 0.5 mM [Fe(^{tbu}dhbpy)][OTf] **1[OTf]** in *N*,*N*-DMF 0.1 M with TBAPF$_6$ at third reduction when varying concentrations of CO2 are added with 0.509 M PhOH. Scan rate is 100 mV/s. Working electrode is glassy carbon (3 mm diameter), counter electrode is Pt wire, and pseudo-reference is Ag/AgCl wire with ferrocene (Fc) added as internal reference.

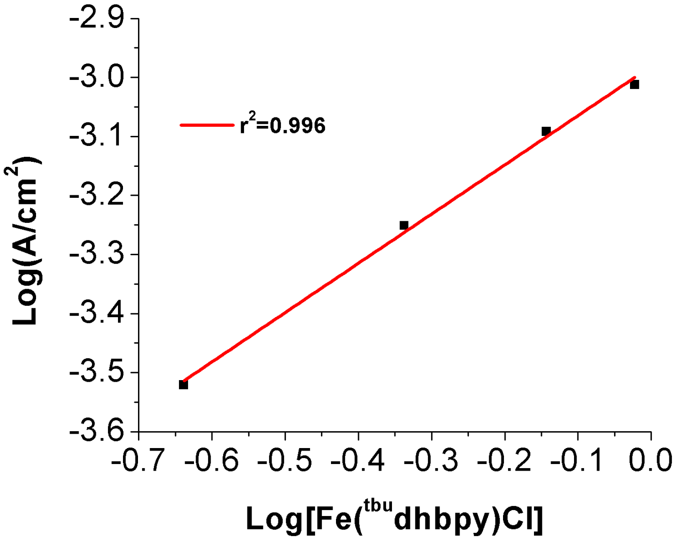

Figure S2.20. Log-log of current density and [Fe(^{tbu}dhbpy)Cl] **1** [mM] under saturated CO2 conditions with 0.5 M PhOH. Slope of 0.83 is indicative of 1st order kinetics with respect to Fe(^{tbu}dhbpy)Cl.

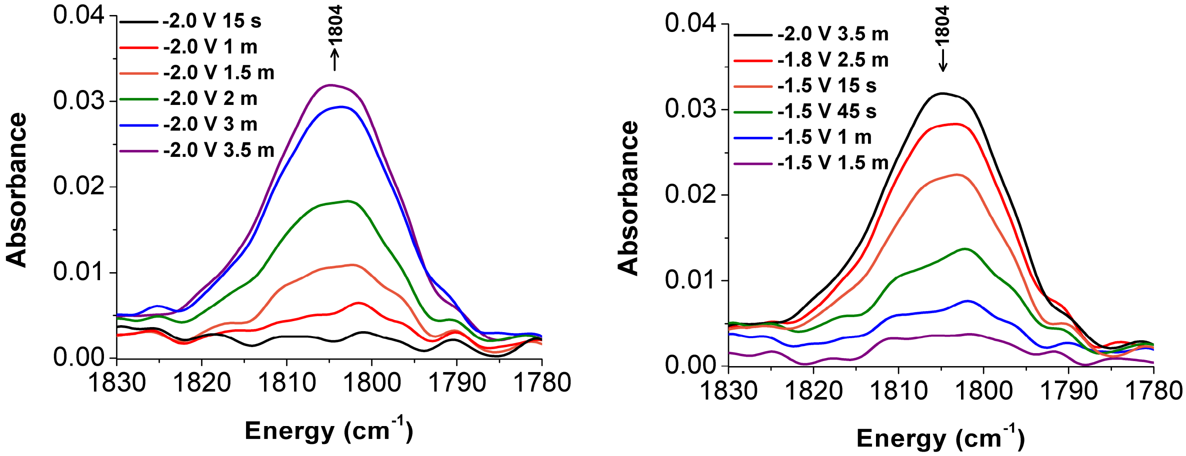

Figure S2.21. IR-SEC experiment with 3 mM Fe(^{tbu}dhbpy)Cl **1** in 0.1 M TBAPF$_6$/*N,N*-DMF supporting electrolyte. CO$_2$ was sparged through the solution for ~20 s. Arrows show growth of intermediate CO$_2$ bound species when potential is held at –2.0 V and reversible loss of this feature when potentials are returned to –1.5 V. Glassy carbon working electrode, Ag metal pseudoreference electrode, glassy carbon counter electrode; referenced to Fc standard.

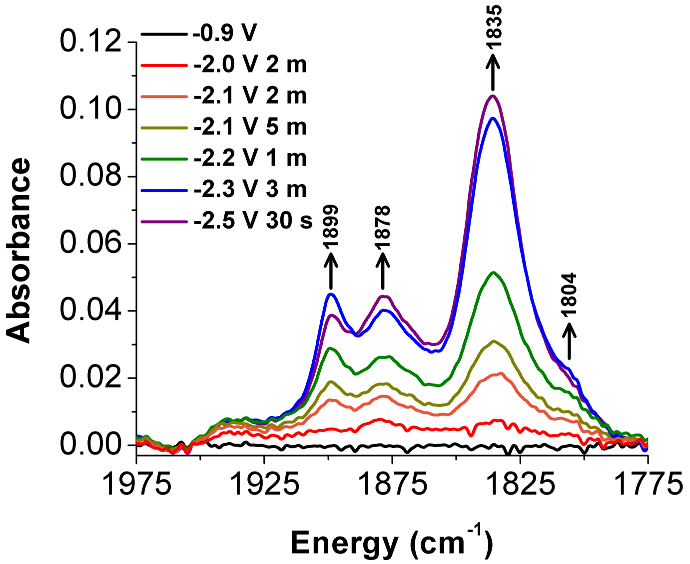

Figure S2.22. IR-SEC experiment with 3 mM Fe(^{tbu}dhbpy)Cl **1** in 0.1 M TBAPF$_6$/*N,N*-DMF supporting electrolyte. ^{13}CO$_2$ was sparged through the solution for ~10 s. Glassy carbon working electrode, Ag metal pseudoreference electrode, glassy carbon counter electrode; referenced to Fc standard.

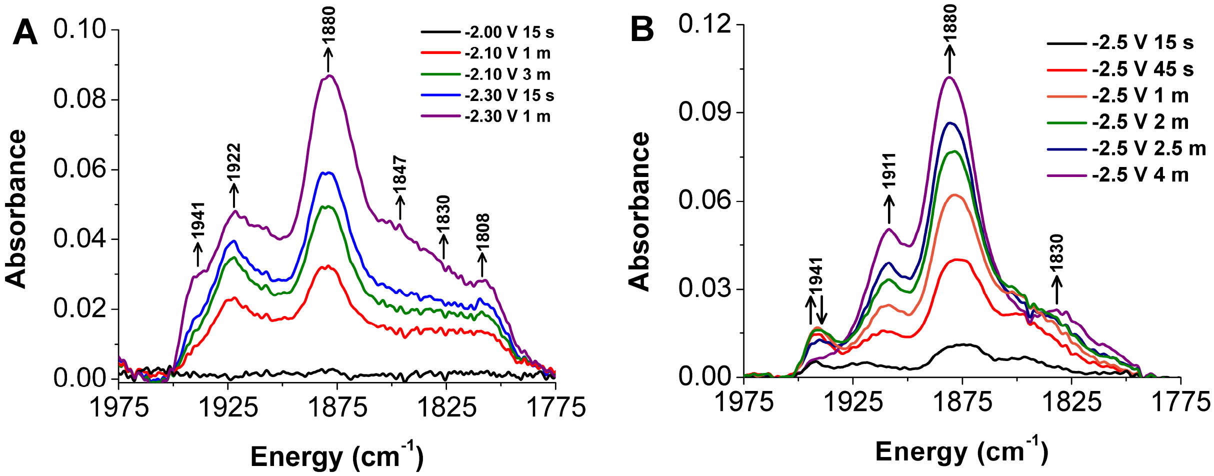

Figure S2.23. (A) IR-SEC spectra of Fe(^{tbu}dhbpy)Cl **1** with CO_2 and 0.5 M PhOH at the Fe(II)/Fe(I) redox wave. Growth of bands at 2nd reduction feature. (B) IR-SEC spectra at the bpy/bpy$^{\bullet-}$ redox wave. Experiments conducted with 3 mM Fe(^{tbu}dhbpy)Cl **1** in 0.1 M $TBAPF_6$/*N,N*-DMF supporting electrolyte. CO_2 was sparged through the solution for approximately 20 s. Glassy carbon working electrode, Ag metal pseudoreference electrode, glassy carbon counter electrode; referenced to Fc standard.

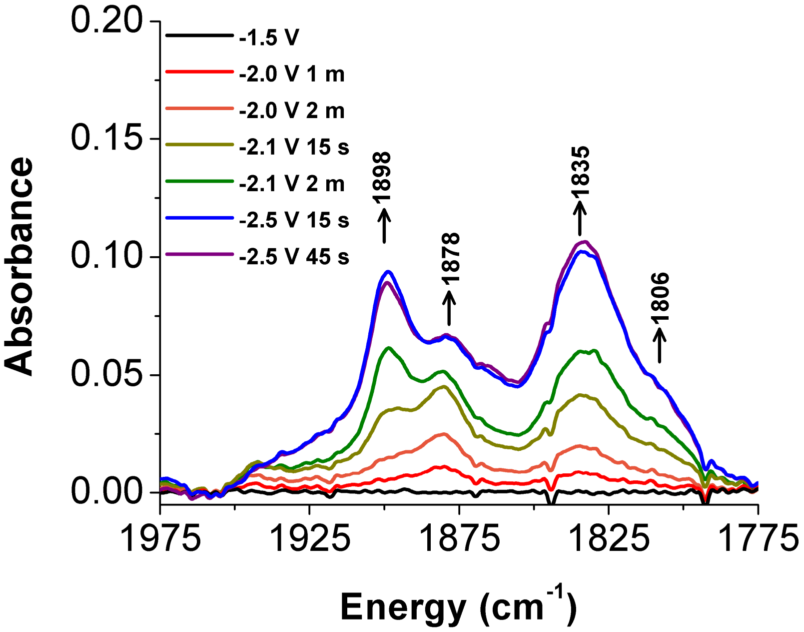

Figure S2.24. IR-SEC experiment with 3 mM Fe(^{tbu}dhbpy)Cl **1** and 0.5 M PhOH in 0.1 M $TBAPF_6$/*N,N*-DMF supporting electrolyte. $^{13}CO_2$ was sparged through the solution for ~10 s. Glassy carbon working electrode, Ag metal pseudoreference electrode, glassy carbon counter electrode; referenced to Fc standard.

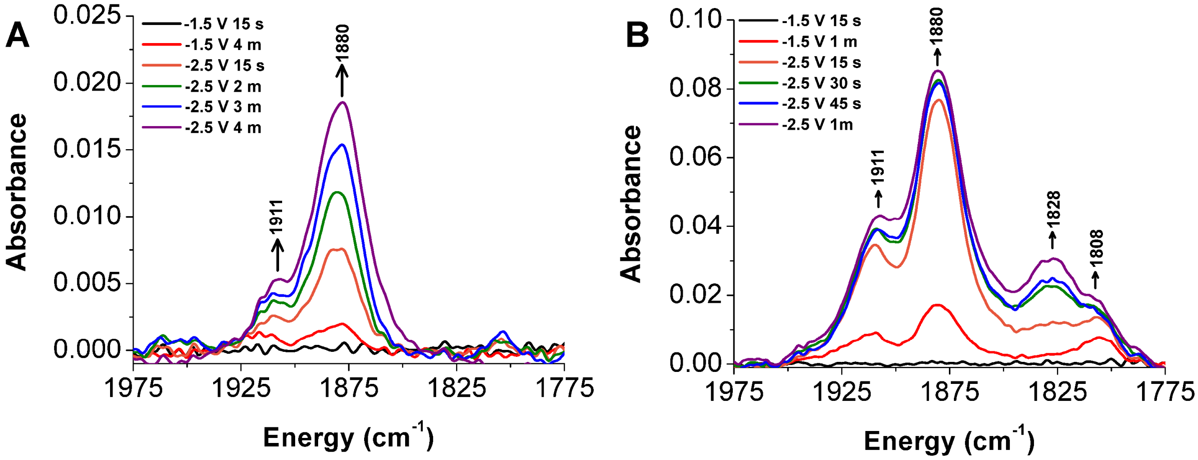

Figure S2.25. IR-SEC experiment with 3 mM Fe(^{tbu}dhbpy)Cl in 0.1 M TBAPF$_6$/*N,N*-DMF supporting electrolyte. (A) CO was sparged through the solution for ~20 s (B) Identical conditions with 0.51 M PhOH added. Arrows show growth of two bands which are consistent to those seen after a CO$_2$ sparge.

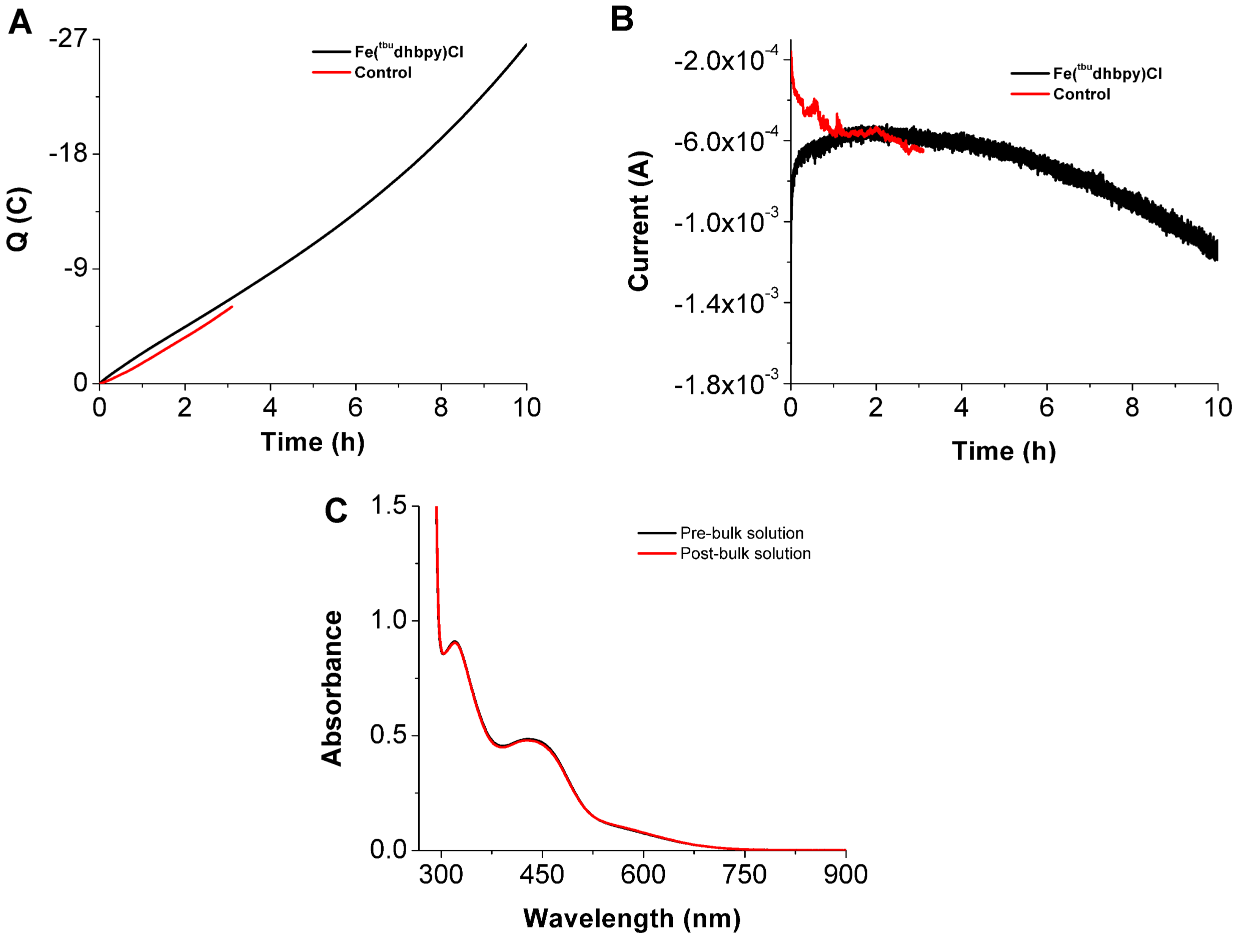

Figure S2.26. (A) Charge passed vs time for bulk electrolysis experiments (B) Current time trace (C) UV-Vis spectrum of Pre (black) and Post (Red) bulk electrolysis solutions after dilution. Conditions were 0.5 mM Fe(^{tbu}dhbpy)Cl **1**, 0.5 M PhOH, and under a CO_2 atmosphere at –2.5 V vs Fc/Fc$^+$ in 0.1 M $TBAPF_6$/*N,N*-DMF supporting electrolyte. 2.7 turnovers for the total system were achieved. Working and counter electrodes were glassy carbon rods. 0.05 M Fc was used as sacrificial oxidant. Reference was non-aqueous Ag/AgCl pseudoreference electrode. Control trace represents identical conditions with no Fe(^{tbu}dhbpy)Cl added.

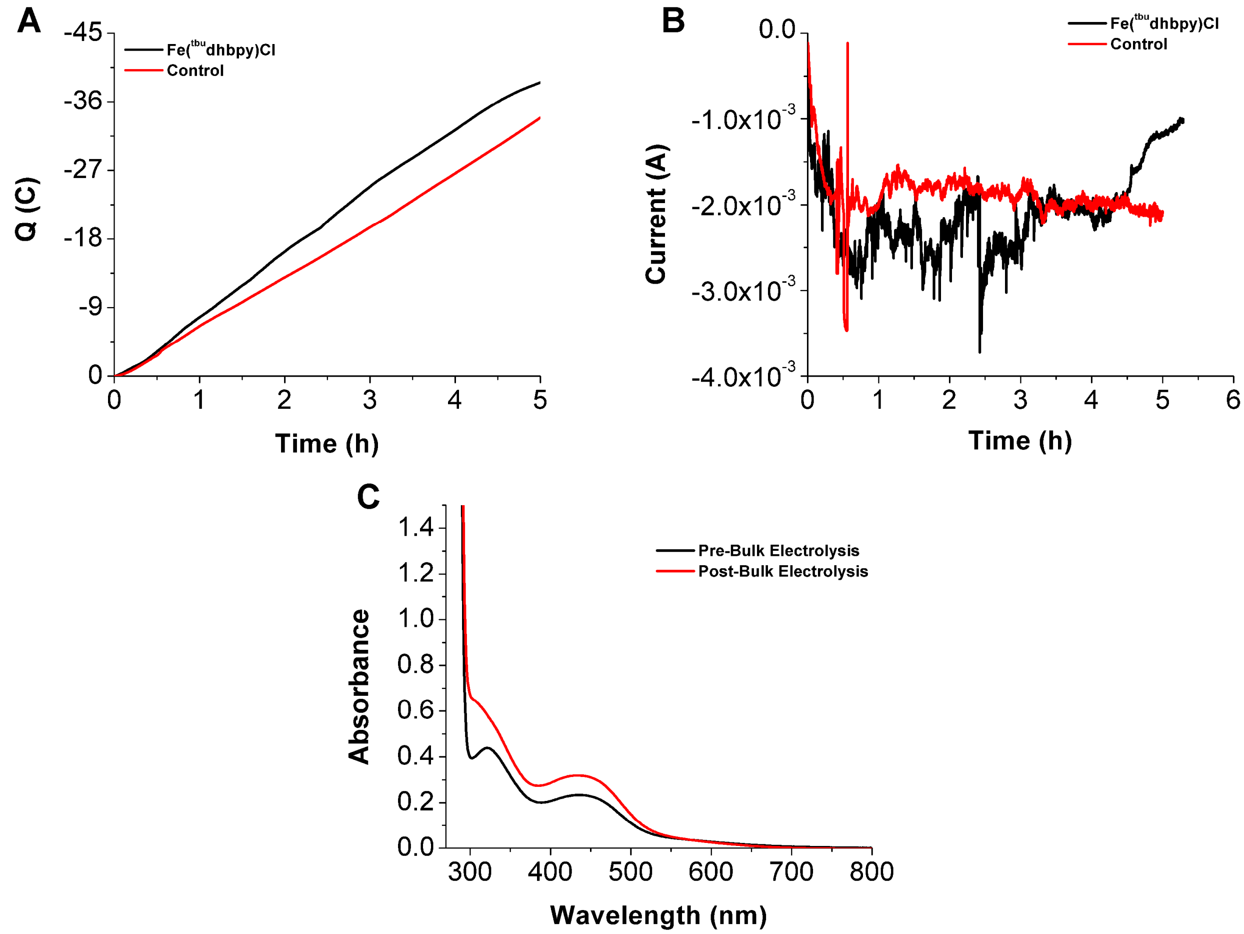

Figure S2.27. (A) Charge passed vs time for bulk electrolysis experiments (B) Current time trace (C) UV-Vis spectrum of Pre (black) and Post (Red) bulk electrolysis solutions after dilution. Conditions were 0.5 mM Fe(^{tbu}dhbpy)Cl **1**, 0.5 M PhOH, and under an Ar atmosphere at –2.5 V vs Fc/Fc^{+} in 0.1 M TBAPF$_6$/*N,N*-DMF supporting electrolyte. 2.7 turnovers for the total system were achieved. Working and counter electrodes were glassy carbon rods. 0.05 M Fc was used as sacrificial oxidant. Reference was non-aqueous Ag/AgCl pseudoreference electrode. Control trace represents identical conditions with no Fe(^{tbu}dhbpy)Cl added.

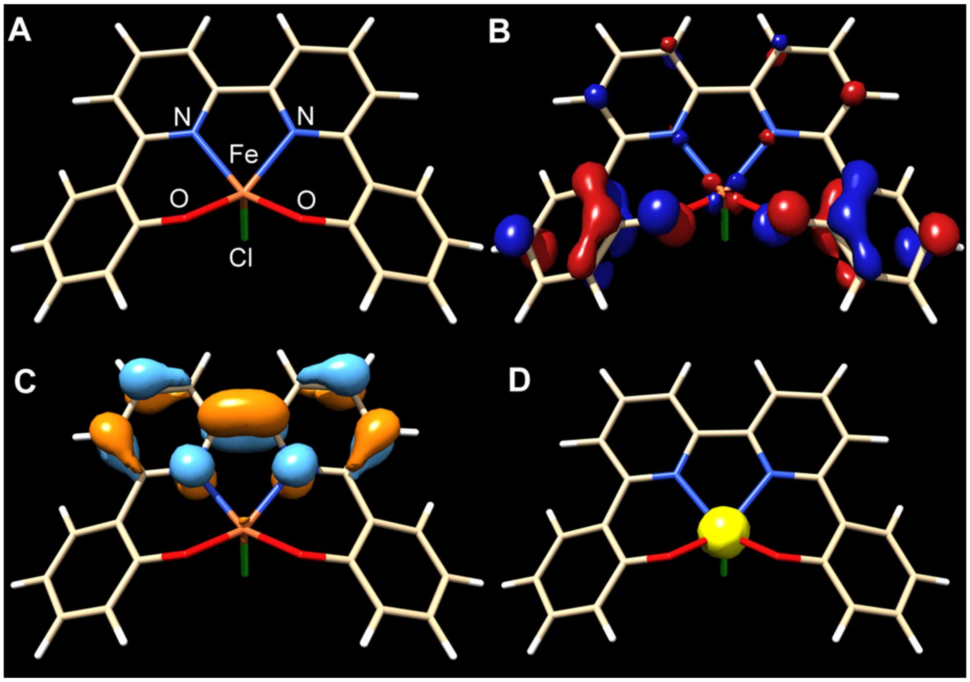

Figure S2.28. Kohn-Sham representations of HOMO (B) and LUMO (C) for model complex Fe(dhbpy)Cl (A); spin density is shown in (D). Used the B3LYP/G[9-13] functional and def2-TZVP[14-15] basis set with the RIJCOSX approximation[16], D3BJ dispersion correction[17-18], and CPCM[19] to model the *N,N*-DMF solvent; 2S + 1 = 6.

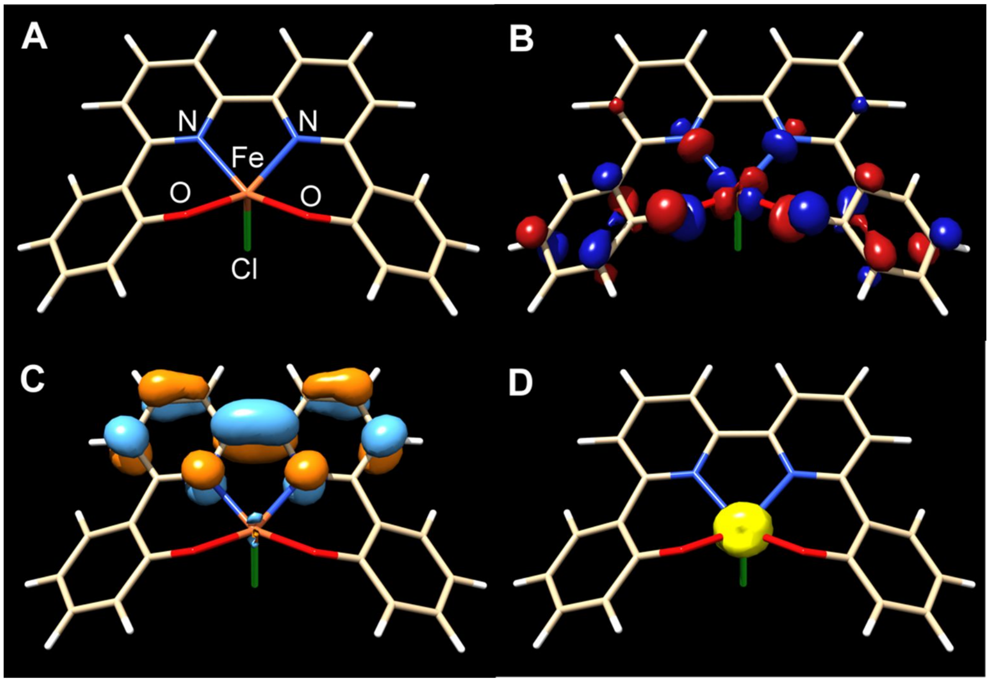

Figure S2.29. Kohn-Sham representations of HOMO (B) and LUMO (C) for model complex $[Fe(dhbpy)Cl]^-$ (A); spin density is shown in (D). Used the B3LYP/G[9-13] functional and def2-TZVP[14-15] basis set with the RIJCOSX approximation[16], D3BJ dispersion correction[17-18], and CPCM[19] to model the *N,N*-DMF solvent; 2S + 1 = 5.

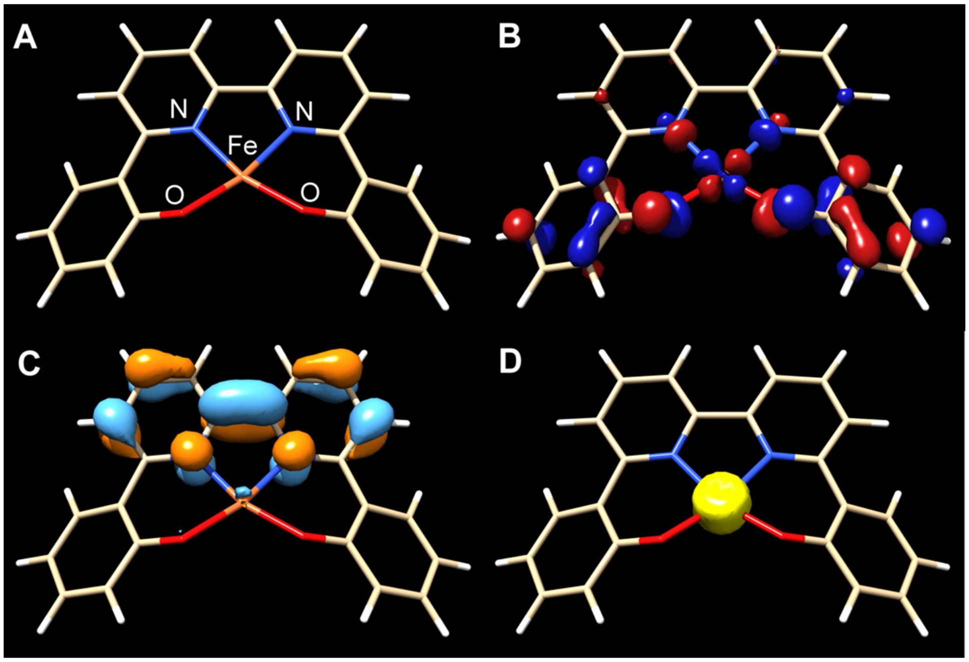

Figure S2.30. Kohn-Sham representations of HOMO (B) and LUMO (C) for model complex [Fe(dhbpy)]^0 (A); spin density is shown in (D). Used the B3LYP/G[9-13] functional and def2-TZVP[14-15] basis set with the RIJCOSX approximation[16], D3BJ dispersion correction[17-18], and CPCM[19] to model the *N,N*-DMF solvent; 2S + 1 = 5.

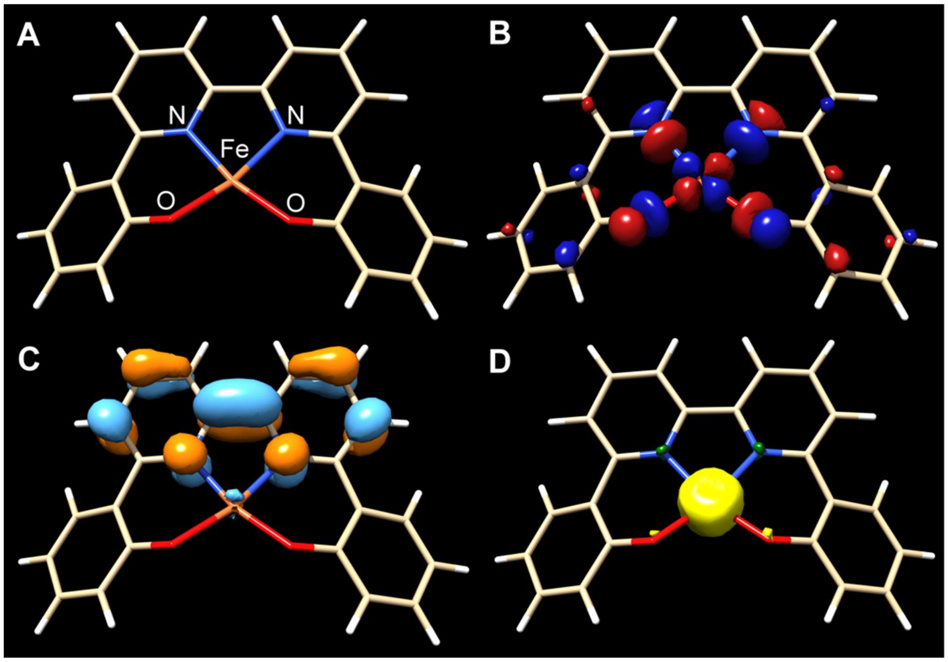

Figure S.31. Kohn-Sham representations of HOMO (B) and LUMO (C) for model complex [Fe(dhbpy)]$^-$ (A); spin density is shown in (D). Used the B3LYP/G[9-13] functional and def2-TZVP[14-15] basis set with the RIJCOSX approximation[16], D3BJ dispersion correction[17-18], and CPCM[19] to model the *N,N*-DMF solvent; 2S + 1 = 4.

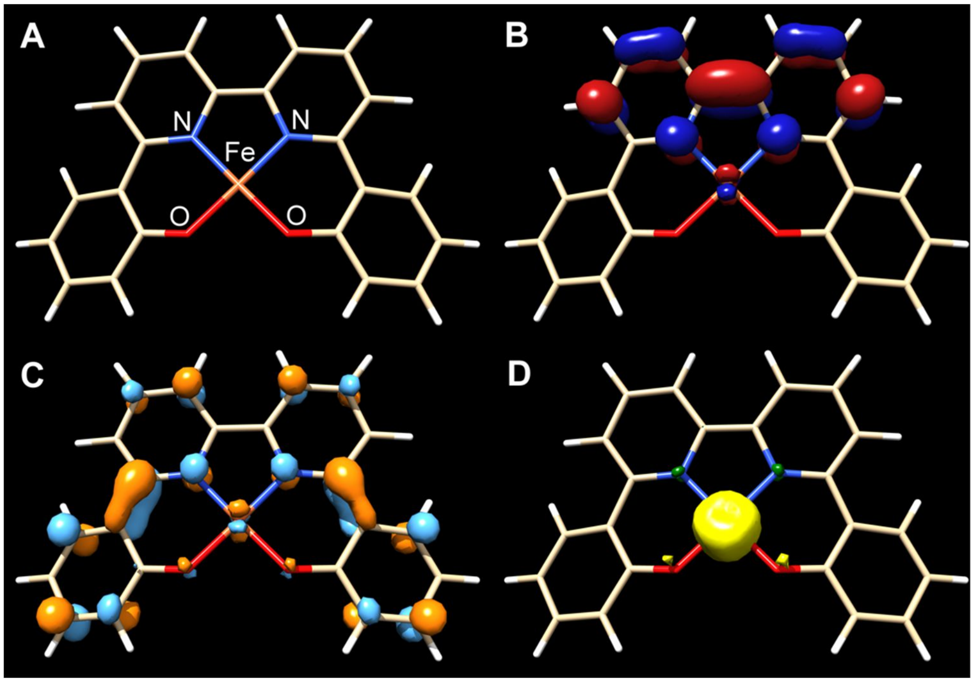

Figure S2.32. Kohn-Sham representations of HOMO (B) and LUMO (C) for model complex [Fe(dhbpy)]$^{2-}$ (A); spin density is shown in (D). Used the B3LYP/G[9-13] functional and def2-TZVP[14-15] basis set with the RIJCOSX approximation[16], D3BJ dispersion correction[17-18], and CPCM[19] to model the *N,N*-DMF solvent; 2S + 1 = 4.

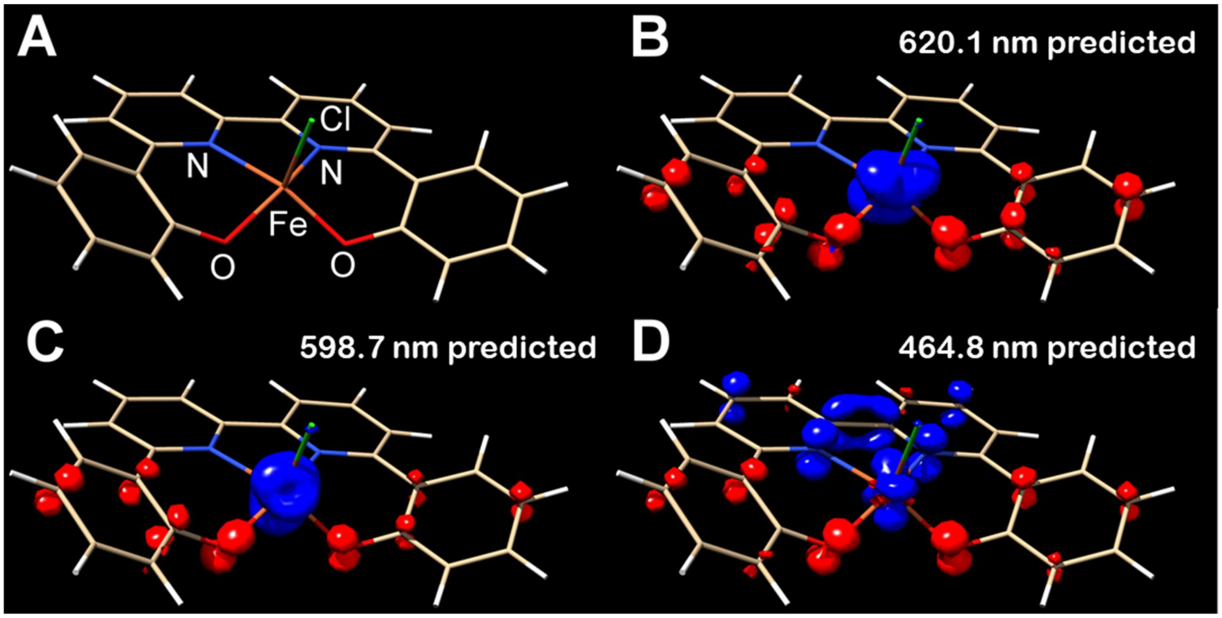

Figure S2.33. Difference densities predicting LMCT in the Visible Region. Used the B3LYP/G[9-13] functional and def2-TZVP[14-15] basis set with CPCM[19] to model the *N,N*-DMF solvent; 2S + 1 = 6.

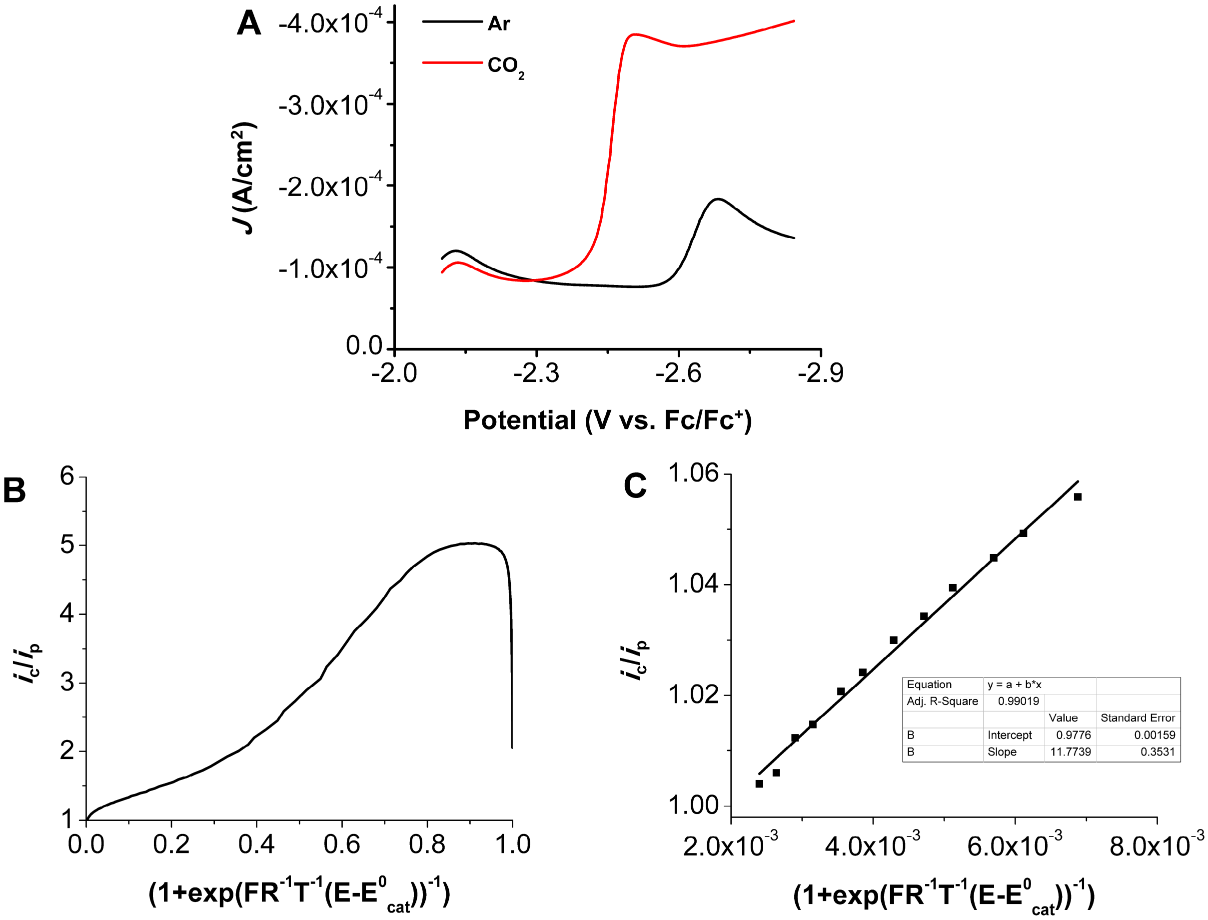

Figure S2.34. (A) CV trace overlays of Ar saturation (black) and CO_2 saturation (red). (B) Full plot of i_c/i_p vs $(1+\exp(FR^{-1}T^{-1}(E-E^0cat))^{-1}$ (C) Linear region from FOWA analysis which gives a slope of 11.8. Conditions are 0.5 mM Fe(^{tbu}dhbpy)Cl in 0.1 M $TBAPF_6$/*N,N*-DMF supporting electrolyte. Working and counter electrodes are glassy carbon. Pseudoreference electrode is Ag/AgCl. All data is referenced to a ferrocene internal standard.

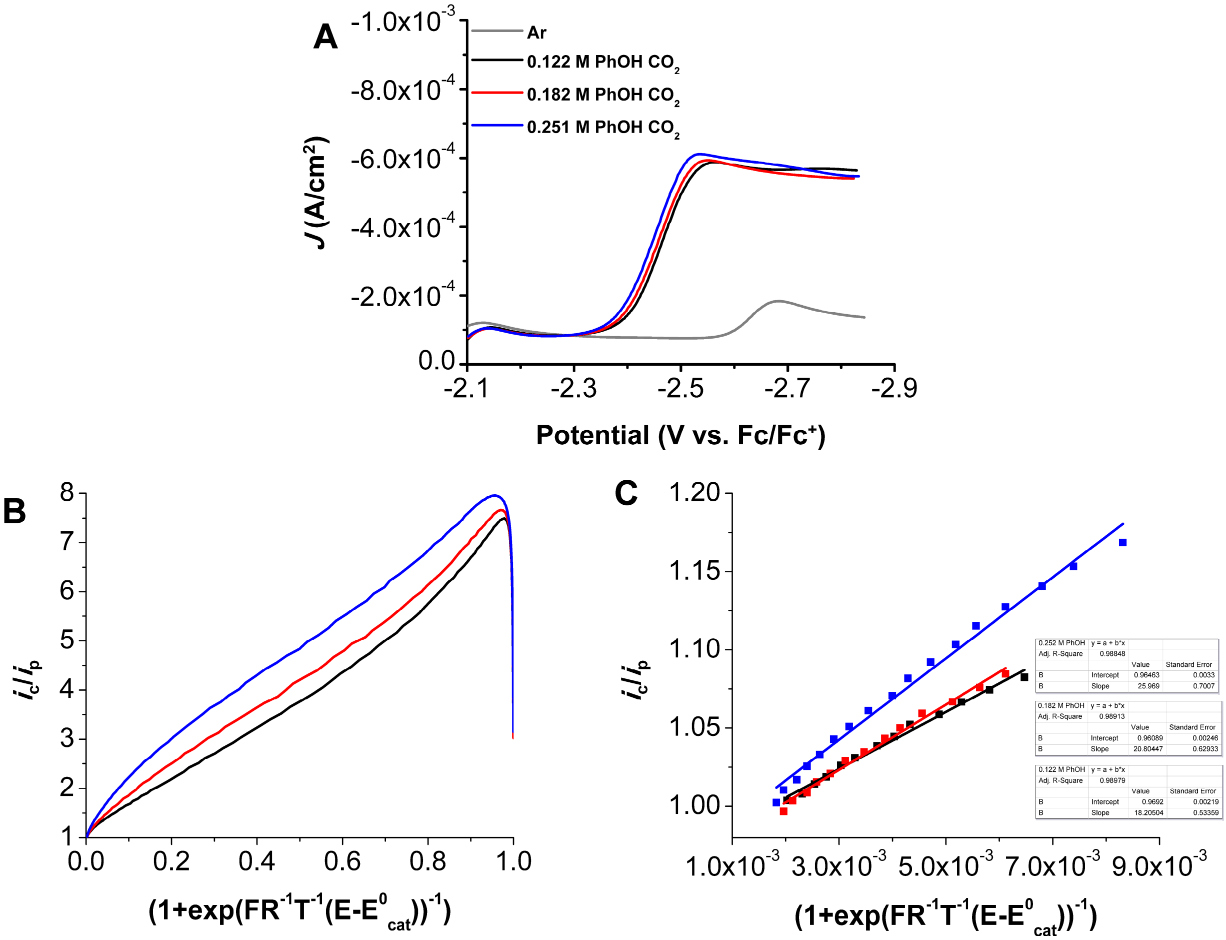

0.252 M PhOH	y = a + b*x		
Adj. R-Square	0.98848		
		Value	Standard Error
B	Intercept	0.96463	0.0033
B	Slope	25.969	0.7007

0.182 M PhOH	y = a + b*x		
Adj. R-Square	0.98913		
		Value	Standard Error
B	Intercept	0.96089	0.00246
B	Slope	20.80447	0.62933

0.122 M PhOH	y = a + b*x		
Adj. R-Square	0.98979		
		Value	Standard Error
B	Intercept	0.9692	0.00219
B	Slope	18.20504	0.53359

Figure S2.35. (A) CV trace overlays of Ar saturation (grey) and CO_2 saturation (red). (B) Full plot of i_c/i_p vs (1+exp(FR^{-1}T^{-1}(E-E^{0}cat))$^{-1}$ (C) Linear region from FOWA analysis which gives slopes of 18.2, 20.8, and 26.0 for 0.122, 0.182, and 0.252 M PhOH, respectively. Conditions are 0.5 mM Fe(^{tbu}dhbpy)Cl in 0.1 M $TBAPF_6$/*N,N*-DMF supporting electrolyte. Working and counter electrodes are glassy carbon. Pseudoreference electrode is Ag/AgCl. All data is referenced to a ferrocene internal standard.

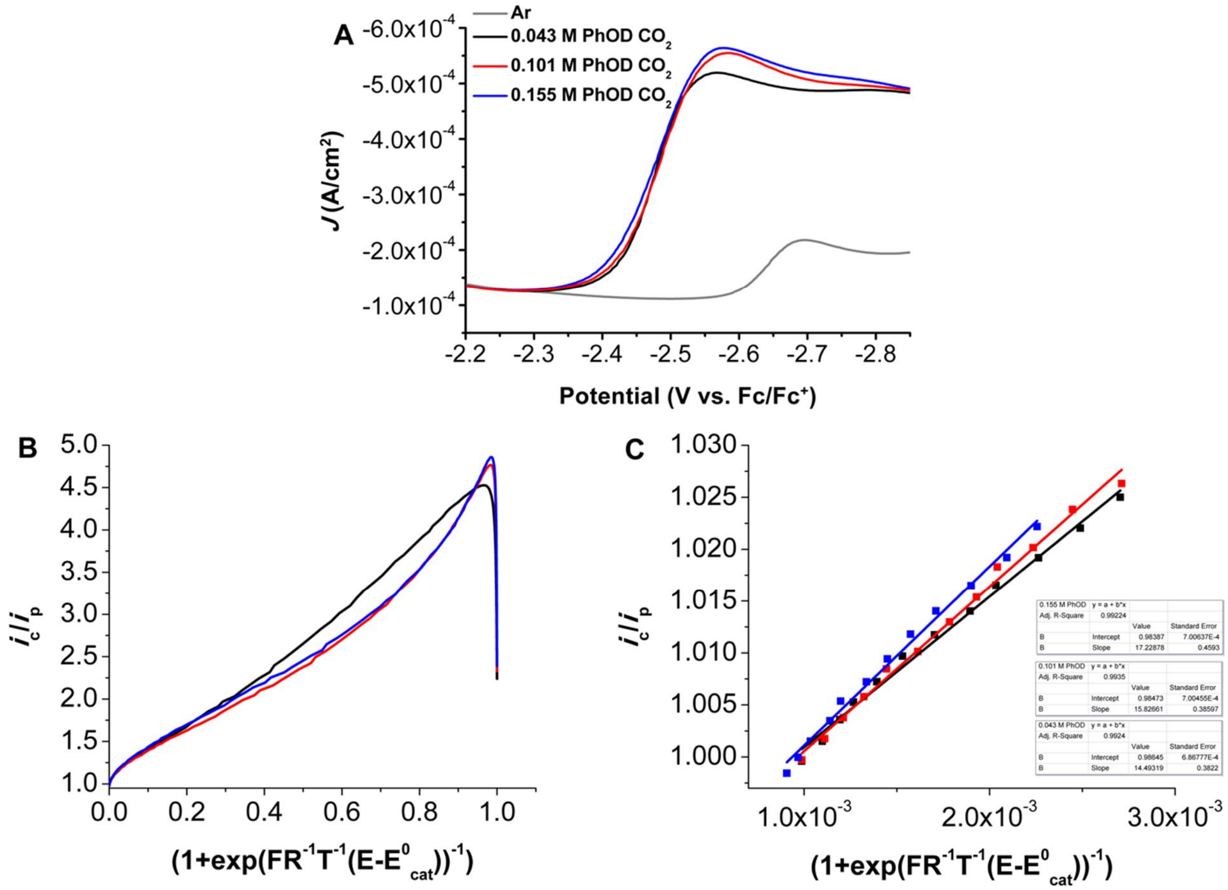

0.155 M PhOD	y = a + b*x		
Adj. R-Square	0.99224		
		Value	Standard Error
B	Intercept	0.98387	7.00637E-4
B	Slope	17.22878	0.4593

0.101 M PhOD	y = a + b*x		
Adj. R-Square	0.9935		
		Value	Standard Error
B	Intercept	0.98473	7.00455E-4
B	Slope	15.82661	0.38597

0.043 M PhOD	y = a + b*x		
Adj. R-Square	0.9924		
		Value	Standard Error
B	Intercept	0.98645	6.86777E-4
B	Slope	14.49319	0.3822

Figure S2.36. (A) CV trace overlays of Ar saturation (grey) and CO$_2$ saturation (red). (B) Full plot of i_c/i_p vs (1+exp(FR^{-1}T^{-1}(E-E^{0}cat))$^{-1}$ (C) Linear region from FOWA analysis which gives slopes of 14.5, 15.8, and 17.2 for 0.045, 0.101, and 0.155 M PhOD, respectively. Conditions are 0.5 mM Fe(^{tbu}dhbpy)Cl in 0.1 M TBAPF$_6$/*N,N*-DMF supporting electrolyte. Working and counter electrodes are glassy carbon. Pseudoreference electrode is Ag/AgCl. All data is referenced to a ferrocene internal standard.

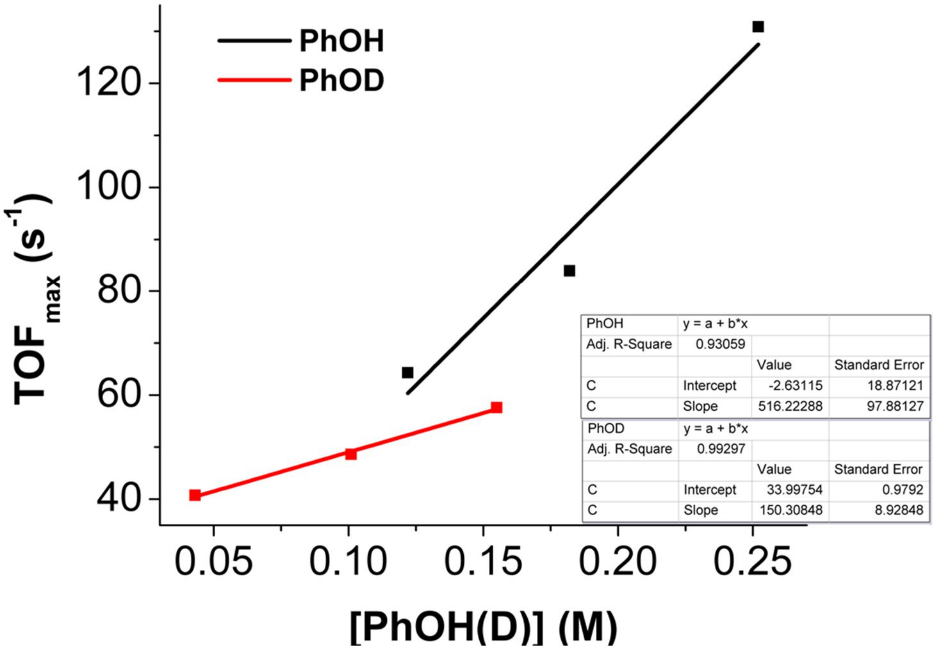

PhOH	y = a + b*x		
Adj. R-Square	0.93059		
		Value	Standard Error
C	Intercept	-2.63115	18.87121
C	Slope	516.22288	97.88127

PhOD	y = a + b*x		
Adj. R-Square	0.99297		
		Value	Standard Error
C	Intercept	33.99754	0.9792
C	Slope	150.30848	8.92848

Figure S2.37. Plots of TOF$_{max}$ vs [PhOH(D)]. A ratio of the slopes of linear fits can be used to determine KIE (k_H/k_D). In this case a KIE of 4.8±0.9 was found.

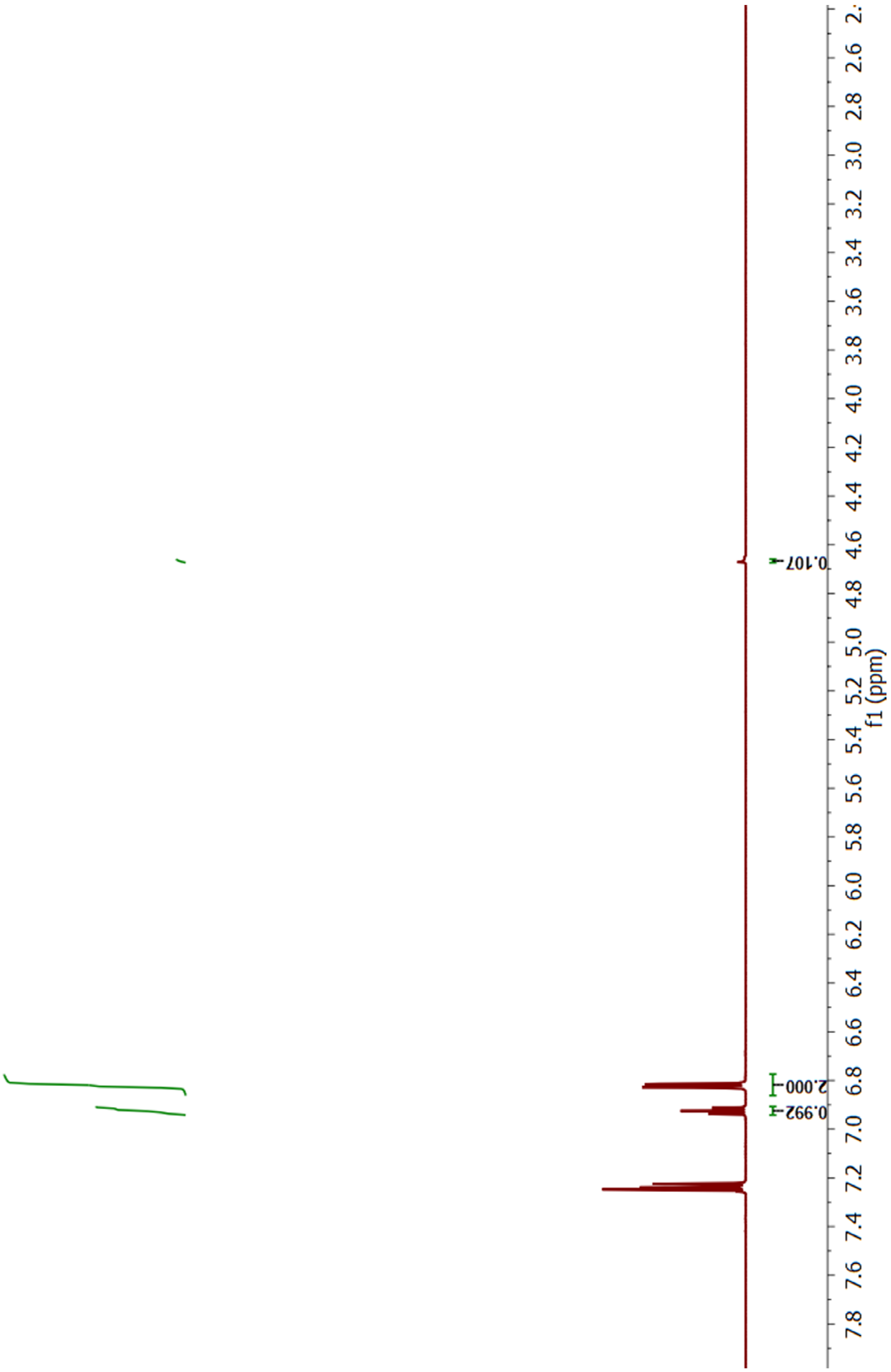

Figure S2.38. ^{1}H NMR of d_1-PhOD in $CDCl_3$. Two sets of aromatic protons not infringed upon by solvent (δ 6.82, 6.92 ppm) integrate to 1 H and 2 H respectively. Phenolic proton (δ 4.67) integrates to 0.107, indicating 89% deuteration. ^{1}H NMR taken in $CDCl_3$ dried on 4 Å molecular sieves for 3 days.

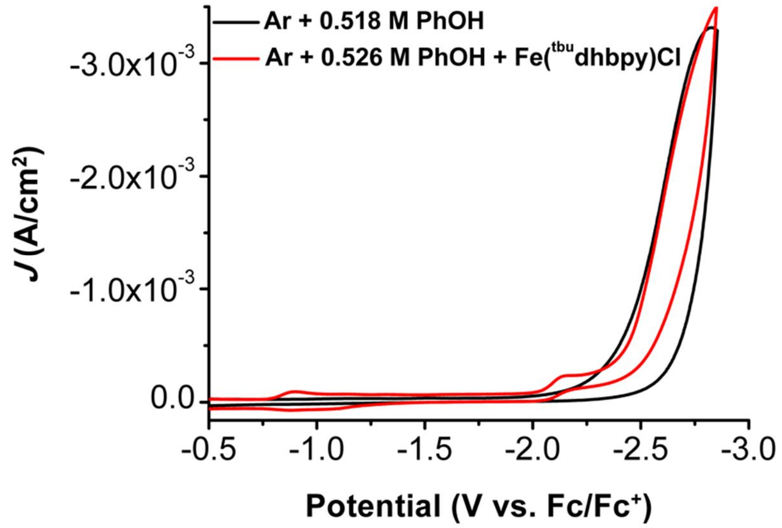

Figure S2.39. Control (black) and 0.5 mM Fe(^{tbu}dhbpy)Cl (Red) upon addition of 0.5 M PhOH as a proton source under a saturated Ar atmosphere in *N*,*N*-DMF 0.1 M with TBAPF$_6$ supporting electrolyte. Scan rate is 100 mV/s. Working electrode is glassy carbon (3 mm diameter), counter electrode is glassy carbon rod, and pseudo-reference is Ag/AgCl wire with ferrocene (Fc) added as internal reference.

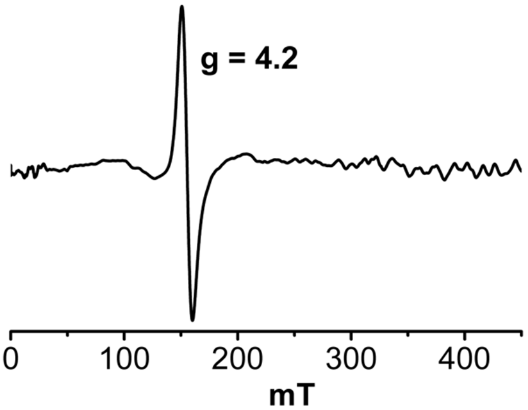

Figure S2.40. X-band EPR spectrum of Fe(^{tbu}dhbpy)Cl in dichloromethane and acetonitrile (1:1) glass mixture. (Experimental parameters: temperature = 77 K, microwave frequency = 9.13 GHz, microwave power = 0.998 mW, modulation frequency = 100 kHz, modulation width = 1 mT, time constant = 0.03 s).

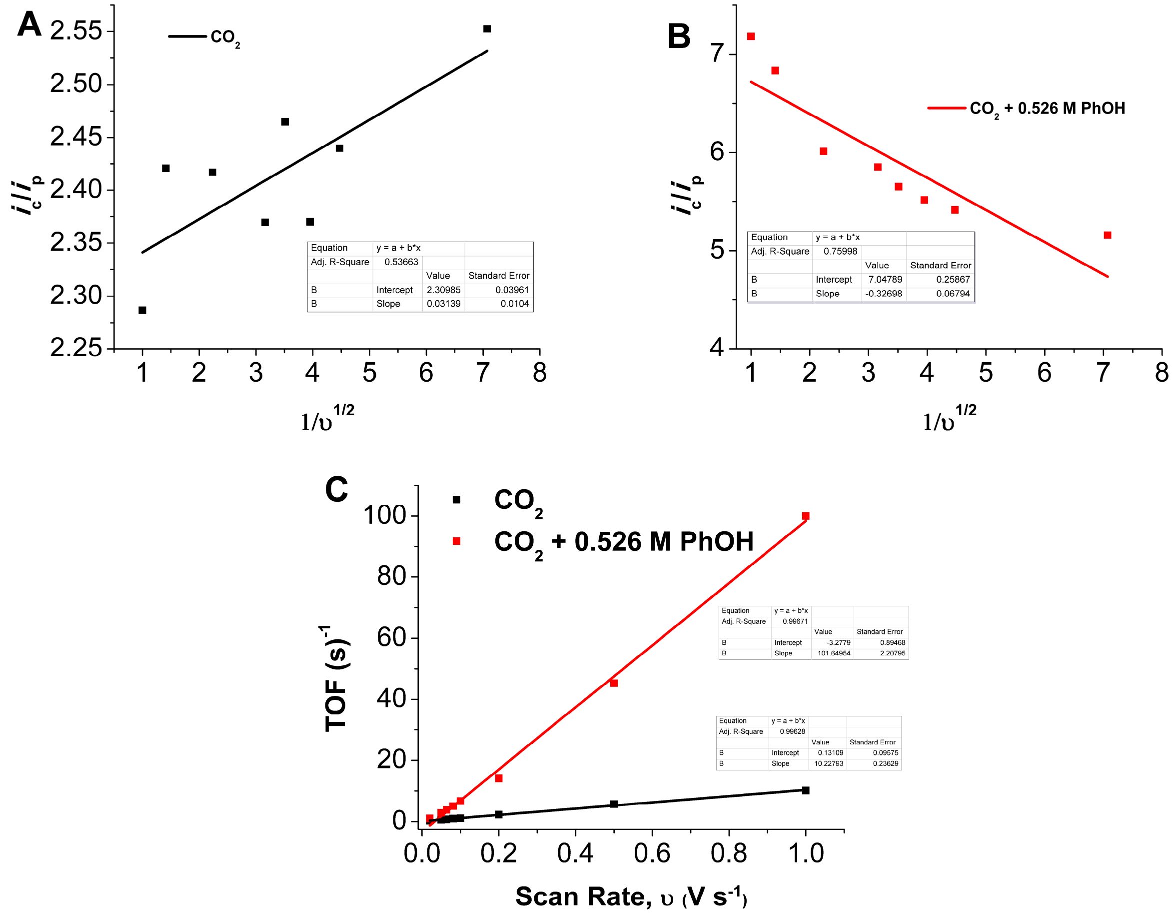

Figure S2.41. Plots of (A) i_c/i_p vs $1/(\upsilon)^{1/2}$ under CO_2 saturation, (B) i_c/i_p vs $1/(\upsilon)^{1/2}$ under CO_2 saturation with 0.526 M PhOH, and (C) TOF vs υ for Fe(^{tbu}dhbpy)Cl **1** under a CO_2 atmosphere (black) and under a CO_2 atmosphere with 0.526 M PhOH. Working electrode is glassy carbon (3 mm diameter), counter electrode is glassy carbon, and pseudo-reference is Ag/AgCl wire with ferrocene (Fc) added as internal reference. These data indicate that this catalyst is not under kinetically controlled steady-state conditions for all non-Faradaic conditions.[20]

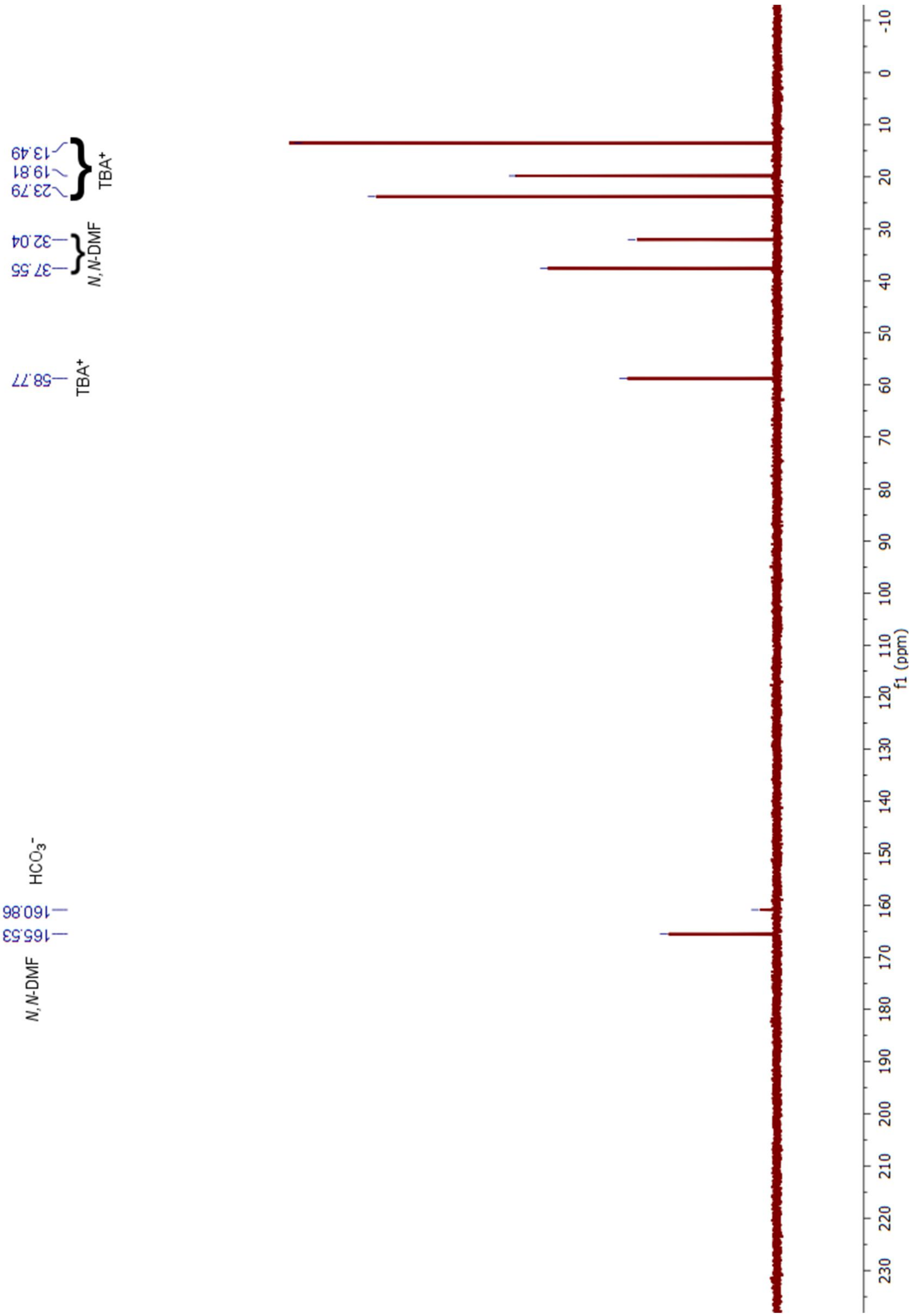

Figure S2.42. ^{13}C{^{1}H} NMR of TBAHCO$_3$ in D$_2$O with a single drop of *N,N*-DMF added for internal reference. Peak at δ 158.48 assigned to HCO$_3^-$. 151 MHz, Varian.

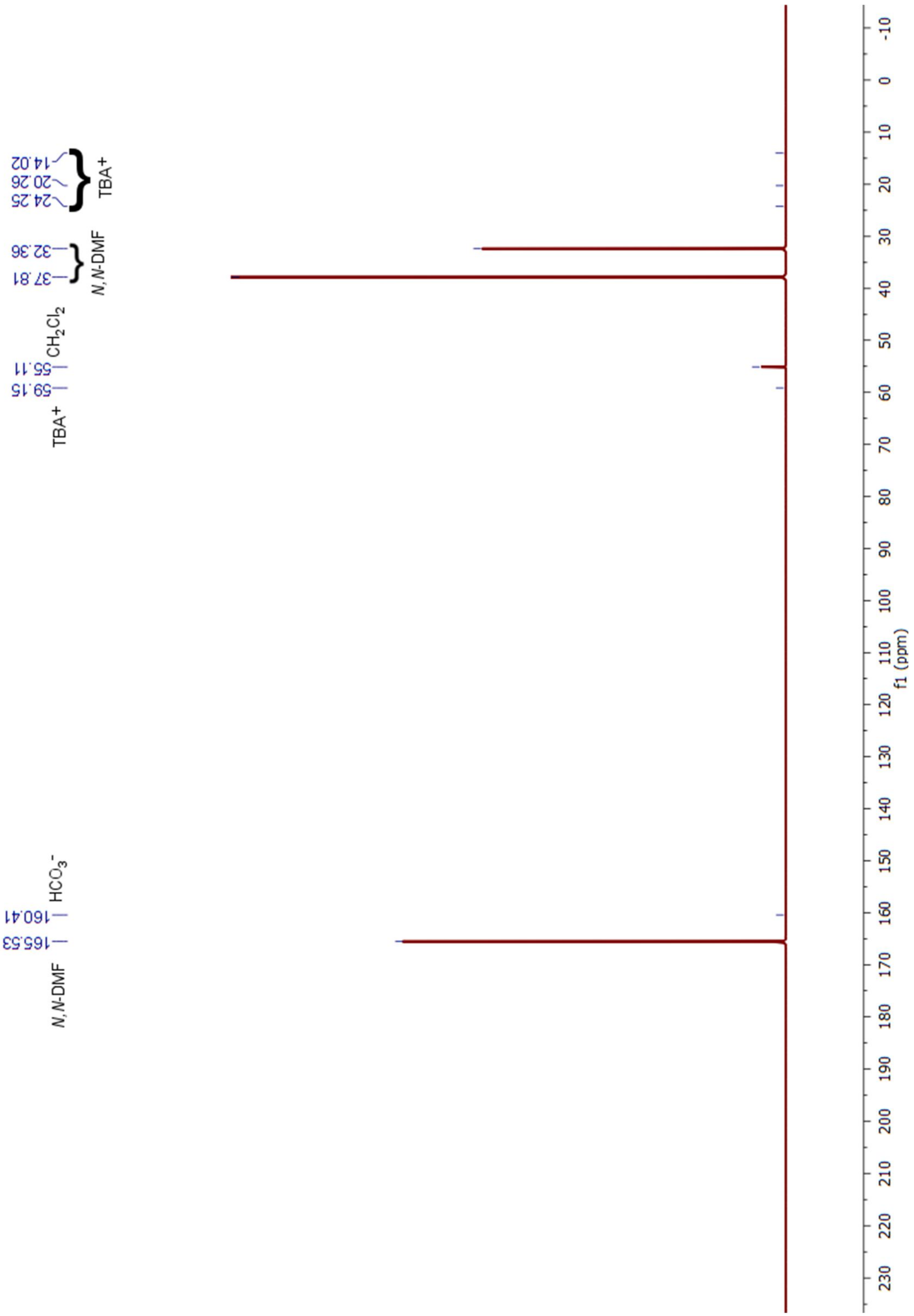

Figure S2.43. $^{13}C\{^1H\}$ NMR of extract from controlled potential electrolysis in D_2O. Peak at δ 158.04 assigned to HCO_3^-. Referenced to residual *N*-*N*-DMF in extract. 151 MHz Varian.

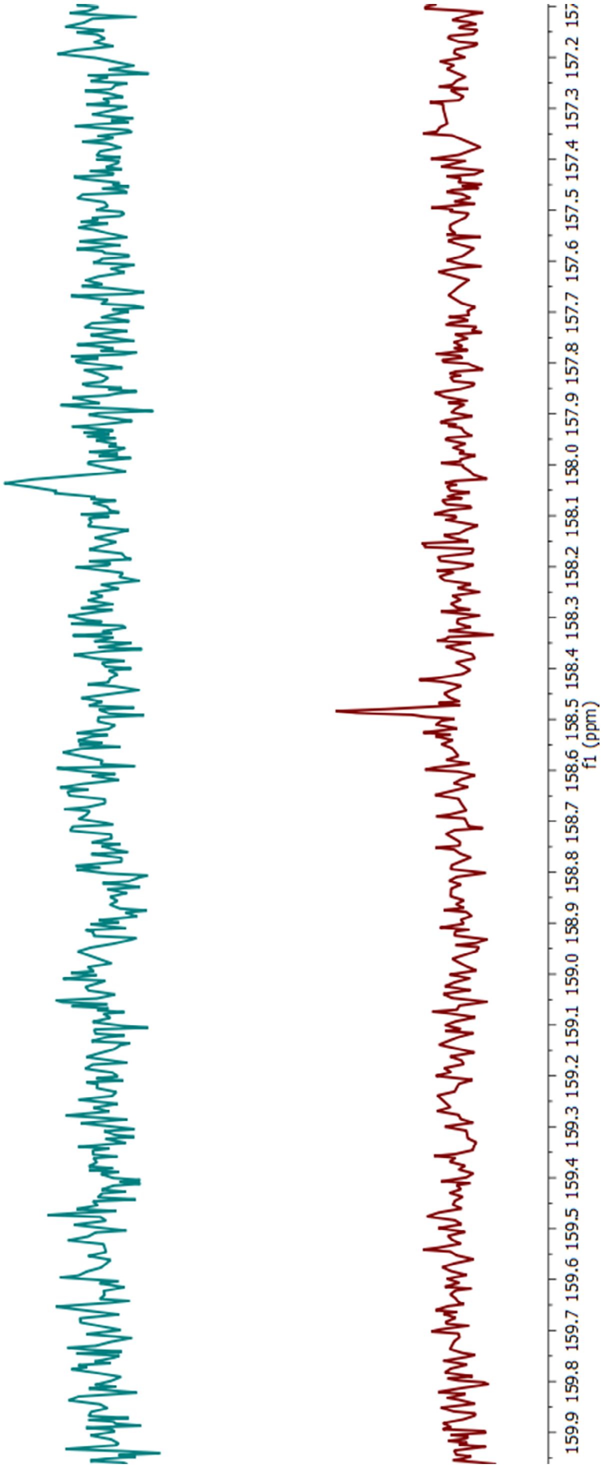

Figure S2.44. $^{13}C\{^{1}H\}$ NMR overlay of $TBAHCO_3$ in D_2O with a single drop of *N,N*-DMF added for reference (Red), and extract from controlled potential electrolysis in D_2O (Green). 151 MHz Varian.

Table S2.1. ΔE_p for variable scan rate experiments under Faradaic conditions and upon the addition of 10.8 mM TBACl. 0.5 mM Fe(^{tbu}dhbpy)Cl in *N*,*N*-DMF with 0.1 M TBAPF$_6$ supporting electrolyte under an atmosphere of Ar. Working electrode is glassy carbon (3 mm diameter), counter electrode is Pt wire, and pseudo-reference is Ag/AgCl wire with ferrocene (Fc) added as internal reference. [a]0.5 M Fe(^{tbu}dhbpy)Cl [b]10.8 mM TBACl [c]Value for Fc internal standard for the same scan.

Scan Rate (mV/s)	**ΔE_p[a] (mV)**	**ΔE_p[a,c] (mV)**	**J_c[a] (A/cm^2) (x10^{-5})**	**J_a[a] (A/cm^2) (x10^{-5})**	**$\lvert J_c/J_a \rvert$[a]**	**ΔE_p[a,b,c] (mV)**	**ΔE_p[a,b,c] (mV)**	**J_c[b] (A/cm^2) (x10^{-5})**	**J_a[b] (A/cm^2) (x10^{-5})**	**$\lvert J_c/J_a \rvert$[b]**
20	98	82	1.96	-1.98	0.99	78	81	1.85	-1.86	0.99
50	96	81	2.87	-2.90	0.99	74	81	2.78	-2.80	0.99
64	101	81	3.20	-3.25	0.98	76	81	3.24	-3.21	1.01
81	102	81	3.53	-3.58	0.99	71	81	3.61	-3.60	1.00
100	104	81	3.96	-4.01	0.99	78	82	3.93	-3.93	1.00
200	111	81	5.55	-5.65	0.98	76	81	5.66	-5.68	1.00
500	129	81	8.71	-9.69	0.90	81	82	9.09	-9.17	0.99
1000	148	81	12.9	-1.40	0.92	76	81	1.38	-1.37	1.01

Table S2.2. $E_{1/2}$ and ΔE_p for variable PhOH concentrations under Ar atmosphere. 0.5 mM Fe(^{tbu}dhbpy)Cl in *N*,*N*-DMF with 0.1 M TBAPF$_6$ supporting electrolyte. Working electrode is glassy carbon (3 mm diameter), counter electrode is Pt wire, and pseudo-reference is Ag/AgCl wire with ferrocene (Fc) added as internal reference. ^{a}First reduction wave of Fe^{tbu}dhbpy. ^{b}Fc for the corresponding scan.

[PhOH] (M)	$E_{1/2}{}^a$ (V)	$\Delta E_p{}^a$ (mV)	$\Delta E_p{}^b$ (mV)
0	-0.9	104	75
0.0612	-0.88	98	73
0.106	-0.88	93	73
0.174	-0.87	88	74
0.214	-0.87	84	73
0.257	-0.86	85	72
0.318	-0.86	80	72
0.368	-0.86	79	73
0.418	-0.85	78	71
0.477	-0.85	71	72
0.531	-0.85	71	72
0.593	-0.85	78	74
0.64	-0.85	72	73
0.705	-0.85	71	74
0.756	-0.85	72	71
0.86	-0.85	69	71
0.916	-0.85	66	73
0.978	-0.85	57	74
1.06	-0.84	52	73
1.3	-0.84	67	74
1.66	-0.84	52	74
1.99	-0.84	61	77
2.3	-0.83	43	77
2.66	-0.83	54	77
3.11	-0.83	62	77

Table S2.3. $E_{1/2}$ and ΔE_p for variable PhOH concentrations under CO_2 atmosphere. 0.5 mM Fe(^{tbu}dhbpy)Cl in *N*,*N*-DMF with 0.1 M $TBAPF_6$ supporting electrolyte. Working electrode is glassy carbon (3 mm diameter), counter electrode is Pt wire, and pseudo-reference is Ag/AgCl wire with ferrocene (Fc) added as internal reference.

[PhOH] (M)	**$E_{1/2}$ (V)**	**ΔE_p (mV)**	**ΔE_p (mV)**
0	-0.9	110	71
0.0489	-0.89	96	72
0.111	-0.88	95	72
0.152	-0.87	90	72
0.202	-0.87	91	73
0.325	-0.86	76	72
0.275	-0.86	86	72
0.388	-0.86	83	71
0.393	-0.86	78	73
0.436	-0.86	78	73
0.5	-0.85	67	75
0.554	-0.85	66	75
0.629	-0.84	64	72
0.642	-0.85	77	73
0.695	-0.84	70	75
0.76	-0.84	54	73
0.868	-0.84	75	74
0.927	-0.84	65	72
0.998	-0.84	66	75
1.12	-0.84	68	72
1.4	-0.84	64	71
1.59	-0.84	66	75
1.83	-0.84	64	75
2.07	-0.83	69	75
2.31	-0.83	65	75
2.6	-0.83	66	77
2.81	-0.83	65	77
3.03	-0.83	63	76

X-Ray Crystallography Data

Table S2.5. Crystal data and structure refinement for $C_{40}H_{49}N_3O_2ClFe$.

Empirical formula	C40 H49 Cl Fe N3 O2	
Formula weight	695.12	
Temperature	153(2) K	
Wavelength	0.71073 Å	
Crystal system	Triclinic	
Space group	P-1	
Unit cell dimensions	a = 9.332(3) Å	a = 9.332(4)°.
	b = 13.545(4) Å	b = 13.54(4)°.
	c = 15.219(5) Å	c = 15.219(4)°.
Volume	1826.8(10) Å^3	
Z	2	
Density (calculated)	1.264 Mg/m^3	
Absorption coefficient	0.524 mm^{-1}	
F(000)	738	
Crystal size	0.390 x 0.210 x 0.030 mm^3	
Theta range for data collection	3.541 to 30.251°.	
Index ranges	-13<=h<=13, -19<=k<=19, -21<=l<=21	
Reflections collected	10572	
Independent reflections	10572 [R(int) = 0.0492]	
Completeness to theta = 25.242°	99.6 %	

Absorption correction	Empirical
Refinement method	Full-matrix least-squares on F^2
Data / restraints / parameters	10572 / 0 / 437
Goodness-of-fit on F^2	1.043
Final R indices [I>2sigma(I)]	R1 = 0.0459, wR2 = 0.1075
R indices (all data)	R1 = 0.0702, wR2 = 0.1142
Largest diff. peak and hole	0.515 and -0.353 e.Å^{-3}

Computational Coordinates

Fe(dhbpy)Cl; 2S + 1 = 6.

Cl	-6.127941	2.496286	16.421569
Fe	-4.069577	2.335406	17.321613
O	-2.790267	2.779134	15.993159
O	-3.773434	3.876781	18.386319
N	-3.525521	0.311062	16.905124
N	-4.424290	1.333995	19.176121
C	-3.014502	0.848216	14.576299
C	-2.818085	2.237281	14.782927
C	-2.638864	3.074265	13.668757
C	-2.699922	2.573653	12.382616
H	-2.574834	3.242284	11.540344
C	-2.938714	1.214672	12.169217
C	-3.083789	0.373787	13.256037
H	-3.281160	-0.674725	13.081734
C	-3.103334	-0.102089	15.692477
C	-3.623071	-0.549571	17.936844
C	-4.109372	0.024364	19.207175
C	-4.245367	-0.726539	20.363136
C	-3.295036	-1.888051	17.797359
C	-4.896831	1.961017	20.273072
C	-5.256330	3.383766	20.215116
C	-4.648016	4.278689	19.299632
C	-4.971993	5.644300	19.362709
C	-5.903165	6.116180	20.268056
H	-6.149436	7.170462	20.284200
C	-6.537296	5.234977	21.145867
C	-6.205116	3.893791	21.116513
H	-6.710488	3.216156	21.790482
C	-2.737299	-1.444322	15.513708
C	-2.839718	-2.332789	16.563286
C	-4.709679	-0.097382	21.510472
C	-5.032015	1.242847	21.469845
H	-2.556846	-3.367925	16.429809
H	-2.354187	-1.774208	14.561636
H	-3.383559	-2.572727	18.625450
H	-3.988543	-1.773179	20.380345
H	-4.808991	-0.653132	22.432918
H	-5.365766	1.746206	22.363025
H	-4.482846	6.311177	18.664739
H	-7.285475	5.593077	21.840135
H	-2.469254	4.127520	13.851368
H	-3.013628	0.820467	11.165025

$[Fe(dhbpy)Cl]^{-}$, 2S + 1 = 5.

Cl	-6.128864	2.622077	16.376433
Fe	-3.907520	2.411264	17.351964
O	-2.642815	2.809495	15.883841
O	-3.717699	4.010595	18.500875
N	-3.503519	0.339611	16.887075
N	-4.409301	1.372103	19.178856
C	-2.996676	0.838823	14.543982
C	-2.734184	2.231091	14.711947
C	-2.552854	3.011934	13.547397
C	-2.680515	2.477812	12.280772
H	-2.551630	3.114728	11.413801
C	-2.990826	1.125508	12.117260
C	-3.134726	0.332270	13.241089
H	-3.385840	-0.711851	13.109806
C	-3.084289	-0.094492	15.679987
C	-3.615446	-0.514550	17.921811
C	-4.103093	0.060767	19.195727
C	-4.245571	-0.707577	20.345495
C	-3.299447	-1.862373	17.793231
C	-4.888012	1.979670	20.284695
C	-5.263156	3.403578	20.246473
C	-4.625584	4.344401	19.384738
C	-4.990380	5.704529	19.510391
C	-5.968423	6.122064	20.390889
H	-6.233373	7.171564	20.441525
C	-6.627538	5.192971	21.199526
C	-6.261732	3.861252	21.121771
H	-6.782325	3.143577	21.741957
C	-2.726008	-1.440323	15.512165
C	-2.840871	-2.322479	16.568446
C	-4.708218	-0.094905	21.499919
C	-5.026561	1.248694	21.473646
H	-2.565890	-3.361343	16.444357
H	-2.342245	-1.781334	14.563584
H	-3.398439	-2.540858	18.625306
H	-3.992351	-1.755319	20.350803
H	-4.810883	-0.662238	22.415381
H	-5.362835	1.741622	22.372367
H	-4.483041	6.414069	18.868049
H	-7.414962	5.504370	21.873027
H	-2.325057	4.061920	13.685631
H	-3.120857	0.702464	11.130239

[Fe(dhbpy)]^0, 2S + 1 = 5.

Fe	-3.497656	2.393317	17.538827
O	-2.710657	2.869659	15.859907
O	-3.637309	4.019465	18.545630
N	-3.450906	0.350733	16.907698
N	-4.366089	1.375439	19.203580
C	-2.981109	0.857344	14.554086
C	-2.796729	2.262372	14.697464
C	-2.676604	3.042831	13.528157
C	-2.780763	2.488676	12.268640
H	-2.695645	3.122095	11.394259
C	-3.008275	1.118471	12.123793
C	-3.098452	0.330353	13.254661
H	-3.293750	-0.725930	13.132338
C	-3.040787	-0.072590	15.693331
C	-3.588692	-0.514032	17.933788
C	-4.102886	0.053189	19.204971
C	-4.320772	-0.728488	20.328711
C	-3.283001	-1.858741	17.796782
C	-4.880191	1.983353	20.293000
C	-5.228940	3.412294	20.256159
C	-4.576353	4.350460	19.407327
C	-4.940516	5.709445	19.510600
C	-5.933351	6.133224	20.370753
H	-6.197649	7.182967	20.410091
C	-6.605043	5.209766	21.174795
C	-6.242356	3.877946	21.112805
H	-6.778318	3.167004	21.726459
C	-2.684933	-1.420713	15.521926
C	-2.807536	-2.306297	16.571267
C	-4.812203	-0.116415	21.474358
C	-5.091990	1.233757	21.461019
H	-2.530986	-3.343995	16.442569
H	-2.297901	-1.760398	14.575000
H	-3.397037	-2.546153	18.619265
H	-4.106982	-1.784865	20.326250
H	-4.970134	-0.695724	22.374077
H	-5.454585	1.717904	22.353652
H	-4.418937	6.413102	18.873989
H	-7.402701	5.526443	21.833266
H	-2.508386	4.104973	13.655572
H	-3.118306	0.676486	11.142854

$[\mathrm{Fe(dhbpy)}]^{-}$, 2S + 1 = 4.

Fe	-3.569980	2.335026	17.526790
O	-2.672106	2.868974	15.882494
O	-3.688293	4.031927	18.477157
N	-3.462501	0.356021	16.917090
N	-4.359531	1.373608	19.184570
C	-2.968291	0.860562	14.562951
C	-2.763905	2.264317	14.717332
C	-2.638065	3.050821	13.550019
C	-2.753847	2.512429	12.283498
H	-2.663389	3.153677	11.414907
C	-3.003509	1.148031	12.129665
C	-3.104310	0.354192	13.258813
H	-3.320355	-0.697842	13.131821
C	-3.038608	-0.086456	15.698508
C	-3.622776	-0.536768	17.957854
C	-4.110357	0.015869	19.189365
C	-4.323575	-0.743396	20.352530
C	-3.307792	-1.895547	17.786271
C	-4.859683	1.979684	20.299520
C	-5.219456	3.414845	20.249195
C	-4.602049	4.352787	19.369041
C	-4.983458	5.710035	19.469524
C	-5.957260	6.138312	20.350260
H	-6.231334	7.186110	20.383428
C	-6.597136	5.215664	21.179128
C	-6.220452	3.885368	21.116420
H	-6.736228	3.173897	21.746858
C	-2.691738	-1.417561	15.516304
C	-2.829096	-2.331917	16.575360
C	-4.776707	-0.124299	21.491685
C	-5.048943	1.254987	21.467208
H	-2.559438	-3.370271	16.433846
H	-2.304509	-1.752059	14.567025
H	-3.431719	-2.589656	18.604332
H	-4.121875	-1.804192	20.353462
H	-4.926389	-0.690357	22.401796
H	-5.394446	1.748610	22.361854
H	-4.487237	6.411319	18.809403
H	-7.383376	5.527747	21.854135
H	-2.455237	4.110105	13.686071
H	-3.126460	0.714120	11.146184

$[Fe(dhbpy)]^{2-}$, 2S + 1 = 3.

Fe	-3.772093	2.133366	17.538195
O	-3.100320	2.906273	15.933698
O	-3.973603	3.917753	18.180340
N	-3.499005	0.347339	16.943991
N	-4.364947	1.343545	19.159922
C	-2.991817	0.878192	14.597043
C	-2.970503	2.295561	14.780325
C	-2.798504	3.114021	13.635590
C	-2.706081	2.598249	12.358984
H	-2.588154	3.264191	11.512212
C	-2.785244	1.216531	12.169941
C	-2.926383	0.396493	13.275477
H	-3.009618	-0.668048	13.108699
C	-3.075054	-0.088962	15.715701
C	-3.668199	-0.597206	17.998208
C	-4.130335	-0.062272	19.188097
C	-4.341083	-0.785385	20.396747
C	-3.332179	-1.963709	17.778275
C	-4.856556	1.962626	20.279516
C	-5.206952	3.399701	20.210067
C	-4.717473	4.281599	19.197957
C	-5.056720	5.654819	19.288732
C	-5.883003	6.152985	20.275726
H	-6.130637	7.207981	20.294454
C	-6.412256	5.283309	21.232172
C	-6.069631	3.943342	21.180811
H	-6.505468	3.279414	21.913676
C	-2.728719	-1.416565	15.509758
C	-2.859002	-2.365297	16.565414
C	-4.769250	-0.137425	21.516494
C	-5.036629	1.262086	21.462600
H	-2.584951	-3.399627	16.395156
H	-2.339602	-1.739583	14.558385
H	-3.449201	-2.673944	18.586482
H	-4.145490	-1.849491	20.417147
H	-4.916022	-0.677478	22.444339
H	-5.367278	1.770557	22.353478
H	-4.653052	6.308525	18.524187
H	-7.089760	5.642793	21.996283
H	-2.758007	4.184492	13.802745
H	-2.746636	0.787976	11.176652

TD-DFT Output

```
-------------------------
TD-DFT/TDA EXCITED STATES
-------------------------
the weight of the individual excitations are printed if larger than 0.01

STATE  1:  E=   0.058626 au      1.595 eV    12866.9 cm**-1
   106b -> 107b  :     0.954729 (c= -0.97710249)
   106b -> 110b  :     0.013515 (c=  0.11625203)
STATE  2:  E=   0.064865 au      1.765 eV    14236.1 cm**-1
    91b -> 107b  :     0.010567 (c=  0.10279823)
   105b -> 107b  :     0.801739 (c= -0.89539904)
   105b -> 110b  :     0.025323 (c=  0.15913067)
   106b -> 108b  :     0.133947 (c= -0.36598710)
STATE  3:  E=   0.066256 au      1.803 eV    14541.5 cm**-1
    92b -> 109b  :     0.011367 (c=  0.10661801)
   104b -> 109b  :     0.011292 (c=  0.10626182)
   106b -> 108b  :     0.026143 (c= -0.16168817)
   106b -> 109b  :     0.932611 (c=  0.96571787)
STATE  4:  E=   0.068674 au      1.869 eV    15072.2 cm**-1
   105b -> 107b  :     0.096372 (c= -0.31043776)
   105b -> 109b  :     0.089146 (c=  0.29857387)
   105b -> 110b  :     0.024094 (c=  0.15522115)
   106b -> 108b  :     0.724142 (c=  0.85096553)
   106b -> 109b  :     0.028789 (c=  0.16967343)
STATE  5:  E=   0.073479 au      1.999 eV    16126.8 cm**-1
    91b -> 108b  :     0.011929 (c=  0.10922210)
   105b -> 108b  :     0.674232 (c= -0.82111634)
   106b -> 110b  :     0.265457 (c=  0.51522565)
STATE  6:  E=   0.075310 au      2.049 eV    16528.7 cm**-1
    91b -> 109b  :     0.011745 (c=  0.10837596)
   105b -> 108b  :     0.018460 (c=  0.13586665)
   105b -> 109b  :     0.829934 (c= -0.91100735)
   105b -> 110b  :     0.016896 (c=  0.12998349)
   106b -> 108b  :     0.067916 (c=  0.26060626)
   106b -> 110b  :     0.029613 (c=  0.17208324)
STATE  7:  E=   0.076098 au      2.071 eV    16701.6 cm**-1
   105b -> 108b  :     0.268347 (c=  0.51802229)
   105b -> 109b  :     0.046475 (c=  0.21558111)
   106b -> 110b  :     0.651571 (c=  0.80719949)
STATE  8:  E=   0.085489 au      2.326 eV    18762.6 cm**-1
   100b -> 109b  :     0.018459 (c= -0.13586380)
   105b -> 107b  :     0.037970 (c= -0.19486011)
   105b -> 110b  :     0.846635 (c= -0.92012764)
```

```
STATE  9:  E=   0.090798 au      2.471 eV    19927.8 cm**-1
   109a -> 112a  :     0.029907 (c=  0.17293583)
   111a -> 112a  :     0.143328 (c= -0.37858662)
   104b -> 107b  :     0.730287 (c=  0.85456803)
   106b -> 111b  :     0.047487 (c= -0.21791566)
STATE 10:  E=   0.098023 au      2.667 eV    21513.6 cm**-1
   111a -> 112a  :     0.659282 (c= -0.81196172)
   104b -> 107b  :     0.207364 (c= -0.45537270)
   104b -> 111b  :     0.017594 (c=  0.13264175)
   106b -> 111b  :     0.042953 (c= -0.20724995)
STATE 11:  E=   0.100171 au      2.726 eV    21985.0 cm**-1
   110a -> 112a  :     0.045623 (c= -0.21359541)
   103b -> 107b  :     0.711197 (c=  0.84332526)
   104b -> 108b  :     0.129360 (c=  0.35966651)
   106b -> 112b  :     0.031906 (c= -0.17862279)
STATE 12:  E=   0.107179 au      2.916 eV    23523.0 cm**-1
   109a -> 112a  :     0.025441 (c=  0.15950357)
   109a -> 113a  :     0.030556 (c= -0.17480188)
   110a -> 114a  :     0.056859 (c= -0.23845147)
   111a -> 112a  :     0.027272 (c=  0.16514279)
   111a -> 113a  :     0.340993 (c=  0.58394591)
   104b -> 107b  :     0.014771 (c= -0.12153440)
   104b -> 109b  :     0.028027 (c=  0.16741322)
   104b -> 110b  :     0.084589 (c=  0.29084173)
   104b -> 111b  :     0.022765 (c=  0.15087949)
   104b -> 113b  :     0.010376 (c= -0.10186398)
   105b -> 112b  :     0.029311 (c= -0.17120398)
   106b -> 111b  :     0.096052 (c= -0.30992304)
   106b -> 112b  :     0.015593 (c= -0.12487032)
   106b -> 113b  :     0.119489 (c=  0.34567115)
STATE 13:  E=   0.099763 au      2.715 eV    21895.4 cm**-1
   110a -> 112a  :     0.030650 (c= -0.17507101)
   111a -> 114a  :     0.013462 (c=  0.11602423)
   103b -> 107b  :     0.065666 (c=  0.25625315)
   104b -> 108b  :     0.808577 (c= -0.89920909)
   104b -> 109b  :     0.012922 (c=  0.11367393)
   106b -> 112b  :     0.022271 (c= -0.14923373)
STATE 14:  E=   0.098741 au      2.687 eV    21671.2 cm**-1
   111a -> 113a  :     0.012511 (c= -0.11185197)
   104b -> 109b  :     0.914875 (c=  0.95649118)
   106b -> 109b  :     0.012376 (c= -0.11124553)
```

```
STATE 15:  E=   0.109201 au      2.972 eV    23966.9 cm**-1
   110a -> 112a  :     0.204190 (c=  0.45187363)
   110a -> 113a  :     0.100240 (c=  0.31660690)
   111a -> 114a  :     0.140687 (c= -0.37508201)
   100b -> 109b  :     0.013927 (c=  0.11801371)
   103b -> 107b  :     0.160059 (c=  0.40007420)
   104b -> 108b  :     0.034456 (c= -0.18562448)
   105b -> 113b  :     0.052761 (c= -0.22969777)
   106b -> 112b  :     0.183689 (c=  0.42858937)
STATE 16:  E=   0.110946 au      3.019 eV    24349.8 cm**-1
   107a -> 112a  :     0.010189 (c=  0.10094023)
   109a -> 112a  :     0.016120 (c= -0.12696406)
   110a -> 114a  :     0.011806 (c= -0.10865531)
   111a -> 112a  :     0.047387 (c= -0.21768662)
   111a -> 113a  :     0.038996 (c=  0.19747358)
   101b -> 107b  :     0.127986 (c= -0.35775121)
   102b -> 107b  :     0.305615 (c=  0.55282424)
   104b -> 110b  :     0.028802 (c= -0.16971220)
   105b -> 112b  :     0.028621 (c= -0.16917785)
   106b -> 111b  :     0.202536 (c=  0.45003969)
   106b -> 113b  :     0.082839 (c=  0.28781805)
STATE 17:  E=   0.105752 au      2.878 eV    23209.9 cm**-1
   111a -> 113a  :     0.013651 (c= -0.11683554)
   102b -> 107b  :     0.034959 (c=  0.18697345)
   104b -> 110b  :     0.822148 (c=  0.90672366)
   106b -> 111b  :     0.038444 (c=  0.19607269)
   106b -> 113b  :     0.016553 (c= -0.12865955)
STATE 18:  E=   0.111118 au      3.024 eV    24387.6 cm**-1
   109a -> 112a  :     0.017478 (c=  0.13220328)
   111a -> 112a  :     0.034783 (c=  0.18650072)
    99b -> 107b  :     0.012506 (c= -0.11182846)
   101b -> 107b  :     0.141756 (c= -0.37650472)
   101b -> 109b  :     0.015900 (c=  0.12609535)
   102b -> 107b  :     0.241061 (c=  0.49097953)
   102b -> 109b  :     0.028675 (c= -0.16933836)
   104b -> 107b  :     0.014057 (c= -0.11856205)
   105b -> 112b  :     0.029912 (c=  0.17294946)
   106b -> 111b  :     0.310420 (c= -0.55715368)
   106b -> 112b  :     0.011668 (c=  0.10801962)
   106b -> 113b  :     0.057818 (c= -0.24045465)
```

```
STATE 19:  E=   0.108966 au      2.965 eV    23915.3 cm**-1
   110a -> 112a  :     0.569460 (c= -0.75462603)
   110a -> 113a  :     0.028707 (c=  0.16943285)
   111a -> 114a  :     0.019397 (c= -0.13927442)
   105b -> 111b  :     0.013048 (c=  0.11422715)
   105b -> 113b  :     0.012149 (c= -0.11022240)
   106b -> 112b  :     0.238281 (c=  0.48814021)
   106b -> 113b  :     0.032294 (c=  0.17970667)
STATE 20:  E=   0.108588 au      2.955 eV    23832.3 cm**-1
   100b -> 108b  :     0.026728 (c= -0.16348844)
   103b -> 108b  :     0.921025 (c=  0.95970035)
   104b -> 110b  :     0.012315 (c= -0.11097144)
STATE 21:  E=   0.112302 au      3.056 eV    24647.4 cm**-1
   110a -> 113a  :     0.020940 (c=  0.14470641)
   111a -> 114a  :     0.027062 (c= -0.16450483)
   100b -> 107b  :     0.013182 (c=  0.11481428)
   100b -> 109b  :     0.032538 (c= -0.18038327)
   103b -> 109b  :     0.724373 (c=  0.85110092)
   103b -> 110b  :     0.020390 (c=  0.14279290)
   105b -> 113b  :     0.014411 (c= -0.12004610)
   106b -> 112b  :     0.042335 (c= -0.20575516)
   106b -> 114b  :     0.053823 (c=  0.23199701)
STATE 22:  E=   0.117879 au      3.208 eV    25871.4 cm**-1
   110a -> 112a  :     0.023788 (c=  0.15423201)
   110a -> 113a  :     0.076020 (c= -0.27571762)
   111a -> 114a  :     0.084353 (c=  0.29043624)
   101b -> 108b  :     0.023837 (c= -0.15439152)
   102b -> 108b  :     0.035191 (c=  0.18759213)
   103b -> 109b  :     0.223773 (c=  0.47304663)
   103b -> 110b  :     0.102698 (c= -0.32046529)
   105b -> 113b  :     0.031334 (c=  0.17701434)
   106b -> 112b  :     0.156310 (c=  0.39536117)
   106b -> 113b  :     0.013499 (c=  0.11618519)
   106b -> 114b  :     0.142322 (c= -0.37725581)
STATE 23:  E=   0.118891 au      3.235 eV    26093.5 cm**-1
    98b -> 107b  :     0.236183 (c=  0.48598636)
   100b -> 107b  :     0.590148 (c=  0.76821087)
   100b -> 109b  :     0.018393 (c= -0.13562083)
   100b -> 111b  :     0.012820 (c= -0.11322536)
   103b -> 107b  :     0.013321 (c=  0.11541834)
   103b -> 109b  :     0.018204 (c= -0.13492333)
   105b -> 111b  :     0.038258 (c= -0.19559763)
```

```
STATE 24:  E=   0.121453 au      3.305 eV    26655.8 cm**-1
   107a -> 112a  :     0.012218 (c= -0.11053407)
   109a -> 112a  :     0.080598 (c=  0.28389784)
   111a -> 112a  :     0.011697 (c=  0.10815104)
   111a -> 113a  :     0.057861 (c= -0.24054283)
    99b -> 109b  :     0.014735 (c= -0.12138902)
   100b -> 108b  :     0.017940 (c= -0.13393907)
   101b -> 107b  :     0.026428 (c= -0.16256640)
   101b -> 108b  :     0.030268 (c=  0.17397674)
   101b -> 109b  :     0.151562 (c= -0.38930955)
   101b -> 110b  :     0.021687 (c= -0.14726476)
   102b -> 107b  :     0.023767 (c=  0.15416412)
   102b -> 108b  :     0.064807 (c= -0.25457159)
   102b -> 109b  :     0.295936 (c=  0.54400015)
   102b -> 110b  :     0.024881 (c=  0.15773613)
   103b -> 108b  :     0.016877 (c= -0.12991329)
   106b -> 113b  :     0.054655 (c=  0.23378510)
STATE 25:  E=   0.121487 au      3.306 eV    26663.3 cm**-1
   109a -> 112a  :     0.012829 (c=  0.11326693)
   111a -> 113a  :     0.010846 (c= -0.10414206)
    98b -> 109b  :     0.010537 (c= -0.10265103)
    99b -> 108b  :     0.018751 (c= -0.13693368)
   100b -> 109b  :     0.048455 (c= -0.22012546)
   100b -> 110b  :     0.023489 (c= -0.15326162)
   101b -> 108b  :     0.166039 (c= -0.40747829)
   101b -> 109b  :     0.023104 (c= -0.15200062)
   102b -> 108b  :     0.368955 (c=  0.60741661)
   102b -> 109b  :     0.046134 (c=  0.21478800)
   103b -> 110b  :     0.146329 (c=  0.38252966)
   105b -> 113b  :     0.010748 (c=  0.10367086)
STATE 26:  E=   0.118027 au      3.212 eV    25904.0 cm**-1
   110a -> 112a  :     0.012672 (c=  0.11256834)
   110a -> 113a  :     0.025348 (c= -0.15920984)
   111a -> 114a  :     0.026394 (c=  0.16246178)
   100b -> 109b  :     0.012166 (c=  0.11029854)
   101b -> 108b  :     0.040541 (c=  0.20134813)
   102b -> 108b  :     0.070155 (c= -0.26486702)
   103b -> 110b  :     0.670963 (c=  0.81912308)
   105b -> 113b  :     0.026320 (c=  0.16223500)
   106b -> 112b  :     0.025209 (c=  0.15877445)
   106b -> 114b  :     0.049395 (c= -0.22224958)
```

```
STATE 27:  E=   0.122720 au      3.339 eV    26934.0 cm**-1
   109a -> 112a  :     0.133339 (c= -0.36515652)
   111a -> 113a  :     0.126160 (c=  0.35518988)
   101b -> 109b  :     0.031579 (c= -0.17770573)
   102b -> 109b  :     0.060349 (c=  0.24565957)
   104b -> 111b  :     0.012934 (c= -0.11372935)
   105b -> 111b  :     0.034412 (c= -0.18550352)
   105b -> 112b  :     0.368668 (c=  0.60718071)
   105b -> 113b  :     0.020413 (c=  0.14287551)
   105b -> 114b  :     0.087282 (c= -0.29543542)
STATE 28:  E=   0.123913 au      3.372 eV    27195.9 cm**-1
   107a -> 112a  :     0.013537 (c= -0.11634788)
   109a -> 112a  :     0.061813 (c=  0.24862146)
   111a -> 113a  :     0.019035 (c= -0.13796616)
    98b -> 108b  :     0.058879 (c=  0.24264994)
    99b -> 110b  :     0.016756 (c=  0.12944594)
   100b -> 108b  :     0.110883 (c=  0.33299080)
   101b -> 110b  :     0.127869 (c=  0.35758829)
   102b -> 110b  :     0.282599 (c= -0.53160036)
   103b -> 108b  :     0.025748 (c=  0.16046177)
   105b -> 111b  :     0.025616 (c= -0.16005122)
   105b -> 112b  :     0.053861 (c=  0.23208005)
   105b -> 114b  :     0.025443 (c= -0.15950755)
   106b -> 111b  :     0.028536 (c=  0.16892672)
   106b -> 113b  :     0.060764 (c=  0.24650369)
STATE 29:  E=   0.116911 au      3.181 eV    25658.9 cm**-1
   108a -> 112a  :     0.014081 (c=  0.11866468)
   110a -> 112a  :     0.045814 (c= -0.21404260)
   100b -> 107b  :     0.024218 (c= -0.15562139)
   105b -> 107b  :     0.010980 (c= -0.10478664)
   105b -> 111b  :     0.748969 (c= -0.86542975)
   105b -> 112b  :     0.026646 (c= -0.16323523)
   105b -> 113b  :     0.012769 (c= -0.11300155)
STATE 30:  E=   0.124247 au      3.381 eV    27269.1 cm**-1
   107a -> 112a  :     0.013377 (c= -0.11566088)
   109a -> 112a  :     0.135096 (c=  0.36755442)
   111a -> 113a  :     0.082409 (c=  0.28706956)
   100b -> 108b  :     0.027350 (c= -0.16537732)
   101b -> 107b  :     0.080718 (c= -0.28410875)
   102b -> 107b  :     0.045505 (c= -0.21331926)
   104b -> 111b  :     0.130002 (c=  0.36055737)
   105b -> 112b  :     0.069189 (c=  0.26303755)
   106b -> 111b  :     0.168995 (c=  0.41109059)
   106b -> 112b  :     0.015546 (c=  0.12468391)
```

```
   106b -> 113b  :     0.123957 (c= -0.35207592)

STATE 31:  E=   0.129798 au      3.532 eV    28487.3 cm**-1
   107a -> 112a  :     0.014548 (c=  0.12061503)
   108a -> 114a  :     0.056092 (c= -0.23683819)
   109a -> 112a  :     0.081173 (c= -0.28490882)
   109a -> 113a  :     0.225088 (c= -0.47443403)
   110a -> 114a  :     0.011104 (c=  0.10537711)
   111a -> 113a  :     0.046544 (c= -0.21574095)
    99b -> 107b  :     0.063866 (c=  0.25271736)
   101b -> 107b  :     0.073764 (c= -0.27159574)
   102b -> 107b  :     0.025245 (c= -0.15888522)
   102b -> 110b  :     0.016856 (c=  0.12983090)
   103b -> 112b  :     0.019027 (c= -0.13793986)
   103b -> 114b  :     0.028402 (c= -0.16852845)
   104b -> 112b  :     0.013546 (c=  0.11638679)
   104b -> 113b  :     0.130362 (c= -0.36105649)
   105b -> 112b  :     0.043744 (c=  0.20915078)
STATE 32:  E=   0.129602 au      3.527 eV    28444.3 cm**-1
   109a -> 112a  :     0.024783 (c= -0.15742719)
   109a -> 113a  :     0.019285 (c= -0.13886898)
    98b -> 108b  :     0.066181 (c= -0.25725725)
   100b -> 108b  :     0.268315 (c= -0.51799121)
   101b -> 109b  :     0.011462 (c= -0.10705933)
   101b -> 110b  :     0.112437 (c=  0.33531553)
   102b -> 109b  :     0.034077 (c=  0.18459990)
   102b -> 110b  :     0.235416 (c= -0.48519663)
   104b -> 113b  :     0.023666 (c= -0.15383859)
   105b -> 112b  :     0.025211 (c= -0.15878092)
   105b -> 114b  :     0.025231 (c=  0.15884410)
   106b -> 113b  :     0.039798 (c= -0.19949486)
STATE 33:  E=   0.128348 au      3.493 eV    28169.2 cm**-1
   109a -> 112a  :     0.013158 (c=  0.11470838)
   109a -> 113a  :     0.059014 (c= -0.24292834)
    97b -> 107b  :     0.024727 (c= -0.15724689)
    99b -> 107b  :     0.436211 (c= -0.66046275)
   101b -> 107b  :     0.209643 (c=  0.45786799)
   101b -> 110b  :     0.020319 (c= -0.14254443)
   102b -> 107b  :     0.033991 (c=  0.18436611)
   102b -> 110b  :     0.019963 (c=  0.14128942)
   104b -> 111b  :     0.017519 (c=  0.13235787)
   104b -> 113b  :     0.033442 (c= -0.18287241)
```

```
STATE 34:  E=   0.132407 au      3.603 eV    29060.1 cm**-1
   108a -> 112a  :     0.047371 (c= -0.21764954)
   108a -> 113a  :     0.110628 (c= -0.33260783)
   109a -> 114a  :     0.172293 (c= -0.41508153)
   110a -> 113a  :     0.107181 (c=  0.32738503)
   111a -> 114a  :     0.025479 (c=  0.15962086)
    98b -> 107b  :     0.012391 (c= -0.11131575)
   103b -> 113b  :     0.103557 (c=  0.32180285)
   104b -> 112b  :     0.125298 (c=  0.35397522)
   104b -> 113b  :     0.011142 (c=  0.10555693)
   104b -> 114b  :     0.067557 (c=  0.25991782)
   105b -> 113b  :     0.042295 (c= -0.20565776)
STATE 35:  E=   0.132077 au      3.594 eV    28987.5 cm**-1
   107a -> 112a  :     0.161997 (c=  0.40248809)
   107a -> 113a  :     0.021438 (c=  0.14641649)
   110a -> 114a  :     0.074003 (c= -0.27203495)
   111a -> 113a  :     0.109693 (c= -0.33119895)
    97b -> 107b  :     0.013319 (c= -0.11540829)
    98b -> 108b  :     0.043776 (c= -0.20922652)
    99b -> 107b  :     0.026928 (c= -0.16409764)
   100b -> 108b  :     0.140968 (c= -0.37545645)
   101b -> 107b  :     0.014838 (c= -0.12181210)
   102b -> 107b  :     0.049529 (c= -0.22255084)
   102b -> 109b  :     0.030815 (c= -0.17554078)
   104b -> 113b  :     0.040996 (c=  0.20247484)
   105b -> 112b  :     0.040690 (c=  0.20171717)
   105b -> 114b  :     0.019851 (c= -0.14089293)
   106b -> 113b  :     0.094210 (c=  0.30693574)
STATE 36:  E=   0.127346 au      3.465 eV    27949.1 cm**-1
   110a -> 113a  :     0.010711 (c= -0.10349591)
    96b -> 107b  :     0.011102 (c= -0.10536676)
    97b -> 108b  :     0.014510 (c= -0.12045911)
    98b -> 107b  :     0.440127 (c= -0.66342098)
    98b -> 110b  :     0.032991 (c= -0.18163466)
    98b -> 111b  :     0.010090 (c=  0.10044901)
    99b -> 108b  :     0.101318 (c= -0.31830459)
   100b -> 107b  :     0.144352 (c=  0.37993639)
   100b -> 109b  :     0.012727 (c= -0.11281357)
   100b -> 110b  :     0.123264 (c= -0.35108961)
   101b -> 108b  :     0.016788 (c=  0.12956671)
```

```
STATE 37:  E=   0.134652 au      3.664 eV    29552.7 cm**-1
   110a -> 113a  :     0.028622 (c=  0.16917966)
   111a -> 114a  :     0.033167 (c= -0.18211766)
    98b -> 107b  :     0.058712 (c= -0.24230585)
    98b -> 109b  :     0.068207 (c=  0.26116556)
    98b -> 110b  :     0.065487 (c=  0.25590476)
   100b -> 107b  :     0.121841 (c=  0.34905779)
   100b -> 109b  :     0.198064 (c=  0.44504350)
   100b -> 110b  :     0.188653 (c=  0.43434205)
   102b -> 108b  :     0.028854 (c=  0.16986568)
   105b -> 113b  :     0.040265 (c=  0.20066196)
   106b -> 112b  :     0.035274 (c= -0.18781318)
   106b -> 114b  :     0.023686 (c= -0.15390218)
STATE 38:  E=   0.134439 au      3.658 eV    29506.0 cm**-1
   109a -> 112a  :     0.026244 (c= -0.16200060)
    97b -> 107b  :     0.054483 (c= -0.23341510)
    98b -> 108b  :     0.026067 (c=  0.16145268)
    99b -> 107b  :     0.290449 (c= -0.53893357)
   100b -> 108b  :     0.039146 (c=  0.19785387)
   101b -> 107b  :     0.210916 (c= -0.45925582)
   102b -> 107b  :     0.135767 (c= -0.36846620)
   102b -> 109b  :     0.035488 (c=  0.18838280)
   104b -> 111b  :     0.034958 (c= -0.18697007)
   105b -> 112b  :     0.032004 (c= -0.17889721)
   106b -> 113b  :     0.016624 (c= -0.12893530)
STATE 39:  E=   0.133361 au      3.629 eV    29269.3 cm**-1
   108a -> 113a  :     0.031511 (c= -0.17751291)
   109a -> 114a  :     0.029576 (c= -0.17197556)
   110a -> 113a  :     0.387808 (c= -0.62274202)
   111a -> 114a  :     0.440233 (c= -0.66350074)
   103b -> 113b  :     0.017027 (c=  0.13048625)
   104b -> 112b  :     0.014346 (c=  0.11977339)
STATE 40:  E=   0.135480 au      3.687 eV    29734.3 cm**-1
   107a -> 112a  :     0.596917 (c=  0.77260375)
   110a -> 114a  :     0.010909 (c=  0.10444521)
   111a -> 112a  :     0.023515 (c=  0.15334497)
    98b -> 108b  :     0.021168 (c=  0.14549209)
   100b -> 108b  :     0.023387 (c=  0.15292885)
   101b -> 107b  :     0.024359 (c=  0.15607443)
   101b -> 109b  :     0.022422 (c= -0.14974136)
   102b -> 107b  :     0.027842 (c=  0.16685821)
   102b -> 109b  :     0.018059 (c=  0.13438372)
   104b -> 111b  :     0.070510 (c=  0.26553778)
   105b -> 112b  :     0.014061 (c= -0.11857753)
```

```
   106b -> 113b  :     0.048201 (c= -0.21954814)

STATE 41:  E=   0.138343 au      3.764 eV    30362.7 cm**-1
   110a -> 113a  :     0.066759 (c=  0.25837749)
   111a -> 114a  :     0.045143 (c= -0.21246880)
    98b -> 107b  :     0.028682 (c=  0.16935709)
    98b -> 109b  :     0.011225 (c=  0.10594936)
    98b -> 110b  :     0.034715 (c= -0.18632079)
    99b -> 108b  :     0.017111 (c=  0.13080915)
   100b -> 109b  :     0.062400 (c=  0.24979961)
   100b -> 110b  :     0.409903 (c= -0.64023641)
   103b -> 110b  :     0.015834 (c= -0.12583158)
   104b -> 112b  :     0.013611 (c= -0.11666832)
   105b -> 113b  :     0.077742 (c=  0.27882196)
   106b -> 112b  :     0.035607 (c= -0.18869804)
   106b -> 114b  :     0.069674 (c= -0.26395818)
STATE 42:  E=   0.130116 au      3.541 eV    28557.1 cm**-1
   110a -> 114a  :     0.038123 (c=  0.19525021)
    96b -> 108b  :     0.026871 (c= -0.16392440)
    98b -> 108b  :     0.651026 (c= -0.80686173)
    98b -> 109b  :     0.010295 (c= -0.10146536)
   100b -> 108b  :     0.211631 (c=  0.46003413)
STATE 43:  E=   0.138453 au      3.768 eV    30387.0 cm**-1
   107a -> 112a  :     0.010166 (c= -0.10082497)
   110a -> 114a  :     0.393290 (c= -0.62712861)
   111a -> 113a  :     0.032427 (c= -0.18007418)
    98b -> 108b  :     0.024048 (c= -0.15507357)
    99b -> 109b  :     0.011963 (c=  0.10937683)
   100b -> 108b  :     0.025556 (c=  0.15986313)
   100b -> 109b  :     0.013398 (c=  0.11575083)
   101b -> 109b  :     0.014608 (c= -0.12086411)
   103b -> 112b  :     0.010764 (c= -0.10375027)
   104b -> 111b  :     0.011568 (c=  0.10755293)
   105b -> 113b  :     0.105538 (c= -0.32486649)
   105b -> 114b  :     0.044788 (c= -0.21163234)
   106b -> 113b  :     0.106993 (c= -0.32709738)
   106b -> 114b  :     0.020604 (c= -0.14354030)
```

```
STATE 44:  E=   0.138820 au      3.777 eV    30467.5 cm**-1
   108a -> 113a  :     0.016090 (c= -0.12684589)
   109a -> 114a  :     0.012455 (c= -0.11160248)
   110a -> 113a  :     0.022342 (c=  0.14947081)
   110a -> 114a  :     0.117535 (c= -0.34283340)
   111a -> 114a  :     0.010386 (c= -0.10191196)
    98b -> 109b  :     0.013388 (c= -0.11570572)
    98b -> 110b  :     0.022704 (c=  0.15067811)
    99b -> 108b  :     0.029720 (c= -0.17239476)
   100b -> 108b  :     0.012884 (c=  0.11350811)
   100b -> 109b  :     0.039871 (c= -0.19967772)
   101b -> 108b  :     0.021724 (c=  0.14739010)
   103b -> 111b  :     0.014447 (c= -0.12019457)
   104b -> 112b  :     0.011510 (c= -0.10728577)
   105b -> 112b  :     0.040230 (c= -0.20057498)
   105b -> 113b  :     0.321259 (c=  0.56679680)
   105b -> 114b  :     0.012107 (c= -0.11003364)
   106b -> 112b  :     0.064441 (c=  0.25385200)
   106b -> 114b  :     0.048193 (c=  0.21952995)
STATE 45:  E=   0.135542 au      3.688 eV    29748.0 cm**-1
    98a -> 112a  :     0.010208 (c=  0.10103539)
   108a -> 112a  :     0.569735 (c=  0.75480808)
   109a -> 115a  :     0.014249 (c= -0.11936855)
   110a -> 112a  :     0.015380 (c= -0.12401448)
   111a -> 114a  :     0.016161 (c=  0.12712700)
   100b -> 109b  :     0.017972 (c=  0.13406046)
   101b -> 108b  :     0.012519 (c=  0.11188966)
   102b -> 108b  :     0.015887 (c=  0.12604279)
   103b -> 111b  :     0.126880 (c= -0.35620260)
   105b -> 111b  :     0.044435 (c=  0.21079669)
   105b -> 113b  :     0.014398 (c= -0.11998994)
   106b -> 114b  :     0.015578 (c=  0.12481316)
STATE 46:  E=   0.141981 au      3.864 eV    31161.3 cm**-1
    98b -> 107b  :     0.020362 (c=  0.14269703)
    98b -> 109b  :     0.012831 (c= -0.11327592)
    98b -> 110b  :     0.194779 (c=  0.44133791)
    99b -> 108b  :     0.209439 (c= -0.45764546)
   100b -> 107b  :     0.012044 (c= -0.10974732)
   100b -> 109b  :     0.011940 (c= -0.10927171)
   101b -> 108b  :     0.192881 (c=  0.43918268)
   102b -> 108b  :     0.022074 (c=  0.14857228)
   105b -> 113b  :     0.038943 (c= -0.19733957)
   106b -> 112b  :     0.011926 (c= -0.10920421)
   106b -> 114b  :     0.135194 (c= -0.36768795)
```

```
STATE 47:  E=   0.139702 au      3.801 eV    30661.0 cm**-1
    99b -> 109b  :     0.241110 (c= -0.49102947)
    99b -> 110b  :     0.039699 (c= -0.19924699)
   101b -> 108b  :     0.011257 (c= -0.10610134)
   101b -> 109b  :     0.437891 (c=  0.66173358)
   102b -> 108b  :     0.011580 (c= -0.10760881)
   102b -> 109b  :     0.154202 (c=  0.39268526)
   104b -> 111b  :     0.013297 (c=  0.11531129)
STATE 48:  E=   0.143481 au      3.904 eV    31490.4 cm**-1
   108a -> 112a  :     0.033500 (c=  0.18303023)
   109a -> 112a  :     0.017569 (c= -0.13254925)
    98b -> 109b  :     0.058747 (c=  0.24237748)
    98b -> 110b  :     0.034600 (c=  0.18601023)
    99b -> 109b  :     0.010095 (c=  0.10047392)
    99b -> 110b  :     0.017460 (c=  0.13213722)
   100b -> 109b  :     0.101854 (c= -0.31914622)
   101b -> 108b  :     0.247813 (c= -0.49780807)
   101b -> 109b  :     0.013604 (c= -0.11663477)
   102b -> 108b  :     0.184850 (c= -0.42994228)
   103b -> 111b  :     0.025328 (c= -0.15914873)
   104b -> 111b  :     0.034968 (c=  0.18699719)
   106b -> 114b  :     0.076802 (c= -0.27713249)
STATE 49:  E=   0.142833 au      3.887 eV    31348.3 cm**-1
   107a -> 112a  :     0.045106 (c= -0.21238107)
   109a -> 112a  :     0.155859 (c= -0.39478928)
    98b -> 109b  :     0.012307 (c= -0.11093788)
    99b -> 109b  :     0.020298 (c=  0.14246959)
    99b -> 110b  :     0.081490 (c=  0.28546394)
   100b -> 109b  :     0.015205 (c=  0.12330747)
   101b -> 108b  :     0.029984 (c=  0.17315823)
   101b -> 109b  :     0.013592 (c=  0.11658479)
   101b -> 110b  :     0.039951 (c= -0.19987746)
   102b -> 108b  :     0.018121 (c=  0.13461512)
   102b -> 109b  :     0.034536 (c=  0.18583752)
   103b -> 112b  :     0.017179 (c=  0.13106945)
   104b -> 111b  :     0.326239 (c=  0.57117337)
   104b -> 113b  :     0.066745 (c=  0.25835115)
```

```
STATE 50:  E=   0.137825 au      3.750 eV    30249.1 cm**-1
    96b -> 109b  :     0.015201 (c= -0.12329256)
    98b -> 109b  :     0.520562 (c= -0.72150009)
    98b -> 110b  :     0.088760 (c= -0.29792553)
    99b -> 108b  :     0.020798 (c= -0.14421670)
   100b -> 109b  :     0.070350 (c=  0.26523603)
   100b -> 110b  :     0.046837 (c=  0.21641871)
   101b -> 108b  :     0.031856 (c= -0.17848233)
   102b -> 108b  :     0.031254 (c= -0.17678782)
   103b -> 111b  :     0.010440 (c= -0.10217828)
   104b -> 112b  :     0.012849 (c= -0.11335476)
   106b -> 114b  :     0.055218 (c= -0.23498429)

-----------------------------------------------------------------------------
        ABSORPTION SPECTRUM VIA TRANSITION ELECTRIC DIPOLE MOMENTS
-----------------------------------------------------------------------------
State   Energy  Wavelength   fosc        T2        TX        TY        TZ
       (cm-1)    (nm)               (au**2)    (au)      (au)      (au)
-----------------------------------------------------------------------------
   1   12866.9    777.2   0.010753836   0.27515   0.18124  -0.20006  -0.44975
   2   14236.1    702.4   0.001162020   0.02687  -0.05458   0.12792  -0.08677
   3   14541.5    687.7   0.000694768   0.01573   0.04339  -0.06071  -0.10080
   4   15072.2    663.5   0.001342500   0.02932   0.06945   0.15206  -0.03710
   5   16126.8    620.1   0.028140886   0.57447  -0.26135   0.28755   0.65075
   6   16528.7    605.0   0.001648269   0.03283  -0.04058   0.11083   0.13747
   7   16701.6    598.7   0.018544077   0.36553  -0.21348   0.22187   0.52032
   8   18762.6    533.0   0.001427267   0.02504   0.07689   0.13638  -0.02306
   9   19927.8    501.8   0.002005876   0.03314   0.06126  -0.07265  -0.15526
  10   21513.6    464.8   0.027982083   0.42820  -0.22245   0.25425   0.56042
  11   21985.0    454.9   0.000005862   0.00009  -0.00486  -0.00723  -0.00344
  12   23523.0    425.1   0.000003915   0.00005  -0.00311   0.00163   0.00652
  13   21895.4    456.7   0.000342650   0.00515  -0.03871  -0.01297  -0.05904
  14   21671.2    461.4   0.001447828   0.02199   0.06467  -0.06371  -0.11728
  15   23966.9    417.2   0.001335417   0.01834  -0.00645  -0.12926   0.03993
  16   24349.8    410.7   0.000849073   0.01148  -0.03529   0.02124   0.09891
  17   23209.9    430.8   0.003561045   0.05051  -0.07946   0.08247   0.19338
  18   24387.6    410.0   0.002056255   0.02776   0.05724  -0.04159  -0.15084
  19   23915.3    418.1   0.001372005   0.01889   0.02818   0.13012  -0.03408
  20   23832.3    419.6   0.000041234   0.00057   0.01311   0.00571  -0.01911
  21   24647.4    405.7   0.001414132   0.01889  -0.04772  -0.12091   0.04463
  22   25871.4    386.5   0.002921943   0.03718   0.02596   0.17531  -0.07600
  23   26093.5    383.2   0.000091152   0.00115   0.02828  -0.00736   0.01720
  24   26655.8    375.2   0.009558994   0.11806   0.08854  -0.13621  -0.30276
  25   26663.3    375.0   0.001589749   0.01963   0.13731  -0.00131  -0.02780
```

```
  26   25904.0    386.0   0.003014817   0.03832  -0.02388   0.17080  -0.09258
  27   26934.0    371.3   0.001497394   0.01830   0.06016  -0.05072  -0.11005
  28   27195.9    367.7   0.004303076   0.05209  -0.08615   0.10626   0.18270
  29   25658.9    389.7   0.000707762   0.00908  -0.01626   0.09204  -0.01859
  30   27269.1    366.7   0.037011489   0.44683  -0.21970   0.27444   0.56854
  31   28487.3    351.0   0.000471243   0.00545   0.01832  -0.02516  -0.06691
  32   28444.3    351.6   0.013257068   0.15344   0.14285  -0.15545  -0.32995
  33   28169.2    355.0   0.003146662   0.03677  -0.05597   0.07555   0.16713
  34   29060.1    344.1   0.000226102   0.00256   0.05027  -0.00451  -0.00378
  35   28987.5    345.0   0.026830899   0.30472  -0.19496   0.21839   0.46799
  36   27949.1    357.8   0.002318280   0.02731   0.15550   0.05098   0.02295
  37   29552.7    338.4   0.031124055   0.34672   0.28737  -0.43135   0.27942
  38   29506.0    338.9   0.034149021   0.38102   0.19816  -0.22375  -0.54008
  39   29269.3    341.7   0.000446228   0.00502   0.03403  -0.05802   0.02224
  40   29734.3    336.3   0.045893109   0.50812   0.24613  -0.30946  -0.59311
  41   30362.7    329.4   0.056995773   0.61798   0.05826  -0.68473   0.38175
  42   28557.1    350.2   0.000219670   0.00253   0.00003  -0.04256  -0.02686
  43   30387.0    329.1   0.012874470   0.13948   0.19346   0.05380  -0.31489
  44   30467.5    328.2   0.020395282   0.22038  -0.10624  -0.44724  -0.09521
  45   29748.0    336.2   0.004940944   0.05468   0.07930   0.20869  -0.06958
  46   31161.3    320.9   0.010833239   0.11445  -0.28244  -0.17247   0.07024
  47   30661.0    326.1   0.005590587   0.06003   0.02780  -0.16217  -0.18153
  48   31490.4    317.6   0.022747581   0.23781   0.11105  -0.45003  -0.15151
  49   31348.3    319.0   0.118005320   1.23926   0.36089  -0.28719  -1.01318
  50   30249.1    330.6   0.008371854   0.09111  -0.09093  -0.27033   0.09883

-----------------------------------------------------------------------------
         ABSORPTION SPECTRUM VIA TRANSITION VELOCITY DIPOLE MOMENTS
-----------------------------------------------------------------------------
State   Energy  Wavelength   fosc        P2         PX        PY        PZ
        (cm-1)   (nm)                 (au**2)     (au)      (au)      (au)
-----------------------------------------------------------------------------
   1   12866.9   777.2   0.003150536   0.00028   0.00534  -0.00623  -0.01448
   2   14236.1   702.4   0.007527164   0.00073  -0.01872   0.01409  -0.01354
   3   14541.5   687.7   0.000035448   0.00000   0.00065  -0.00129   0.00120
   4   15072.2   663.5   0.003850511   0.00040   0.01602   0.01176   0.00127
   5   16126.8   620.1   0.000069670   0.00001   0.00033  -0.00218  -0.00168
   6   16528.7   605.0   0.002131756   0.00024   0.00645   0.01346  -0.00426
   7   16701.6   598.7   0.000059611   0.00001  -0.00104  -0.00237  -0.00028
   8   18762.6   533.0   0.000324969   0.00004  -0.00557   0.00123  -0.00301
   9   19927.8   501.8   0.000933811   0.00013   0.00365  -0.00457  -0.00964
  10   21513.6    464.8   0.001855831   0.00027  -0.00513   0.00687   0.01412
  11   21985.0    454.9   0.000713132   0.00011   0.00663   0.00792  -0.00069
  12   23523.0    425.1   0.000090111   0.00001   0.00187  -0.00074  -0.00324
  13   21895.4    456.7   0.000385508   0.00006  -0.00701   0.00193  -0.00219
  14   21671.2    461.4   0.000152836   0.00002   0.00074   0.00127   0.00453
```

15	23966.9	417.2	0.000100539	0.00002	0.00328	-0.00181	0.00154
16	24349.8	410.7	0.000099765	0.00002	-0.00222	-0.00035	0.00340
17	23209.9	430.8	0.000776730	0.00012	0.00335	-0.00454	-0.00956
18	24387.6	410.0	0.001327173	0.00022	0.00668	-0.00313	-0.01291
19	23915.3	418.1	0.003212447	0.00053	0.01527	0.01707	0.00072
20	23832.3	419.6	0.000041520	0.00001	0.00189	0.00107	-0.00143
21	24647.4	405.7	0.002619201	0.00044	-0.01262	-0.01677	0.00091
22	25871.4	386.5	0.003783141	0.00067	0.01392	0.02150	-0.00356
23	26093.5	383.2	0.000290136	0.00005	-0.00623	-0.00357	-0.00042
24	26655.8	375.2	0.007010090	0.00128	-0.01302	0.01309	0.03059
25	26663.3	375.0	0.000468986	0.00009	0.00190	0.00596	0.00681
26	25904.0	386.0	0.001829643	0.00032	0.00701	0.01608	-0.00404
27	26934.0	371.3	0.001473951	0.00027	-0.00402	0.00640	0.01464
28	27195.9	367.7	0.000042590	0.00001	0.00098	0.00240	0.00110
29	25658.9	389.7	0.001273475	0.00022	0.01209	0.00715	-0.00509
30	27269.1	366.7	0.000021198	0.00000	0.00156	0.00063	-0.00106
31	28487.3	351.0	0.002027055	0.00039	0.00639	-0.00752	-0.01724
32	28444.3	351.6	0.002503432	0.00049	-0.00745	0.00853	0.01893
33	28169.2	355.0	0.000969332	0.00019	0.00536	-0.00493	-0.01156
34	29060.1	344.1	0.000117549	0.00002	0.00004	0.00137	0.00463
35	28987.5	345.0	0.018613262	0.00369	0.01992	-0.02284	-0.05262
36	27949.1	357.8	0.000500717	0.00010	0.00569	0.00795	-0.00023
37	29552.7	338.4	0.006666908	0.00135	0.01368	-0.02826	0.01899
38	29506.0	338.9	0.005905804	0.00119	-0.01224	0.01409	0.02903
39	29269.3	341.7	0.000614002	0.00012	0.00925	-0.00161	0.00590
40	29734.3	336.3	0.016086605	0.00327	-0.02087	0.02017	0.04926
41	30362.7	329.4	0.007450156	0.00155	-0.01851	-0.03458	0.00279
42	28557.1	350.2	0.000035660	0.00001	-0.00215	-0.00141	0.00061
43	30387.0	329.1	0.006878215	0.00143	-0.00150	0.02261	0.03025
44	30467.5	328.2	0.006374927	0.00133	-0.02922	-0.01211	0.01808
45	29748.0	336.2	0.003198540	0.00065	0.01494	0.02057	-0.00193
46	31161.3	320.9	0.001744627	0.00037	-0.01606	-0.00635	-0.00856
47	30661.0	326.1	0.000672265	0.00014	-0.00748	0.00168	0.00906
48	31490.4	317.6	0.001341162	0.00029	-0.00469	-0.01402	0.00837
49	31348.3	319.0	0.001481626	0.00032	-0.00533	0.01241	0.01161
50	30249.1	330.6	0.002033052	0.00042	-0.01235	-0.01621	0.00227

Chapter Three

Electrocatalytic CO_2 Reduction to Formate with Molecular Fe(III) Complexes Containing Pendent Proton Relays

Published as: Nichols, A. W., Hooe, S. L., Kuehner, J. S., Dickie, D.A., Machan, C. W. *Inorganic Chemistry* **2020**, *59*, 5854–5864.

3.1 Abstract

Previously, we reported an iron (III) complex with 6,6'-([2,2'-bipyridine]-6,6'-diyl)bis(2,4-ditertbutyl-phenol) as a ligand (Fe(^{tbu}dhbpy)Cl, **1**) as catalytically competent for the electrochemical reduction of CO_2 to formate (Faradaic efficiency FE_{HCO2-} = 68±4%). In mechanistic experiments, an essential component was found to be a pre-equilibrium reaction involving the association of the proton donor with the catalyst, which preceded proton transfer to the Fe-bound O atoms upon reduction of the Fe center. Here, we report the synthesis, structural characterization, and reactivity of two iron(III) compounds with 6,6′-([2,2′-bipyridine]-6,6′-diyl)bis(2-methoxy-4-methylphenol (^{me}crebpy[H]$_2$, Fe(^{me}crebpy)Cl, **2**) and 6,6'-([2,2'-bipyridine]-6,6'-diyl)bis(4-(tert-butyl)benzene-1,2-diol) (^{tbu}catbpy[H]$_4$, Fe(^{tbu}catbpy), **3**) as ligands, where pendent –OMe and –OH groups are poised to modify the protonation reaction involving the Fe-bound O atoms. Differences in selectivity and activity for the electrocatalytic reduction of carbon dioxide (CO_2) to formate (HCO_2^-) between complexes **1**-**3** were assessed via cyclic voltammetry (CV) and controlled potential electrolysis (CPE) experiments in *N,N*-dimethylformamide (*N,N*-DMF). Mechanistic studies suggest that the O atoms in the secondary coordination sphere are important for relaying the exogenous proton donor to the active site through a pre-concentration effect, which leads to the J_{HCO2-} (partial catalytic current density for formate) increasing by 3.3-fold for **2** and 1.2-fold for **3** in comparison to the J_{HCO2-} **1**. These results also suggest that there is a difference in the strength of the interaction between the pendent functional groups and the sacrificial proton donor between **2** and **3**, resulting in quantifiable differences in catalytic activity and

efficiency. CPE experiments demonstrate an increased FE_{HCO2-} = 85±2% for **2**, whereas **3** had a lower FE_{HCO2-} = 71±3%, with CO and H_2 generated as co-products in each case to reach mass balance. These results indicate that using secondary sphere moieties to modulate metal-ligand interactions and multisite electron and proton transfer reactivity in the primary coordination sphere through reactant pre-concentration can be a powerful strategy for enhancing electrocatalytic activity and selectivity.

3.2 Introduction

The steadily increasing market share of electricity from renewable sources continues to generate interest in developing electrochemical transformations for storing energy in chemical bonds.[1] One compelling approach is to direct energy from these sources towards electrochemical transformations of CO_2, a byproduct of fossil fuel usage and a greenhouse gas, into useful fuel precursors and commodity chemicals.[1-2] In comparison to molecular electrocatalysts developed for the reduction of CO_2 to CO, relatively few catalysts have been developed which selectively produce formate.[3-5] Formate is currently used as an organic hydride source in synthesis,[6] an energy source in fuel cells,[7] and an H_2 storage material.[8]

Previously, we identified a molecular Fe(III) chloride complex (Fe(^{tbu}dhbpy)Cl, **1**; **Figure 3.1**) based upon a 6,6′-di(3,5-di-tert-butyl-2-hydroxybenzene)-2,2′-bipyridine (^{tbu}dhbpy[H]$_2$) ligand which produced formate (HCO_2^-) with a FE of 68±4% from CO_2 in the presence of 0.5 M phenol (PhOH) at an $E_{cat/2}$ of –2.45 V versus the ferrocenium/ferrocene redox couple (Fc^+/Fc).[9] Mechanistic studies suggested that a non-catalytic electrochemical reaction was vital to the observed reactivity: the Fe-bound oxygen atoms underwent protonation upon the Fe(III)/(II) reduction, a type of multi-site electron and proton transfer (MS-EPT) reaction.[9-12] MS-EPT mechanisms involving ligand protonation upon metal redox changes in the primary coordination sphere are generally invoked for metal oxime and dithiolene complexes which catalytically generate hydrogen (H_2)[13-17]; similar mechanisms are underdeveloped for other substrates.[3] MS-EPT has been explored broadly in photochemical and chemical systems, including the photosynthetic oxidation of tyrosine-Z,[18] ruthenium-based model compounds for phenol oxidation,[19] and mixed TEMPOH/organic base/chemical oxidant systems.[20] Under electrochemical conditions, MS-EPT has also been studied in the context of tyrosine oxidation by $[M(bpy)_3]^{3+/2+}$ systems (M = Os, Ru, Fe; bpy = 2,2′-bipyridine).[21]

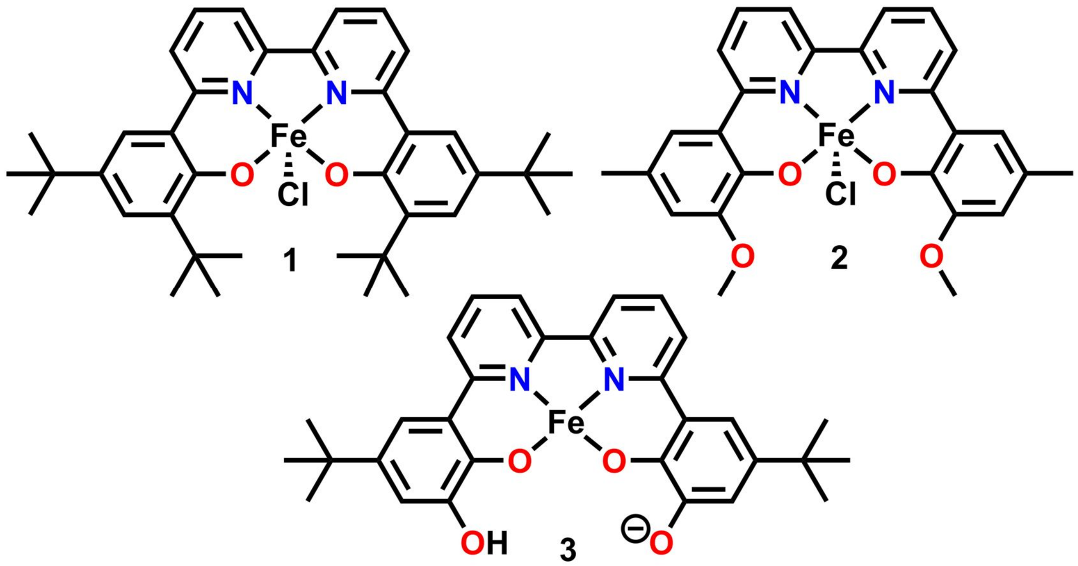

Figure 3.1. Molecular electrocatalysts for CO_2 reduction to formate (HCO_2^-) studied previously (**1**; Fe(^{tbu}dhbpy)Cl)[9] and in this work (**2**; Fe(^{me}crebpy)Cl and **3**; Fe(^{tbu}catbpy).

A successful strategy for improving the activity, selectivity, and thermodynamic efficiency of molecular electrocatalysts which facilitate the transformation of CO_2 is the incorporation of pendent proton shuttles in their secondary coordination spheres.[22-24] The utility of these functional groups holds for many electrocatalytic transformations: examples exist for the H_2 evolution,[25-27] oxygen reduction,[28-30] and CO_2 reduction[22, 31-34] reactions. In studies on molecular electrocatalysts for CO_2 reduction, the design emphasis is generally placed on positioning the pendent relay such that it can interact with CO_2 bound to the active site of the complex to stabilize intermediates, act as a proton (or proton donor) relay, and/or to provide access to new reaction pathways to lower the energy input and increase catalytic rates.[22-23, 34-41]

Intrigued by our initial observations of the MS-EPT reaction and its relationship to the catalytic response,[9] we have synthesized two new ligand frameworks containing secondary-sphere hydrogen bond -donor and -acceptor groups which are instead oriented to interact with the Fe-bound O atoms that are protonated upon reduction of the metal center (**Figure 3.1**; complexes **2** and **3**).[37-40] By tuning the ability of the secondary sphere moiety to direct the exogenous sacrificial proton donor to the proton-sensitive Fe-bound O atom, an increased current density for formate production (J_{HCO2-}) and selectivity for HCO_2^- is achieved. Importantly, this demonstrates that non-catalytic MS-EPT reactions can be optimized via analogous strategies to those used for enhanced protonation rates of activated substrate at the metal center.

Here, we report the synthesis, characterization, and electrochemical behavior of two new Fe(III) complexes containing pendent hydroxy or methoxy moieties oriented to direct proton donors to the Fe-bound oxygen atoms of an N_2O_2 coordination environment. These complexes contain the ligands 6,6'-([2,2'-bipyridine]-6,6'-diyl)bis(2-methoxy-4-methylphenol) (^{me}crebpy[H]$_2$) for Fe(^{me}crebpy)Cl (**2**; **Figure 3.1**) and 6,6'-([2,2'-bipyridine]-6,6'-diyl)bis(4-(tert-butyl)benzene-1,2-diol) (^{tbu}catbpy[H]$_4$) for Fe(^{tbu}catbpy) (**3**; **Figure 3.1**). Initial studies have shown complex **2** to be an excellent catalyst for the reduction of CO_2 to HCO_2^-, with a 3.3-fold enhancement in partial catalytic current density corresponding to HCO_2^- production in comparison to **1**. Complex **2** also shows an enhanced FE_{HCO2-} (FE_{HCO2-} **2** = 85±2%) in comparison to the 68±4% FE_{HCO2-} previously observed for **1**[9] under analogous conditions. In contrast, **3** is only slightly more active than **1** with a 1.2-fold enhancement in terms of catalytic current density for HCO_2^- production; no significant increase in FE_{HCO2-} is observed (FE_{HCO2-} **3** = 71±3%). We propose that the improvements in selectivity and activity for **2** arise from beneficial interactions between the secondary sphere moieties, exogenous proton donor, and inner-sphere Fe-bound oxygen atom, which contribute to the pre-concentration of the proton donor and kinetic selectivity.

3.3 Results

3.3.1 Synthesis and Characterization of 2 and 3

The isolation of the [^{me}crebpy(H)$_2$] and [^{tbu}catbpy(H)$_4$] ligands was accomplished through Pd-catalyzed cross-coupling procedures analogous to the previously reported synthesis of [^{tbu}dhbpy(H)$_2$] (see **Experimental Methods**).[9] The corresponding Fe(III) complexes were obtained by refluxing the respective ligands in ethanol in the presence of equimolar $FeCl_3•6H_2O$ with NaOAc as a proton scavenger. Single crystals of sufficient quality for X-ray diffraction studies were obtained for both **2** and **3** by the slow cooling of supersaturated acetonitrile solutions from refluxing temperatures. The solid-state structure of complex **2** is a dimeric species, with a single oxygen atom from each ligand framework coordinated to an axial position of a second Fe complex to create a hexadentate coordination environment (**Figure 3.2**). Likewise, complex **3** also exists as a dimeric species in the solid state, however in this case hexadentate coordination is instead facilitated by the partial deprotonation of one of each of the pendent –OH moieties per equivalent of **3** in the dimeric structure, replacing the Cl^- ligand for both Fe centers (**Figure S3.1**). Microanalysis of the as-synthesized **3** confirmed that complete chloride loss occurs for the bulk material, with charge for the Fe(III) center balanced by the partial deprotonation in the secondary coordination sphere (**3**; **Figure 3.1**). In both cases the solution-phase behavior suggests that these are monomeric species: UV-Vis spectra of **2** and **3** obtained in *N,N*-DMF maintain linearity upon dilution, which is consistent with the absence of an equilibrium process (**Figure S3.2** and **S3.3**). Diffusion coefficients for **2** and **3** determined by RDE methods using the Levich equation are consistent with those determined for **1** (**Table S3.1**, **Figures S3.4-S3.6**).[42] Finally, the magnetic moments determined by Evans' method of 5.9±0.1 and 6.0±0.1 Bohr magnetons obtained for **2** and **3**, respectively, are consistent with a monomeric high spin S = 5/2 Fe(III) species in each case.[9]

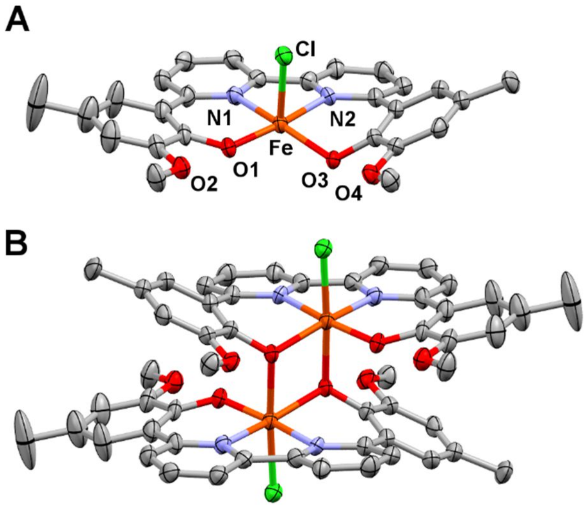

Figure 3.2. (A) Unit cell and (B) overall dimer structure for Fe(^{me}crebpy)Cl **2**; each equivalent of **2** is generated by symmetry and not crystallographically distinct. C = grey, O = red, N= blue, Fe = orange, Cl = green. Thermal ellipsoids set to 50%. Occluded acetonitrile molecules and hydrogen atoms omitted for clarity.

3.3.2 Electrochemistry

3.3.2.1 Electrochemical Response under Ar Saturation

Cyclic voltammetry (CV) experiments conducted in 0.1 M $TBAPF_6$/*N,N*-DMF under Ar with each complex demonstrated redox processes at similar potentials to **1**.[9] Complex **2** exhibits four total redox processes: one irreversible reduction with $E_{p,a}$ = –1.45 V vs Fc^+/Fc, two quasi-reversible $1e^-$ reductions with $E_{1/2}$ = –0.84 and –2.55 V vs Fc^+/Fc, and one reversible $1e^-$ reduction with $E_{1/2}$ = –1.93 V vs. Fc^+/Fc (**Figure 3.3**, black, **Figure S3.7**, and **Tables S3.2-S3.4**). The irreversible reduction with $E_{p,a}$ = –1.45 V vs Fc^+/Fc disappears at fast scan rates upon the addition of TBACl as a source of Cl^- (**Figure S3.8**), suggesting that it corresponds to the product of an equilibrium reaction involving Cl^- loss. Complex **3** exhibits four total redox processes as well: two reversible, $1e^-$ reductions with $E_{1/2}$ = –1.01 V and –1.65 V vs Fc^+/Fc, respectively, followed by two $1e^-$ irreversible reductions with $E_{1/2}$ = –2.24 V and $E_{p.a}$ = –2.58 V vs Fc^+/Fc (**Figure 3.3**, red, **Figure S3.9**, and **Tables S3.5** and **S3.6**). On the return sweep to oxidizing potentials with **3**, a feature with $E_{p,c}$ = –1.39 V vs Fc^+/Fc is observed when the CV switching potential is ~–2.7 V vs Fc^+/Fc, indicating that this CV feature is associated with the final two reduction waves (**Figure 3.3**, red). Interestingly, a scan rate-dependent relationship is observed between the final two reduction features for **3** (**Figure S3.10**). The reduction at –2.24 V vs Fc^+/Fc produces larger current densities at slow scan rates (<200 mV/s), but the reduction feature at –2.58 V vs Fc^+/Fc becomes relatively more prominent at faster scan rates; the ratio between the two decreases asymptotically (**Figure S3.10**).

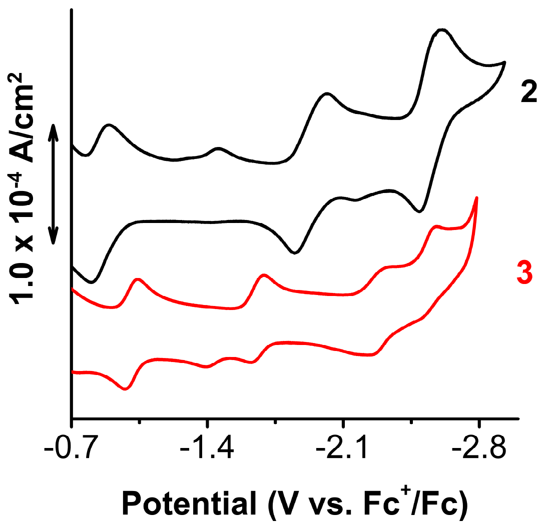

Figure 3.3. Cyclic Voltammograms of 0.5 mM Fe(^{me}crebpy)Cl **2** (black) and Fe(^{tbu}catbpy) **3** (red) under an Ar atmosphere in 0.1 M TBAPF$_6$/*N,N*-DMF supporting electrolyte. Working electrode is glassy carbon, counter electrode is a glassy carbon rod, AgCl/Ag pseudoreference electrode. Referenced to Fc$^+$/Fc from internal decamethylferrocene (Cp$_2$*Fe) standard; 100 mV/s scan rate.

Variable scan rate experiments indicate the electrochemical response of both **2** and **3** is in a diffusion-limited regime for the first two reversible reductions (**Figures S3.11** and **S3.12**, respectively).[43] CVs of the corresponding Zn analogues of **2** and **3** (Zn(^{me}crebpy) and Zn(^{tbu}catbpy), respectively) show redox features only at potentials similar to the final two reductions for each, suggesting that the frontier orbital configuration in highly reduced states incorporates contributions from the ligand manifold (**Figures S3.13** and **S3.14**). As we have shown previously, the initial Fe(III)/(II) reduction feature is sensitive to the presence of a proton donor.[9] For complex **2** (**Figure S3.15**) and complex **3** (**Figure S3.16**): distinct shifts to positive potentials and the coalescence of the more positive reduction features occur upon addition of phenol (PhOH) as a proton donor. These changes are not conducive to the simple equilibrium modelling used previously,[9] which we attribute to multiple competitive equilibria involving the pendent moieties, the Fe-bound O atoms and PhOH at reducing potentials. In an attempt to deconvolute these processes for the pre-catalytic complexes, we also examined the interactions between PhOH and both **2** and **3** using UV-vis spectroscopy, however, no well-defined isosbestic points were observed in the relevant concentration ranges (**Figures S3.17** and **S3.18**).

3.3.2.1 Electrochemical Response under CO_2 Saturation

In the presence of CO_2 under aprotic conditions, **2** and **3** exhibit an increase in current, with i_c/i_p values of 5.5 and 13, with $E_{p,c}$ = –2.50 V and –2.37 V vs Fc^+/Fc, respectively (**Figure 3.4**, red).[44] Upon the addition of (PhOH) under CO_2 saturation conditions (0.23 M)[45], each complex shows an increase in current relative to aprotic conditions, consistent with the electrocatalytic response observed previously for **1** (**Figure 3.4**, black, **S3.19** and **S3.20**). Stepwise titrations of PhOH show that current saturation is reached at 0.9 M PhOH for **2** with $E_{cat/2}$ = –2.33 V vs Fc^+/Fc and at 0.5 M PhOH for **3** with $E_{cat/2}$ = –2.33 V vs Fc^+/Fc (100 mV/s scan rate; **Figures S3.21** and **S3.22**).

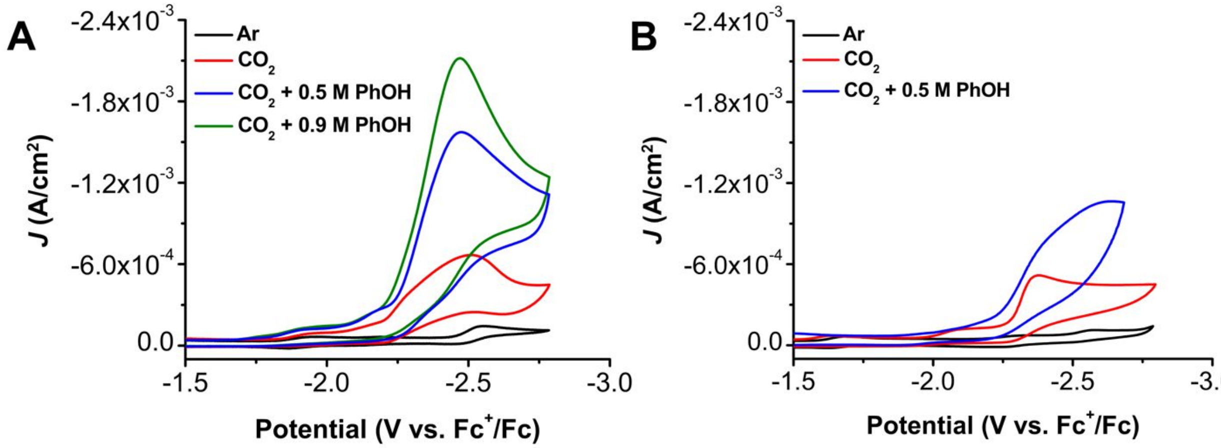

Figure 3.4. CVs of (A) Fe(^{me}crebpy)Cl **2** and (B) Fe(^{tbu}catbpy) **3** under Ar (black) and CO_2 (red, blue, and green) saturation conditions. Blue and green traces are in the presence of PhOH added as a proton source. Working electrode is glassy carbon, counter electrode is a glassy carbon rod, AgCl/Ag pseudoreference electrode. Referenced to Fc^+/Fc from internal Cp_2*Fe standard. 100 mV/s scan rate.

3.3.2.3 Comparative Analysis

In our previous study, we noted that, in the presence of CO_2 and PhOH, **1** showed: (A) decreased current densities under increasing CO_2 concentrations due to the suppression of competitive HER activity, (B) saturation of the catalytic current at a PhOH concentration of 0.2 M, and (C) a first-order dependence on catalyst concentration.[9] For **2**, current saturation was observed above concentrations of 0.04 M CO_2 in the presence of 1.0 M PhOH (**Figure S3.23**), and a first-order concentration dependence on PhOH was observed under CO_2 saturation conditions (**Figure S3.24**). We again observed electrocatalytic current saturation above 0.04 M CO_2 for complex **3** (**Figure S3.25**); however, varied PhOH concentrations under saturated CO_2 give a slope of 0.16, which we attribute to the role of the –OH relay (**Figure S3.26**). A fractional reaction order for the added sacrificial proton donor in a proton-dependent reaction suggests that transfer of proton equivalents or PhOH from the relay to the active site is extremely facile for **3** relative to **1** and **2**. Plots comparing the current response to the [catalyst] were linear for both **2** and **3**, suggesting the reaction is first order with respect to each, consistent with our prior study (**Figures S3.27** and **S3.28**).[9]

These results indicate that a different mechanism is occurring for **2** and **3**, in comparison to **1**, which we hypothesize is the result of a pre-concentration of PhOH through favorable non-covalent equilibrium interactions with the O atoms in the secondary coordination sphere of the ligand (**Figure 3.5**). In our previous studies on complex **1**, we noted that electrochemical behavior consistent with the redox-dependent protonation of the Fe-bound oxygen atoms occurred; a quantifiable equilibrium response was obtained for the Fe(III)/(II) reduction potential with respect to the concentration of added PhOH.[9]

This experimentally observed equilibrium potential shift requires an appreciable concentration of a non-covalent assembly between complex **1** and PhOH, ‘pre-loading’ the complex for subsequent proton-dependent reduction reactions.[46] Therefore, we reason that the related shifts in reduction potential observed for complexes **2** and **3** which do not conform to our previous model (**Figures S3.15-S3.16**) represent multiple related pre-equilibria involving PhOH. Importantly, we expect several differences from **1** at applied potential based on the inclusion of the pendent –OMe/–OH functional groups in the secondary coordination sphere: as mentioned above for **2** and **3**, the possibility of multi-point hydrogen bonding interactions between PhOH and the ligand framework (**2[PhOH]** and **3[PhOH]**; **Figures 3.5A** and **3.5B**) implies that a significant pre-concentration of the sacrificial proton donor relative to **1** is possible. We note that these non-covalent adducts are expected to be in equilibrium with the products of formal proton transfer to the Fe-bound oxygen atom, **3(H$^+$)** and **2(H$^+$)** (**Figure 3.5**). For complex **3**, however, there is the added possibility of greater homoconjugation-type interactions[47] between the ligand framework and phenol/phenolate, **3(H$^+$)[PhO$^-$]** versus **3[PhO$^-$]** in **Figure 3.5B-C**, which have previously been implicated as possible determinants of both kinetic and thermodynamic reaction parameters for electrochemical reactions.[11, 48-50] We describe the observed difference in catalytic response with respect to [PhOH] for **2** and **3** to the ability of the –OH groups to form both hydrogen-bond donor and acceptor interactions, resulting in a pre-concentration of the sacrificial proton donor.

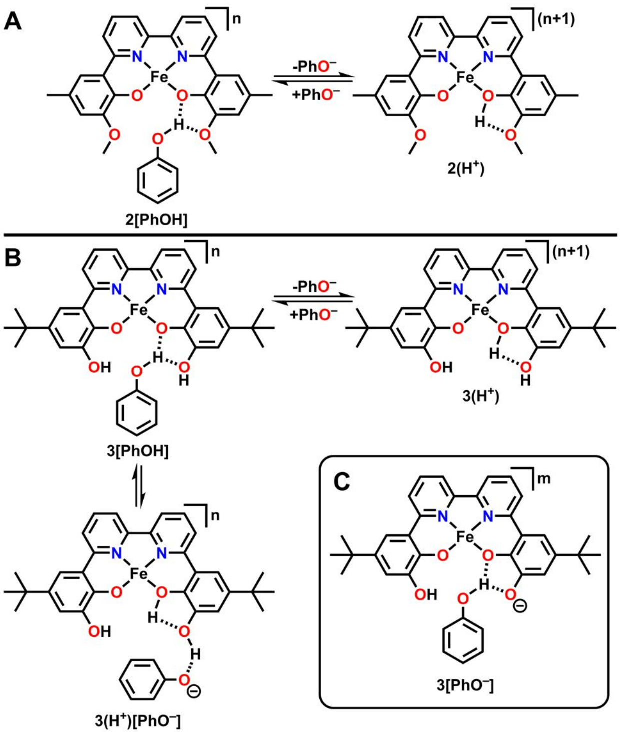

Figure 3.5. Diagram of select possible equilibria involving complexes **2** (A) and **3** (B) and (**C**) in the reduced state. In previous studies, formal proton transfer to the O atom of the ligand was implicated for **1**; the effect of multipoint hydrogen-bonding interactions for **2** and **3** with PhOH is observed in their concentration-dependent electrochemical responses. Where **n** = 0 or -1 and **m** = 0, -2, or -2.

Partial catalytic current densities for formate production (J_{HCO2-}) were determined for each complex utilizing Faradaic efficiencies from controlled potential electrolysis experiments under the saturation conditions optimized from CV studies. At 0.5 M PhOH, **3** exhibits J_{HCO2-} = 0.7 mA/cm^2. At 1.0 M PhOH, **2** exhibits an increased J_{HCO2-} = 2.0 mA/cm^2. By treating the catalytic response observed for **1** with the same method at 0.5 M concentration of PhOH, a J_{HCO2-} = 0.6 mA/cm^2 is obtained. Under these conditions, **2** exhibits an increase in current at the second reduction potential at –1.93 V vs. Fc$^+$/Fc, as well as a new pre-wave feature at more reducing potentials, in the voltammetric response (**Figure 3.4A**). We attribute these changes to the formation of intermediate species containing a non-covalent assembly of the complex and PhOH (or several PhOH equivalents) under reducing conditions, e.g. **[2][PhOH]**, **Figure 3.5A**, prior to the formation of the active catalyst species capable of net hydride transfer to CO_2.

3.3.3 Product Analysis

The catalytic efficiencies and selectivities of **2** and **3** for the reduction of CO_2 were determined by controlled potential electrolysis (CPE) experiments at the peak catalytic potentials for their respective PhOH saturation concentrations (**Table 3.1**, entries 2 and 8). CPE at –2.50 V vs Fc^+/Fc with **2** and 0.9 M PhOH under CO_2 saturation conditions produced HCO_2^- at 85±2% FE_{HCO2-} with the remainder of current going to H_2 (12±4%) and CO (5±1%) through 11.0 TON (22 electron equivalents passed per catalyst molecule, **Figure S3.29**). CPE at –2.60 V vs Fc^+/Fc with **3** and 0.5 M PhOH under CO_2 saturation conditions yielded 71±3% FE_{HCO2-}, with the remainder of current going to H_2 (23±9%) and CO (0.8±0.1%) (**Figure S3.30**). Following these electrolysis experiments, the working electrode was rinsed with ethanol and allowed to air dry before a second electrolysis experiment was conducted where the putative molecular precatalyst was omitted under otherwise identical conditions of proton donor concentration and CO_2 saturation (**Figures S3.29** and **S3.30**, blue). The rinse test with both **2** and **3** indicated no HCO_2^- production (**Table 3.1**, entries 5 and 11). Additional control experiments with no added catalyst material and a freshly polished electrode generated no HCO_2^- under either set of conditions (**Table 3.1**, entries 6 and 12). To confirm that the observed HCO_2^- product originated from CO_2 rather than *N,N*-DMF, isotopically labeled $^{13}CO_2$ was utilized under identical conditions to previous CPE experiments. ^1H NMR spectra from these experiments with **2** and **3** indicate that the observed HCO_2^- is generated from $^{13}CO_2$: a doublet reflecting ^1H-^{13}C coupling (J_{CH} = 133.1 Hz) is seen in the spectra where a singlet for HCO_2^- is observed in electrolysis experiments using CO_2 with a normal isotopic abundance (**Figures S3.31**-**S3.34**).[51]

For comparison with the results discussed above, CO_2 reduction activity was examined by CPE under aprotic conditions with both **2** and **3** at –2.5 V vs Fc^+/Fc (**Figures S3.35** and **S3.36**). Both **2** and **3** show appreciable production of CO under these conditions (30±6% FE_{CO} for **2** and 17±3% FE_{CO} for **3**; **Table 3.1**, entries 3 and 9). This observation is in stark contrast to **1**, which only showed ~1% FE_{CO} after 15 h under these conditions.[9] Comparable CPE experiments were also conducted to examine the inherent HER activity in the absence of CO_2 (**Figure S3.37** and **S3.38**). For **2**, 51±9% FE_{H2} was observed with no CO or HCO_2^- detected after 9.5 TON (**Table 3.1**, entry 4). For **3**, 48±8% FE_{H2} was observed with no CO or HCO_2^- detected after 13 TON (**Table 3.1**, entry 10). A CPE experiment with **3** in the absence of PhOH under Ar saturation did not result in H_2 production from the pendent proton remaining on the ligand framework (**Figure S3.39**).

Table 3.1. Summary of Controlled Potential Electrolysis Data.[a]

Trial	**Complex**	**Atmosphere**	**[PhOH] (M)**	**$E_{applied}$**	**TON**	**Formate[b] (HCO_2^-)**	**CO[b]**	**H_2[b]**
1	**2**	CO_2	0.9	-2.5	9.0	85±2	9±2	10±2
2[c]	**2**	CO_2	0.9	-2.5	11.0	84±1	5±1	12±4
3	**2**	CO_2	0	-2.5	3.9	-	30±6	-
4	**2**	Ar	0.9	-2.5	9.5	-	-	51±9
5	Rinse **2**	CO_2	0.9	-2.5	-	ND	6±2	32±4
6	**-**	CO_2	0.9	-2.5	-	ND	ND	60±10
7	**3**	CO_2	0.5	-2.6	9.4	70±8	2±1	28±4
8[d]	**3**	CO_2	0.5	-2.6	9.8	71±3	0.8±0.1	23±9
9	**3**	CO_2	0	-2.45	3.6	-	17±3	-
10	**3**	Ar	7.5	-2.6	12.9	-	-	48±8
11	Rinse **3**	CO_2	0.5	-2.6	-	ND	4±1	ND
12	**-**	CO_2	0.5	-2.6	-	ND	1.0±0.5	17±7

[a]Conditions were 0.1 M $TBAPF_6$/*N,N*-DMF supporting electrolyte with 0.5 M Fc as sacrificial oxidant. Working and counter electrodes were graphite rods, pseudoreference was Ag/AgCl. [b]Faradaic efficiency determined by ^{1}H NMR. [c]Duplicate of Trial 1. [d]Duplicate of Trial 7.

3.3.4 Electrochemistry with a Sterically Hindered Proton Donor

To assess the proposed mechanism of proton donor pre-concentration by the pendent functional groups for **2** and **3**, CV experiments were repeated using 2,4,6-tri-*tert*-butyl-phenol (ΔpK_a^{DMSO} = 0.2[52], pK_a values are known to scale well between DMSO and *N,N*-DMF[53]) as a sterically hindered proton source (**Figure S3.40**).[54] At concentrations of 2,4,6-tri-*tert*-butyl-phenol comparable to that of PhOH at saturation of the catalytic response, only **2** showed a catalytic increase in current relative to the background electrode current (**Figure S3.40**, green). This is consistent with the proposal that the pendent methoxy group in **2** is more competent for facilitating the net transfer of proton equivalents from the sacrificial donor to the active site than the hydroxy/phenolate moieties present in **3**.[31]

3.4 Discussion

In the case of both **2** and **3**, an enhanced J_{HCO2-} in comparison to our original report with **1** is observed under catalytic conditions. Only complex **2** shows increased selectivity for HCO_2^-, which suggests that under catalytic conditions, the production of H_2 is suppressed in comparison to **1** and **3**. We ascribe this in part to differences in the efficiency of the transfer of proton donors from the secondary coordination sphere relay mechanism and to corresponding differences in the effective pK_a of the exogenous proton donor resulting in lower rates of putative metal hydride protonation.[55] To enhance an intrinsic molecular electrocatalytic response, the combined forward reaction rate constants of net proton transfer from the exogenous proton through the relay and to the active site during the electrocatalytic response must compare favorably to that for the catalytic response in the absence of a relay mechanism, where the proton donor interacts directly with the Fe center (**Figure 3.6**).[31] We propose that the existence of the zwitterionic state of **3** in the secondary sphere as synthesized is suggestive of possible deleterious effects on catalyst turnover due to the partial or complete deprotonation of the pendent –OH groups during the course of the reaction (**Figure 3.5C**). The experimental observation of near zero-order dependence of catalytic current on [PhOH] for complex **3** (**Figure S3.26**) indicates that a significant pre-concentration of the proton donor is occurring (**Figure 3.6A**). This pre-concentration allows the 'pre-loaded' proton donor relay to accumulate in excess at reducing potentials because of a mismatch with the rate of electrocatalytic formate production. Deprotonation of the ligand during the catalytic turnover of **3** will induce non-covalent homoconjugation interactions with the sacrificial proton donor which are much stronger than those possible for the neutral methoxy groups in complex **2** for purely electrostatic reasons (**Figure 3.5**).[47, 53, 56] The effectiveness of this pre-concentration effect for **3** is likely also the origin of the diminished activity relative to **2**, since the same effects are likely to cause steric hindrance at the active site, as well as alter the barrier for net CO_2 insertion into the putative metal hydride intermediate (**Figure 3.6B-C**).

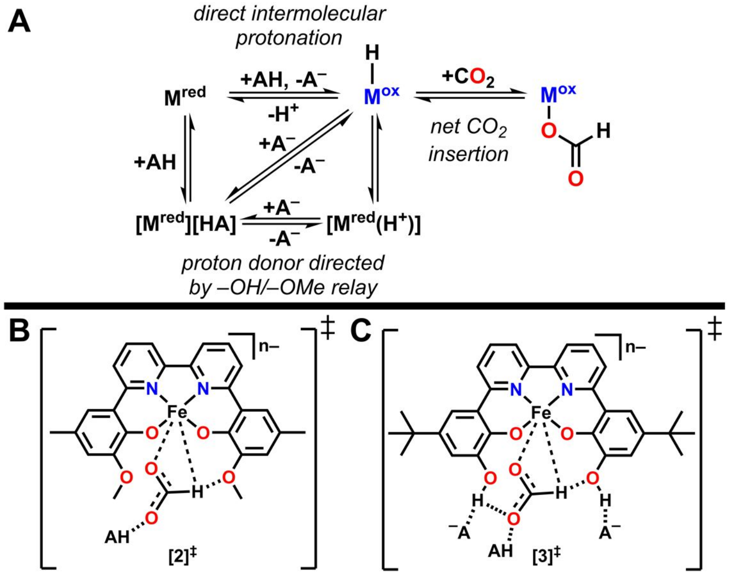

Figure 3.6. Summary of the basic relay mechanism of the exogenous proton donor. For boosting effects to be observable in an electrocatalytic response, the forward reaction rate constants of the relay need to be competitive with the rate of direct protonation.[31] AH and A^- are PhOH and its conjugate base PhO^-.

Future studies will attempt to deconvolute the relevant equilibrium processes involving the proton donors and pendent functional groups at applied potential. We note that the propensity of Fe(III) ions to coordinate phenolate is well-known and represents an as yet unquantified contribution to the driving force for the association of the exogenous proton donor with the pendent relay which will need to be considered. These data implicate that both the proton donor-shuttling mechanism and the intermolecular protonation of the active site result in the formation of a common metal hydride intermediate, the net transfer of which to CO_2 will result in formate production (**Figure 3.6A**). The experimental observation of identical $E_{cat/2}$ values for both **2** and **3** is consistent with the existence of a comparable intermediate metal hydride for both catalysts, suggesting that the electronic difference between the two active sites is minimal. This indirectly indicates that the activity difference between complexes **2** and **3** arises from a difference in the kinetic parameters of proton donor loading through the –OMe/–OH groups.[55]

Consistent with this interpretation, a pre-wave feature appears in the electrocatalytic response of **2**, indicative of the formation of a new intermediate species when the proton donor is present, which we ascribe to adducts of the proton donor and the two-electron reduction product of **2** (**Figure 3.5A**); the formation of new intermediate species is also suggested by the proton-dependence of the preceding reduction features (**Figure S3.15**). Further, the experimental results with a sterically hindered proton source demonstrate catalytic current increases only for **2** (**Figure S3.40**). This suggests facile transfer of proton donor equivalents from solution through the relay to the active site for complex **2** in comparison to **3**. Consistent with our postulation that the outer-sphere pendent Lewis basic –OMe site generates less hindering non-covalent interactions with PhOH than those implied for **3**, the electrocatalytic response of **2** achieves greater J_{HCO2-} than that for **1** or **3**. This putative kinetic preference in the proton donor-shuttling mechanism also results in an improvement in selectivity for **2** ($\mathrm{Fe}_{\mathrm{HCO2-}}$ = 85±2%) in comparison to **1** ($\mathrm{Fe}_{\mathrm{HCO2-}}$ = 68±4%) and **3** ($\mathrm{Fe}_{\mathrm{HCO2-}}$ = 71±3%). While it cannot be explicitly discounted that the hydricity or pK_a values of the putative Fe hydride intermediates for **2** and **3** are different, we emphasize again that there is no observed difference between their $E_{\mathrm{cat/2}}$, suggesting that the proposed catalytically proposed iron hydride intermediates are analogous.[55, 57]

3.5 Conclusions

We have reported the synthesis, characterization, and reactivity for the electrocatalytic reduction of CO_2 to HCO_2^- of two new Fe(III) complexes with pendent functional groups capable of pre-concentrating the sacrificial proton donor PhOH. Enhancement of the catalytic rate constant is observed for both methyl-ether and hydroxy pendent functional groups. However, enhanced selectivity was only observed for the methyl-ether pendent functional group, suggesting that the strength of interaction between the external proton donor and the pendent relay site has a nuanced effect on reaction control. These results further demonstrate that the pre-catalytic MS-EPT mechanism we observed in our original report is vital to the intrinsic catalytic properties and that its overall effect can be modulated through non-covalent secondary sphere interactions to optimize the catalytic response. This suggests that secondary sphere moieties which do not interact directly with substrate bound at the active site are a complementary way to modulate activity and selectivity in this class of catalysts.

3.6 Experimental and Methods

3.6.1 General.

All chemicals and solvents (ACS or HPLC grade) were commercially available and used as received unless otherwise indicated. For all air-sensitive reactions and electrochemical experiments, solvents were obtained as anhydrous and air-free from a PPT Glass Contour Solvent Purification System. Gas cylinders were obtained from Praxair (Ar as 5.0; CO_2 as 4.0) and passed through molecular sieves prior to use. $^{13}CO_2$ was obtained from Sigma (99.0% enriched, <3.0% ^{16}O). NMR spectra were obtained on a Varian 600 MHz or Bruker 800 MHz instrument and referenced to the residual solvent signal. Microwave reactions were carried out using an Anton-Parr Multiwave Pro SOLV, NXF-8 microwave reactor. Flash chromatography columns were run utilizing Teledyne ISCO CombiFlashRf+. UV-vis absorbance spectra were obtained on a Cary 60 from Agilent. Gas phase products were analyzed on an Agilent 7890B Gas Chromatograph with an Agilent J&W Select Permanent Gases/CO_2 column and thermal conductivity detector; eluent retention times and product characterization were determined by standard injections. Formate was quantified by a previously reported NMR method.[9] HRMS data were obtained by the Mass Spectrometry Lab at the University of Illinois at Urbana-Champaign or on an Agilent 6545 Q-TOF LC/MS at UVA and elemental analyses were performed by Midwest Microlab. All synthetic procedures are summarized in **Scheme 1** and **Scheme 2** below.

3.6.2 Electrochemistry.

All electroanalytical experiments were performed using a Metrohm Autolab PGSTAT302N or Biologic SP-50 potentiostats. Glassy carbon working (3 mm) and non-aqueous silver/silver chloride pseudoreference electrodes behind PTFE tips were obtained from CH Instruments. The pseudoreference electrodes were obtained by depositing chloride on bare silver wire in 10% HCl at oxidizing potentials and stored in a solution of 0.1 M tetrabutylammonium hexafluorophosphate ($TBAPF_6$) in *N,N*-dimethylformamide (DMF) prior to use. The counter electrode was a glassy carbon rod (Alfa Aesar, 99.95%, 3 mm diameter). All CV experiments were performed in a modified scintillation vial (20 mL volume) as a single-chamber cell with a cap modified with ports for all electrodes and a sparging needle.

Controlled potential electrolysis (CPE) experiments were performed in a H-cell with a porous glass frit separating the working and counter chambers. Prior to electrolysis, a CV of ferrocene was obtained to reference the cell. CPE experiments were run with graphite working and counter electrodes (Electron Microscopy Sciences, type A, 3 mm diameter) a custom silver/silver chloride pseudoreference electrode (BASi, non-aqueous reference electrode kit), and ports for head-space sampling and gas sparging via needles through septa. To generate an oxygen free environment under the correct atmosphere, the H-Cell was degassed for eight minutes with the corresponding gas, with the exception of $^{13}CO_2$ labelled experiments. In this case, Ar was sparged for 8 minutes followed by a 30 s sparge with $^{13}CO_2$. The working chamber was separated from the counter and pseudoreference electrodes utilizing a porous glass frit, and 0.05 M ferrocene was added to the counter chamber as a sacrificial reductant. $TBAPF_6$ was purified by recrystallization from ethanol and dried in a vacuum oven before being stored in a desiccator. All data were referenced to an internal decamethylferrocene (Cp^*_2Fe) standard (decamethylferricenium/decamethylferrocene reduction potential under stated conditions) which was subsequently corrected relative to the relative $E_{1/2}$ of ferrocene[58] unless otherwise specified.

Scheme 3.1. Synthesis of ^{me}crebpy[H$_2$].

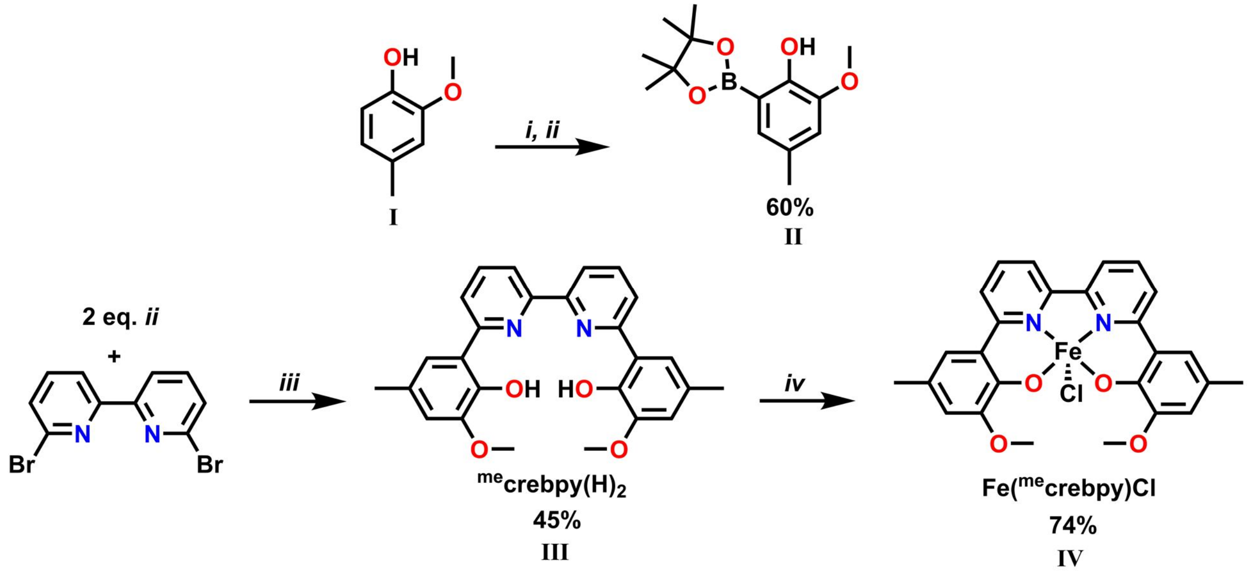

(*a*) (*i*) 4,4,5,5-tetramethyl-1,3,2-dioxaborolane, RT, 10 m. (*ii*) 4,4,5,5-tetramethyl-2-(4,4,5,5-tetramethyl-1,3,2-dioxaborolan-2-yl)-1,3,2-dioxaborolane, 4-tert-butyl-2-(4-tert-butyl-2-pyridyl)pyridine, Ir[(cod)(OMe)]$_2$, cyclohexane, 90 °C 21 h. (*b*) Pd(PPh$_3$)$_4$, K$_3$PO$_4$, 1,4-dioxane, 130 °C, 72 h. (*c*) FeCl$_3$•6H$_2$O, NaOAc, EtOH, 78 °C, 12 h.

3.6.3 Synthesis of 2-methoxy-4-methyl-6-(4,4,5,5-tetramethyl-1,3,2-dioxaborolan-2-yl)phenol[59], II.

In a glovebox, 2-methoxy-4-methyl-phenol (2.5 mL, 19.7 mmol) and 4,4,5,5-tetramethyl-1,3,2-dioxaborolane (2.5 mL, 21.7 mmol) were combined and stirred for 10 m in a 250 mL pressure flask, during which time vigorous effervescence was observed. Subsequently, 4,4,5,5-tetramethyl-2-(4,4,5,5-tetramethyl-1,3,2-dioxaborolan-2-yl)-1,3,2-dioxaborolane (3.51 g, 13.8 mmol), 4-tert-butyl-2-(4-tert-butyl-2-pyridyl)pyridine (0.318 g, 6 mol %), Ir[(cod)(OMe)]$_2$ (0.392 g, 3 mol %), and 100 mL of dry cyclohexane were added. The flask was capped and heated to 90 °C for 21 h. When the flask cooled to room temperature after being removed from the heat source, 10 g of silica gel was added, and solvent was removed under reduced pressure. A silica gel column was run using a Combiflash purification system (ramp 0 to 10 % EtOAc/Hexanes) and the fraction which eluted after the starting material was isolated (very little UV-Vis absorbance is observed for the product). Solvent was removed to yield 2.52 g of a pale-yellow solid. Yield: 48.4%. Characterization was consistent with prior reports.[59]

3.6.4 Synthesis of ^{me}crebpy[H]$_2$, III.

A 500 mL pressure flask with stir bar was charged with 6,6′-dibromobipyridine (0.7 g, 2.23 mmol), K_3PO_4 (2.56 g, 12 mmol), 2-methoxy-4-methyl-6-(4,4,5,5-tetramethyl-1,3,2-dioxaborolan-2-yl)phenol (1.77 g, 6.69 mmol), $Pd(PPh_3)_4$ (0.260 g, 0.22 mmol), and dioxane (250 mL). After this time, the mixture was cooled to RT, diluted with brine (250 mL), and extracted with toluene (6x50 ml) and CH_2Cl_2 (6x50 mL). The organic layers were combined and dried with $MgSO_4$, filtered, and dried under vacuum. The yellow product elutes from a CH_2Cl_2/MeOH ramp of 0-5 % MeOH using a Combiflash purification system. Recrystallization of the product fraction from CH_2Cl_2/hexanes yields pure product. Yield: 0.430 g, 45%. ESI-MS (*m/z*) $[M+H]^+$: Calc'd 429.181 Found: 429.181. CHN analysis: Theory (CHN): C: 72.88, H: 5.65, N: 6.54. Found: C: 72.59, H: 5.53, N: 6.32. ^1H NMR (DMSO-d_6, 600 MHz, **Figure S3.43**): δ (ppm) 2.34 (s, 6H), 3.82 (s, 6H), 6.92 (s, 2H), 7.50 (s, 2H), 8.13 (d, 2H), 8.21 (t, 2H), 8.29 (d, 2H), 13.18 (s, 2H). $^{13}C\{^1H\}$ NMR (DMSO-d_6, 600 MHz, **Figure S3.44**): δ (ppm) 20.82, 55.79, 114.71, 119.11, 119.18, 119.25, 121.60, 127.17, 139.59, 146.37, 148.50, 151.86, 157.10.

3.6.5 Synthesis of Fe(^{me}crebpy)Cl, 2, IV.

Ferric chloride hexahydrate ($Fe(Cl)_3 \cdot 6H_2O$, 0.088 g, 0.33 mmol), sodium acetate (NaOAc, 0.052 g, 0.64 mmol), and 6,6'-([2,2'-bipyridine]-6,6'-diyl)bis(2-methoxy-4-methylphenol) (0.133 g, 0.310 mmol) were combined in a 100 mL round-bottom flask (RBF) equipped with stir bar. EtOH (20 mL) was added to the solids and the solution was brought to reflux overnight for 16 h. The resulting suspension was removed from heat and the dark red-black solid was collected by vacuum filtration, washed with water (3x10 mL) and diethyl ether (3x5 mL). Crystals suitable for X-ray diffraction were grown by slow cooling a boiling acetonitrile solution saturated with **2**. Yield: 0.120 g, 74.1%. UV-vis in *N,N*- DMF: λ_{max}: 354 nm (ε: 28000 M^{-1} cm^{-1}) and 473 nm (ε: 5300 M^{-1} cm^{-1}). CHN Analysis: Theory ($FeC_{26}H_{22}N_2O_4$•$0.5H_2O$): C: 60.31, H: 4.28, N: 5.41. Found: C: 59.15, H: 4.21, N: 5.09. ESI-MS (*m/z*) $[M+Na]^+$: Calc'd 540.052 Found: 540.045. Magnetic Moment: 5.9±0.1 BM.

3.6.6 Synthesis of Zn(^{me}crebpy).

6,6'-([2,2'-bipyridine]-6,6'-diyl)bis(2-methoxy-4-methylphenol) (0.61 g, 0.142 mmol), sodium acetate (23.9 mg, 0.29 mmol), zinc dichloride (0.020 g, 0.149 mmol), and absolute ethanol (20 mL) were combined in a 100 mL RBF equipped with stir bar and condenser. The mixture was brought to reflux (78 °C) overnight (16 h). The resultant yellow-orange precipitate was collected via vacuum filtration, washed with DI water (1x5 mL) and diethyl ether (1x5 mL). Yield: 21 mg, 30%. CHN analysis Theory ($ZnC_{26}H_{22}N_2O_4$•$3H_2O$): C: 57.21, H: 5.17, N: 5.13. Found: C: 56.90, H: 4.26, N: 5.05. ^1H NMR (DMSO-d_6, 600 MHz): δ (ppm) 2.25 (s, 6H), 3.76 (s, 6H), 6.65 (s, 2H), 7.10 (s, 2H), 8.01 (d, 2H), 8.13 (t, 2H), 8.31 (d, 2H). $^{13}C\{^1H\}$ NMR (DMSO-d_6, 600 MHz): (**L^1**) δ (ppm) 21.04, 55.10, 112.39, 117.82, 120.17, 123.24, 140.03, 147.76, 152.31, 156.88, 159.23.

Scheme 3.2. Synthesis for Fe(^{tbu}catbpy).

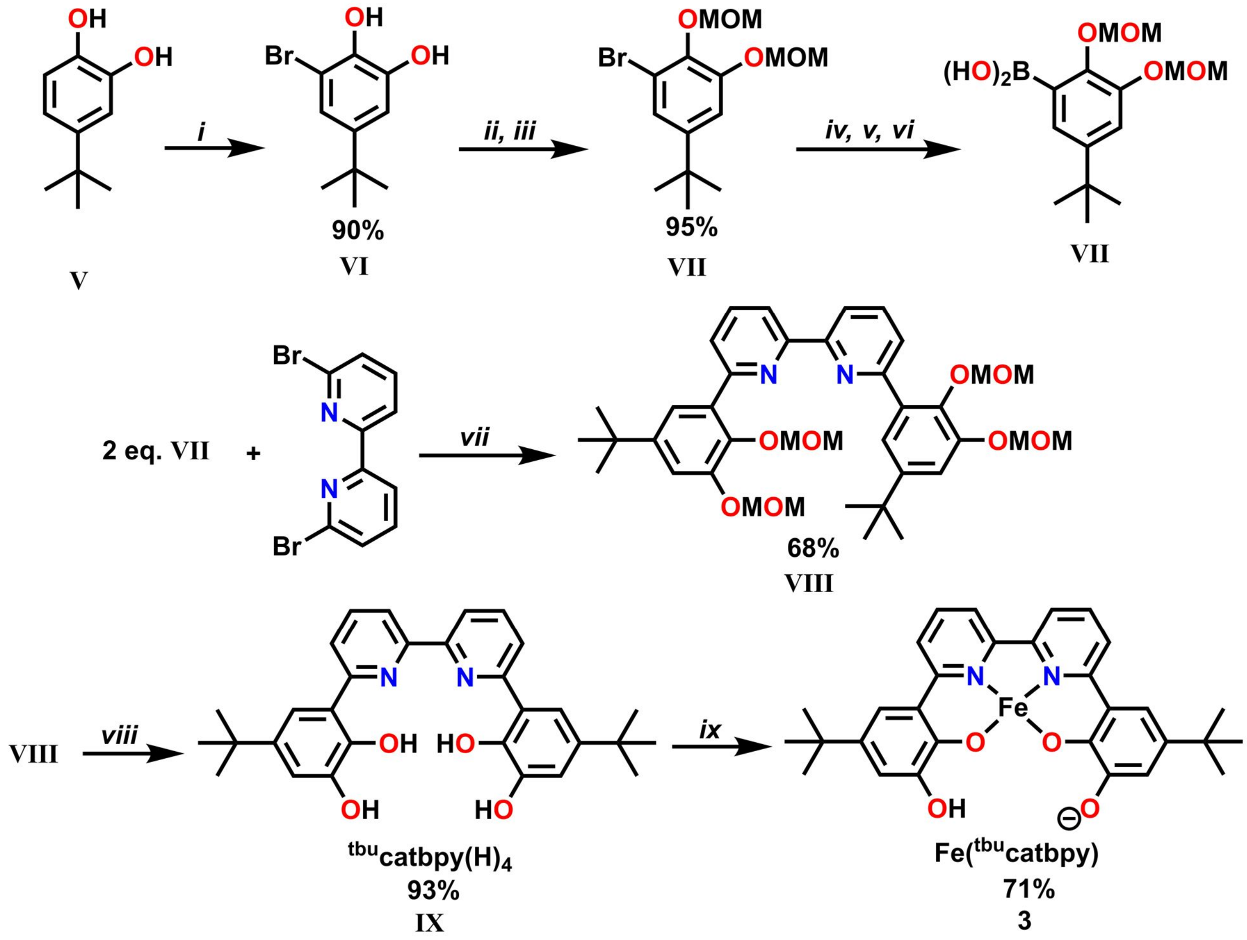

(*a*) NBS, *N,N*-DMF, N_2, room temperature, 2 h. (*b*) (*i*) DIPEA, N_2, CH_2Cl_2. (*ii*) MOMCl, 0°C→RT, 5 h. (*c*) (*i*) ^{n}BuLi, –78 °C→RT, 2 h. (*ii*) $B(OMe)_3$, –78 °C→RT, 16 h. (*iii*) 2 M HCl. (*d*) $Pd(PPh_3)_4$, Na_2CO_3, toluene, MeOH, H_2O, 280 W microwave irradiation, 5 h. (*e*) HCl(g), EtOAc. (*f*) $FeCl_3{\bullet}6H_2O$, NaOAc, EtOH, 78 °C, 3 h.

3.6.7 Synthesis of 3-bromo-5-tert-butyl-benzene-1,2-diol60, VI.

4-*tert*-butyl catechol **(V)** (10.0 g, 0.0602 mol) was dissolved in *N,N*-DMF (25 mL) in a 200 mL Schlenk RBF with a stir bar under nitrogen. A 2.0 M solution of *N*-bromosuccinimide in *N,N*-DMF (30.0 mL, 0.0662 mol) was added to the solution dropwise via syringe with vigorous stirring. After 2 h the solution was diluted with 100 mL ethyl acetate, washed with water (3x50 mL) and then with brine (3x50 mL). The organic fraction was collected, dried over $MgSO_4$, filtered, and the solvent was removed under reduced pressure to yield a dark red oil. Note: the oil can be used without further purification, however, sublimation of the oil produces white X-ray quality crystals of analytical purity. (Yield: 13.2 g, 89.5%). ES-MS (*m/z*) $[M]^+$: Calc'd 244.0099 Found: 244.0098. ^{1}H NMR ($CDCl_3$, 600 MHz, **Figure S3.46**): δ (ppm) 1.26 (s, 9H), 6.92 (d, 1H), 6.99 (d, 1H). $^{13}C\{^1H\}$ NMR ($CDCl_3$, 600 MHz, **Figure S3.47**): (**L^1**) δ (ppm) 31.43, 34.55, 109.23, 112.69, 120.16, 137.98, 144.08, 145.78.

3.6.8 Synthesis of 1-bromo-5-tert-butyl-2,3-bis(methoxymethoxy)benzene, VII.

Dry dichloromethane (50 mL) was dispensed in an oven-dried RBF (250 mL). To this flask, an oven-dried stir bar, 3-bromo-5-*tert*-butyl-benzene-1,2-diol (8.67 g, 35.4 mmol) were added. The headspace was flushed with nitrogen and diisopropylethylamine (21.6 mL, 124.0 mmol) was added. A color change from brown to maroon was observed. The RBF was cooled to 0 °C using an ice bath. Methoxymethylchloride (8.1 mL, 110 mmol) was added dropwise with vigorous stirring. After the addition, the ice bath was removed and the solution was allowed to stir for 5 h. The reaction was quenched with aqueous NH_4OH (2 N, 120 mL), the organic layer was separated, and the aqueous layer was extracted using diethyl ether (3x50 mL). The organic fractions were combined, washed with brine (3x50 mL), dried over $MgSO_4$, and condensed in vacuo to yield a red oil. Yield 11.2 g, 94.9 %. EI-MS (*m/z*) $[M]^+$: Calc'd 332. Found: 332. ^{1}H NMR ($CDCl_3$, 600 MHz, **Figure S49**): δ (ppm) 1.28 (s, 9H), 3.51 (s, 3H), 3.67 (s, 3H), 5.16 (s, 2H), 5.18 ppm (s, 2H) 7.10 (d, 1H), 7.21 (d, 1H). $^{13}C\{^1H\}$ NMR (CD_2Cl_2, 600 MHz, **Figure S50**): δ (ppm) 31.39, 34.91, 56.52, 58.08, 95.83, 98.97, 114.07, 117.42, 123.81, 142.04, 148.99, 150.64.

3.6.9 Synthesis of bis(MOM)catbpy, IX.

A 500 mL Schlenk flask with stir bar was charged with 1-bromo-5-*tert*-butyl-2,3-bis(methoxymethoxy)benzene (11.2 g, 33.6 mmol) and dry diethyl ether (100 mL). The resulting solution was cooled to –78 °C under N_2. *n*-Butyllithium (1.6 M in hexanes) was added dropwise via syringe (23.1 mL, 36.9 mmol) still under N_2, after which the solution was allowed to warm to room temperature with vigorous stirring. At this point the reaction mixture was a brown suspension. After two hours the solution was returned to –78 °C. Trimethyl borate was then added rapidly by syringe (3.95 mL, 35.3 mmol) with vigorous stirring and left for 10 minutes before the cold bath was removed and the mixture left overnight under N_2 (16 h). After this time the reaction was quenched with deionized water (50 mL) and opened to air. The suspension was extracted and the aqueous and organic layers separated. The aqueous layer was carefully neutralized to pH = 7 with ~0.1 M HCl, washed with diethyl ether (3x50 mL), and all organic fractions were combined. The combined layers were then washed with brine (3x50 mL). The resulting solution was dried with $MgSO_4$ for 10 minutes, before the mixture was filtered to remove solid and the solvent was removed under reduced pressure. The resulting dark orange oil was used as isolated without further purification.

A microwave-assisted Suzuki-Miyaura coupling reaction was performed with 6,6′-dibromo-2,2′-bipyridine and the crude boronic acid generated above using an Anton Paar Multiwave Pro equipped with Rotor 8NXF100. Two PTFE reaction tubes were equipped with a magnetic stir bar and charged with 6,6′-dibromo-2,2′-bipyridine (1.0 g, 3.2 mmol) and Na_2CO_3 (2.0 g, 38 mmol), each. Deionized water and methanol were degassed with Ar. The loaded PTFE tubes, solvents, and crude boronic acid were pumped into a N_2

glovebox. $Pd(PPh_3)_4$ (0.18 g, 0.16 mmol) was added to each tube. The boronic acid was added to this suspension by diluting in toluene (20 mL total volume) and splitting this stock solution equally between the two PTFE vessels. Methanol (10 mL), deionized water (10 mL), and toluene (30 mL) were added to the vessels. The vessels were sealed, and loaded into the microwave. The power was ramped to 280 W for 10 m, and then held at this value for 5 h. After cooling to room temperature, the tubes were combined, and the organic and aqueous layers were separated. The aqueous layer was extracted with CH_2Cl_2 (3x50 mL) and all organic fractions were combined, dried with $MgSO_4$, filtered to remove solids, and condensed under vacuum to yield a crude red oil. This oil was left overnight at room temperature, and an off-white crystalline solid formed overnight. This solid was collected, and washed with hexanes. Upon combination of the hexanes wash and the initial fraction, more crystalline material was produced. Characterization of each fraction was consistent with the desired product. Yield 2.85 g, 67.7 %. EI-MS (*m/z*) $[M-H]^+$: Calc'd 661.3489. Found: 661.3486. Theory (CHN): C: 69.07, H: 68.83, N: 7.32. Found: C: 68.83, H: 7.24, N: 4.02. ^1H NMR ($CDCl_3$, 600 MHz, **Figure S3.52**): δ (ppm) 1.39 (s, 18H), 3.12 (s, 6H), 3.56 (s, 6H), 4.96 (s, 4H), 5.27 ppm (s, 4H), 7.27 (d, 2H), 7.55 (d, 2H)), 7.81-7.88 (m, 4H), 8.53 (d, 2H). $^{13}C\{^1H\}$ NMR ($CDCl_3$, 600 MHz, **Figure S3.53**): δ (ppm) 31.60, 34.91, 56.45, 57.23, 95.89, 99.37, 115.17, 119.45, 121.54, 125.57, 134.95, 136.76, 142.57, 147.85, 150.04, 155.96.

3.6.10 Synthesis of ^{tbu}catbpy[H]4, X.

6,6'-bis(5-(tert-butyl)-2,3-bis(methoxymethoxy)phenyl)-2,2'-bipyridine (2.50 g, 3.78 mmol) was dissolved in minimal EtOAc (~100 mL) in a 250 mL RBF equipped with stir bar. Excess anhydrous HCl was generated by adding concentrated H_2SO_4 dropwise to solid NaCl in an airtight vessel that vented through the EtOAc solution via PTFE cannula transfer. The residual HCl was quenched by venting through an outlet flask containing saturated aq. $NaHCO_3$. The flask containing EtOAc was then sealed and left to stir overnight. During the ~9 h of stirring, the EtOAc solution changed from colorless to yellow, and a solid precipitated from solution. After purging the EtOAc solution with N_2, saturated aq. $NaHCO_3$ was added to ensure neutralization. The resultant solid was collected via vacuum filtration, washed with water, and triturated with $CHCl_3$ to yield the desired product as an orange powder. Yield: 1.71 g, 93.3 %. EI-MS (*m/z*) $[M-H]^+$: Calc'd 485.2440. Found: 485.2435. CHN analysis: Theory ($C_{30}H_{32}N_2O_4$•$0.8CHCl_3$): C: 63.77, H: 5.70, N: 4.83. Found: C: 63.84, H: 5.69, N: 4.69. ^1H NMR (DMSO-d_6, 600 MHz, **Figure S3.55**): δ (ppm) 1.31 (s, 18H), 6.89 (s, 2H), 7.49 (s, 2H), 8.04-8.20 (m, 4H), 8.45 (s, 2H). $^{13}C\{^1H\}$ NMR (DMSO-d_6, 600 MHz, **Figure S3.56**): δ (ppm) 31.33, 33.94, 113.88, 114.71, 118.78, 118.92, 121.44, 139.64, 141.06, 145.01, 145.86, 151.91, 157.70.

3.6.11 Synthesis of Fe(^{tbu}catbpy), 3.

6,6'-([2,2'-bipyridine]-6,6'-diyl)bis(4-(*tert*-butyl)benzene-1,2-diol) (0.150 g, 0.310 mmol), NaOAc (52 mg, 0.63 mmol), $Fe(Cl)_3$•$6H_2O$ (0.088 g, 0.33 mmol), and absolute ethanol (20 mL) were combined in a 100 mL RBF equipped with stir bar and condenser. The mixture was brought to reflux (78 °C) overnight (16 h). The resulting black suspension was removed from heat and the volume reduced to ~10 mL *in vacuo* before DI H_2O (5 mL) was added, inducing the formation of a black precipitate. The solid was collected by vacuum filtration and washed with H_2O (3 x 5 mL) and Et_2O (3x5 mL). Yield: 0.119 g, 71%. UV-vis in *N,N*- DMF: λ_{max}: 290, 345, and 560 nm. ε: 31000, 20000, and 3700 M^{-1} cm^{-1}, respectively EI-MS (*m/z*) $[M-H]^+$: Calc'd 535.1555. Found: 535.1553. CHNCl analysis: Theory ($FeC_{30}H_{29}N_2O_4 \cdot 2H_2O$): C: 62.84, H: 5.80, N: 4.89, Cl: None. Found: C: 63.08, H: 5.26, N: 4.92, Cl: None. Magnetic Moment: 6.1±0.1 BM.

3.6.12 Synthesis of Zn(^{tbu}catbpy).

6,6'-([2,2'-bipyridine]-6,6'-diyl)bis(4-(*tert*-butyl)benzene-1,2-diol) (0.052 g, 0.108 mmol), sodium acetate (18.1 mg, 0.22 mmol), zinc dichloride (0.015 g, 0.11 mmol), and absolute ethanol (20 mL) were combined in a 100 mL RBF equipped with stir bar and condenser. The mixture was brought to reflux (78 °C) overnight (16 h). After this time, a yellow-orange precipitate formed and was collected via vacuum filtration, washed with DI water (1x5 ml) and diethyl ether (1x5mL). Yield: 39 mg, 68%. CHN analysis Theory: C: 65.76, H: 5.52, N: 5.11. Found: C: 65.20, H: 5.29, N: 4.90. ^{1}H NMR (DMSO-d_6, 600 MHz): δ (ppm) 1.26 (s, 18H), 6.80 (s, 2H), 7.02 (s, 2H)), 8.05 (d, 2H), 8.15 (t, 2H), 8.34 (d, 2H). ^{13}C{^{1}H} NMR (DMSO-d_6, 600 MHz): δ (ppm) 31.47, 33.75, 110.26, 114.18, 116.55, 118.00, 135.09, 140.47, 147.74, 149.71, 154.32, 159.82.

3.7 Supporting Information for Chapter 3

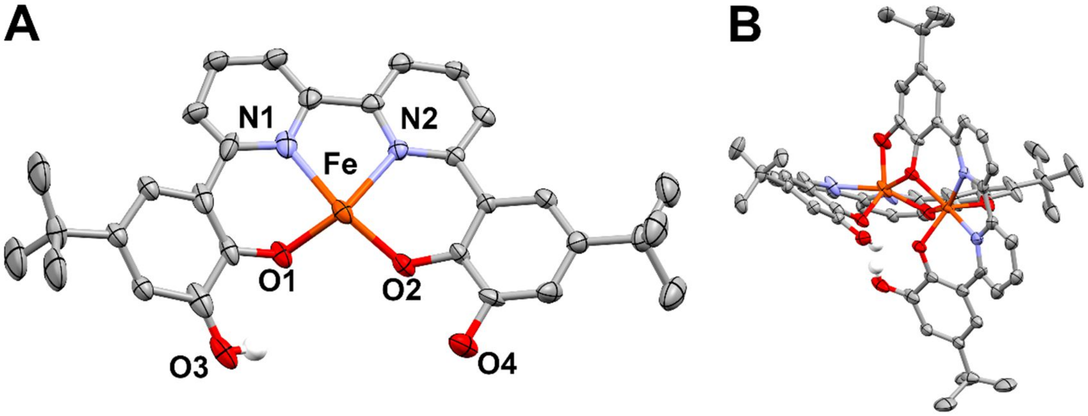

Figure S3.1. (A) Representative monomer structure (one of two structurally inequivalent units crystallographically) from (B) overall dimeric structure of Fe(^{tbu}catbpy) **3**. C = grey, O = red, N= blue, Fe = orange, H = white. Thermal ellipsoids set to 30%. Non-catecholate H-atoms, occluded MeCN and second set of coordinates for disordered *tert*-butyl groups and bpy ring omitted for clarity. All hydrogen atoms in Fe(^{tbu}catbpy) **3**, including the O–H hydrogens, were placed in calculated positions.

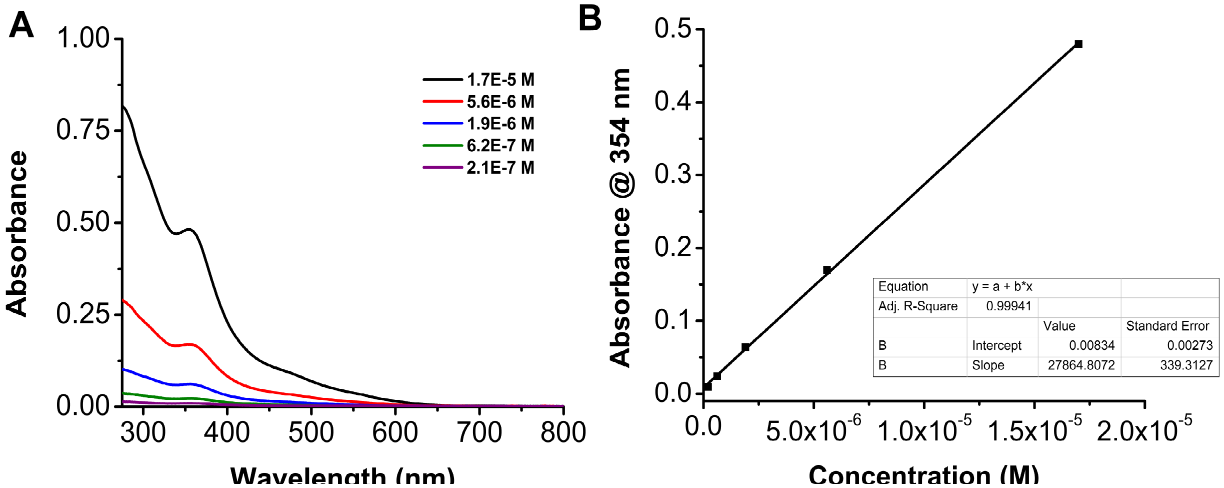

Equation	y = a + b*x		
Adj. R-Square	0.99941		
		Value	Standard Error
B	Intercept	0.00834	0.00273
B	Slope	27864.8072	339.3127

Figure S3.2. (A) UV-Vis absorbance spectra of serial dilutions of Fe(^{me}crebpy)Cl **2** in *N,N*-DMF showing absence of equillibrium processes. Quartz call with 1 cm pathlength. (B) Plot of absorbance versus concentration for complex **2** in *N,N*-DMF at 354 nm (28000 $M^{-1}cm^{-1}$).

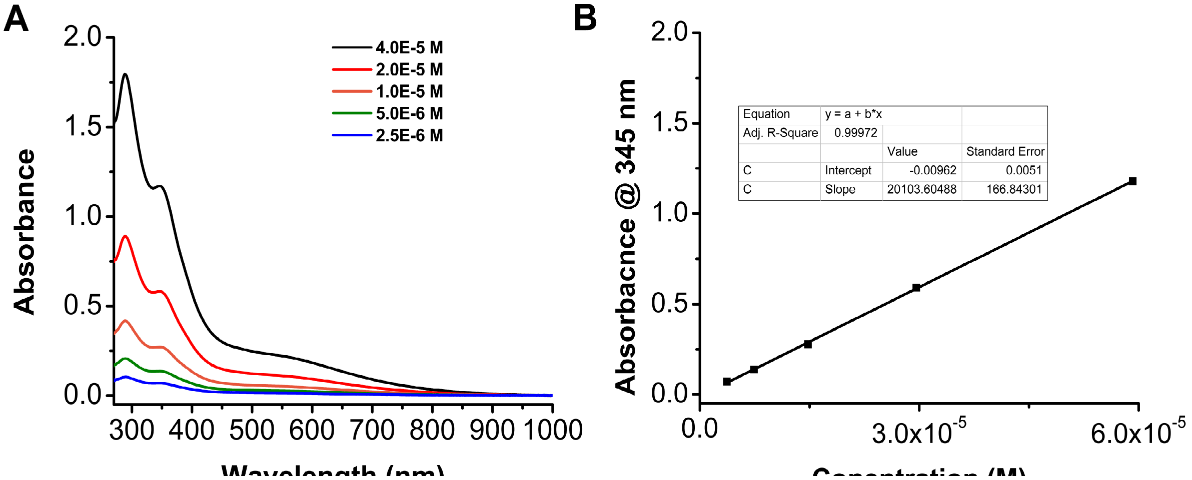

Figure S3.3. (A) UV-vis absorbance spectra of serial dilutions of Fe(^{tbu}catbpy) **3** in *N,N*-DMF showing absence of equillibrium processes. Quartz call with 1 cm pathlength. (B) Plot of absorbance versus concentration for complex **3** in *N,N*-DMF at 345 nm (20000 M^{-1}cm^{-1}).

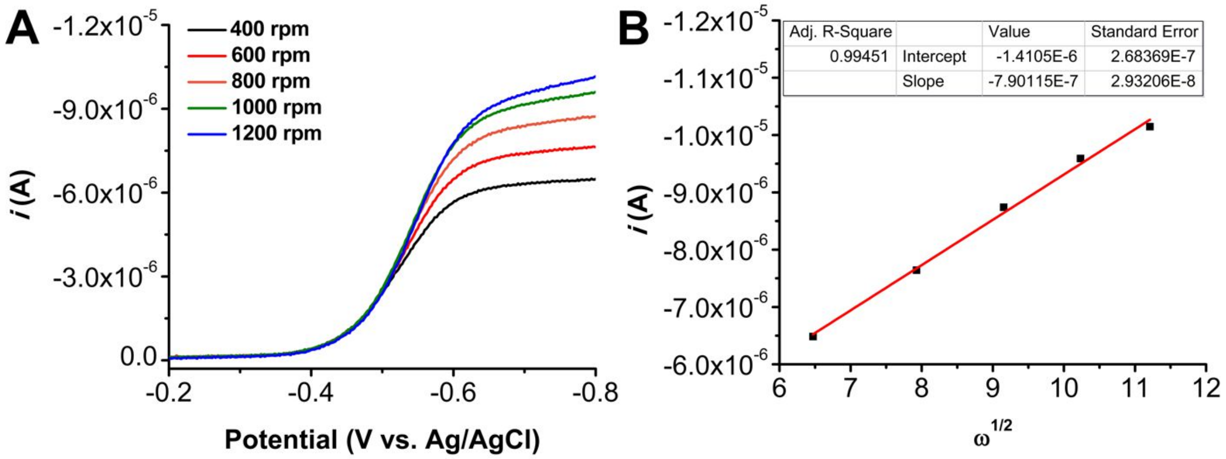

Figure S3.4. (A) Linear Sweep Voltammograms of RRDE experiment Fe(^{tbu}dhbpy)Cl **1** (0.25 mM) at various rotation rates under Ar saturation conditions. (B) Levich plot from data obtained from linear sweep voltammograms of Fe(^{tbu}dhbpy)Cl **1** (0.25 mM) at various rotation rates under Ar saturation conditions. Conditions: 0.25 mM analyte in 0.1 M TBAPF$_6$/*N,N*-DMF; glassy carbon working electrode, glassy carbon rod counter electrode, Ag/AgCl pseudoreference electrode; scan rate 0.01 V/s.

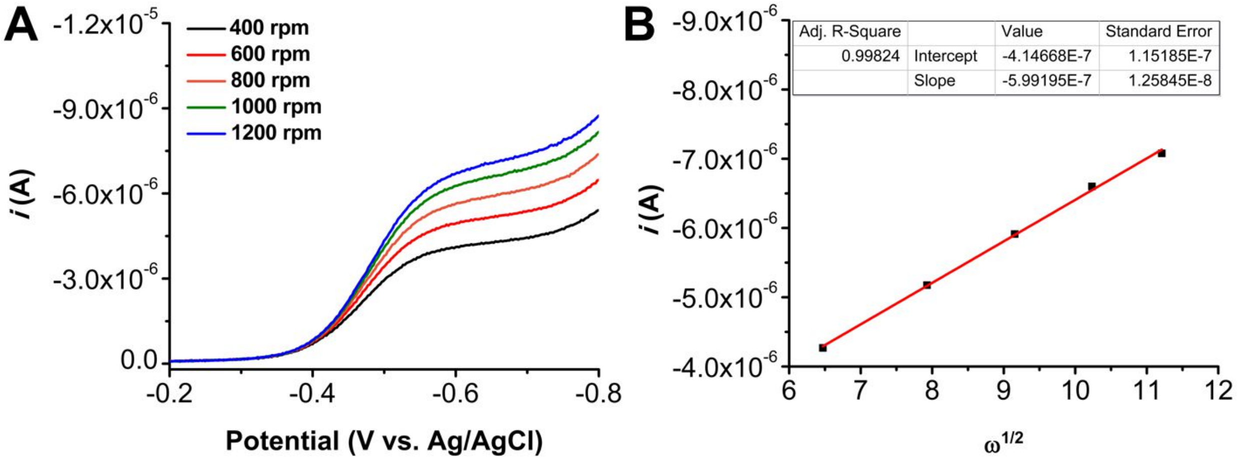

Adj. R-Square		Value	Standard Error
0.99824	Intercept	-4.14668E-7	1.15185E-7
	Slope	-5.99195E-7	1.25845E-8

Figure S3.5. (A) Linear Sweep Voltammograms of RRDE experiment Fe(^{me}crebpy)Cl **2** (0.25 mM) at various rotation rates under Ar saturation conditions. (B) Levich plot from data obtained from linear sweep voltammograms of Fe(^{me}crebpy)Cl **2** (0.25 mM) at various rotation rates under Ar saturation conditions. Conditions: 0.25 mM analyte in 0.1 M TBAPF$_6$/*N,N*-DMF; glassy carbon working electrode, glassy carbon rod counter electrode, Ag/AgCl pseudoreference electrode; scan rate 0.01 V/s.

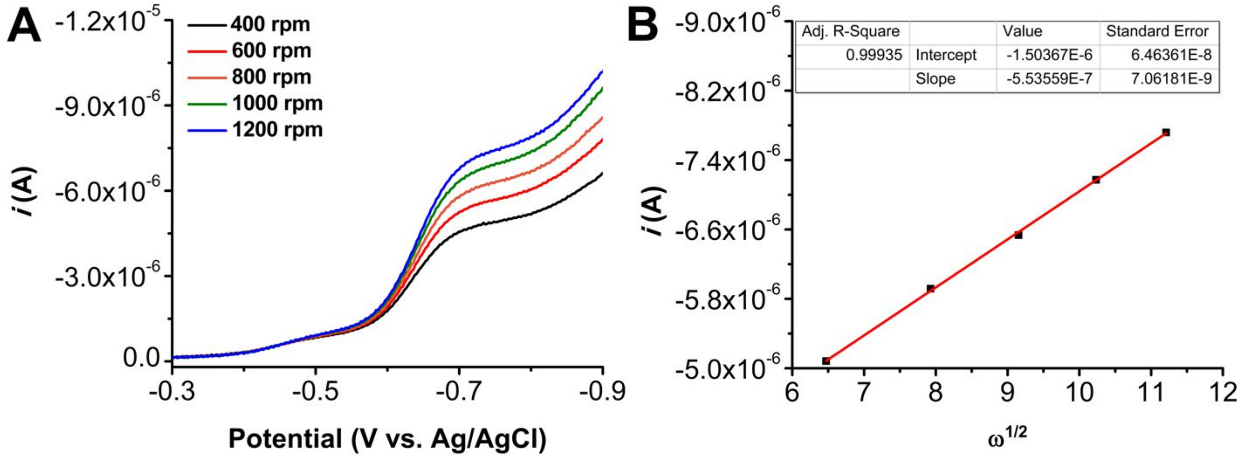

Adj. R-Square		Value	Standard Error
0.99935	Intercept	-1.50367E-6	6.46361E-8
	Slope	-5.53559E-7	7.06181E-9

Figure S3.6. (A) Linear Sweep Voltammograms of RRDE experiment Fe(^{tbu}catbpy) **3** (0.25 mM) at various rotation rates under Ar saturation conditions. (B) Levich plot from data obtained from linear sweep voltammograms of Fe(^{tbu}catbpy) **3** (0.25 mM) at various rotation rates under Ar saturation conditions. Conditions: 0.25 mM analyte in 0.1 M TBAPF$_6$/*N,N*-DMF; glassy carbon working electrode, glassy carbon rod counter electrode, Ag/AgCl pseudoreference electrode; scan rate 0.01 V/s.

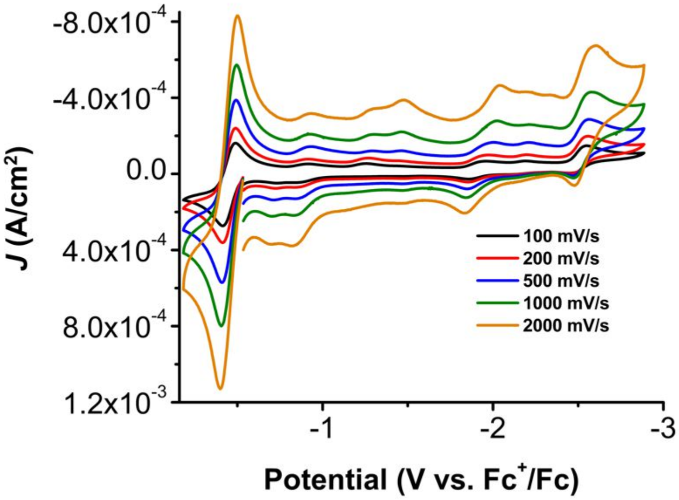

Figure S3.7. CVs of Fe($^{\text{me}}$crebpy)Cl **2** at various scan rates under Ar saturation conditions. Conditions: 0.5 mM analyte in 0.1 M TBAPF$_6$/*N,N*-DMF; glassy carbon working and counter electrodes, Ag/AgCl pseudoreference electrode, referenced to Fc$^+$/Fc from internal decamethylferrocene (Cp$_2$*Fe) standard.

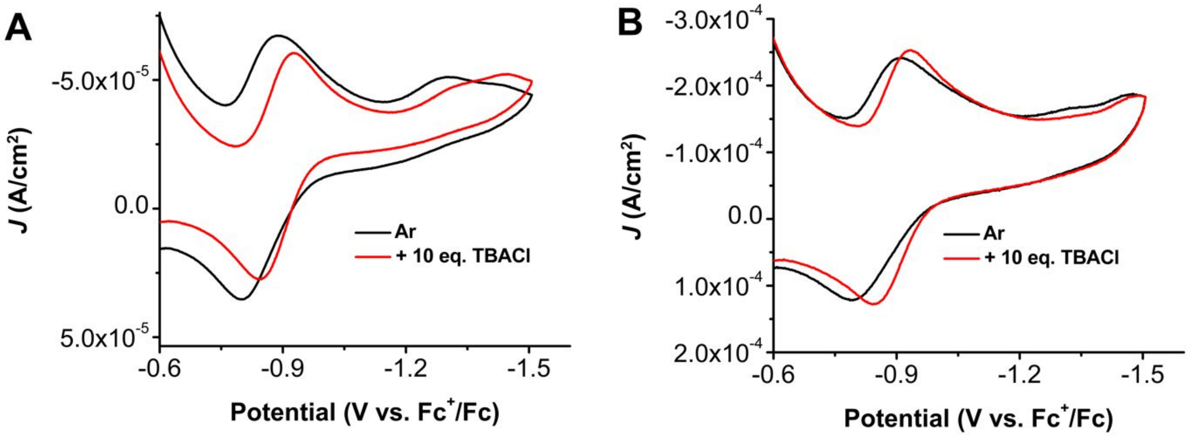

Figure S3.8. CVs of Fe($^{\text{me}}$crebpy)Cl **2** upon addition of TBACl under Ar saturation conditions at 100 mV/s (A) and at 1000 mV/s (B) illustrating that at fast scan rates, the reduction at –1.45 V vs Fc$^+$/Fc dissapears. Conditions: 0.5 mM analyte in 0.1 M TBAPF$_6$/*N,N*-DMF; glassy carbon working and counter electrodes, Ag/AgCl pseudoreference electrode, referenced to Fc$^+$/Fc from internal decamethylferrocene (Cp$_2$*Fe) standard.

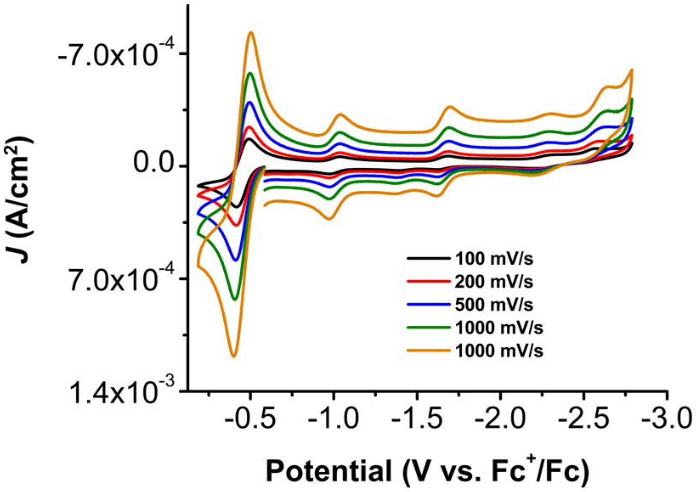

Figure S3.9. CVs of Fe(^{tbu}catbpy) **3** at various scan rates under Ar saturation conditions. Conditions: 0.5 mM analyte in 0.1 M TBAPF$_6$/*N,N*-DMF; glassy carbon working and counter electrodes, Ag/AgCl pseudoreference electrode, referenced to Fc$^+$/Fc from internal decamethylferrocene (Cp$_2$*Fe) standard.

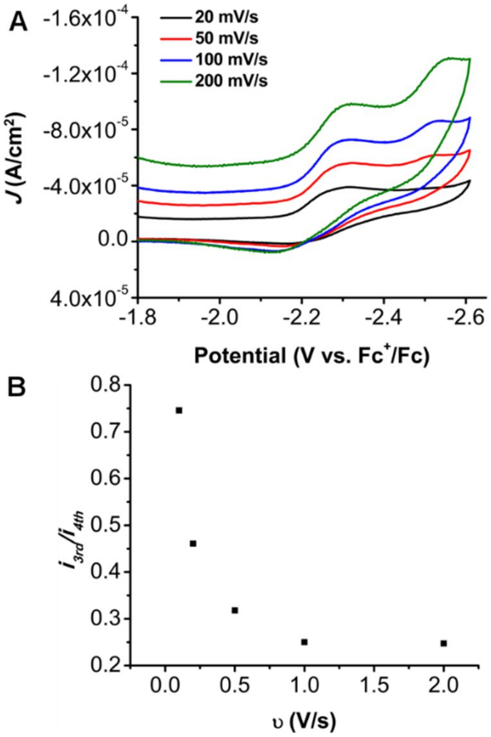

Figure S3.10. (A) Plots of CVs of 3rd and 4th reductions of Fe(^{tbu}catbpy) **3** at variable scan rates under Ar saturation conditions showing scan rate dependence of the relative current response of these two features. (B) Plot of the ratio of the peak current of the 3rd and 4th reductions of Fe(^{tbu}catbpy) **3** vs. scan rate. Conditions: 0.5 mM analyte in 0.1 M TBAPF$_6$/*N,N*-DMF; glassy carbon working and counter electrodes, Ag/AgCl pseudoreference electrode, referenced to Fc$^+$/Fc from internal decamethylferrocene (Cp$_2$*Fe) standard.

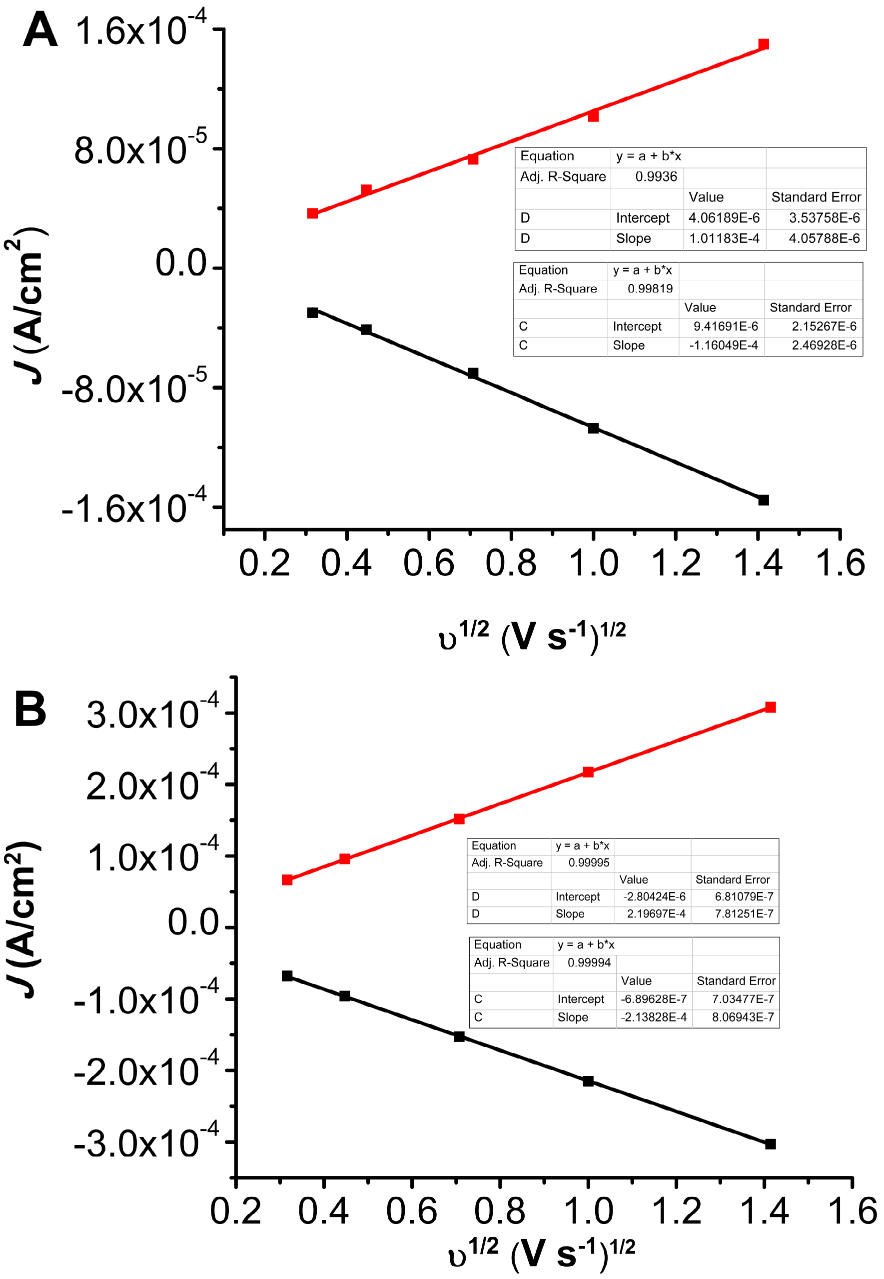

Equation	y = a + b*x		
Adj. R-Square	0.9936		
		Value	Standard Error
D	Intercept	4.06189E-6	3.53758E-6
D	Slope	1.01183E-4	4.05788E-6

Equation	y = a + b*x		
Adj. R-Square	0.99819		
		Value	Standard Error
C	Intercept	9.41691E-6	2.15267E-6
C	Slope	-1.16049E-4	2.46928E-6

Equation	y = a + b*x		
Adj. R-Square	0.99995		
		Value	Standard Error
D	Intercept	-2.80424E-6	6.81079E-7
D	Slope	2.19697E-4	7.81251E-7

Equation	y = a + b*x		
Adj. R-Square	0.99994		
		Value	Standard Error
C	Intercept	-6.89628E-7	7.03477E-7
C	Slope	-2.13828E-4	8.06943E-7

Figure S3.11. Plots of current density vs $\upsilon^{1/2}$ for the reductions with $E_{1/2}$ = –0.84 V (A) and –1.93 V (B) vs Fc^+/Fc for Fe(^{me}crebpy)Cl **2**. Linearity indicates Fe(^{me}crebpy)Cl **2** is operating in a diffusion limited regime. Conditions: 0.5 mM analyte in 0.1 M $TBAPF_6$/*N,N*-DMF; glassy carbon working and counter electrodes, Ag/AgCl pseudoreference electrode, referenced to Fc^+/Fc from internal decamethylferrocene (Cp_2*Fe) standard.

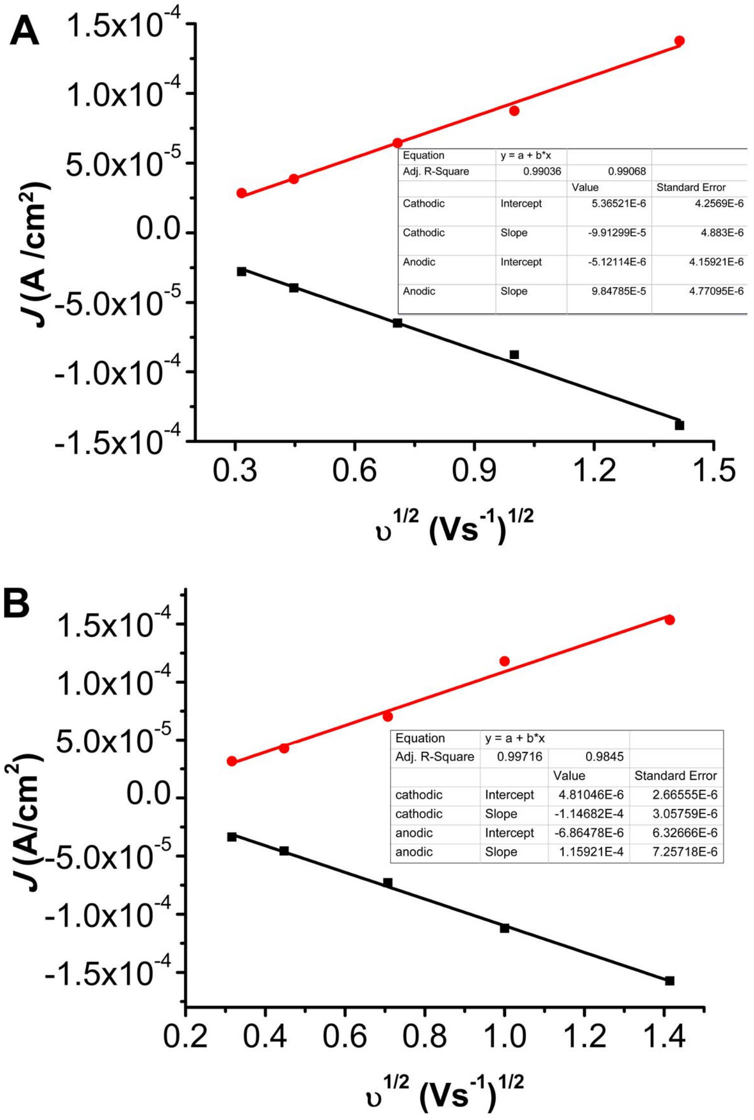

Equation	y = a + b*x		
Adj. R-Square	0.99036	0.99068	
		Value	Standard Error
Cathodic	Intercept	5.36521E-6	4.2569E-6
Cathodic	Slope	-9.91299E-5	4.883E-6
Anodic	Intercept	-5.12114E-6	4.15921E-6
Anodic	Slope	9.84785E-5	4.77095E-6

Equation	y = a + b*x		
Adj. R-Square	0.99716	0.9845	
		Value	Standard Error
cathodic	Intercept	4.81046E-6	2.66555E-6
cathodic	Slope	-1.14682E-4	3.05759E-6
anodic	Intercept	-6.86478E-6	6.32666E-6
anodic	Slope	1.15921E-4	7.25718E-6

Figure S3.12. Plots of current density vs $\upsilon^{1/2}$ for the reductions with $E_{1/2}$ = –1.01 V (A) and –1.65 V (B) vs Fc$^+$/Fc for Fe(^{tbu}catbpy) **3**. Linearity indicates Fe(^{tbu}catbpy) **3** is operating in a diffusion limited regime. Conditions: 0.5 mM analyte in 0.1 M TBAPF$_6$/*N,N*-DMF; glassy carbon working and counter electrodes, Ag/AgCl pseudoreference electrode, referenced to Fc$^+$/Fc from internal decamethylferrocene (Cp$_2$*Fe) standard.

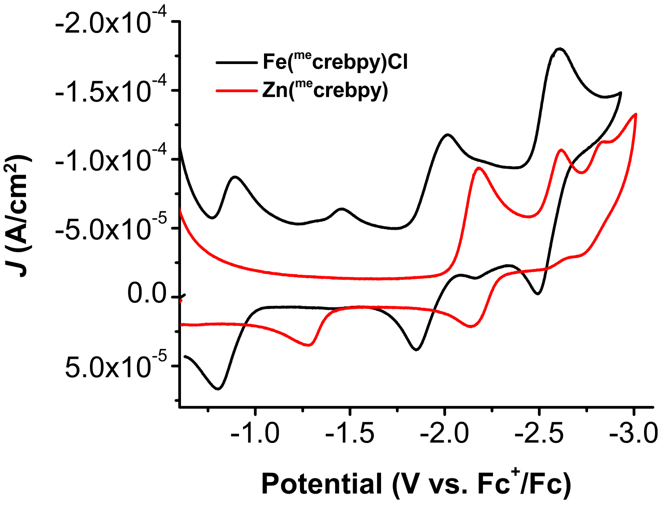

Figure S3.13. Cyclic voltammogram of 0.5 mM Fe(^{me}crebpy)Cl **2** (black) or Zn(^{me}crebpy) (red) under Ar saturation conditions. Conditions: 0.5 mM analyte in 0.1 M $TBAPF_6$/ *N,N*-DMF; glassy carbon working and counter electrodes, Ag/AgCl pseudoreference electrode, referenced to Fc$^+$/Fc from internal decamethylferrocene (Cp_2*Fe) standard, 100 mV/s scan rate.

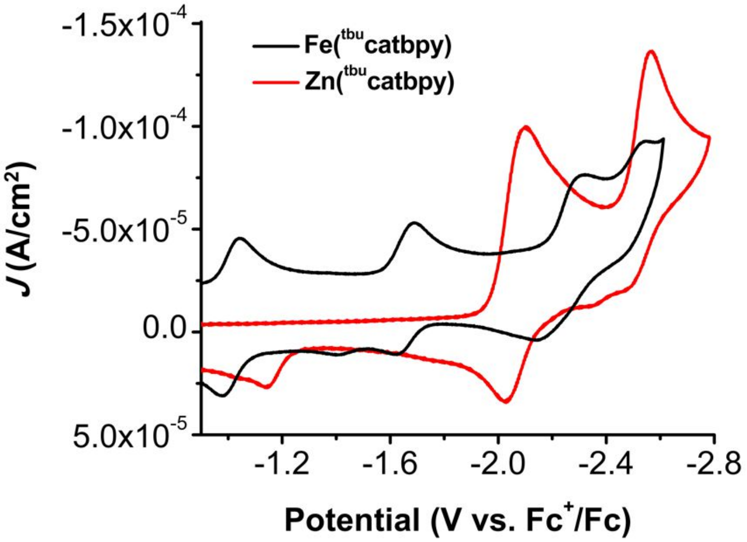

Figure S3.14. Cyclic voltammogram of 0.5 mM Fe(^{tbu}catbpy) **3** (black) or Zn(^{tbu}catbpy) (red) under Ar saturation conditions. Conditions: 0.5 mM analyte in 0.1 M $TBAPF_6$/*N,N*-DMF; glassy carbon working and counter electrodes, Ag/AgCl pseudoreference electrode, referenced to Fc$^+$/Fc from eitherinternal Cp_2*Fe or Cp_2Co standard, 100 mV/s scan rate.

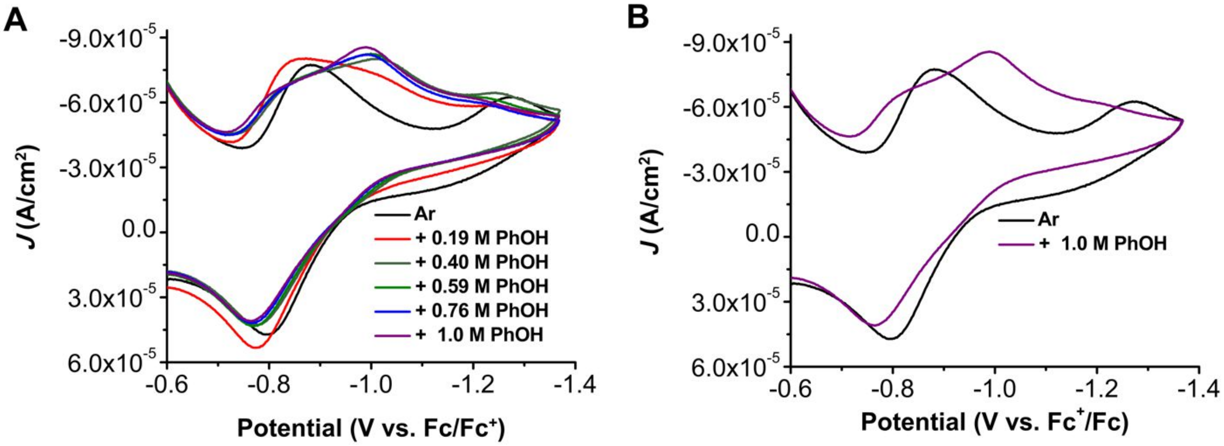

Figure S3.15. Cyclic voltammograms of 0.5 mM Fe(^{me}crebpy)Cl **2** under Ar saturation conditions with varied amounts of PhOH showing a shift in the first two reduction features. Conditions: 0.5 mM analyte in 0.1 M TBAPF$_6$/*N,N*-DMF; glassy carbon working and counter electrodes, Ag/AgCl pseudoreference electrode, referenced to Fc$^+$/Fc from internal decamethylferrocene (Cp$_2$*Fe) standard, 100 mV/s scan rate.

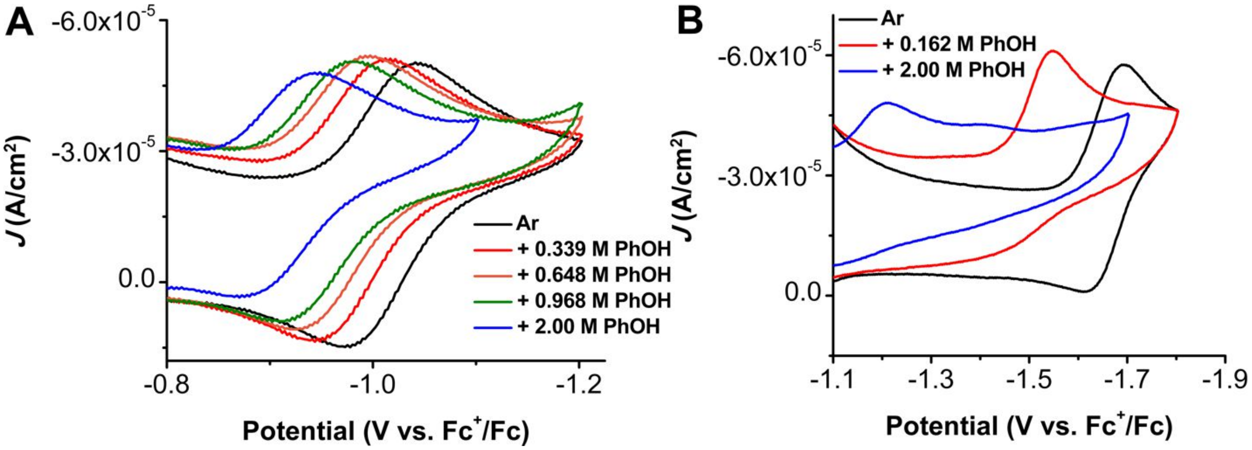

Figure S3.16. Cyclic voltammograms of 0.5 mM Fe(^{tbu}catbpy) **3** under Ar saturation conditions with varied amounts of PhOH showing a shift in the first two reduction features. Conditions: 0.5 mM analyte in 0.1 M TBAPF$_6$/*N,N*-DMF; glassy carbon working and counter electrodes, Ag/AgCl pseudoreference electrode, referenced to Fc$^+$/Fc from internal decamethylferrocene (Cp$_2$*Fe) standard, 100 mV/s scan rate.

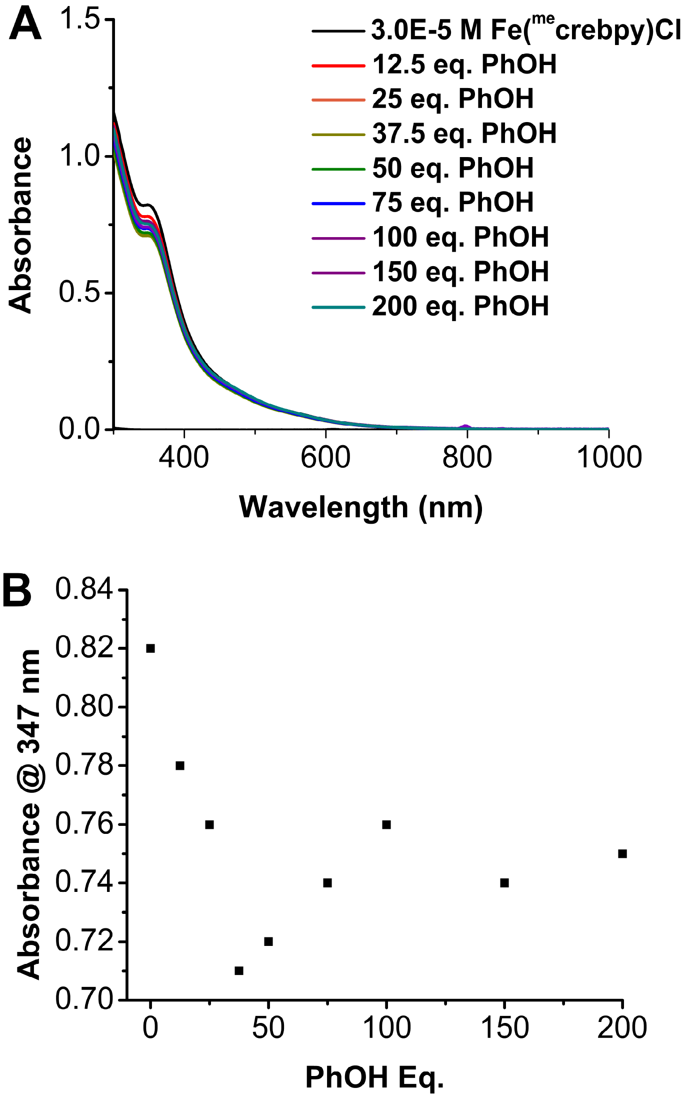

Figure S3.17. (A) UV-vis titration of PhOH into a solution of Fe(^{me}crebpy)Cl **2** in *N,N*-DMF. Quartz cell of 1 cm pathlength. (B) Plot of absorbance at 347 nm versus PhOH equivalents.

Figure S3.18. (A) UV-vis titration of PhOH into a solution of Fe($^{\text{tbu}}$catbpy) **3** in *N,N*-DMF. Quartz cell of 1 cm pathlength. (B) Plot of absorbance at 335 nm versus PhOH equivalents. (C) Plot of absorbance at 463 nm versus PhOH equivalents.

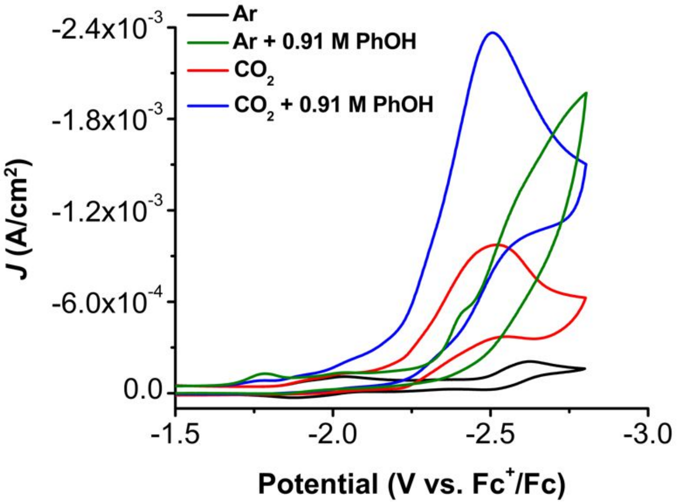

Figure S3.19. Cyclic voltammograms of 0.5 mM Fe(^{me}crebpy)Cl **2** under labeled conditions. Conditions: 0.5 mM analyte in 0.1 M TBAPF$_6$/*N,N*-DMF; glassy carbon working and counter electrodes, Ag/AgCl pseudoreference electrode, referenced to Fc$^+$/Fc from internal decamethylferrocene (Cp$_2$*Fe) standard, 100 mV/s scan rate.

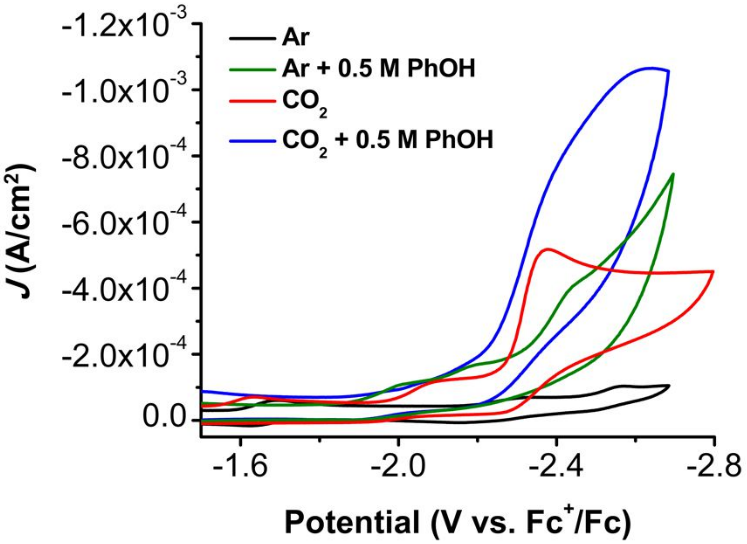

Figure S3.20. Cyclic voltammograms of 0.5 mM Fe(^{tbu}catbpy) **3** under labeled conditions. Conditions: 0.5 mM analyte in 0.1 M TBAPF$_6$/*N,N*-DMF; glassy carbon working and counter electrodes, Ag/AgCl pseudoreference electrode, referenced to Fc$^+$/Fc from internal decamethylferrocene (Cp$_2$*Fe) standard, 100 mV/s scan rate.

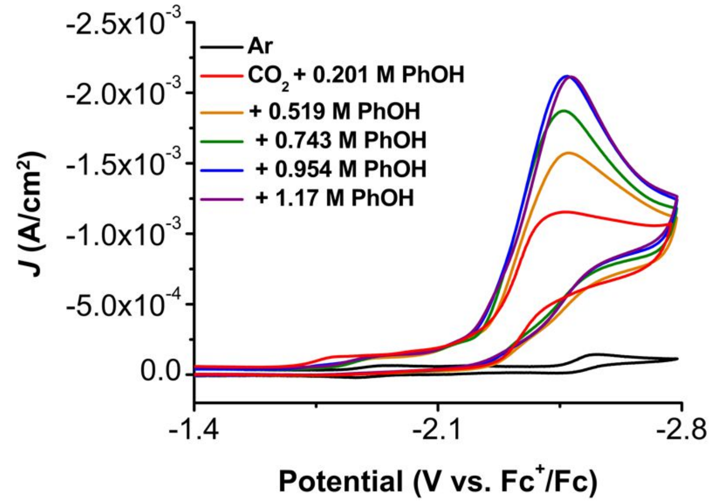

Figure S3.21. Cyclic Voltammograms of 0.5 mM Fe(^{me}crebpy)Cl **2** under CO_2 saturation conditions with scans to the catalytic wave showing current saturation occurs at ~0.9 M PhOH. Conditions: 0.5 mM analyte in 0.1 M $TBAPF_6$/*N,N*-DMF; glassy carbon working and counter electrodes, Ag/AgCl pseudoreference electrode, referenced to Fc^+/Fc from internal decamethylferrocene (Cp_2*Fe) standard, 100 mV/s scan rate.

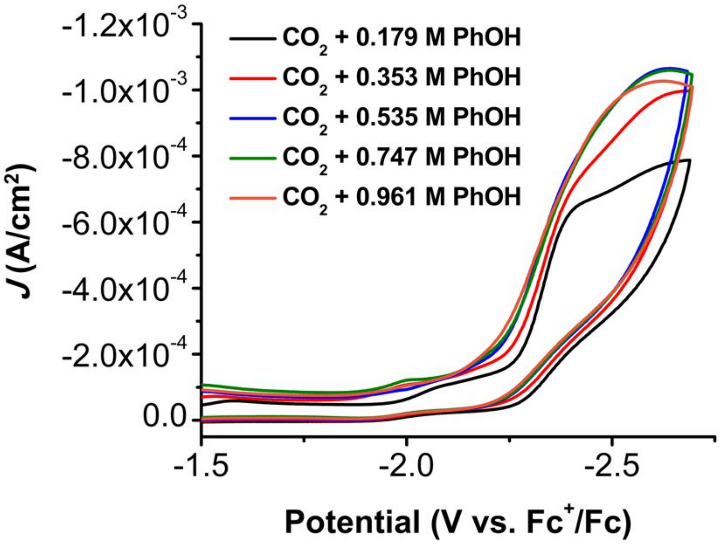

Figure S3.22. Cyclic Voltammograms of 0.5 mM Fe(^{tbu}catbpy) **3** under CO_2 saturation conditions with scans to the catalytic wave showing current saturation occurs at 0.5 M PhOH. Conditions: 0.5 mM analyte in 0.1 M $TBAPF_6$/*N,N*-DMF; glassy carbon working and counter electrodes, Ag/AgCl pseudoreference electrode, referenced to Fc^+/Fc from internal decamethylferrocene (Cp_2*Fe) standard, 100 mV/s scan rate.

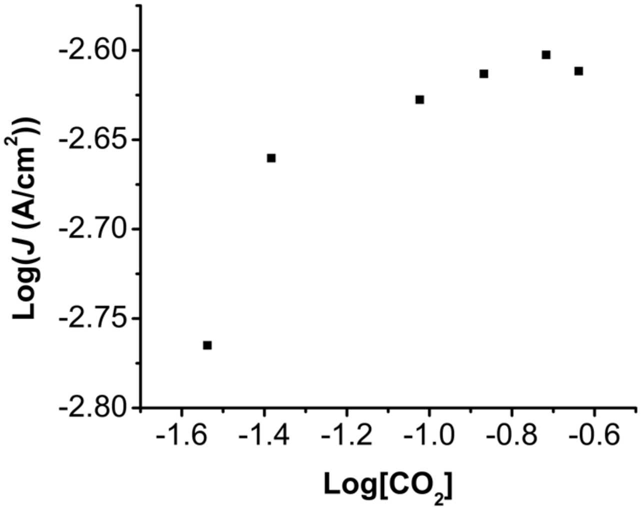

Figure S3.23. Log-log plot of peak current density versus [CO_2] for 0.5 mM Fe(^{me}crebpy)Cl **2** with 1.0 M PhOH. Kinetic current saturation is observed above 0.04 M CO_2. Conditions: 0.5 mM analyte in 0.1 M $TBAPF_6$/*N,N*-DMF; glassy carbon working and counter electrodes, Ag/AgCl pseudoreference electrode, referenced to Fc^+/Fc from internal decamethylferrocene (Cp_2*Fe) standard, 100 mV/s scan rate.

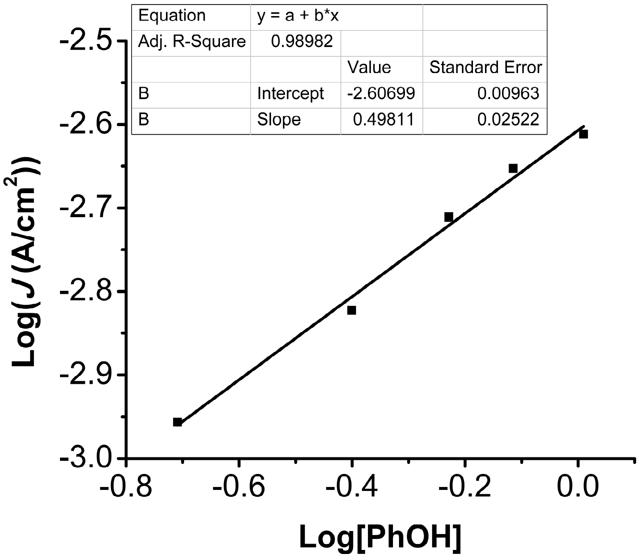

Figure S3.24. Log-log plot of peak current density versus [PhOH] for 0.5 mM Fe(^{me}crebpy)Cl **2** under CO_2 saturation conditions. Slope of 0.5 is indicative of 1st order kinetics with respect to [PhOH].[1] Conditions: 0.5 mM analyte in 0.1 M $TBAPF_6$/*N,N*-DMF; glassy carbon working and counter electrodes, Ag/AgCl pseudoreference electrode, referenced to Fc^+/Fc from internal decamethylferrocene (Cp_2*Fe) standard, 100 mV/s scan rate.

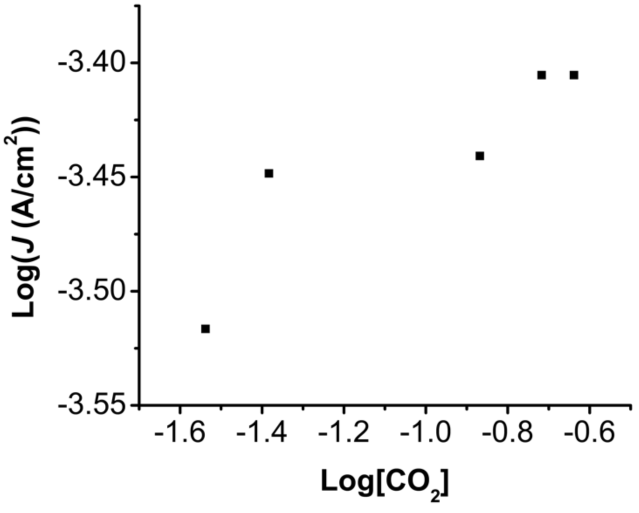

Figure S3.25. Log-log plot of peak current density versus [CO_2] for 0.5 mM Fe(^{tbu}catbpy) **3** with 0.5 M PhOH. Kinetic current saturation is observed above 0.04 M CO_2. Conditions: 0.5 mM analyte in 0.1 M $TBAPF_6$/*N,N*-DMF; glassy carbon working and counter electrodes, Ag/AgCl pseudoreference electrode, referenced to Fc^+/Fc from internal decamethylferrocene (Cp_2*Fe) standard, 100 mV/s scan rate.

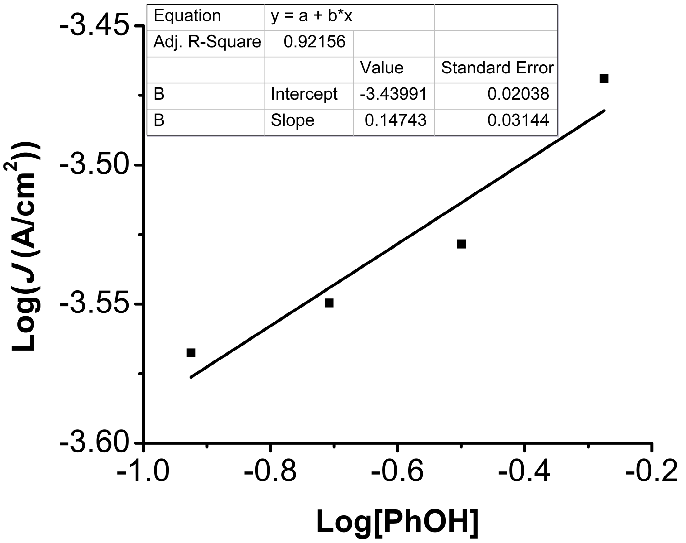

Figure S3.26. Log-log plot of peak current density versus [PhOH] for 0.5 mM Fe(^{tbu}catbpy) **3** under CO_2 saturation conditions. Conditions: 0.5 mM analyte in 0.1 M $TBAPF_6$/*N,N*-DMF; glassy carbon working and counter electrodes, Ag/AgCl pseudoreference electrode, referenced to Fc^+/Fc from internal decamethylferrocene (Cp_2*Fe) standard, 100 mV/s scan rate.

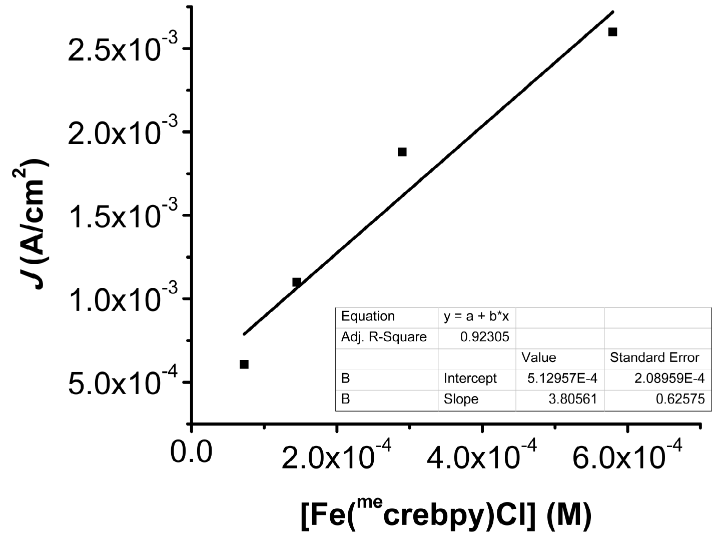

Figure S3.27. Plot of peak current density versus [**2**], Fe(^{me}crebpy)Cl under CO_2 saturation conditions with 1.0 M PhOH. Linearity is consistent with 1st order kinetics with respect to [**2**].[1] Conditions: 0.5 mM analyte in 0.1 M $TBAPF_6$/*N,N*-DMF; glassy carbon working and counter electrodes, Ag/AgCl pseudoreference electrode, referenced to Fc^+/Fc from internal decamethylferrocene (Cp_2*Fe) standard, 100 mV/s scan rate.

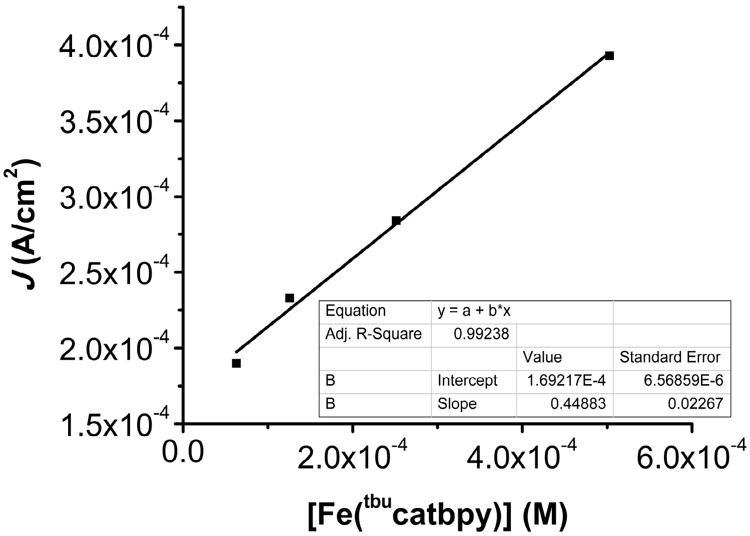

Figure S3.28. Plot of peak current density and [**3**], Fe(^{tbu}catbpy) under CO_2 saturation conditions with 0.5 M PhOH. Linearity is consistent with 1st order kinetics with respect to [**3**].[1] Conditions: 0.5 mM analyte in 0.1 M $TBAPF_6$/*N,N*-DMF; glassy carbon working and counter electrodes, Ag/AgCl pseudoreference electrode, referenced to Fc^+/Fc from internal decamethylferrocene (Cp_2*Fe) standard, 100 mV/s scan rate.

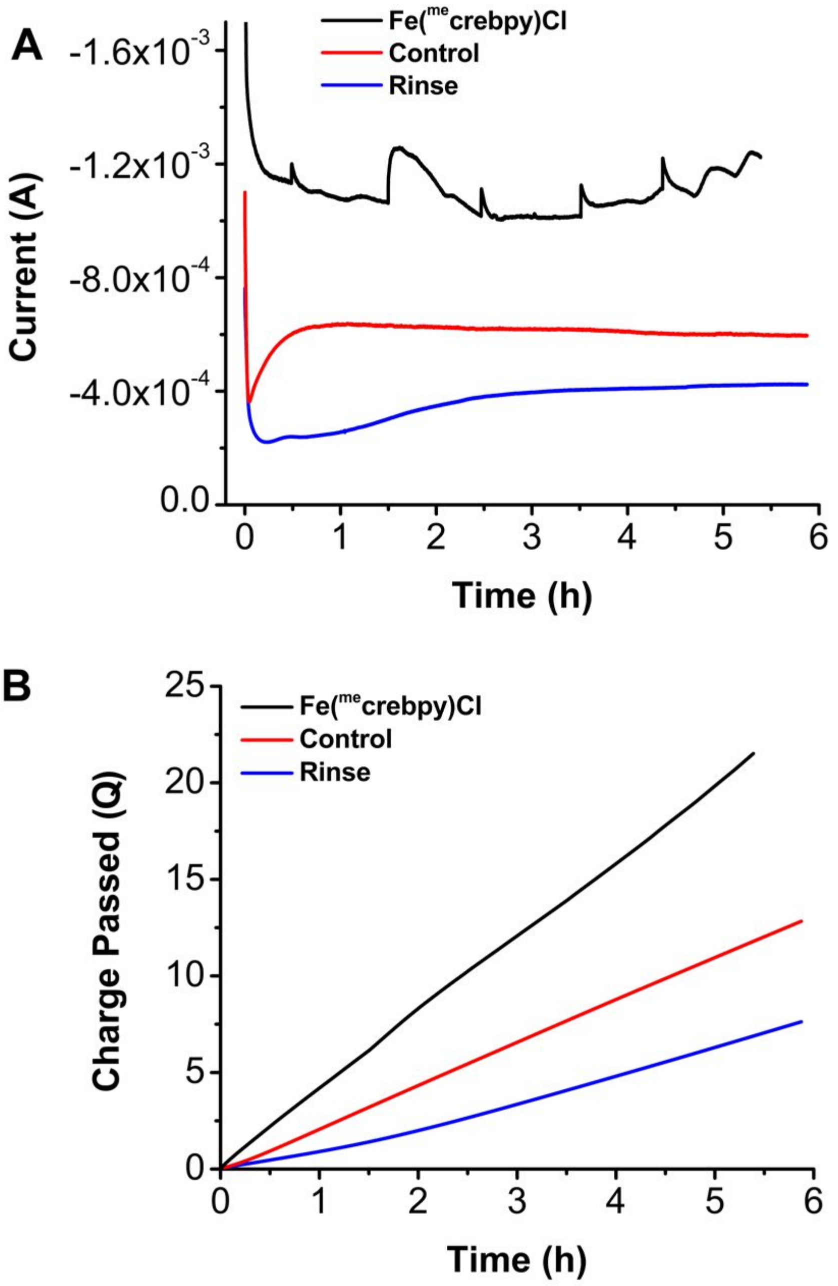

Figure S3.29. Current vs. Time and (A) Charge Passed vs. Time (B) plots for CPE experiments at –2.50 V vs Fc$^+$/Fc Conditions: Black: 0.5 mM Fe(^{me}crebpy)Cl **2**, 0.9 M PhOH, and CO_2 atmosphere; Blue: Ethanol rinsed working electrode from black experiment, 0.5 M PhOH and CO_2 atmosphere; Red: 0.5 M PhOH and CO_2 atmosphere. 0.1 M $TBAPF_6$/*N,N*-DMF electrolyte; graphite working and counter electrodes were used; reference electrode nonaqueous Ag/AgCl pseudoreference electrode which was referenced to Fc$^+$/Fc before each run; 0.05 M Fc was used as sacrificial oxidant

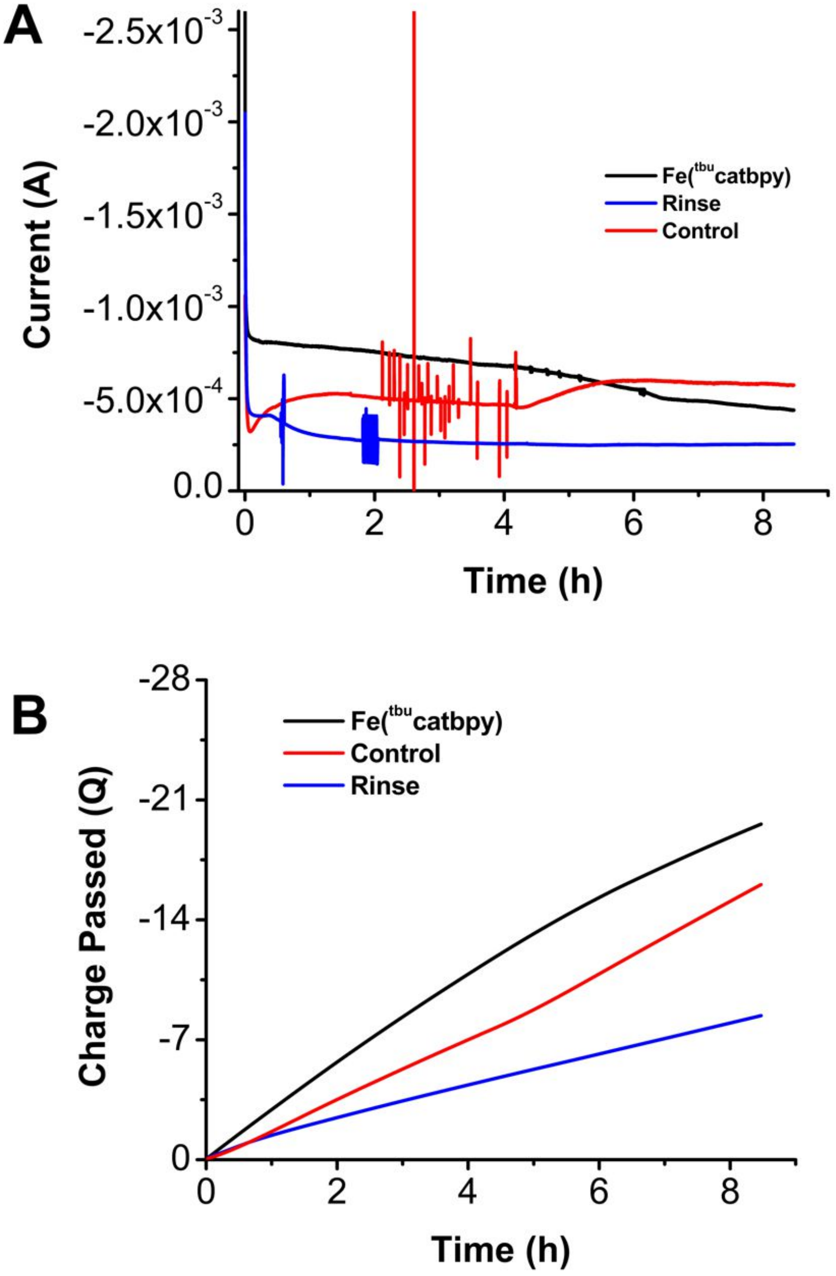

Figure S3.30. Current vs. Time (A) and Charge Passed vs. Time (B) plots for CPE experiments at –2.60 V vs Fc$^+$/Fc with Black: 0.5 mM Fe(^{tbu}catbpy) **3**, 0.5 M PhOH, and CO_2 atmosphere; Blue: Ethanol rinsed working electrode from black experiment, 0.5 M PhOH and CO_2 atmosphere; Red: 0.5 M PhOH and CO_2 atmosphere. 0.1 M $TBAPF_6$/*N,N*-DMF electrolyte; graphite working and counter electrodes were used; reference electrode nonaqueous Ag/AgCl pseudoreference electrode which was referenced to Fc$^+$/Fc before each run; 0.05 M Fc was used as sacrificial oxidant

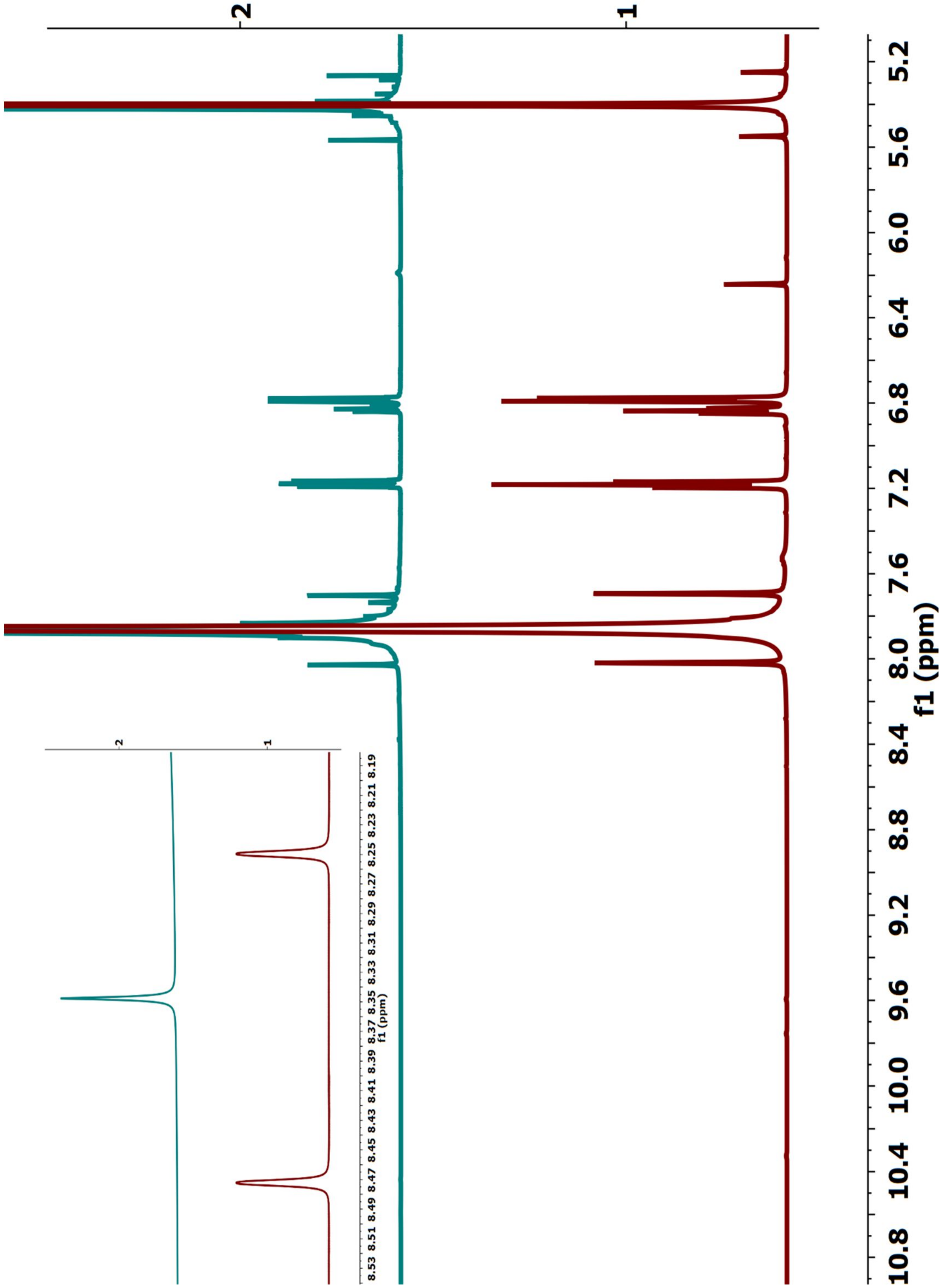

Figure S3.31. ^{1}H NMR spectra showing (green) HCO_2^- generated during CPE experiments under a CO_2 atmosphere with Fe(^{me}crebpy)Cl **2** and (red) $H^{13}CO_2^-$ generated under a $^{13}CO_2$ atmosphere under identical conditions (inset) after extraction with D_2O and washing with CH_2Cl_2 (600 MHz).

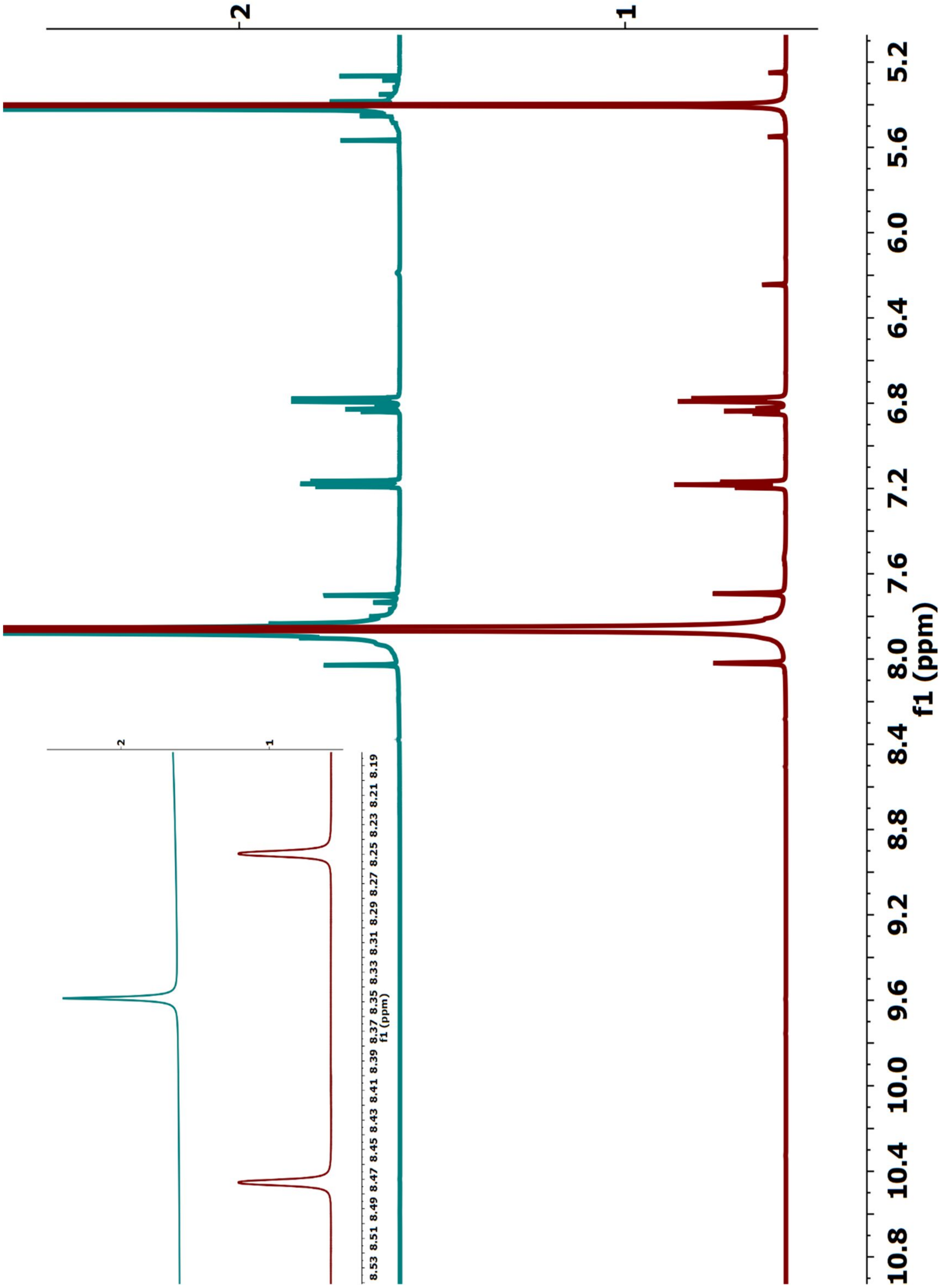

Figure S3.32. ^1H NMR spectra showing (green) HCO_2^- generated during CPE experiments under a CO_2 atmosphere with Fe(^{tbu}catbpy) **3** and (red) $H^{13}CO_2^-$ generated under a $^{13}CO_2$ atmosphere under identical conditions (inset) after extraction with D_2O and washing with CH_2Cl_2 (600 MHz).

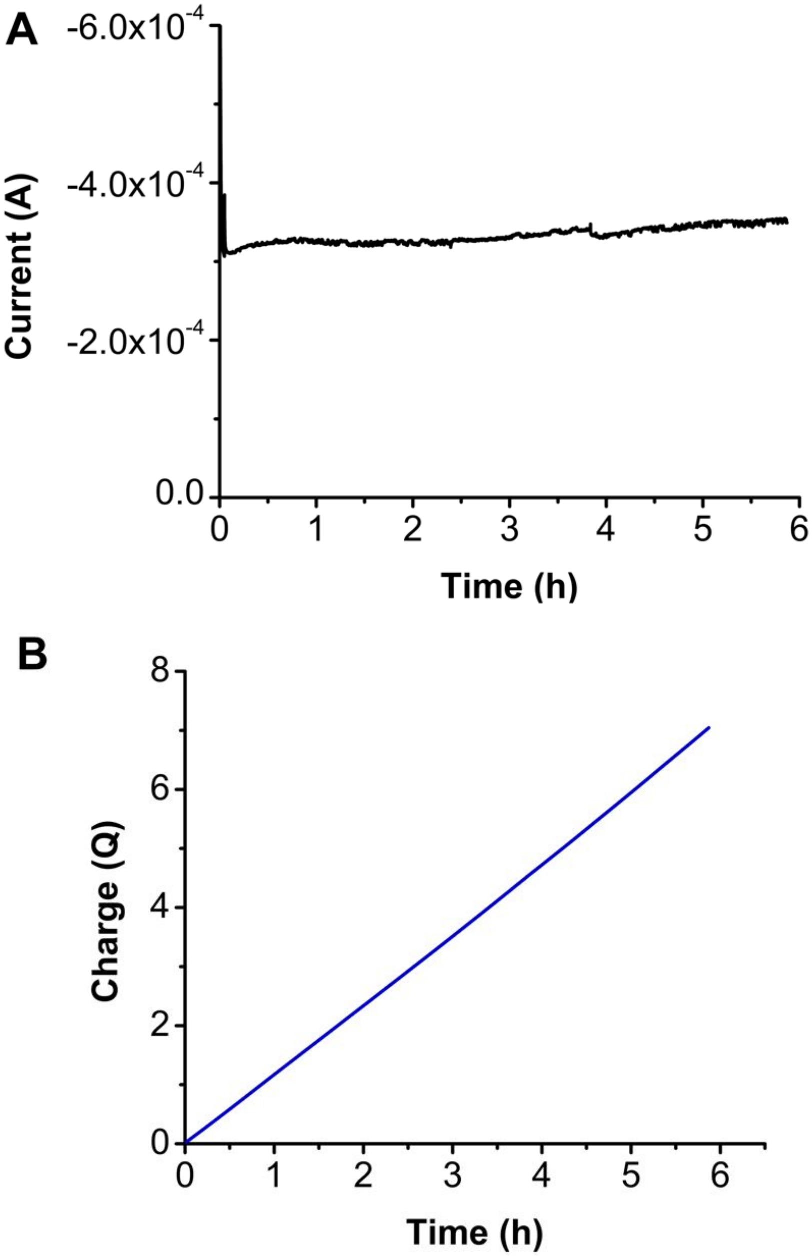

Figure S3.33. Current vs. Time (A) and Charge Passed vs. Time plots (B) for CPE experiments at –2.50 V vs Fc$^+$/Fc with 0.5 mM Fe(^{me}crebpy)Cl **2,** 0.5 M PhOH and $^{13}CO_2$ atmosphere. 0.1 M $TBAPF_6$/*N,N*-DMF electrolyte; graphite working and counter electrodes were used; reference electrode nonaqueous Ag/AgCl pseudoreference electrode which was referenced to Fc$^+$/Fc before each run; 0.05 M Fc was used as sacrificial oxidant

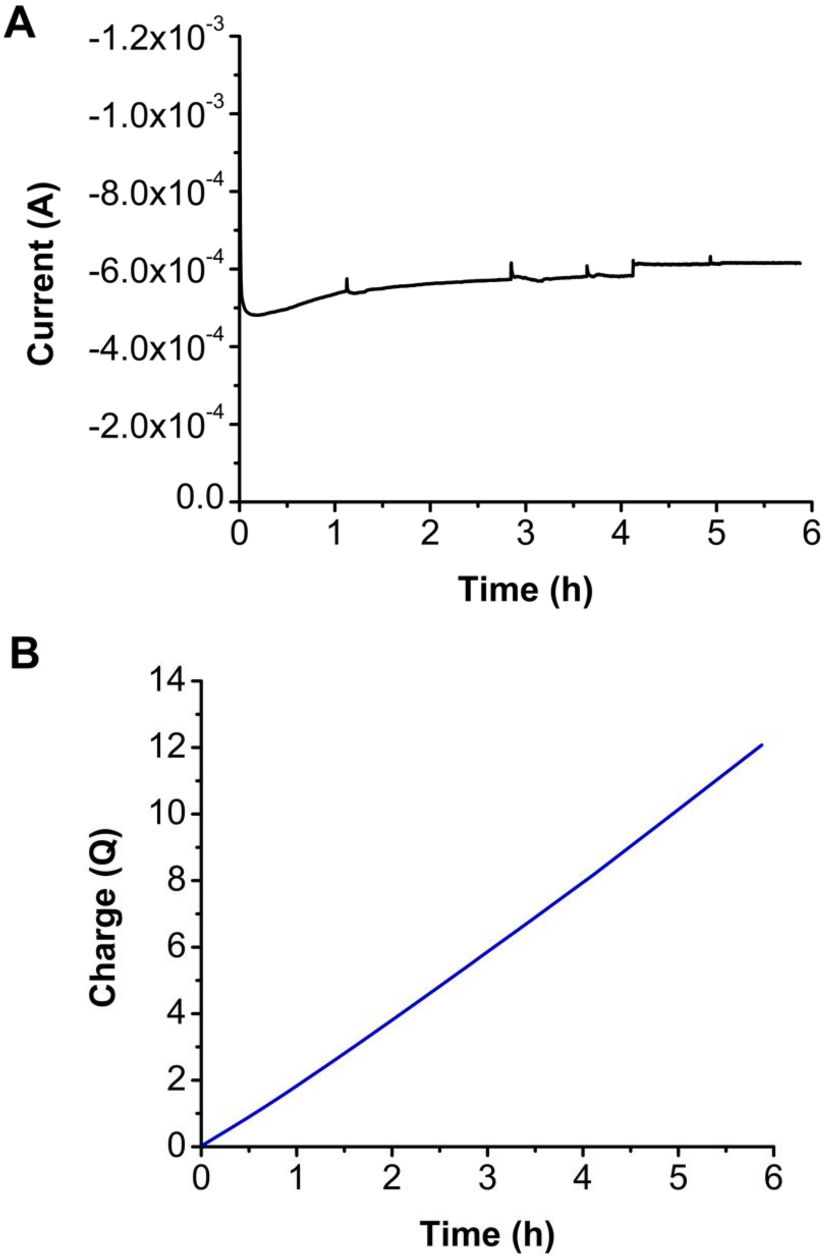

Figure S3.34. Current vs. Time (A) and Charge Passed vs. Time plots (B) for CPE experiments at –2.60 V vs Fc$^+$/Fc with 0.5 mM Fe(^{tbu}catbpy) **3,** 0.5 M PhOH and $^{13}CO_2$ atmosphere. 0.1 M TBAPF$_6$/*N,N*-DMF electrolyte; graphite working and counter electrodes were used; reference electrode nonaqueous Ag/AgCl pseudoreference electrode which was referenced to Fc$^+$/Fc before each run; 0.05 M Fc was used as sacrificial oxidant

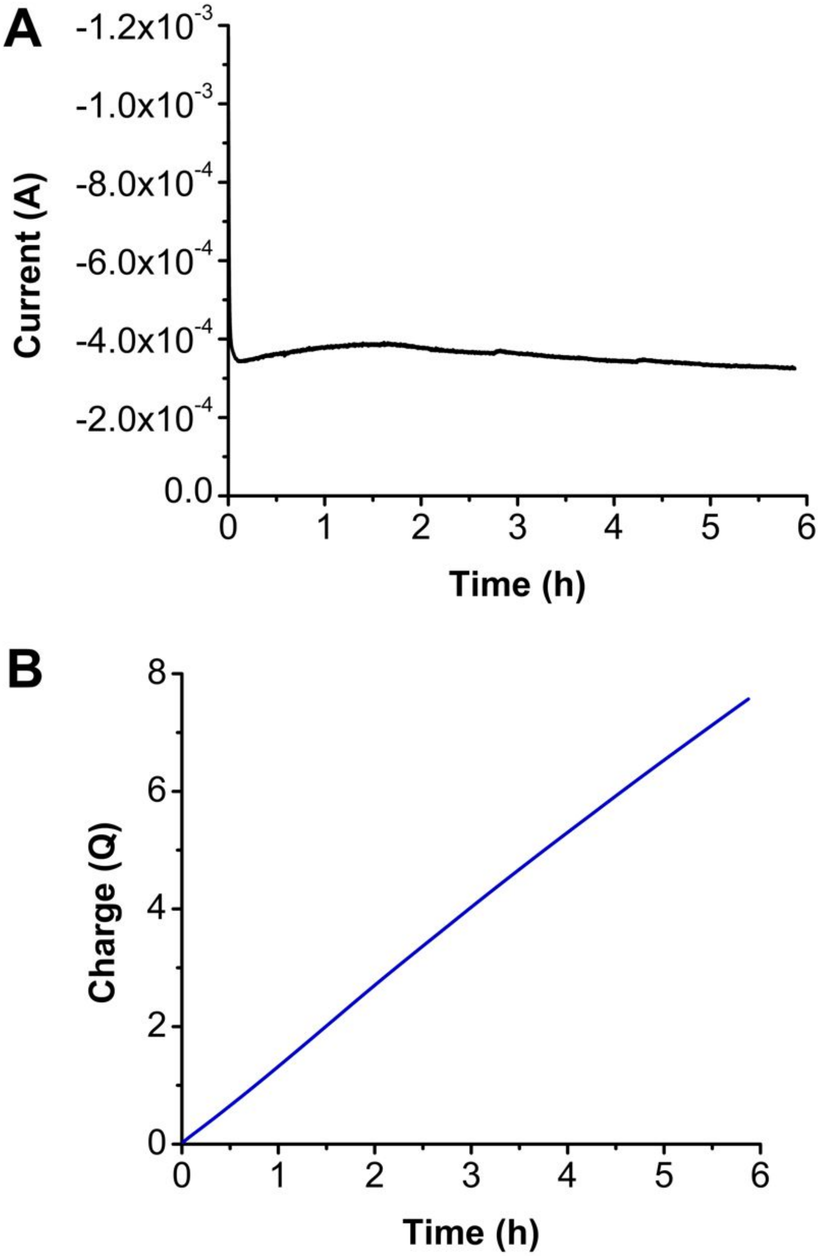

Figure S3.35. Current vs. Time (A) and Charge Passed vs. Time (B) Plots for CPE experiments at –2.50 V vs Fc$^+$/Fc with 0.5 mM Fe(^{me}crebpy)Cl **2** and CO$_2$ atmosphere. 0.1 M TBAPF$_6$/*N,N*-DMF electrolyte; graphite working and counter electrodes were used; reference electrode nonaqueous Ag/AgCl pseudoreference electrode which was referenced to Fc$^+$/Fc before each run; 0.05 M Fc was used as sacrificial oxidant

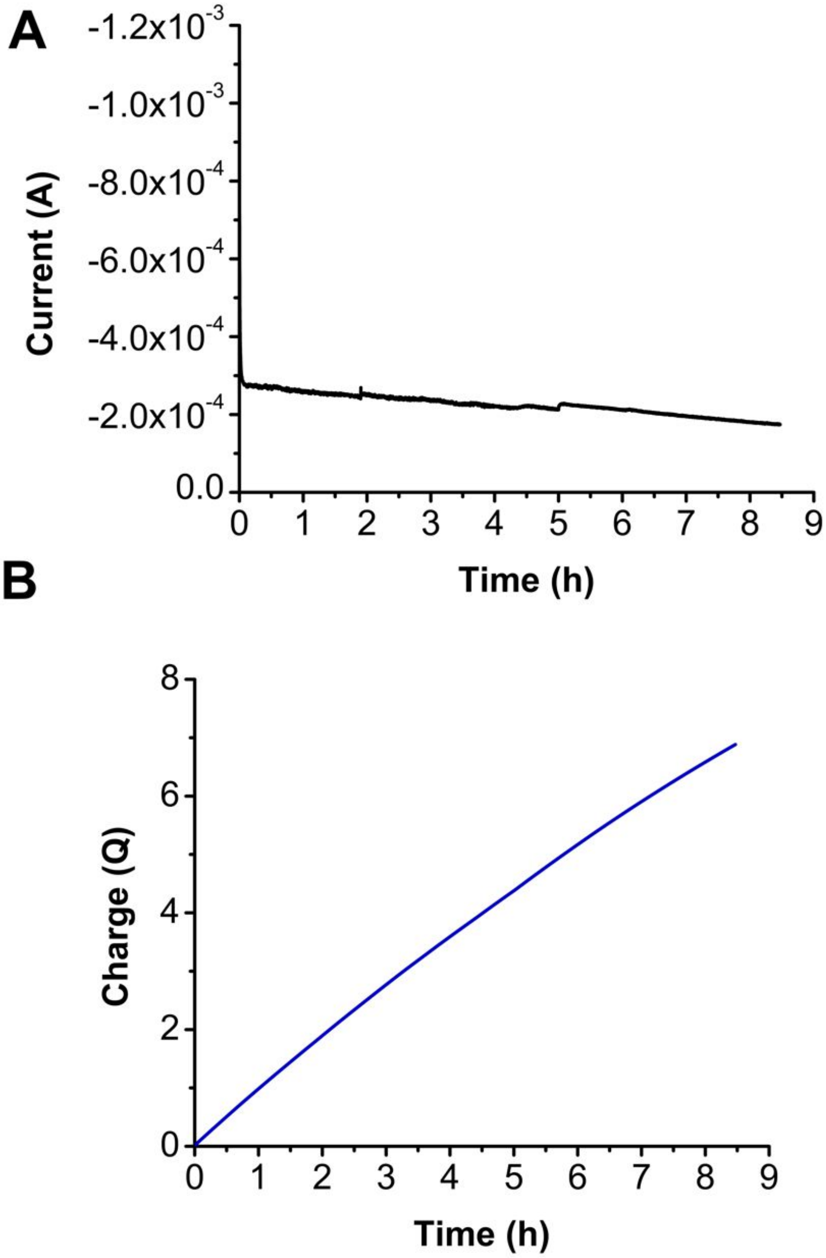

Figure S3.36. Current vs. Time (A) and Charge Passed vs. Time plots (B) for CPE experiments at –2.60 V vs Fc$^+$/Fc with 0.5 mM Fe($^{\text{tbu}}$catbpy) **3** and CO_2 atmosphere. 0.1 M $TBAPF_6$/*N,N*-DMF electrolyte; graphite working and counter electrodes were used; reference electrode nonaqueous Ag/AgCl pseudoreference electrode which was referenced to Fc$^+$/Fc before each run; 0.05 M Fc was used as sacrificial oxidant

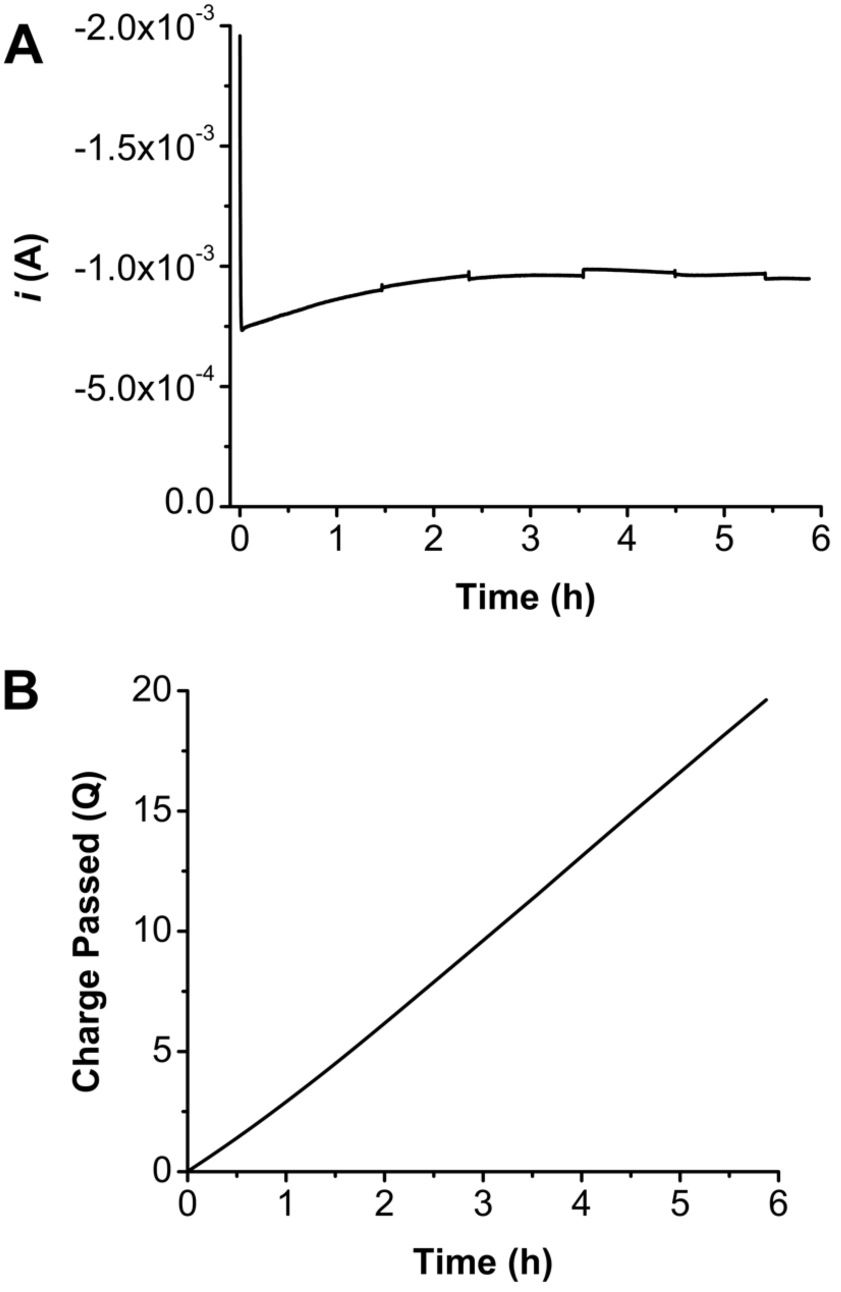

Figure S3.37. Current vs. Time (A) and Charge Passed vs. Time plots (B) for CPE experiments at –2.60 V vs Fc^+/Fc with 0.5 mM Fe(^{me}crebpy)Cl **2**, 0.9 M PhOH, and Ar atmosphere. 0.1 M $TBAPF_6$/*N,N*-DMF electrolyte; graphite working and counter electrodes were used; reference electrode nonaqueous Ag/AgCl pseudoreference electrode which was referenced to Fc^+/Fc before each run; 0.05 M Fc was used as sacrificial oxidant

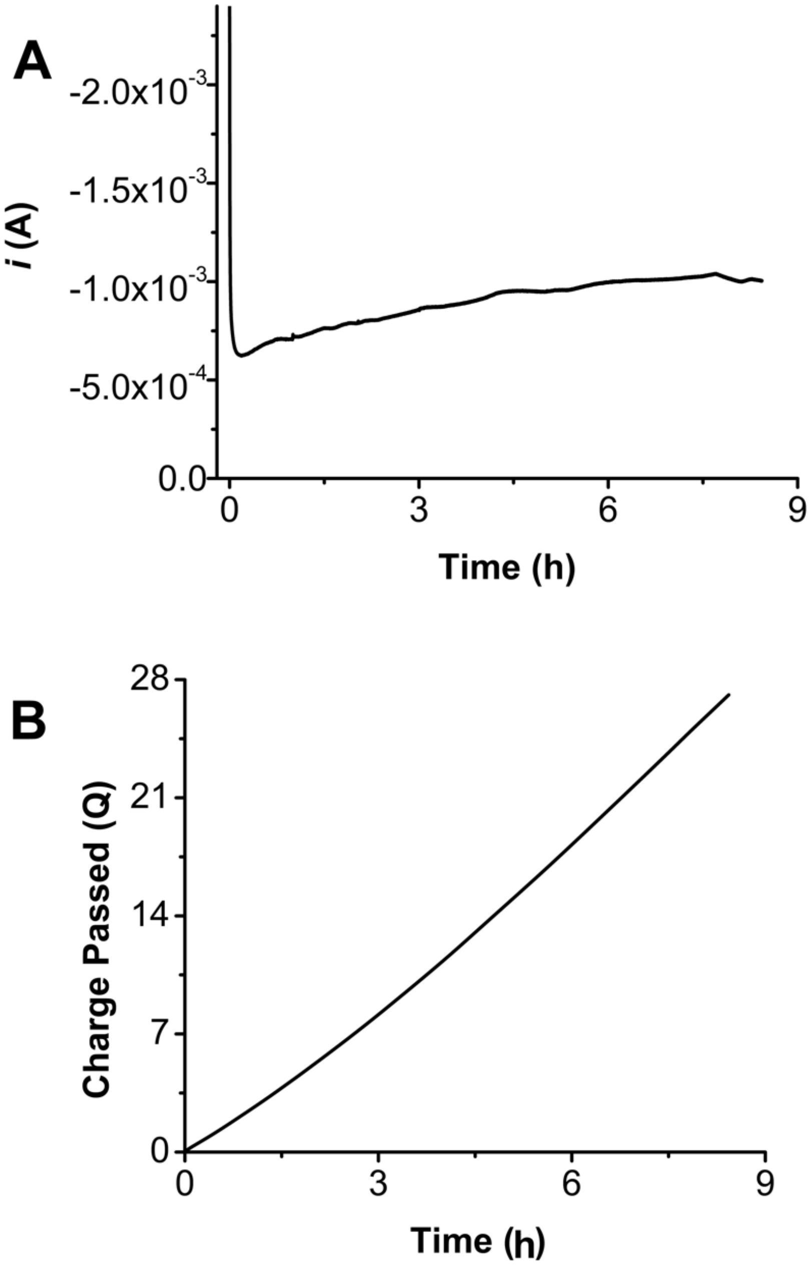

Figure S3.38. Current vs. Time (A) and Charge Passed vs. Time plots (B) for CPE experiments at –2.60 V vs Fc^+/Fc with 0.5 mM Fe(^{tbu}catbpy) **3**, 0.5 M PhOH, and Ar atmosphere. 0.1 M $TBAPF_6$/*N,N*-DMF electrolyte; graphite working and counter electrodes were used; reference electrode nonaqueous Ag/AgCl pseudoreference electrode which was referenced to Fc^+/Fc before each run; 0.05 M Fc was used as sacrificial oxidant

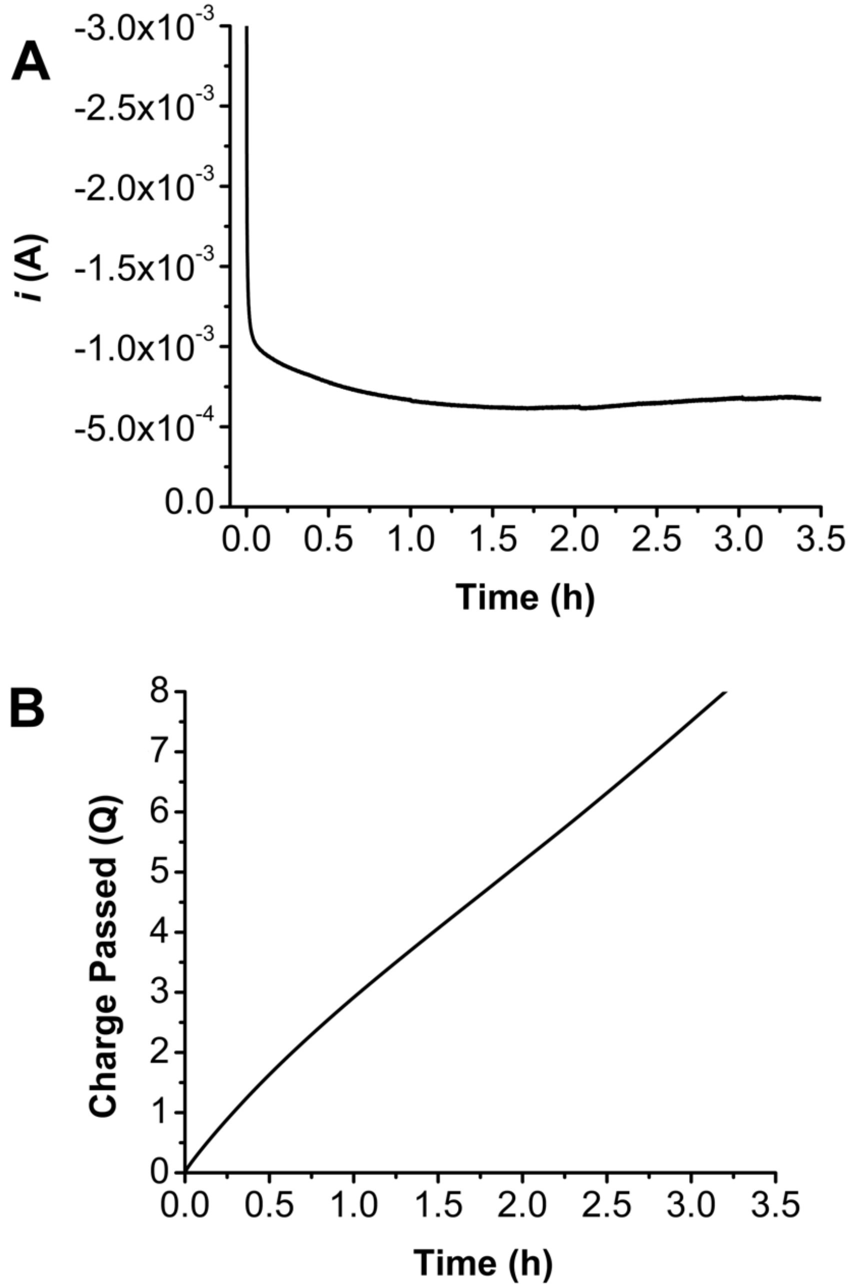

Figure S3.39. Current vs. Time (A) and Charge Passed vs. Time plots (B) for CPE experiments at –2.60 V vs Fc$^+$/Fc with 0.5 mM Fe(^{tbu}catbpy) **3** and Ar atmosphere. 0.1 M TBAPF$_6$/*N,N*-DMF electrolyte; graphite working and counter electrodes were used; reference electrode nonaqueous Ag/AgCl pseudoreference electrode which was referenced to Fc$^+$/Fc before each run; 0.05 M Fc was used as sacrificial oxidant

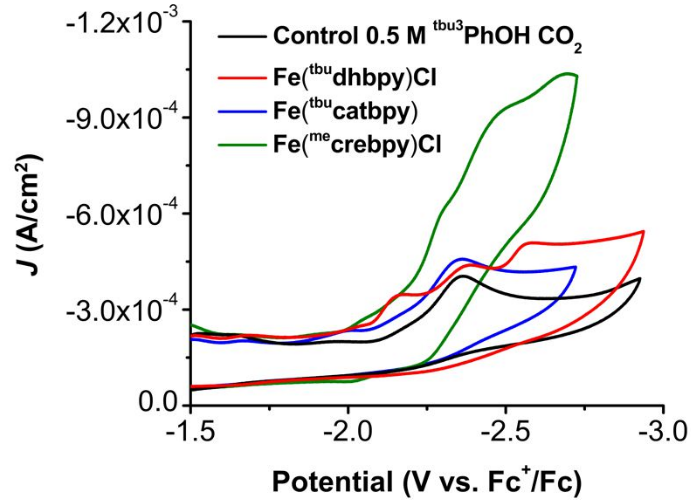

Figure S3.40. Cyclic Voltammograms of 0.5 mM Fe(^{tbu}dhbpy)Cl **1** (red), Fe(^{me}crebpy)Cl **2** (green)**,** and Fe(^{tbu}catbpy) **3** (blue) with 0.5 M 2,4,6-tri-*tert*-butyl-phenol (^{tbu3}PhOH) under CO_2 saturation conditions. Control experiment is under identical conditions with no catalyst material added. Conditions: 0.5 mM analyte in 0.1 M $TBAPF_6$/ *N,N*-DMF; glassy carbon working and counter electrodes, Ag/AgCl pseudoreference electrode, referenced to Fc^+/Fc from internal decamethylferrocene (Cp_2*Fe) standard, 100 mV/s scan rate.

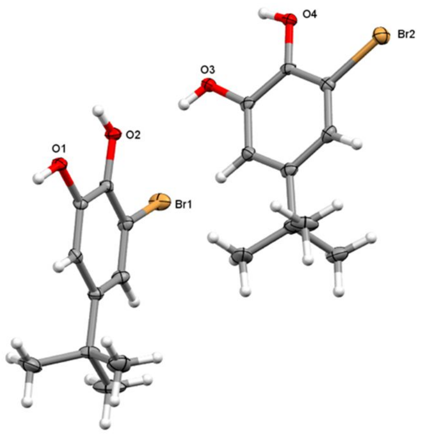

Figure S3.41. Crystal structure of 3-bromo-5-*tert*-butyl-benzene-diol. Grown by sublimation. Thermal ellipsoids set to 50%. C = carbon, Br = orange, O = red, H = white. CCDC: 1940614

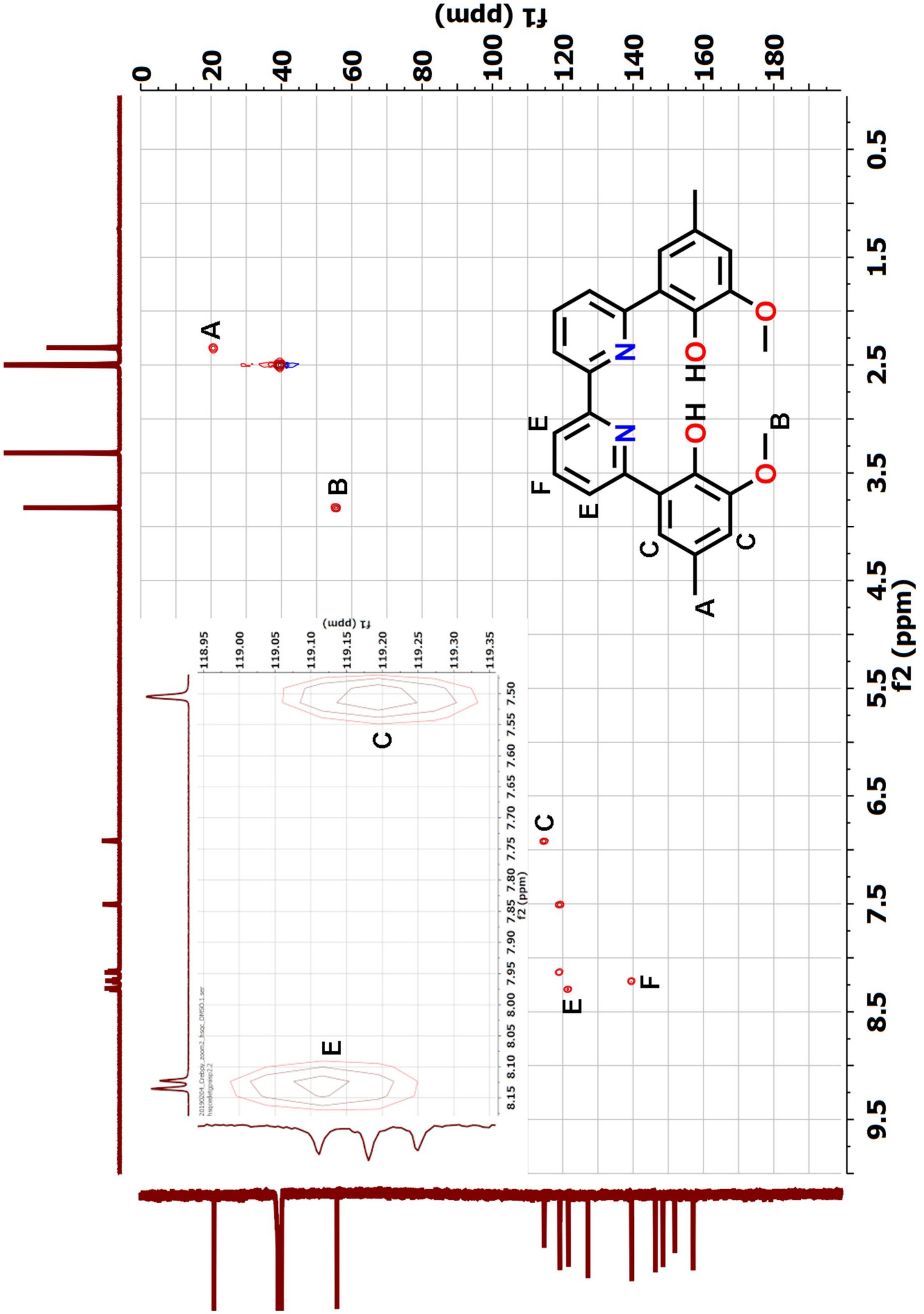

Figure S3.42. ^{1}H–^{13}C HSQC NMR of **$^{\mathrm{me}}$crebpy** (DMSO-d_6, ^{1}H 600 MHz; ^{13}C 151 MHz).

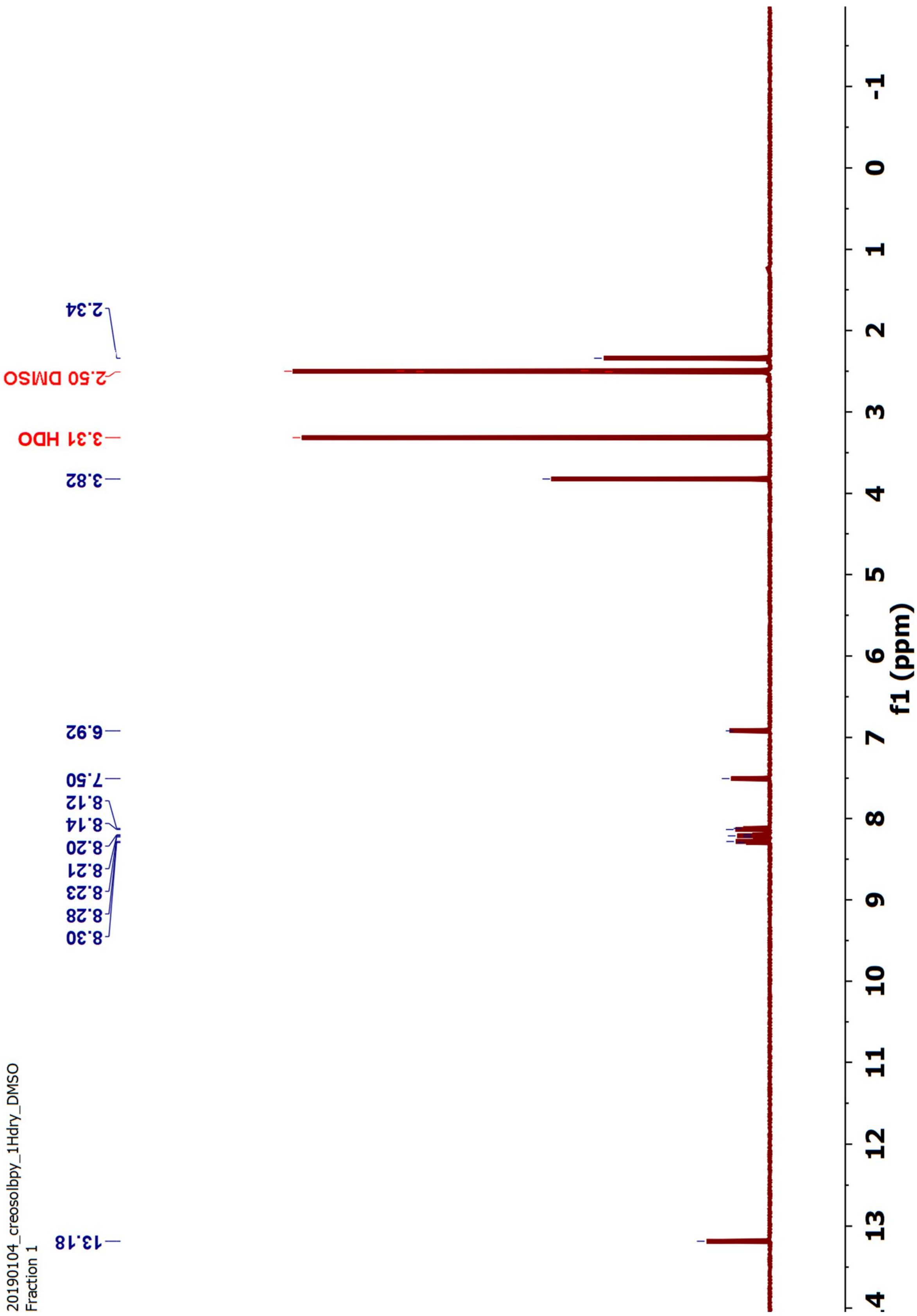

Figure S3.43. ^{1}H NMR of **$^{\mathbf{me}}$crebpy** (DMSO-d_6, 600 MHz).

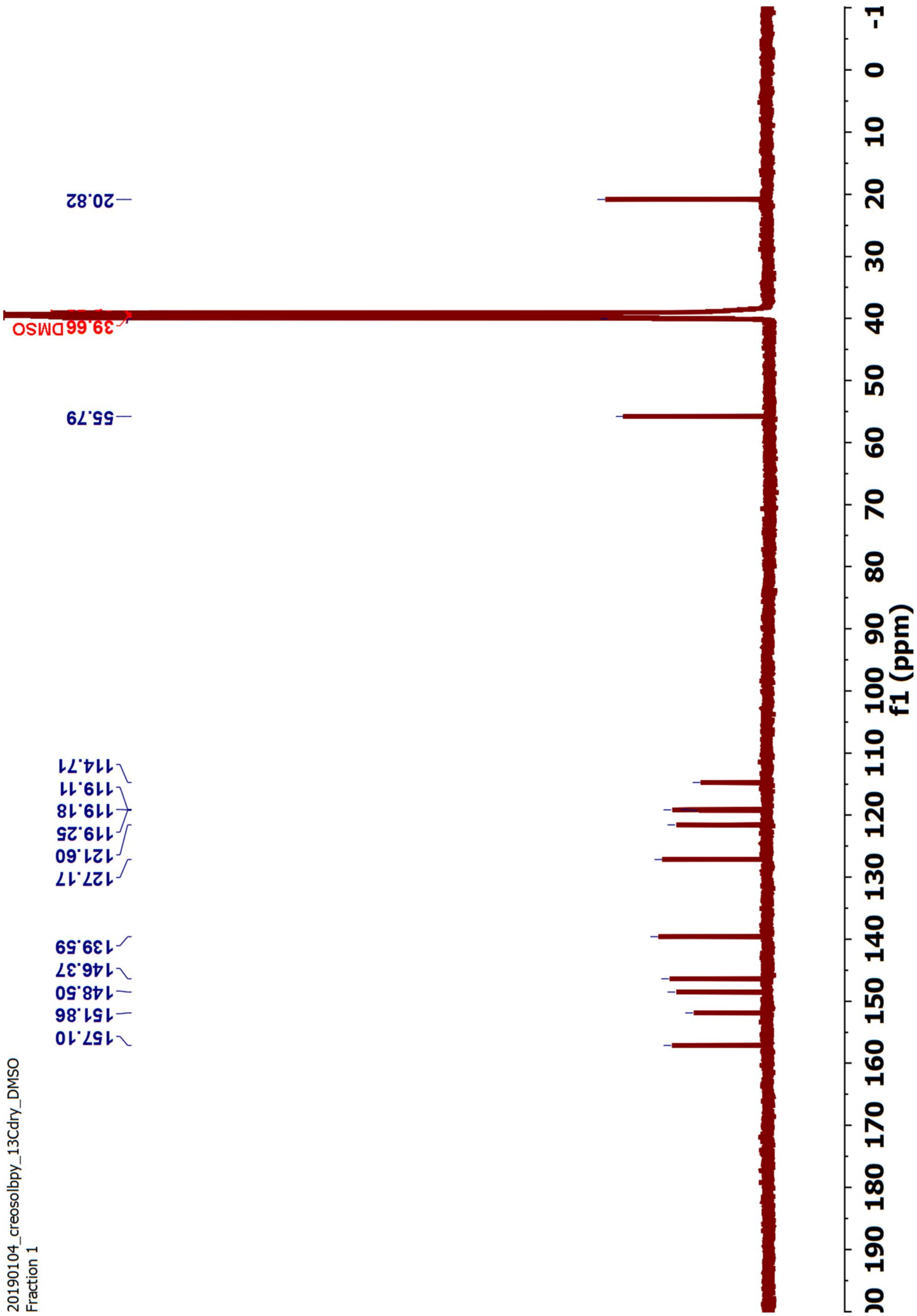

Figure S3.44. $^{13}C\{^{1}H\}$ NMR of **^{me}crebpy** (DMSO-*d*$_6$, 151 MHz).

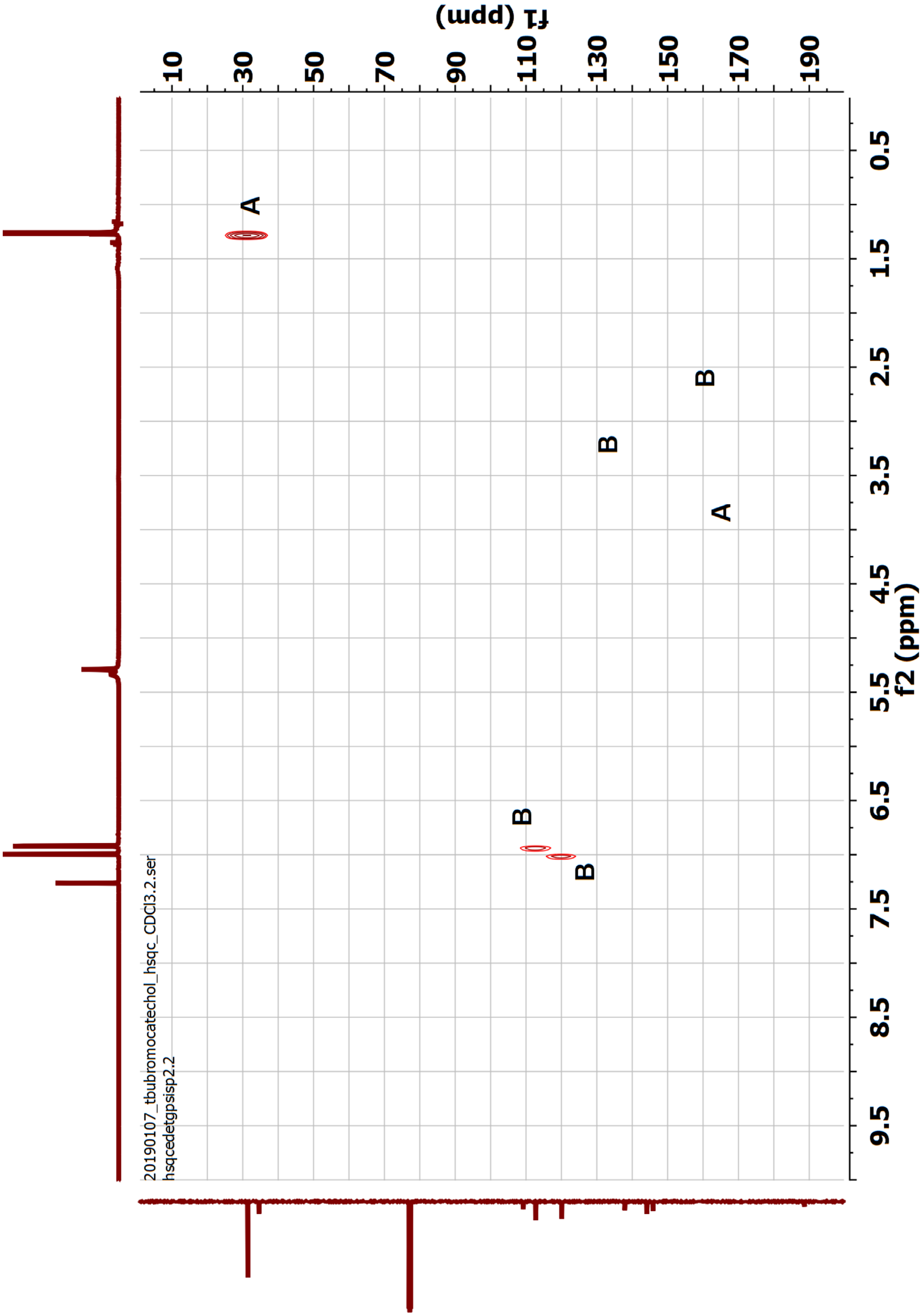

Figure S3.45. ^{1}H–^{13}C HSQC NMR of **VI** (CDCl$_3$, ^{1}H 600 MHz; ^{13}C 151 MHz).

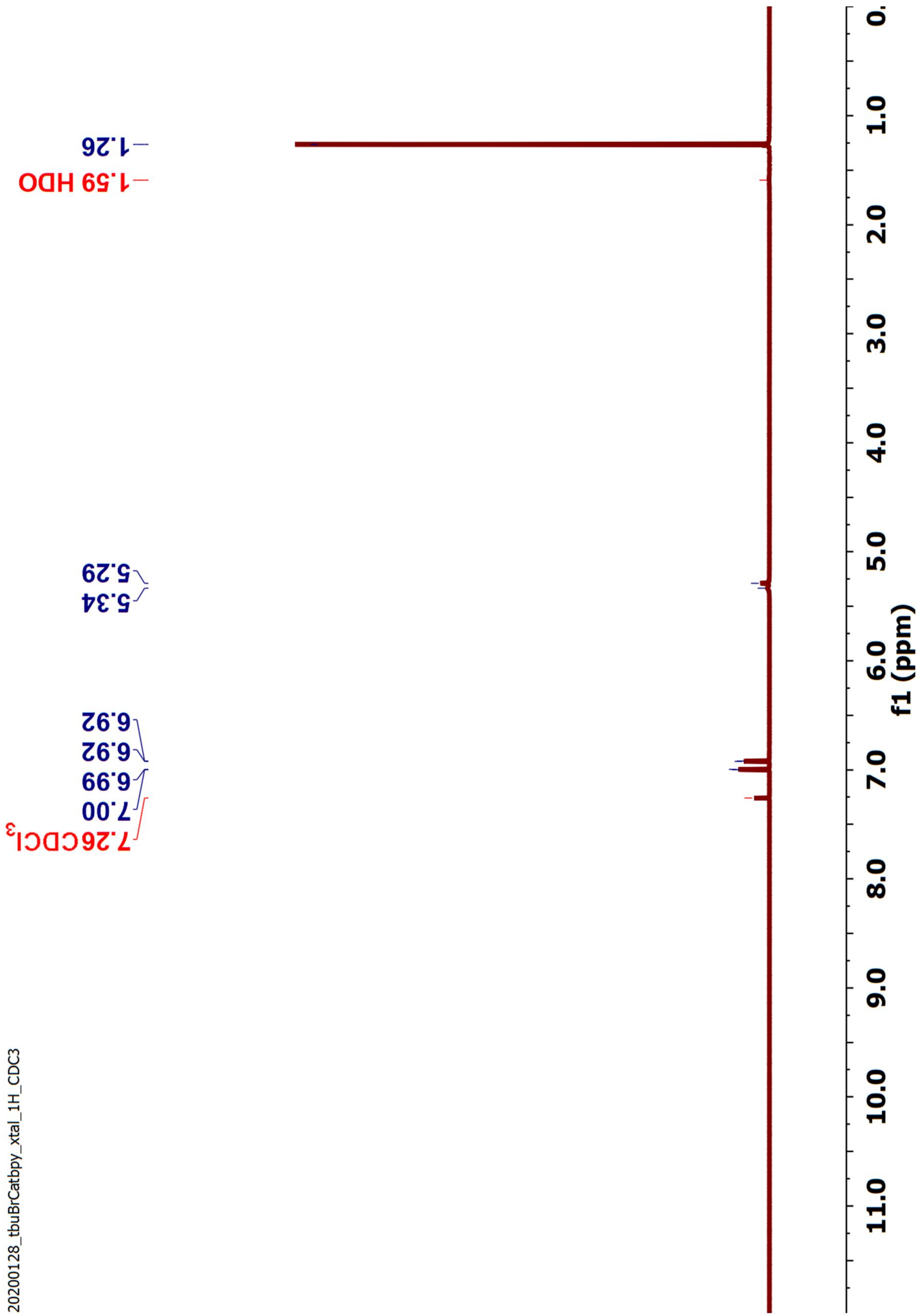

Figure S3.46. ^{1}H NMR of **VI** ($CDCl_3$, 600 MHz).

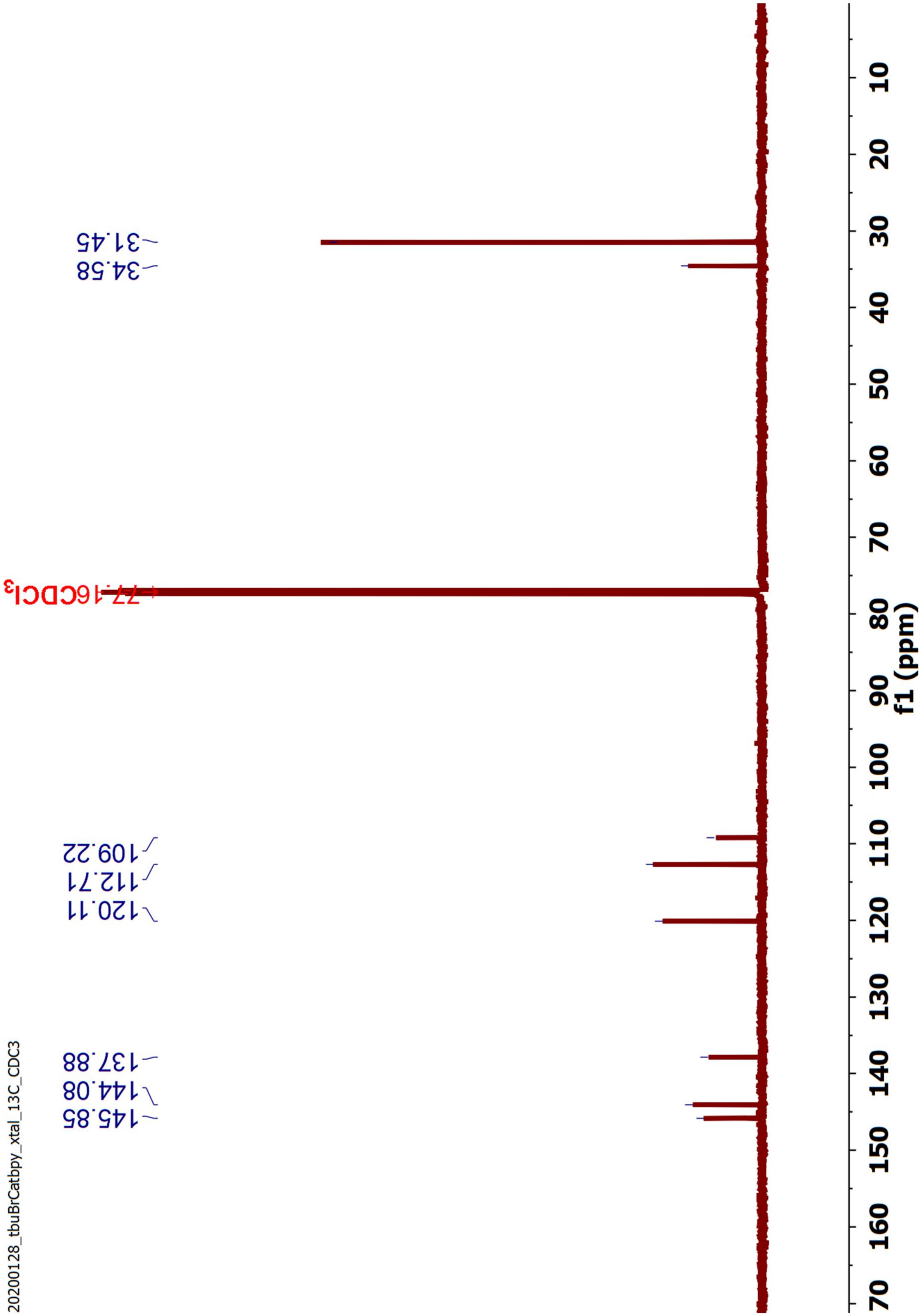

Figure S3.47. $^{13}C\{^1H\}$ NMR of **VI** ($CDCl_3$, 151 MHz).

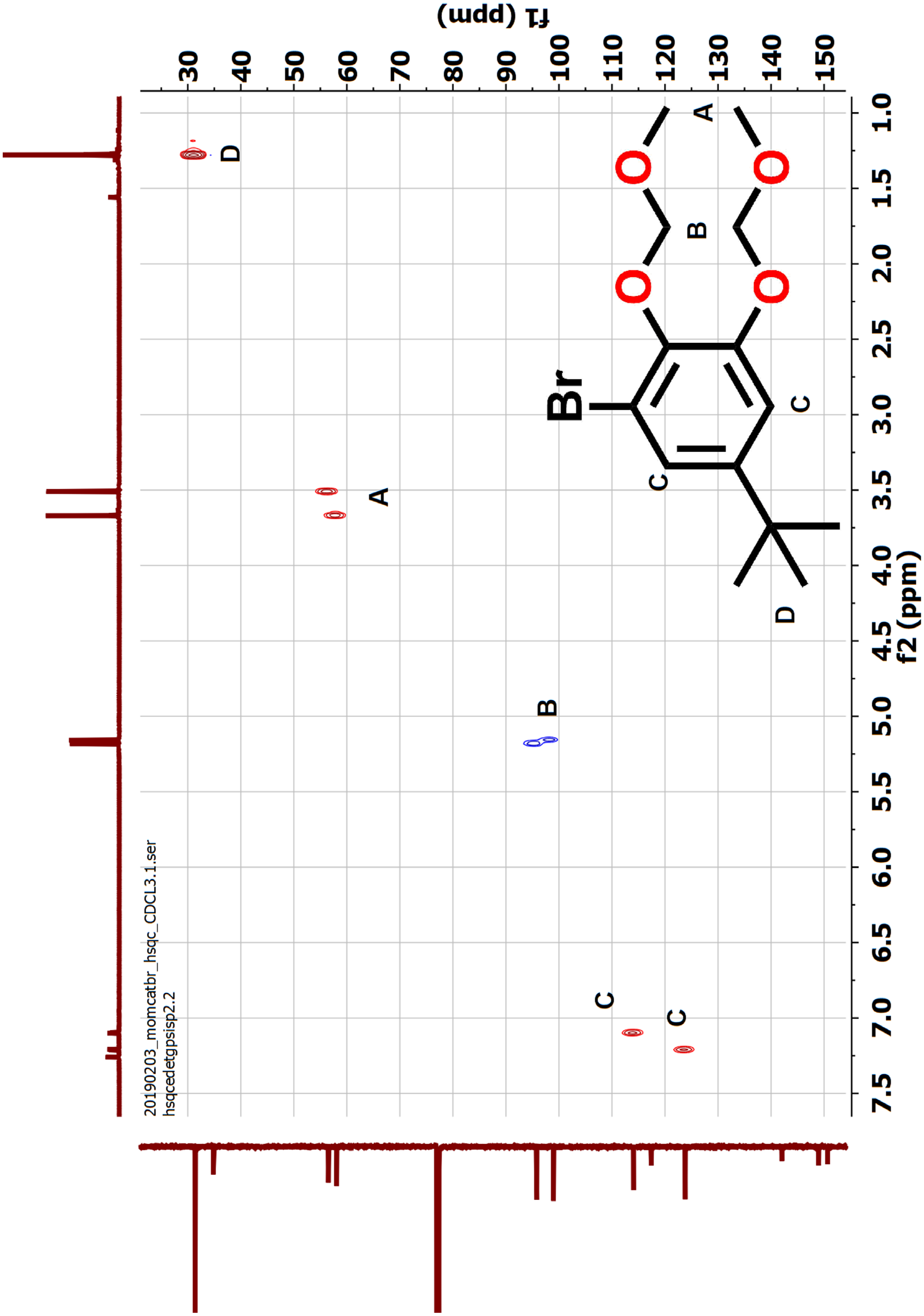

Figure S3.48. ^{1}H–^{13}C HSQC NMR of **VII** (CDCl$_3$, ^{1}H 600 MHz; ^{13}C 151 MHz).

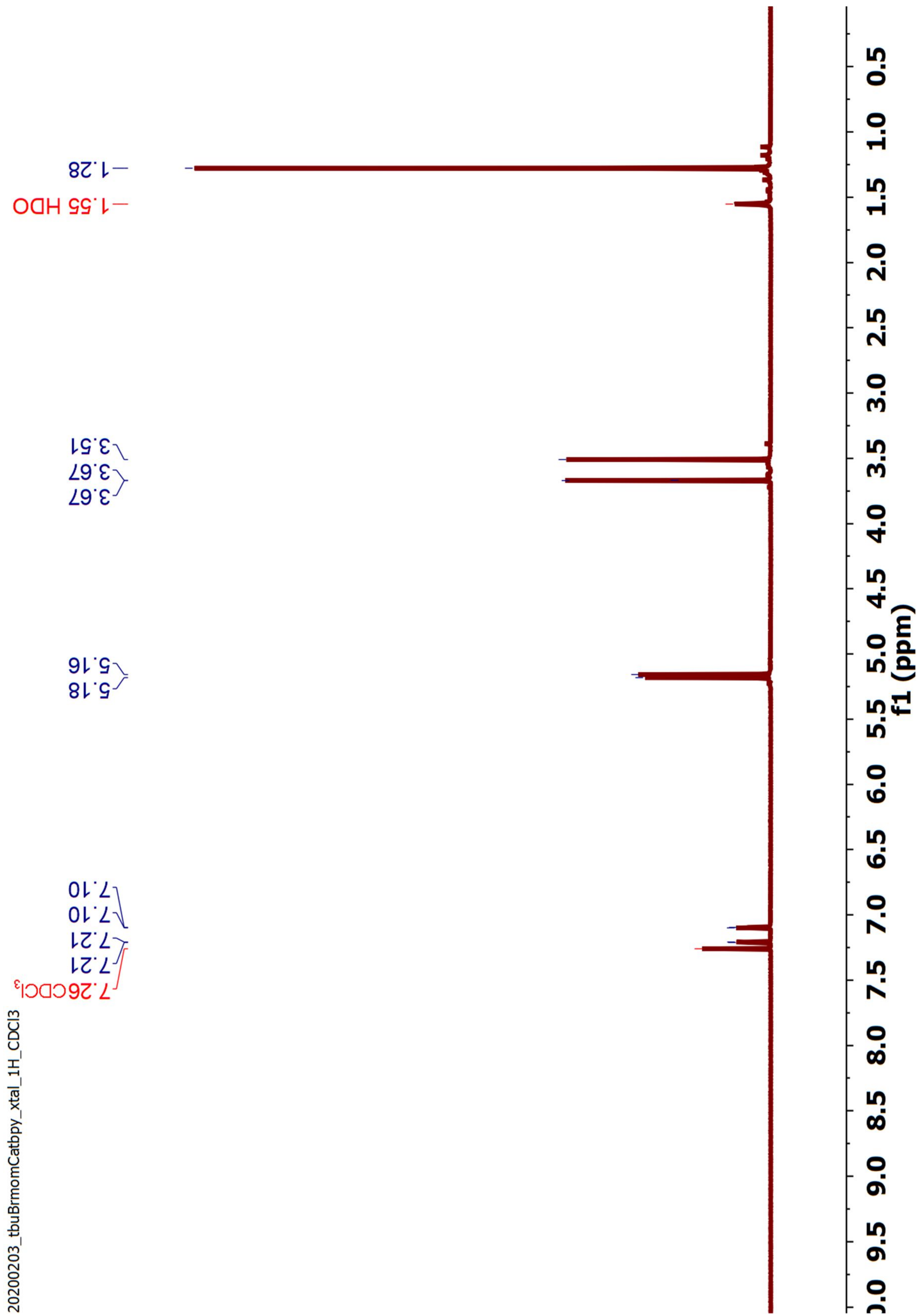

Figure S3.49. ^{1}H NMR of **VII** (CDCl$_3$, 600 MHz).

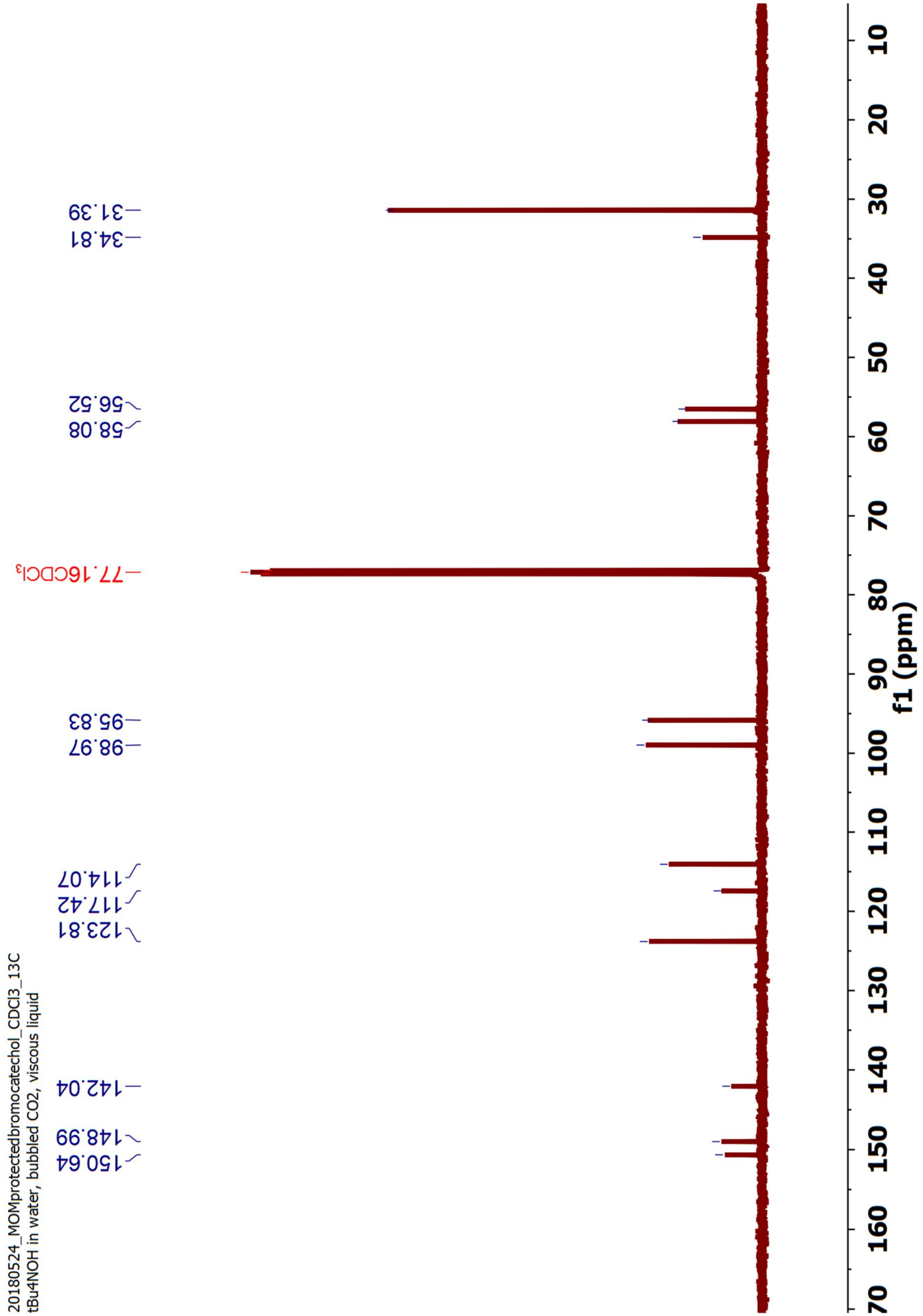

Figure S3.50. $^{13}C\{^{1}H\}$ NMR of **VII** ($CDCl_3$, 151 MHz).

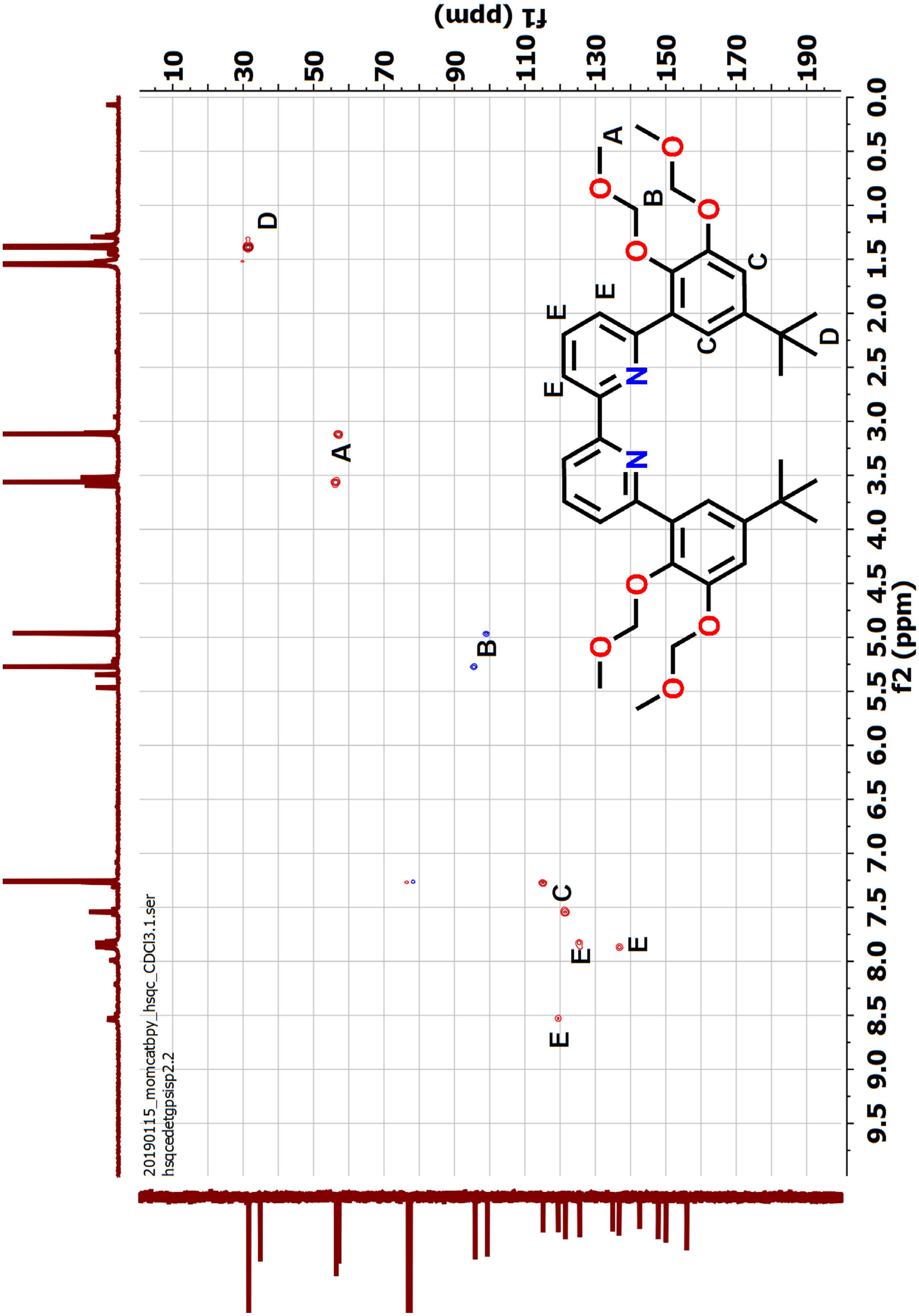

Figure S3.51. ^{1}H–^{13}C HSQC-DPT NMR of **IX** (CDCl$_3$, ^{1}H 600 MHz; ^{13}C 151 MHz).

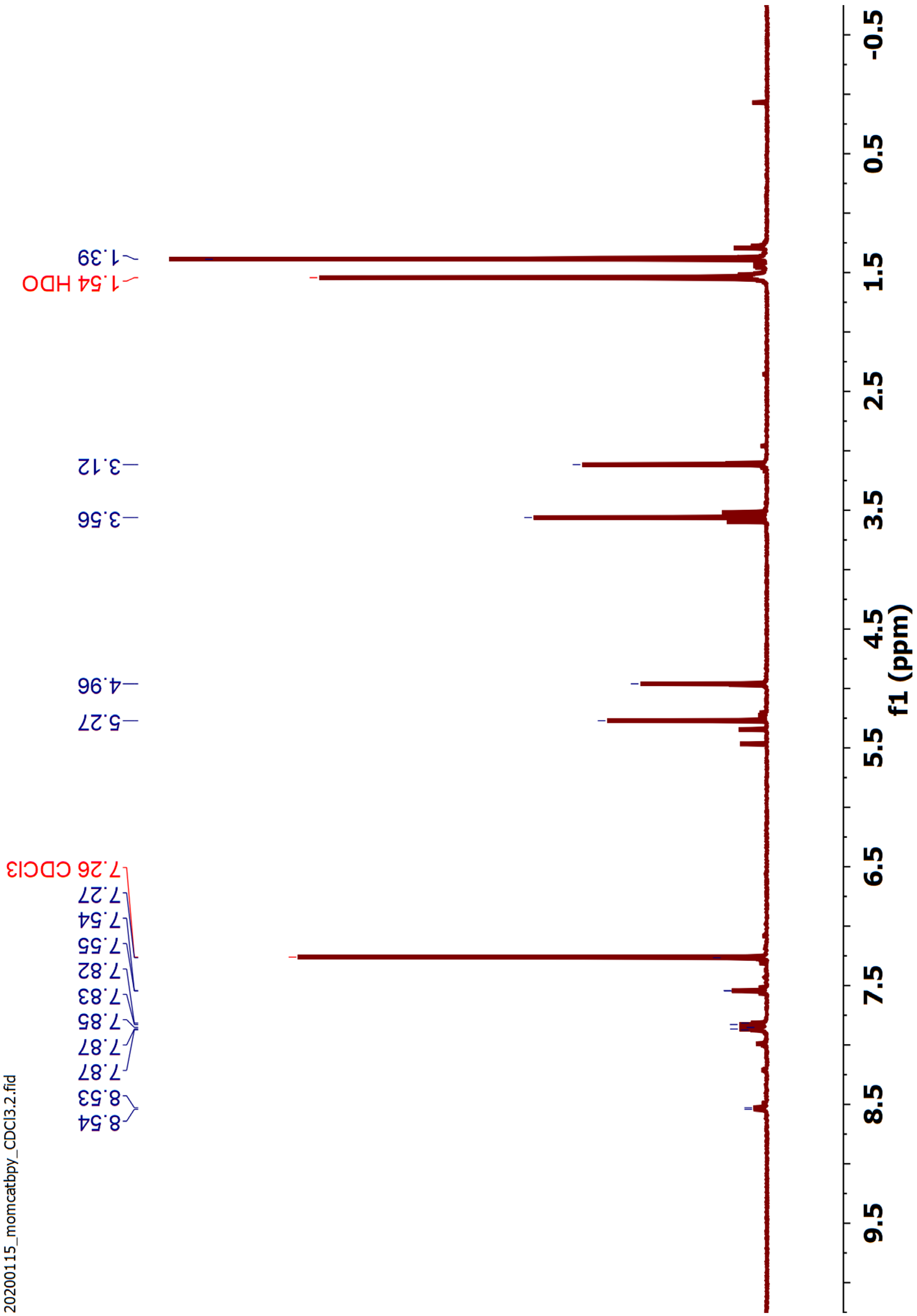

Figure S3.52. ^{1}H NMR of **IX** ($CDCl_3$, 600 MHz).

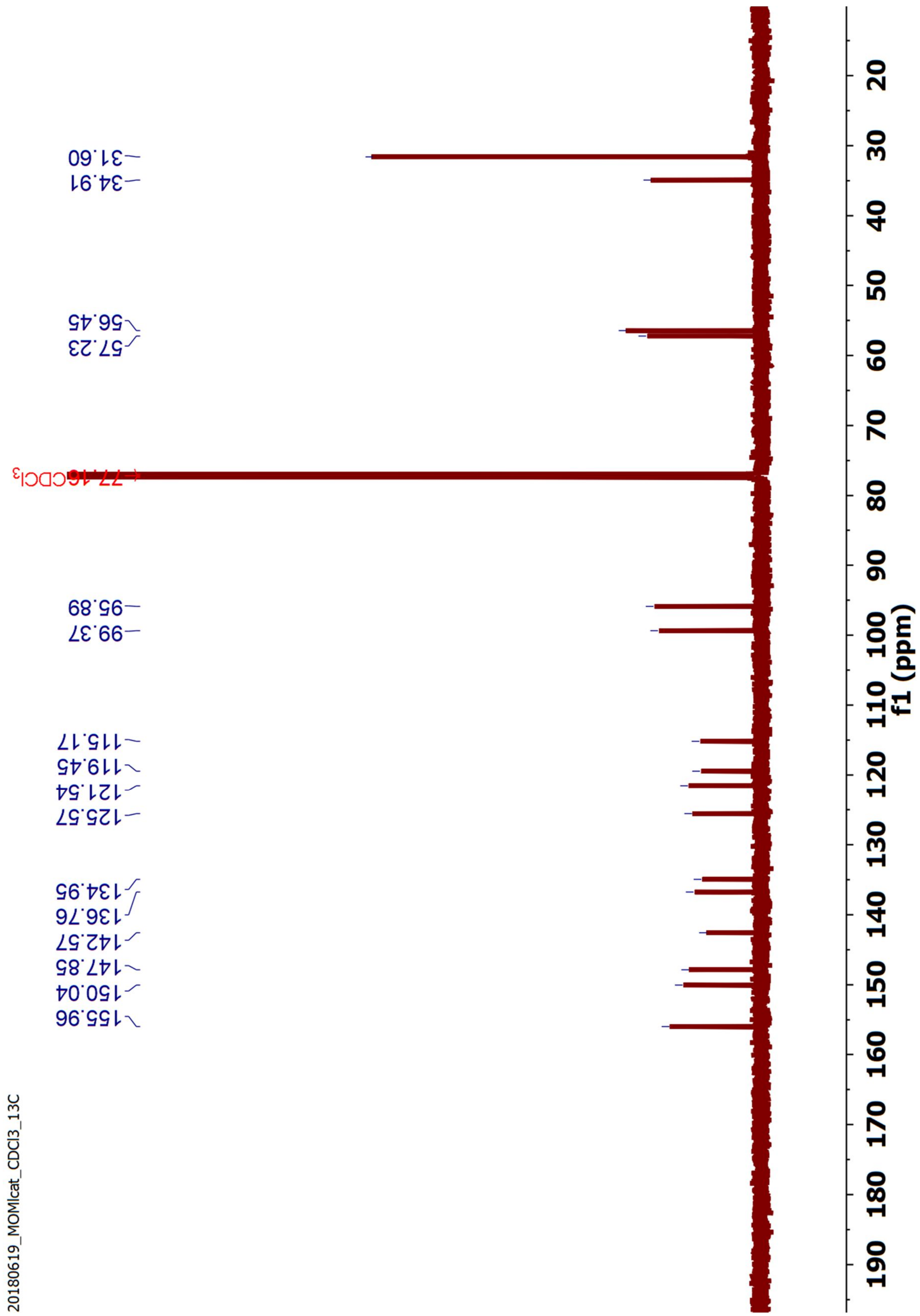

Figure S3.53. $^{13}C\{^{1}H\}$ NMR of **IX** ($CDCl_3$, 151 MHz).

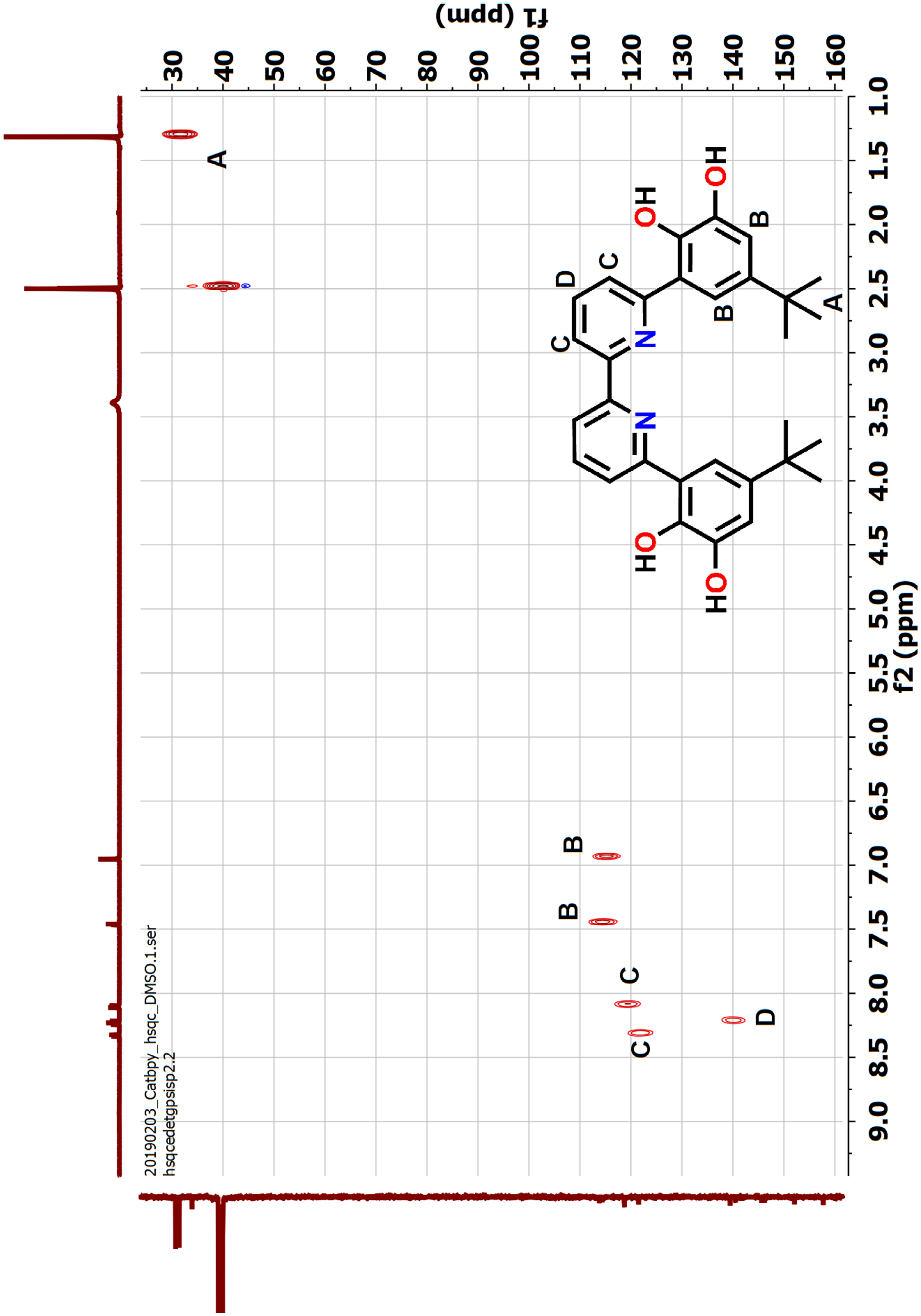

Figure S3.54. ^{1}H–^{13}C HSQC-DPT NMR of **^{tbu}catbpy** (DMSO-d_6, ^{1}H 600 MHz; ^{13}C 151 MHz).

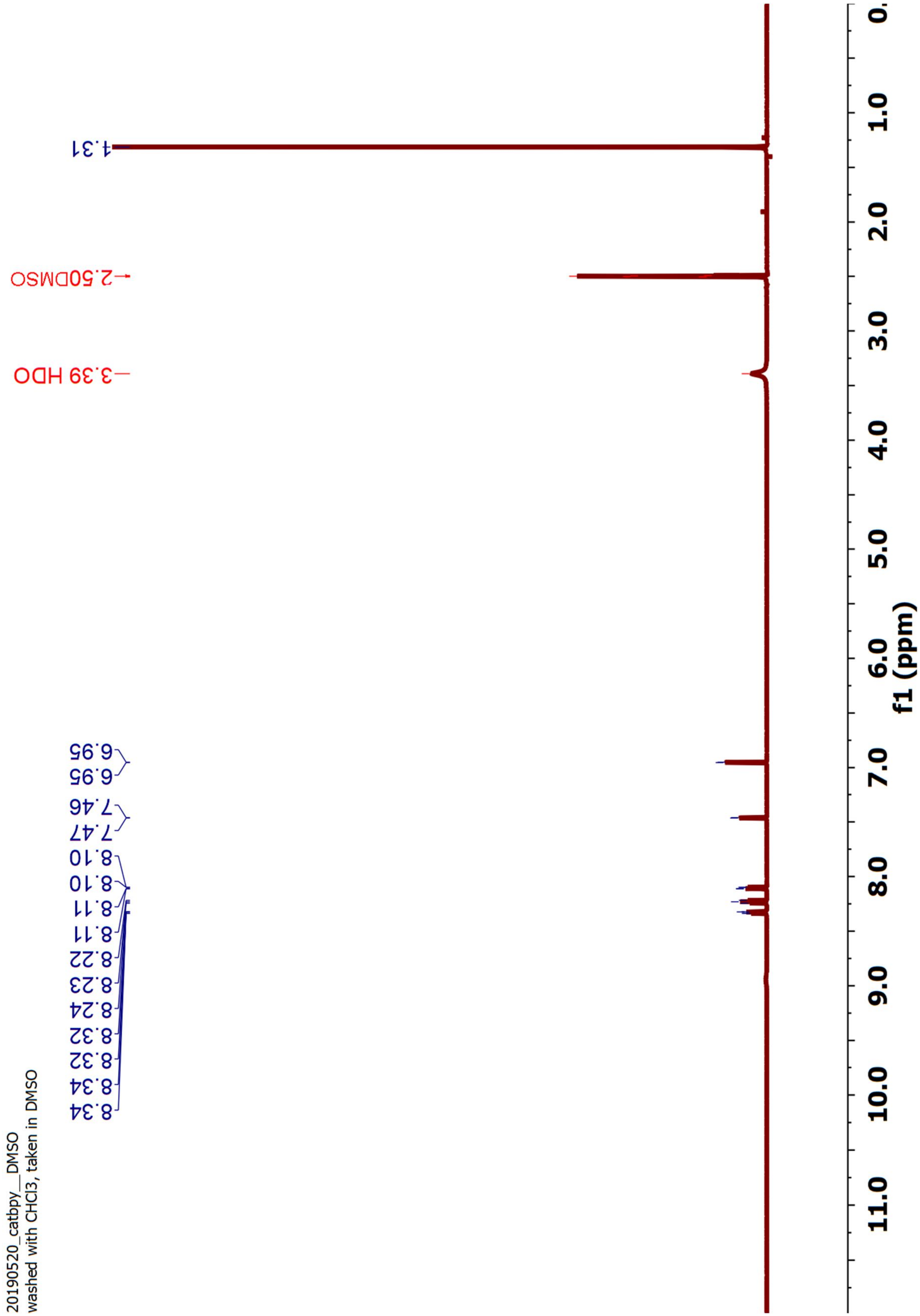

Figure S3.55. ^{1}H NMR of **$^{\mathbf{tbu}}$catbpy** (DMSO-d_6, 600 MHz).

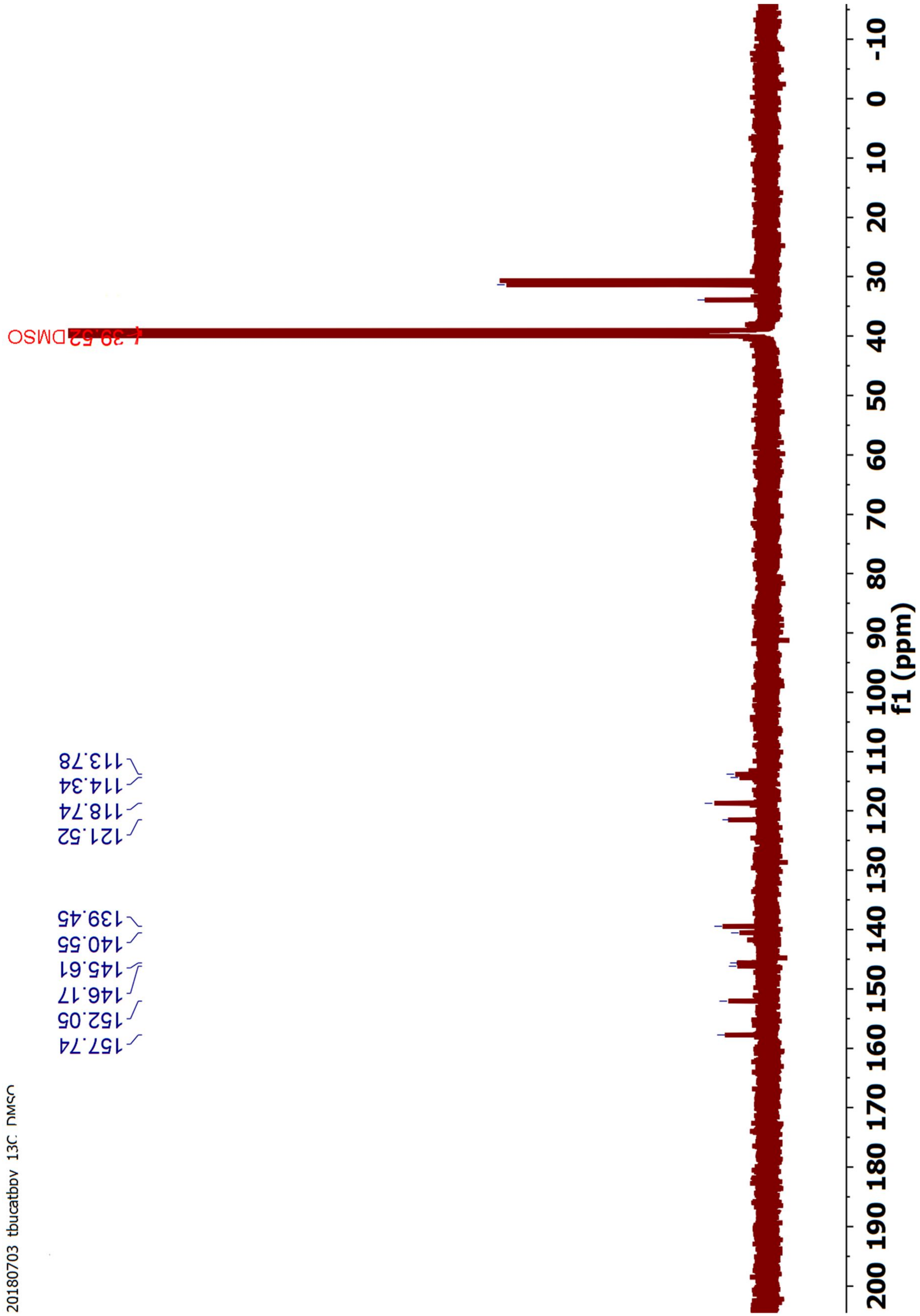

Figure S3.56. ^{13}C{^{1}H} NMR of **^{tbu}catbpy** (DMSO-*d*$_6$, 600 MHz).

Table S3.1. Average diffusion coefficient for the first reduction feature for each of the Fe complexes

Fe Complex	**Diffusion Coefficient (cm^2/s) RDE**
1	2.1×10^{-6} ($\pm 1 \times 10^{-7}$)
2	1.20×10^{-6} ($\pm 3 \times 10^{-8}$)
3	1.4×10^{-6} ($\pm 1 \times 10^{-7}$)

Table S3.2. ΔE_p and $i_{p,c}/i_{p,a}$ for **2** at the first reduction feature under various scan rates.

ν (V/s)	**ΔE_p (mV)**	**$i_{p,c}/i_{p,a}$**	**ΔE_p Cp_2*Fc (mV)**
0.1	97	0.81644	72
0.2	97	0.78578	76
0.5	105	0.96342	78
1	115	1.05517	87
2	122	1.03559	96

Table S3.3. ΔE_p and $i_{p,c}/i_{p,a}$ for **2** at the second reduction feature under various scan rates.

ν (V/s)	**ΔE_p (mV)**	**$i_{p,c}/i_{p,a}$**	**ΔE_p Cp_2*Fc (mV)**
0.1	170	1.01287	74
0.2	179	1.00365	73
0.5	201	1.00858	80
1	217	0.98877	90
2	239	0.98247	101

Table S3.4. ΔE_p and $i_{p,c}/i_{p,a}$ for **2** at the third reduction feature under various scan rates.

ν (V/s)	**ΔE_p (mV)**	**$i_{p,c}/i_{p,a}$**	**ΔE_p Cp_2*Fc (mV)**
0.1	99	0.866972	75
0.2	94	0.873759	75
0.5	96	0.917196	82
1	109	0.94919	90
2	125	0.911843	100

Table S3.5. ΔE_p and $i_{p,c}/i_{p,a}$ for **3** at the first reduction feature under various scan rates.

ν (V/s)	**ΔE$_p$ (mV)**	**$i_{p,c}/i_{p,a}$**	**ΔE$_p$ Cp$_2$*Fc (mV)**
0.1	72	1.006826	75
0.2	72	0.995181	78
0.5	71	1.004573	83
1	73	1.003185	92
2	72	0.997817	101

Table S3.6. ΔE_p and $i_{p,c}/i_{p,a}$ for **3** at the second reduction feature under various scan rates.

ν (V/s)	**ΔE$_p$ (mV)**	**$i_{p,c}/i_{p,a}$**	**ΔE$_p$ Cp$_2$*Fc (mV)**
0.1	72	0.994551	75
0.2	72	1.004357	79
0.5	74	0.998179	83
1	75	1.018182	92
2	77	0.987342	101

Chapter 4

Reduction of dioxygen to water by a Co(N_2O_2) complex with a 2,2′-bipyridine backbone

Published as: Nichols, A. W., Kuehner, J. S., Huffman, B. L., Miedaner, P. R., Dickie, D. A., Machan, C. W. *Chem. Commun*., **2021**, *57*, 516-519.

4.1 Abstract

We report a Co-based complex for the reduction of O_2 to H_2O utilizing decamethylferrocene as chemical reductant and acetic acid as a proton donor in methanol solution. Despite structural similarities to previously reported $Co(N_2O_2)$ complexes capable of catalytic O_2 reduction, this system shows selectivity for the four-electron/four-proton reduction product, H_2O, instead of the two-electron/two-proton reduction product, H_2O_2. Mechanistic studies show that the overall rate law is analogous to previous examples, suggesting that the key selectivity difference arises in part from increased favorability of protonation at the distal O position of the key intermediate Co(III)-hydroperoxide, instead of the proximal one. Interestingly, no product selectivity dependence is observed with respect to the presence of pyridine, which is proposed to bind *trans* to O_2 during catalysis.

4.2 Introduction

The reduction of dioxygen (O_2) to hydrogen peroxide (H_2O_2, $2e^-$, $2H^+$) or water (H_2O, $4e^-$, $4H^+$) is important for the development of new energy storage technologies, in the study of biological systems, and relevant to the discovery of new chemical oxidations via reactive oxygen species.[1] For the catalytic reduction of O_2 to be made more efficient, mechanistic studies are required to understand the requirements to develop molecular catalysts which operate at low overpotentials (additional energy required above the thermodynamic minimum) with high rates.[2-3]

Mononuclear cobalt N_4 macrocycles including derivatives of porphyrins,[4-14] corroles[15-16], phthalocyanines[17-21], chlorins,[22-23] and cyclam[11, 24-28] have been studied in great detail for ORR, with the majority demonstrating selectivity for H_2O_2. However, Brønsted acid scaling relationships can be used to alter product selectivity through thermodynamic bracketing.[1, 10] Cobalt complexes containing non-macrocyclic N_2O_2 salen, salophen, and acen derivatives have been known to bind dioxygen since the 1930s, but relatively few studies have been performed on their activity towards ORR (**Scheme 4.1**, top).[10, 29-34]

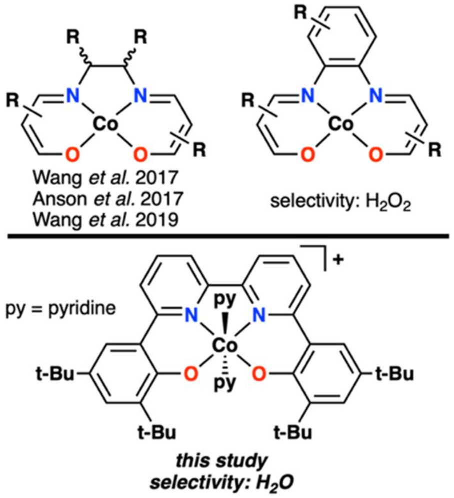

Scheme 4.1. General summary of known $Co(N_2O_2)$ catalysts for homogeneous ORR, emphasizing the known diversity of the diimine ligand backbone (top). The $[Co(^{tbu}dhbpy)(py)_2][PF_6]$ (**1**) catalyst reported here shows selectivity for H_2O (bottom).

Prior work from Stahl and co-workers has shown that $Co(N_2O_2)$ complexes are effective catalysts for the reduction of O_2 to H_2O_2 in methanol solution with acetic acid (AcOH) as a proton donor and decamethylferrocene (Cp^*_2Fe) as a chemical reductant.[31] As part of this study, the authors determined that the catalytic rate law for ORR mediated by one of the acen derivatives was overall second order, with a first-order dependence of the reaction rate on both [catalyst] and [AcOH]. The catalytic reaction exhibited no dependence on the partial pressure of O_2 (P_{O2}) due to the spontaneous formation of a Co(III)-superoxo species upon the addition of O_2 to a solution of $Co(N_2O_2)$ in MeOH.[31] Based on the observed correlation between the log(TOF) and effective overpotentials for the presented salen, salophen, and acen derivatives, as well as their identical product selectivities, they were proposed to follow the same general rate law. The rate-determining step was later proposed to be protonation of a Co hydroperoxo species at the oxygen atom proximal to the Co center to generate H_2O_2.[34]

We have previously studied the ORR utilizing a Mn complex which contained a bpy-based N_2O_2 analogue of salen/salophen ligands (^{tbu}dhbpy[H]$_2$) for the selective reduction of O_2 to H_2O_2 utilizing both electrochemical and spectrochemical methods.[35-36] Notably, prior studies from Thomas and co-workers have shown that a structurally analogous Co-based species Co(II)(^{tbu}dhbpy)(py) (pyridine = py) forms a relatively stable superoxo species.[37] Reasoning that the structural similarity between Co(II)(^{tbu}dhbpy) and Co(II)(salen), as well as their comparable ability to bind O_2, could be relevant to catalytic ORR behaviour, we synthesized **[Co(^{tbu}dhbpy)(py)$_2$][PF$_6$]** (**1**) to examine how: 1) changes in the ligand framework alter ORR selectivity and activity in comparison to other Co(II)-N_2O_2 complexes and 2) how the inclusion of axial ligands alters the rate law, selectivity, and overpotential in this family of catalysts utilizing electrochemistry and UV-vis kinetic studies. Importantly, **1** does not have the high selectivity for H_2O_2 during O_2 reduction that is observed for other reported monomeric Co(N_2O_2) complexes, displaying 71±5% selectivity for H_2O instead, while the rate law remains identical, *vide infra*.[1, 31]

4.3 Results and Discussion

4.3.1 Synthesis and Characterization of Co[(^{tbu}dhbpy)(py)$_2$][PF$_6$] (1)

Synthesis of **1** was achieved by the stoichiometric addition of Co(OAc)$_2$•4H_2O to a refluxing suspension of ^{tbu}dhbpy[H]$_2$ in MeOH. After 3 h at reflux, excess pyridine (py) and ammonium hexafluorophosphate (NH_4PF_6) were added to the reaction mixture. Following an additional 10 min under reflux, the suspension was cooled to room temperature, filtered, the volatile components were removed under reduced pressure, and the resultant solid recrystallized from a saturated methanol solution to yield a red-brown diamagnetic crystalline solid.

UV-vis spectroscopy in MeOH solution revealed three absorbances with λ_{max} at 332, 395, and 475 nm with $\varepsilon = 1.2 \times 10^3$, 1.2×10^3, and 4.1×10^2 M^{-1} cm^{-1}, respectively (**Figure S4.1**). X-ray quality crystals were obtained over the course of several days by layering of a concentrated CH_2Cl_2 solution with hexanes. Both X-ray structural data and NMR spectroscopies are consistent with a low-spin Co(III) metal center coordinated by the dianionic ^{tbu}dhbpy ligand in a tetradentate fashion about the equatorial plane of the molecule (**Figures 4.1, S4.2-S4.4**). ^{1}H NMR data obtained in d_4-MeOH demonstrate that pyridine dissociation occurs even in the Co(III) oxidation state, which we propose is facilitated by MeOH coordination (**Figure S4.5**). *Nota bene,* in the Co(II) state, it has been previously reported that this compound is stable as a five-coordinate species with a single equivalent of bound py, even when crystallized from neat py.[37] The square planar Co(II) species [Co(^{tbu}dhbpy)] was prepared according to previously reported procedures.[37]

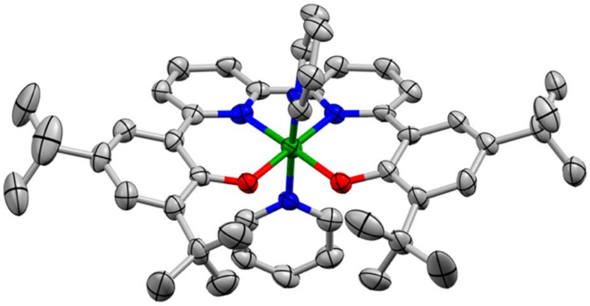

Figure 4.1. X-ray crystal structure of **1**. C = gray; N = blue; O = red; Co = green. Thermal ellipsoids set to 50%, H atoms and PF_6^- omitted for clarity, CCDC: 2035029.

4.3.2 Electrochemistry

Initial differential pulse voltammetry experiments in MeOH of **1** revealed one major species present in solution with $E_{1/2}$ = –0.23 V vs $Cp^*_2Fe^+/Cp^*_2Fe$ and two minor species located at $E_{1/2}$ = –0.01 V and 0.23 V vs $Cp^*_2Fe^+/Cp^*_2Fe$, respectively (**Figure S4.6**). Based on the ^{1}H NMR studies conducted in d_4-MeOH which show free py exists in solution (**Figure S4.5**), it is likely that the minor species correspond to the partial and/or complete substitution of axial py ligands with MeOH. All reduction potentials are located within the approximate range of previously studied $Co(N_2O_2)$ compounds, with the major reduction feature approximately 0.17 V more negative than the most reducing $Co(N_2O_2)$ complex reported for ORR.[31] CVs of **1** in the presence of 25 mM AcOH and a buffered mixture of 25 mM AcOH/tetrabutylammonium acetate (TBAOAc) buffer demonstrate minimal shifts in reduction potentials (**Figure S4.7**). Addition of 10 mM py to a fixed concentration of **1** suggests that the major reduction feature represents the $[Co(^{tbu}dhbpy)(py)_2]^+$ species in solution, since the reduction wave at 0.23 V vs $Cp^*_2Fe^+/Cp^*_2Fe$ disappears upon addition and the wave at –0.01 V vs $Cp^*_2Fe^+/Cp^*_2Fe$ decreases with a concomitant increase in current and shift towards negative potentials of the wave at –0.23 V $Cp^*_2Fe^+/Cp^*_2Fe$ (**Figure S4.8**). Overall, these observations are consistent with the proposed equilibrium between a six-coordinate Co(III) structure with two py ligands (**Figure 4.1**) and at least two other more easily reduced forms where one or two py equivalents have been displaced from **1**.[37] Kinetic and selectivity information for ORR could not be obtained through electroanalytical methods; the system operates at more negative potentials than the heterogenous ORR response of the glassy carbon electrode.

4.3.3 Spectrochemical Kinetic Studies

Catalytic ORR experiments with **1** were run under spectrochemical conditions with Cp^*_2Fe as a chemical reductant. Spectral changes in the visible region were monitored using scanning kinetics studies by following the rate of appearance of $[Cp^*_2Fe]^+$ under O_2

saturation conditions with added AcOH in methanol solution (**Figure 4.2**). Selectivity for the ORR reaction was determined via an iodometric titration using sodium iodide (NaI) as previously reported.[22, 31] A calibration curve was obtained to ensure that the method was functioning properly; the slope is within error of what is expected from the reported molar absorptivity value of I_3^- (**Figure S4.9**).[22, 31] Control experiments indicate that no H_2O_2 disproportionation occurs under catalytic conditions (**Figure S4.10**). However, in contrast to previous observations, selectivity for H_2O_2 was diminished to 29±5% for **1** (**Figure S4.11**).[31] Notably, when 20 equivalents of py were added to otherwise identical conditions, a minimal change in product selectivity for H_2O_2 (25±3%) was observed (**Figure S4.12**). Lastly, we examined the possibility of a 2+2 type mechanism, by placing **1** under anaerobic conditions with acid, the reducing agent, and urea•H_2O_2 present (**Figure S4.13**): no activity for H_2O_2 reduction was observed, 97% of the H_2O_2 remained after 30 min. Overall, these data indicate 71±5% selectivity for H_2O, corresponding to the consumption of 3.4 electrons consumed per catalyst turnover.

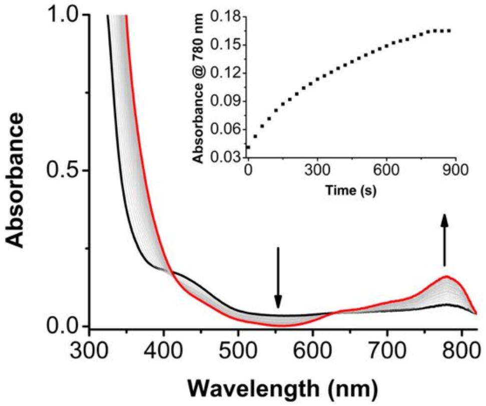

Figure 4.2. Representative UV-Vis changes under catalytic conditions in MeOH over a timeframe of 15 min. Concentrations: 40 μM **1**, 25 mM AcOH, 0.9 mM Cp^*_2Fe, 9 mM O_2.[31, 38-40] Inset: absorbance changes at 780 nm are due to the formation of $Cp^*_2Fe^+$.

The catalytic rate law was determined for the ORR by independently varying the concentrations of **1** (**Figure S4.14**), AcOH (**Figure S4.15**), Cp^*_2Fe (**Figure S4.16**), O_2

(**Figure S4.17**), and py (**Figure S4.18**) through initial rates. According to these data, the catalytic response has a first-order dependence on both [**1**] and [AcOH], and is independent of [O_2], [Cp^*_2Fe], and [py]. This is consistent with results reported previously for other Co(N_2O_2) complexes.[31, 41] The TOF was determined to be 1.03±0.03 x 10^{-2} s^{-1} (40 μM **1** and 25 mM AcOH) utilizing the data from the variable [**1**] experiment; the second-order rate constant was found to be 4.1±0.2 x 10^{-1} $M^{-1}s^{-1}$ (see **Supporting Information**).

Balanced reactions for H_2O_2 and H_2O production:

$$O_2 + 2Cp_2^*Fe + 2AcOH \xrightarrow{\mathbf{1}} H_2O_2 + 2Cp_2^*Fe^+ + 2AcO^- \quad (4.1)$$

$$O_2 + 4Cp_2^*Fe + 4AcOH \xrightarrow{\mathbf{1}} 2H_2O + 4Cp_2^*Fe^+ + 4AcO^- \quad (4.2)$$

Observed rate law:

$$rate = k_{cat}[Co]^1[AcOH]^1[O_2]^0[py]^0[Cp_2^*Fe]^0 \quad (4.3)$$

Utilizing previously reported ORR standard potentials for the production of H_2O_2 (+0.46 V vs $Cp^*{}_2Fe$)[31], we estimate the overpotential for the production of H_2O_2 as 0.69 V. Considering the difference between the standard potentials for the production of H_2O_2 and H_2O in aqueous systems (1.23 V vs NHE – 0.68 V vs NHE = 0.55 V)[31, 42-43] yields an estimated overpotential for the production of H_2O of 1.24 V. To evaluate if py was responsible for the shift in product selectivity, reactions were run with Co(salen) in the presence of two equiv of added py and the py-free Co(^{tbu}dhbpy). Co(salen) remained selective for H_2O_2 (98±4%; **Figure S4.19**) with added pyridine and Co(^{tbu}dhbpy) was 73±3% selective for H_2O (27±3% H_2O_2 detected, **Figure S4.20**). Lastly, given that py is proposed to be essential to the catalytic mechanism, the observed zero-order initial rate dependence for [py] is best described as resulting from saturation kinetics.

4.3.4 Proposed Mechanism

Based on prior reports and the experiments conducted here, we propose that the catalytic cycle mediated by **1** is initiated by the net loss of a single py ligand and one-electron reduction by an equiv Cp^*_2Fe. Subsequently, O_2 binding to the resultant five-coordinate $[Co(II)(L)(py)]^0$ species occurs to generate a formally Co(III)-superoxo species stabilized by py in the opposite axial position (**Scheme 4.2**).[37] This superoxo species is protonated and reduced through a proton-coupled electron transfer (PCET) step to generate the proposed resting state of the catalytic cycle, a Co(III)-hydroperoxo species.[31] We note that the observed first order-dependence of the initial ORR rate upon [**1**] (**Figure S4.14**) and [AcOH] (**Figure S4.15**) is consistent with the protonation of the bound Co(III)-hydroperoxo species, at the oxygen atom distal to the Co center being the rate-limiting step.[31, 34, 41, 44-45] As mentioned above, since a 2+2 type mechanism was ruled out utilizing anaerobic tests for H_2O_2 reduction, this means that the concerted four-electron/four-proton pathway to H_2O must be operative and kinetically competitive with the two-electron/two-proton pathway for the alternate product H_2O_2.

Scheme 4.2. Proposed catalytic mechanism for ORR mediated by **1** in MeOH with AcOH as a proton donor and Cp^*_2Fe as a chemical reductant. L = $[^{tbu}dhbpy]^{2-}$.

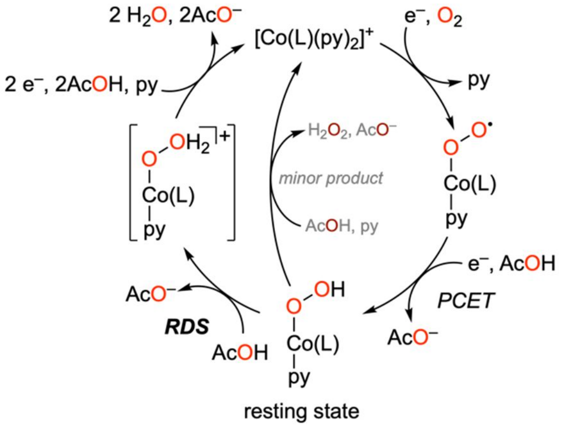

4.4 Conclusions

We have synthesized and tested a novel $Co(N_2O_2)$ complex, **$[Co(^{tbu}dhbpy)(py)_2][PF_6]$ 1**, and found it competent for the $4H^+/4e^-$ reduction of dioxygen to H_2O with 71±5% selectivity and an estimated TOF = $1.03\pm0.03 \times 10^{-2}$ s^{-1} at an overpotential of 1.24 V. The preferential reduction of O_2 to H_2O has not been previously observed for monomeric $Co(N_2O_2)$ complexes utilized for ORR in the absence of an electron–proton transfer ediator[1, 31-32, 41] and suggests further tuning of this system will allow for increased selectivity towards H_2O. We hypothesize that the stronger π-acidity of the bpy backbone relative to other N_2O_2 ligands leads to this change in selectivity. Backbonding interactions from Co-based orbitals into bpy could stabilize the key intermediate Co(III)-hydroperoxo species by accommodating stronger π donation from O to Co, disfavoring the net protonation and dissociation that generates H_2O_2.[31] In summary, we have determined that the resting state of the ORR catalytic cycle mediated by **1** is similar to previously studied $Co(N_2O_2)$ complexes, with the rate-determining step also serving as selectivity determining. Notably, py coordination plays no apparent role in product selectivity, suggesting that the primary determinant is the $[Co(^{tbu}dhbpy)]$

fragment. The relationship of the choice of axial ligand and electronic structure of the bpy backbone to the observed activity and selectivity is being examined in ongoing studies.

4.5 Supporting Information for Chapter 4

4.5.1 Experimental and Methods

4.5.1.1 General

All chemicals and solvents (ACS or HPLC grade) were commercially available and used as received unless otherwise indicated; Co(salen) was obtained from TCI America (>95.0%). For all air-sensitive reactions and electrochemical experiments, HPLC-grade solvents were obtained as anhydrous and air-free from a PPT Glass Contour Solvent Purification System, with the exception of methanol. Gas cylinders were obtained from Praxair (Ar as 5.0; O_2 as 4.0) and passed through activated molecular sieves prior to use. UV-vis absorbance spectra were obtained on a Cary 60 from Agilent. HRMS and elemental analyses were performed at the University of Virginia utilizing an Agilent 6545B QTOF and PerkinElmer 2400 Series II CHNS/O Analyser instruments. An Anton-Parr Multiwave Pro SOLV, NXF-8 microwave reactor was used for microwave syntheses. Single-crystal X-ray diffraction data was collected on a Bruker Kappa APEXII Duo diffractometer equipped with a graphite monochromator and a Mo K_α fine-focus sealed tube.

4.5.1.2 Electrochemistry

All electroanalytical experiments were performed using a Metrohm Autolab PGSTAT302N potentiostat. Glassy carbon working (⌀ = 3 mm) and non-aqueous silver/silver chloride pseudoreference electrodes behind CoralPor frits were obtained from CH Instruments. The pseudoreference electrodes were obtained by depositing chloride on bare silver wire in 10% HCl at oxidizing potentials and stored under light-free conditions in 0.1 M tetrabutylammonium hexafluorophosphate/acetonitrile solution prior to use. The counter electrode was a glassy carbon rod (⌀ = 3 mm). All CV experiments were performed in a modified scintillation vial (20 mL volume) as a single-chamber cell with a cap modified with ports for all electrodes and a sparging needle. Tetrabutylammonium hexafluorophosphate ($TBAPF_6$) was purified by recrystallization from ethanol and dried in a vacuum oven before being stored in a desiccator. All data were referenced to an internal ferrocene standard (ferricenium/ferrocene reduction potential under stated conditions) unless otherwise specified. All voltammograms were corrected for internal resistance.

4.5.1.3 Synthesis of ^{tbu}dhbpy[H]$_2$

^{tbu}dhbpy was synthesized according to our previously reported procedures.[1-2]

4.5.1.4 Synthesis of [Co(^{tbu}dhbpy)(py)$_2$][PF$_6$] (1)

A two-necked round-bottom flask (100 mL) was charged with a stir bar, ^{tbu}dhbpyh[H]$_2$ (0.150 g, 0.266 mmol), and methanol (25 mL). The suspension was capped with a septum and a condenser was attached before it was brought to reflux (65 °C) under aerobic conditions. $Co(OAc)_2$•$4H_2O$ (0.066 g, 0.27 mmol) was dissolved in minimal MeOH (~5 mL) and added to the suspension via syringe. A color change from yellow (ligand) to black was observed. After 3 h, excess pyridine (1.0 mL, 13 mmol) and NH_4PF_6 (0.216 g, 1.33 mmol) were added. Color change from black to red was observed following this addition. The suspension was allowed to reflux for an additional 10 m, then allowed to cool to room temperature. The suspension was filtered to remove excess ligand, solvent was removed under reduced pressure, and the isolated solid was recrystallized from minimal hot methanol. After 48 h in the freezer, 92 mg (44% yield) was recovered via vacuum filtration. Elemental Analysis for $CoC_{48}H_{56}F_6N_4O_2P$ Calc'd: C 62.33 H 6.10 N 6.06; Found: C 61.98

H 6.05 N 5.94. ESI-MS: Calc'd (M-2py$^+$): 621.289 Found: 621.2887 ^{1}H NMR (600 MHz): δ 8.26 (dd, 2H), 8.21 (t, 2H), 8.15 (dd, 2H), 7.67 (dd, 4H) 7.57 (t, 2H), 7.50 (2H, d), 7.44 (2H, d), 6.99 (4H, t), 1.53 (18H, s), 1.31 (18H, s).^{13}C NMR (600 MHz): δ 160.68, 158.47, 156.88, 152.02, 144.63, 140.29, 139.85, 138.39, 129.30, 125.62, 125.35, 122.70, 120.61, 115.60, 36.82, 34.62, 31.65, 31.01.

4.5.1.5 Synthesis of Co(^{tbu}dhbpy)^3

A two-necked round-bottom flask (100 mL) was charged with stir bar, ^{tbu}dhbpy(H)$_2$ (0.150 g, 0.266 mmol), and methanol (25 mL). The suspension was capped with a septum and a condenser was attached before it was brought to reflux (65 °C) under aerobic conditions. $Co(OAc)_2 \cdot 4H_2O$ (0.066 g, 0.27 mmol) was dissolved in minimal MeOH (~5 mL) and added to the suspension via syringe. A color change from yellow (ligand) to black was observed. The suspension was then refluxed for 3 h prior to cooling to room temperature. Product was obtained via vacuum filtration: 100 mg (60.6% yield). Elemental Analysis for $C_{38}H_{46}N_2O_2Co$ Calc'd: C 73.41 H 7.46 N 4.51; Found: C 73.67 H 7.50 N 4.41.

4.5.2 Figures

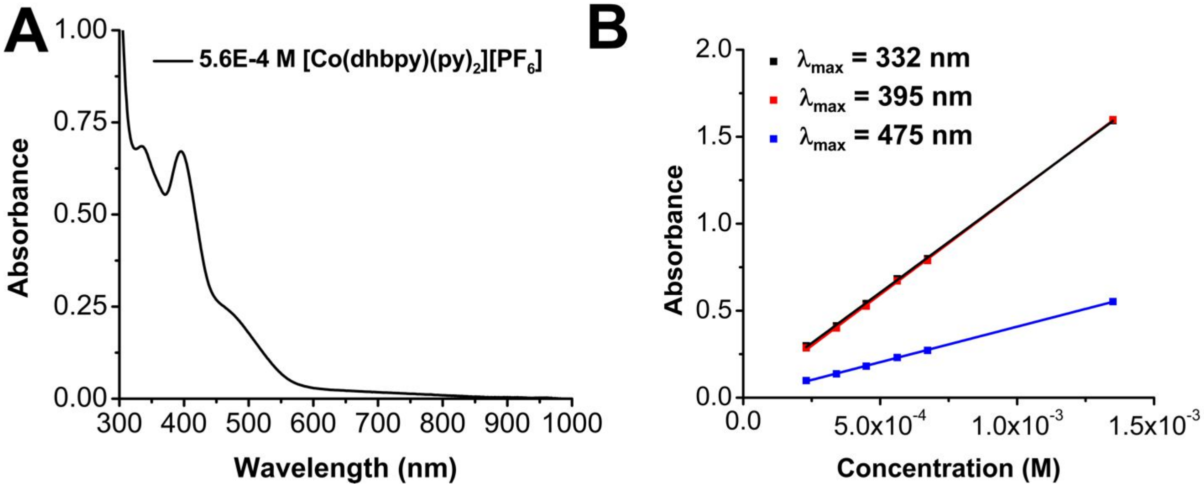

Figure S4.1. (A) UV-vis spectra of **1** in MeOH. (B) determination of ε for **1**.

Equation	y = mx + b		
		Value	**Std Err**
Abs @ 322 nm	b	2.42E-02	5.5E-03
--	m	1.16E+03	1E+01
Adj. R-Square	0.99977		
		Value	**Std Err**
Abs @ 395 nm	b	4.34E-03	6.86E-03
	m	1.18E+03	1E+01
Adj. R-Square	0.99966		
		Value	**Std. Err**
Abs @ 475 nm	b	1.08E-04	2.4E-03
	m	4.08E+02	3E+00
Adj. R-Square	0.99966		

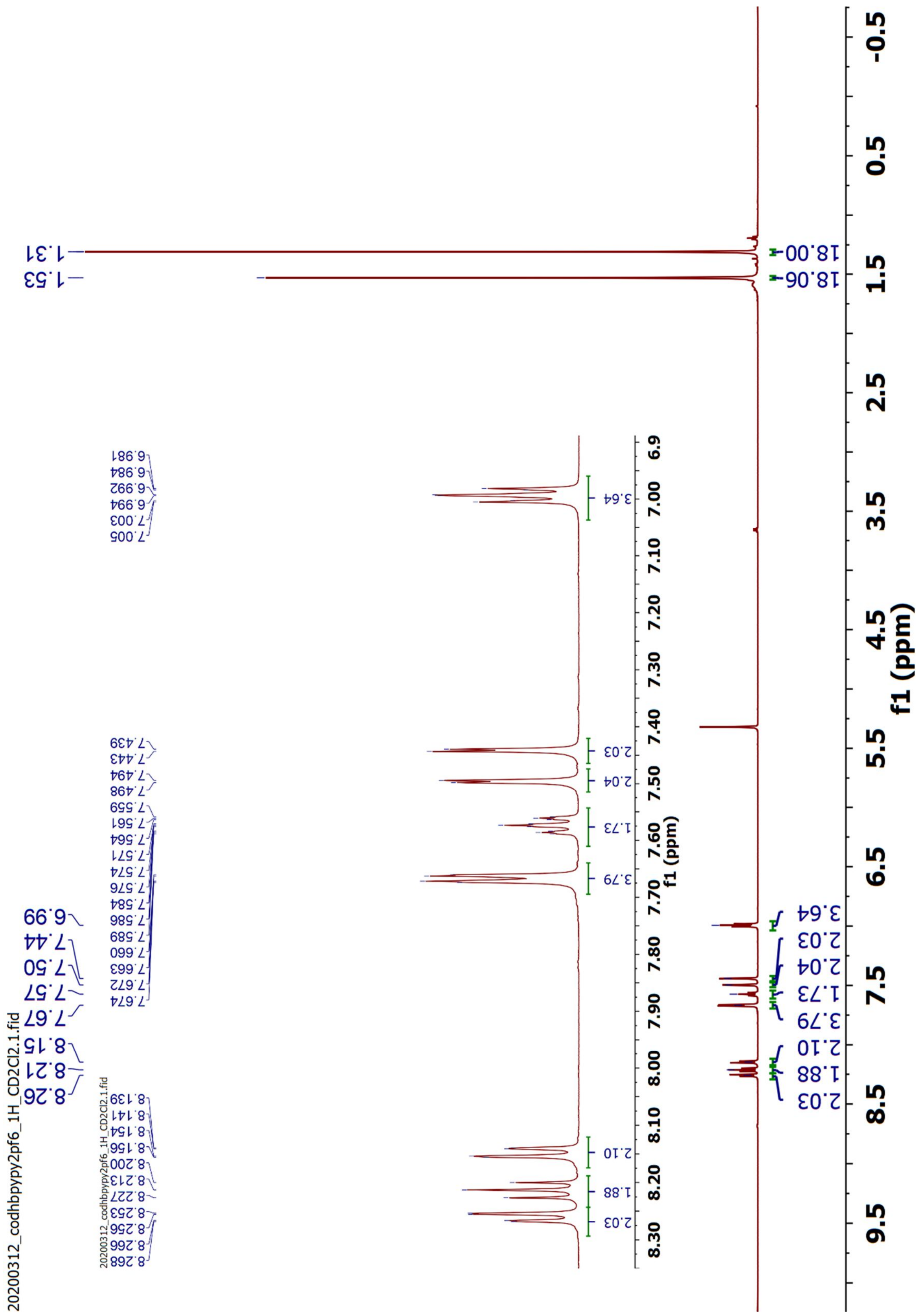

Figure S4.2. ^{1}H NMR spectra of **1** in CD_2Cl_2. (600 MHz, Varian)

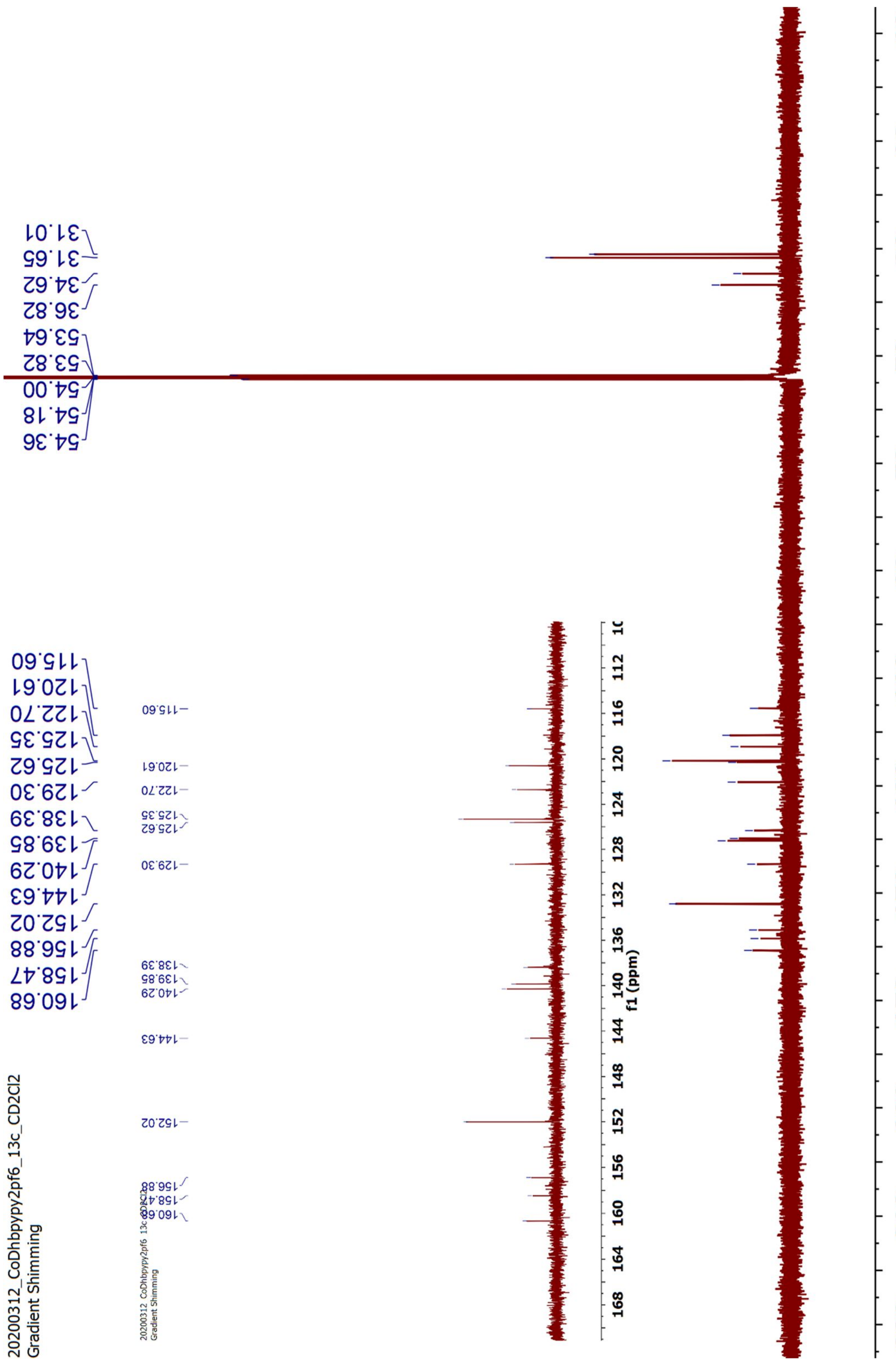

Figure S4.3. ^{13}C NMR of **1** in CD_2Cl_2. (151 MHz, Varian). Inset is region from 110-170 ppm.

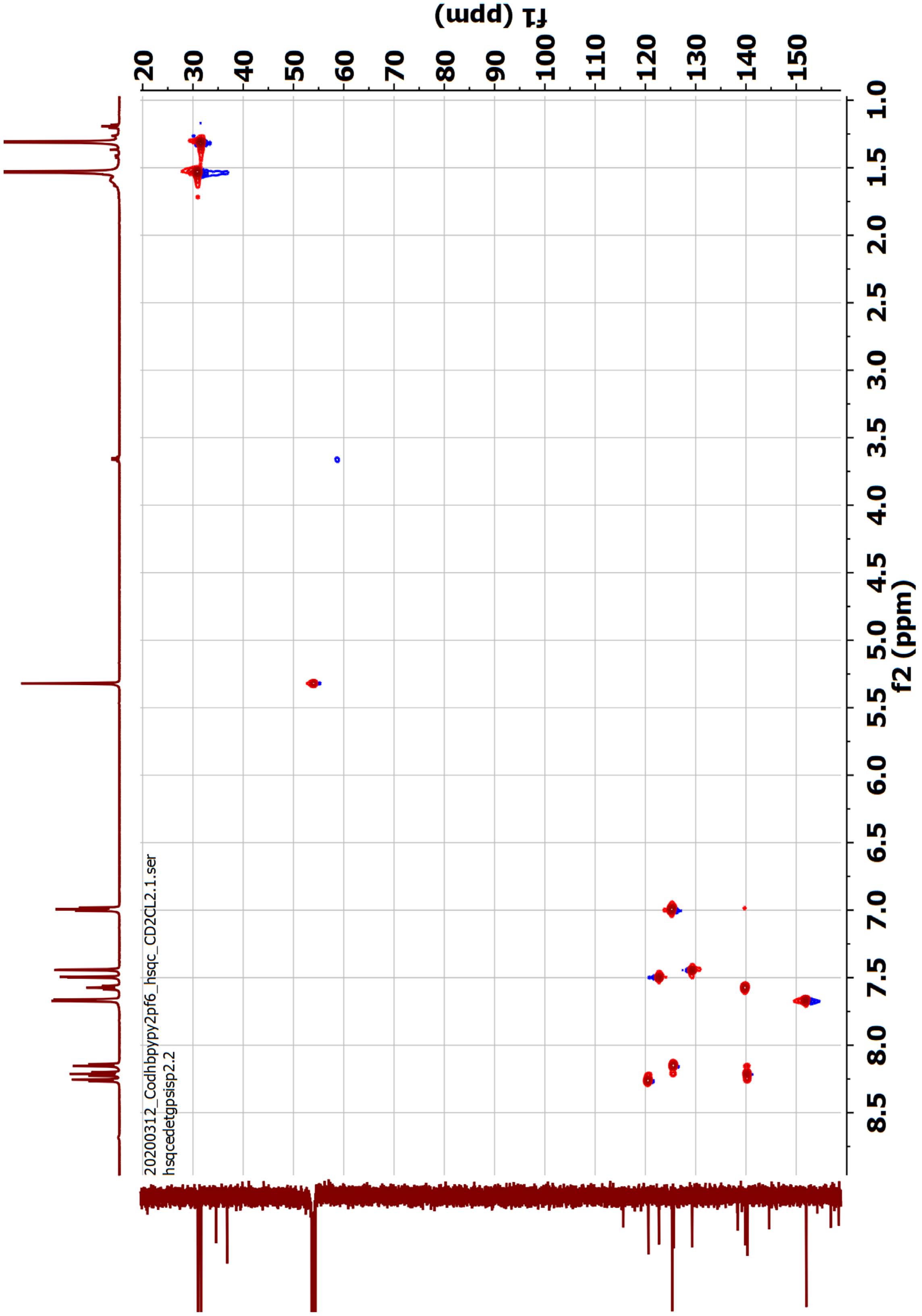

Figure S4.4. ^{1}H-^{13}C HSQC NMR of **1** in CD_2Cl_2. (^{1}H 600 MHz; ^{13}C 151 MHz, Bruker).

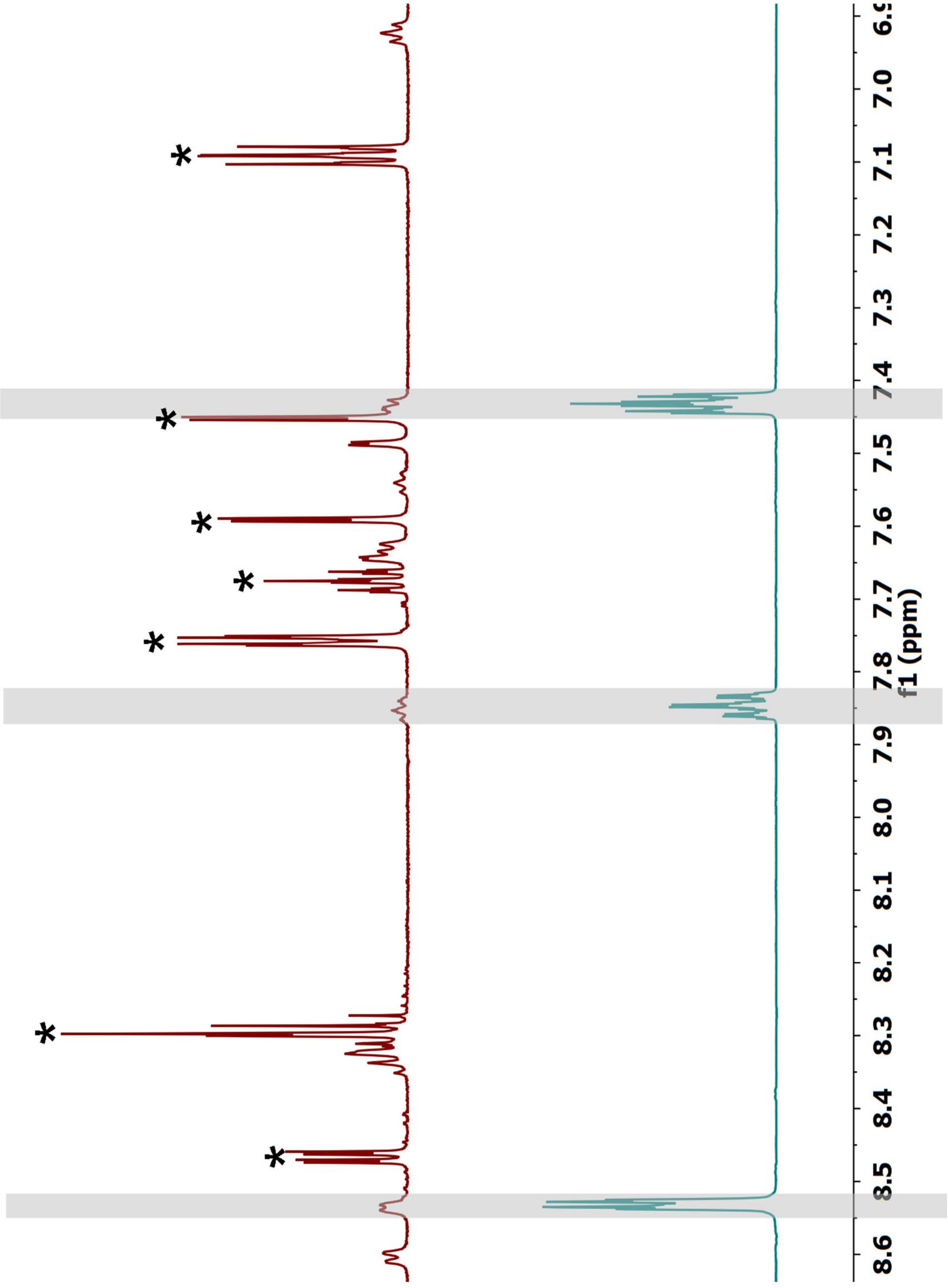

Figure S4.5. Stacked 1H NMR spectra of 1 and py in d4-MeOH. (600 MHz, Varian). Grey boxes indicate free py; asterisks indicate [Co(^{tbu}dhbpy)(py)$_2$]$^+$.

4.5.2.1 Electrochemical Experiments

Complex **1** was analyzed by differential pulse voltammetry and cyclic voltammetry in 0.1 M $TBAPF_6$/MeOH electrolyte under Ar with no additional additives, 25 mM AcOH, and 25 mM AcOH/TBAOAc buffer to ensure the redox potential did not shift upon addition of AcOH or under catalytic conditions once AcO^- is generated. Standard reduction potentials ($E_{1/2}$) were determined from DPV utilizing the Parry-Osteryoung Equation (**Eq (4.4)**)[4] where E_p is the peak potential and ΔE is the modulation amplitude:

$$E_{1/2} = E_p + \frac{\Delta E}{2} \quad (4.4)$$

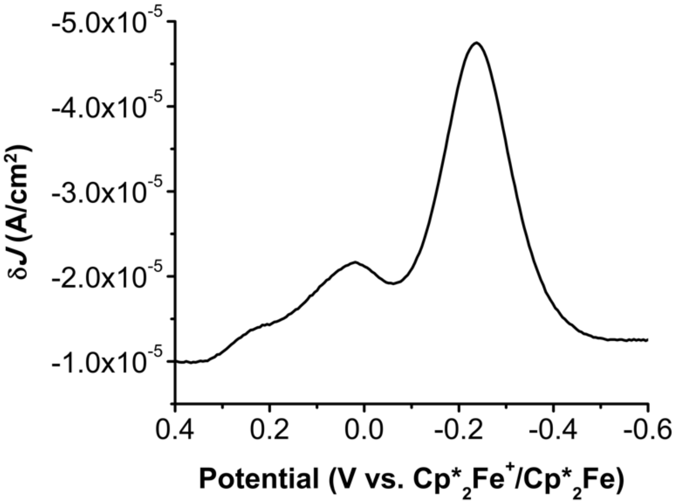

Figure S4.6. DPV of 1 mM **1** under Ar. Conditions: 0.1 M $TBAPF_6$/MeOH, glassy carbon working electrode, glassy carbon counter electrode, Ag/AgCl pseudoreference electrode, ΔE = 0.025 V, modulation time 0.01 s, interval time 0.1 s, scan rate 50.354 mV/s. Referenced to external Cp^*_2Fe solution under the same conditions.

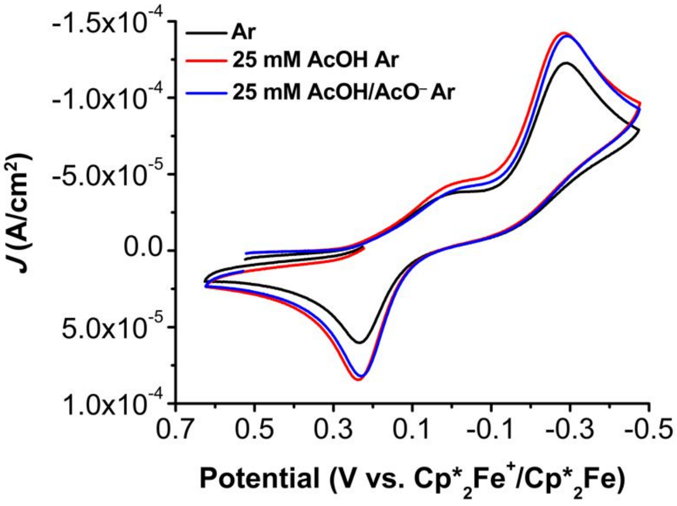

Figure S4.7. CVs of **1** under Ar (black), with added 25 mM AcOH (red), and with an added buffer comprised of 25 mM AcOH and 25 mM TBAOAc (blue). Conditions: **1** mM 1, 0.1 M TBAPF6/MeOH; glassy carbon working electrode, glassy carbon counter electrode, Ag/AgCl pseudoreference electrode, scan rate 100 mV/s; referenced to external decamethylferrocene standard.

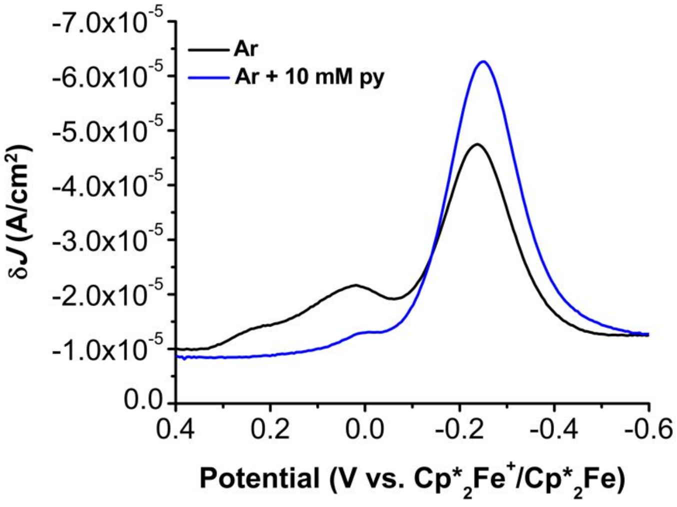

Figure S4.8. DPVs of 1 under Ar (black), and with 10 mM py under aprotic conditions. Conditions: 1 mM **1**, 0.1 M TBAPF$_6$/MeOH; glassy carbon working electrode, glassy carbon counter electrode, Ag/AgCl pseudoreference electrode, ΔE = 0.025 V, modulation time 0.01 s, interval time 0.1 s, scan rate 50.354 mV/s. Referenced to external Cp*$_2$Fe solution under the same conditions.

4.5.2.2 Iodometric Titration for Determination of Product Selectivity for ORR.

The concentration of catalytically produced H_2O_2 was determined by titration with NaI as previously reported in the literature.[5-6] A calibration curve was obtained through a serial dilution of a stock solution of urea•H_2O_2 in MeOH while monitoring the appearance of the I_3^- absorbance at 361 nm. For each dilution, 30 µL of the stock solution was added to 2.97 mL of acetonitrile (MeCN). An initial UV-vis spectrum was collected to ensure no background absorbance occurred, and then excess NaI (0.1-0.2 M) was added to the solution, and a final UV-Vis spectrum was collected after approximately 1 h.

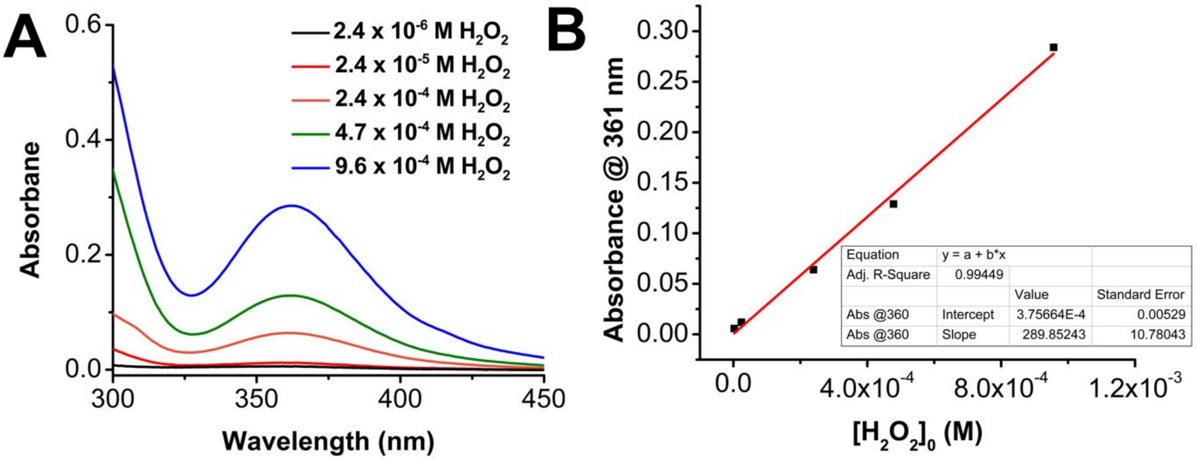

Figure S4.9. Iodometric titration calibration curve. (A) Serial dilution of urea•H_2O_2 in methanol treated using the above method for iodometric titration. (B) Calibration curve made utilizing a serial dilution of urea•H_2O_2 in MeOH, the observed slope of 290±10 is consistent with reported molar absorptivity of 2.8 x 10^4 M^{-1} cm^{-1}.

To ensure Co complex **1** does not facilitate H_2O_2 disproportionation or interfere with iodometric titrations, a known amount of urea•H_2O_2 in MeOH (0.5 mM final concentration) was added to each Co complex (40 μM final concentration) in MeOH along with 25 mM AcOH/TBAOAc buffer. These were then left for the full reaction time of a catalytic run (30 min) prior to diluting a 30 μL aliquot with 2.97 mL of MeCN. A UV-vis spectrum was collected before excess NaI (0.1-0.2 M) was added to the solution and the quantification reaction monitored utilizing scanning kinetics. The difference between the final and initial traces was taken at 361 nm, and used to quantify the final H_2O_2 concentration. With no cobalt complex present, 98% of the H_2O_2 was recovered; for **1**, 100% H_2O_2 was recovered.

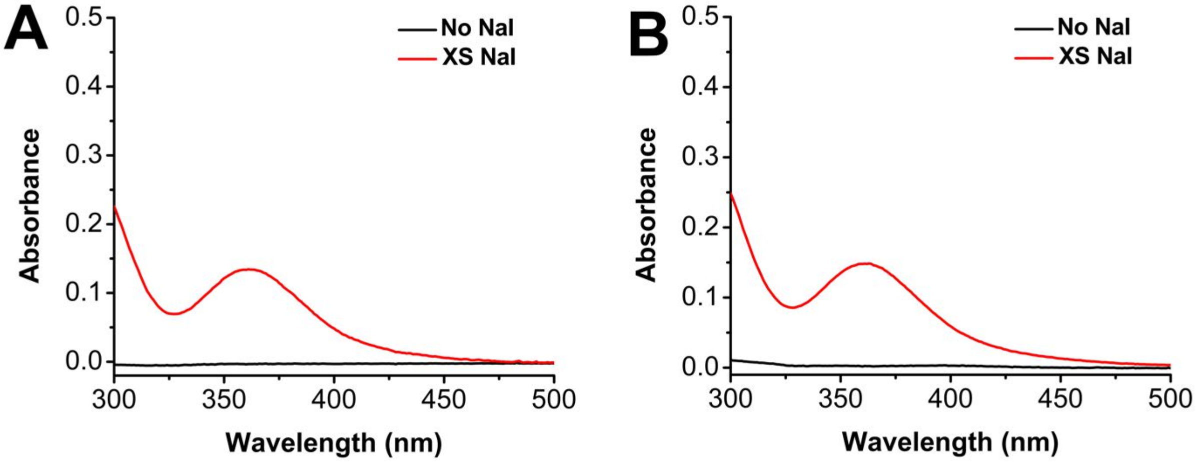

Figure S4.10. H_2O_2 disproportionation test. Iodometric titrations of MeOH solutions of 0 (A) or 40 μM (B) of **1** in the presence of 25 mM AcOH/TBAOAc and 0.5 mM urea•H_2O_2 to determine if the 1 interacted with I_3^- or urea•H_2O_2.

To determine the selectivity of **1** for the ORR reaction, catalytic reaction mixtures (40 µM Co, 0.45 mM Cp^*_2Fc, 0.9 mM O_2, 25 mM AcOH in MeOH) were run to completion (30 min) prior to obtaining a 30 µL aliquot and diluting it into 2.97 mL of MeCN. A UV-vis spectrum was obtained, and excess NaI (0.1-0.2 M) was added. The solution was then monitored by scanning kinetics to determine when a stable concentration of I_3^- had formed.

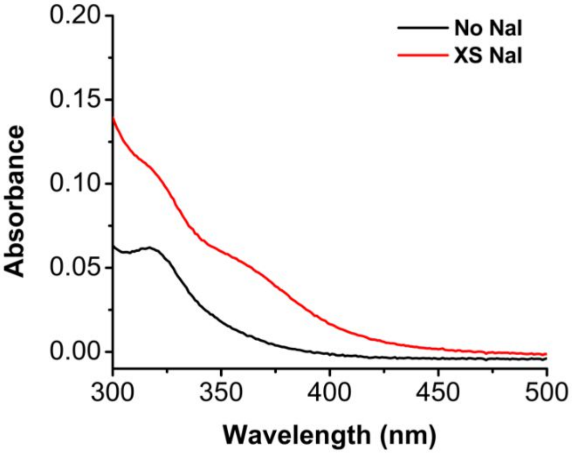

Figure S4.11. Iodometric titration of **1**. Black trace is prior to the address of NaI. Red trace is after the addition of NaI.

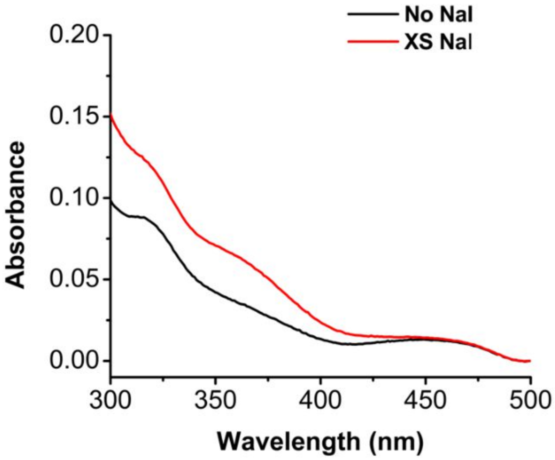

Figure S4.12. Iodometric titration of **1** in the presence of 20 equivalents of py. Black trace is prior to the addition of NaI. Red trace is after the addition of NaI.

4.5.2.3 Mechanistic Studies of the 2+2 Mechanism.

A 0.15 mL volume of 4 mM urea•H_2O_2 in MeOH was added to a 2.7 mL N_2-saturated MeOH solution containing 1 mM $Cp^*{}_2Fe$. To this mixture, a 0.15 mL N_2-saturated MeOH solution of cobalt complex **1** (800 μM) and 0.5 M AcOH was rapidly added. The reaction mixture was vigorously shaken for 30 sec and the absorbance was monitored at 780 nm by UV-vis spectroscopy, minimal changes were observed. An Iodometric titration, as described above was performed and indicated 97% of H_2O_2 remained.

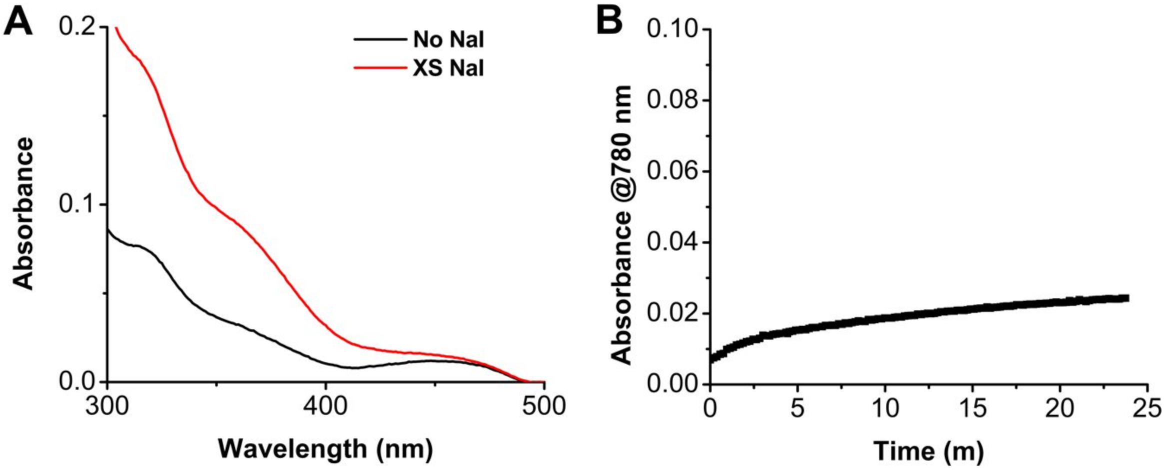

Figure S4.13. Iodometric titration of 40 μM **1** in MeOH. (A) Effect of NaI addition after 30 min reaction time in the presence of 0.9 mM $Cp^*{}_2Fe$, 0.2 mM urea•H_2O_2, and 25 mM AcOH under anaerobic conditions. (B) Monitoring of the growth of $[Cp^*{}_2Fe]^+$ at 780 nm, which indicates that a negligible amount of catalytic reduction of H_2O_2 occurs.

4.5.2.4 Determination of the Catalytic Rate Law for 1.

[**1**]

A 0.3 mL N_2-saturated MeOH solution of cobalt complex **1** (100, 200, 300, 400, and 500 μM) was rapidly added to a 2.7 mL O_2-saturated (O_2 saturation concentration in MeOH is 10 mM)[6-9] MeOH solution containing 1 mM Cp^*_2Fe before 4.2 μL AcOH was added. The reaction mixture was vigorously shaken for 30 sec and the absorbance was monitored at 780 nm by UV-vis spectroscopy. Experiments were repeated in triplicate, figure axes show final concentrations; initial rates procedure described on Page 249.[5-6]

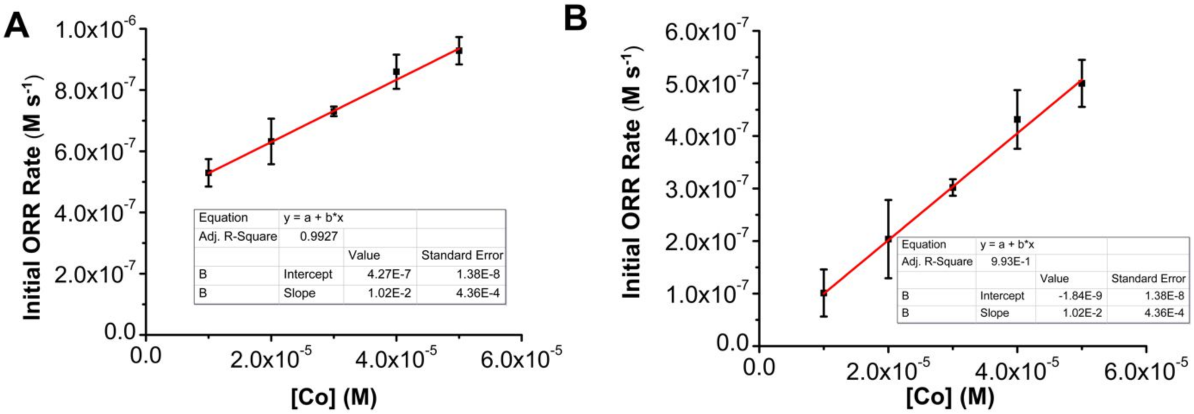

Figure S4.14. Determination of ORR reaction dependence upon [**1**]. (A) Uncorrected for background O_2 reduction. (B) Corrected for background O_2 reduction.

[**AcOH**]

A 0.3 mL N_2-saturated MeOH solution of complex **1** (400 μM) was rapidly added into a 2.7 mL O_2-saturated MeOH solution containing 1 mM Cp^*_2Fe before AcOH (0.9, 1.6, 2.6, 3.2, 5.2 μL) was added to the reaction mixture. The reaction mixture was vigorously shaken for 30 sec and the absorbance was monitored at 780 nm by UV-visible spectroscopy. Experiments were repeated in triplicate, figure axes show final concentrations; initial rates procedure described on Page 249.

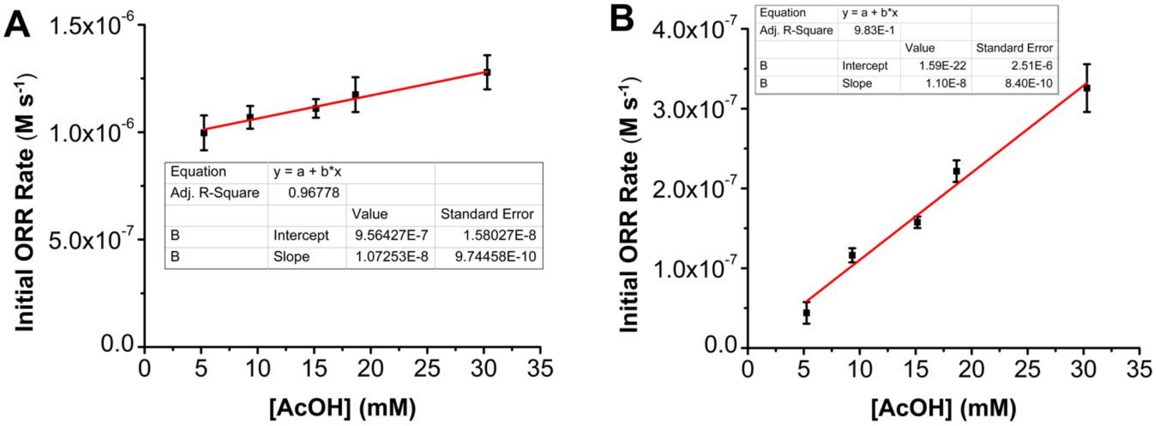

Figure S4.15. Determination of ORR reaction dependence upon [AcOH]. (A) Uncorrected for background O_2 reduction. (B) Corrected for background O_2 reduction, note that the background reaction is assumed to have minimal initial ORR rate dependence on [AcOH] relative to the reaction catalyzed by **1**.

[Cp*$_2$Fe]

A 0.3 mL N_2-saturated MeOH solution of cobalt complex **1** (400 μM) and AcOH (4.2 μL) were rapidly added into a 2.7 mL O_2-saturated MeOH solution containing Cp*$_2$Fe (0.37, 0.52, 0.63, 0.78 and 1 mM) before AcOH (4.2 μL) was added to the reaction mixture. Then the reaction mixture was vigorously shaken for 30 sec and the absorbance was monitored at 780 nm by UV-visible spectroscopy. Experiments were repeated in triplicate, figure axis shows final concentration; initial rates procedure described on Page 249.

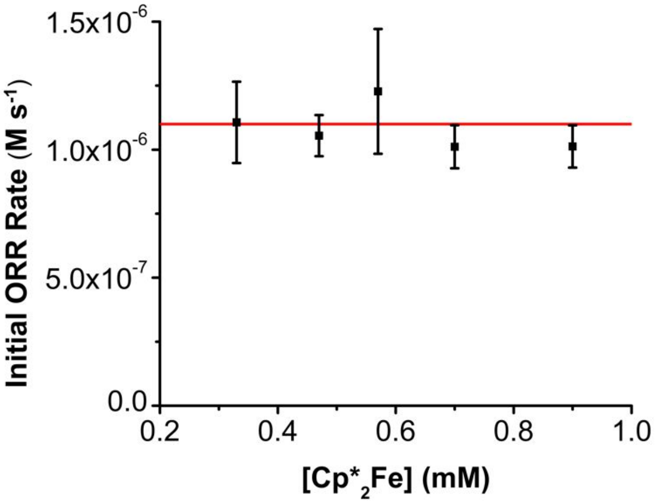

Figure S4.16. Determination of ORR reaction dependence upon [Cp*$_2$Fe]. Horizontal line represents the global average rate observed across all experiments described for variable [Cp*$_2$Fe].

[O_2]

(1) A 0.3 mL N_2-saturated MeOH solution of cobalt complex **1** (400 µM) was rapidly added into an O_2-saturated MeOH solution of 1 mM $Cp^*{}_2Fe$ before 4.2 µL of AcOH was added to the reaction mixture. Then the reaction mixture was vigorously shaken for 30 sec and the absorbance was monitored at 780 nm by UV-visible spectroscopy ([O_2] 9 mM). Experiments were repeated in triplicate, figure axis shows final concentration; initial rates procedure described on Page 249.

(2) A 0.3 mL air-saturated MeOH (20% O_2) solution of cobalt complex **1** (400 µM) was rapidly added into an air-saturated MeOH solution of 1 mM $Cp^*{}_2Fe$ before 4.2 µL of AcOH was added to the reaction mixture. Then the reaction mixture was vigorously shaken for 30 sec and the absorbance was monitored at 780 nm by UV-visible spectroscopy ([O_2] 2 mM). Experiments were repeated in triplicate, figure axis shows final concentration; initial rates procedure described on Page 249.

(3) A 1.5 mL O_2-saturated MeOH solution containing 0.9 mM $Cp^*{}_2Fe$ and 40 µM cobalt complex **1** was mixed with a 1.5 mL N_2-saturated MeOH solution containing 0.9 mM $Cp^*{}_2Fe$ and 40 µM cobalt complex **1**. A 4.2 µL volume of AcOH was rapidly added into the above mixed solution (3 mL), then the reaction mixture was vigorously shaken for 30 sec and the absorbance was monitored at 780 nm by UV-visible spectroscopy ([O_2] 5 mM). Experiments were repeated in triplicate, figure axis shows final concentration; initial rates procedure described on Page 249.

(4) A 2 mL O_2-saturated MeOH solution containing 0.9 mM $Cp^*{}_2Fe$ and 40 µM cobalt complex **1** was mixed with a 1 mL N_2-saturated MeOH solution containing 0.9 mM $Cp^*{}_2Fe$ and 40 µM cobalt complex **1**. A 4.2 µL volume of AcOH was rapidly added into the above mixed solution (3 mL), then the reaction mixture was vigorously shaken for 30 sec and the absorbance was monitored at 780 nm by UV-visible spectroscopy ([O_2] 6.7 mM). Experiments were repeated in triplicate, figure axis shows final concentration; initial rates procedure described on Page 249.

(5) A 1 mL O_2-saturated MeOH solution containing 0.9 mM $Cp^*{}_2Fe$ and 40 µM cobalt complex **1** was mixed with a 2 mL N_2-saturated MeOH solution containing 0.9 mM $Cp^*{}_2Fe$ and 40 µM cobalt complex **1**. A 4.2 µL volume of AcOH was rapidly added into the above mixed solution (3 mL), then the reaction mixture was vigorously shaken for 30 sec and the absorbance was monitored at 780 nm by UV-visible spectroscopy ([O_2] 3.3 mM). Experiments were repeated in triplicate, figure axis shows final concentration; initial rates procedure described on Page 249.

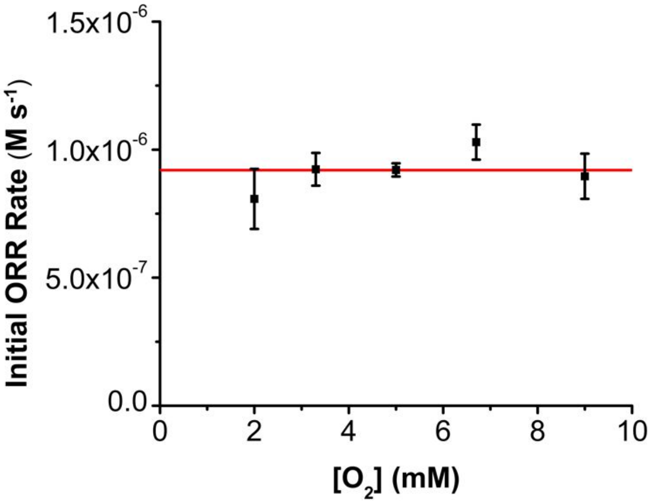

Figure S4.17. Determination of ORR reaction dependence upon [O_2]. Horizontal line represents the global average rate observed across all experiments described for variable [O_2].

[py]

A 0.15 mL N_2-saturated MeOH to solution of py (0.8, 1.6, 4.0, 8.0, and 16 mM) was added to a 2.7 mL O_2-saturated MeOH solution containing 1 mM Cp^*_2Fe. A 0.15 mL N_2-saturated MeOH solution of cobalt complex **1** (800 μM) and 0.5 M acetic acid was rapidly added. The reaction mixture was vigorously shaken for 30 sec and the absorbance was monitored at 780 nm by UV-vis spectroscopy. Experiments were repeated in triplicate, figure axis shows final concentration; initial rates procedure described on Page 248.

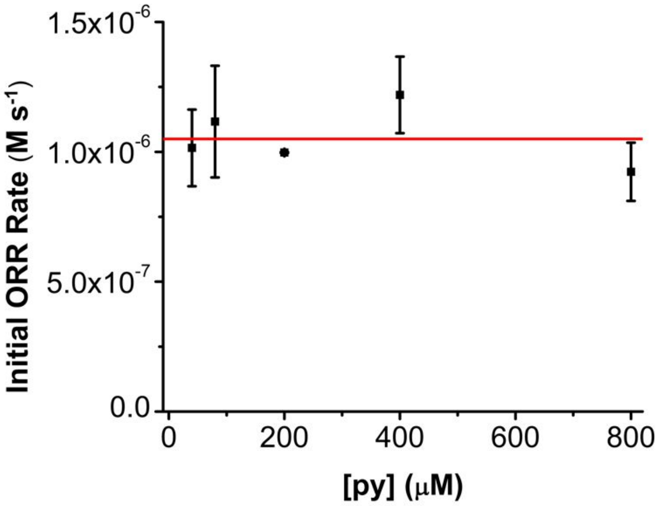

Figure S4.18. Determination of ORR reaction dependence upon [py]. Horizontal line represents the global average rate observed across all experiments described for variable [py].

4.5.2.5 Determination of rate constant, k_{cat} (adapted[6]).

The initial observed rate of ORR ($Rate_{obs}$, units of M s^{-1}) is a combination of the catalytic rate ($Rate_{cat}$) and background rate ($Rate_{background}$) of Cp^*_2Fe oxidation as follows:

$$Rate_{obs} = Rate_{cat} + Rate_{background}$$

In all cases, $Rate_{obs}$ values were obtained by taking the results of a linear fit of the initial region of $[Cp^*_2Fe]^+$ growth at 780 nm (units = relative absorbance/minute) to a minimum R^2 of 0.99. The results of the linear fit were processed to reflect the rate of ORR by converting relative absorbance units to concentration using the molar extinction coefficient of $[Cp^*_2Fe]^+$ (ε = 440 M^{-1} cm^{-1} as determined by serial dilution of a chemically prepared sample of $[Cp^*_2Fc][BF_4]$), correcting for the number of electrons passed during catalysis (n_{cat} = 3.4), and converting from minutes to seconds.

$Rate_{cat}$ is equivalent to the following based on the experimentally determined rate law:

$$Rate_{cat} = k_{cat}[\mathbf{1}][AcOH]$$

By substitution:

$$Rate_{obs} = k_{cat}[\mathbf{1}][AcOH] + Rate_{background}$$

Utilizing **Figure S4.14**, both k_{cat} and $Rate_{background}$ can be determined. At [**1**] = 0, (*y*-intercept), $Rate_{background}$ is the only observed rate, so $Rate_{background}$ = 4.3±0.2 x 10^{-7} M s^{-1} (rate of O_2 reduction). To determine $k_{cat,}$ we can simply divide the slope (Rate/[**1**]) by [AcOH] (2.5 x 10^{-2} M), giving a second-order rate constant k_{cat} = 4.1±0.2 x 10^{-1} $M^{-1}s^{-1}$.

We can also determine the TOF for this complex utilizing the individual initial rates ($Rate_{[0]}$) from this graph, subtracting the background rate, and dividing by the catalyst concentration.

$$TOF = \frac{Rate_{[0]} - Rate_{background}}{[1]}$$

This gives TOF = 1.03±0.03 x 10^{-2} s^{-1} at 0.025 M AcOH.

Using an identical procedure, an estimated $Rate_{background}$ = 9.5±0.1 x 10^{-7} M s^{-1} was obtained from **Figure S4.15**. Given that the background reaction is expected to have a dependence on [AcOH], this value was not used to determine k_{cat}, but was used as an approximate correction to establish the rate dependence of the catalytic reaction mediated by **1** as described above. We note, however, that it shows good agreement with the value obtained from **Figure S4.14**.

4.5.2.6 Py Controls for Selectivity Testing with Co(salen) and Co(^{tbu}dhbpy)

A 0.15 mL volume of N_2-saturated MeOH solution of 1.6 μM py was added to 2.7 mL of an O_2-saturated MeOH solution containing 1 mM Cp^*_2Fe. To this solution, a 0.15 mL volume of N_2-saturated MeOH solution of Co(salen) (800 μM) and 0.5 M acetic acid was rapidly added. The reaction mixture was vigorously shaken. After 30 min an iodometric titration was performed. Co(salen) with two equivalents of pyridine present was determined to be 98±4% selective for H_2O_2 under these conditions (experiments were run in triplicate).

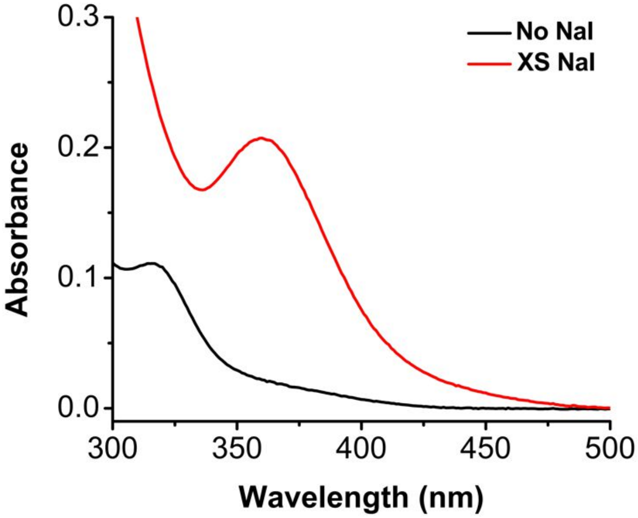

Figure S4.19. Iodometric titration of Co(salen) in the presence of two equivalents of py under conditions identical to testing of **1**.

A 20 μM solution of Co(^{tbu}dhbpy) was degassed for 15 minutes by bubbling with Ar. A 6.8 mg sample of $Cp^*{}_2Fe$ was placed under Ar in a round-bottom flask and 21 mL of the degassed Co(^{tbu}dhbpy) solution was added under positive Ar pressure. The solution was degassed for another 5 min. To a 3 mL aliquot of this solution, 4.2 μL AcOH was added and the mixture sparged with O_2 for 60 s. The reaction mixture was then vigorously shaken. After 45 min, an iodometric titration was performed: the reaction was determined to be 27±3% selective for H_2O_2 under these conditions (experiment was run in triplicate).

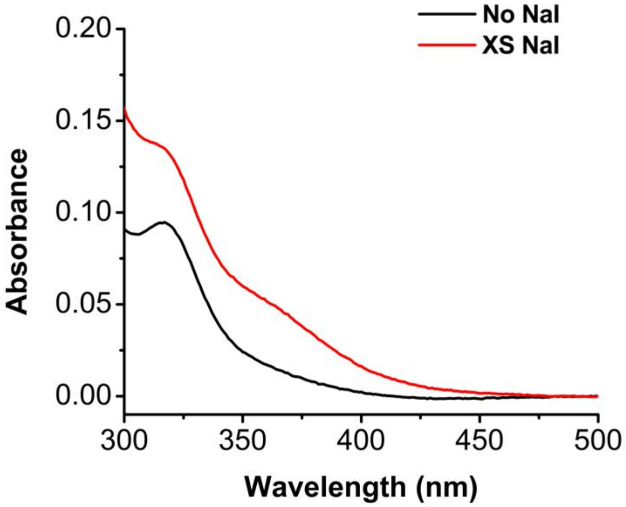

Figure S4.20. Iodometric titration of 20 μM **Co(^{tbu}dhbpy)** in the presence of 25 mM AcOH and O_2 saturation.

Chapter 5

Reduction of Dioxygen by bpy-based Co-N_2O_2 Complexes: Optimizing Efficiency for Water and H_2O_2

Submitted as: Nichols, A. W.; Miedaner, P. R.; Cook, N.C.; Machan, C. W. **2021**.

5.1 Abstract

Generally, cobalt-N_2O_2 complexes show selectivity for hydrogen peroxide during electrochemical dioxygen (O_2) reduction. We recently reported a Co(III)-N_2O_2 complex with a 2,2′-bipyridine-based ligand backbone which showed alternative selectivity: H_2O was observed as the primary reduction product from O_2 (71±5%) using decamethylferrocene as a chemical reductant and acetic acid as a proton donor in methanol solution. We hypothesized that the key selectivity difference in this case arises in part from increased favorability of protonation at the distal O position of the key intermediate Co(III)-hydroperoxide species. To interrogate this hypothesis, we have prepared a new Co(III) compound which contains pendent –OMe groups poised to direct protonation towards the proximal O atom of this hydroperoxo intermediate. Mechanistic studies in acetonitrile solution reveal two regimes are possible in the catalytic response, dependent on added acid strength and the presence of the pendent proton donor relay. In the presence of stronger acids, the complex containing pendent relays becomes O_2 dependent, implying a switch to a protonation-assisted O_2 binding step. Interestingly, selectivity for H_2O without a pendent relay is high in MeCN (81-100%), while the relay instead results in primarily H_2O_2 (76-87%), despite no quantifiable difference between the standard reduction potential of the two catalysts.

5.2 Introduction

The reduction of dioxygen (ORR) to water (H_2O, $4e^-$, $4H^+$) or hydrogen peroxide (H_2O_2, $2e^-$, $2H^+$) is important for the development of new technologies for energy storage, understanding dioxygen-dependent biological systems, and the development of new oxidative chemical transformations via reactive oxygen species.[1-2] Understanding reaction mechanisms and controlling selectivity between the two pathways is vital: for both energy storage and the biological systems like cytochrome *c* oxidase (C*c*O), H_2O is the desired product.[3-5] In energy storage technologies, the generation of H_2O_2 or other reactive oxygen species can be damaging to the cell-dividing membranes.[3-4] While H_2O is the desired product for the study of energy conversion and biomimetic use of ORR to simultaneously drive chemical oxidation reactions, the selective generation of reactive oxygen species or hydrogen peroxide is an attractive route to the discovery of new direct oxidation reactions using O_2 as the terminal oxidant.[2]

The study of molecular Co complexes for the reduction of dioxygen (O_2) has been examined extensively with N_4 macrocyclic ligand frameworks, including derivatives of porphyrins,[6-16] corroles,[17-18] phthalocyanines[19-23], chlorins,[24-25] and cyclam,[13, 26-30] with the majority demonstrating selectivity for H_2O_2. For certain catalysts, Brønsted acid-scaling relationships have been used to alter product selectivity through thermodynamic bracketing; by thermodynamically excluding the H_2O_2 pathway through the tuning of proton activity, a selectivity switch to H_2O is observed.[1, 12]

Cobalt complexes containing non-macrocyclic N_2O_2 salen, salophen, and acen derivatives were recently examined by Stahl and coworkers and found to be competent catalysts for the reduction of O_2 to H_2O_2 in methanol (MeOH) solution with acetic acid (AcOH) as a proton donor and decamethylferrocene (Cp^*_2Fe) as a chemical reductant.[31-33] However, our own report employing a bipyridine-based Co(III)(N_2O_2) complex **[Co(^{tbu}dhbpy)(py)$_2$][PF$_6$]** (**1**) showed selectivity for the production of H_2O (71±5%) under identical conditions (**Figure 5.1**).[34] Here, $[^{tbu}\text{dhbpy}]^{2-}$ = 6,6′-di(3,5-di-*tert*-butyl-2-phenolate)-2,2′-bipyridine and py = pyridine. We hypothesized that the Co(III) hydroperoxo resting state was resistant to net protonation and H_2O_2 release due to stronger *π*-backbonding of the Co center with the bpy backbone relative to other N_2O_2 ligands. The relative decrease in electron density at Co from *π*-backbonding into the bpy fragment allows the hydroperoxo moiety to donate more *π* electron density to Co, favoring protonation at the distal O atom relative to the Co center and directing product selectivity towards two equivalents of H_2O.

The study of secondary-sphere effects based on hydrogen-bonding motifs in O_2 reduction stems from an understanding of similar effects in bioinorganic processes like the C*c*O mechanism. In C*c*O, selectivity is proposed to derive from hydrogen atom transfer from a tyrosine residue to O_2 bound at a heterobimetallic active site, yielding a tyrosyl radical, Fe(IV)(O), and a Cu(II)(OH) species as the result of net O–O bond cleavage.[35] This proposed mechanism has led to the development of a variety of "hangman"-type designs where hydrogen-bonding residues are placed above the active site of catalysis and facilitate O_2 binding, often leading to enhanced rates of O–O bond scission through interaction with the distal O atom of intermediate O_2 adducts.[36-39]

In this work we take a different approach: hydrogen-bond acceptor –OMe moieties are placed such that they can direct protonation towards the proximal O atom of O_2 fragments bound to Co in a similar fashion to a strategy we have previously used to enhance electrocatalytic CO_2 reduction to formate.[40] Here we present the synthesis, characterization, and ORR reactivity of **$[Co(^{pro}bpy)(py)_2][PF_6]$**, **2** (**Figure 5.1**) and its comparison to **1** in acetonitrile (MeCN) employing benzoic acid derivatives (AH) with varying proton activity, where $[^{pro}bpy]^{2-}$ = 6,6′-di(3-methoxy-5-*n*-propyl-2-phenolate)-2,2′-bipyridine. While **1** demonstrates higher selectivity for H_2O (81-100%) than our original report with AcOH, **2** has comparable selectivity for H_2O_2 (76-87%) with faster turnover frequencies (TOFs). Complex **2** also undergoes a change in mechanism at high proton activities, with the observed rate showing a dependence on [O_2]. To the best of our knowledge, comparable kinetic control for H_2O_2 with high efficiency has not previously been demonstrated for homogeneous ORR catalysts.

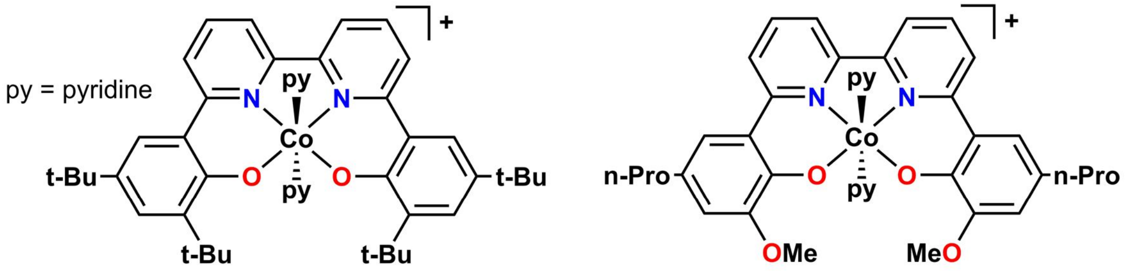

[Co(^{tbu}dhbpy)(py)$_2$][PF$_6$], 1
MeCN: 81-100% selectivity H_2O
MeOH: 71% selectivity H_2O

[Co(^{pro}bpy)(py)$_2$][PF$_6$], 2
MeCN: 76-87% selectivity H_2O_2
MeOH: 91% selectivity H_2O_2

Figure 5.1. Summary of complexes studied in this work and their ORR selectivity.

Both complexes operate at lower overpotentials than our previous work in MeOH. Consistent with the proposed kinetic relay effect, although **1** and **2** have identical standard reduction potentials, vastly different product selectivity is observed under otherwise identical conditions. Further, examining **2** in MeOH solution also results in near quantitative production of H_2O_2, demonstrating that the inclusion of pendent relay can switch the system between the selective production of either reaction product regardless of solvent and proton donor activity.

5.3 Results

5.3.1 Synthesis and Characterization

The synthesis of ^{pro}bpy[H]$_2$ was completed through modification of our previously reported procedure (**Supporting Information**).[40] Isolation of **2** was achieved by adding equivalent amounts of ^{pro}bpy[H]$_2$ and Co(OAc)$_2$•4H_2O to a refluxing MeOH solution, followed by the addition of excess pyridine and ammonium hexafluorophosphate. After a 16h reflux, the solution was cooled to room temperature, filtered, and the volatile components were removed under reduced pressure. The isolated solid was recrystallized from a saturated MeOH solution to yield a red-brown diamagnetic crystalline solid. UV-vis spectroscopy in an MeCN solution (**Figure S5.1**) revealed two absorbances with λ_{max} of 253 (ε = 2.2 x 10^4 M^{-1} cm^{-1}) and 395 nm (ε = 5.9x10^3 M^{-1} cm^{-1}). Complex **1** was synthesized according to our previously reported procedure.[34]

5.3.2 Initial Reactivity Screening

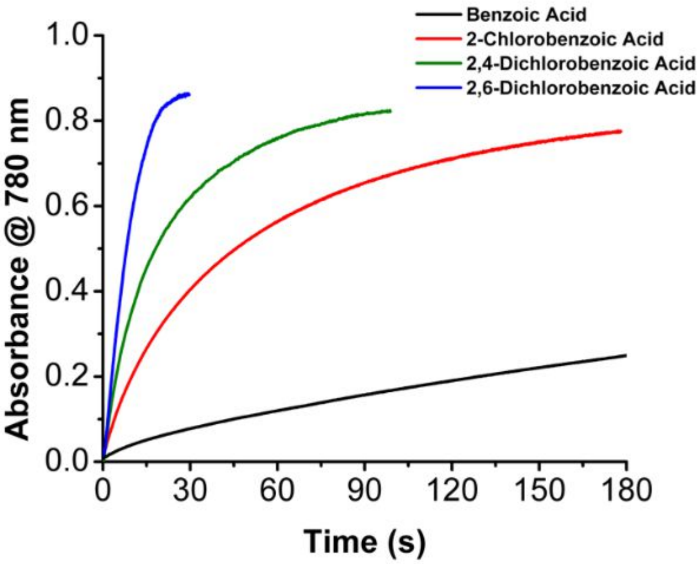

Figure 5.2. Observed changes in UV-Vis absorbance at 780 nm resulting from catalytic ORR utilizing 40 uM 2, 25 mM AH, 1.5 mM Cp^*_2Fe, and 8.1 mM O_2.

Initial testing for ORR was carried out in MeCN with decamethylferrocene (Cp^*_2Fe) and acids of varying pK_a under O_2 saturation conditions. Suitable conditions for ORR in terms of rate were found with benzoic acid (pK_a(MeCN) = 20.4).[41] A structurally homologous series of benzoic acid derivatives (AH) of increasing strength was chosen for subsequent mechanistic study: 2-chlorobenzoic Acid (pK_a(MeCN) = 19), 2,4-

dichlorobenzoic acid (pK_a(MeCN) = 18.4), and 2,6-dichlorobenzoic acid (pK_a(MeCN) = 17.6) (**Figure 5.2**).[41]

5.3.2 Electrochemistry

Differential pulse voltammetry (DPV) was employed to examine the catalytically relevant electrochemical responses of **1** and **2** under Ar and O_2 saturation. For **1**, a single reduction feature is observed with $E_{1/2}$ = –0.76 V vs Fc^+/Fc. Under aprotic conditions, O_2 saturation presents a shift in the reduction potential of **1** to –0.85 V vs Fc^+/Fc, consistent with O_2 binding (**Figure S4**). Upon the addition of the 25 mM of each AH under Ar saturation, shifts in the reduction potential of **1** of 30-50 mV towards more *negative* potentials are observed (**Figures S5-S8, Table S1**). Addition of 25 mM 1:1 buffers of each AH:A^- pair led to a shift towards negative potentials of ~0.4 V in all cases, consistent with displacement of py from Co(III) and coordination of A^- (**Figures S5.5-S5.8, Table S5.1**).

With **2**, a reduction is observed at the same potential as **1,** $E_{1/2}$ = –0.76 V vs Fc^+/Fc. Under aprotic conditions, O_2 saturation causes a positive shift in the reduction potential of **2** to –0.65 V vs Fc^+/Fc, and a second reduction event is observed at –0.94 V vs Fc^+/Fc consistent with O_2 binding and further reduction (**Figure S5.9**). Upon the addition of each of the four acids under Ar saturation, shifts in the first reduction potential of **2** of 10-20 mV towards more *positive* potentials are observed (**Figures S5.10-S5.13, Table S5.1**). Addition of 25 mM 1:1 buffers of each AH:A^- pair again led to a shift in towards negative potentials, although for **2** these amounted to only ~0.1 V in all cases (**Figures S5.10-S5.13, Table S5.1**). Note that interference from heterogenous ORR by the glassy carbon working electrode precludes electrochemical analysis of both **1** and **2** in the presence of O_2 and all of the chosen AH.

5.3.3 Selectivity

Table 5.1. Summary of selectivity for different acids with complexes 1 and 2.

AH (pK_a)	$[Co(^{tbu}dhbpy)(py)_2][PF_6]$ H_2O_2 Selectivity (n_{cat})	$[Co(^{pro}bpy)(py)_2][PF_6]$ H_2O_2 Selectivity (n_{cat})	$\eta_{H2O}{}^a$	$\eta_{H2O2}{}^a$
Benzoic Acid (20.7)	14±3% (3.72)	81±7% (2.38)	0.81	0.33
2-Chlorobenzoic Acid (19)	15±3% (3.70)	87±2% (2.26)	0.91	0.44
2,4-Dichlorobenzoic Acid (18.4)	19±2% (3.62)	81±3% (2.38)	0.95	0.47
2,6-Dichlorobenzoic Acid (17.6)	0±2% (4.00)	76±3% (2.48)	0.99	0.52

Conditions: 40 μM Co, 25 mM AH, air saturation, 0.9 or 1.5 mM Cp^*_2Fe. Values for n_{cat} are shown in parentheses. Overpotential calculations described in supporting information.
[a] - Values for η are consistent between both complexes **1** and **2**.

Selectivity for H_2O_2 was determined by a modified spectrophotometric titration method using an acidified $Ti(O)SO_4$ solution (**Figure S5.14**).[42-43] Briefly, air-saturated solutions of **1** or **2** and AH were added to an air-saturated solution of Cp^*_2Fe to give final concentrations of 40 μM catalyst, 25 mM AH, and 0.9-1.5 mM Cp^*_2Fe. For **1**, the final concentration of $[Cp^*_2Fe]^+$ was determined by UV-vis spectroscopy at 780 nm to give a theoretical concentration of H_2O_2. For **2** the reaction was allowed to run to completion based on the kinetic studies discussed below. Complex **1** is near quantitatively selective for H_2O, producing H_2O_2 in a range from 0-19% (**Table 5.1, Figures S5.15-S5.18**). This selectivity for H_2O is enhanced in comparison to our previous work with **1** in MeOH solution with acetic acid as the proton donor, suggesting that protic solutions favor the net protonation and dissociation of H_2O_2, presumably through hydrogen-bonding interactions with the protic solvent.[34]

For complex **2**, a range in H_2O_2 selectivity from 76-87% was observed (**Table 5.1, Figures S5.19-S5.22**). We postulate that the shift of selectivity is consistent with the enhancement of the rate of protonation at the proximal O atom in the bound Co(III)-hydroperoxo species relative to the distal O atom. We emphasize that there is no difference in the catalytically relevant standard potentials of **1** and **2**, suggesting that the pendent –OMe relay places the system under kinetic control during the ORR. Control experiments indicate that no H_2O_2 disproportionation occurs under catalytic conditions with either **1** and **2** for any AH (**Figure S5.23-S5.30**). Overpotentials of 0.33-0.52 V were calculated for the production of H_2O_2 **Eq (5.1)** and 0.81-0.99 V for the production of H_2O **Eq (5.2)** for complexes **1** and **2**, dependent upon AH. We emphasize again that these values are *consistent between the two complexes under otherwise identical conditions*.

Balanced reactions for H_2O_2 and H_2O production:

$$O_2 + 2Cp_2^*Fe + 2AH \overset{\text{Co}}{\rightarrow} H_2O_2 + 2Cp_2^*Fe^+ + 2A^- \quad (5.1)$$

$$O_2 + 4Cp_2^*Fe + 4AH \overset{\text{Co}}{\rightarrow} 2H_2O + 4Cp_2^*Fe^+ + 4A^- \quad (5.2)$$

5.3.4 Spectrochemical Kinetic Studies

Kinetic studies were undertaken with Cp^*_2Fe as a chemical reductant using initial rates. Spectral changes in the visible region were monitored by following the rate of appearance of $[Cp^*_2Fe]^+$ under O_2 saturation conditions with added AH in MeCN, λ_{max} = 780 nm (ε = 461 M^{-1} cm^{-1} as determined by spectrophotometric titration). Selectivity data was used to determine number of electrons transferred (n_{cat}) for each set of conditions. According to these data for **1**, the catalytic response has a first-order dependence on both [**1**] (**Figures S5.31-S5.34**) and [AH] (**Figures S5.37-S5.40**); the reaction rate is also independent of [Cp^*_2Fe] (**Figures S5.43-S5.46**) and [O_2] (**Figures S5.49-S5.52**). This catalytic rate law **eq(3)** is consistent with our previously reported results in MeOH and those for other $Co(N_2O_2)$ complexes reported in MeOH.[31-32, 34] From these variable catalyst concentration studies, TOF values were determined with 25 mM AH (**Table 5.2**). For **2**, the same rate law **Eq (5.3)** is maintained with benzoic acid and 2-chlorobenzoic acid (**Figures S5.35-S5.36**, **S5.41-S5.42, S5.47-S5.48, S5.53-S5.54**). However, with 2,4-dichlorobenzoic acid (at [O_2] < 4mM) and 2,6-dichlorobenzoic acid are added, the rate law demonstrates a first-order dependence on [**2**], [HA], and [O_2] (**Figures S5.55-S5.62**). We propose that this shift to [O_2] dependence **Eq (5.4)** is consistent with a favorable equilibrium O_2 binding, with a subsequent proton transfer step as the rate-determining one, *vide infra*.

$$rate = k_{cat}[Co]^1[AH]^1[O_2]^0[Cp_2^*Fe]^0 \quad (5.3)$$

$$rate = k_{cat}[Co]^1[AH]^1[O_2]^1[Cp_2^*Fe]^0 \quad (5.4)$$

Table 5.2. Summary of turnover frequencies (TOF) for different acids with complexes **1** and **2**.

AH (p*K*$_a$)	**[Co(^{tbu}dhbpy)(py)$_2$][PF$_6$]**	**[Co(probpy)(py)$_2$][PF$_6$]**
Benzoic Acid (20.7)	$1.1 \times 10^{-3} \pm 0.1 \times 10^{-3}$ s^{-1}	$1.0 \times 10^{-1} \pm 0.1 \times 10^{-1}$ s^{-1}
2-Chlorobenzoic Acid (19)	$1.7 \times 10^{-3} \pm 0.1 \times 10^{-3}$ s^{-1}	$3.3 \times 10^{-1} \pm 0.1 \times 10^{-1}$ s^{-1}
2,4-Dichlorobenzoic Acid (18.4)	$2.8 \times 10^{-3} \pm 0.1 \times 10^{-3}$ s^{-1}	$7.8 \times 10^{-1} \pm 0.1 \times 10^{-1}$ s^{-1}
2,6-Dichlorobenzoic Acid (17.6)	$3.1 \times 10^{-3} \pm 0.4 \times 10^{-3}$ s^{-1} (O–H) $3.0 \times 10^{-3} \pm 0.2 \times 10^{-3}$ s^{-1} (O–D)	1.9 ± 0.1 s^{-1} (O–H) 0.94 ± 0.05 s^{-1} (O–D)

Conditions: variable [Co], 25 mM AH, O_2 saturation, 1.5 mM Cp^*_2Fe. The deuterated 2,6-dichlorobenzoic acid substrate was prepared with 92% O–D substitution

5.3.5 Determination of Kinetic Isotope Effect

To elucidate the cause of differing mechanisms with **2** when a stronger proton source is present, we evaluated the kinetic isotope effect (KIE, k_H/k_D) for **1** and **2** with the strongest acid: 2,6-dichlorobenzoic acid. Catalytic reaction rates for both naturally abundant (O–H) and deuterated (O–D) 2,6-dichlorobenzoic acid substrate under variable acid concentration are summarized in **Table 5.2**. Under these conditions, KIE values of 1.2±0.1 and 2.4±0.2 were obtained for **1** and **2**, respectively (**Figure 5.3** and **Figure S5.62**).

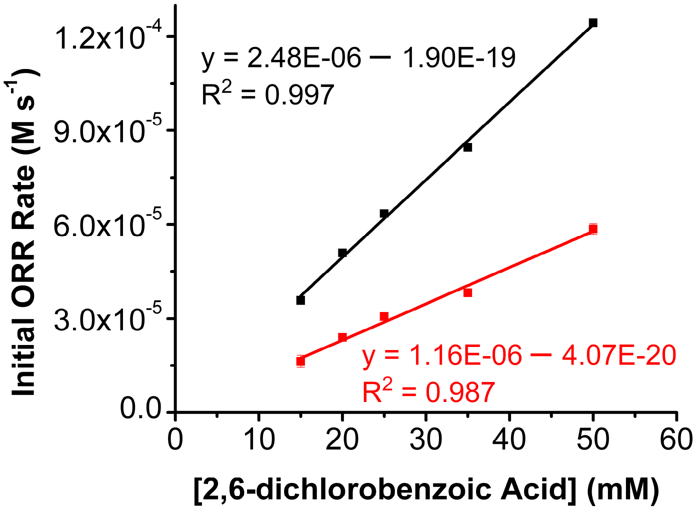

Figure 5.3. Kinetic isotope effect determination for complex **2**. Black line is with naturally abundant 2,6-dichlorobenzoic acid (O-H). Red line is with isotopically enriched (92%) d_1-2,6-dichlorobenzoic acid (O-D).

5.4 Discussion

Complex **1** maintains high selectivity for H_2O under all conditions in MeCN, while **2** was 76-87% selective for H_2O_2. This is noteworthy, *given that there is no quantifiable difference in their standard reduction potentials*. We propose the enhanced kinetic selectivity for H_2O_2 with **2** is the result of the alkyl ether pendent relay enhancing proton transfer to the proximal O atom of a Co(III)(OOH) intermediate, accelerating H_2O_2 dissociation. The consequences of an overall increased protonation rate are also observed in the change in the rate law when stronger acids are utilized with **2**. With complex **1**, the rate is dependent only on [Co] and [AH] for all added acids (**Figure 5.4A**). With complex **2**, the rate is dependent on only [Co] and [AH] for weakest acids: benzoic acid and 2-chlorobenzoic acid. Once 2,4-dichlorobenzoic acid and 2,6-dichlorobenzoic acid are used as a proton source, the rate becomes dependent on [O_2]. Based on these observations, we propose that resting state of catalysis for **2** (**Figure 5.4B**) with the stronger acids shifts to $[Co(II)(^{pro}bpy)(py)_2]^+$ (***i***), where a subsequent favorable equilibrium reaction with O_2 precedes rate-limiting protonation. The absence of a concentration dependence on the added reductant suggests that this step is no longer a PCET reaction and that proton transfer precedes electron transfer to generate (***iii***). From (***iii***) protons are directed more towards the proximal O atom by the pendent –OMe groups, resulting in the net protonation and dissociation of H_2O_2 (**Figures 5.4B and 5.5**). Stronger proton donors have a stronger hydrogen-bonding interaction with the secondary-sphere –OMe groups, leading to an enhancement of rate.[44]

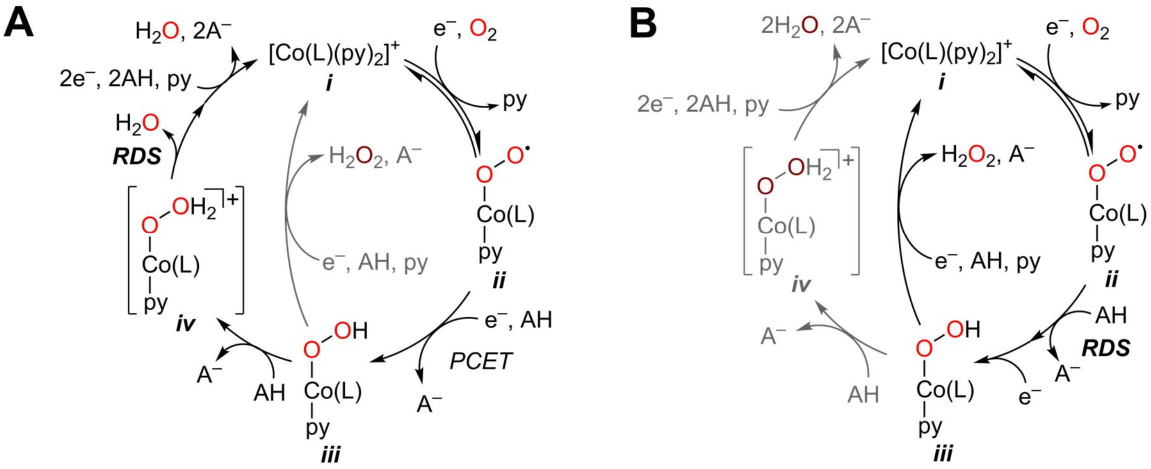

Figure 5.4. (A) General proposed ORR mechanism for complex **1**. (B) General proposed ORR mechanism for complex **2**.

The observed rate-law of **2** with stronger acids is in contrast to other Co-N_2O_2 complexes, where the protonation step to form the intermediate Co(III)-hydroperoxo (***iii***) has been proposed to be concerted with electron transfer.[31-33] These data instead suggest **2** operates in a mechanistically similar fashion to [Fe(porphyrin)]$^+$ derivatives, where the rate-determining protonation step is sensitive to equilibrium O_2 binding.[33, 45] Evidence of proton transfer being the rate-determining step is directly obtained from the KIE data. With **1**, a KIE of 1.2±0.1 is observed, which is consistent with proton transfer being complete *before* the rate-determining oxygen-oxygen bond cleavage (**Figure**

5.4A). With **2**, a KIE of 2.4±0.2 is observed, which is consistent with rate-determining proton transfer (**Figure 5.4B**).[46-47] The absence of a dependence on the concentration of the reductant suggests that this proton transfer is decoupled from electron transfer.

We note that DPV experiments described above with 1:1 buffered conditions of HA:A⁻ indicate coordination by benzoate anions in the Co(III) oxidation state, which has previously been shown to alter reaction mechanism in other systems for ORR.[48] This suggests that over time, as the reaction proceeds to completion, the resting state of the catalyst and the observed rate are both likely to change as benzoate anion concentrations increase and change the catalyst standard potential.

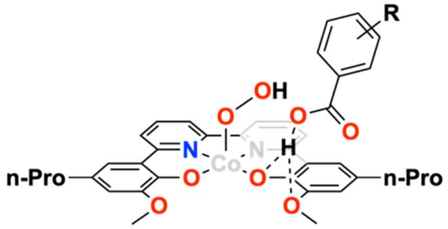

Figure 5.5. Proposed pendent relay interaction relevant to the ORR mechanism for complex **2**.

Comparison of overpotentials, selectivity, and rates with our previous report leads to a few interesting observations. First, high selectivity for H_2O is observed during ORR mediated by **1** in MeCN with benzoic acid derivatives. With **2**, 76-81% selectivity for H_2O_2 is instead observed in MeCN solution <u>at the same overpotentials</u> as **1**. In MeOH solution with AcOH, 91±5% selectivity for H_2O_2 during ORR mediated by **2** is achieved (**Figure S5.59**).[34] There is also a marked enhancement of TOF when **2** is utilized across all conditions, with three orders of magnitude of increase in comparison to **1** in MeCN and two orders of magnitude increase in MeOH. These results indicate the kinetic role of the alkyl ether pendent relay has almost quantitative control over ORR selectivity for this family of Co(N_2O_2) catalysts in these two solvent systems.

5.5 Conclusions

We have reported a new Co(III)(N_2O_2) complex bearing pendent –OMe relays for the ORR. Kinetic studies revealed a change in mechanism at high proton activities when the pendent –OMe residues were present, with the reaction shifting to [O_2] dependence. This change is consistent with an enhanced rate of protonation and a dependence upon the equilibrium reaction between Co(II) and O_2 to generate a Co(III)($O_2^{\bullet-}$) (***ii***) intermediate prior to rate-determining protonation. This assignment is supported by KIE studies and the absence of a concentration dependence on the reductant.

With **1**, enhanced selectivity for water (81–100%) is observed in MeCN with TOFs = 1.1×10^{-3} to 3.1×10^{-3} s^{-1} and estimated overpotentials of 810-990 mV. With **2**, selectivity for H_2O_2 (76–81% H_2O_2) is observed in MeCN with TOF = 1.0×10^{-1} to 1.5 s^{-1} and estimated overpotentials of 330-520 mV. Since both complexes have the same standard reduction potential, these results indicate that the alkyl ethers in **2** put the reaction almost completely under kinetic control. In MeOH, the selectivity of **2** during ORR shifts almost quantitatively to H_2O_2 (91±5%), consistent with the protic solvent favoring enhanced kinetic selectivity in conjunction with the pendent relay. This work helps broaden the understanding of the ORR utilizing non-macrocyclic Co complexes and has the potential to lead to active catalysts for the ORR to either H_2O_2 or H_2O with high selectivity and activity. Further studies on solvent effects, utilization of a broader range of acids, and axial ligand effects are underway.

Supporting Information for Chapter 5

5.6 Experimental and Methods

5.6.1 General

All chemicals and solvents (ACS or HPLC grade) were commercially available and used as received unless otherwise indicated. For all air-sensitive reactions and electrochemical experiments, HPLC-grade solvents were obtained as anhydrous and air-free from a PPT Glass Contour Solvent Purification System. Gas cylinders were obtained from Praxair (Ar as 5.0; O_2 as 4.0) and passed through activated molecular sieves prior to use. UV-vis absorbance spectra were obtained on a Cary 60 from Agilent. HRMS and elemental analyses were performed at the University of Virginia utilizing an Agilent 6545B QTOF and PerkinElmer 2400 Series II CHNS/O Analyser instruments. An Anton-Parr Multiwave Pro SOLV, NXF-8 microwave reactor was used for microwave syntheses.

5.6.2 Electrochemistry

All electroanalytical experiments were performed using a Metrohm Autolab PGSTAT302N potentiostat. Glassy carbon working (⌀ = 3 mm) and non-aqueous silver/silver chloride pseudoreference electrodes behind CoralPor frits were obtained from CH Instruments. The pseudoreference electrodes were obtained by depositing chloride on bare silver wire in 10% HCl at oxidizing potentials and stored under light-free conditions in 0.1 M tetrabutylammonium hexafluorophosphate/acetonitrile solution prior to use. The counter electrode was a glassy carbon rod (⌀ = 3 mm). All DPV experiments were performed in a modified scintillation vial (20 mL volume) as a single-chamber cell with a cap modified with ports for all electrodes and a sparging needle. Tetrabutylammonium hexafluorophosphate ($TBAPF_6$) was purified by recrystallization from ethanol and dried in a vacuum oven before being stored in a desiccator. All data were referenced to an internal ferrocene standard (ferricenium/ferrocene reduction potential under stated conditions) unless otherwise specified. All voltammograms were corrected for internal resistance.

5.6.3 Synthesis of ^{tbu}dhbpy[H]$_2$ and [Co(^{tbu}dhbpy)(py)$_2$][PF$_6$] (1)

^{tbu}dhbpy and **1** were synthesized according to our previously reported procedures.[1-3]

5.6.4 Synthesis of 2-methoxy-4-propyl-6-(4,4,5,5-tetramethyl-1,3,2-dioxaborolan-2-yl)phenol

In the glovebox, 2-methoxy-4-propyl-phenol (3.0 mL, 19 mmol) and 4,4,5,5-tetramethyl-1,3,2-dioxaborolane (3.0 mL, 21 mmol) were added to an oven-dried 500 mL pressure flask with stir bar and stirred for 10 minutes; vigorous H_2 effervescence was observed. After this time, [Ir(cod)(OMe)]$_2$ (0.37 g, 3 mol %), 4,4,5,5-tetramethyl-2-(4,4,5,5-tetramethyl-1,3,2-dioxaborolan-2-yl)-1,3,2-dioxaborolane (3.3 g, 13 mmol), and 4-*tert*-butyl-2-(4-*tert*-butyl-2-pyridyl)pyridine (0.30 g, 6.0 mol %), and cyclohexane (200 mL) were added. The flask was capped and heated to 90 °C for 16 h. After this time, the flask was allowed to cool to dryness, and 15 g of silica gel was added, after which volatiles were removed under vacuum. The dry loaded sample was then separated by column chromatography with hexanes and ethyl acetate as eluent. Solvent mixture was initially 100% hexanes and gradually adjusted to 100% ethyl acetate. The first fraction was collected and solvent was removed to yield an off-white solid. Recrystallization from hot hexanes yielded 1.61 g, 29.4 % yield. ^{1}H NMR (CDCl$_3$, 600 MHz): δ (ppm) 0.92 (t, 3H), 1.37 (s, 12H) 1.61 (m, 2H), 1.72 (t, 2H), 3.87 (s, 3H), 6.81 (s, 1H), 7.01 (s, 1H), 7.63 (s, 1H).

5.6.5 Synthesis of ^{pro}bpy[H]$_2$

In the glovebox, a 500 mL pressure flask was charged with 6,6′-dibromobipyridine (0.75 g, 2.4 mmol), 2-methoxy-4-propyl-6-(4,4,5,5-tetramethyl-1,3,2-dioxaborolan-2-yl)phenol (1.6 g, 5.5 mmol), $Pd(PPh_3)_4$ (0.28 g, 2.4 mmol), K_3PO_4 (2.7 g, 13 mmol), 1,4 dioxane (150 mL), and degassed H_2O (15 mL). This suspension was heated to 130 °C for 72 h, at which point all solids were dissolved. Upon cooling to room temperature, a yellow precipitate formed. This was collected by vacuum filtration and determined to be the desired product. 0.41 g, 43%. ESI-MS (m/z) [M + H]+: Calcd 485.244. Found: 485.2437. CHN analysis: theory (CHN, $C_{30}H_{32}N_2O_4{\bullet}H_2O$): C: 71.69, H: 6.82, N: 5.57. Found: C: 72.14, H: 6.65, N: 5.50. ^{1}H NMR (CD_2Cl_2, 600 MHz): δ (ppm) 0.99 (t, 6H), 1.69 (m, 4H) 2.61 (t, 4H), 3.91 (s, 6H), 6.83 (d, 2H), 7.32 (d, 2H), 8.05 (m, 2H), 8.16 (dd, 2H). ^{13}C{^{1}H} (CD_2Cl_2, 151 MHz) δ (ppm) 14.14, 25.45, 38.49, 56.57, 114.53, 118.34, 118.83, 119.64, 120.82, 133.21, 139.80, 148.51, 149.72, 152.53, 158.63.

5.6.6 Synthesis of [Co(^{pro}bpy)py)$_2$][PF$_6$]

A two-necked round-bottom flask (100 mL) was charged with a stir bar, ^{pro}bpy[H]$_2$ (0.100 g, 0.201 mmol), Co(OAc)$_2$•H$_2$O (0.050 g, 0.20 mmol), and methanol (25 mL) The suspension was capped with a septum and a condenser was attached before it was brought to reflux (65 °C) under aerobic conditions. A color change from yellow (ligand) to black was observed. After 3 h, excess pyridine (1.0 mL, 13 mmol) and NH$_4$PF$_6$ (0.163 g, 1.00 mmol) were added. Color change from black to red was observed following this addition. The suspension was allowed to reflux for 16 h, then allowed to cool to room temperature. The suspension was filtered to remove excess ligand, solvent was removed under reduced pressure, and the isolated solid was recrystallized from minimal hot methanol. After 48 h in the freezer a red-brown solid was recovered via vacuum filtration. Final recrystallization from CH$_2$Cl$_2$/hexanes yielded 65 mg (46%). Elemental Analysis for CoC$_{40}$H$_{40}$F$_6$N$_4$O$_4$P•2/3CH$_2$Cl$_2$ Calc'd: C 54.19 H 4.62 N 6.22; Found: C 53.79 H 4.75 N 5.91. ESI-MS: Calc'd (M-2Py$^+$): 541.154 Found: 541.1208; ^{1}H NMR (600 MHz): δ 8.22 (m, 6H), 7.72 (s, 4H), 7.54 (t, 2H), 7.01 (t, 4H) 6.95 (s, 2H), 6.67 (s, 2H), 4.00 (s, 6H), 2.46 (t, 4H), 2.58 (m, 4H), 0.88 (t, 6H).^{13}C NMR (201 MHz): δ 13.94, 25.02, 38.18, 56.61, 114.32, 120.23, 120.45, 121.31, 123.39, 125.80, 125.84, 132.56, 140.13, 14177, 151.98, 154.42, 156.95, 157.58.

5.6.7 Figures and Tables

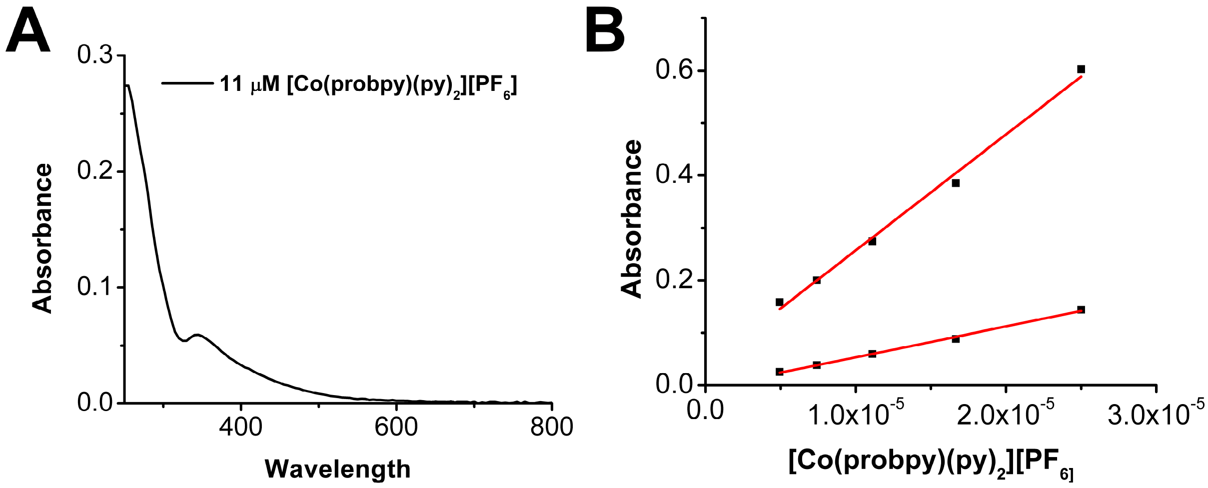

Figure S5.1. (A) UV-vis spectra of **2** in MeCN. (B) determination of ε for **2**.

Equation	**y = mx + b**		
		Value	**Std Err**
Abs @ 253 nm	b	3.60E-02	1.50E-02
--	m	2.21E+04	1.01E+03
Adj. R-Square	0.99171		
		Value	**Std Err**
Abs @ 395 nm	b	-5.94E-03	2.68E-03
	m	5.90E+03	1.90E+02
Adj. R-Square	0.99628		

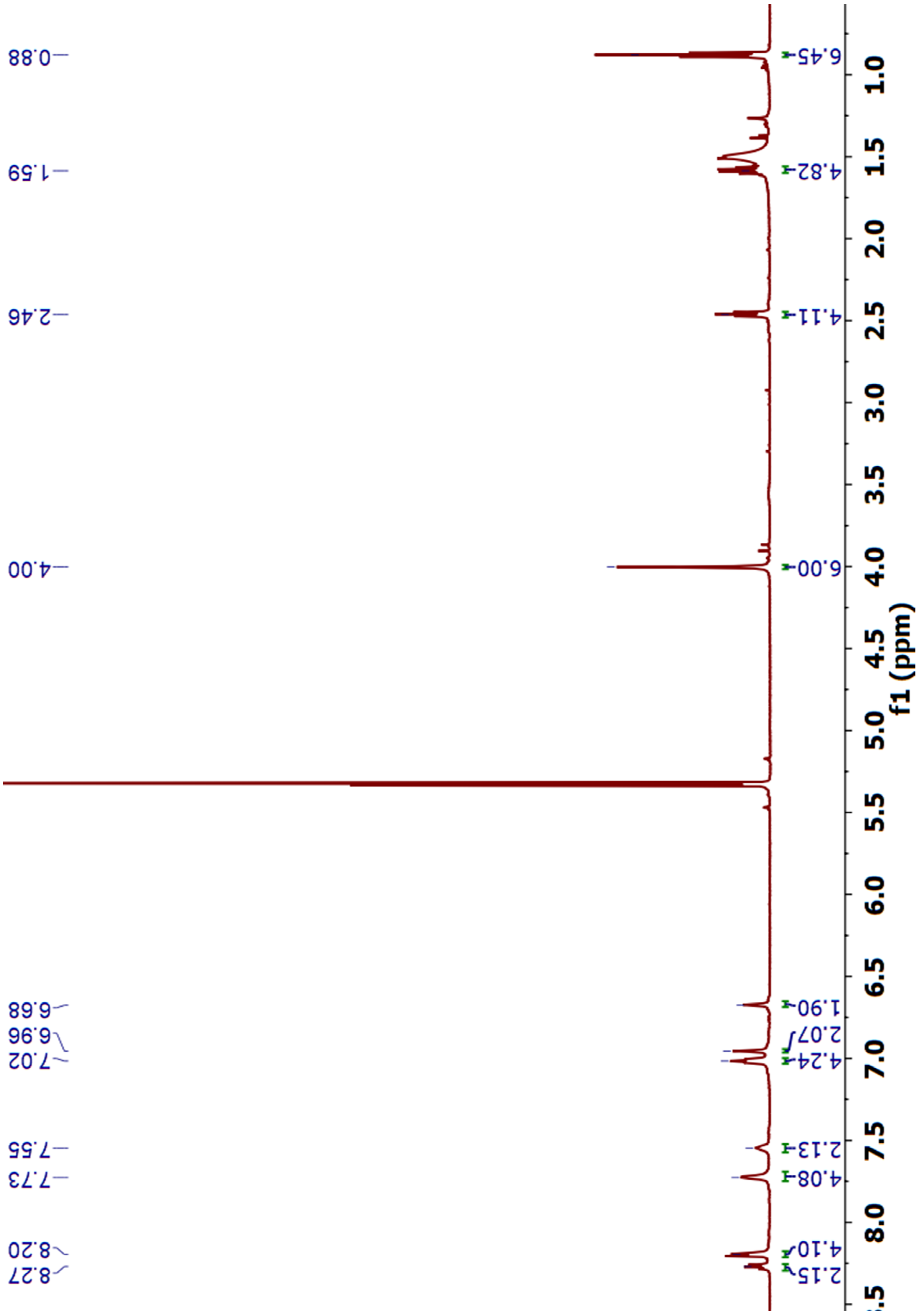

Figure S5.2. ^{1}H NMR spectra of 2 in CD_2Cl_2. (600 MHz, Varian)

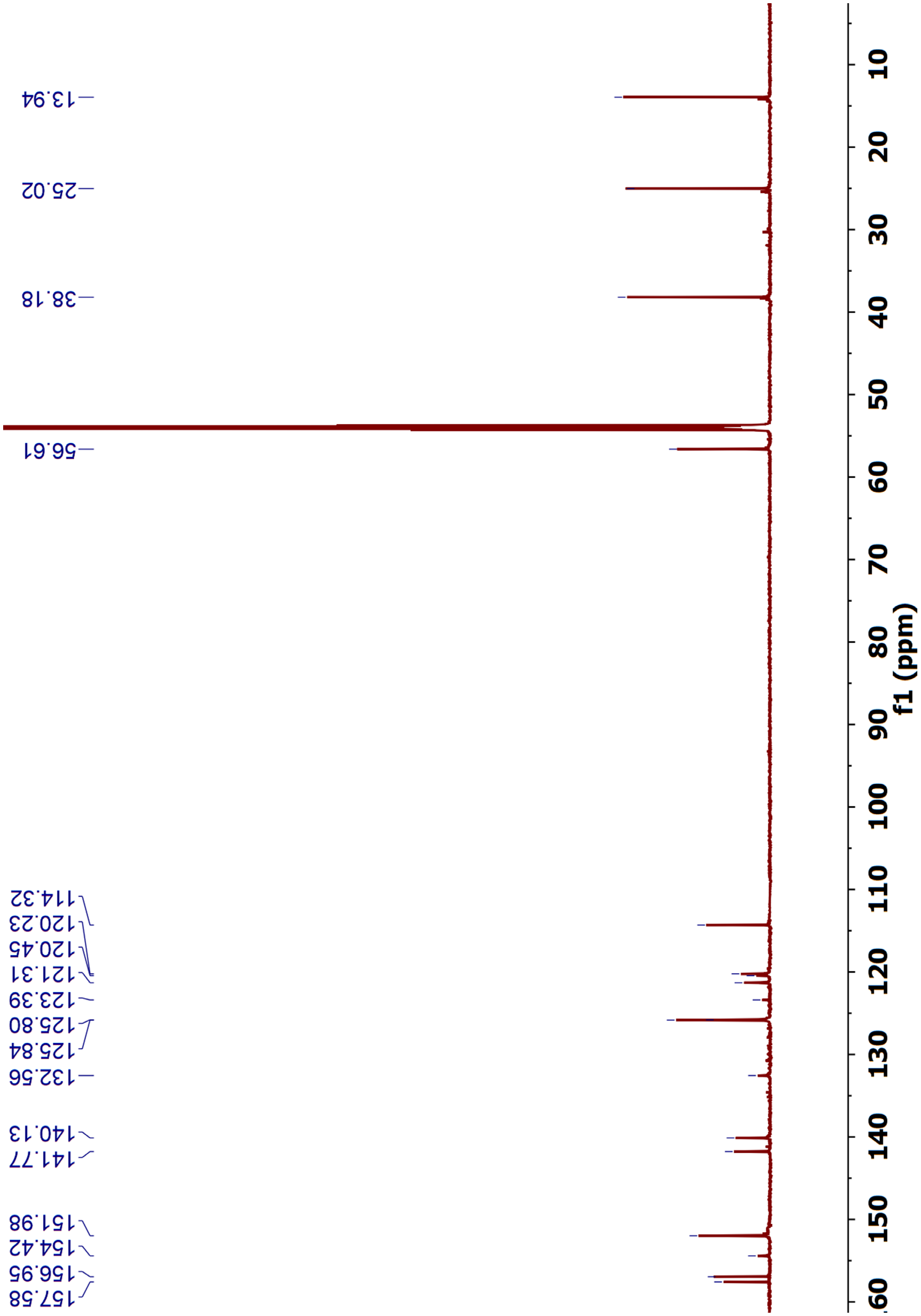

Figure S5.3. ^{13}C NMR of 2 in CD_2Cl_2. (201 MHz, Bruker).

5.6.7.1 Electrochemical Experiments

Complex **1** and **2** were analyzed by differential pulse voltammetry in 0.1 M $TBAPF_6$/MeCN electrolyte under Ar with (1) no additional additives, (2) 25 mM added benzoic acid derivative, and (3) 25 mM of a 1:1 buffer of each benzoic acid derivative.

Standard reduction potentials ($E_{1/2}$) were determined from DPV utilizing the Parry-Osteryoung **Eq 5.5**[4] where E_p is the peak potential and ΔE is the modulation amplitude:

$$E_{1/2} = E_p + \frac{\Delta E}{2} \qquad (5.5)$$

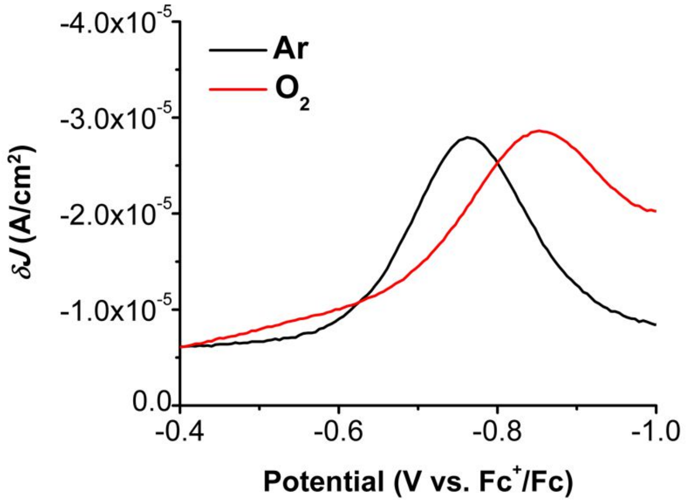

Figure S5.4. DPV of 0.5 mM **1** under Ar (black) and O_2 (red) saturation. Conditions: 0.1 M $TBAPF_6$/MeCN, glassy carbon working electrode, glassy carbon counter electrode, Ag/AgCl pseudoreference electrode, ΔE = 0.025 V, modulation time 0.01 s, interval time 0.1 s, scan rate 50.354 mV/s. Referenced to internal ferrocene standard.

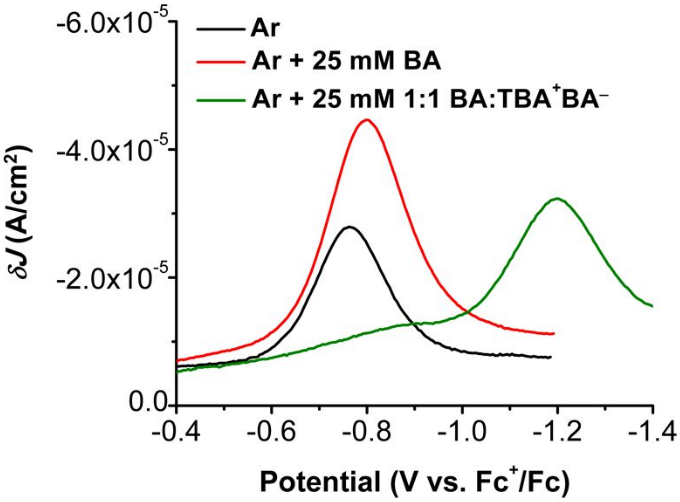

Figure S5.5. DPVs of **1** under Ar (black), with added 25 mM benzoic acid (red), and with an added buffer comprised of 25 mM benzoic acid and 25 mM tetra-n-butylammonium benzoate (green). Conditions: 0.5 mM **1**, 0.1 M TBAPF$_6$/MeCN; glassy carbon working electrode, glassy carbon counter electrode, Ag/AgCl pseudoreference electrode, ΔE = 0.025 V, modulation time 0.01 s, interval time 0.1 s, scan rate 50.354 mV/s. Referenced to internal ferrocene standard.

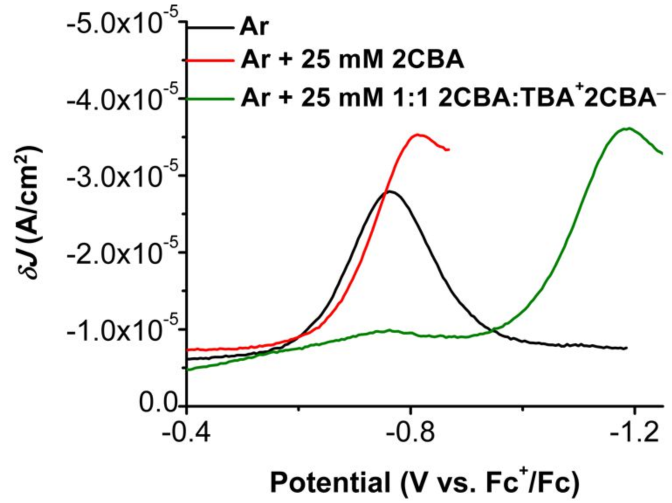

Figure S5.6. DPVs of **1** under Ar (black), with added 25 mM 2-chlorobenzoic acid (red), and with an added buffer comprised of 25 mM 2-chlorobenzoic acid and 25 mM tetra-n-butylammonium 2-chlorobenzoate (green). Conditions: 0.5 mM 1, 0.1 M TBAPF$_6$/MeCN; glassy carbon working electrode, glassy carbon counter electrode, Ag/AgCl pseudoreference electrode, ΔE = 0.025 V, modulation time 0.01 s, interval time 0.1 s, scan rate 50.354 mV/s. Referenced to internal ferrocene internal standard.

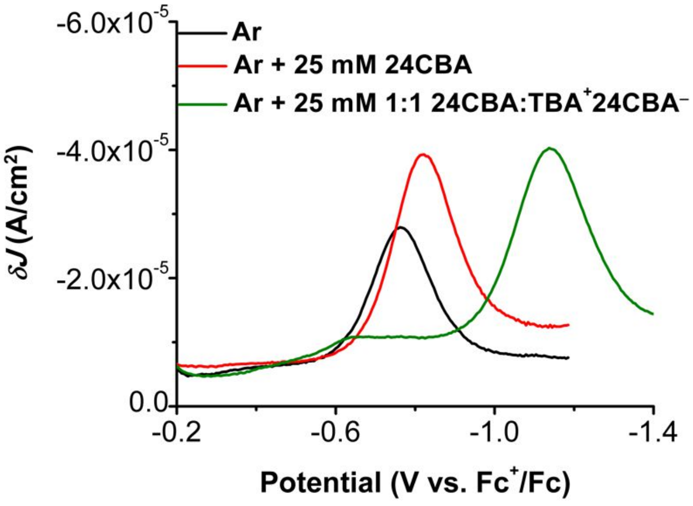

Figure S5.7. DPVs of **1** under Ar (black), with added 25 mM 2,4-dichlorobenzoic acid (red), and with an added buffer comprised of 25 mM 2,4-dichlorobenzoic acid and 25 mM tetra-n-butylammonium 2,4-dichlorobenzoate (green). Conditions: 0.5 mM **1**, 0.1 M $TBAPF_6$/MeCN; glassy carbon working electrode, glassy carbon counter electrode, Ag/AgCl pseudoreference electrode, ΔE = 0.025 V, modulation time 0.01 s, interval time 0.1 s, scan rate 50.354 mV/s. Referenced to internal ferrocene standard.

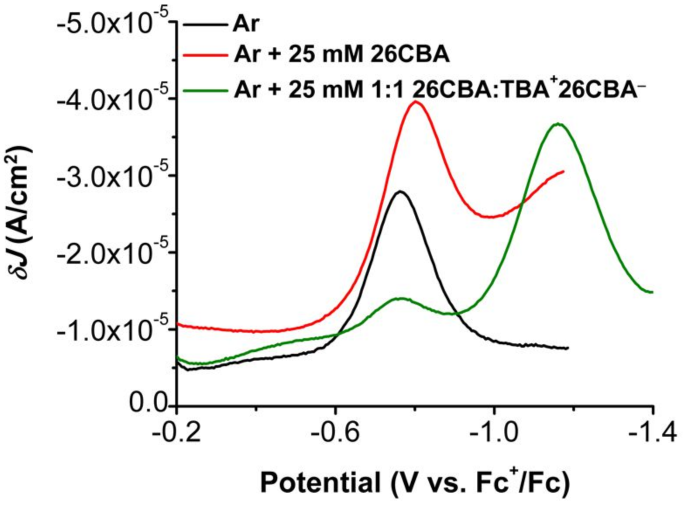

Figure S5.8. DPVs of **1** under Ar (black), with added 25 mM 2,6-dichlorobenzoic acid (red), and with an added buffer comprised of 25 mM 2,6-dichlorobenzoic acid and 25 mM tetra-n-butylammonium 2,6-dichlorobenzoate (green). Conditions: 0.5 mM **1**, 0.1 M $TBAPF_6$/MeCN; glassy carbon working electrode, glassy carbon counter electrode, Ag/AgCl pseudoreference electrode, ΔE = 0.025 V, modulation time 0.01 s, interval time 0.1 s, scan rate 50.354 mV/s. Referenced to internal ferrocene standard

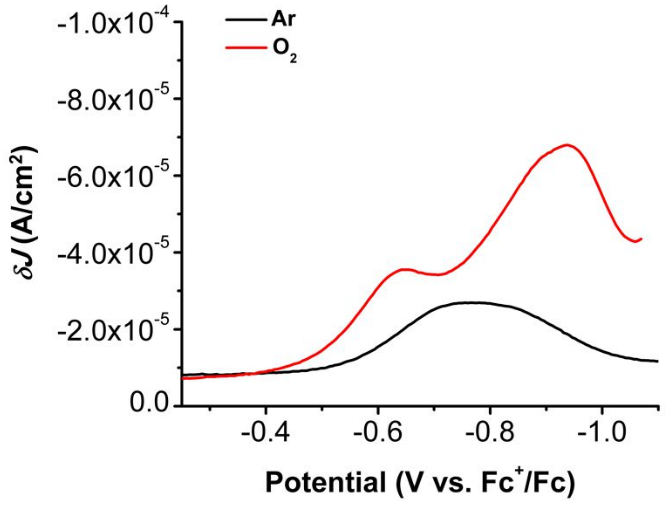

Figure S5.9. DPV of 0.5 mM **2** under Ar (black) and O_2 (red) saturation. Conditions: 0.1 M $TBAPF_6$/MeCN, glassy carbon working electrode, glassy carbon counter electrode, Ag/AgCl pseudoreference electrode, ΔE = 0.025 V, modulation time 0.01 s, interval time 0.1 s, scan rate 50.354 mV/s. Referenced to internal ferrocene standard.

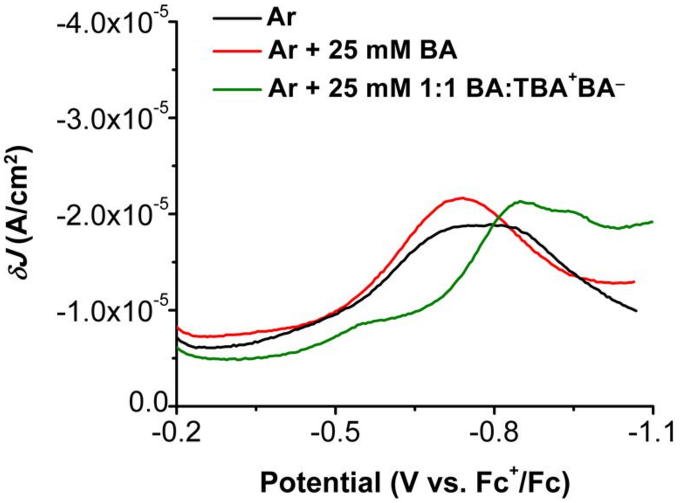

Figure S5.10. DPVs of **2** under Ar (black), with added 25 mM benzoic acid (red), and with an added buffer comprised of 25 mM benzoic acid and 25 mM tetra-n-butylammonium benzoate (green). Conditions: 0.5 mM **2**, 0.1 M $TBAPF_6$/MeCN; glassy carbon working electrode, glassy carbon counter electrode, Ag/AgCl pseudoreference electrode, ΔE = 0.025 V, modulation time 0.01 s, interval time 0.1 s, scan rate 50.354 mV/s. Referenced to internal ferrocene internal standard.

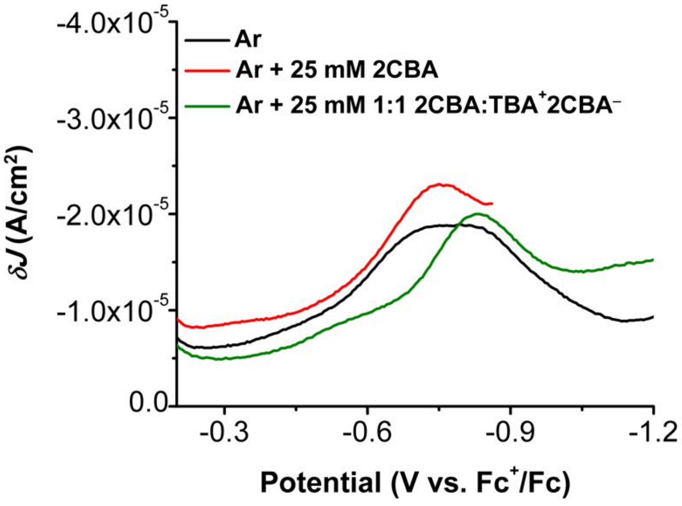

Figure S5.11. DPVs of **2** under Ar (black), with added 25 mM 2-chlorobenzoic acid (red), and with an added buffer comprised of 25 mM 2-chlorobenzoic acid and 25 mM tetra-n-butylammonium 2-chlorobenzoate (green). Conditions: 0.5 mM **2**, 0.1 M TBAPF$_6$/MeCN; glassy carbon working electrode, glassy carbon counter electrode, Ag/AgCl pseudoreference electrode, ΔE = 0.025 V, modulation time 0.01 s, interval time 0.1 s, scan rate 50.354 mV/s. Referenced to internal ferrocene standard.

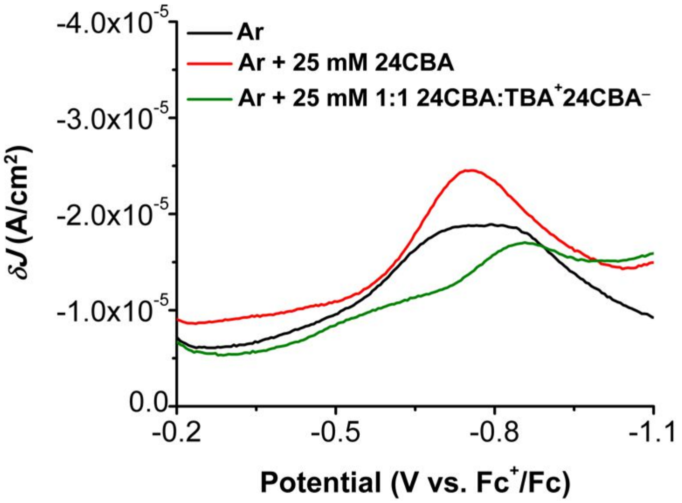

Figure S5.12. DPVs of **2** under Ar (black), with added 25 mM 2,4-dichlorobenzoic acid (red), and with an added buffer comprised of 25 mM 2,4-dichlorobenzoic acid and 25 mM tetra-n-butylammonium 2,4-dichlorobenzoate (green). Conditions: 0.5 mM **2**, 0.1 M TBAPF$_6$/MeCN; glassy carbon working electrode, glassy carbon counter electrode, Ag/AgCl pseudoreference electrode, ΔE = 0.025 V, modulation time 0.01 s, interval time 0.1 s, scan rate 50.354 mV/s. Referenced to internal ferrocene standard.

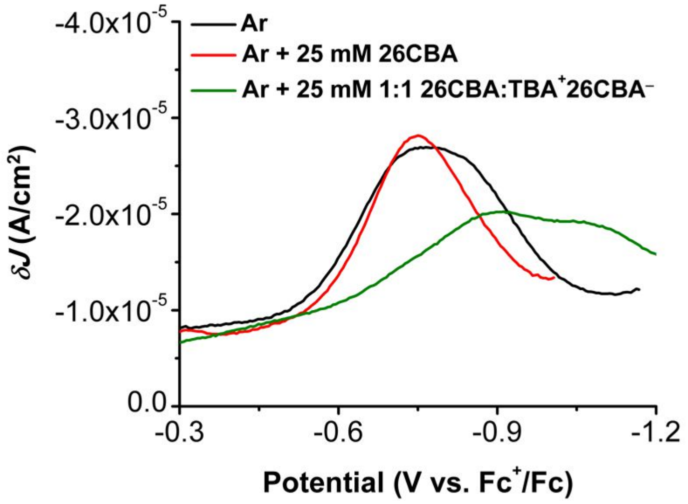

Figure S5.13. DPVs of **2** under Ar (black), with added 25 mM 2,6-dichlorobenzoic acid (red), and with an added buffer comprised of 25 mM 2,4-dichlorobenzoic acid and 25 mM tetra-n-butylammonium 2,6-dichlorobenzoate (green). Conditions: 0.5 mM **2**, 0.1 M TBAPF$_6$/MeCN; glassy carbon working electrode, glassy carbon counter electrode, Ag/AgCl pseudoreference electrode, ΔE = 0.025 V, modulation time 0.01 s, interval time 0.1 s, scan rate 50.354 mV/s. Referenced to internal ferrocene standard.

Table S5.1. Summary of redox potentials of each complex under conditions studied.

Compound	Ar	O$_2$	Benzoic Acid	2-chlorobenzoic acid	2,4-dichlorobenzoic acid	2,6-dichlorobenzoic acid
1	–0.76	–0.85	–	–	–	–
1 unbuffered	–	–	–0.80	–0.81	–0.82	–0.80
1 buffered	–	–	–1.20	–1.19	–1.14	–1.16
2	–0.76	–0.65	–	–	–	–
2 unbuffered	–	–	–0.74	–0.75	–0.76	–0.75
2 buffered	–	–	–0.85	–0.84	–0.86	–0.91

Potentials are referenced to Fc$^+$/Fc.

5.6.7.2 Determination of product selectivity for ORR.

The concentration of catalytically produced H_2O_2 was determined by titration with Ti(O)SO_4 as previously reported in the literature.[5-6] A calibration curve was obtained through a serial dilution of a stock solution of urea•H_2O_2 in MeCN. Aliquots (2 mL) at each concentration were diluted with 5 mL of DI H_2O, after which a UV-vis spectrum was obtained. Subsequently, 0.1 mL of a 0.1 M Ti(O)SO_4 solution in 2.0 M H_2SO_4 was added and a second UV-vis spectrum was collected. The absorbance at 405 nm was observed and the difference in the two spectra was utilized to obtain a calibration curve.[5, 7]

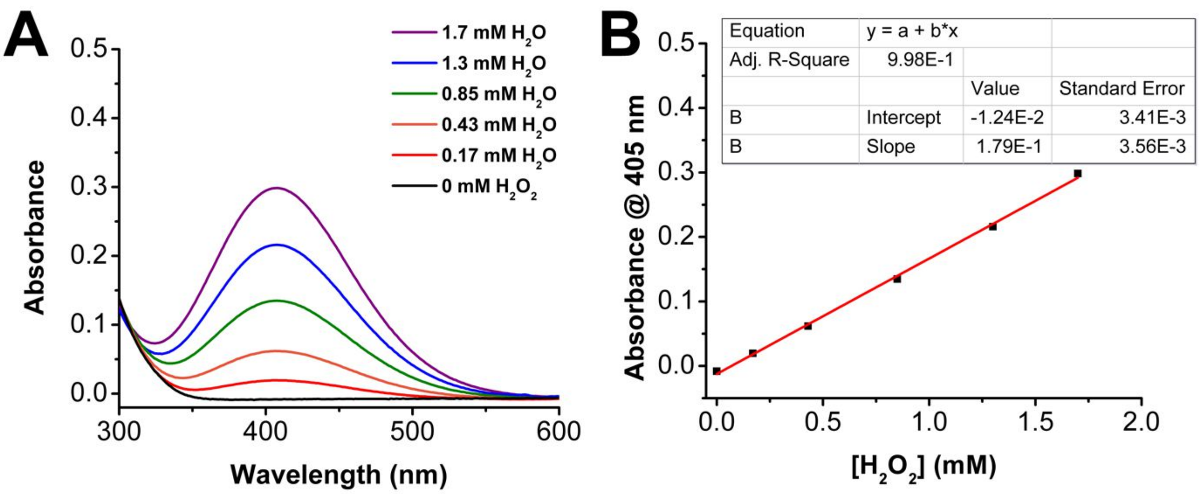

Equation	y = a + b*x		
Adj. R-Square	9.98E-1		
		Value	Standard Error
B	Intercept	-1.24E-2	3.41E-3
B	Slope	1.79E-1	3.56E-3

Figure S5.14. Calibration curve for H_2O_2 quantification utilizing TiO(SO_4) addition. (A) Serial dilution of urea•H_2O_2 in 2 mL of MeCN diluted by 5 mL of H_2O. (B) Calibration curve made utilizing a serial dilution of urea•H_2O_2 in MeCN.

To determine the selectivity of **1** for the ORR reaction, catalytic reaction mixtures (40 μM Co, 1.5 mM $Cp^*{}_2Fc$, air saturation, and 25 mM benzoic acid derivative in MeCN) were run overnight and $[Cp^*{}_2Fe]^+$ concentration was determined by UV-vis spectroscopy prior to obtaining a 2 mL aliquot, diluting to 7 total mL with water. 2 mL of this solution were collected and a UV-vis spectrum was obtained. To this 2 mL solution, 0.1 mL of Ti(O)SO_4 stock solution was added and characterized.

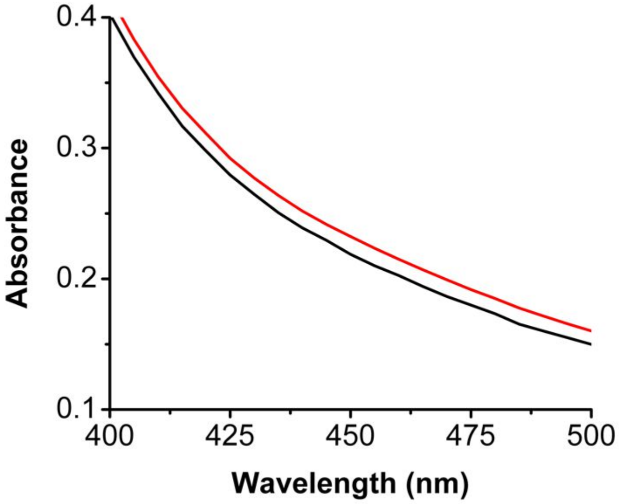

Figure S5.15. Ti(O)SO_4 titration of **1** with benzoic acid. Black trace is prior to the addition of Ti(O)SO_4. Red trace is after the addition of Ti(O)SO_4.

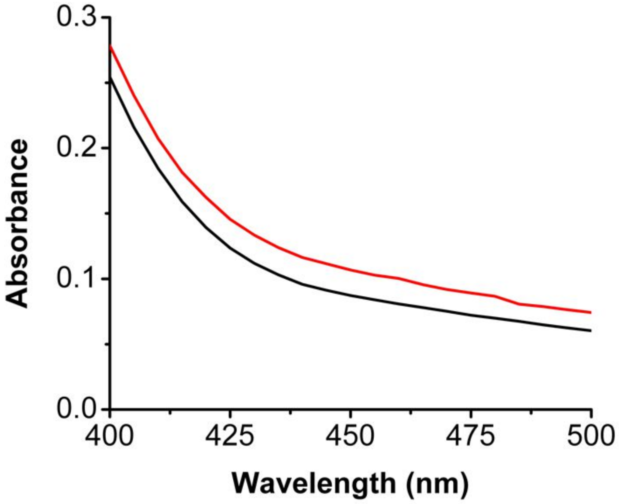

Figure S5.16. Ti(O)SO_4 titration of **1** with 2-chlorobenzoic acid. Black trace is prior to the addition of Ti(O)SO_4. Red trace is after the addition of Ti(O)SO_4.

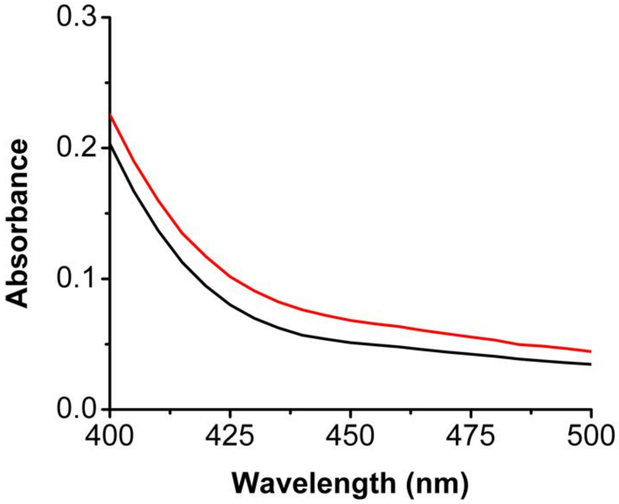

Figure S5.17. Ti(O)SO_4 titration of **1** with 2,4-dichlorobenzoic acid. Black trace is prior to the addition of Ti(O)SO_4. Red trace is after the addition of Ti(O)SO_4.

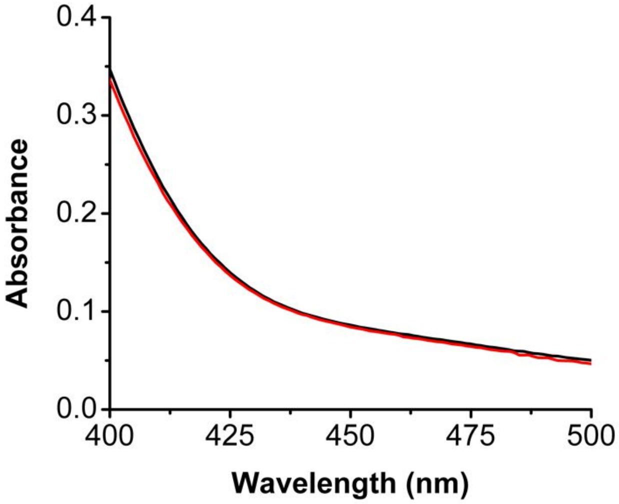

Figure S5.18. Ti(O)SO_4 titration of **1** with 2,6-dichlorobenzoic acid. Black trace is prior to the addition of Ti(O)SO_4. Red trace is after the addition of Ti(O)SO_4.

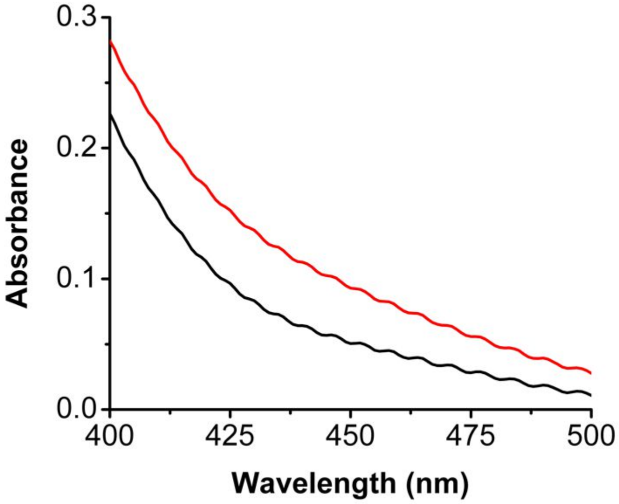

Figure S5.19. Ti(O)SO_4 titration of **2** with benzoic acid. Black trace is prior to the addition of Ti(O)SO_4. Red trace is after the addition of Ti(O)SO_4.

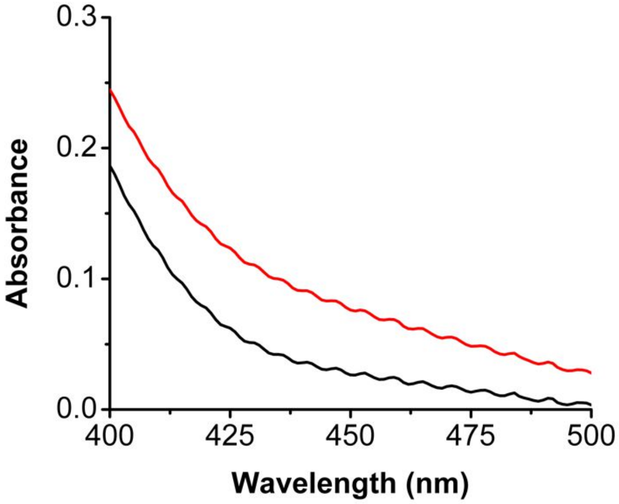

Figure S5.20. Ti(O)SO_4 titration of **2** with 2-chlorobenzoic acid. Black trace is prior to the addition of Ti(O)SO_4. Red trace is after the addition of Ti(O)SO_4.

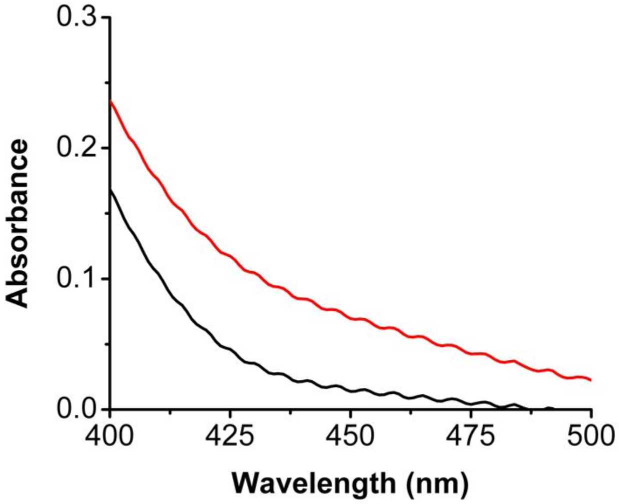

Figure S5.21. Ti(O)SO_4 titration of **2** with 2,4-dichlorobenzoic acid. Black trace is prior to the addition of Ti(O)SO_4. Red trace is after the addition of Ti(O)SO_4.

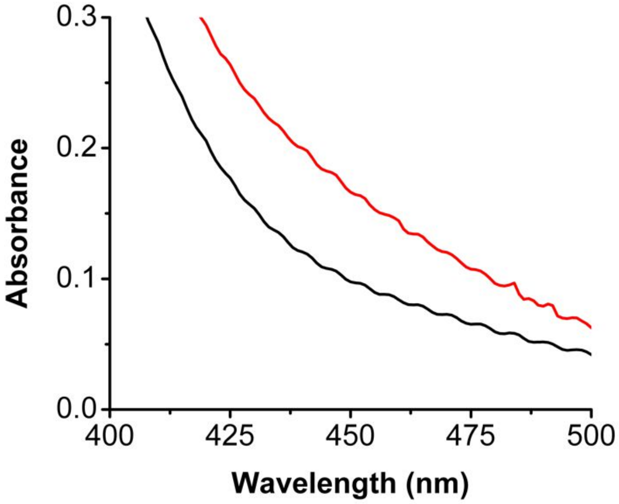

Figure S5.22. Ti(O)SO_4 titration of **2** with 2,6-dichlorobenzoic acid. Black trace is prior to the addition of Ti(O)SO_4. Red trace is after the addition of Ti(O)SO_4.

To ensure Co complexes **1** and **2** do not facilitate H_2O_2 disproportionation or interfere with iodometric titrations, a known amount of urea•H_2O_2 in MeCN (0.45 or 0.60 mM final concentration, as labeled) was added to each Co complex (40 µM final concentration) in MeOH along with 25 mM of each benzoic acid derivative. These were then left for the quantification time utilized for ORR (16 h for **1,** 1 h for **2**). Aliquots (2 mL) at each concentration were diluted with 5 mL of DI H_2O, after which a UV-vis spectrum was obtained. Subsequently, 0.1 mL of a 0.1 M $Ti(O)SO_4$ solution in 2.0 M H_2SO_4 was added, and a second UV-Vis spectrum was collected. The absorbance at 431 nm was observed and the difference in the two spectra was utilized to obtain a calibration curve.

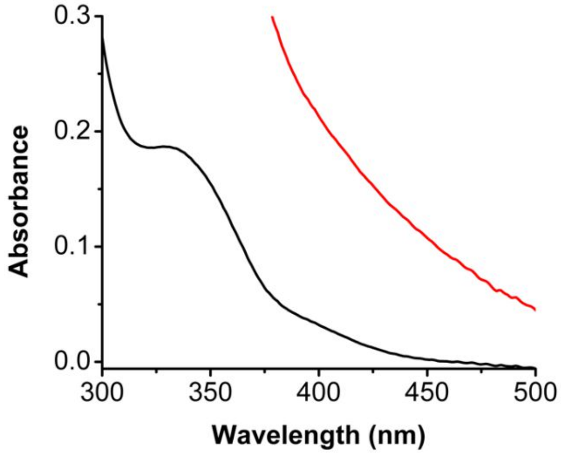

Figure S5.23. H_2O_2 disproportionation test. $Ti(O)SO_4$ titrations of **1** in the presence of 25 mM benzoic acid and 0.60 mM urea•H_2O_2. Black trace is prior to the addition of $Ti(O)SO_4$. Red trace is after the addition of $Ti(O)SO_4$. 98±2% H_2O_2 recovered

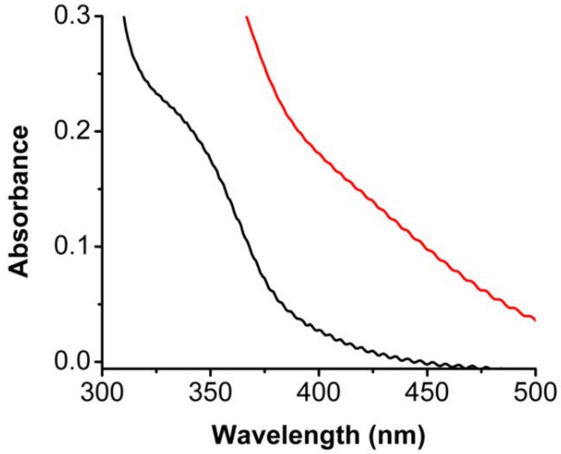

Figure S5.24. H_2O_2 disproportionation test. $Ti(O)SO_4$ titrations of **1** in the presence of 25 mM 2-chlorobenzoic acid and 0.60 mM urea•H_2O_2. Black trace is prior to the addition of $Ti(O)SO_4$. Red trace is after the addition of $Ti(O)SO_4$. 96±2% H_2O_2 recovered.

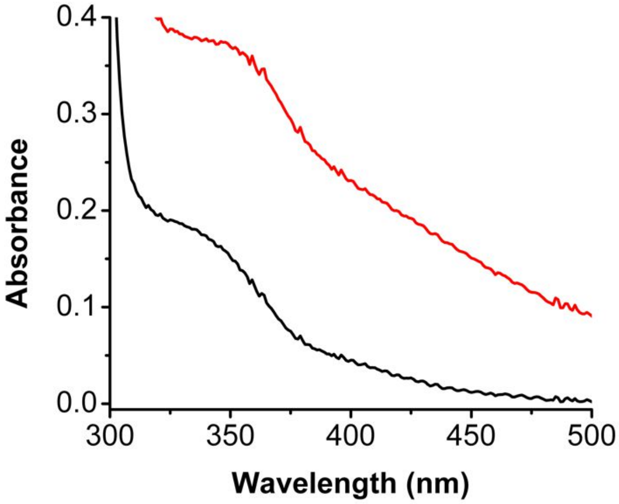

Figure S5.25. H_2O_2 disproportionation test. Ti(O)SO_4 titrations of **1** in the presence of 25 mM 2,4-dichlorobenzoic acid and 0.60 mM urea•H_2O_2. Black trace is prior to the addition of Ti(O)SO_4. Red trace is after the addition of Ti(O)SO_4. 104±2% H_2O_2 recovered.

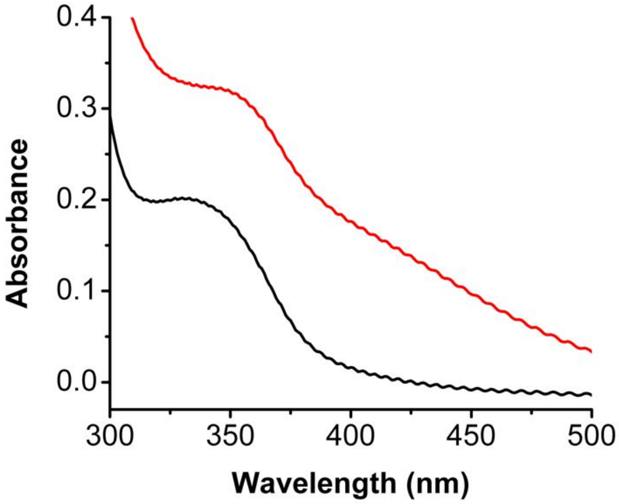

Figure S5.26. H_2O_2 disproportionation test. Ti(O)SO_4 titrations of **1** in the presence of 25 mM 2,6-dichlorobenzoic acid and 0.60 mM urea•H_2O_2. Black trace is prior to the addition of Ti(O)SO_4. Red trace is after the addition of Ti(O)SO_4. 102±2% H_2O_2 recovered.

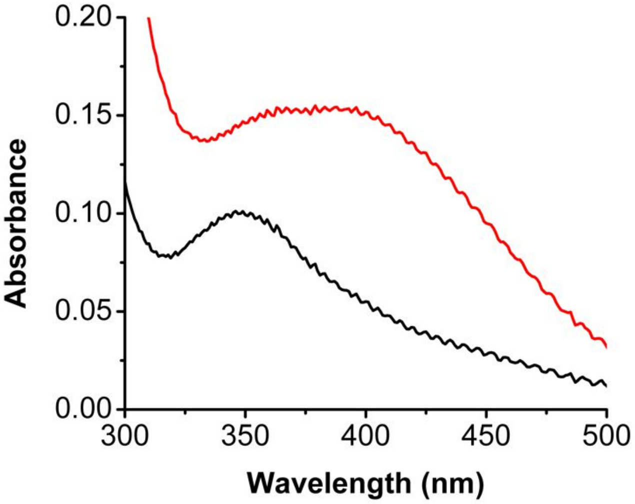

Figure S5.27. H_2O_2 disproportionation test. Ti(O)SO_4 titrations of **2** in the presence of 25 mM benzoic acid and 0.45 mM urea•H_2O_2. Black trace is prior to the addition of Ti(O)SO_4. Red trace is after the addition of Ti(O)SO_4. 103±4% H_2O_2 recovered.

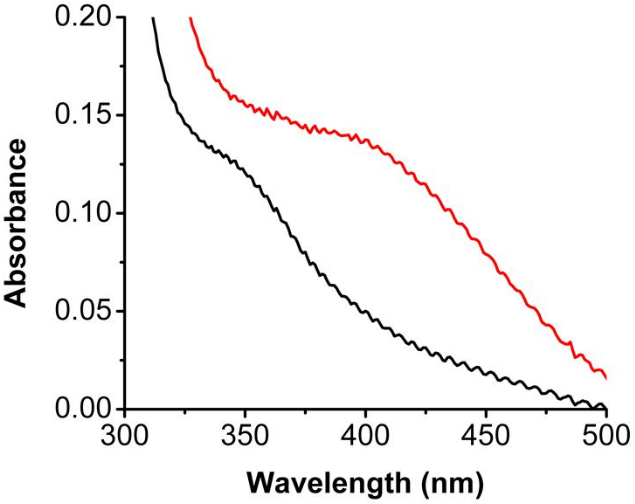

Figure S5.28. H_2O_2 disproportionation test. Ti(O)SO_4 titrations of **2** in the presence of 25 mM 2-chlorobenzoic acid and 0.45 mM urea•H_2O_2. Black trace is prior to the addition of Ti(O)SO_4. Red trace is after the addition of Ti(O)SO_4. 95±4% H_2O_2 recovered.

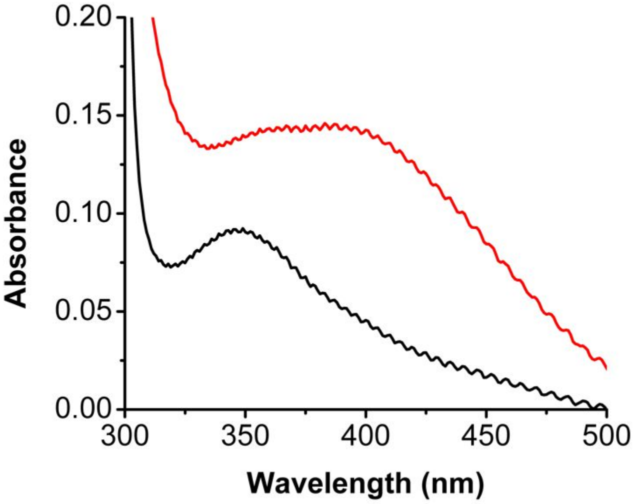

Figure S5.29. H_2O_2 disproportionation test. Ti(O)SO_4 titrations of **2** in the presence of 25 mM 2,4-dichlorobenzoic acid and 0.45 mM urea•H_2O_2. Black trace is prior to the addition of Ti(O)SO_4. Red trace is after the addition of Ti(O)SO_4. 101±3% H_2O_2 recovered.

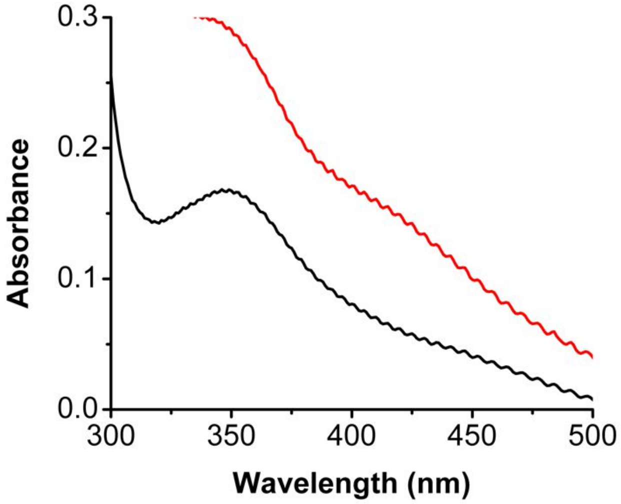

Figure S5.30. H_2O_2 disproportionation test. Ti(O)SO_4 titrations of **2** in the presence of 25 mM 2,6-dichlorobenzoic acid and 0.45 mM urea•H_2O_2. Black trace is prior to the addition of Ti(O)SO_4. Red trace is after the addition of Ti(O)SO_4. 93±4% H_2O_2 recovered.

5.6.7.3 Determination of the Catalytic Rate Law for 1 with all acids and 2 with benzoic acid and 2-chlorobenzoic acid.

[1 or 2]

A 1.0 mL O_2-saturated MeCN solution of cobalt complex **1** or **2** (40, 60, 80, 120, and 160 μM) containing 50 mM benzoic acid derivative was rapidly added to a 1 mL O_2-saturated (O_2 saturation concentration in MeCN is 8.1 mM)[8] MeCN solution containing 3 mM Cp^*_2Fe. The absorbance was monitored at 780 nm by UV-vis spectroscopy. Experiments were repeated in triplicate, figure axes show final concentrations; initial rates procedure and background correction described on Page 309.[9-10]

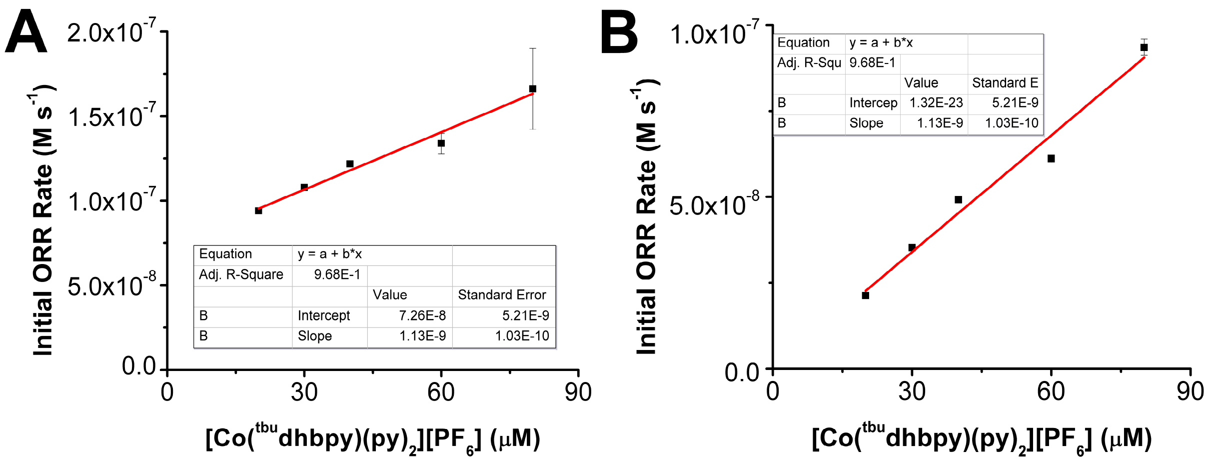

Figure S5.31. Determination of ORR reaction dependence upon [**1**] with benzoic acid. (A) Uncorrected for background O_2 reduction. (B) Corrected for background O_2 reduction.

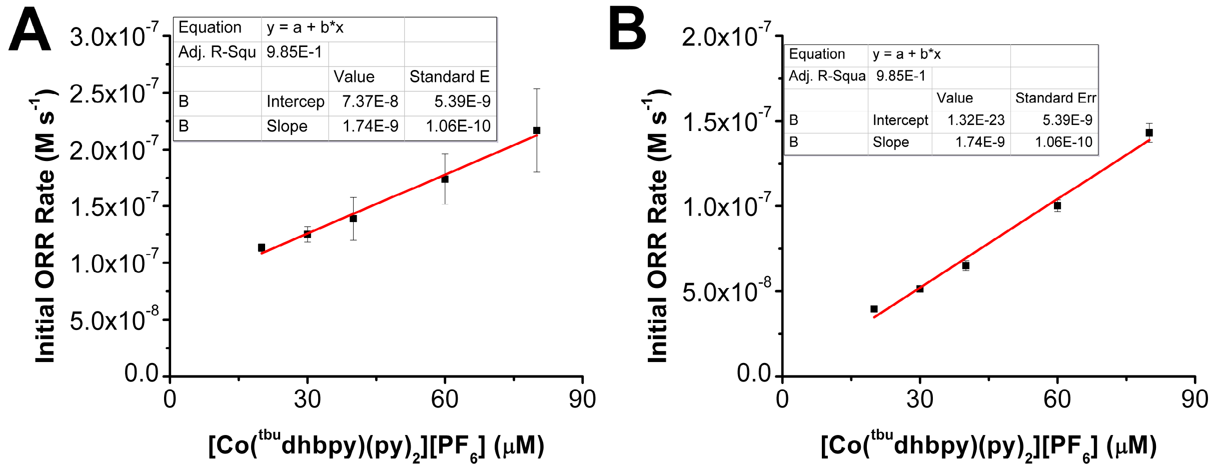

Figure S5.32. Determination of ORR reaction dependence upon [**1**] with 2-chlorobenzoic acid. (A) Uncorrected for background O2 reduction. (B) Corrected for background O2 reduction.

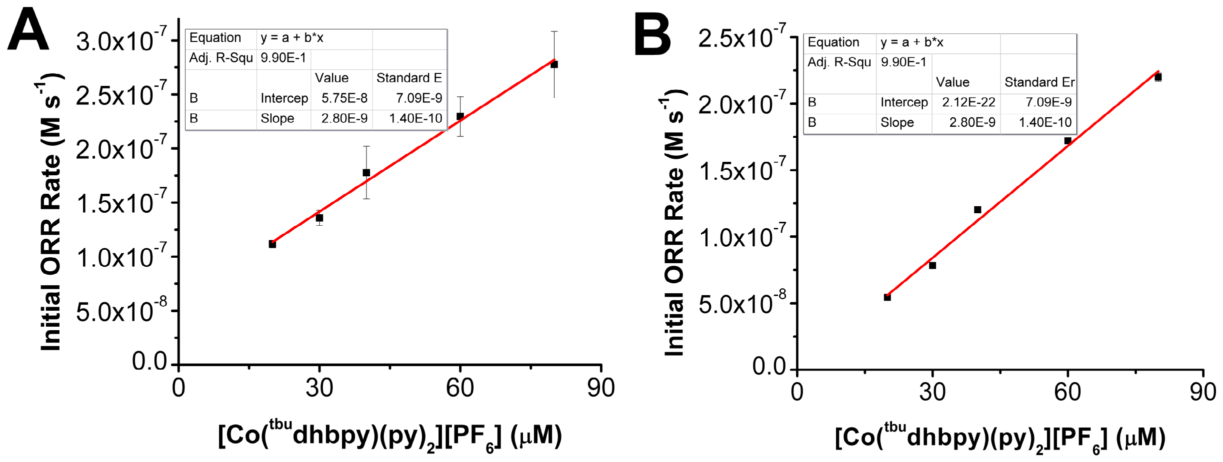

Figure S5.33. Determination of ORR reaction dependence upon [**1**] with 2,4-dichlorobenzoic acid. (A) Uncorrected for background O2 reduction. (B) Corrected for background O2 reduction.

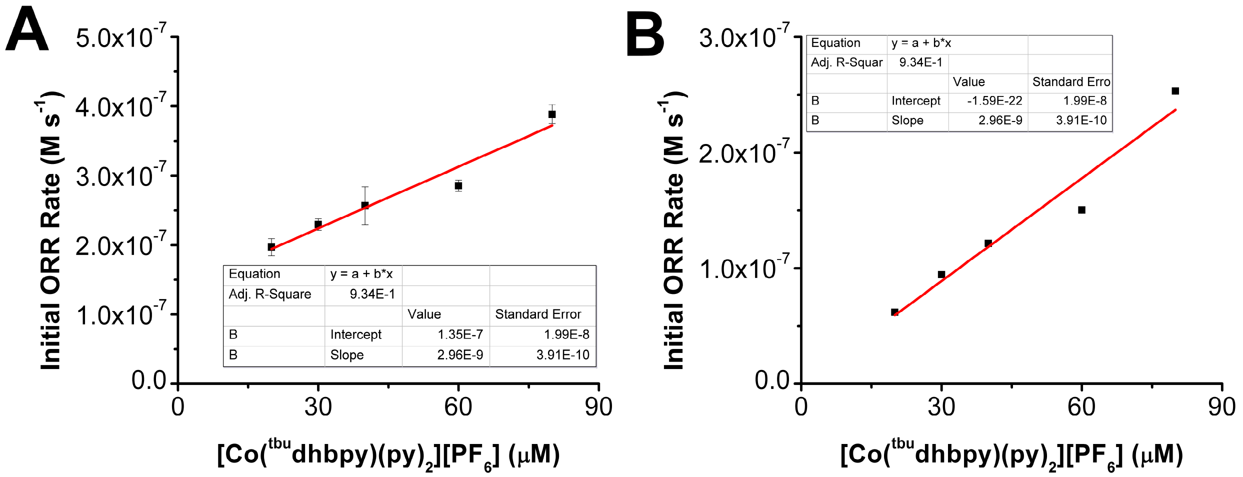

Figure S5.34. Determination of ORR reaction dependence upon [**1**] with 2,6-dichlorobenzoic acid. (A) Uncorrected for background O_2 reduction. (B) Corrected for background O_2 reduction.

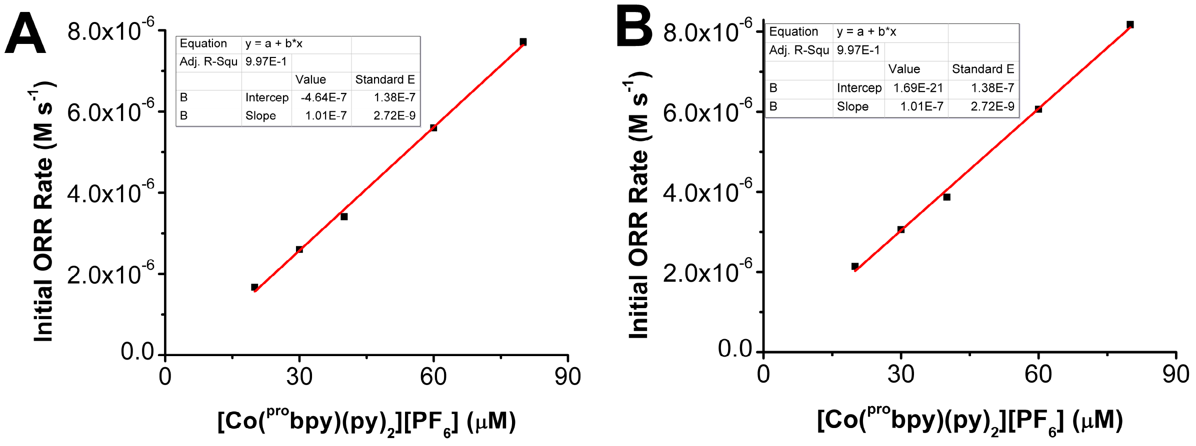

Figure S5.35. Determination of ORR reaction dependence upon [**2**] with benzoic acid. (A) Uncorrected for background O_2 reduction. (B) Corrected for background O_2 reduction.

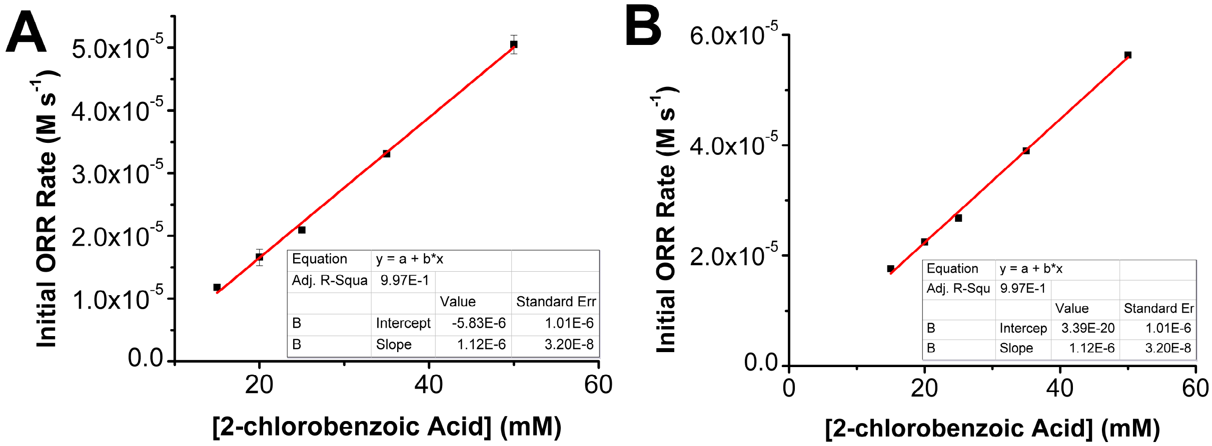

Equation	y = a + b*x		
Adj. R-Squa	9.97E-1		
		Value	Standard Err
B	Intercept	-5.83E-6	1.01E-6
B	Slope	1.12E-6	3.20E-8

Equation	y = a + b*x		
Adj. R-Squ	9.97E-1		
		Value	Standard Er
B	Intercep	3.39E-20	1.01E-6
B	Slope	1.12E-6	3.20E-8

Figure S5.36. Determination of ORR reaction dependence upon [**2**] with 2-chlorobenzoic acid. (A) Uncorrected for background O_2 reduction. (B) Corrected for background O_2 reduction.

[**Benzoic Acid Derivatives**]

A 1.0 mL O_2-saturated MeCN solution of complex **1** or **2** (80 µM) containing varied benzoic acid derivative concentrations (30, 40, 50, 70, 100 mM) was rapidly added into a 1.0 mL O_2-saturated MeCN solution containing 3 mM Cp^*_2Fe. The absorbance was monitored at 780 nm by UV-visible spectroscopy. Experiments were repeated in triplicate, figure axes show final concentrations; initial rates and background correction procedure described on Page 309.

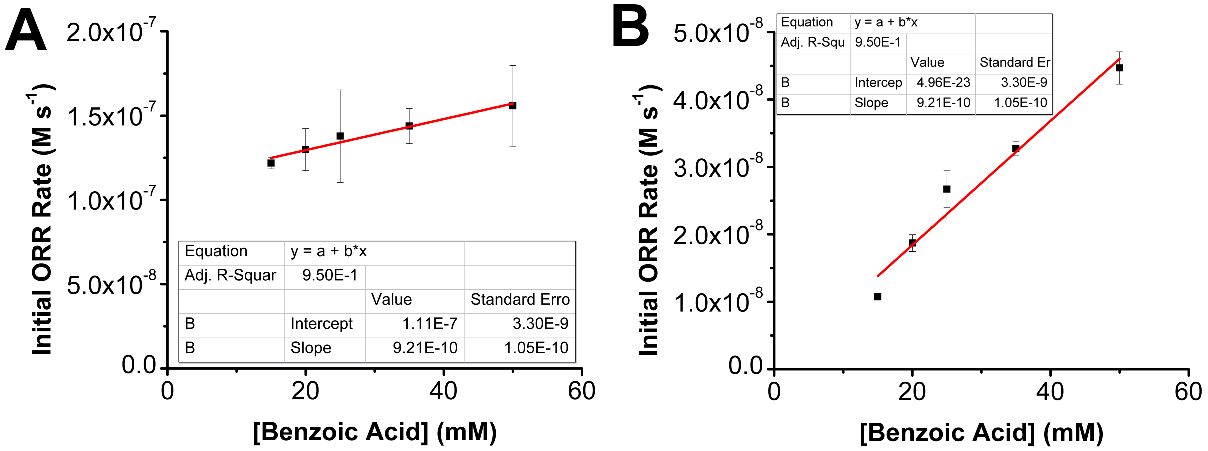

Figure S5.37. Determination of ORR reaction dependence upon [Benzoic Acid] with **1**. (A) Uncorrected for background O2 reduction. (B) Corrected for background O2 reduction, note that the background reaction is assumed to have minimal initial ORR rate dependence on [Benzoic Acid] relative to the reaction catalyzed by **1**.

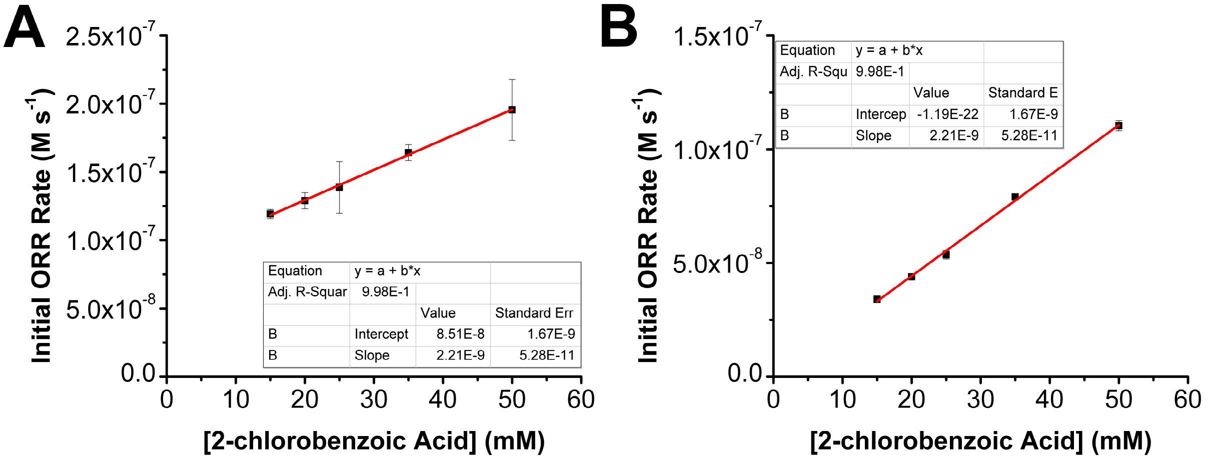

Figure S5.38. Determination of ORR reaction dependence upon [2-chlorobenzoic Acid] with **1**. (A) Uncorrected for background O2 reduction. (B) Corrected for background O2 reduction, note that the background reaction is assumed to have minimal initial ORR rate dependence on [2-chlorobenzoic Acid] relative to the reaction catalyzed by **1**.

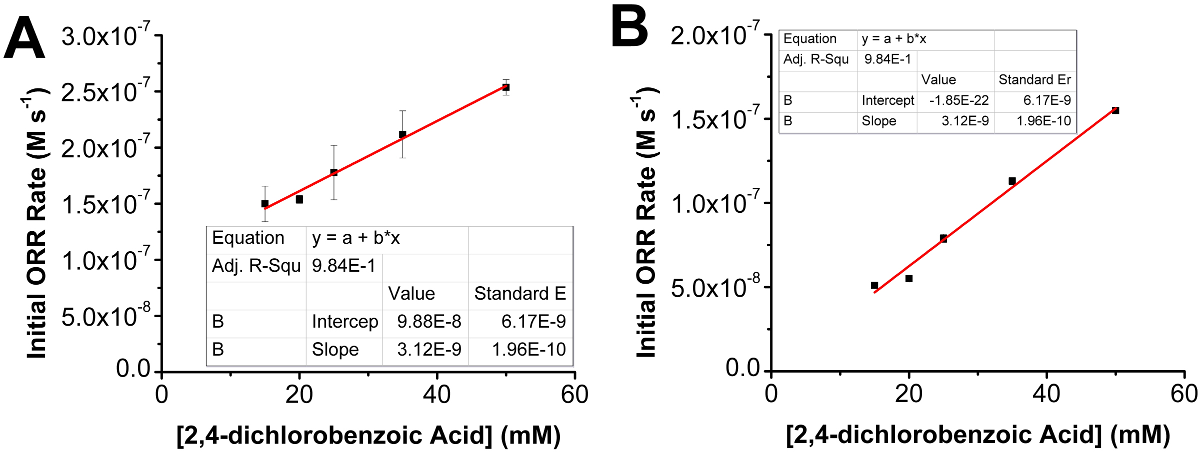

Figure S5.39. Determination of ORR reaction dependence upon [2,4-chlorobenzoic Acid] with **1**. (A) Uncorrected for background O_2 reduction. (B) Corrected for background O_2 reduction, note that the background reaction is assumed to have minimal initial ORR rate dependence on [2,4-dichlorobenzoic Acid] relative to the reaction catalyzed by **1**.

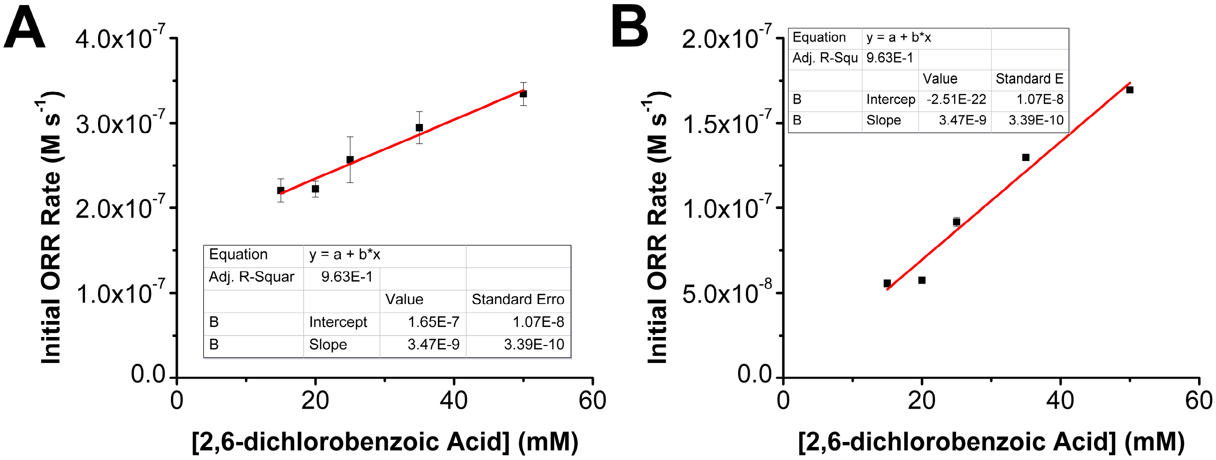

Figure S5.40. Determination of ORR reaction dependence upon [2,6-chlorobenzoic Acid] with **1**. (A) Uncorrected for background O_2 reduction. (B) Corrected for background O_2 reduction, note that the background reaction is assumed to have minimal initial ORR rate dependence on [2,6-dichlorobenzoic Acid] relative to the reaction catalyzed by **1**.

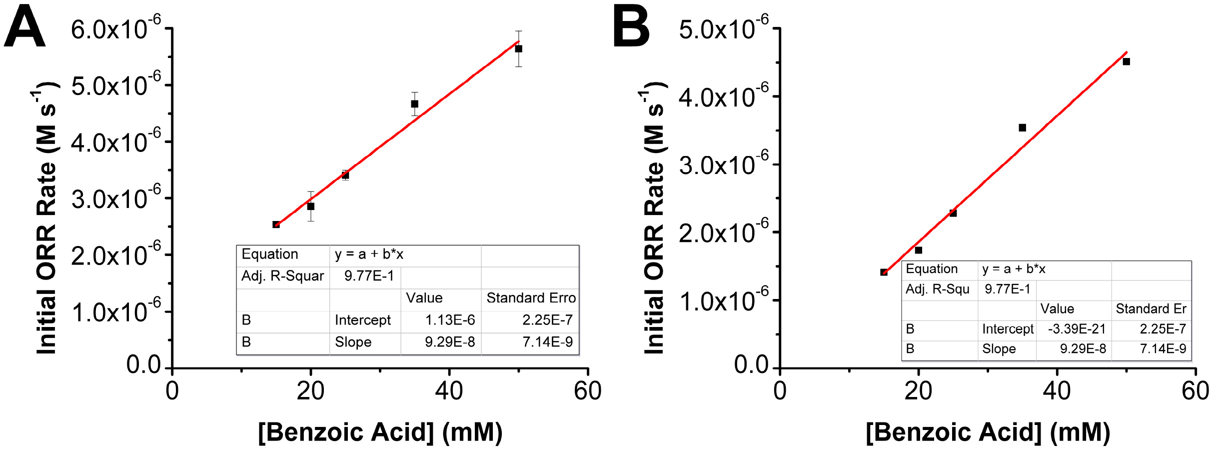

Figure S5.41. Determination of ORR reaction dependence upon [Benzoic Acid] with **2**. (A) Uncorrected for background O_2 reduction. (B) Corrected for background O_2 reduction, note that the background reaction is assumed to have minimal initial ORR rate dependence on [Benzoic Acid] relative to the reaction catalyzed by **2**.

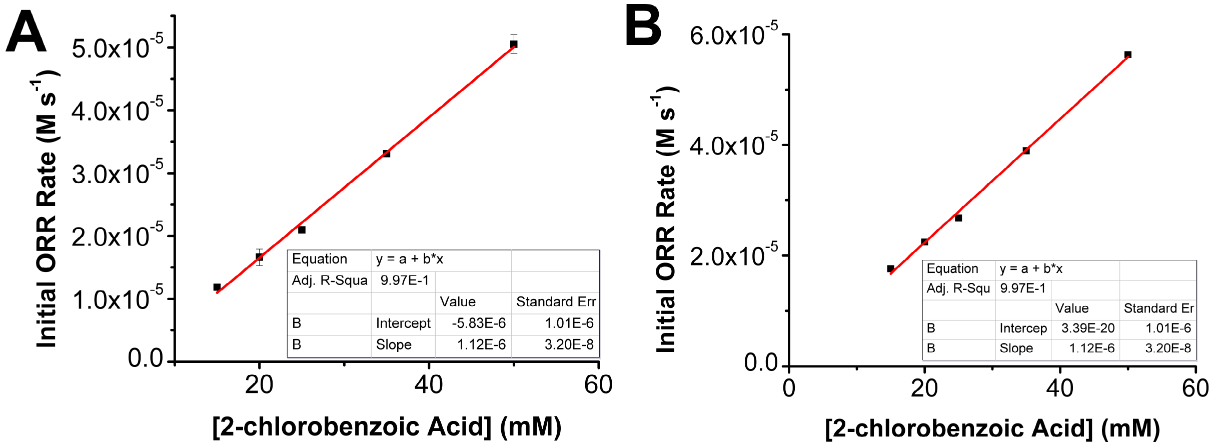

Figure S5.42. Determination of ORR reaction dependence upon [2-chlorobenzoic Acid] with **2**. (A) Uncorrected for background O_2 reduction. (B) Corrected for background O_2 reduction, note that the background reaction is assumed to have minimal initial ORR rate dependence on [2-chlorobenzoic Acid] relative to the reaction catalyzed by **2**.

[Cp^*_2Fe]

A 1.0 mL O_2-saturated MeCN solution of cobalt complex **1** (80 μM) and benzoic acid derivative (50 mM) were rapidly added into a 1.0 mL O_2-saturated MeCN solution containing Cp^*_2Fe (1.5, 2.0, 2.4, 2.8, and 3.0 mM). Then the reaction mixture was monitored at 780 nm by UV-visible spectroscopy. Experiments were repeated in triplicate, figure axis shows final concentration; initial rates procedure described on Page 309.

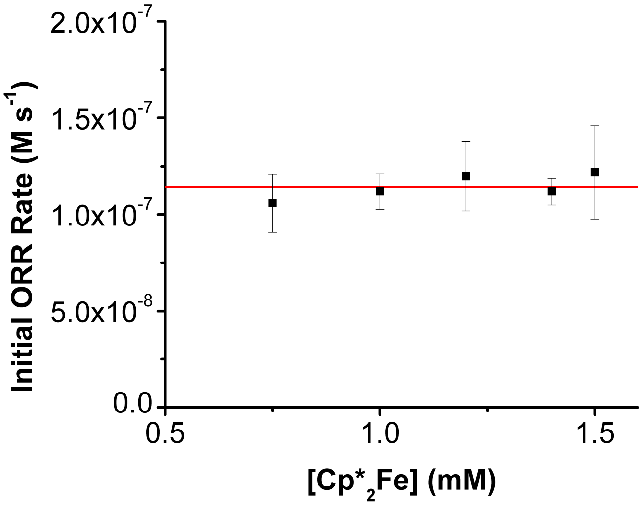

Figure S5.43. Determination of ORR reaction dependence upon [Cp*$_2$Fe] with **1** and benzoic acid. Horizontal line represents the global average rate observed across all experiments described for variable [Cp*$_2$Fe].

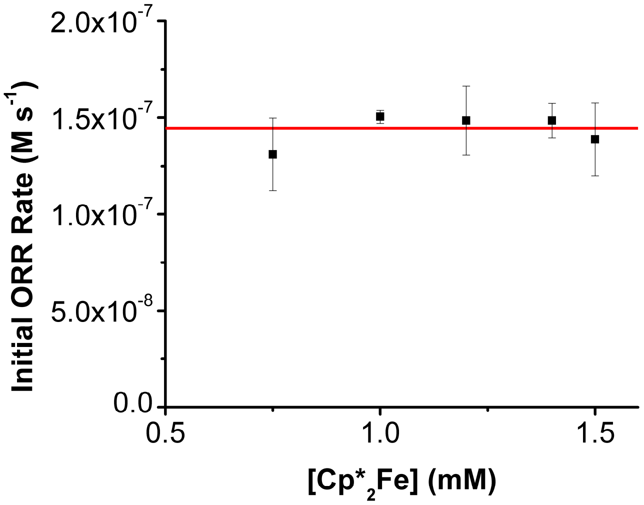

Figure S5.44. Determination of ORR reaction dependence upon [Cp*$_2$Fe] with **1** and 2-chlorobenzoic acid. Horizontal line represents the global average rate observed across all experiments described for variable [Cp*$_2$Fe].

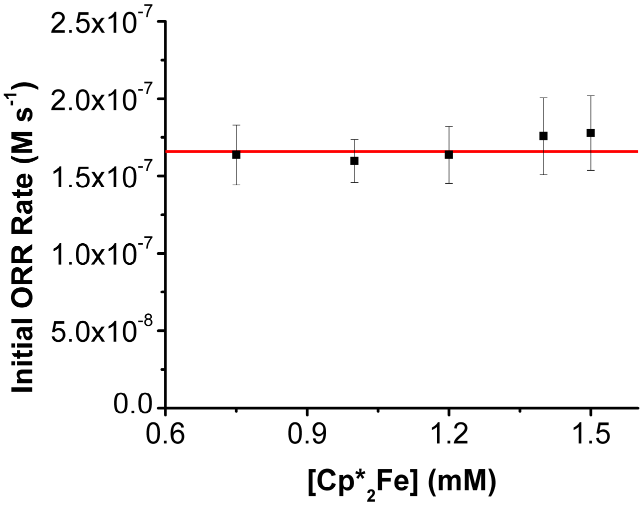

Figure S5.45. Determination of ORR reaction dependence upon [Cp*$_2$Fe] with **1** and 2,4-dichlorobenzoic acid. Horizontal line represents the global average rate observed across all experiments described for variable [Cp*$_2$Fe].

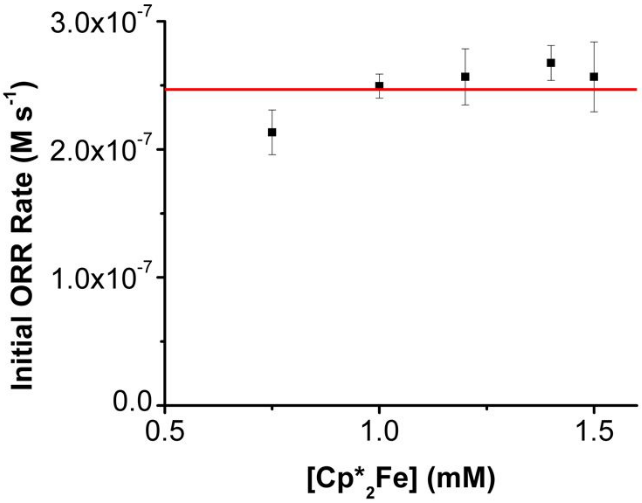

Figure S5.46. Determination of ORR reaction dependence upon [Cp*$_2$Fe] with **1** and 2,6-dichlorobenzoic acid. Horizontal line represents the global average rate observed across all experiments described for variable [Cp*$_2$Fe].

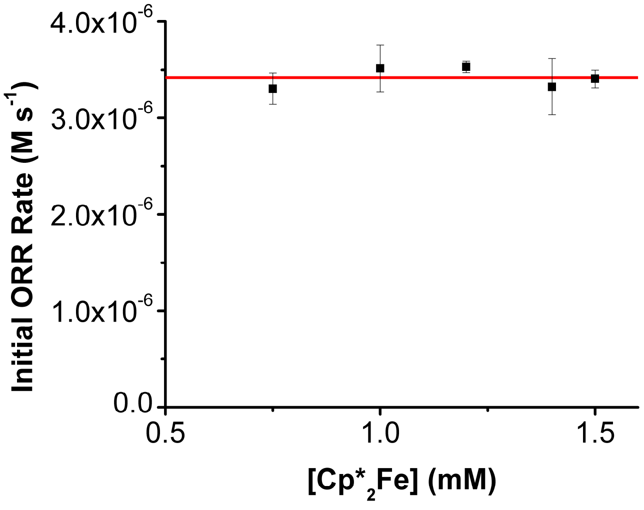

Figure S5.47. Determination of ORR reaction dependence upon [Cp*$_2$Fe] with 2 and benzoic acid. Horizontal line represents the global average rate observed across all experiments described for variable [Cp*$_2$Fe].

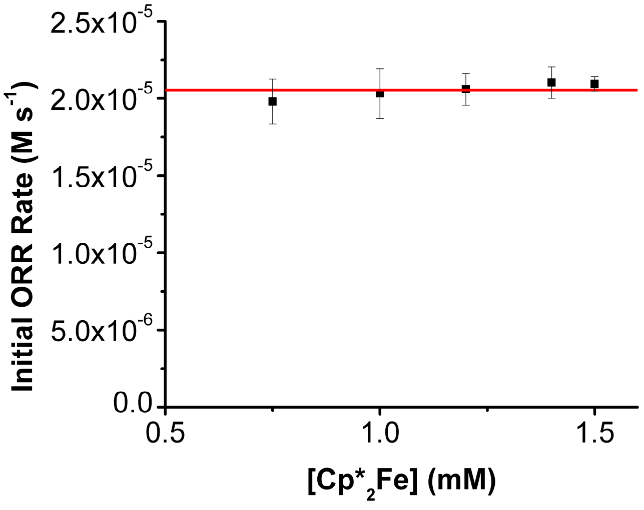

Figure S5.48. Determination of ORR reaction dependence upon [Cp*$_2$Fe] with **2** and 2-chlorobenzoic acid. Horizontal line represents the global average rate observed across all experiments described for variable [Cp*$_2$Fe].

[**O_2**]

(1) A 1.0 mL O_2-saturated MeCN solution of cobalt complex **1** (80 μM) containing benzoic acid derivative (50 mM) was rapidly added into an O_2-saturated MeCN solution of 3 mM $Cp^*{}_2Fe$. The absorbance was monitored at 780 nm by UV-visible spectroscopy ([O_2] 8.1 mM). Experiments were repeated in triplicate, figure axis shows final concentration; initial rates procedure described on Page 309.

(2) A 1.0 mL O_2-saturated MeCN solution of cobalt complex **1** (80 μM) containing benzoic acid derivative (50 mM) was rapidly added into an air-saturated MeCN solution of 3 mM $Cp^*{}_2Fe$. The absorbance was monitored at 780 nm by UV-visible spectroscopy ([O_2] 5.8 mM). Experiments were repeated in triplicate, figure axis shows final concentration; initial rates procedure described on Page 309.

(3 A 1.0 mL O_2-saturated MeCN solution of cobalt complex **1** (80 μM) containing benzoic acid derivative (50 mM) was rapidly added into an Ar-saturated MeCN solution of 3 mM then the absorbance was monitored at 780 nm by UV-visible spectroscopy ([O_2] 4.1 mM). Experiments were repeated in triplicate, figure axis shows final concentration; initial rates procedure described on Page 309.

(4) A 1.0 mL air-saturated MeCN solution of cobalt complex **1** (80 μM) containing benzoic acid derivative (50 mM) was rapidly added into an air-saturated MeCN solution of 3 mM and the absorbance was monitored at 780 nm by UV-visible spectroscopy ([O_2] 1.7 mM). Experiments were repeated in triplicate, figure axis shows final concentration; initial rates procedure described on Page 309.

(5) A 1.0 mL air-saturated MeCN solution of cobalt complex **1** (80 μM) containing benzoic acid derivative (50 mM) was rapidly added into an Ar-saturated MeCN solution of 3 mM

and the absorbance was monitored at 780 nm by UV-visible spectroscopy ([O_2] 0.85 mM). were repeated in triplicate, figure axis shows final concentration; initial rates procedure described on Page 309.

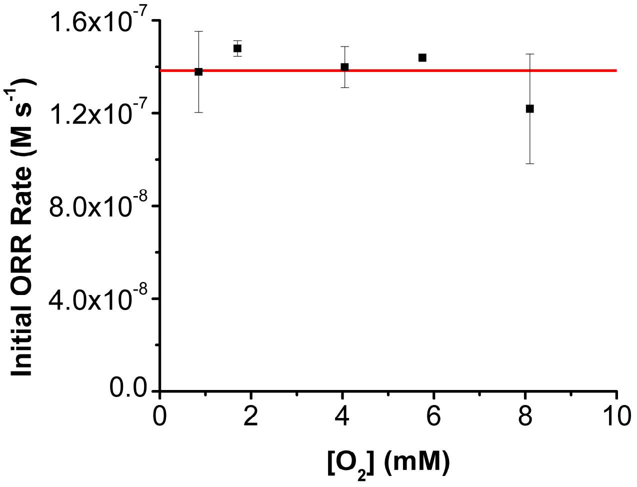

Figure S5.49. Determination of ORR reaction dependence upon [O_2] with **1** and benzoic acid. Horizontal line represents the global average rate observed across all experiments described for variable [O_2].

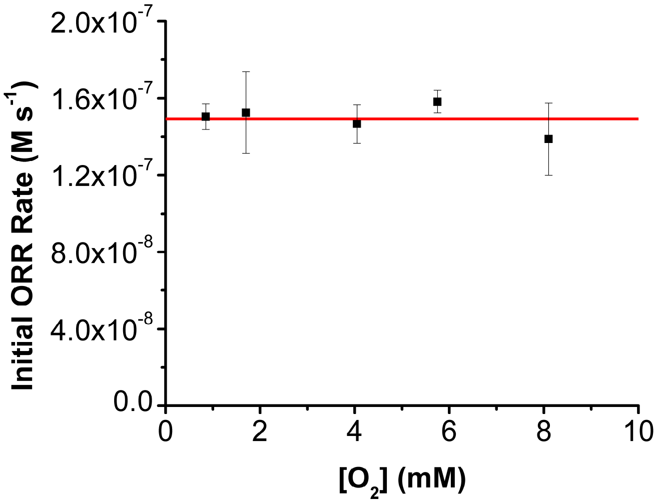

Figure S5.50. Determination of ORR reaction dependence upon [O_2] with **1** and 2-chlorobenzoic acid. Horizontal line represents the global average rate observed across all experiments described for variable [O_2].

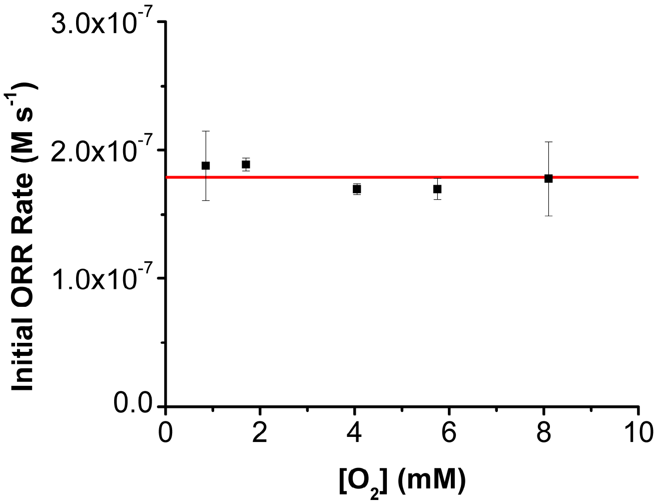

Figure S5.51. Determination of ORR reaction dependence upon [O2] with **1** and 2,4-dichlorobenzoic acid. Horizontal line represents the global average rate observed across all experiments described for variable [O2].

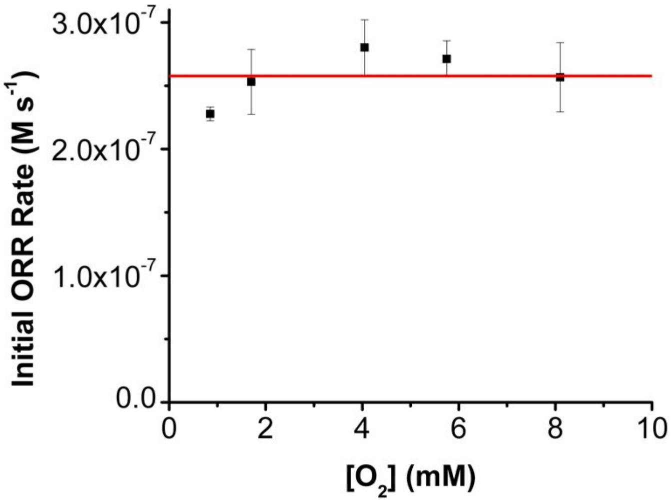

Figure S5.52. Determination of ORR reaction dependence upon [O2] with **1** and 2,6-dichlorobenzoic acid. Horizontal line represents the global average rate observed across all experiments described for variable [O2].

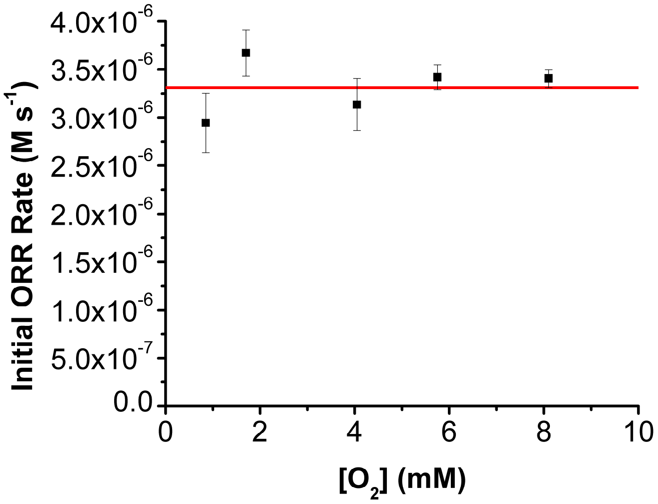

Figure S5.53. Determination of ORR reaction dependence upon [O$_2$] with **2** and benzoic acid. Horizontal line represents the global average rate observed across all experiments described for variable [O$_2$].

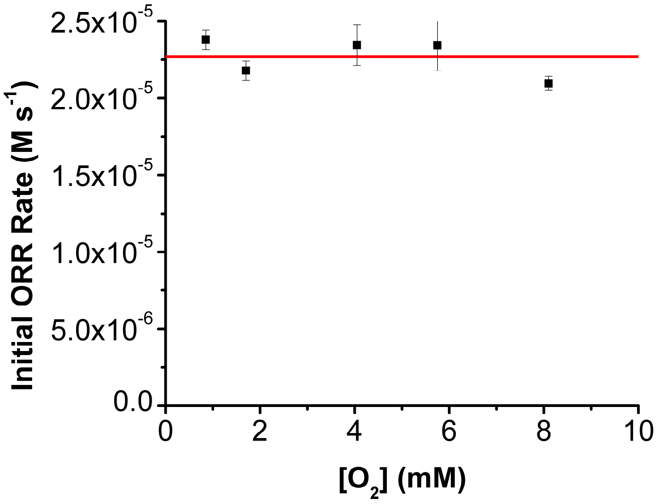

Figure S5.54. Determination of ORR reaction dependence upon [O$_2$] with **2** and 2-chlorobenzoic acid. Horizontal line represents the global average rate observed across all experiments described for variable [O$_2$].

5.6.7.4 Determination of the Catalytic Rate Law for 2 with 2,4-dichlorobenzoic acid and 2,6-dichlorobenzoic acid.

For this combination of acids and Co complex **2**, the reaction rate was too fast to be reliably measured by initial rates using the Agilent Cary 60 UV-vis spectrometer. Stopped-flow rapid-mixing spectrochemical studies were performed with a CSF-61DX2 stopped-flow system from Hi-Tech Scientific with monitoring at 780 nm using Kinetic Studio Software. All data fits were performed within the Kinetic Studio 4.0 Software Suite. For each concentration combination three sets of five-run data sets were collected and then the average of each five-run data set was fit. Prior to experiments, dried MeCN was passed through all syringes and the cell block before reagents were loaded. In a typical experiment, syringes were loaded with known concentrations of reagents. All concentrations are reported as mixed concentrations, which are half of the syringe concentrations.

[**2**]

An O_2-saturated MeOH solution of cobalt complex **2** (40, 60, 80, 120, and 160 μM) containing 50 mM benzoic acid derivative was mixed with an O_2-saturated (O_2 saturation concentration in MeCN is 8.1 mM) MeCN solution containing 3 mM Cp^*_2Fe. The absorbance was monitored at 780 nm by UV-vis spectroscopy. Experiments were repeated in triplicate, figure axes show final concentrations; initial rates and background correction procedure described on Page 309.[9-10]

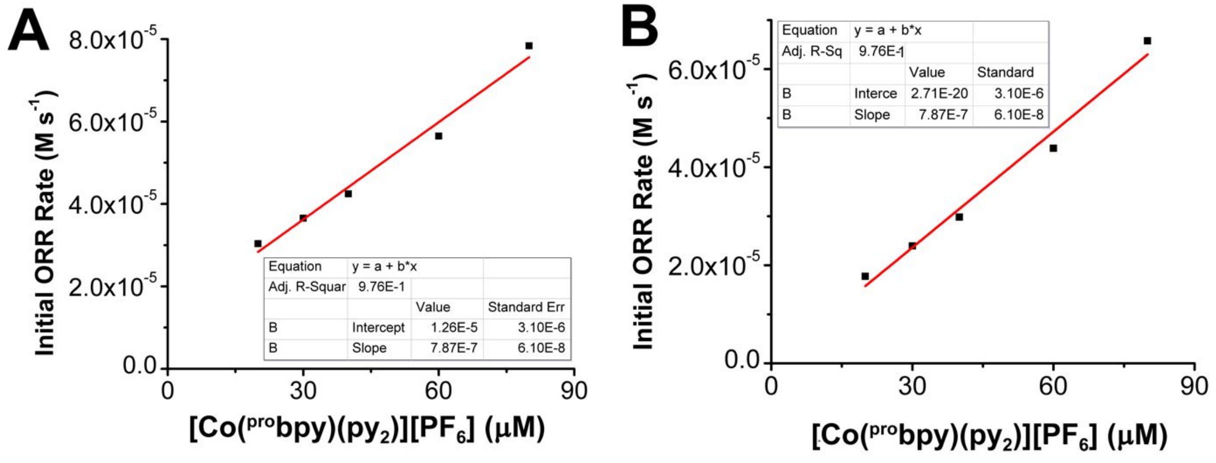

Figure S5.55. Determination of ORR reaction dependence upon [**2**] with 2,4-dichlorobenzoic acid. (A) Uncorrected for background O_2 reduction. (B) Corrected for background O_2 reduction.

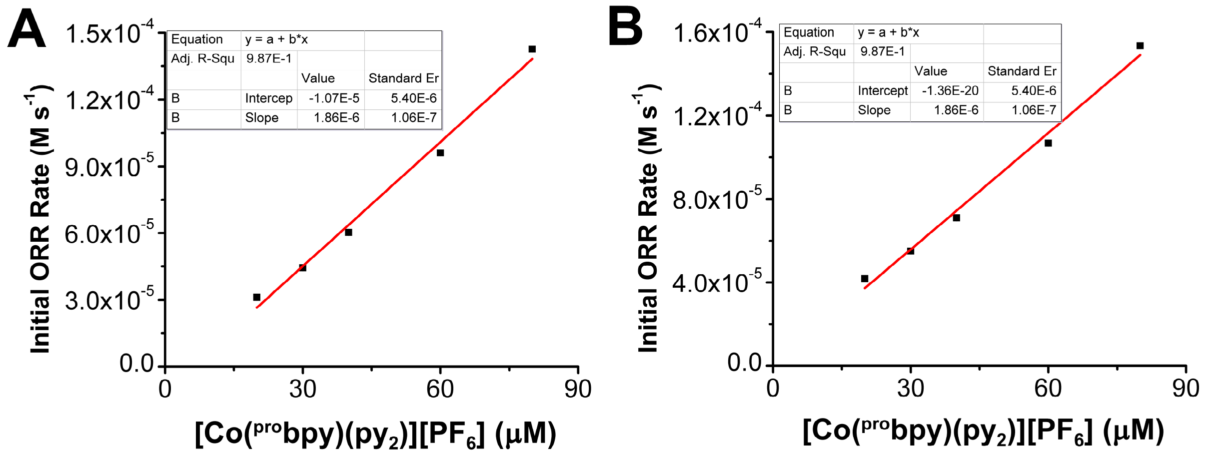

Figure S5.56. Determination of ORR reaction dependence upon [**2**] with 2,6-dichlorobenzoic acid. (A) Uncorrected for background O_2 reduction. (B) Corrected for background O_2 reduction.

[Benzoic Acid Derivative]

A O_2-saturated MeCN solution of complex 2 (80 μM) containing varied benzoic acid derivative concentrations (30, 40, 50, 70, 100 mM) was mixed with an O_2-saturated MeCN solution containing 3 mM $Cp*_2Fe$. The absorbance was monitored at 780 nm by UV-visible spectroscopy. Experiments were repeated in triplicate, figure axes show final concentrations; initial rates and background correction procedure described on Page 309.

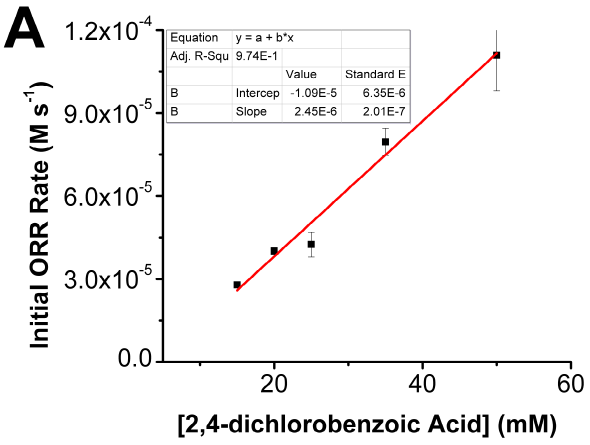

Equation	y = a + b*x		
Adj. R-Squ	9.74E-1		
		Value	Standard E
B	Intercep	-1.09E-5	6.35E-6
B	Slope	2.45E-6	2.01E-7

Equation	y = a + b*x		
Adj. R-Squ	9.74E-1		
		Value	Standard E
B	Intercep	2.57E-19	6.35E-6
B	Slope	2.45E-6	2.01E-7

Figure S5.57. Determination of ORR reaction dependence upon [2,4-dichlorobenzoic acid] with **2**. (A) Uncorrected for background O2 reduction. (B) Corrected for background O2 reduction, note that the background reaction is assumed to have minimal initial ORR rate dependence on [2,4-dichlorobenzoic Acid] relative to the reaction catalyzed by **2.**

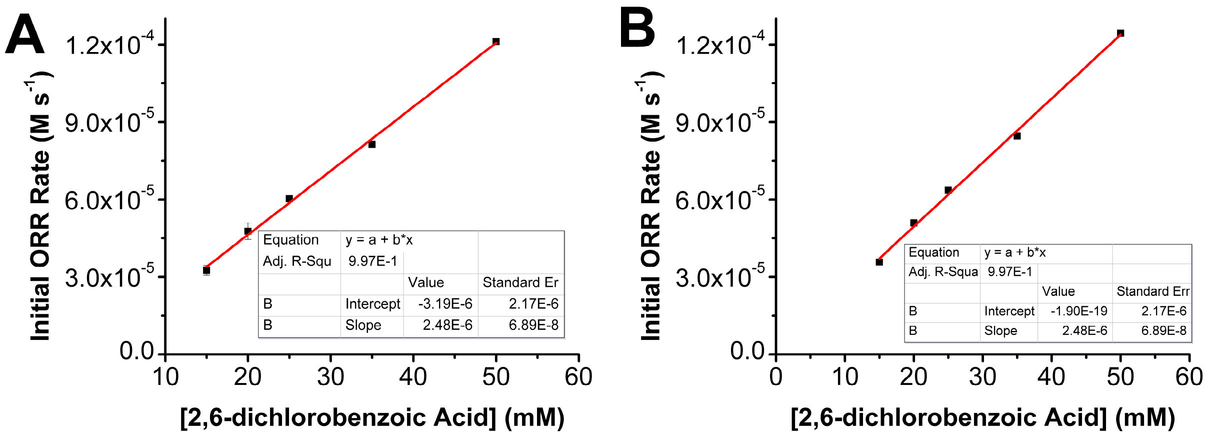

Equation	y = a + b*x		
Adj. R-Squ	9.97E-1		
		Value	Standard Er
B	Intercept	-3.19E-6	2.17E-6
B	Slope	2.48E-6	6.89E-8

Equation	y = a + b*x		
Adj. R-Squa	9.97E-1		
		Value	Standard Err
B	Intercept	-1.90E-19	2.17E-6
B	Slope	2.48E-6	6.89E-8

Figure S5.58. Determination of ORR reaction dependence upon [2,6-dichlorobenzoic Acid] with **2**. (A) Uncorrected for background O2 reduction. (B) Corrected for background O2 reduction, note that the background reaction is assumed to have minimal initial ORR rate dependence on [2,6-dichlorobenzoic Acid] relative to the reaction catalyzed by **2**.

[Cp*$_2$Fe]

A O_2-saturated MeCN solution of cobalt complex **2** (80 μM) and benzoic acid derivative (50 mM) was mixed with 1.0 mL O_2-saturated MeCN solution containing Cp*$_2$Fe (1.5, 2.0, 2.4, 2.8, and 3.0 mM). Then the reaction mixture was monitored at 780 nm by UV-visible spectroscopy. Experiments were repeated in triplicate, figure axis shows final concentration; initial rates procedure described on Page 309.

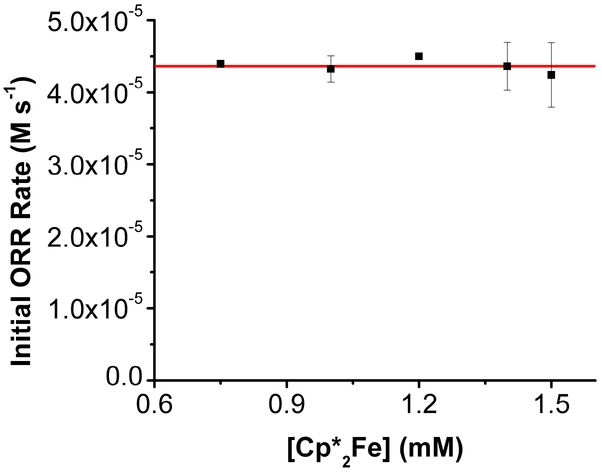

Figure S5.59. Determination of ORR reaction dependence upon [Cp*$_2$Fe] with **2** and 2,4-dichlorobenzoic acid. Horizontal line represents the global average rate observed across all experiments described for variable [Cp*$_2$Fe].

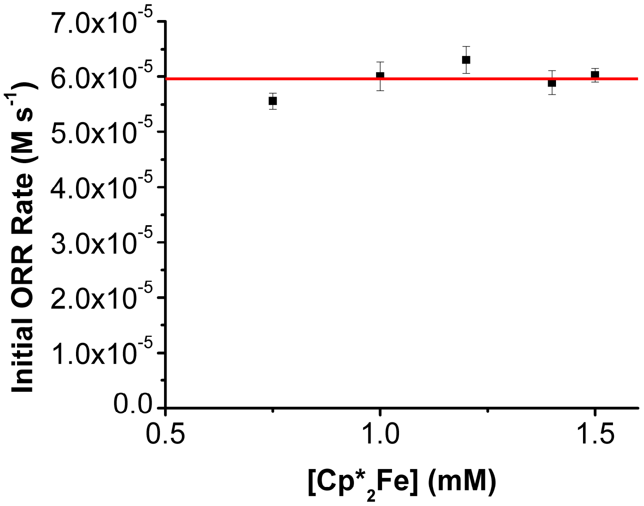

Figure S5.60. Determination of ORR reaction dependence upon [Cp*$_2$Fe] with **2** and 2,6-dichlorobenzoic acid. Horizontal line represents the global average rate observed across all experiments described for variable [Cp*$_2$Fe].

[O$_2$]

(1) A O$_2$-saturated MeCN solution of cobalt complex **2** (80 μM) containing benzoic acid derivative (50 mM) was mixed with an O$_2$-saturated MeCN solution of 3 mM Cp*$_2$Fe. The absorbance was monitored at 780 nm by UV-visible spectroscopy ([O$_2$] 8.1 mM). Experiments were repeated in triplicate, figure axis shows final concentration; initial rates procedure described on Page 309.

(2) A O$_2$-saturated MeCN solution of cobalt complex **2** (80 μM) containing benzoic acid derivative (50 mM) was mixed with air-saturated MeCN solution of 3 mM Cp*$_2$Fe. The absorbance was monitored at 780 nm by UV-visible spectroscopy ([O$_2$] 5.8 mM). Experiments were repeated in triplicate, figure axis shows final concentration; initial rates procedure described on Page 309.

(3 A O$_2$-saturated MeCN solution of cobalt complex **2** (80 μM) containing benzoic acid derivative (50 mM) was mixed with an Ar saturated MeCN solution of 3 mM then the

absorbance was monitored at 780 nm by UV-visible spectroscopy ([O_2] 4.1 mM). Experiments were repeated in triplicate, figure axis shows final concentration; initial rates procedure described on Page 309.

(4) An air-saturated MeCN solution of cobalt complex **2** (80 μM) containing benzoic acid derivative (50 mM) was mixed with an air-saturated MeCN solution of 3 mM and the absorbance was monitored at 780 nm by UV-visible spectroscopy ([O_2] 1.7 mM). Experiments were repeated in triplicate, figure axis shows final concentration; initial rates procedure described on Page 309.

(5) An air-saturated MeCN solution of cobalt complex **2** (80 μM) containing benzoic acid derivative (50 mM) was mixed with an Ar saturated MeCN solution of 3 mM and the absorbance was monitored at 780 nm by UV-visible spectroscopy ([O_2] 0.85 mM). Experiments were repeated in triplicate, figure axis shows final concentration; initial rates procedure described on Page 309.

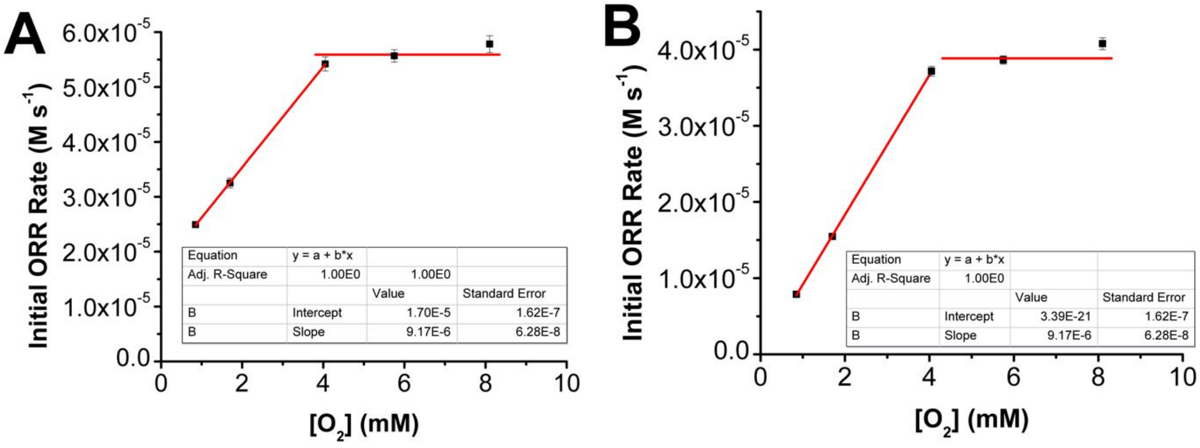

Figure S5.61. Determination of ORR reaction dependence upon [O_2] with **2** and 2,4-dichlorobenzoic acid. Horizontal line represents the global average rate observed across experiments from 4.1-8.1 mM O_2 described for variable [O_2].

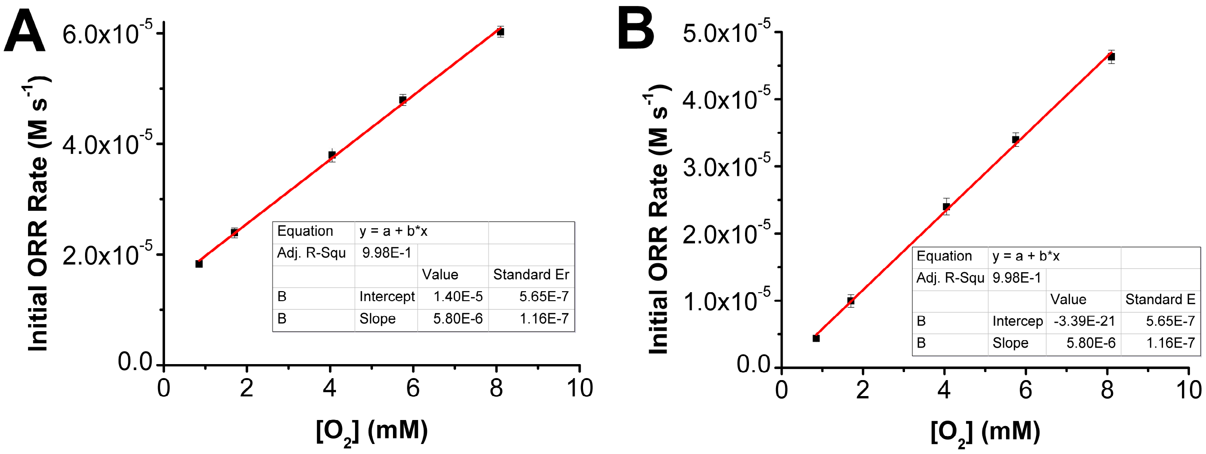

Figure S5.62. Determination of ORR reaction dependence upon [O_2] with **2** and 2,6-dichlorobenzoic acid. (A) Uncorrected for background O_2 reduction. (B) Corrected for background O_2 reduction, note that the background reaction is assumed to have minimal initial ORR rate dependence on [O_2] relative to the reaction catalyzed by 2.

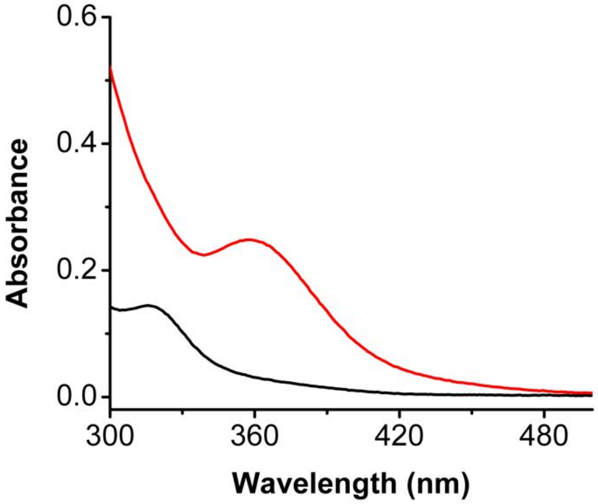

Figure S5.63. Iodometric titration of a catalytic reaction of **2** with 0.9 mM $Cp*_2Fe$, 25 mM AcOH, and O_2 saturation in MeOH to determine ORR selectivity by our previously reported method.[3]

Determination of turnover frequency (TOF) (adapted[9]).

The initial observed rate of ORR ($Rate_{obs}$, units of M s^{-1}) is a combination of the catalytic rate ($Rate_{cat}$) and background rate ($Rate_{background}$) of $Cp*_2Fe$ oxidation as follows:

$$Rate_{obs} = Rate_{cat} + Rate_{background} \quad (5.6)$$

In all cases, $Rate_{obs}$ values were obtained by taking the results of a linear fit of the initial region of $[Cp*_2Fe]^+$ growth at 780 nm (units = relative absorbance/minute) to a minimum R^2 of 0.99 utilizing Kinetic Studio 4.0 Software Suite. The results of the linear fit were processed to reflect the rate of ORR by converting relative absorbance units to concentration using the molar extinction coefficient of $[Cp*_2Fe]^+$ (ε = 461 M^{-1} cm^{-1} as determined by serial dilution of a chemically prepared sample of $[Cp*_2Fc][BF_4]$), correcting for the number of electrons passed during catalysis.

Rate_{cat}

$Rate_{cat}$ is equivalent to the following based on the experimentally determined rate law, where x = 0 for **1** with all HA, 0 for **2** with benzoic acid and 2-chlorobenzoic acid, and 1 for **2** with 2,4-dichlorobenzoic acid and 2,6-dichlorobenzoic acid:

$$Rate_{cat} = k_{cat}[\mathbf{1}][HA][O_2]^x \quad (5.7)$$

By substitution:

$$Rate_{obs} = k_{cat}[\mathbf{1}][benzoic\ acid\ derivative][O_2]^x + Rate_{background} \quad (5.8)$$

We can also determine the TOF for this complex utilizing the individual initial rates ($Rate_{[0]}$) from this graph, subtracting the background rate, and dividing by the catalyst concentration.

$$TOF = \frac{Rate_{[0]} - Rate_{background}}{[1]} \qquad (5.9)$$

5.6.7.5 Determination of Overpotential:

Overpotential calculations for this system is complicated by the inability to utilize buffered acids for kinetic or electrochemical studies. Utilizing reported pK_a and $\log(K_f)$ (K_f is the equilibrium constant for homoconjugation of a given HA) , we have corrected for standard reduction potentials using the following equations:[11]

$$E^0_{H2O} = 1.21 - 0.0592pK_a + \frac{2.303RT}{4F}\log(4K_f) \qquad (5.10)$$

$$E^0_{H2O2} = 0.68 - 0.0592pK_a + \frac{2.303RT}{2F}\log(2K_f) \qquad (5.11)$$

5.6.7.6 Determination of KIE (adapted[1])

d_1-2,6-dichlorobenzoic acid (O-D) was synthesized by stirring 2,6-dichlorobenzoic acid in a Schlenk flask with 5:1 D_2O:MeOD for 3 h under an N_2 atmosphere, followed by solvent removal by reduced pressure. *d_1*-2,6-dichlorobenzoic acid (O–D) was stored under positive N_2 pressure until use. ^{1}H-NMR in were taken in CD_2Cl_2 (dried on 4 Å mol sieves for 4 days) to determine % deuteration (92%, **Figure S5.60-S5.61**).

After correction for background ORR rate, the slopes of the plots of initial ORR rate vs [HA] give pseudo-first order rate constants k_H and k_d directly **Eq 5.12**.

$$Initial\ ORR\ Rate = k_{H/D}[AH] \qquad \text{eq}(5.12)$$

Since [O_2] is constant under O_2 saturation conditions, it follows that by taking a direct ratio of the slopes obtained with 2,6-dichlorobenzoic acid and d_1-2,6-dichlorobenzoic acid, a KIE can be obtained eq(8). k_H is for 2,6-dichlorobenzoic acid of normal isotopic abundance; k_D is for d_1-2,6-dichlorobenzoic acid. To correct for non-stoichiometric deuteration, consider **Eq 5.13** which gives the observed slope for deuteration as a function of the mol fraction (χ_H/χ_D) and the known slope for naturally abundant O–H. This leads to **Eq 5.14** to give the corrected KIE. The uncorrected value for k_h/k_d for **1** is 1.1±0.1, the corrected value obtained using **Eq 5.15** to correct for incomplete deuteration is 1.2±0.1. The uncorrected value for k_h/k_d for **2** is 2.1±0.1, the corrected value obtained using equation 6 to correct for incomplete deuteration is 2.4±0.2.

$$\frac{Slope_H}{Slope_D} = \frac{k_H[O_2]}{k_D[O_2]} = \frac{k_H}{k_D} \qquad (5.13)$$

$$Slope_D = \frac{(Slope_{obs} - (\chi_H \times slope_H)}{\chi_D} \qquad (5.14)$$

$$\frac{\mathrm{k_H}}{\mathrm{k_D}} = \frac{\chi_\mathrm{D} \times \mathrm{Slope_H}}{\mathrm{Slope_{obs}} \text{- } (\chi_\mathrm{H} \times \mathrm{Slope_{H)}}} \qquad (5.15)$$

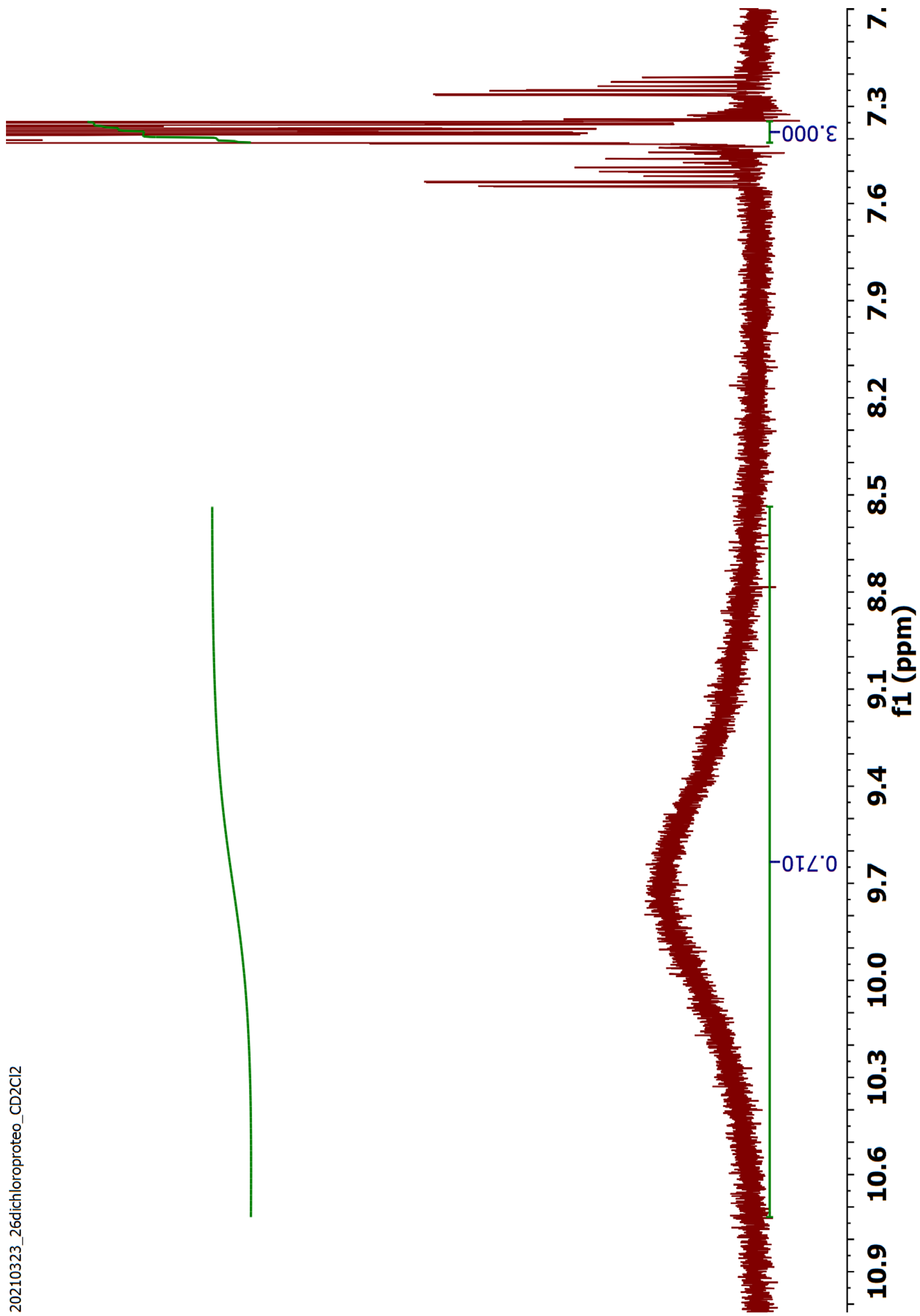

Figure S5.64. ^{1}H NMR of 2,6-dichlorobenzoic acid (O-H) in dry CD_2Cl_2.

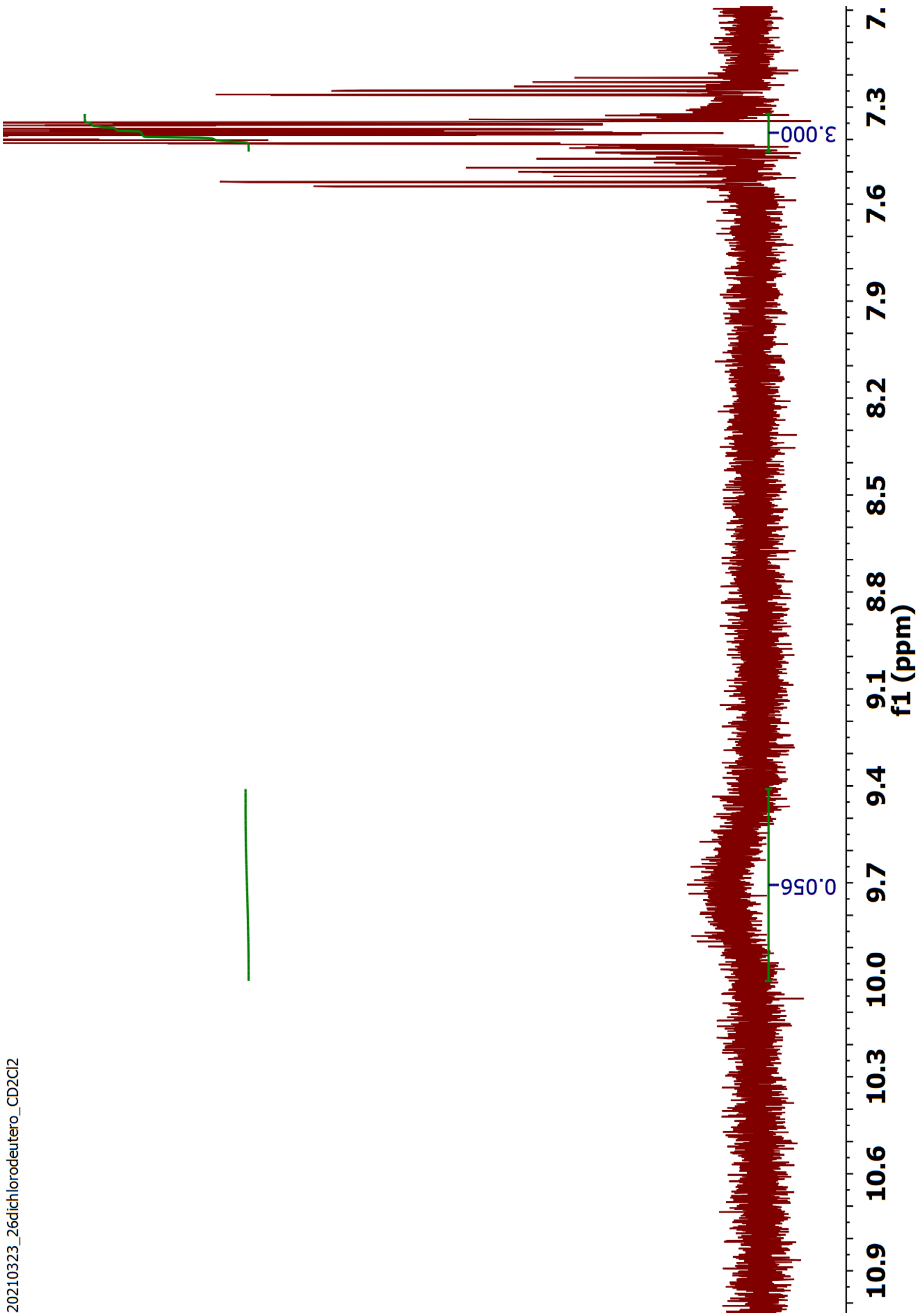

Figure S5.65. ^{1}H NMR of d_1-2,6-dichlorobenzoic acid (O-D) in dry CD_2Cl_2.

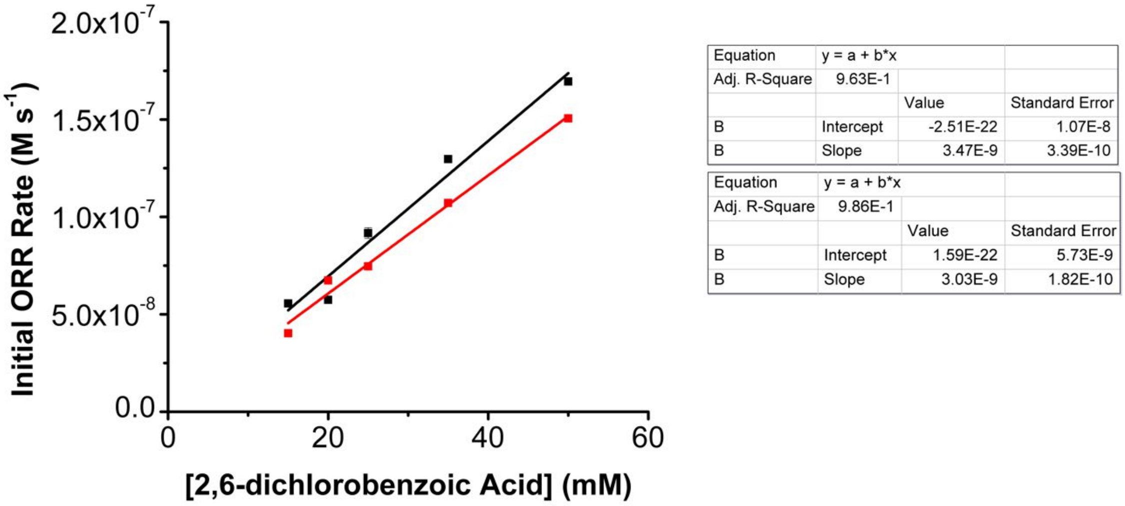

Equation	y = a + b*x		
Adj. R-Square	9.63E-1		
		Value	Standard Error
B	Intercept	-2.51E-22	1.07E-8
B	Slope	3.47E-9	3.39E-10

Equation	y = a + b*x		
Adj. R-Square	9.86E-1		
		Value	Standard Error
B	Intercept	1.59E-22	5.73E-9
B	Slope	3.03E-9	1.82E-10

Figure S5.66. Determination of KIE with **1**. Corrected ratio of slopes gives a KIE of 1.2±0.1.

Chapter 6

Conclusions and Future Work

6.1 Introduction

This thesis has detailed a series of projects that investigated the use of N_2O_2 ligands in the CO_2RR and the ORR. The utilization of an Fe metal center enabled the production of HCO_2^- from CO_2 in the presence of phenol under electrochemically reducing conditions. When the metal center was switched to Co, ORR capabilities were observed, with the major product being H_2O. In both systems, addition of secondary-sphere moieties led to enhanced rates and altered selectivity. This work has led to new understanding of design principles in molecular electrocatalysis for each reaction, with uniquely positioned secondary-sphere moieties providing novel reactivity changes in comparison to typically designed systems. Following a summary of the previous chapters, future directions and preliminary results are briefly summarized.

6.2 Summary and Conclusions

Chapter 2 of this dissertation focused on synthesis, characterization, and reactivity of **Fe(^{tbu}dhbpy)Cl** towards CO_2 under electrochemically reducing conditions in the presence of phenol.[1] In the presence of CO_2 under aprotic conditions, this complex mediates the 2e⁻ reductive disproportionation of two equivalents of CO_2 to CO and CO_3^{2-}, with long-term degradation to Fe-carbonyl species observed. When phenol is added to the system, mechanistic studies indicate that the phenolate moieties coordinated to Fe are sensitive to protonation in the reduced state, which led us to propose that cooperative pendent proton interactions were involved in CO_2 reduction. Experiments with phenol under CO_2 atmosphere generated HCO_2^- (68±4% Faradaic efficiency) with H_2 and CO completing the Faradaic mass balance. This work led to the development of the ligands discussed in Chapters 3 and 5.

Chapter 3 focused on studying how secondary-sphere moieties oriented towards the protonation-sensitive Fe-bound phenolate ligands would affect catalytic reactivity towards CO_2.[2] Two new ligands, ^{me}crebpy and ^{tbu}catbpy, and their Fe complexes were synthesized, characterized, and their reactivity towards CO_2 under electrochemically reducing conditions with added phenol was examined. Enhanced partial current density for HCO_2^- and selectivity were observed with Fe(^{me}crebpy)Cl in comparison to the Fe(^{tbu}dhbpy)Cl (Chapter 2). Fe(^{tbu}catbpy) was only observed to have slightly higher partial current densities for HCO_2^-, while selectivity was the same as observed for Fe(^{tbu}dhbpy)Cl. These results led us to propose a mechanism whereby proton transfer is enhanced through pre-concentration of added phenol in close proximity to the active site by these pendent moieties, with stronger hydrogen-bonding interactions present in Fe(^{tbu}catbpy) leading to less favorable proton transfer. This work demonstrates a novel strategy for altering proton transfer reactivity through secondary-sphere moieties oriented towards protonation-responsive, coordinated O atoms rather than above the active site to interact with bound substrate.

Chapter 4 examines a Co complex of ^{tbu}dhbpy, [Co(^{tbu}dhbpy)(py)$_2$][PF$_6$] (py = pyridine).[3] Previous work from Stahl and co-workers showed Co(N_2O_2) compounds to be active for the reduction of O_2 to H_2O_2 (>96%) in methanol solution with acetic acid as proton donor and Cp*$_2$Fe as reductant.[4] Earlier work from Thomas and coworkers showed Co(^{tbu}dhbpy) was reactive with O_2 to form a Co(III)($O_2^{\bullet-}$) species in pyridine solution.[5] With these two studies in mind, we synthesized, characterized, and examined the reactivity towards oxygen reduction of [Co(^{tbu}dhbpy)(py)$_2$][PF$_6$] under the conditions previously studied by Stahl and co-workers. Interestingly, we observed divergent selectivity in comparison to this work ([Co(^{tbu}dhbpy)(py)$_2$][PF$_6$] = 29±5% H_2O_2) while the rate law was maintained. This led us to propose a similar mechanism to that proposed previously for Co(N_2O_2) compounds, with the key selectivity-determining step governed by the stronger π-accepting ability of the bipyridine ligand relative to salen, salophen, and acen derivatives, allowing for facile protonation of the distal O atom of the bound Co hydroperoxo species.

Chapter 5 was built upon the knowledge generated in Chapter 3 regarding non-traditional secondary-sphere effects for CO_2 reduction. This knowledge was applied to generate [Co(^{pro}bpy)(py)$_2$][PF$_6$] to study how secondary-sphere can affect the oxygen reduction reaction. This new compound has secondary-sphere pendent –OMe groups poised to direct protonation to the proximal O atom of the bound hydroperoxo species. A comparative study with [Co(^{tbu}dhbpy)(py)$_2$][PF$_6$] in acetonitrile with a homologous series of benzoic acids with varied pK_a was carried out, and results showed an enhancement in ORR rate and altered selectivity towards H_2O_2 production with [Co(^{pro}bpy)(py)$_2$][PF$_6$] relative to [Co(^{tbu}dhbpy)(py)$_2$][PF$_6$].

6.3 Preliminary Results and Future Directions

6.3.1 CO_2 Reduction with Fe Compounds in the presence of Lewis Acids

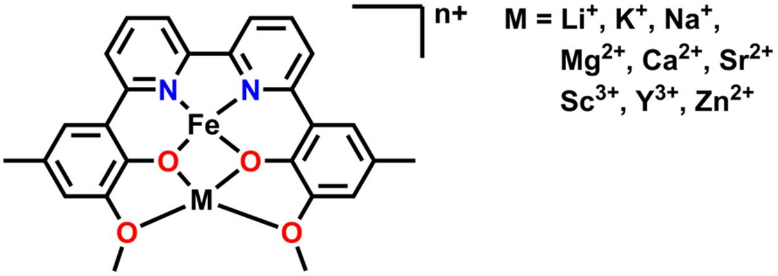

Figure 6.1. Proposed structures of secondary-sphere supported Lewis acid additives for CO_2 reduction.

Another way to use the ligands we designed for secondary-sphere interactions described in Chapter 3 and Chapter 5 is to use the secondary-sphere pocket to incorporate a second metal ion (**Figure 6.1**). For the majority of ligand frameworks, synthetic challenges prevent the inclusion of a secondary metal ion and reports are limited of heterobimetallic molecular systems for the CO_2 reduction reaction.[6] Both ^{me}crebpy and ^{pro}bpy have structural characteristics which allow access to two metal ions in close proximity which are bridged by a heteroatom in a similar structural pattern to what is seen in carbon monoxide (CO) dehydrogenases and formic acid (FA) dehydrogenases as discussed in Chapter 1.[7] This strategy has been used in similar N_2O_2 compounds to alter their redox properties[8-9] or reactivity, including systems for hydrogen evolution[10], asymmetric catalysis[11-15], and N-N bond formation.[16] However, only one heterobimetallic system has been studied for CO_2 reduction to this point.[17]

It is important to note that both the CO and FA dehydrogenase enzymes use a secondary metal center which is proposed to be redox active during catalysis; however, an initial study of non-redox active metals in the secondary sphere position in synthetic systems will allow for an understanding of how introduced charge effects the electronic and reactive properties of the primary metal center.[8-9] CO_2 reduction studies have used both alkali, alkaline earth, and a few other Lewis acidic metal centers to enhance catalysis in the absence of a proton donor.[18-21] It should be noted that in most cases, the use of Lewis acid additives leads to the precipitation of insoluble metal carbonates[18-20], but when $[Zn(cyclam)]^{2+}$ was employed as a Lewis acid additive its function was co-catalytic and no insoluble carbonates were detected.[21] These results led to a brief study of Fe(^{me}crebpy)Cl with added Lewis acidic metal triflate $M(OTf)_n$ salts to look for conditions where the cations could be stabilized within the secondary-sphere pocket and potentially operate in a co-catalytic fashion.

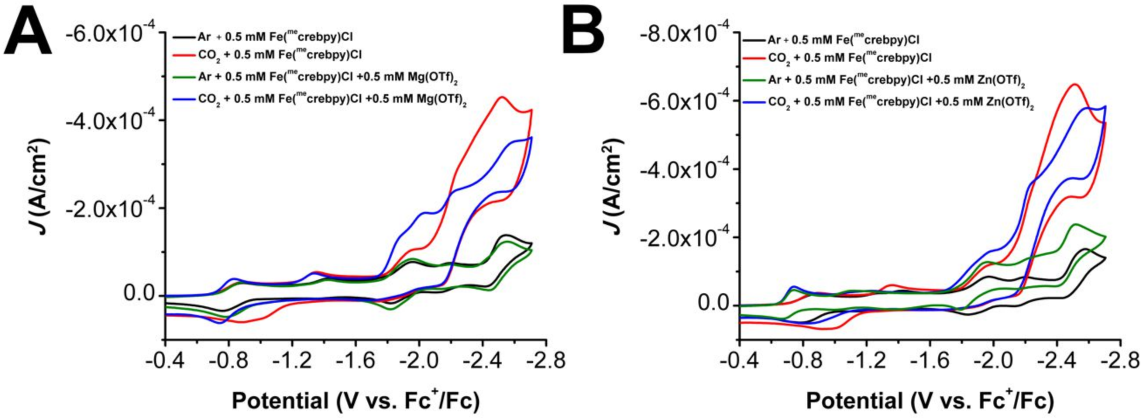

Figure 6.2. Cyclic voltammograms of 0.5 mM Fe(^{me}crebpy)Cl in 0.1M TBAPF$_6$/*N,N*-DMF supporting electrolyte with no added Lewis acid under Ar (black) or CO$_2$ (red) atmospheres and upon the addition of equimolar (0.5 mM) Mg(OTf)$_2$ or Zn(OTf)$_2$ under Ar (green) or CO$_2$ (blue) atmospheres. Working electrode: 3 mM diameter glassy carbon; counter electrode: glassy carbon; reference electrode Ag/AgCl pseudoreference. Potentials referenced to internal ferrocene standard.

Upon the addition of 0.5 mM of either Mg(OTf)$_2$ or Zn(OTf)$_2$ to solutions of 0.5 mM Fe(^{me}crebpy)Cl in 0.1 M TBAPF$_6$/*N,N*-DMF supporting electrolyte under aprotic conditions changes in the redox properties were observed. Under Ar with added Mg(OTf)$_2$, a slight shift towards negative potentials at the first reduction feature is observed, which could indicate association of the Mg^{2+} cation to the secondary-sphere binding pocket upon the generation of an anionic species (**Figure 6.2A**). However, the observed shift is quite minimal, and one would expect shifts in the other reduction features upon the introduction of the local electric field if this were the case.[8-9] In contrast, under Ar with added Zn^{2+}, a shift of the first reduction potential by ~200 mV towards positive potential indicates that Zn^{2+} has likely associated with the binding pocket (**Figure 6.2B**).[8-9] More negative reduction features are shifted by smaller amounts (20-60 mV), but this is consistent with their assignment as metal-ligand mixed redox features.

When aprotic conditions under CO_2 saturation with 0.5 mM $Mg(OTf)_2$ or $Zn(OTf)_2$ added to solutions of 0.5 mM Fe(^{me}crebpy)Cl in 0.1 M $TBAPF_6$/*N,N*-DMF supporting electrolyte were tested, additional changes in the CV waveform were observed in comparison to the conditions with no Lewis acid additive described above. Under CO_2 with added $Mg(OTf)_2$, four distinct reduction waves are observed near or more negative than the approximate potential for CO_2 binding in the absence of a Lewis acid additive (**Figure 6.2A**). The potentials at half wave height for each reduction feature are approximately –1.81 V, –1.96 V, –2.17 V, and –2.5 V vs Fc^+/Fc. The first wave is approximately 50 mV more positive than the potential of CO_2 binding in the absence of Mg^{2+}, and current densities greater than that in the absence of Mg^{2+} are observed from –1.75 V to –2.18 V vs Fc^+/Fc. After –2.18 V vs Fc, two separate plateaus are achieved.

Under a CO_2 atmosphere with added Zn^{2+}, three distinct reduction waves are observed near or more negative than the approximate potential for CO_2 binding in the absence of a Lewis acid additive (**Figure 6.2B**). The potentials at half wave height for each reduction feature are approximately –1.83 V, –2.18 V, and –2.5 V vs Fc^+/Fc. The first wave is approximately 30 mV more positive than the potential of CO_2 binding in the absence of Zn^{2+} and current densities greater than that in the absence of Zn^{2+} are observed from –1.75 V to –2.25 V vs Fc^+/Fc. After –2.18 V vs Fc, one plateau is achieved. Importantly, *this reactivity is not observed in the absence of Fe(^{me}crebpy)Cl under these conditions* (**Figure 6.3**). Controlled potential electrolysis studies with 0.5 mM $Zn(OTf)_2$ and 0.5 mM Fe(^{me}crebpy)Cl at –2.5 V vs Fc^+/Fc generated substantial amounts of oxalate, which is not observed with either component in the absence of the either component, consistent with the heterobimetallic active site favoring a new reaction pathway.

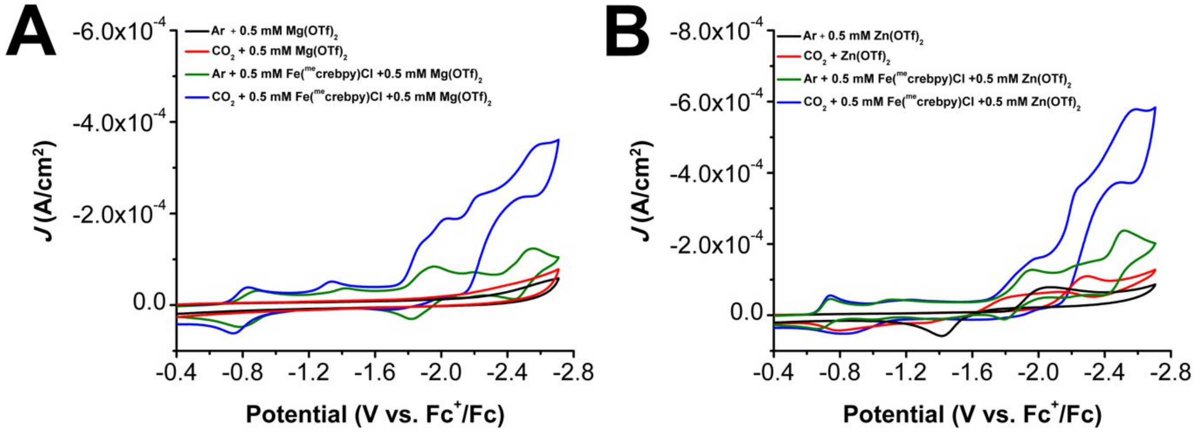

Figure 6.3. Cyclic voltammograms of 0.5 mM (A) $Mg(OTf)_2$ or (B) $Zn(OTf)_2$ in 0.1 M $TBAPF_6$/*N,N*-DMF supporting electrolyte with no added Fe(^{me}crebpy)Cl under Ar (black) or CO_2 (red) atmospheres and upon the addition of equimolar Fe(^{me}crebpy)Cl under Ar (green) or CO_2 (blue) atmospheres. Working electrode: 3 mM diameter glassy carbon; counter electrode: glassy carbon; reference electrode Ag/AgCl pseudoreference. Potentials referenced to internal ferrocene standard.

While this preliminary study shows promise for the development of a system which utilizes a heterobimetallic construct that enhances CO_2 reduction, an in-depth mechanistic study is required for optimization. Abstraction of $Cl^–$ from the system with the introduction of non-coordinating anions will allow for more precise judgement of the Lewis acid's affinity for the secondary-sphere pocket, as $Cl^–$ release has an effect on the first reduction species of this family of Fe complexes.[1] UV-vis spectroelectrochemical studies will allow for the elucidation of the electronic structure of the heterobimetallic species which have been proposed to exist under these conditions.[22] Infrared spectroelectrochemistry will allow for a more thorough understanding of how the Lewis acids alter the binding mode of CO_2 to the metal center, and potentially allow for the determination of the individual species generated within each wave in the CV for each respective Lewis acid.[23] Finally, comprehensive controlled potential electrolysis studies are necessary to determine the CO_2 reduction products generated at different applied potentials. In future studies, the addition of Brønsted acids to these systems could also be assessed, to determine if unique product distributions are generated under electrochemically reducing conditions. At each stage of this project, comparison to the parent monometallic complexes should be used to enhance the understanding of the observed electronic structures and reactivity.

In summary, the generation of heterobimetallic molecular species for CO_2 reduction has not been highly studied even with most examples in nature relying upon these structural motifs.[24] Initial investigations of Lewis acid additives to Fe(^{me}crebpy)Cl show promising results, but a significant amount of work is still required to fully understand the system. Successful completion of this project will lead to an understanding of how a second metal center will interact with this type of ligand framework, and the lessons learned can be applied to other metal centers which have been studied within our lab for small molecule activation with the parent ^{tbu}dhbpy ligand framework.[3, 25-26]

6.3.2 CO_2 Reduction with Co(^{tbu}dhbpy) and [Co(^{tbu}dhbpy)(py)$_2$][PF_6]

Both Co(^{tbu}dhbpy) and [Co(^{tbu}dhbpy)(py)$_2$][PF_6] have also been evaluated for CO_2 reduction activity in the presence of phenol. Initial CV testing under Ar in MeCN reveals three distinct reduction potentials for Co(^{tbu}dhbpy) and four distinct reduction potentials for [Co(^{tbu}dhbpy)(py)$_2$][PF_6] (**Figure 6.4**). Co(^{tbu}dhbpy) has two reversible reduction features with $E_{1/2}$ of –0.36 and –1.64 V vs Fc^+/Fc and one quasi-reversible reduction feature with $E_{1/2}$ of –2.69 V in MeCN. [Co(^{tbu}dhbpy)(py)$_2$][PF_6] has three irreversible reductions with E_{pc} of –0.76, –2.26. and –2.7 V vs Fc^+/Fc and one quasi-reversible reduction with $E_{1/2}$ of –1.61 V vs Fc^+/Fc.

Under a CO_2 atmosphere, Co(^{tbu}dhbpy) has an increase in current at its most negative reduction feature with an i_c/i_p = 2.1 and an $E_{p/2}$ of –2.57 V vs Fc^+/Fc with a new oxidative feature on the return sweep with E_p = –1.89 V vs Fc^+/Fc. With [Co(^{tbu}dhbpy)(py)$_2$][PF_6], an increase in current is observed at the most negative reduction feature with an i_c/i_p = 4.6 and an $E_{p/2}$ of –2.41 V vs Fc^+/Fc. These results indicate reactivity with CO_2 is present under electrochemically reducing conditions.

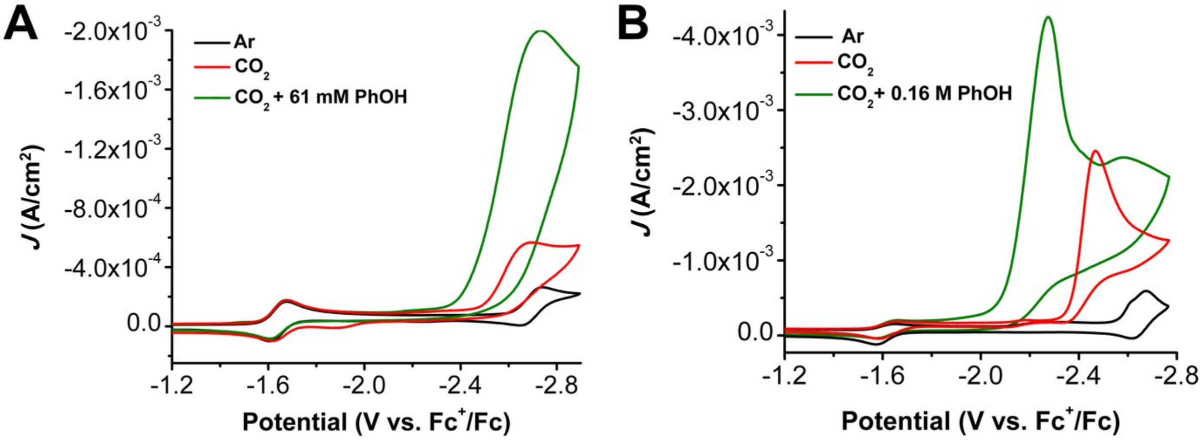

Figure 6.4. CVs of (A) Co(^{tbu}dhbpy) and (B) [Co(^{tbu}dhbpy)(py)$_2$][PF_6] under an Ar atmosphere, under a CO_2 atmosphere with optimized PhOH concentrations.

Upon addition of PhOH under a CO_2 atmosphere, a current increase is again observed at the third reduction feature with maximal current increase observed with 61 mM PhOH added with Co(^{tbu}dhbpy). At this concentration of PhOH, an i_c/i_p = 10 is observed with an $E_{p/2}$ = –2.56 V. With [Co(^{tbu}dhbpy)(py)$_2$][PF_6], maximal current increases with added PhOH are observed at 0.16 M PhOH. At this concentration of PhOH, an i_c/i_p = 8.2 is observed with an $E_{p/2}$ = –2.18 V. These results indicate reactivity with CO_2 is present under electrochemically reducing conditions in the presence of PhOH as a proton donor.

With these results in mind, we began to test the system for product distribution utilizing controlled potential electrolysis. Unfortunately, all electrolysis attempts to date have yet to reveal gaseous or solution phase CO_2 reduction products. Analysis of post-electrolysis electrodes via show no indication of Co deposition. Unknown issues stemming from catalyst deactivation are likely occurring, given the experimental variability. Further testing of catalytic conditions with varied co-substrates and co-catalysts like proton donors of varied strengths, Lewis acids, more strongly coordination axial ligands, and varied concentration or potential during electrolysis may lead to discovery of suitable reaction conditions for desired reactivity for CO_2. Further investigations into this reactivity are underway.

6.3.3 Application of N_2O_2 Ligands with Non-innocent Secondary-Sphere Moieties to Mn and Cr Electrocatalyst Systems

Other projects in the group have examined the structure and reactivity of Mn and Cr cations within the ^{tbu}dhbpy ligand framework (**Figure 6.5**).[25-28] These initial studies have given promising results: Mn(^{tbu}dhbpy)Cl is an active catalyst for the reduction of O_2 to H_2O_2 under both electrochemical[25] and spectrochemical[27] conditions, while Cr(^{tbu}dhbpy)(H_2O)Cl is the first active and selective molecular Group 6 electrocatalyst for reduction of CO_2.[26, 28] In both cases, initial mechanistic studies indicate the O atoms of the ligand framework bound to the metal center are susceptible to protonation or PhOH association.[25-26] With this in mind and the modified ligands which have been shown to be effective at altering this reactivity pathway in Chapter 3 and Chapter 5 through preconcentration, the complexes in **Figure 6.5** will be synthesized and studied for their reactivity in these reactions. This work is currently underway.

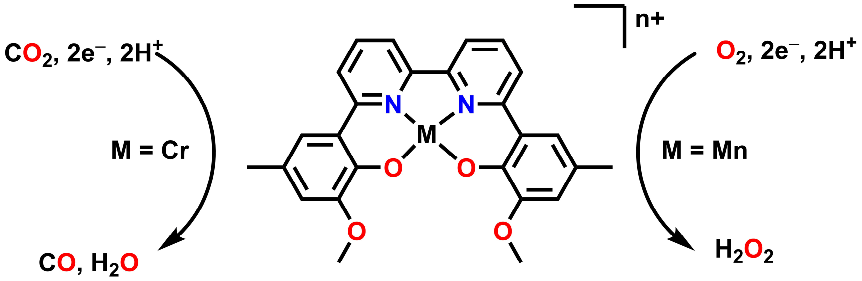

Figure 6.5. Proposed structures of Cr and Mn catalysts with secondary-sphere –OMe groups for CO_2 and O_2 reduction, respectively.

6.4 Perspective

Both CO_2 reduction and O_2 reduction reactions are important research avenues to help address energy issues we see today. The work presented in Chapters 2-5 of this thesis provides a solid foundation upon which interesting future work can be built, specifically in the area of secondary-sphere effects to control activity and selectivity. Each of the projects detailed in this chapter have the potential to have a significant impact on the fields of small molecule activation, energy storage and utilization in the long term.

Chapter 1 References

1. Senftle, T. P.; Carter, E. A., The Holy Grail: Chemistry Enabling an Economically Viable CO_2 Capture, Utilization, and Storage Strategy. *Accounts of Chemical Research* **2017,** *50*, 472-475.
2. Centi, G.; Perathoner, S., Opportunities and prospects in the chemical recycling of carbon dioxide to fuels. *Catalysis Today* **2009,** *148*, 191-205.
3. Benson, E. E.; Kubiak, C. P.; Sathrum, A. J.; Smieja, J. M., Electrocatalytic and homogeneous approaches to conversion of CO_2 to liquid fuels. *Chemical Society Reviews* **2009,** *38*, 89-99.
4. Rountree, E. S.; McCarthy, B. D.; Eisenhart, T. T.; Dempsey, J. L., Evaluation of homogeneous electrocatalysts by cyclic voltammetry. Inorganic Chemistry, **2014**, *53,* 9983-10002.
5. Jiang, C.; Nichols, A. W.; Machan, C. W., A look at periodic trends in d-block molecular electrocatalysts for CO_2 reduction. *Dalton Transactions* **2019**, *48*, 9454-9468.
6. Costentin, C.; Drouet, S.; Robert, M.; Savéant, J.-M., A Local Proton Source Enhances CO_2 Electroreduction to CO by a Molecular Fe Catalyst. *Science* **2012,** *338*, 90.
7. Sampson, M. D.; Nguyen, A. D.; Grice, K. A.; Moore, C. E.; Rheingold, A. L.; Kubiak, C. P., Manganese Catalysts with Bulky Bipyridine Ligands for the Electrocatalytic Reduction of Carbon Dioxide: Eliminating Dimerization and Altering Catalysis. *Journal of the American Chemical Society* **2014,** *136*, 5460-5471.
8. Ngo, K. T.; McKinnon, M.; Mahanti, B.; Narayanan, R.; Grills, D. C.; Ertem, M. Z.; Rochford, J., Turning on the Protonation-First Pathway for Electrocatalytic CO_2 Reduction by Manganese Bipyridyl Tricarbonyl Complexes. *Journal of the American Chemical Society* **2017,** *139*, 2604-2618.
9. Costentin, C.; Passard, G.; Robert, M.; Savéant, J.-M., Pendant Acid–Base Groups in Molecular Catalysts: H-Bond Promoters or Proton Relays? Mechanisms of the Conversion of CO_2 to CO by Electrogenerated Iron(0)Porphyrins Bearing Prepositioned Phenol Functionalities. *Journal of the American Chemical Society* **2014,** *136*, 11821-11829.
10. Azcarate, I.; Costentin, C.; Robert, M.; Saveant, J.-M., Through-Space Charge Interaction Substituent Effects in Molecular Catalysis Leading to the Design of the Most Efficient Catalyst of CO_2-to-CO Electrochemical Conversion. *Journal of the American Chemical Society* **2016,** *138*, 16639-16644.
11. Costentin, C.; Passard, G.; Robert, M.; Savéant, J.-M., Ultraefficient homogeneous catalyst for the CO_2-to-CO electrochemical conversion. *Proceedings of the National Academy of Sciences* **2014,** *111* (42), 14990-14994.
12. Himeda, Y.; Onozawa-Komatsuzaki, N.; Sugihara, H.; Kasuga, K., Simultaneous Tuning of Activity and Water Solubility of Complex Catalysts by Acid− Base Equilibrium of Ligands for Conversion of Carbon Dioxide. *Organometallics* **2007,** *26*, 702-712.
13. Hull, J. F.; Himeda, Y.; Wang, W. H.; Hashiguchi, B.; Periana, R.; Szalda, D. J.; Muckerman, J. T.; Fujita, E., Reversible hydrogen storage using CO_2 and a proton-

switchable iridium catalyst in aqueous media under mild temperatures and pressures. *Nature Chemistry* **2012,** *4*, 383-8.

14. Wang, W.; Muckerman, J. T.; Fujita, E.; Himeda, Y., Mechanistic Insight through Factors Controlling Effective Hydrogenation of CO_2 Catalyzed by Bioinspired Proton-Responsive Iridium(III) Complexes. *ACS Catalysis* **2013,** *3*, 856-860.
15. Suna, Y.; Ertem, M. Z.; Wang, W.-H.; Kambayashi, H.; Manaka, Y.; Muckerman, J. T.; Fujita, E.; Himeda, Y., Positional effects of hydroxy groups on catalytic activity of proton-responsive half-sandwich Cp* Iridium (III) complexes. *Organometallics* **2014,** *33*, 6519-6530.
16. Wang, W.-H.; Muckerman, J. T.; Fujita, E.; Himeda, Y., Mechanistic insight through factors controlling effective hydrogenation of CO_2 catalyzed by bioinspired proton-responsive iridium (III) complexes. *ACS Catalysis* **2013,** *3*, 856-860.
17. Himeda, Y.; Onozawa-Komatsuzaki, N.; Sugihara, H.; Arakawa, H.; Kasuga, K., Half-sandwich complexes with 4, 7-dihydroxy-1, 10-phenanthroline: water-soluble, highly efficient catalysts for hydrogenation of bicarbonate attributable to the generation of an oxyanion on the catalyst ligand. *Organometallics* **2004,** *23*, 1480-1483.
18. Himeda, Y.; Onozawa-Komatsuzaki, N.; Sugihara, H.; Kasuga, K., Recyclable catalyst for conversion of carbon dioxide into formate attributable to an oxyanion on the catalyst ligand. *Journal of the American Chemical Society* **2005,** *127*, 13118-13119.
19. Manaka, Y.; Wang, W.-H.; Suna, Y.; Kambayashi, H.; Muckerman, J. T.; Fujita, E.; Himeda, Y., Efficient H2 generation from formic acid using azole complexes in water. *Catalysis Science & Technology* **2014,** *4*, 34-37.
20. Wang, W. H.; Xu, S.; Manaka, Y.; Suna, Y.; Kambayashi, H.; Muckerman, J. T.; Fujita, E.; Himeda, Y., Formic acid dehydrogenation with bioinspired iridium complexes: a kinetic isotope effect study and mechanistic insight. *ChemSusChem* **2014,** *7*, 1976-1983.
21. Cammarota, R. C.; Vollmer, M. V.; Xie, J.; Ye, J.; Linehan, J. C.; Burgess, S. A.; Appel, A. M.; Gagliardi, L.; Lu, C. C., A Bimetallic Nickel–Gallium Complex Catalyzes CO_2 Hydrogenation via the Intermediacy of an Anionic d10 Nickel Hydride. *Journal of the American Chemical Society* **2017,** *139*, 14244-14250.
22. Helm, M. L.; Stewart, M. P.; Bullock, R. M.; DuBois, M. R.; DuBois, D. L., A Synthetic Nickel Electrocatalyst with a Turnover Frequency Above 100,000 s^{-1} for H_2 Production. *Science* **2011,** *333*, 863.
23. DuBois, M. R.; DuBois, D. L., The roles of the first and second coordination spheres in the design of molecular catalysts for H_2 production and oxidation. *Chemical Society Reviews* **2009,** *38*, 62-72.
24. Gloaguen, F.; Rauchfuss, T. B., Small molecule mimics of hydrogenases: hydrides and redox. *Chemical Society Reviews* **2009,** *38*, 100-108.
25. Ginovska-Pangovska, B.; Dutta, A.; Reback, M. L.; Linehan, J. C.; Shaw, W. J., Beyond the active site: the impact of the outer coordination sphere on electrocatalysts for hydrogen production and oxidation. *Accounts of Chemical Research* **2014,** *47*, 2621-2630.
26. Reback, M. L.; Ginovska-Pangovska, B.; Ho, M. H.; Jain, A.; Squier, T. C.; Raugei, S.; Roberts, J. A.; Shaw, W. J., The Role of a Dipeptide Outer-Coordination Sphere

on H2-Production Catalysts: Influence on Catalytic Rates and Electron Transfer. *Chemistry – A European Journal* **2013,** *19*, 1928-1941.

27. Jacobsen, G. M.; Shoemaker, R. K.; McNevin, M. J.; Rakowski DuBois, M.; DuBois, D. L., Syntheses and structural characterizations of iron (II) complexes containing cyclic diphosphine ligands with positioned pendant nitrogen bases. *Organometallics* **2007,** *26*, 5003-5009.
28. Jacobsen, G. M.; Shoemaker, R.; Rakowski DuBois, M.; DuBois, D. L., Syntheses and reactions of iron (II) complexes containing diphosphine ligands with pendant nitrogen bases. *Organometallics* **2007,** *26*, 4964-4971.
29. Henry, R. M.; Shoemaker, R. K.; Newell, R. H.; Jacobsen, G. M.; DuBois, D. L.; Rakowski DuBois, M., Stereochemical control of iron (II) complexes containing a diphosphine ligand with a pendant nitrogen base. *Organometallics* **2005,** *24*, 2481-2491.
30. Henry, R. M.; Shoemaker, R. K.; DuBois, D. L.; DuBois, M. R., Pendant bases as proton relays in iron hydride and dihydrogen complexes. *Journal of the American Chemical Society* **2006,** *128*, 3002-3010.
31. Fraze, K.; Wilson, A. D.; Appel, A. M.; Rakowski DuBois, M.; DuBois, D. L., Thermodynamic Properties of the Ni− H Bond in Complexes of the Type $[HNi(P_2RN_2R')_2](BF_4)$ and Evaluation of Factors That Control Catalytic Activity for Hydrogen Oxidation/Production. *Organometallics* **2007,** *26*, 3918-3924.
32. Curtis, C. J.; Miedaner, A.; Ciancanelli, R.; Ellis, W. W.; Noll, B. C.; Rakowski DuBois, M.; DuBois, D. L., $[Ni(Et_2PCH_2NMeCH_2PEt_2)_2]^{2+}$ as a functional model for hydrogenases. *Inorganic Chemistry* **2003,** *42*, 216-227.
33. Wilson, A. D.; Newell, R. H.; McNevin, M. J.; Muckerman, J. T.; Rakowski DuBois, M.; DuBois, D. L., Hydrogen oxidation and production using nickel-based molecular catalysts with positioned proton relays. *Journal of the American Chemical Society* **2006,** *128*, 358-366.
34. Dutta, A.; Lense, S.; Hou, J.; Engelhard, M. H.; Roberts, J. A.; Shaw, W. J., Minimal proton channel enables H_2 oxidation and production with a water-soluble nickel-based catalyst. *Journal of the American Chemical Society* **2013,** *135*, 18490-18496.
35. Dutta, A.; Roberts, J. A.; Shaw, W. J., Arginine-Containing Ligands Enhance H_2 Oxidation Catalyst Performance. *Angewandte Chemie International Edition* **2014,** *53*, 6487-6491.
36. Galan, B. R.; Reback, M. L.; Jain, A.; Appel, A. M.; Shaw, W. J., Electrocatalytic Oxidation of Formate with Nickel Diphosphine Dipeptide Complexes: Effect of Ligands Modified with Amino Acids. *European Journal of Inorganic Chemistry* **2013,** *2013*, 5366-5371.
37. Galan, B. R.; Schöffel, J.; Linehan, J. C.; Seu, C.; Appel, A. M.; Roberts, J. A.; Helm, M. L.; Kilgore, U. J.; Yang, J. Y.; DuBois, D. L., Electrocatalytic oxidation of formate by $[Ni(PR_2NR'_2)_2(CH_3CN)]^{2+}$ complexes. *Journal of the American Chemical Society* **2011,** *133*, 12767-12779.
38. Seu, C. S.; Appel, A. M.; Doud, M. D.; DuBois, D. L.; Kubiak, C. P., Formate oxidation via β-deprotonation in $[Ni(PR_2NR'_2)_2(CH_3CN)]^{2+}$ complexes. *Energy & Environmental Science* **2012,** *5*, 6480-6490.

39. Fukuzumi, S.; Ohkubo, K.; Lee, Y. M.; Nam, W., Lewis Acid Coupled Electron Transfer of Metal–Oxygen Intermediates. *Chemistry – A European Journal* **2015,** *21*, 17548-17559.
40. Hong, S.; Lee, Y.-M.; Ray, K.; Nam, W., Dioxygen activation chemistry by synthetic mononuclear nonheme iron, copper and chromium complexes. *Coordination Chemistry Reviews* **2017,** *334*, 25-42.
41. Sahu, S.; Goldberg, D. P., Activation of dioxygen by iron and manganese complexes: a heme and nonheme perspective. *Journal of the American Chemical Society* **2016,** *138*, 11410-11428.
42. Nam, W., Synthetic mononuclear nonheme iron–oxygen intermediates. *Accounts of Chemical Research* **2015,** *48*, 2415-2423.
43. Ray, K.; Pfaff, F. F.; Wang, B.; Nam, W., Status of reactive non-heme metal–oxygen intermediates in chemical and enzymatic reactions. *Journal of the American Chemical Society* **2014,** *136*, 13942-13958.
44. Mase, K.; Ohkubo, K.; Fukuzumi, S., Efficient Two-Electron Reduction of Dioxygen to Hydrogen Peroxide with One-Electron Reductants with a Small Overpotential Catalyzed by a Cobalt Chlorin Complex. *Journal of the American Chemical Society* **2013,** *135*, 2800-2808.
45. Collman, J. P.; Boulatov, R.; Sunderland, C. J.; Fu, L., Functional analogues of cytochrome c oxidase, myoglobin, and hemoglobin. *Chemical Reviews* **2004,** *104*, 561-588.
46. Collman, J. P., Synthetic models for the oxygen-binding hemoproteins. *Accounts of Chemical Research* **1977,** *10*, 265-272.
47. Mirica, L. M.; Ottenwaelder, X.; Stack, T. D. P., Structure and spectroscopy of copper− dioxygen complexes. *Chemical Reviews* **2004,** *104*, 1013-1046.
48. Lewis, E. A.; Tolman, W. B., Reactivity of dioxygen−copper systems. *Chemical Reviews* **2004,** *104*, 1047-1076.
49. Elwell, C. E.; Gagnon, N. L.; Neisen, B. D.; Dhar, D.; Spaeth, A. D.; Yee, G. M.; Tolman, W. B., Copper–oxygen complexes revisited: structures, spectroscopy, and reactivity. *Chemical Reviews* **2017,** *117*, 2059-2107.
50. Sinha, S.; Ghosh, M.; Warren, J. J., Changing the Selectivity of O_2 Reduction Catalysis with One Ligand Heteroatom. *ACS Catalysis* **2019,** *9*, 2685-2691.
51. Zahran, Z. N.; Mohamed, E. A.; Naruta, Y., Bio-inspired cofacial Fe porphyrin dimers for efficient electrocatalytic CO_2 to CO conversion: Overpotential tuning by substituents at the porphyrin rings. *Scientific Reports* **2016,** *6*, 24533.
52. Margarit, C. G.; Schnedermann, C.; Asimow, N. G.; Nocera, D. G., Carbon Dioxide Reduction by Iron Hangman Porphyrins. *Organometallics* **2018**.
53. Mohamed, E. A.; Zahran, Z. N.; Naruta, Y., Efficient electrocatalytic CO_2 reduction with a molecular cofacial iron porphyrin dimer. *Chemical Communications* **2015,** *51*, 16900-16903.
54. Nichols, E. M.; Derrick, J. S.; Nistanaki, S. K.; Smith, P. T.; Chang, C. J., Positional effects of second-sphere amide pendants on electrochemical CO_2 reduction catalyzed by iron porphyrins. *Chemical Science* **2018,** *9*, 2952-2960.
55. Sinha, S.; Warren, J. J., Unexpected Solvent Effect in Electrocatalytic CO_2 to CO Conversion Revealed Using Asymmetric Metalloporphyrins. *Inorganic Chemistry* **2018,** *57*, 12650-12656.

56. Manbeck, G. F.; Muckerman, J. T.; Szalda, D. J.; Himeda, Y.; Fujita, E., Push or Pull? Proton Responsive Ligand Effects in Rhenium Tricarbonyl CO_2 Reduction Catalysts. *The Journal of Physical Chemistry B* **2015,** *119*, 7457-7466.
57. Agarwal, J.; Shaw, T. W.; Schaefer, H. F.; Bocarsly, A. B., Design of a Catalytic Active Site for Electrochemical CO_2 Reduction with Mn(I)-Tricarbonyl Species. *Inorganic Chemistry* **2015,** *54*, 5285-5294.
58. Franco, F.; Cometto, C.; Vallana, F. F.; Sordello, F.; Priola, E.; Minero, C.; Nervi, C.; Gobetto, R., A local proton source in a $[Mn(bpy\text{-}R)(CO)_3Br]$-type redox catalyst enables CO_2 reduction even in the absence of Brønsted acids. *Chemical Communications* **2014,** *50*, 14670-14673.
59. Bourrez, M.; Molton, F.; Chardon-Noblat, S.; Deronzier, A., $[Mn(bipyridyl)(CO)_3Br]$: An abundant metal carbonyl complex as efficient electrocatalyst for CO2 reduction. *Angewandte Chemie International Edition* **2011,** *123*, 10077-10080.
60. Chabolla, S. A.; Machan, C. W.; Yin, J.; Dellamary, E. A.; Sahu, S.; Gianneschi, N. C.; Gilson, M. K.; Tezcan, F. A.; Kubiak, C. P., Bio-inspired CO_2 reduction by a rhenium tricarbonyl bipyridine-based catalyst appended to amino acids and peptidic platforms: incorporating proton relays and hydrogen-bonding functional groups. *Faraday Discussions* **2017,** *198*, 279-300.
61. Chabolla, S. A.; Dellamary, E. A.; Machan, C. W.; Tezcan, F. A.; Kubiak, C. P., Combined steric and electronic effects of positional substitution on dimethyl-bipyridine rhenium (I) tricarbonyl electrocatalysts for the reduction of CO_2. *Inorganica Chimica Acta* **2014,** *422*, 109-113.
62. Wong, K.-Y.; Chung, W.-H.; Lau, C.-P., The effect of weak Brönsted acids on the electrocatalytic reduction of carbon dioxide by a rhenium tricarbonyl bipyridyl complex. *Journal of Electroanalytical Chemistry* **1998,** *453*, 161-170.
63. Riplinger, C.; Carter, E. A., Influence of Weak Brønsted Acids on Electrocatalytic CO_2 Reduction by Manganese and Rhenium Bipyridine Catalysts. *ACS Catalysis* **2015,** *5*, 900-908.
64. Smieja, J. M.; Sampson, M. D.; Grice, K. A.; Benson, E. E.; Froehlich, J. D.; Kubiak, C. P., Manganese as a Substitute for Rhenium in CO_2 Reduction Catalysts: The Importance of Acids. *Inorganic Chemistry* **2013,** *52*, 2484-2491.
65. Riplinger, C.; Sampson, M. D.; Ritzmann, A. M.; Kubiak, C. P.; Carter, E. A., Mechanistic Contrasts between Manganese and Rhenium Bipyridine Electrocatalysts for the Reduction of Carbon Dioxide. *Journal of the American Chemical Society* **2014,** *136*, 16285-16298.
66. Sahu, S.; Cheung, P. L.; Machan, C. W.; Chabolla, S. A.; Kubiak, C. P.; Gianneschi, N. C., Charged Macromolecular Rhenium Bipyridine Catalysts with Tunable CO_2 Reduction Potentials. *Chemistry – A European Journal* **2017,** *23*, 8619-8622.
67. Machan, C. W.; Yin, J.; Chabolla, S. A.; Gilson, M. K.; Kubiak, C. P., Improving the Efficiency and Activity of Electrocatalysts for the Reduction of CO_2 through Supramolecular Assembly with Amino Acid-Modified Ligands. *Journal of the American Chemical Society* **2016,** *138*, 8184-8193.
68. Machan, C. W.; Kubiak, C. P., Interrogating heterobimetallic co-catalytic responses for the electrocatalytic reduction of CO_2 using supramolecular assembly. *Dalton Transactions* **2016,** *45*, 15942-15950.

69. Machan, C. W.; Chabolla, S. A.; Kubiak, C. P., Reductive Disproportionation of Carbon Dioxide by an Alkyl-Functionalized Pyridine Monoimine Re(I) fac-Tricarbonyl Electrocatalyst. *Organometallics* **2015,** *34*, 4678-4683.
70. Machan, C. W.; Chabolla, S. A.; Yin, J.; Gilson, M. K.; Tezcan, F. A.; Kubiak, C. P., Supramolecular Assembly Promotes the Electrocatalytic Reduction of Carbon Dioxide by Re(I) Bipyridine Catalysts at a Lower Overpotential. *Journal of the American Chemical Society* **2014,** *136*, 14598-14607.
71. Beley, M.; Collin, J.-P.; Ruppert, R.; Sauvage, J.-P., Nickel (II)-cyclam: an extremely selective electrocatalyst for reduction of CO_2 in water. *Journal of the Chemical Society, Chemical Communications* **1984,** 19, 1315-1316.
72. Barefield, E. K.; Freeman, G. M.; Van Derveer, D. G., Electrochemical and structural studies of nickel (II) complexes of N-alkylated cyclam ligands: x-ray structures of trans-$[Ni(C_{14}H_{32}N_4)(OH_2)_2]Cl_2 \cdot 2H_2O$ and $[Ni(C_{14}H_{32}N_4)](O_3SCF_3)_2$. *Inorganic Chemistry* **1986,** *25*, 552-558.
73. Balazs, G. B.; Anson, F. C., Effects of CO on the electrocatalytic activity of Ni $(cyclam)^{2+}$ toward the reduction of CO_2. *Journal of Electroanalytical Chemistry* **1993,** *361*, 149-157.
74. Kelly, C. A.; Blinn, E. L.; Camaioni, N.; D'Angelantonio, M.; Mulazzani, Q. G., Mechanism of CO_2 and H^+ reduction by $Ni(cyclam)^+$ in aqueous solution. A pulse and continuous radiolysis study. *Inorganic Chemistry* **1999,** *38*, 1579-1584.
75. Froehlich, J. D.; Kubiak, C. P., Homogeneous CO_2 Reduction by Ni(cyclam) at a Glassy Carbon Electrode. *Inorganic Chemistry* **2012,** *51*, 3932-3934.
76. Song, J.; Klein, E. L.; Neese, F.; Ye, S., The Mechanism of Homogeneous CO_2 Reduction by Ni(cyclam): Product Selectivity, Concerted Proton–Electron Transfer and C–O Bond Cleavage. *Inorganic Chemistry* **2014,** *53*, 7500-7507.
77. Nichols, E. M.; Chang, C. J., Urea-Based Multipoint Hydrogen-Bond Donor Additive Promotes Electrochemical CO2 Reduction Catalyzed by Nickel Cyclam. *Organometallics* **2019,** *38*, 1213-1218.
78. Appel, A. M.; Bercaw, J. E.; Bocarsly, A. B.; Dobbek, H.; DuBois, D. L.; Dupuis, M.; Ferry, J. G.; Fujita, E.; Hille, R.; Kenis, P. J. A.; Kerfeld, C. A.; Morris, R. H.; Peden, C. H. F.; Portis, A. R.; Ragsdale, S. W.; Rauchfuss, T. B.; Reek, J. N. H.; Seefeldt, L. C.; Thauer, R. K.; Waldrop, G. L., Frontiers, Opportunities, and Challenges in Biochemical and Chemical Catalysis of CO_2 Fixation. *Chemical Reviews* **2013,** *113*, 6621-6658.
79. Kroneck, P. M.; Torres, M. E. S., *The metal-driven biogeochemistry of gaseous compounds in the environment*. Springer: 2014.
80. Dobbek, H.; Gremer, L.; Kiefersauer, R.; Huber, R.; Meyer, O., Catalysis at a dinuclear [CuSMo(O)OH] cluster in a CO dehydrogenase resolved at 1.1-Å resolution. *Proceedings of the National Academy of Sciences* **2002,** *99*, 15971-15976.
81. Hille, R., The molybdenum oxotransferases and related enzymes. *Dalton Transactions* **2013,** *42*, 3029-3042.
82. Dobbek, H.; Gremer, L.; Meyer, O.; Huber, R., *Handbook of Metalloproteins*. John Wiley & Sons Ltd., Chichester, United Kingdom: 2001; Vol. 2, p 1136-1147.
83. Jeoung, J.-H.; Dobbek, H., Carbon Dioxide Activation at the Ni,Fe-Cluster of Anaerobic Carbon Monoxide Dehydrogenase. *Science* **2007,** *318*, 1461-1464.

84. Boyington, J. C.; Gladyshev, V. N.; Khangulov, S. V.; Stadtman, T. C.; Sun, P. D., Crystal Structure of Formate Dehydrogenase H: Catalysis Involving Mo, Molybdopterin, Selenocysteine, and an Fe4S4 Cluster. *Science* **1997,** *275*, 1305-1308.
85. Sawers, G., The hydrogenases and formate dehydrogenases of Escherichia coli. *Antonie Van Leeuwenhoek* **1994,** *66*, 57-88.
86. Costentin, C.; Drouet, S.; Robert, M.; Savéant, J.-M., Turnover numbers, turnover frequencies, and overpotential in molecular catalysis of electrochemical reactions. Cyclic voltammetry and preparative-scale electrolysis. *Journal of the American Chemical Society* **2012,** *134*, 11235-11242.
87. Costentin, C.; Savéant, J. M., Multielectron, multistep molecular catalysis of electrochemical reactions: Benchmarking of homogeneous catalysts. *ChemElectroChem* **2014,** *1*, 1226-1236.
88. Savéant, J.-M., Molecular Catalysis of Electrochemical Reactions. Cyclic Voltammetry of Systems Approaching Reversibility. *ACS Catalysis* **2018,** *8*, 7608-7611.
89. Savéant, J.-M., Molecular Catalysis of Electrochemical Reactions. Mechanistic Aspects. *Chemical Reviews* **2008,** *108*, 2348-2378.
90. Costentin, C.; Savéant, J.-M., Homogeneous Catalysis of Electrochemical Reactions: The Steady-State and Nonsteady-State Statuses of Intermediates. *ACS Catalysis* **2018,** *8*, 5286-5297.
91. Appel, A. M.; Helm, M. L., Determining the overpotential for a molecular electrocatalyst. *ACS Catalysis* **2014,** *4*, 630-633.
92. Costentin, C.; Savéant, J.-M., Homogeneous Molecular Catalysis of Electrochemical Reactions: Manipulating Intrinsic and Operational Factors for Catalyst Improvement. *Journal of the American Chemical Society* **2018,** *140*, 16669-16675.
93. Pegis, M. L.; Wise, C. F.; Koronkiewicz, B.; Mayer, J. M., Identifying and Breaking Scaling Relations in Molecular Catalysis of Electrochemical Reactions. *Journal of the American Chemical Society* **2017,** *139*, 11000-11003.
94. Gennaro, A.; Isse, A. A.; Severin, M.-G.; Vianello, E.; Bhugun, I.; Saveant, J.-M., Mechanism of the electrochemical reduction of carbon dioxide at inert electrodes in media of low proton availability. *Journal of the Chemical Society, Faraday Transactions* **1996,** *92*, 3963-3968.
95. Bhugun, I.; Lexa, D.; Savéant, J.-M., Catalysis of the electrochemical reduction of carbon dioxide by iron (0) porphyrins: Synergystic effect of weak Brönsted acids. *Journal of the American Chemical Society* **1996,** *118*, 1769-1776.
96. Bhugun, I.; Lexa, D.; Saveant, J.-M., Ultraefficient selective homogeneous catalysis of the electrochemical reduction of carbon dioxide by an iron (0) porphyrin associated with a weak Broensted acid cocatalyst. *Journal of the American Chemical Society* **1994,** *116*, 5015-5016.
97. Bonin, J.; Maurin, A.; Robert, M., Molecular catalysis of the electrochemical and photochemical reduction of CO_2 with Fe and Co metal based complexes. Recent advances. *Coordination Chemistry Reviews* **2017,** *334*, 184-198.

98. Fukuzumi, S.; Lee, Y.-M.; Ahn, H. S.; Nam, W., Mechanisms of catalytic reduction of CO_2 with heme and nonheme metal complexes. *Chemical Science* **2018,** *9*, 6017-6034.
99. Sen, P.; Mondal, B.; Saha, D.; Rana, A.; Dey, A., Role of 2nd sphere H-bonding residues in tuning the kinetics of CO_2 reduction to CO by iron porphyrin complexes. *Dalton Transactions* **2019,** *48*, 5965-5977.
100. Gotico, P.; Roupnel, L.; Guillot, R.; Sircoglou, M.; Leibl, W.; Halime, Z.; Aukauloo, A., Atropisomeric Hydrogen Bonding Control for CO_2 Binding and Enhancement of Electrocatalytic Reduction at Iron Porphyrins. *Angewandte Chemie International Edition* **2020,** *59*, 22451-22455.
101. Gotico, P.; Boitrel, B.; Guillot, R.; Sircoglou, M.; Quaranta, A.; Halime, Z.; Leibl, W.; Aukauloo, A., Second-Sphere Biomimetic Multipoint Hydrogen-Bonding Patterns to Boost CO_2 Reduction of Iron Porphyrins. *Angewandte Chemie International Edition* **2019,** *58*, 4504-4509.
102. Costentin, C.; Savéant, J.-M.; Tard, C., Ligand “noninnocence” in coordination complexes vs. kinetic, mechanistic, and selectivity issues in electrochemical catalysis. *Proceedings of the National Academy of Sciences* **2018,** *115*, 9104-9109.
103. Grice, K.; Kubiak, C., *Chapter Five – Recent Studies of Rhenium and Manganese Bipyridine Carbonyl Catalysts for the Electrochemical Reduction of CO_2*. 2013; 66, 163-188.
104. Hawecker, J.; Lehn, J.-M.; Ziessel, R., Electrocatalytic reduction of carbon dioxide mediated by $Re(bipy)(CO)_3Cl$ (bipy = 2,2′-bipyridine). *Journal of the Chemical Society, Chemical Communications* **1984,** , 328-330.
105. Grills, D. C.; Farrington, J. A.; Layne, B. H.; Lymar, S. V.; Mello, B. A.; Preses, J. M.; Wishart, J. F., Mechanism of the Formation of a Mn-Based CO_2 Reduction Catalyst Revealed by Pulse Radiolysis with Time-Resolved Infrared Detection. *Journal of the American Chemical Society* **2014,** *136*, 5563-5566.
106. Sullivan, B. P.; Bolinger, C. M.; Conrad, D.; Vining, W. J.; Meyer, T. J., One-and two-electron pathways in the electrocatalytic reduction of CO_2 by fac-$Re(bpy)(CO)_3Cl$ (bpy= 2, 2′-bipyridine). *Journal of the Chemical Society, Chemical Communications* **1985,** 20, 1414-1416.
107. Keith, J. A.; Grice, K. A.; Kubiak, C. P.; Carter, E. A., Elucidation of the Selectivity of Proton-Dependent Electrocatalytic CO_2 Reduction by fac-$Re(bpy)(CO)_3Cl$. *Journal of the American Chemical Society* **2013,** *135*, 15823-15829.
108. Sampson, M. D.; Froehlich, J. D.; Smieja, J. M.; Benson, E. E.; Sharp, I. D.; Kubiak, C. P., Direct observation of the reduction of carbon dioxide by rhenium bipyridine catalysts. *Energy & Environmental Science* **2013,** *6*, 3748-3755.
109. Smieja, J. M.; Benson, E. E.; Kumar, B.; Grice, K. A.; Seu, C. S.; Miller, A. J. M.; Mayer, J. M.; Kubiak, C. P., Kinetic and structural studies, origins of selectivity, and interfacial charge transfer in the artificial photosynthesis of CO. *Proceedings of the National Academy of Sciences* **2012,** *109*, 15646-15650.
110. Clark, M. L.; Cheung, P. L.; Lessio, M.; Carter, E. A.; Kubiak, C. P., Kinetic and Mechanistic Effects of Bipyridine (bpy) Substituent, Labile Ligand, and Brønsted Acid on Electrocatalytic CO_2 Reduction by Re(bpy) Complexes. *ACS Catalysis* **2018,** *8*, 2021-2029.

111. Benson, E. E.; Sampson, M. D.; Grice, K. A.; Smieja, J. M.; Froehlich, J. D.; Friebel, D.; Keith, J. A.; Carter, E. A.; Nilsson, A.; Kubiak, C. P., The Electronic States of Rhenium Bipyridyl Electrocatalysts for CO_2 Reduction as Revealed by X-ray Absorption Spectroscopy and Computational Quantum Chemistry. *Angewandte Chemie International Edition* **2013,** *52*, 4841-4844.
112. Haviv, E.; Azaiza-Dabbah, D.; Carmieli, R.; Avram, L.; Martin, J. M. L.; Neumann, R., A Thiourea Tether in the Second Coordination Sphere as a Binding Site for CO_2 and a Proton Donor Promotes the Electrochemical Reduction of CO_2 to CO Catalyzed by a Rhenium Bipyridine-Type Complex. *Journal of the American Chemical Society* **2018,** *140*, 12451-12456.
113. Rotundo, L.; Garino, C.; Priola, E.; Sassone, D.; Rao, H.; Ma, B.; Robert, M.; Fiedler, J.; Gobetto, R.; Nervi, C., Electrochemical and Photochemical Reduction of CO2 Catalyzed by Re(I) Complexes Carrying Local Proton Sources. *Organometallics* **2019,** *38*, 1351-1360.
114. Sung, S.; Kumar, D.; Gil-Sepulcre, M.; Nippe, M., Electrocatalytic CO_2 Reduction by Imidazolium-Functionalized Molecular Catalysts. *Journal of the American Chemical Society* **2017,** *139*, 13993-13996.
115. Johnson, F. P.; George, M. W.; Hartl, F.; Turner, J. J., Electrocatalytic Reduction of CO_2 Using the Complexes $[Re(bpy)(CO)_3L]^n$ (n = +1, L = $P(OEt)_3$, CH_3CN; n = 0, L= Cl^-, Otf^-; bpy= 2, 2'-Bipyridine; Otf^-= CF_3SO_3) as Catalyst Precursors: Infrared Spectroelectrochemical Investigation. *Organometallics* **1996,** *15*, 3374-3387.
116. Sampson, M. D.; Kubiak, C. P., Manganese Electrocatalysts with Bulky Bipyridine Ligands: Utilizing Lewis Acids To Promote Carbon Dioxide Reduction at Low Overpotentials. *Journal of the American Chemical Society* **2016,** *138*, 1386-1393.
117. Ashley, K.; Pons, S., Infrared spectroelectrochemistry. *Chemical Reviews* **1988,** *88*, 673-695.
118. Machan, C. W.; Sampson, M. D.; Chabolla, S. A.; Dang, T.; Kubiak, C. P., Developing a mechanistic understanding of molecular electrocatalysts for CO_2 reduction using infrared spectroelectrochemistry. *Organometallics* **2014,** *33*, 4550-4559.
119. Zavarine, I. S.; Kubiak, C. P., A versatile variable temperature thin layer reflectance spectroelectrochemical cell. *Journal of Electroanalytical Chemistry* **2001,** *495*, 106-109.
120. Best, S.; Crumbliss, A.; Dunsch, L.; Haga, M.-a.; Hartl, F.; Kubiak, C.; Winter, R.; Yellowlees, L.; Salsman, C.; Murray, P., *Spectroelectrochemistry*. Royal Society of Chemistry: 2008.
121. Kaim, W.; Fiedler, J., Spectroelectrochemistry: the best of two worlds. *Chemical Society Reviews* **2009,** *38*, 3373-3382.
122. Sung, S.; Li, X.; Wolf, L. M.; Meeder, J. R.; Bhuvanesh, N. S.; Grice, K. A.; Panetier, J. A.; Nippe, M., Synergistic Effects of Imidazolium-Functionalization on fac-$Mn(CO)_3$ Bipyridine Catalyst Platforms for Electrocatalytic Carbon Dioxide Reduction. *Journal of the American Chemical Society* **2019,** *141*, 6569-6582.
123. Fisher, B. J.; Eisenberg, R., Electrocatalytic reduction of carbon dioxide by using macrocycles of nickel and cobalt. *Journal of the American Chemical Society* **1980,** *102*, 7361-7363.

124. Schneider, J.; Jia, H.; Kobiro, K.; Cabelli, D. E.; Muckerman, J. T.; Fujita, E., Nickel (II) macrocycles: highly efficient electrocatalysts for the selective reduction of CO_2 to CO. *Energy & Environmental Science* **2012,** *5*, 9502-9510.
125. Neri, G.; Aldous, I. M.; Walsh, J. J.; Hardwick, L. J.; Cowan, A. J., A highly active nickel electrocatalyst shows excellent selectivity for CO_2 reduction in acidic media. *Chemical Science* **2016,** *7*, 1521-1526.
126. Dobbek, H.; Svetlitchnyi, V.; Gremer, L.; Huber, R.; Meyer, O., Crystal Structure of a Carbon Monoxide Dehydrogenase Reveals a [Ni-4Fe-5S] Cluster. *Science* **2001,** *293*, 1281-1285.
127. Smith, P. T.; Benke, B. P.; Cao, Z.; Kim, Y.; Nichols, E. M.; Kim, K.; Chang, C. J., Iron Porphyrins Embedded into a Supramolecular Porous Organic Cage for Electrochemical CO_2 Reduction in Water. *Angewandte Chemie International Edition* **2018,** *57*, 9684-9688.
128. Rail, M. D.; Berben, L. A., Directing the reactivity of $[HFe_4N(CO)_{12}]^-$ toward H^+ or CO_2 reduction by understanding the electrocatalytic mechanism. *Journal of the American Chemical Society* **2011,** *133*, 18577-18579.
129. Taheri, A.; Thompson, E. J.; Fettinger, J. C.; Berben, L. A., An Iron Electrocatalyst for Selective Reduction of CO_2 to Formate in Water: Including Thermochemical Insights. *ACS Catalysis* **2015,** *5*, 7140-7151.
130. Taheri, A.; Berben, L. A., Tailoring Electrocatalysts for Selective CO_2 or H^+ Reduction: Iron Carbonyl Clusters as a Case Study. *Inorganic Chemistry* **2016,** *55*, 378-385.
131. Loewen, N. D.; Neelakantan, T. V.; Berben, L. A., Renewable Formate from C–H Bond Formation with CO_2: Using Iron Carbonyl Clusters as Electrocatalysts. *Accounts of Chemical Research* **2017,** *50*, 2362-2370.
132. Loewen, N. D.; Thompson, E. J.; Kagan, M.; Banales, C. L.; Myers, T. W.; Fettinger, J. C.; Berben, L. A., A pendant proton shuttle on $[Fe_4N(CO)_{12}]^-$ alters product selectivity in formate vs. H_2 production via the hydride $[H–Fe_4N(CO)_{12}]^-$. *Chemical Science* **2016,** *7*, 2728-2735.
133. Bruckmeier, C.; Lehenmeier, M. W.; Reithmeier, R.; Rieger, B.; Herranz, J.; Kavakli, C., Binuclear rhenium (I) complexes for the photocatalytic reduction of CO_2. *Dalton Transactions* **2012,** *41*, 5026-5037.
134. Cheung, P. L.; Kapper, S. C.; Zeng, T.; Thompson, M. E.; Kubiak, C. P., Improving Photocatalysis for the Reduction of CO_2 through Non-covalent Supramolecular Assembly. *Journal of the American Chemical Society* **2019,** *141*, 14961-14965.
135. Yang, W.; Sinha Roy, S.; Pitts, W. C.; Nelson, R. L.; Fronczek, F. R.; Jurss, J. W., Electrocatalytic CO_2 Reduction with Cis and Trans Conformers of a Rigid Dinuclear Rhenium Complex: Comparing the Monometallic and Cooperative Bimetallic Pathways. *Inorganic Chemistry* **2018,** *57*, 9564-9575.
136. Wilting, A.; Stolper, T.; Mata, R. A.; Siewert, I., Dinuclear Rhenium Complex with a Proton Responsive Ligand as a Redox Catalyst for the Electrochemical CO_2 Reduction. *Inorganic Chemistry* **2017,** *56*, 4176-4185.
137. Sinha, S.; Berdichevsky, E. K.; Warren, J. J., Electrocatalytic CO_2 reduction using rhenium(I) complexes with modified 2-(2′-pyridyl)imidazole ligands. *Inorganica Chimica Acta* **2017,** *460*, 63-68.

138. Roy, S.; Sharma, B.; Pécaut, J.; Simon, P.; Fontecave, M.; Tran, P. D.; Derat, E.; Artero, V., Molecular cobalt complexes with pendant amines for selective electrocatalytic reduction of carbon dioxide to formic acid. *Journal of the American Chemical Society* **2017,** *139*, 3685-3696.
139. Nichols, A. W.; Chatterjee, S.; Sabat, M.; Machan, C. W., Electrocatalytic Reduction of CO_2 to Formate by an Iron Schiff Base Complex. *Inorganic Chemistry* **2018,** *57*, 2111-2121.
140. Nichols, A. W.; Hooe, S. L.; Kuehner, J. S.; Dickie, D. A.; Machan, C. W., Electrocatalytic CO2 Reduction to Formate with Molecular Fe(III) Complexes Containing Pendent Proton Relays. *Inorganic Chemistry* **2020,** *59*, 5854-5864.
141. Chapovetsky, A.; Do, T. H.; Haiges, R.; Takase, M. K.; Marinescu, S. C., Proton-Assisted Reduction of CO_2 by Cobalt Aminopyridine Macrocycles. *Journal of the American Chemical Society* **2016,** *138*, 5765-5768.
142. Chapovetsky, A.; Welborn, M.; Luna, J. M.; Haiges, R.; Miller, T. F.; Marinescu, S. C., Pendant Hydrogen-Bond Donors in Cobalt Catalysts Independently Enhance CO_2 Reduction. *ACS Central Science* **2018,** *4*, 397-404.
143. Maynard, E. L.; Lindahl, P. A., Catalytic Coupling of the Active Sites in Acetyl-CoA Synthase, a Bifunctional CO-Channeling Enzyme. *Biochemistry* **2001,** *40*, 13262-13267.
144. Kuhl, K. P.; Cave, E. R.; Abram, D. N.; Jaramillo, T. F., New insights into the electrochemical reduction of carbon dioxide on metallic copper surfaces. *Energy & Environmental Science* **2012,** *5*, 7050.
145. Weng, Z.; Jiang, J.; Wu, Y.; Wu, Z.; Guo, X.; Materna, K. L.; Liu, W.; Batista, V. S.; Brudvig, G. W.; Wang, H., Electrochemical CO_2 Reduction to Hydrocarbons on a Heterogeneous Molecular Cu Catalyst in Aqueous Solution. *Journal of the American Chemical Society* **2016,** *138*, 8076-8079.
146. Gong, M.; Cao, Z.; Liu, W.; Nichols, E. M.; Smith, P. T.; Derrick, J. S.; Liu, Y.-S.; Liu, J.; Wen, X.; Chang, C. J., Supramolecular Porphyrin Cages Assembled at Molecular–Materials Interfaces for Electrocatalytic CO Reduction. *ACS Central Science* **2017,** *3*, 1032-1040.
147. Shirley, H.; Su, X.; Sanjanwala, H.; Talukdar, K.; Jurss, J. W.; Delcamp, J. H., Durable Solar-Powered Systems with Ni-Catalysts for Conversion of CO_2 or CO to CH_4. *Journal of the American Chemical Society* **2019,** *141*, 6617-6622.
148. Rao, H.; Schmidt, L. C.; Bonin, J.; Robert, M., Visible-light-driven methane formation from CO_2 with a molecular iron catalyst. *Nature* **2017,** *548*, 74.
149. Matsumoto, T.; Kim, K.; Nakai, H.; Hibino, T.; Ogo, S., Organometallic Catalysts for Use in a Fuel Cell. *ChemCatChem* **2013,** *5*, 1368-1373.
150. Kadirov, M. K.; Karasik, A. A.; Nizameev, I. R.; Strelnik, I. D.; Kholin, K. V.; Kadirov, D. M.; Ismaev, T. I.; Budnikova, Y. G.; Sinyashin, O. G., Organometallic Polymer Electrolyte Membrane Fuel Cell Bis-Ligand Nickel(Ii) Complex of 1,5-Di-P-Tolyl-3,7-Dipyridine-1,5,3,7-Diazadiphosphacyclo-Octane Catalyst. *Energy Technology* **2018,** *6*, 1088-1095.
151. Matsumoto, T.; Kim, K.; Ogo, S., Molecular Catalysis in a Fuel Cell. *Angewandte Chemie International Edition* **2011,** *123*, 11398-11401.

152. Pegis, M. L.; Wise, C. F.; Martin, D. J.; Mayer, J. M., Oxygen reduction by homogeneous molecular catalysts and electrocatalysts. *Chemical Reviews* **2018,** *118*, 2340-2391.
153. Bratsch, S. G., Standard electrode potentials and temperature coefficients in water at 298.15 K. *Journal of Physical and Chemical Reference Data* **1989,** *18*, 1-21.
154. Wang, Y.-H.; Schneider, P. E.; Goldsmith, Z. K.; Mondal, B.; Hammes-Schiffer, S.; Stahl, S. S., Brønsted Acid Scaling Relationships Enable Control Over Product Selectivity from O_2 Reduction with a Mononuclear Cobalt Porphyrin Catalyst. *ACS Central Science* **2019,** *5*, 1024-1034.
155. Martin, D. J.; Wise, C. F.; Pegis, M. L.; Mayer, J. M., Developing Scaling Relationships for Molecular Electrocatalysis through Studies of Fe-Porphyrin-Catalyzed O_2 Reduction. *Accounts of Chemical Research* **2020,** *53*, 1056-1065.
156. Martin, D. J.; Mercado, B. Q.; Mayer, J. M., Combining scaling relationships overcomes rate versus overpotential trade-offs in O_2 molecular electrocatalysis. *Science Advances* **2020,** *6*, eaaz3318.
157. Chan, R. J.; Su, Y. O.; Kuwana, T., Electrocatalysis of oxygen reduction. 5. oxygen to hydrogen peroxide conversion by cobalt (II) tetrakis (N-methyl-4-pyridyl) porphyrin. *Inorganic Chemistry* **1985,** *24*, 3777-3784.
158. Sazou, D.; Araullo-McAdams, C.; Han, B.; Franzen, M.; Kadish, K. M., The use of an electrogenerated cobalt (I) porphyrin for the homogeneous catalytic reduction of dioxygen in dimethylformamide. Reactions of $[(TMpyP)CoII]^{4+}$ and $[(TMpyP)CoI]^{3+}$ where TMpyP= meso-tetrakis (1-methylpyridinium-4-yl) porphyrin. *Journal of the American Chemical Society* **1990,** *112*, 7879-7886.
159. He, Q.; Mugadza, T.; Hwang, G.; Nyokong, T., Mechanisms of electrocatalysis of oxygen reduction by metal porphyrins in trifluoromethane sulfonic acid solution. *International Journal of Electrochemical Science* **2012,** *7*, 7045-7064.
160. D'Souza, F.; Hsieh, Y.-Y.; Deviprasad, G., Electrocatalytic reduction of molecular oxygen using non-planar cobalt tetrakis-(4-sulfonatophenyl)-β-octabromoporphyrin. *Journal of Electroanalytical Chemistry* **1997,** *426*, 17-21.
161. D'Souza, F.; Deviprasad, R.; Hsieh, Y.-Y., Synthesis and studies on the electrocatalytic reduction of molecular oxygen by non-planar cobalt (II) tetrakis-(N-methyl pyridyl)-β-octabromoporphyrin. *Journal of Electroanalytical Chemistry* **1996,** *411*, 167-171.
162. Geiger, T.; Anson, F. C., Homogeneous catalysis of the electrochemical reduction of dioxygen by a macrocyclic cobalt (III) complex. *Journal of the American Chemical Society* **1981,** *103*, 7489-7496.
163. Kang, C.; Anson, F. C., Effects of Coordination to a Macrocyclic Cobalt Complex on the Electrochemistry of Dioxygen, Superoxide, and Hydroperoxide. *Inorganic Chemistry* **1995,** *34*, 2771-2780.
164. Kobayashi, N.; Nishiyama, Y., Catalytic electroreduction of molecular oxygen using iron or cobalt 4, 4', 4'', 4'''-tetracarboxyphthalocyanine. *The Journal of Physical Chemistry* **1985,** *89*, 1167-1170.
165. Anson, F. C.; Shi, C.; Steiger, B., Novel multinuclear catalysts for the electroreduction of dioxygen directly to water. *Accounts of Chemical Research* **1997,** *30*, 437-444.

166. Fukuzumi, S.; Mochizuki, S.; Tanaka, T., Efficient reduction of dioxygen with ferrocene derivatives, catalyzed by metalloporphyrins in the presence of perchloric acid. *Inorganic Chemistry* **1989,** *28*, 2459-2465.
167. Fukuzumi, S.; Mochizuki, S.; Tanaka, T., Metalloporphyrin-catalyzed reduction of dioxygen by ferrocene derivatives. *Chemistry Letters* **1989,** *18*, 27-30.
168. Trojanek, A.; Langmaier, J.; Kvapilová, H.; Záliš, S.; Samec, Z. k., Inhibitory effect of water on the oxygen reduction catalyzed by cobalt (II) tetraphenylporphyrin. *The Journal of Physical Chemistry A* **2014,** *118*, 2018-2028.
169. Honda, T.; Kojima, T.; Fukuzumi, S., Proton-coupled electron-transfer reduction of dioxygen catalyzed by a saddle-distorted cobalt phthalocyanine. *Journal of the American Chemical Society* **2012,** *134*, 4196-4206.
170. Kadish, K. M.; Shen, J.; Frémond, L.; Chen, P.; El Ojaimi, M.; Chkounda, M.; Gros, C. P.; Barbe, J.-M.; Ohkubo, K.; Fukuzumi, S., Clarification of the oxidation state of cobalt corroles in heterogeneous and homogeneous catalytic reduction of dioxygen. *Inorganic Chemistry* **2008,** *47*, 6726-6737.
171. Mase, K.; Ohkubo, K.; Fukuzumi, S., Much enhanced catalytic reactivity of cobalt chlorin derivatives on two-electron reduction of dioxygen to produce hydrogen peroxide. *Inorganic Chemistry* **2015,** *54*, 1808-1815.
172. Fukuzumi, S.; Okamoto, K.; Gros, C. P.; Guilard, R., Mechanism of four-electron reduction of dioxygen to water by ferrocene derivatives in the presence of perchloric acid in benzonitrile, catalyzed by cofacial dicobalt porphyrins. *Journal of the American Chemical Society* **2004,** *126*, 10441-10449.
173. Oldacre, A. N.; Friedman, A. E.; Cook, T. R., A self-assembled cofacial cobalt porphyrin prism for oxygen reduction catalysis. *Journal of the American Chemical Society* **2017,** *139*, 1424-1427.
174. Kobayashi, N.; Nevin, W. A., Electrocatalytic Reduction of Oxygen Using Water-Soluble Iron and Cobalt Phthalocyanines and Porphyrins. *Applied organometallic chemistry* **1996,** *10*, 579-590.
175. Han, S.-B.; Kwak, D.-H.; Park, H. S.; Choi, I.-A.; Park, J.-Y.; Ma, K.-B.; Won, J.-E.; Kim, D.-H.; Kim, S.-J.; Kim, M.-C., Chemically regenerative redox fuel cells using iron redox couples as a liquid catalyst with cocatalysts. *ACS Catalysis* **2016,** *6*, 5302-5306.
176. Kuwana, T.; Fujihira, M.; Sunakawa, K.; Osa, T., Catalytic electroreduction of molecular oxygen using water soluble iron porphyrin. *Journal of Electroanalytical Chemistry and Interfacial Electrochemistry* **1978,** *88*, 299-303.
177. Bettelheim, A.; Kuwana, T., Rotating-ring-disk analysis of iron tetra (N-methylpyridyl) porphyrin in electrocatalysis of oxygen. *Analytical Chemistry* **1979,** *51*, 2257-2260.
178. Su, Y. O.; Kuwana, T.; Chen, S.-M., Electrocatalysis of oxygen reduction by water-soluble iron porphyrins: thermodynamic and kinetic advantage studies. *Journal of Electroanalytical Chemistry and Interfacial Electrochemistry* **1990,** *288*, 177-195.
179. Costentin, C.; Dridi, H.; Savéant, J.-M., Molecular catalysis of O_2 reduction by iron porphyrins in water: heterogeneous versus homogeneous pathways. *Journal of the American Chemical Society* **2015,** *137*, 13535-13544.
180. Matson, B. D.; Carver, C. T.; Von Ruden, A.; Yang, J. Y.; Raugei, S.; Mayer, J. M., Distant protonated pyridine groups in water-soluble iron porphyrin electrocatalysts

promote selective oxygen reduction to water. *Chemical Communications* **2012,** *48*, 11100-11102.

181. Pegis, M. L.; McKeown, B. A.; Kumar, N.; Lang, K.; Wasylenko, D. J.; Zhang, X. P.; Raugei, S.; Mayer, J. M., Homogenous electrocatalytic oxygen reduction rates correlate with reaction overpotential in acidic organic solutions. *ACS Central Science* **2016,** *2*, 850-856.
182. Wasylenko, D. J.; Rodríguez, C.; Pegis, M. L.; Mayer, J. M., Direct comparison of electrochemical and spectrochemical kinetics for catalytic oxygen reduction. *Journal of the American Chemical Society* **2014,** *136*, 12544-12547.
183. Carver, C. T.; Matson, B. D.; Mayer, J. M., Electrocatalytic oxygen reduction by iron tetra-arylporphyrins bearing pendant proton relays. *Journal of the American Chemical Society* **2012,** *134*, 5444-5447.
184. Huang, X.; Xuan, Y.; Xie, L.; Su, B., Unraveling the Phase-Transfer Catalysis Mechanism of Oxygen Reduction Catalyzed by Iron (III) meso-tetra-(4-N-Methyl-pyridyl) Porphine at the Liquid/Liquid Interface. *ChemElectroChem* **2016,** *3*, 1781-1786.
185. Anderson, B. L.; Maher, A. G.; Nava, M.; Lopez, N.; Cummins, C. C.; Nocera, D. G., Ultrafast Photoinduced Electron Transfer from Peroxide Dianion. *The Journal of Physical Chemistry B* **2015,** *119*, 7422-7429.
186. Bernhard, P.; Anson, F. C., Hydrogen atom abstraction from amine complexes of iron (II), cobalt (II), and ruthenium (II) by superoxide: influence of driving force on rate. *Inorganic Chemistry* **1988,** *27*, 4574-4577.
187. Mittra, K.; Chatterjee, S.; Samanta, S.; Dey, A., Selective $4e^-/4H^+$ O_2 reduction by an iron (tetraferrocenyl) porphyrin complex: from proton transfer followed by electron transfer in organic solvent to proton coupled electron transfer in aqueous medium. *Inorganic Chemistry* **2013,** *52*, 14317-14325.
188. Collman, J. P.; Ghosh, S.; Dey, A.; Decréau, R. A.; Yang, Y., Catalytic reduction of O_2 by cytochrome c using a synthetic model of cytochrome c oxidase. *Journal of the American Chemical Society* **2009,** *131*, 5034-5035.
189. Halime, Z.; Kotani, H.; Li, Y.; Fukuzumi, S.; Karlin, K. D., Homogeneous catalytic O_2 reduction to water by a cytochrome c oxidase model with trapping of intermediates and mechanistic insights. *Proceedings of the National Academy of Sciences* **2011,** *108*, 13990-13994.
190. Soo, H. S.; Komor, A. C.; Iavarone, A. T.; Chang, C. J., A hydrogen-bond facilitated cycle for oxygen reduction by an acid-and base-compatible iron platform. *Inorganic Chemistry* **2009,** *48*, 10024-10035.
191. Kobayashi, N.; Saiki, H.; Osa, T., Catalytic electroreduction of molecular oxygen using [5, 10, 15, 20-tetrakis-(1-methylpyridinium-4-yl) porphinato] manganese. *Chemistry Letters* **1985,** *14*, 1917-1920.
192. Jung, J.; Liu, S.; Ohkubo, K.; Abu-Omar, M. M.; Fukuzumi, S., Catalytic Two-Electron Reduction of Dioxygen by Ferrocene Derivatives with Manganese (V) Corroles. *Inorganic Chemistry* **2015,** *54*, 4285-4291.
193. Sheriff, T. S., Production of hydrogen peroxide from dioxygen and hydroxylamine or hydrazine catalysed by manganese complexes. *Journal of the Chemical Society, Dalton Transactions* **1992,** 6, 1051-1058.

194. Shook, R. L.; Peterson, S. M.; Greaves, J.; Moore, C.; Rheingold, A. L.; Borovik, A., Catalytic reduction of dioxygen to water with a monomeric manganese complex at room temperature. *Journal of the American Chemical Society* **2011,** *133*, 5810-5817.
195. Fukuzumi, S.; Kotani, H.; Lucas, H. R.; Doi, K.; Suenobu, T.; Peterson, R. L.; Karlin, K. D., Mononuclear copper complex-catalyzed four-electron reduction of oxygen. *Journal of the American Chemical Society* **2010,** *132*, 6874-6875.
196. Kakuda, S.; Peterson, R. L.; Ohkubo, K.; Karlin, K. D.; Fukuzumi, S., Enhanced catalytic four-electron dioxygen (O_2) and two-electron hydrogen peroxide (H_2O_2) reduction with a copper (II) complex possessing a pendant ligand pivalamido group. *Journal of the American Chemical Society* **2013,** *135* (17), 6513-6522.
197. Asahi, M.; Yamazaki, S.-i.; Itoh, S.; Ioroi, T., Electrochemical reduction of dioxygen by copper complexes with pyridylalkylamine ligands dissolved in aqueous buffer solution: the relationship between activity and redox potential. *Dalton Transactions* **2014,** *43*, 10705-10709.
198. Fukuzumi, S.; Tahsini, L.; Lee, Y.-M.; Ohkubo, K.; Nam, W.; Karlin, K. D., Factors that control catalytic two-versus four-electron reduction of dioxygen by copper complexes. *Journal of the American Chemical Society* **2012,** *134*, 7025-7035.
199. Tahsini, L.; Kotani, H.; Lee, Y.-M.; Cho, J.; Nam, W.; Karlin, K. D.; Fukuzumi, S., Electron-transfer reduction of dinuclear copper peroxo and bis-μ-oxo complexes leading to the catalytic four-electron reduction of dioxygen to water. *Chemistry* **2012,** *18*, 1084.
200. Tang, Y. H.; Lin, Y. C.; Hsu, S. C.; Liou, S. T.; Chen, H. Y.; Hsieh, K. C.; Chuang, W. J.; Chiu, L. T.; Chen, Y. L.; Kao, C. L., Cooperative effects in copper polyamidoamine dendrimer complexes catalyzing the reduction of molecular oxygen. *European Journal of Inorganic Chemistry* **2015,** *2015*, 4839-4847.
201. Das, D.; Lee, Y.-M.; Ohkubo, K.; Nam, W.; Karlin, K. D.; Fukuzumi, S., Temperature-independent catalytic two-electron reduction of dioxygen by ferrocenes with a copper (II) tris[2-(2-pyridyl)ethyl]amine catalyst in the presence of perchloric acid. *Journal of the American Chemical Society* **2013,** *135*, 2825-2834.
202. Meng, J.; Lei, H.; Li, X.; Zhang, W.; Cao, R., The Trans Axial Ligand Effect on Oxygen Reduction. Immobilization Method May Weaken Catalyst Design for Electrocatalytic Performance. *The Journal of Physical Chemistry C* **2020,** *124*, 16324-16331.
203. Mho, S. i.; Ortiz, B.; Doddapaneni, N.; Park, S. M., Electrochemical and Spectroelectrochemical Studies on Metallophthalocyanine-Oxygen Interactions in Nonaqueous Solutions. *Journal of the Electrochemical Society* **1995,** *142*, 1047.
204. Patir, I. H., Fluorinated-cobalt phthalocyanine catalyzed oxygen reduction at liquid/liquid interfaces. *Electrochimica Acta* **2013,** *87*, 788-793.
205. Wong, C.-L.; Switzer, J. A.; Balakrishnan, K.; Endicott, J. F., Oxidation-reduction reactions of complexes with macrocyclic ligands. Oxygen uptake kinetics, equilibriums and intermediates in aqueous CoII(N_4) systems. *Journal of the American Chemical Society* **1980,** *102*, 5511-5518.

206. Wong, C.-L.; Endicott, J. F., Oxidation-reduction reactions of complexes with macrocyclic ligands. Role of intermediates in reactions of μ-peroxo-dicobalt complexes. *Inorganic Chemistry* **1981,** *20*, 2233-2239.
207. Kumar, K.; Endicott, J. F., Oxidation-reduction reactions of complexes with macrocyclic ligands. Electron-transfer reactivity of a 1:1 cobalt(II)-dioxygen adduct. *Inorganic Chemistry* **1984,** *23*, 2447-2452.
208. Tsumaki, T., Nebenvalenzringverbindungen. IV. Über einige innerkomplexe Kobaltsalze der Oxyaldimine. *Bulletin of the Chemical Society of Japan* **1938,** *13*, 252-260.
209. Hughes, E. W.; Wilmarth, W. K.; Calvin, M., The Oxygen-carrying Synthetic Chelate Compounds. V. Equilibrium with the Solid Compounds 1a. *Journal of the American Chemical Society* **1946,** *68*, 2273-2278.
210. Wang, Y.-H.; Pegis, M. L.; Mayer, J. M.; Stahl, S. S., Molecular Cobalt Catalysts for O2 Reduction: Low-Overpotential Production of H_2O_2 and Comparison with Iron-Based Catalysts. *Journal of the American Chemical Society* **2017,** *139*, 16458-16461.
211. Anson, C. W.; Stahl, S. S., Cooperative Electrocatalytic O_2 Reduction Involving Co(salophen) with p-Hydroquinone as an Electron–Proton Transfer Mediator. *Journal of the American Chemical Society* **2017,** *139*, 18472-18475.
212. Carter, M. J.; Rillema, D. P.; Basolo, F., Oxygen carrier and redox properties of some neutral cobalt chelates. Axial and in-plane ligand effects. *Journal of the American Chemical Society* **1974,** *96*, 392-400.
213. Wang, Y.-H.; Goldsmith, Z. K.; Schneider, P. E.; Anson, C. W.; Gerken, J. B.; Ghosh, S.; Hammes-Schiffer, S.; Stahl, S. S., Kinetic and Mechanistic Characterization of Low-Overpotential, H_2O_2-Selective Reduction of O_2 Catalyzed by N_2O_2-Ligated Cobalt Complexes. *Journal of the American Chemical Society* **2018,** *140*, 10890-10899.
214. Nichols, A. W.; Chatterjee, S.; Sabat, M.; Machan, C. W., Electrocatalytic Reduction of CO_2 to Formate by an Iron Schiff Base Complex. *Inorganic Chemistry* **2018,** *57*, 2111-2121.
215. Nichols, A. W.; Kuehner, J. S.; Huffman, B. L.; Miedaner, P. R.; Dickie, D. A.; Machan, C. W., Reduction of dioxygen to water by a Co(N_2O_2) complex with a 2,2′-bipyridine backbone. *Chemical Communications* **2021,** *57*, 516-519.
216. Andrez, J.; Guidal, V.; Scopelliti, R.; Pécaut, J.; Gambarelli, S.; Mazzanti, M., Ligand and Metal Based Multielectron Redox Chemistry of Cobalt Supported by Tetradentate Schiff Bases. *Journal of the American Chemical Society* **2017,** *139*, 8628-8638.
217. Pearce, D. J.; Pletcher, D., A study of the mechanism for the electrocatalysis of carbon dioxide reduction by nickel and cobalt square planar complexes in solution. *Journal of Electroanalytical Chemistry and Interfacial Electrochemistry* **1986,** *197* (1-2), 317-330.
218. Isse, A. A.; Gennaro, A.; Vianello, E.; Floriani, C., Electrochemical reduction of carbon dioxide catalyzed by [CoI(salophen)Li]. *Journal of Molecular Catalysis* **1991,** *70*, 197-208.
219. Cozzi, P. G., Metal–Salen Schiff base complexes in catalysis: practical aspects. *Chemical Society Reviews* **2004,** *33*, 410-421.

Chapter 2 References

1. Benson, E. E.; Kubiak, C. P.; Sathrum, A. J.; Smieja, J. M., Electrocatalytic and homogeneous approaches to conversion of CO_2 to liquid fuels. *Chemical Society Reviews* **2009,** *38*, 89-99.
2. Senftle, T. P.; Carter, E. A., The Holy Grail: Chemistry Enabling an Economically Viable CO_2 Capture, Utilization, and Storage Strategy. *Accounts of Chemical Research* **2017,** *50*, 472-475.
3. Savéant, J.-M., Molecular Catalysis of Electrochemical Reactions. Mechanistic Aspects. *Chemical Reviews* **2008,** *108*, 2348-2378.
4. Chen, J.; Szalda, D. J.; Fujita, E.; Creutz, C., Iron(II) and ruthenium(II) complexes containing P, N, and H ligands: structure, spectroscopy, electrochemistry, and reactivity. *Inorganic Chemistry* **2010,** *49*, 9380-91.
5. Hull, J. F.; Himeda, Y.; Wang, W. H.; Hashiguchi, B.; Periana, R.; Szalda, D. J.; Muckerman, J. T.; Fujita, E., Reversible hydrogen storage using CO_2 and a proton-switchable iridium catalyst in aqueous media under mild temperatures and pressures. *Nature Chemistry* **2012,** *4*, 383-388.
6. Clarke, H. T.; Gillespie, H. B.; Weisshaus, S. Z., The Action of Formaldehyde on Amines and Amino Acids 1. *Journal of the American Chemical Society* **1933,** *55*, 4571-4587.
7. Moore, M. L., The Leuckart Reaction. In *Organic Reactions*, John Wiley & Sons, Inc.: 2004.
8. Sampson, M. D.; Nguyen, A. D.; Grice, K. A.; Moore, C. E.; Rheingold, A. L.; Kubiak, C. P., Manganese catalysts with bulky bipyridine ligands for the electrocatalytic reduction of carbon dioxide: eliminating dimerization and altering catalysis. *Journal of the American Chemical Society* **2014,** *136*, 5460-71.
9. Elgrishi, N.; Chambers, M. B.; Wang, X.; Fontecave, M., Molecular polypyridine-based metal complexes as catalysts for the reduction of CO_2. *Chemical Society Reviews* **2017,** *46*, 761-796.
10. Azcarate, I.; Costentin, C.; Robert, M.; Saveant, J.-M., Through-Space Charge Interaction Substituent Effects in Molecular Catalysis Leading to the Design of the Most Efficient Catalyst of CO_2-to-CO Electrochemical Conversion. Journal of the American Chemical Society **2016,** *138*, 16639-16644.
11. Bhugun, I.; Lexa, D.; Savéant, J.-M., Catalysis of the Electrochemical Reduction of Carbon Dioxide by Iron(0) Porphyrins: Synergystic Effect of Weak Brönsted Acids. *Journal of the American Chemical Society* **1996,** *118*, 1769-1776.
12. Costentin, C.; Drouet, S.; Robert, M.; Savéant, J.-M., A Local Proton Source Enhances CO_2 Electroreduction to CO by a Molecular Fe Catalyst. *Science* **2012,** *338*, 90.
13. Costentin, C.; Passard, G.; Robert, M.; Savéant, J.-M., Ultraefficient homogeneous catalyst for the CO_2-to-CO electrochemical conversion. *Proceedings of the National Academies of Science* **2014,** *111*, 14990-14994.
14. Taheri, A.; Thompson, E. J.; Fettinger, J. C.; Berben, L. A., An Iron Electrocatalyst for Selective Reduction of CO_2 to Formate in Water: Including Thermochemical Insights. *ACS Catalysis* **2015,** *5*, 7140-7151.

15. Taheri, A.; Berben, L. A., Tailoring Electrocatalysts for Selective CO_2 or H^+ Reduction: Iron Carbonyl Clusters as a Case Study. *Inorganic Chemistry* **2016,** *55*, 378-385.
16. Rail, M. D.; Berben, L. A., Directing the reactivity of $[HFe_4N(CO)_{12}]^-$ toward H^+ or CO_2 reduction by understanding the electrocatalytic mechanism. *Journal of the American Chemical Society* **2011,** *133*, 18577-18579.
17. Roy, S.; Sharma, B.; Pécaut, J.; Simon, P.; Fontecave, M.; Tran, P. D.; Derat, E.; Artero, V., Molecular cobalt complexes with pendant amines for selective electrocatalytic reduction of carbon dioxide to formic acid. *Journal of the American Chemical Society* **2017,** *139*, 3685-3696.
18. Ceballos, B. M.; Tsay, C.; Yang, J. Y., CO_2 reduction or HCO_2^- oxidation? Solvent-dependent thermochemistry of a nickel hydride complex. *Chemical Communications* **2017,** *53*, 7405-7408.
19. Tsay, C.; Livesay, B. N.; Ruelas, S.; Yang, J. Y., Solvation Effects on Transition Metal Hydricity. *Journal of the American Chemical Society* **2015,** *137*, 14114-14121.
20. Pun, S.-N.; Chung, W.-H.; Lam, K.-M.; Guo, P.; Chan, P.-H.; Wong, K.-Y.; Che, C.-M.; Chen, T.-Y.; Peng, S.-M., Iron(I) complexes of 2,9-bis(2-hydroxyphenyl)-1,10-phenanthroline (H_2dophen) as electrocatalysts for carbon dioxide reduction. X-Ray crystal structures of $[Fe(dophen)Cl]_2 \cdot 2HCON(CH_3)_2$ and $[Fe(dophen)(N\text{-}MeIm)_2]ClO_4$ (N-MeIm = 1-methylimidazole). *Journal of the Chemical Society, Dalton Transactions* **2002,** 4, 575.
21. Khusnutdinova, J. R.; Milstein, D., Metal–Ligand Cooperation. *Angewandte Chemie International Edition* **2015,** *54*, 12236-12273.
22. Luca, O. R.; Crabtree, R. H., Redox-active ligands in catalysis. *Chemical Society Reviews* **2013,** *42*, 1440-1459.
23. Bourrez, M.; Molton, F.; Chardon-Noblat, S.; Deronzier, A., $[Mn(bipyridyl)(CO)_3Br]$: An abundant metal carbonyl complex as efficient electrocatalyst for CO_2 reduction. *Angewandte Chemie International Edition* **2011,** *123*, 10077-10080.
24. Ngo, K. T.; McKinnon, M.; Mahanti, B.; Narayanan, R.; Grills, D. C.; Ertem, M. Z.; Rochford, J., Turning on the Protonation-First Pathway for Electrocatalytic CO_2 Reduction by Manganese Bipyridyl Tricarbonyl Complexes. *Journal of the American Chemical Society* **2017,** *139*, 2604-2618.
25. Andrez, J.; Guidal, V.; Scopelliti, R.; Pecaut, J.; Gambarelli, S.; Mazzanti, M., Ligand and Metal Based Multielectron Redox Chemistry of Cobalt Supported by Tetradentate Schiff Bases. *Journal of the American Chemical Society* **2017,** *139*, 8628-8638.
26. Lee, K. J.; Elgrishi, N.; Kandemir, B.; Dempsey, J. L., Electrochemical and spectroscopic methods for evaluating molecular electrocatalysts. *Nature Reviews Chemistry* **2017,** *1*, 0039.
27. Machan, C. W.; Chabolla, S. A.; Kubiak, C. P., Reductive Disproportionation of Carbon Dioxide by an Alkyl-Functionalized Pyridine Monoimine Re(I) fac-Tricarbonyl Electrocatalyst. *Organometallics* **2015,** *34*, 4678-4683.
28. Baleizão, C.; Garcia, H., Chiral Salen Complexes: An Overview to Recoverable and Reusable Homogeneous and Heterogeneous Catalysts. *Chemical Reviews* **2006,** *106*, 3987-4043.

29. Cozzi, P. G., Metal-Salen Schiff base complexes in catalysis: practical aspects. *Chemical Society Reviews* **2004,** *33*, 410-21.
30. Gupta, K.; Sutar, A. K., Catalytic activities of Schiff base transition metal complexes. *Coordination Chemistry Reviews* **2008,** *252*, 1420-1450.
31. Pearce, D. J.; Pletcher, D., A study of the mechanism for the electrocatalysis of carbon dioxide reduction by nickel and cobalt square planar complexes in solution. *Journal of Electroanalytical Chemistry* **1986,** *197*, 317-330.
32. Isse, A. A.; Gennaro, A.; Vianello, E.; Floriani, C., Electrochemical reduction of carbon dioxide catalyzed by [CoI(salophen)Li]. *Journal of Molecular Catalysis* **1991,** *70*, 197-208.
33. Wong, H. L.; Tian, Y.; Chan, K. S., Electronically controlled asymmetric cyclopropanation catalyzed by a new type of chiral 2,2′-bipyridine. *Tetrahedron Letters* **2000,** *41*, 7723-7726.
34. Lin, Y.-Y.; Chan, S.-C.; Chan, M. C. W.; Hou, Y.-J.; Zhu, N.; Che, C.-M.; Liu, Y.; Wang, Y., Structural, Photophysical, and Electrophosphorescent Properties of Platinum(II) Complexes Supported by Tetradentate N_2O_2 Chelates. *Chemistry – A European Journal* **2003,** *9*, 1263-1272.
35. Hooe, S.; Rheingold, A. L.; Machan, C. W., Electrocatalytic Reduction of Dioxygen to Hydrogen Peroxide by a Molecular Manganese Complex with a Bipyridine-Containing Schiff Base Ligand. *Journal of the American Chemical Society* **2018,** *9,* 3232-3241.
36. Arora, H.; Philouze, C.; Jarjayes, O.; Thomas, F., Co(II), Ni(II), Cu(II) and Zn(II) complexes of a bipyridine bis-phenol conjugate: generation and properties of coordinated radical species. *Dalton Transactions* **2010,** *39*, 10088-98.
37. Dietrick-Buchecker, C.; Marnot, P.; Sauvage, J., Direct synthesis of disubstituted aromatic polyimine chelates. *Tetrahedron Letters* **1982,** *23*, 5291-5294.
38. Campbell, I. B.; Walker, A. L.; Box, P. C.; Giblin, G. M. P.; Tranter, G. E. Bipyridine manganese complexes. US 6177419, January 3, 2001.
39. Capdevielle, P.; Maumy, M.; Audebert, P.; Plaza, B., Electoactive Polymers Exchanging Transition Metal Ions; Synthesis of New Monomers And Polymers Based on 6, 6'-Bis (2-Hydroxyphenyl) Bipyridine Complexes. *New Journal of Chemistry* **1994,** *18*, 519-524.
40. Pegis, M. L.; McKeown, B. A.; Kumar, N.; Lang, K.; Wasylenko, D. J.; Zhang, X. P.; Raugei, S.; Mayer, J. M., Homogenous electrocatalytic oxygen reduction rates correlate with reaction overpotential in acidic organic solutions. *ACS Central Science* **2016,** *2*, 850-856.
41. Zavarine, I. S.; Kubiak, C. P., A versatile variable temperature thin layer reflectance spectroelectrochemical cell. *Journal of Electroanalytical Chemistry* **2001,** *495*, 106-109.
42. Machan, C. W.; Sampson, M. D.; Chabolla, S. A.; Dang, T.; Kubiak, C. P., Developing a mechanistic understanding of molecular electrocatalysts for CO_2 reduction using infrared spectroelectrochemistry. *Organometallics* **2014,** *33*, 4550-4559.
43. Neese, F., The ORCA program system. *Wiley Interdisciplinary Reviews: Computational Molecular Science* **2012,** *2*, 73-78.

44. Vosko, S. H.; Wilk, L.; Nusair, M., Accurate spin-dependent electron liquid correlation energies for local spin density calculations: a critical analysis. *Canadian Journal of Physics* **1980,** *58*, 1200-1211.
45. Lee, C.; Yang, W.; Parr, R. G., Development of the Colle-Salvetti correlation-energy formula into a functional of the electron density. *Physical Review B* **1988,** *37*, 785-789.
46. Becke, A. D., Density-functional thermochemistry. III. The role of exact exchange. *Journal of Chemical Physics* **1993,** *98*, 5648-5652.
47. Becke, A. D., A new mixing of Hartree–Fock and local density-functional theories. *Journal of Chemical Physics* **1993,** *98*, 1372-1377.
48. Stephens, P. J.; Devlin, F. J.; Chabalowski, C. F.; Frisch, M. J., Ab Initio Calculation of Vibrational Absorption and Circular Dichroism Spectra Using Density Functional Force Fields. *Journal of Physical Chemistry* **1994,** *98*, 11623-11627.
49. Schäfer, A.; Horn, H.; Ahlrichs, R., Fully optimized contracted Gaussian basis sets for atoms Li to Kr. *Journal of Chemical Physics* **1992,** *97*, 2571-2577.
50. Weigend, F.; Ahlrichs, R., Balanced basis sets of split valence, triple zeta valence and quadruple zeta valence quality for H to Rn: Design and assessment of accuracy. *Physical Chemistry Chemical Physics* **2005,** *7*, 3297-3305.
51. Izsák, R.; Neese, F., An overlap fitted chain of spheres exchange method. *Journal of Chemical Physics* **2011,** *135*, 144105.
52. Grimme, S.; Antony, J.; Ehrlich, S.; Krieg, H., A consistent and accurate ab initio parametrization of density functional dispersion correction (DFT-D) for the 94 elements H-Pu. *Journal of Chemical Physics* **2010,** *132*, 154104.
53. Grimme, S.; Ehrlich, S.; Goerigk, L., Effect of the damping function in dispersion corrected density functional theory. *Journal of Computational Chemistry* **2011,** *32*, 1456-1465.
54. Cossi, M.; Rega, N.; Scalmani, G.; Barone, V., Energies, structures, and electronic properties of molecules in solution with the C-PCM solvation model. *Journal of Computational Chemistry* **2003,** *24*, 669-681.
55. Bain, G. A.; Berry, J. F., Diamagnetic Corrections and Pascal's Constants. *Journal of Chemical Education* **2008,** *85*, 532.
56. Piguet, C., Paramagnetic Susceptibility by NMR: The "Solvent Correction" Removed for Large Paramagnetic Molecules. *Journal of Chemical Education* **1997,** *74*, 815.
57. Chatterjee, S.; Sheet, D.; Paine, T. K., Catalytic and regiospecific extradiol cleavage of catechol by a biomimetic iron complex. *Chemical Communications* **2013,** *49*, 10251-10253.
58. Murav'ev, V., EPR spectra and structures of spin-variable iron (III) complexes. *Russian Journal of Coordination Chemistry* **2011,** *37*, 861-867.
59. Ramesh, K.; Mukherjee, R., Trends in the spectral and redox potential data of mononuclear iron (III)(S= 5/2) phenolate complexes. *Journal of the Chemical Society, Dalton Transactions* **1992,** , 83-89.
60. Pyrz, J. W.; Roe, A. L.; Stern, L. J.; Que Jr, L., Model studies of iron-tyrosinate proteins. *Journal of the American Chemical Society* **1985,** *107*, 614-620.
61. Ainscough, E. W.; Brodie, A. M.; Plowman, J. E.; Brown, K. L.; Addison, A. W.; Gainsford, A. R., Small molecule analogs for the specific iron-binding site of

lactoferrin: a single-crystal x-ray structure of bis(methanol) bis[2-(5-methylpyrazol-3-yl) phenolato] iron (III) nitrate-methanol and spectroscopic studies on iron (III) phenolate complexes. *Inorganic Chemistry* **1980,** *19*, 3655-3663.

62. Lubben, M.; Meetsma, A.; Van Bolhuis, F.; Feringa, B. L.; Hage, R., Synthesis, crystal and molecular structures, UV-Vis spectroscopy and electrochemical properties of two iron (III) phenolate complexes. *Inorganica Chimica Acta* **1994,** *215*, 123-129.
63. Zanello, P., *Inorganic electrochemistry: theory, practice and application*. Royal Society of Chemistry: 2007.
64. Miomandre, F.; Audebert, P.; Maumy, M.; Uhl, L., Electrochemical behaviour of iron (III) salen and poly (iron–salen). Application to the electrocatalytic reduction of hydrogen peroxide and oxygen. *Journal of Electroanalytical Chemistry* **2001,** *516*, 66-72.
65. Bard, A. J.; Faulkner, L. R., *Electrochemical Methods: Fundamentals and Applications*. 2nd ed.; John Wiley & Sons, Inc.: Hoboken, NJ, 2001.
66. Machan, C. W.; Sampson, M. D.; Kubiak, C. P., A Molecular Ruthenium Electrocatalyst for the Reduction of Carbon Dioxide to CO and Formate. *Journal of the American Chemical Society* **2015,** *137*, 8564-71.
67. Gagne, R. R.; Ingle, D. M., Intramolecular electron transfer and valence isomerization in mononuclear nickel-macrocyclic ligand complexes: formation of paramagnetic nickel (I)-carbonyl complexes. *Journal of the American Chemical Society* **1980,** *102*, 1444-1446.
68. Gagne, R. R.; Allison, J. L.; Ingle, D. M., Unusual structural and reactivity types for copper (I). Equilibrium constants for the binding of monodentate ligands to several four-coordinate copper (I) complexes. *Inorganic Chemistry* **1979,** *18*, 2767-2774.
69. Fujita, E.; Creutz, C.; Sutin, N.; Szalda, D. J., Carbon dioxide activation by cobalt (I) macrocycles: factors affecting carbon dioxide and carbon monoxide binding. *Journal of the American Chemical Society* **1991,** *113*, 343-353.
70. Sathrum, A. J.; Kubiak, C. P., Kinetics and Limiting Current Densities of Homogeneous and Heterogeneous Electrocatalysts. *Journal of Physical Chemistry Letters* **2011,** *2*, 2372-2379.
71. Ashley, K.; Pons, S., Infrared spectroelectrochemistry. *Chemical Reviews* **1988,** *88*, 673-695.
72. Kaim, W.; Fiedler, J., Spectroelectrochemistry: the best of two worlds. *Chemical Society Reviews* **2009,** *38*, 3373-3382.
73. Best, S.; Crumbliss, A.; Dunsch, L.; Haga, M.-a.; Hartl, F.; Kubiak, C.; Winter, R.; Yellowlees, L.; Salsman, C.; Murray, P., *Spectroelectrochemistry*. Royal Society of Chemistry: 2008.
74. Cargill, R. W., *Solubility Data Series: Carbon Monoxide*. Elsevier: 2013; Vol. 43.
75. Costentin, C.; Savéant, J. M., Multielectron, multistep molecular catalysis of electrochemical reactions: Benchmarking of homogeneous catalysts. *ChemElectroChem* **2014,** *1*, 1226-1236.
76. Gómez-Gallego, M.; Sierra, M. A., Kinetic isotope effects in the study of organometallic reaction mechanisms. *Chemical Reviews* **2011,** *111*, 4857-4963.
77. Smieja, J. M.; Benson, E. E.; Kumar, B.; Grice, K. A.; Seu, C. S.; Miller, A. J.; Mayer, J. M.; Kubiak, C. P., Kinetic and structural studies, origins of selectivity, and

interfacial charge transfer in the artificial photosynthesis of CO. *Proceedings of the National Academies of Science* **2012,** *109*, 15646-15650.

78. Costentin, C.; Drouet, S.; Passard, G.; Robert, M.; Savéant, J.-M., Proton-coupled electron transfer cleavage of heavy-atom bonds in electrocatalytic processes. Cleavage of a C–O bond in the catalyzed electrochemical reduction of CO_2. *Journal of the American Chemical Society* **2013,** *135*, 9023-9031.

Chapter 2 SI References

1. Piguet, C., Paramagnetic Susceptibility by NMR: The "Solvent Correction" Removed for Large Paramagnetic Molecules. *Journal of Chemical Education* **1997,** *74*, 815.
2. Bain, G. A.; Berry, J. F., Diamagnetic Corrections and Pascal's Constants. *Journal of Chemical Education* **2008,** *85*, 532.
3. Gagne, R. R.; Allison, J. L.; Ingle, D. M., Unusual structural and reactivity types for copper (I). Equilibrium constants for the binding of monodentate ligands to several four-coordinate copper (I) complexes. *Inorganic Chemistry* **1979,** *18*, 2767-2774.
4. Harris, D. C., *Quantitative Chemical Analysis*. 7th ed.; W.H. Freeman and Company: New York, NY, 2007.
5. Cargill, R. W., *Solubility Data Series: Carbon Monoxide*. Elsevier: 2013; Vol. 43.
6. Atkins, P.; De Paula, J.; Friedman, R., *Quanta, matter, and change: a molecular approach to physical chemistry*. Oxford University Press: 2009.
7. Cheng, S. C.; Blaine, C. A.; Hill, M. G.; Mann, K. R., Electrochemical and IR spectroelectrochemical studies of the electrocatalytic reduction of carbon dioxide by $[Ir_2 (dimen)_4]^{2+}$ (dimen= 1, 8-Diisocyanomenthane). *Inorganic Chemistry* **1996,** *35*, 7704-7708.
8. Sathrum, A. J.; Kubiak, C. P., Kinetics and Limiting Current Densities of Homogeneous and Heterogeneous Electrocatalysts. *Journal of Physical Chemistry Letters* **2011,** *2*, 2372-2379.
9. Vosko, S. H.; Wilk, L.; Nusair, M., Accurate spin-dependent electron liquid correlation energies for local spin density calculations: a critical analysis. *Canadian Journal of Physics* **1980,** *58*, 1200-1211.
10. Lee, C.; Yang, W.; Parr, R. G., Development of the Colle-Salvetti correlation-energy formula into a functional of the electron density. *Physical Review B* **1988,** *37*, 785-789.
11. Becke, A. D., Density-functional thermochemistry. III. The role of exact exchange. *Journal of Chemical Physics* **1993,** *98*, 5648-5652.
12. Becke, A. D., A new mixing of Hartree–Fock and local density-functional theories. *Journal of Chemical Physics* **1993,** *98*, 1372-1377.
13. Stephens, P. J.; Devlin, F. J.; Chabalowski, C. F.; Frisch, M. J., Ab Initio Calculation of Vibrational Absorption and Circular Dichroism Spectra Using Density Functional Force Fields. *Journal of Physical Chemistry* **1994,** *98*, 11623-11627.
14. Schäfer, A.; Horn, H.; Ahlrichs, R., Fully optimized contracted Gaussian basis sets for atoms Li to Kr. *Journal of Chemical Physics* **1992,** *97*, 2571-2577.
15. Weigend, F.; Ahlrichs, R., Balanced basis sets of split valence, triple zeta valence and quadruple zeta valence quality for H to Rn: Design and assessment of accuracy. *Physical Chemistry Chemical Physics* **2005,** *7*, 3297-3305.

16. Izsák, R.; Neese, F., An overlap fitted chain of spheres exchange method. *Journal of Chemical Physics* **2011,** *135*, 144105.
17. Grimme, S.; Antony, J.; Ehrlich, S.; Krieg, H., A consistent and accurate ab initio parametrization of density functional dispersion correction (DFT-D) for the 94 elements H-Pu. *Journal of Chemical Physics* **2010,** *132*, 154104.
18. Grimme, S.; Ehrlich, S.; Goerigk, L., Effect of the damping function in dispersion corrected density functional theory. *Journal of Computational Chemistry* **2011,** *32*, 1456-1465.
19. Cossi, M.; Rega, N.; Scalmani, G.; Barone, V., Energies, structures, and electronic properties of molecules in solution with the C-PCM solvation model. *Journal of Computational Chemistry* **2003,** *24*, 669-681.
20. Ngo, K. T.; McKinnon, M.; Mahanti, B.; Narayanan, R.; Grills, D. C.; Ertem, M. Z.; Rochford, J., Turning on the Protonation-First Pathway for Electrocatalytic CO_2 Reduction by Manganese Bipyridyl Tricarbonyl Complexes. *Journal of the American Chemical Society* **2017,** *139*, 2604-2618.

Chapter 3 References

1. Senftle, T. P.; Carter, E. A., The Holy Grail: Chemistry Enabling an Economically Viable CO_2 Capture, Utilization, and Storage Strategy. *Accounts of Chemical Research* **2017,** *50*, 472-475.
2. De Luna, P.; Hahn, C.; Higgins, D.; Jaffer, S. A.; Jaramillo, T. F.; Sargent, E. H., What would it take for renewably powered electrosynthesis to displace petrochemical processes? *Science* **2019,** *364*, eaav3506.
3. Francke, R.; Schille, B.; Roemelt, M., Homogeneously Catalyzed Electroreduction of Carbon Dioxide—Methods, Mechanisms, and Catalysts. *Chemical Reviews* **2018,** *118*, 4631-4701.
4. Witt, S. E.; White, T. A.; Li, Z.; Dunbar, K. R.; Turro, C., Cationic dirhodium(ii,ii) complexes for the electrocatalytic reduction of CO2 to HCOOH. *Chemical Communications* **2016,** *52*, 12175-12178.
5. Roy, S.; Sharma, B.; Pécaut, J.; Simon, P.; Fontecave, M.; Tran, P. D.; Derat, E.; Artero, V., Molecular cobalt complexes with pendant amines for selective electrocatalytic reduction of carbon dioxide to formic acid. *Journal of the American Chemical Society* **2017,** *139*, 3685-3696.
6. Clarke, H. T.; Gillespie, H. B.; Weisshaus, S. Z., The Action of Formaldehyde on Amines and Amino Acids 1. *Journal of the American Chemical Society* **1933,** *55*, 4571-4587.
7. Rice, C.; Ha, S.; Masel, R.; Waszczuk, P.; Wieckowski, A.; Barnard, T., Direct formic acid fuel cells. *Journal of Power Sources* **2002,** *111*, 83-89.
8. Hull, J. F.; Himeda, Y.; Wang, W.-H.; Hashiguchi, B.; Periana, R.; Szalda, D. J.; Muckerman, J. T.; Fujita, E., Reversible hydrogen storage using CO_2 and a proton-switchable iridium catalyst in aqueous media under mild temperatures and pressures. *Nature Chemistry* **2012,** *4*, 383.
9. Nichols, A. W.; Chatterjee, S.; Sabat, M.; Machan, C. W., Electrocatalytic Reduction of CO_2 to Formate by an Iron Schiff Base Complex. *Inorganic Chemistry* **2018,** *57*, 2111-2121.

10. Lieske, L. E.; Hooe, S. L.; Nichols, A. W.; Machan, C. W., Electrocatalytic reduction of dioxygen by Mn(iii) meso-tetra(N-methylpyridinium-4-yl)porphyrin in universal buffer. *Dalton Transactions* **2019,** *48*, 8633-8641.
11. Hooe, S. L.; Machan, C. W., Dioxygen Reduction to Hydrogen Peroxide by a Molecular Mn Complex: Mechanistic Divergence between Homogeneous and Heterogeneous Reductants. *Journal of the American Chemical Society* **2019,** *141*, 4379-4387.
12. Huynh, M. H. V.; Meyer, T. J., Proton-Coupled Electron Transfer. *Chemical Reviews* **2007,** *107*, 5004-5064.
13. Solis, B. H.; Yu, Y.; Hammes-Schiffer, S., Effects of Ligand Modification and Protonation on Metal Oxime Hydrogen Evolution Electrocatalysts. *Inorganic Chemistry* **2013,** *52*, 6994-6999.
14. Kaeffer, N.; Chavarot-Kerlidou, M.; Artero, V., Hydrogen Evolution Catalyzed by Cobalt Diimine-Dioxime Complexes. *Accounts of Chemical Research* **2015,** *48*, 1286-1295.
15. Downes, C. A.; Yoo, J. W.; Orchanian, N. M.; Haiges, R.; Marinescu, S. C., H_2 evolution by a cobalt selenolate electrocatalyst and related mechanistic studies. *Chemical Communications* **2017,** *53*, 7306-7309.
16. Zarkadoulas, A.; Field, M. J.; Artero, V.; Mitsopoulou, C. A., Proton-Reduction Reaction Catalyzed by Homoleptic Nickel-bis-1,2-dithiolate Complexes: Experimental and Theoretical Mechanistic Investigations. *ChemCatChem* **2017,** *9*, 2308-2317.
17. Chen, J.; Sit, P. H.-L., Density Functional Theory and Car–Parrinello Molecular Dynamics Study of the Hydrogen-Producing Mechanism of the $Co(dmgBF_2)_2$ and $Co(dmgH)_2$ Cobaloxime Complexes in Acetonitrile–Water Solvent. *The Journal of Physical Chemistry A* **2017,** *121*, 3515-3525.
18. McEvoy, J. P.; Brudvig, G. W., Water-splitting chemistry of photosystem II. *Chemical Reviews* **2006,** *106*, 4455-4483.
19. Manner, V. W.; DiPasquale, A. G.; Mayer, J. M., Facile Concerted Proton− Electron Transfers in a Ruthenium Terpyridine-4′-Carboxylate Complex with a Long Distance Between the Redox and Basic Sites. *Journal of the American Chemical Society* **2008,** *130*, 7210-7211.
20. Warren, J. J.; Tronic, T. A.; Mayer, J. M., Thermochemistry of proton-coupled electron transfer reagents and its implications. *Chemical Reviews* **2010,** *110*, 6961-7001.
21. Fecenko, C. J.; Thorp, H. H.; Meyer, T. J., The Role of Free Energy Change in Coupled Electron−Proton Transfer. *Journal of the American Chemical Society* **2007,** *129*, 15098-15099.
22. Ngo, K. T.; McKinnon, M.; Mahanti, B.; Narayanan, R.; Grills, D. C.; Ertem, M. Z.; Rochford, J., Turning on the Protonation-First Pathway for Electrocatalytic CO_2 Reduction by Manganese Bipyridyl Tricarbonyl Complexes. *Journal of the American Chemical Society* **2017,** *139*, 2604-2618.
23. Costentin, C.; Drouet, S.; Robert, M.; Savéant, J.-M., A Local Proton Source Enhances CO_2 Electroreduction to CO by a Molecular Fe Catalyst. *Science* **2012,** *338*, 90–94.

24. Roy, S.; Sharma, B.; Pécaut, J.; Simon, P.; Fontecave, M.; Tran, P. D.; Derat, E.; Artero, V., Molecular Cobalt Complexes with Pendant Amines for Selective Electrocatalytic Reduction of Carbon Dioxide to Formic Acid. *Journal of the American Chemical Society* **2017,** *139*, 3685-3696.
25. Curtis, C. J.; Miedaner, A.; Ciancanelli, R.; Ellis, W. W.; Noll, B. C.; Rakowski DuBois, M.; DuBois, D. L., $[Ni(Et_2PCH_2NMeCH_2PEt_2)_2]^{2+}$ as a functional model for hydrogenases. *Inorganic Chemistry* **2003,** *42*, 216-227.
26. Henry, R. M.; Shoemaker, R. K.; DuBois, D. L.; DuBois, M. R., Pendant bases as proton relays in iron hydride and dihydrogen complexes. *Journal of the American Chemical Society* **2006,** *128*, 3002-3010.
27. Fraze, K.; Wilson, A. D.; Appel, A. M.; Rakowski DuBois, M.; DuBois, D. L., Thermodynamic Properties of the Ni− H Bond in Complexes of the Type $[HNi(P_2RN_2R')_2](BF_4)$ and Evaluation of Factors That Control Catalytic Activity for Hydrogen Oxidation/Production. *Organometallics* **2007,** *26*, 3918-3924.
28. Mukherjee, S.; Mukherjee, M.; Mukherjee, A.; Bhagi-Damodaran, A.; Lu, Y.; Dey, A., O_2 reduction by biosynthetic models of cytochrome c oxidase: insights into role of proton transfer residues from perturbed active sites models of CcO. *ACS Catalysis* **2018,** *8*, 8915-8924.
29. Passard, G.; Dogutan, D. K.; Qiu, M.; Costentin, C.; Nocera, D. G., Oxygen reduction reaction promoted by manganese porphyrins. *ACS Catalysis* **2018,** *8*, 8671-8679.
30. McGuire Jr, R.; Dogutan, D. K.; Teets, T. S.; Suntivich, J.; Shao-Horn, Y.; Nocera, D. G., Oxygen reduction reactivity of cobalt (II) hangman porphyrins. *Chemical Science* **2010,** *1*, 411-414.
31. Savéant, J.-M., Proton Relays in Molecular Catalysis of Electrochemical Reactions: Origin and Limitations of the Boosting Effect. *Angewandte Chemie, International Edition* **2019,** *58*, 2125-2128.
32. Azcarate, I.; Costentin, C.; Robert, M.; Saveant, J.-M., Through-Space Charge Interaction Substituent Effects in Molecular Catalysis Leading to the Design of the Most Efficient Catalyst of CO_2-to-CO Electrochemical Conversion. *Journal of the American Chemical Society* **2016,** *138*, 16639-16644.
33. Costentin, C.; Passard, G.; Robert, M.; Savéant, J.-M., Pendant Acid–Base Groups in Molecular Catalysts: H-Bond Promoters or Proton Relays? Mechanisms of the Conversion of CO_2 to CO by Electrogenerated Iron(0)Porphyrins Bearing Prepositioned Phenol Functionalities. *Journal of the Chemical Society* **2014,** *136*, 11821-11829.
34. Jiang, C.; Nichols, A. W.; Machan, C. W., A look at periodic trends in d-block molecular electrocatalysts for CO_2 reduction. *Dalton Transactions* **2019**.
35. Costentin, C.; Passard, G.; Robert, M.; Saveant, J.-M., Ultraefficient homogeneous catalyst for the CO_2-to-CO electrochemical conversion. *Proceedings of the National Academy of Sciences* **2014,** *111*, 14990-14994.
36. Nichols, A. W.; Machan, C. W., Secondary-Sphere Effects in Molecular Electrocatalytic CO_2 Reduction. *Front. Chem.* **2019,** *7*, https://doi.org/10.3389/fchem.2019.00397.
37. Franco, F.; Cometto, C.; Nencini, L.; Barolo, C.; Sordello, F.; Minero, C.; Fiedler, J.; Robert, M.; Gobetto, R.; Nervi, C., Local Proton Source in Electrocatalytic CO_2

Reduction with [Mn (bpy–R)$(CO)_3$Br] Complexes. *Chemistry – A European Journal* **2017,** *23*, 4782-4793.

38. Agarwal, J.; Shaw, T. W.; Schaefer III, H. F.; Bocarsly, A. B., Design of a catalytic active site for electrochemical CO_2 reduction with Mn (I)-tricarbonyl species. *Inorganic Chemistry* **2015,** *54*, 5285-5294.
39. Franco, F.; Cometto, C.; Vallana, F. F.; Sordello, F.; Priola, E.; Minero, C.; Nervi, C.; Gobetto, R., A local proton source in a [Mn(bpy-R)$(CO)_3$Br]-type redox catalyst enables CO_2 reduction even in the absence of Brønsted acids. *Chemical Communications* **2014,** *50*, 14670-14673.
40. Fokin, I.; Denisiuk, A.; Würtele, C.; Siewert, I., The Impact of a Proton Relay in Binuclear α-Diimine-Mn$(CO)_3$ Complexes on the CO2 Reduction Catalysis. *Inorganic Chemistry* **2019,** *58*, 10444-10453.
41. Chapovetsky, A.; Welborn, M.; Luna, J. M.; Haiges, R.; Miller, T. F.; Marinescu, S. C., Pendant Hydrogen-Bond Donors in Cobalt Catalysts Independently Enhance CO_2 Reduction. *ACS Central Science* **2018,** *4*, 397-404.
42. Lexa, D.; Rentien, P.; Savéant, J. M.; Xu, F., Methods for investigating the mechanistic and kinetic role of ligand exchange reactions in coordination electrochemistry: Cyclic voltammetry of chloroiron(III)tetraphenylporphyrin in dimethylformamide. *Journal of Electroanalytical Chemistry and Interfacial Electrochemistry* **1985,** *191*, 253-279.
43. Bard, A. J.; Faulkner, L. R., *Electrochemical Methods: Fundamentals and Applications*. 2nd ed.; John Wiley & Sons, Inc.: Hoboken, NJ, 2001.
44. Appel, A. M.; Helm, M. L., Determining the Overpotential for a Molecular Electrocatalyst. *ACS Catal.* **2014,** *4*, 630-633.
45. Jödecke, M.; Pérez-Salado Kamps, Á.; Maurer, G., An Experimental Investigation of the Solubility of CO2 in (N,N-Dimethylmethanamide + Water). *Journal of Chemical & Engineering Data* **2012,** *57*, 1249-1266.
46. Savéant, J.-M., *Elements of molecular and biomolecular electrochemistry: an electrochemical approach to electron transfer chemistry*. John Wiley & Sons: 2006; Vol. 13.
47. Nielsen, M. F.; Hammerich, O., The Effect of Hydrogen Bonding between Methyl-Substituted Phenols and Dipolar Aprotic Solvents on the Rate Constants for. *Acta Chemica Scandinavica* **1992,** *46*, 883-896.
48. McCarthy, B. D.; Dempsey, J. L., Decoding Proton-Coupled Electron Transfer with Potential–pKa Diagrams. *Inorganic Chemistry* **2017,** *56*, 1225-1231.
49. Machan, C. W., Advances in the Molecular Catalysis of Dioxygen Reduction. *ACS Catalysis* **2020,** *10*, 2640-2655.
50. Pegis, M. L.; Wise, C. F.; Koronkiewicz, B.; Mayer, J. M., Identifying and breaking scaling relations in molecular catalysis of electrochemical reactions. *Journal of the American Chemical Society* **2017,** *139*, 11000-11003.
51. Zimmermann, P.; Hoof, S.; Braun-Cula, B.; Herwig, C.; Limberg, C., A Biomimetic Nickel Complex with a Reduced CO_2 Ligand Generated by Formate Deprotonation and Its Behaviour towards CO_2. *Angewandte Chemie International Edition* **2018,** *57*, 7230-7233.

52. Bordwell, F. G.; Cheng, J., Substituent effects on the stabilities of phenoxyl radicals and the acidities of phenoxyl radical cations. *Journal of the American Chemical Society* **1991,** *113*, 1736-1743.
53. Clare, B.; Cook, D.; Ko, E.; Mac, Y.; Parker, A., Solvation of Ions. IX. 1 The Effect of Anion Solvation on Acid Dissociation Constants in Methanol, Water, Dimethylformamide, and Dimethyl Sulfoxide. *Journal of the American Chemical Society.* **1966,** *88*, 1911-1916.
54. Machan, C. W.; Yin, J.; Chabolla, S. A.; Gilson, M. K.; Kubiak, C. P., Improving the Efficiency and Activity of Electrocatalysts for the Reduction of CO_2 through Supramolecular Assembly with Amino Acid-Modified Ligands. *Journal of the American Chemical Society* **2016,** *138*, 8184-8193.
55. Waldie, K. M.; Ostericher, A. L.; Reineke, M. H.; Sasayama, A. F.; Kubiak, C. P., Hydricity of Transition-Metal Hydrides: Thermodynamic Considerations for CO_2 Reduction. *ACS Catalysis* **2018,** *8*, 1313-1324.
56. Sinha, S.; Warren, J. J., Unexpected Solvent Effect in Electrocatalytic CO_2 to CO Conversion Revealed Using Asymmetric Metalloporphyrins. *Inorganic Chemistry* **2018,** *57*, 12650-12656.
57. Wiedner, E. S.; Chambers, M. B.; Pitman, C. L.; Bullock, R. M.; Miller, A. J. M.; Appel, A. M., Thermodynamic Hydricity of Transition Metal Hydrides. *Chemical Reviews* **2016,** *116*, 8655-8692.
58. Noviandri, I.; Brown, K. N.; Fleming, D. S.; Gulyas, P. T.; Lay, P. A.; Masters, A. F.; Phillips, L., The Decamethylferrocenium/Decamethylferrocene Redox Couple: A Superior Redox Standard to the Ferrocenium/Ferrocene Redox Couple for Studying Solvent Effects on the Thermodynamics of Electron Transfer. *Journal of Physical Chemistry B* **1999,** *103*, 6713-6722.
59. Chattopadhyay, B.; Dannatt, J. E.; Andujar-De Sanctis, I. L.; Gore, K. A.; Maleczka, R. E.; Singleton, D. A.; Smith, M. R., Ir-Catalyzed ortho-Borylation of Phenols Directed by Substrate–Ligand Electrostatic Interactions: A Combined Experimental/in Silico Strategy for Optimizing Weak Interactions. *Journal of the American Chemical Society* **2017,** *139*, 7864-7871.
60. Greenaway, K.; Dambruoso, P.; Ferrali, A.; Hazelwood, A. J.; Sladojevich, F.; Dixon, D. J., Enantioselective Organocatalytic Aryloxylation of β-Keto Esters. *Synthesis* **2011,** *2011*, 1880-1886.

Chapter 3 SI References

1. Sathrum, A. J.; Kubiak, C. P., *The Journal of Physical Chemistry Letters* **2011,** *2*, 2372-2379.

Chapter 4 References

1. Pegis, M. L.; Wise, C. F.; Martin, D. J.; Mayer, J. M., Oxygen Reduction by Homogeneous Molecular Catalysts and Electrocatalysts. *Chemical Reviews* **2018,** *118*, 2340-2391.
2. Pegis, M. L.; Wise, C. F.; Koronkiewicz, B.; Mayer, J. M., Identifying and breaking scaling relations in molecular catalysis of electrochemical reactions. *Journal of the American Chemical Society* **2017,** *139*, 11000-11003.

3. Machan, C. W., Advances in the Molecular Catalysis of Dioxygen Reduction. *ACS Catalysis* **2020,** *10*, 2640-2655.
4. He, Q.; Mugadza, T.; Hwang, G.; Nyokong, T., Mechanisms of electrocatalysis of oxygen reduction by metal porphyrins in trifluoromethane sulfonic acid solution. *International Journal of Electrochemical Science* **2012,** *7*, 7045-7064.
5. Chan, R. J.; Su, Y. O.; Kuwana, T., Electrocatalysis of oxygen reduction. 5. oxygen to hydrogen peroxide conversion by cobalt (II) tetrakis (N-methyl-4-pyridyl) porphyrin. *Inorganic Chemistry* **1985,** *24*, 3777-3784.
6. Sazou, D.; Araullo-McAdams, C.; Han, B.; Franzen, M.; Kadish, K. M., The use of an electrogenerated cobalt (I) porphyrin for the homogeneous catalytic reduction of dioxygen in dimethylformamide. Reactions of [(TMpyP) CoII]$^{4+}$ and [(TMpyP) CoI]$^{3+}$ where TMpyP= meso-tetrakis (1-methylpyridinium-4-yl) porphyrin. *Journal of the American Chemical Society* **1990,** *112*, 7879-7886.
7. D'Souza, F.; Deviprasad, R.; Hsieh, Y.-Y., Synthesis and studies on the electrocatalytic reduction of molecular oxygen by non-planar cobalt (II) tetrakis-(N-methyl pyridyl)-β-octabromoporphyrin. *Journal of Electroanalytical Chemistry* **1996,** *411*, 167-171.
8. D'Souza, F.; Hsieh, Y.-Y.; Deviprasad, G., Electrocatalytic reduction of molecular oxygen using non-planar cobalt tetrakis-(4-sulfonatophenyl)-β-octabromoporphyrin. *Journal of Electroanalytical Chemistry* **1997,** *426*, 17-21.
9. Trojanek, A.; Langmaier, J.; Kvapilová, H.; Záliš, S.; Samec, Z. k., Inhibitory effect of water on the oxygen reduction catalyzed by cobalt (II) tetraphenylporphyrin. *The Journal of Physical Chemistry A* **2014,** *118*, 2018-2028.
10. Wang, Y.-H.; Schneider, P. E.; Goldsmith, Z. K.; Mondal, B.; Hammes-Schiffer, S.; Stahl, S. S., Brønsted Acid Scaling Relationships Enable Control Over Product Selectivity from O_2 Reduction with a Mononuclear Cobalt Porphyrin Catalyst. *ACS Central Science* **2019,** *5*, 1024-1034.
11. Fukuzumi, S.; Mochizuki, S.; Tanaka, T., Efficient reduction of dioxygen with ferrocene derivatives, catalyzed by metalloporphyrins in the presence of perchloric acid. *Inorganic Chemistry* **1989,** *28*, 2459-2465.
12. Fukuzumi, S.; Mochizuki, S.; Tanaka, T., Metalloporphyrin-catalyzed reduction of dioxygen by ferrocene derivatives. *Chemistry Letters* **1989,** *18*, 27-30.
13. Fukuzumi, S.; Okamoto, K.; Gros, C. P.; Guilard, R., Mechanism of four-electron reduction of dioxygen to water by ferrocene derivatives in the presence of perchloric acid in benzonitrile, catalyzed by cofacial dicobalt porphyrins. *Journal of the American Chemical Society* **2004,** *126*, 10441-10449.
14. Oldacre, A. N.; Friedman, A. E.; Cook, T. R., A self-assembled cofacial cobalt porphyrin prism for oxygen reduction catalysis. *Journal of the American Chemical Society* **2017,** *139*, 1424-1427.
15. Kadish, K. M.; Shen, J.; Frémond, L.; Chen, P.; El Ojaimi, M.; Chkounda, M.; Gros, C. P.; Barbe, J.-M.; Ohkubo, K.; Fukuzumi, S., Clarification of the oxidation state of cobalt corroles in heterogeneous and homogeneous catalytic reduction of dioxygen. *Inorganic Chemistry* **2008,** *47*, 6726-6737.
16. Meng, J.; Lei, H.; Li, X.; Zhang, W.; Cao, R., The Trans Axial Ligand Effect on Oxygen Reduction. Immobilization Method May Weaken Catalyst Design for

Electrocatalytic Performance. *The Journal of Physical Chemistry C* **2020,** *124*, 16324-16331.

17. Honda, T.; Kojima, T.; Fukuzumi, S., Proton-coupled electron-transfer reduction of dioxygen catalyzed by a saddle-distorted cobalt phthalocyanine. *Journal of the American Chemical Society* **2012,** *134*, 4196-4206.
18. Kobayashi, N.; Nevin, W. A., Electrocatalytic Reduction of Oxygen Using Water-Soluble Iron and Cobalt Phthalocyanines and Porphyrins. *Applied Organometallic Chemistry* **1996,** *10*, 579-590.
19. Kobayashi, N.; Nishiyama, Y., Catalytic electroreduction of molecular oxygen using iron or cobalt 4, 4', 4", 4'"-tetracarboxyphthalocyanine. *The Journal of Physical Chemistry* **1985,** *89*, 1167-1170.
20. Mho, S. I.; Ortiz, B.; Doddapaneni, N.; Park, S. M., Electrochemical and Spectroelectrochemical Studies on Metallophthalocyanine-Oxygen Interactions in Nonaqueous Solutions. *Journal of the Electrochemical Society* **1995,** *142*, 1047.
21. Patir, I. H., Fluorinated-cobalt phthalocyanine catalyzed oxygen reduction at liquid/liquid interfaces. *Electrochimica Acta* **2013,** *87*, 788-793.
22. Mase, K.; Ohkubo, K.; Fukuzumi, S., Efficient Two-Electron Reduction of Dioxygen to Hydrogen Peroxide with One-Electron Reductants with a Small Overpotential Catalyzed by a Cobalt Chlorin Complex. *Journal of the American Chemical Society* **2013,** *135*, 2800-2808.
23. Mase, K.; Ohkubo, K.; Fukuzumi, S., Much enhanced catalytic reactivity of cobalt chlorin derivatives on two-electron reduction of dioxygen to produce hydrogen peroxide. *Inorganic Chemistry* **2015,** *54*, 1808-1815.
24. Geiger, T.; Anson, F. C., Homogeneous catalysis of the electrochemical reduction of dioxygen by a macrocyclic cobalt (III) complex. *Journal of the American Chemical Society* **1981,** *103*, 7489-7496.
25. Kang, C.; Anson, F. C., Effects of Coordination to a Macrocyclic Cobalt Complex on the Electrochemistry of Dioxygen, Superoxide, and Hydroperoxide. *Inorganic Chemistry* **1995,** *34*, 2771-2780.
26. Wong, C.-L.; Switzer, J. A.; Balakrishnan, K.; Endicott, J. F., Oxidation-reduction reactions of complexes with macrocyclic ligands. Oxygen uptake kinetics, equilibriums and intermediates in aqueous CoII(N_4) systems. *Journal of the American Chemical Society* **1980,** *102*, 5511-5518.
27. Wong, C.-L.; Endicott, J. F., Oxidation-reduction reactions of complexes with macrocyclic ligands. Role of intermediates in reactions of μ-peroxo-dicobalt complexes. *Inorganic Chemistry* **1981,** *20*, 2233-2239.
28. Kumar, K.; Endicott, J. F., Oxidation-reduction reactions of complexes with macrocyclic ligands. Electron-transfer reactivity of a 1: 1 cobalt (II)-dioxygen adduct. *Inorganic Chemistry* **1984,** *23*, 2447-2452.
29. Tsumaki, T., Nebenvalenzringverbindungen. IV. Über einige innerkomplexe Kobaltsalze der Oxyaldimine. *Bulletin of the Chemical Society of Japan* **1938,** *13*, 252-260.
30. Hughes, E. W.; Wilmarth, W. K.; Calvin, M., The Oxygen-carrying Synthetic Chelate Compounds. V. Equilibrium with the Solid Compounds1a. *Journal of the American Chemical Society* **1946,** *68*, 2273-2278.

31. Wang, Y.-H.; Pegis, M. L.; Mayer, J. M.; Stahl, S. S., Molecular Cobalt Catalysts for O_2 Reduction: Low-Overpotential Production of H2O2 and Comparison with Iron-Based Catalysts. *Journal of the American Chemical Society* **2017,** *139*, 16458-16461.
32. Anson, C. W.; Stahl, S. S., Cooperative Electrocatalytic O_2 Reduction Involving Co(salophen) with p-Hydroquinone as an Electron–Proton Transfer Mediator. *Journal of the American Chemical Society* **2017,** *139*, 18472-18475.
33. Carter, M. J.; Rillema, D. P.; Basolo, F., Oxygen carrier and redox properties of some neutral cobalt chelates. Axial and in-plane ligand effects. *Journal of the American Chemical Society* **1974,** *96*, 392-400.
34. Wang, Y.-H.; Goldsmith, Z. K.; Schneider, P. E.; Anson, C. W.; Gerken, J. B.; Ghosh, S.; Hammes-Schiffer, S.; Stahl, S. S., Kinetic and Mechanistic Characterization of Low-Overpotential, H_2O_2-Selective Reduction of O_2 Catalyzed by N_2O_2-Ligated Cobalt Complexes. *Journal of the American Chemical Society* **2018,** *140*, 10890-10899.
35. Hooe, S. L.; Machan, C. W., Dioxygen Reduction to Hydrogen Peroxide by a Molecular Mn Complex: Mechanistic Divergence between Homogeneous and Heterogeneous Reductants. *Journal of the American Chemical Society* **2019,** *141*, 4379-4387.
36. Hooe, S. L.; Rheingold, A. L.; Machan, C. W., Electrocatalytic Reduction of Dioxygen to Hydrogen Peroxide by a Molecular Manganese Complex with a Bipyridine-Containing Schiff Base Ligand. *Journal of the American Chemical Society* **2018,** *140*, 3232-3241.
37. Arora, H.; Philouze, C.; Jarjayes, O.; Thomas, F., CoII, NiII, CuII and ZnII complexes of a bipyridine bis-phenol conjugate: Generation and properties of coordinated radical species. *Dalton Transactions* **2010,** *39*, 10088-10098.
38. Battino, R.; Rettich, T. R.; Tominaga, T., The solubility of oxygen and ozone in liquids. *Journal of Physical and Chemical Reference Data* **1983,** *12*, 163-178.
39. Sato, T.; Hamada, Y.; Sumikawa, M.; Araki, S.; Yamamoto, H., Solubility of oxygen in organic solvents and calculation of the Hansen solubility parameters of oxygen. *Industrial & Engineering Chemistry Research* **2014,** *53*, 19331-19337.
40. Su, B.; Hatay, I.; Ge, P. Y.; Mendez, M.; Corminboeuf, C.; Samec, Z.; Ersoz, M.; Girault, H. H., Oxygen and proton reduction by decamethylferrocene in non-aqueous acidic media. *Chemical Communications* **2010,** *46*, 2918-2919.
41. Wang, Y.-H.; Mondal, B.; Stahl, S. S., Molecular Cobalt Catalysts for O2 Reduction to H2O2: Benchmarking Catalyst Performance via Rate–Overpotential Correlations. *ACS Catalysis* **2020**, 12031-12039.
42. Pegis, M. L.; Roberts, J. A. S.; Wasylenko, D. J.; Mader, E. A.; Appel, A. M.; Mayer, J. M., Standard Reduction Potentials for Oxygen and Carbon Dioxide Couples in Acetonitrile and N , N-Dimethylformamide. *Inorganic Chemistry* **2015,** *54*, 11883-11888.
43. Bratsch, S. G., Standard electrode potentials and temperature coefficients in water at 298.15 K. *Journal of Physical and Chemical Reference Data* **1989,** *18*, 1-21.
44. Nguyen, A. I.; Hadt, R. G.; Solomon, E. I.; Tilley, T. D., Efficient C–H bond activations via O_2 cleavage by a dianionic cobalt(ii) complex. *Chemical Science* **2014,** *5*, 2874-2878.

45. Brezny, A. C.; Johnson, S. I.; Raugei, S.; Mayer, J. M., Selectivity-Determining Steps in O2 Reduction Catalyzed by Iron(tetramesitylporphyrin). *Journal of the American Chemical Society* **2020,** *142*, 4108-4113.

Chapter 4 SI References

1. Nichols, A. W.; Chatterjee, S.; Sabat, M.; Machan, C. W., Electrocatalytic Reduction of CO_2 to Formate by an Iron Schiff Base Complex. *Inorganic Chemistry* **2018,** *57*, 2111-2121.
2. Hooe, S. L.; Dressel, J. M.; Dickie, D. A.; Machan, C. W., Highly Efficient Electrocatalytic Reduction of CO2 to CO by a Molecular Chromium Complex. *ACS Catalysis* **2020,** *10*, 1146-1151.
3. Arora, H.; Philouze, C.; Jarjayes, O.; Thomas, F., CoII, NiII, CuII and ZnII complexes of a bipyridine bis-phenol conjugate: Generation and properties of coordinated radical species. *Dalton Transactions* **2010,** *39*, 10088-10098.
4. Parry, E. P.; Osteryoung, R. A., Evaluation of Analytical Pulse Polarography. *Analytical Chemistry* **1965,** *37*,1634-1637.
5. Mase, K.; Ohkubo, K.; Fukuzumi, S., Efficient Two-Electron Reduction of Dioxygen to Hydrogen Peroxide with One-Electron Reductants with a Small Overpotential Catalyzed by a Cobalt Chlorin Complex. *Journal of the American Chemical Society* **2013,** *135,* 2800-2808.
6. Wang, Y.-H.; Pegis, M. L.; Mayer, J. M.; Stahl, S. S., Molecular Cobalt Catalysts for O_2 Reduction: Low-Overpotential Production of H_2O_2 and Comparison with Iron-Based Catalysts. *Journal of the American Chemical Society* **2017,** *139*, 16458-16461.

Chapter 5 References

1. Pegis, M. L.; Wise, C. F.; Martin, D. J.; Mayer, J. M., Oxygen Reduction by Homogeneous Molecular Catalysts and Electrocatalysts. *Chemical Reviews* **2018,** *118*, 2340-2391.
2. Machan, C. W., Advances in the Molecular Catalysis of Dioxygen Reduction. *ACS Catalysis* **2020,** *10*, 2640-2655.
3. Steele, B. C. H.; Heinzel, A., Materials for fuel-cell technologies. In *Materials for Sustainable Energy: A Collection of Peer-Reviewed Research and Review Articles from Nature Publishing Group*, Dusastre, V., Ed. World Scientific: 2011; 224-231.
4. Borup, R.; Meyers, J.; Pivovar, B.; Kim, Y. S.; Mukundan, R.; Garland, N.; Myers, D.; Wilson, M.; Garzon, F.; Wood, D., Scientific aspects of polymer electrolyte fuel cell durability and degradation. *Chemical Reviews* **2007,** *107*, 3904-3951.
5. Collman, J. P.; Boulatov, R.; Sunderland, C. J.; Fu, L., Functional analogues of cytochrome c oxidase, myoglobin, and hemoglobin. *Chemical Reviews* **2004,** *104*, 561-588.
6. He, Q.; Mugadza, T.; Hwang, G.; Nyokong, T., Mechanisms of Electrocatalysis of Oxygen Reduction by Metal Porphyrins in Trifluoromethane Sulfonic Acid Solution *International Journal of Electrochemical Science* **2012,** *7*, 7045 - 7064.
7. Chan, R. J.; Su, Y. O.; Kuwana, T., Electrocatalysis of oxygen reduction. 5. oxygen to hydrogen peroxide conversion by cobalt (II) tetrakis (N-methyl-4-pyridyl) porphyrin. *Inorganic Chemistry* **1985,** *24*, 3777-3784.

8. Sazou, D.; Araullo-McAdams, C.; Han, B.; Franzen, M.; Kadish, K. M., The use of an electrogenerated cobalt (I) porphyrin for the homogeneous catalytic reduction of dioxygen in dimethylformamide. Reactions of $[(TMpyP)CoII]^{4+}$ and $[(TMpyP)CoI]^{3+}$ where TMpyP= meso-tetrakis (1-methylpyridinium-4-yl) porphyrin. *Journal of the American Chemical Society* **1990,** *112*, 7879-7886.
9. D'Souza, F.; Deviprasad, R.; Hsieh, Y.-Y., Synthesis and studies on the electrocatalytic reduction of molecular oxygen by non-planar cobalt (II) tetrakis-(N-methyl pyridyl)-β-octabromoporphyrin. *Journal of Electroanalytical Chemistry* **1996,** *411*, 167-171.
10. D'Souza, F.; Hsieh, Y.-Y.; Deviprasad, G., Electrocatalytic reduction of molecular oxygen using non-planar cobalt tetrakis-(4-sulfonatophenyl)-β-octabromoporphyrin. *Journal of Electroanalytical Chemistry* **1997,** *426*, 17-21.
11. Trojanek, A.; Langmaier, J.; Kvapilová, H.; Záliš, S.; Samec, Z. k., Inhibitory effect of water on the oxygen reduction catalyzed by cobalt (II) tetraphenylporphyrin. *The Journal of Physical Chemistry A* **2014,** *118*, 2018-2028.
12. Wang, Y.-H.; Schneider, P. E.; Goldsmith, Z. K.; Mondal, B.; Hammes-Schiffer, S.; Stahl, S. S., Brønsted Acid Scaling Relationships Enable Control Over Product Selectivity from O_2 Reduction with a Mononuclear Cobalt Porphyrin Catalyst. *Acs Central Science* **2019,** *5*, 1024-1034.
13. Fukuzumi, S.; Mochizuki, S.; Tanaka, T., Efficient reduction of dioxygen with ferrocene derivatives, catalyzed by metalloporphyrins in the presence of perchloric acid. *Inorganic Chemistry* **1989,** *28*, 2459-2465.
14. Fukuzumi, S.; Mochizuki, S.; Tanaka, T., Metalloporphyrin-catalyzed reduction of dioxygen by ferrocene derivatives. *Chemistry Letters* **1989,** *18*, 27-30.
15. Fukuzumi, S.; Okamoto, K.; Gros, C. P.; Guilard, R., Mechanism of four-electron reduction of dioxygen to water by ferrocene derivatives in the presence of perchloric acid in benzonitrile, catalyzed by cofacial dicobalt porphyrins. *Journal of the American Chemical Society* **2004,** *126*, 10441-10449.
16. Oldacre, A. N.; Friedman, A. E.; Cook, T. R., A self-assembled cofacial cobalt porphyrin prism for oxygen reduction catalysis. *Journal of the American Chemical Society* **2017,** *139*, 1424-1427.
17. Kadish, K. M.; Shen, J.; Frémond, L.; Chen, P.; El Ojaimi, M.; Chkounda, M.; Gros, C. P.; Barbe, J.-M.; Ohkubo, K.; Fukuzumi, S., Clarification of the oxidation state of cobalt corroles in heterogeneous and homogeneous catalytic reduction of dioxygen. *Inorganic Chemistry* **2008,** *47*, 6726-6737.
18. Meng, J.; Lei, H.; Li, X.; Zhang, W.; Cao, R., The Trans Axial Ligand Effect on Oxygen Reduction. Immobilization Method May Weaken Catalyst Design for Electrocatalytic Performance. *The Journal of Physical Chemistry C* **2020,** *124*, 16324-16331.
19. Honda, T.; Kojima, T.; Fukuzumi, S., Proton-Coupled Electron-Transfer Reduction of Dioxygen Catalyzed by a Saddle-Distorted Cobalt Phthalocyanine. *Journal of the American Chemical Society* **2012,** *134*, 4196-4206.
20. Kobayashi, N.; Nevin, W. A., Electrocatalytic Reduction of Oxygen Using Water-Soluble Iron and Cobalt Phthalocyanines and Porphyrins. *Applied Organometallic Chemistry* **1996,** *10*, 579-590.

21. Kobayashi, N.; Nishiyama, Y., Catalytic electroreduction of molecular oxygen using iron or cobalt 4, 4', 4'', 4'''-tetracarboxyphthalocyanine. *Journal of Physical Chemistry* **1985,** *89*, 1167-1170.
22. Mho, S. i.; Ortiz, B.; Doddapaneni, N.; Park, S. M., Electrochemical and Spectroelectrochemical Studies on Metallophthalocyanine-Oxygen Interactions in Nonaqueous Solutions. *Journal of Electroanalytical Chemistry* **1995,** *142*, 1047.
23. Patir, I. H., Fluorinated-cobalt phthalocyanine catalyzed oxygen reduction at liquid/liquid interfaces. *Electrochimica Acta* **2013,** *87*, 788-793.
24. Mase, K.; Ohkubo, K.; Fukuzumi, S., Efficient Two-Electron Reduction of Dioxygen to Hydrogen Peroxide with One-Electron Reductants with a Small Overpotential Catalyzed by a Cobalt Chlorin Complex. *Journal of the American Chemical Society* **2013,** *135*, 2800-2808.
25. Mase, K.; Ohkubo, K.; Fukuzumi, S., Much Enhanced Catalytic Reactivity of Cobalt Chlorin Derivatives on Two-Electron Reduction of Dioxygen to Produce Hydrogen Peroxide. *Inorganic Chemistry* **2015,** *54*, 1808-1815.
26. Geiger, T.; Anson, F. C., Homogeneous catalysis of the electrochemical reduction of dioxygen by a macrocyclic cobalt (III) complex. *Journal of the American Chemical Society* **1981,** *103*, 7489-7496.
27. Kang, C.; Anson, F. C., Effects of Coordination to a Macrocyclic Cobalt Complex on the Electrochemistry of Dioxygen, Superoxide, and Hydroperoxide. *Inorganic Chemistry* **1995,** *34*, 2771-2780.
28. Wong, C.-L.; Switzer, J. A.; Balakrishnan, K.; Endicott, J. F., Oxidation-reduction reactions of complexes with macrocyclic ligands. Oxygen uptake kinetics, equilibriums and intermediates in aqueous CoII (N_4) systems. *Journal of the American Chemical Society* **1980,** *102*, 5511-5518.
29. Wong, C.-L.; Endicott, J. F., Oxidation-reduction reactions of complexes with macrocyclic ligands. Role of intermediates in reactions of. mu.-peroxo-dicobalt complexes. *Inorganic Chemistry* **1981,** *20*, 2233-2239.
30. Kumar, K.; Endicott, J. F., Oxidation-reduction reactions of complexes with macrocyclic ligands. Electron-transfer reactivity of a 1: 1 cobalt (II)-dioxygen adduct. *Inorganic Chemistry* **1984,** *23*, 2447-2452.
31. Wang, Y.-H.; Mondal, B.; Stahl, S. S., Molecular Cobalt Catalysts for O_2 Reduction to H_2O_2: Benchmarking Catalyst Performance via Rate–Overpotential Correlations. *ACS Catalysis* **2020,** *10*, 12031-12039.
32. Wang, Y.-H.; Goldsmith, Z. K.; Schneider, P. E.; Anson, C. W.; Gerken, J. B.; Ghosh, S.; Hammes-Schiffer, S.; Stahl, S. S., Kinetic and Mechanistic Characterization of Low-Overpotential, H_2O_2-Selective Reduction of O_2 Catalyzed by N_2O_2-Ligated Cobalt Complexes. *Journal of the American Chemical Society* **2018,** *140*, 10890-10899.
33. Wang, Y.-H.; Pegis, M. L.; Mayer, J. M.; Stahl, S. S., Molecular Cobalt Catalysts for O_2 Reduction: Low-Overpotential Production of H_2O_2 and Comparison with Iron-Based Catalysts. *Journal of the American Chemical Society* **2017,** *139*, 16458-16461.
34. Nichols, A. W.; Kuehner, J. S.; Huffman, B. L.; Miedaner, P. R.; Dickie, D. A.; Machan, C. W., Reduction of dioxygen to water by a Co(N_2O_2) complex with a 2,2′-bipyridine backbone. *Chemical Communications* **2021,** *57*, 516-519.

35. Yoshikawa, S.; Shimada, A., Reaction mechanism of cytochrome c oxidase. *Chemical Reviews* **2015,** *115*, 1936-1989.
36. Rosenthal, J.; Nocera, D. G., Role of proton-coupled electron transfer in O–O bond activation. *Accounts of Chemical Research* **2007,** *40*, 543-553.
37. Baran, J. D.; Grönbeck, H.; Hellman, A., Analysis of Porphyrines as Catalysts for Electrochemical Reduction of O2 and Oxidation of H_2O. *Journal of the American Chemical Society* **2014,** *136*, 1320-1326.
38. Ohta, T.; Nagaraju, P.; Liu, J.-G.; Ogura, T.; Naruta, Y., The secondary coordination sphere and axial ligand effects on oxygen reduction reaction by iron porphyrins: a DFT computational study. *Journal of Biological Inorganic Chemistry* **2016,** *21*, 745-755.
39. Chng, L. L.; Chang, C. J.; Nocera, D. G., Catalytic O−O Activation Chemistry Mediated by Iron Hangman Porphyrins with a Wide Range of Proton-Donating Abilities. *Organic Letters* **2003,** *5*, 2421-2424.
40. Nichols, A. W.; Hooe, S. L.; Kuehner, J. S.; Dickie, D. A.; Machan, C. W., Electrocatalytic CO2 Reduction to Formate with Molecular Fe(III) Complexes Containing Pendent Proton Relays. *Inorganic Chemistry* **2020,** *59*, 5854-5864.
41. Izutsu, K., *Acid-base dissociation constants in dipolar aprotic solvents*. Blackwell Scientific Publications: Oxford; Boston : Brookline Village, Mass, 1990; Vol. 35.
42. Anson, C. W.; Stahl, S. S., Cooperative Electrocatalytic O_2 Reduction Involving Co(salophen) with p-Hydroquinone as an Electron–Proton Transfer Mediator. *Journal of the American Chemical Society* **2017,** *139*, 18472-18475.
43. Hooe, S. L.; Machan, C. W., Dioxygen Reduction to Hydrogen Peroxide by a Molecular Mn Complex: Mechanistic Divergence between Homogeneous and Heterogeneous Reductants. *Journal of the American Chemical Society* **2019,** *141*, 4379-4387.
44. Savéant, J.-M., Proton Relays in Molecular Catalysis of Electrochemical Reactions: Origin and Limitations of the Boosting Effect. *Angewandte Chemie, International Edition* **2019,** *58*, 2125-2128.
45. Wasylenko, D. J.; Rodríguez, C.; Pegis, M. L.; Mayer, J. M., Direct Comparison of Electrochemical and Spectrochemical Kinetics for Catalytic Oxygen Reduction. *Journal of the American Chemical Society* **2014,** *136*, 12544-12547.
46. Hammes-Schiffer, S.; Iordanova, N., Theoretical studies of proton-coupled electron transfer reactions. *Biochimica et Biophysica Acta - Bioenergetics* **2004,** *1655*, 29-36.
47. Iordanova, N.; Decornez, H.; Hammes-Schiffer, S., Theoretical study of electron, proton, and proton-coupled electron transfer in iron bi-imidazoline complexes. *Journal of the American Chemical Society* **2001,** *123*, 3723-3733.
48. Martin, D. J.; Wise, C. F.; Pegis, M. L.; Mayer, J. M., Developing Scaling Relationships for Molecular Electrocatalysis through Studies of Fe-Porphyrin-Catalyzed O_2 Reduction. *Accounts of Chemical Research* **2020,** *53*, 1056-1065.

Chapter 5 SI References

1. Nichols, A. W.; Chatterjee, S.; Sabat, M.; Machan, C. W., Electrocatalytic Reduction of CO_2 to Formate by an Iron Schiff Base Complex. *Inorganic Chemistry* **2018,** *57*, 2111-2121.

2. Hooe, S. L.; Dressel, J. M.; Dickie, D. A.; Machan, C. W., Highly Efficient Electrocatalytic Reduction of CO_2 to CO by a Molecular Chromium Complex. *ACS Catalysis* **2020,** *10*, 1146-1151.
3. Nichols, A. W.; Kuehner, J. S.; Huffman, B. L.; Miedaner, P. R.; Dickie, D. A.; Machan, C. W., Reduction of dioxygen to water by a $Co(N_2O_2)$ complex with a 2,2′-bipyridine backbone. *Chem. Commun.* **2021,** *57*, 516-519.
4. Parry, E. P.; Osteryoung, R. A., Evaluation of Analytical Pulse Polarography. *Analytical Chemistry* **1965,** *37*, 1634-1637.
5. Anson, C. W.; Stahl, S. S., Cooperative Electrocatalytic O_2 Reduction Involving Co(salophen) with p-Hydroquinone as an Electron–Proton Transfer Mediator. *Journal of the American Chemical Society* **2017,** *139*, 18472-18475.
6. Hooe, S. L.; Machan, C. W., Dioxygen Reduction to Hydrogen Peroxide by a Molecular Mn Complex: Mechanistic Divergence between Homogeneous and Heterogeneous Reductants. *Journal of the American Chemical Society* **2019,** *141*, 4379-4387.
7. Hooe, S. L.; Machan, C. W., Dioxygen Reduction to Hydrogen Peroxide by a Molecular Mn Complex: Mechanistic Divergence between Homogeneous and Heterogeneous Reductants. *Journal of the American Chemical Society* **2019,** *141*, 4379-4387.
8. Achord, J. M.; Hussey, C. L., Determination of dissolved oxygen in nonaqueous electrochemical solvents. *Analytical Chemistry* **1980,** *52*, 601-602.
9. Wang, Y.-H.; Pegis, M. L.; Mayer, J. M.; Stahl, S. S., Molecular Cobalt Catalysts for O_2 Reduction: Low-Overpotential Production of H2O2 and Comparison with Iron-Based Catalysts. *Journal of the American Chemical Society Soc.* **2017,** *139*, 16458-16461.
10. Mase, K.; Ohkubo, K.; Fukuzumi, S., Efficient Two-Electron Reduction of Dioxygen to Hydrogen Peroxide with One-Electron Reductants with a Small Overpotential Catalyzed by a Cobalt Chlorin Complex. *Journal of the American Chemical Society* **2013,** *135*, 2800-2808.
11. Pegis, M. L.; Roberts, J. A. S.; Wasylenko, D. J.; Mader, E. A.; Appel, A. M.; Mayer, J. M., Standard Reduction Potentials for Oxygen and Carbon Dioxide Couples in Acetonitrile and N ,N-Dimethylformamide. *Inorganic Chemistry* **2015,** *54*, 11883-11888.

Chapter 6 References

1. Nichols, A. W.; Chatterjee, S.; Sabat, M.; Machan, C. W., Electrocatalytic Reduction of CO_2 to Formate by an Iron Schiff Base Complex. *Inorganic Chemistry* **2018,** *57*, 2111-2121.
2. Nichols, A. W.; Hooe, S. L.; Kuehner, J. S.; Dickie, D. A.; Machan, C. W., Electrocatalytic CO_2 Reduction to Formate with Molecular Fe(III) Complexes Containing Pendent Proton Relays. *Inorganic Chemistry* **2020,** *59*, 5854-5864.
3. Nichols, A. W.; Kuehner, J. S.; Huffman, B. L.; Miedaner, P. R.; Dickie, D. A.; Machan, C. W., Reduction of dioxygen to water by a $Co(N_2O_2)$ complex with a 2,2′-bipyridine backbone. *Chemical Communications* **2021,** *57*, 516-519.
4. Wang, Y.-H.; Pegis, M. L.; Mayer, J. M.; Stahl, S. S., Molecular Cobalt Catalysts for O_2 Reduction: Low-Overpotential Production of H_2O_2 and Comparison with

Iron-Based Catalysts. *Journal of the American Chemical Society* **2017,** *139*, 16458-16461.

5. Arora, H.; Philouze, C.; Jarjayes, O.; Thomas, F., CoII, NiII, CuII and ZnII complexes of a bipyridine bis-phenol conjugate: Generation and properties of coordinated radical species. *Dalton Transactions* **2010,** *39*, 10088-10098.
6. Mouchfiq, A.; Todorova, T. K.; Dey, S.; Fontecave, M.; Mougel, V., A bioinspired molybdenum–copper molecular catalyst for CO_2 electroreduction. *Chemical Science* **2020,** *11*, 5503-5510.
7. Nichols, A. W.; Machan, C. W., Secondary-Sphere Effects in Molecular Electrocatalytic CO_2 Reduction. *Frontiers in Chemistry* **2019,** *7*, https://doi.org/10.3389/fchem.2019.00397.
8. Kang, K.; Fuller, J.; Reath, A. H.; Ziller, J. W.; Alexandrova, A. N.; Yang, J. Y., Installation of internal electric fields by non-redox active cations in transition metal complexes. *Chemical Science* **2019,** *10*, 10135-10142.
9. Reath, A. H.; Ziller, J. W.; Tsay, C.; Ryan, A. J.; Yang, J. Y., Redox Potential and Electronic Structure Effects of Proximal Nonredox Active Cations in Cobalt Schiff Base Complexes. *Inorganic Chemistry* **2017,** *56*, 3713-3718.
10. Shao, H.; Muduli, S. K.; Tran, P. D.; Soo, H. S., Enhancing electrocatalytic hydrogen evolution by nickel salicylaldimine complexes with alkali metal cations in aqueous media. *Chemical Communications* **2016,** *52*, 2948-2951.
11. Handa, S.; Gnanadesikan, V.; Matsunaga, S.; Shibasaki, M., Heterobimetallic Transition Metal/Rare Earth Metal Bifunctional Catalysis: A Cu/Sm/Schiff Base Complex for Syn-Selective Catalytic Asymmetric Nitro-Mannich Reaction. *Journal of the American Chemical Society* **2010,** *132*, 4925–4934.
12. Handa, S.; Nagawa, K.; Sohtome, Y.; Matsunaga, S.; Shibasaki, M., A Heterobimetallic Pd/La/Schiff Base Complex for anti-Selective Catalytic Asymmetric Nitroaldol Reactions and Applications to Short Syntheses of β-Adrenoceptor Agonists. *Angewandte Chemie International Edition* **2008,** *47*, 3230–3233.
13. Handa, S.; Gnanadesikan, V.; Matsunaga, S.; Shibasaki, M., syn-Selective Catalytic Asymmetric Nitro-Mannich Reactions Using a Heterobimetallic Cu−Sm−Schiff Base Complex. *Journal of the American Chemical Society* **2007,** *129*, 4900-4901.
14. Shibasaki, M.; Sasai, H.; Arai, T., Asymmetric Catalysis with Heterobimetallic Compounds. *Angewandte Chemie International Edition* **1997,** *36*, 1236–1256.
15. Mihara, H.; Xu, Y.; Shepherd, N. E.; Matsunaga, S.; Shibasaki, M., A Heterobimetallic Ga/Yb-Schiff Base Complex for Catalytic Asymmetric α-Addition of Isocyanides to Aldehydes. *Journal of the American Chemical Society* **2009,** *131*, 8384-8385.
16. Chantarojsiri, T.; Reath, A. H.; Yang, J. Y., Cationic Charges Leading to an Inverse Free-Energy Relationship for N−N Bond Formation by MnVI Nitrides. *Angewandte Chemie International Edition* **2018,** *57*, 14037-14042.
17. Gambarotta, S.; Arena, F.; Floriani, C.; Zanazzi, P. F., Carbon dioxide fixation: bifunctional complexes containing acidic and basic sites working as reversible carriers. *Journal of the American Chemical Society* **1982,** *104*, 5082-5092.

18. Bhugun, I.; Lexa, D.; Savéant, J. M., Catalysis of the Electrochemical Reduction of Carbon Dioxide by Iron(0) Porphyrins. Synergistic Effect of Lewis Acid Cations. *The Journal of Physical Chemistry* **1996,** *100*, 19981-19985.
19. Sampson, M. D.; Kubiak, C. P., Manganese Electrocatalysts with Bulky Bipyridine Ligands: Utilizing Lewis Acids To Promote Carbon Dioxide Reduction at Low Overpotentials. *Journal of the American Chemical Society* **2016,** *138*, 1386-1393.
20. Hammouche, M.; Lexa, D.; Momenteau, M.; Saveant, J. M., Chemical catalysis of electrochemical reactions. Homogeneous catalysis of the electrochemical reduction of carbon dioxide by iron("0") porphyrins. Role of the addition of magnesium cations. *Journal of the American Chemical Society* **1991,** *113*, 8455–8466.
21. Zhanaidarova, A.; Steger, H.; Reineke, M. H.; Kubiak, C. P., Chelated $[Zn(cyclam)]^{2+}$ Lewis acid improves the reactivity of the electrochemical reduction of CO_2 by Mn catalysts with bulky bipyridine ligands. *Dalton Transactions* **2017,** *46*, 12413-12416.
22. Kaim, W.; Fiedler, J., Spectroelectrochemistry: the best of two worlds. *Chemical Society Reviews.* **2009,** *38*, 3373-3382.
23. Machan, C. W.; Sampson, M. D.; Chabolla, S. A.; Dang, T.; Kubiak, C. P., Developing a mechanistic understanding of molecular electrocatalysts for CO_2 reduction using infrared spectroelectrochemistry. *Organometallics* **2014,** *33*, 4550-4559.
24. Kroneck, P. M.; Torres, M. E. S., *The metal-driven biogeochemistry of gaseous compounds in the environment*. Springer: 2014.
25. Hooe, S. L.; Rheingold, A. L.; Machan, C. W., Electrocatalytic Reduction of Dioxygen to Hydrogen Peroxide by a Molecular Manganese Complex with a Bipyridine-Containing Schiff Base Ligand. *Journal of the American Chemical Society* **2018,** *140*, 3232-3241.
26. Hooe, S. L.; Dressel, J. M.; Dickie, D. A.; Machan, C. W., Highly Efficient Electrocatalytic Reduction of CO_2 to CO by a Molecular Chromium Complex. *ACS Catalysis* **2020,** *10*, 1146-1151.
27. Hooe, S. L.; Machan, C. W., Dioxygen Reduction to Hydrogen Peroxide by a Molecular Mn Complex: Mechanistic Divergence between Homogeneous and Heterogeneous Reductants. *Journal of the American Chemical Society* **2019,** *141*, 4379-4387.
28. Moreno, J. J.; Hooe, S. L.; Machan, C. W., DFT Study on the Electrocatalytic Reduction of CO_2 to CO by a Molecular Chromium Complex. *Inorganic Chemistry* **2021,** *60*, 3635-3650.

Asa W. Nichols

Curriculum Vitae

Phone: 304-483-1891
asawnichols@gmail.com
awn5fd@virginia.edu
Department of Chemistry, 409 McCormick Rd.
Charlottesville, VA 22904

CURRENT AND PAST POSITIONS

Current Positions

02/2018-present	**Ph.D. Candidate,** Machan Research Laboratory, Department Chemistry, University of Virginia. Charlottesville, VA.
08/2016-present	**Graduate Student**, Department Chemistry, University of Virginia. Charlottesville, VA.

Past Positions

0282016-05/2018	**Graduate Teaching Assistant**, Department Chemistry, University of Virginia. Charlottesville, VA.
06/2015-08/2015	**Science Undergraduate Research Intern**, SULI, under the supervision of Dr. Nathan R. Neale and Dr. Lance M. Wheeler.
05/2014-08/2014	**Research Intern.** NANOSafe NSF-REU, West Virginia University, Morgantown, WV 26506. Laboratory of Dr. Bjorn C.G. Soderberg.

EDUCATION

PhD, Inorganic Chemistry, 2016-Present
University of Virginia; Charlottesville, Virginia
Dissertation Topic: Storage of energy in chemical bonds utilizing Earth-abundant molecular electrocatalysts: Improving catalyst design through understanding mechanism.

BS, Chemistry, 2012-2016
Minors: Mathematics and Physics
West Virginia Wesleyan College; Buckhannon, West Virginia

PUBLICATIONS AND PATENTS

ORCiD: 0000-0002-8480-5118

Manuscripts (13)

Lucas A. Freeman, Akachukwu D. Obi, Haleigh R. Machost, Andrew Molino, **Asa W. Nichols**, Diane A. Dickie, David J. D. Wilson, Charles W. Machan, Robert J. Gilliard. Soluble, Crystalline, and Thermally Stable Alkali CO_2^- and Carbonite (CO_2^{2-}) Clusters Supported by Cyclic (Alkyl)(Amino)Carbenes. *Chem. Sci.,* 2021, *12*, 3544-3550.

Asa W. Nichols, Joseph S. Kuehner, Brittany L. Huffman, Peter R. Miedaner, Diane A. Dickie, Charles W. Machan. Reduction of dioxygen to water by a $Co(N_2O_2)$ complex with a 2,2′-bipyridine backbone. *Chem. Commun*., 2021, *57*, 516-519.

Prince K. Verma, Luke D. Huelsenbeck, **Asa W. Nichols**, Timur Islamoglu, Charles W. Machan, Guarav Giri. Controlling Polymorphism and Orientation of NU-901/NU-1000 Metal–Organic Frameworks Thin Films. *Chem. Mater.,* 2020, *32*, *24*, 10556-10565.

Yanay Popowski, Juan J. Moreno, **Asa W. Nichols**, Shelby L. Hooe, Caitin J. Bouchey, Nigam P. Rath, Charles W. Machan, and William B. Tolman. Mechanistic insight into initiation and regioselectivity in the copolymerization of epoxides and anhydrides by Al complexes. *Chem. Commun.,* 2020, *56*, 14027-14030.

Asa W. Nichols, Shelby Hooe, Joseph S. Kuehner, Diane A. Dickie, Charles W. Machan. Electrocatalytic CO_2 Reduction to Formate with Molecular Fe(III) Complexes Containing Pendent Proton Relays. *Inorg. Chem.*, 2020, *59*, 5854–5864**.**

Changcheng Jiang, **Asa W. Nichols**, John Walzer, Charles W. Machan. Electrochemical CO_2 Reduction in a Continuous Non-Aqueous Flow Configuration with $[Ni(cyclam)]^{2+}$ Catalyst. *Inorg. Chem.*, 2020, *59*, 1883-1892.

Asa W. Nichols and Charles W. Machan. Secondary-Sphere Effects in Molecular Electrocatalytic CO_2 Reduction. *Frontiers in Chemistry,* 2019, 7*.*

L.E. Lieske, S.L. Hooe, **A.W. Nichols**, C.W. Machan. Electrocatalytic Reduction of Oxygen by Mn(III) meso-Tetra(*N*-methyl-4-pyridyl) Porphyrin in Universal Buffer. *Dalton Trans.,* 2019, *48*, 8633-8641*.*

Changcheng Jiang, **Asa W. Nichols**, and Charles W. Machan. A look at periodic trends in d-block molecular electrocatalysts for CO_2 reduction. *Dalton Trans.,* 2019, *48*, 9454-9468.

F. Li, R.L. Meyer, S.H. Carpenter, L.E. VanGelder, **A.W. Nichols**, C W. Machan, M.L. Neidig, and E.M. Matson. Nitric oxide activation facilitated by cooperative multimetallic electron transfer within an iron-functionalized polyoxobanadate-alkoxide cluster. *Chem. Sci.* 2018, *9*, 6379-6389.

Asa W. Nichols, Sayanti Chatterjee, Michal Sabat, and Charles W. Machan. Electrocatalytic Reduction of CO_2 to Formate by an Iron Schiff Base Complex. *Inorg. Chem.*, 2018, *57*, 2111-2121.

Lance M. Wheeler**, Asa W. Nichols**, Nicholas C. Anderson, Boris D. Chernomordik, Matthew C. Beard, and Nathan R. Neale. Cationic Ligand Exchange on Germanium Nanocrystals. *Nano Lett.*, 2016, *16*, 1949-1954.

In preparation or review

Asa W. Nichols, Peter R. Miedaner, Emma N. Cook, Charles W. Machan. Reduction of Dioxygen by bpy-based N_2O_2 Complexes: Optimizing Efficiency for Water and H_2O_2. *In Peer Review.*

Patents (1)

Lance M. Wheeler, **Asa W. Nichols**, Boris D. Chernomordik, Nicholas C. Anderson, Matthew C. Beard, Nathan R. Neale. Group IV nanocrystals with ion-exchangeable surface ligands and methods of making the same. U.S. Patent 9,862,841.

PRESENTATIONS

2020

Asa W. Nichols *Electrocatalytic Reduction of CO_2 with Molecular Fe Complexes*. Oral Presentation. Department of Chemistry Synthetic Chemistry Colloquium Series. Charlottesville, Virginia. January 2020.

2019

Asa W. Nichols, Joseph S. Kuehner, Diane A. Dickie, and Charles W. Machan. *Electrocatalytic CO_2 Reduction with Fe(III) Schiff Base-Type Complexes Containing Pendent Proton Relays*. Poster presentation at 2019 Annual Chemistry Department Retreat. Crozet, Virginia. October 2019 **Selected as third place poster by attendees**.

Asa W. Nichols, Joseph S. Kuehner, Diane A. Dickie, and Charles W. Machan. *Electrocatalytic CO_2 Reduction with Fe(III) Schiff Base-Type Complexes Containing Pendent Proton Relays*. Poster presentation at ACS Fall 2019 National Meeting & Exposition, San Diego, California.

Asa W. Nichols and Charles W. Machan. *Non-traditional Secondary Sphere Interactions for CO_2 Reduction to Formate by Fe Complexes*. Oral presentation at ACS Fall 2019 National Meeting & Exposition, San Diego, California.

Asa W. Nichols, Diane A. Dickie, and Charles W. Machan. *Electrocatalytic CO_2 Reduction with Fe(III) Schiff Base-Type Complexes Containing Pendent Proton Relays*. Poster presentation at 2019 Poster Session for 3rd Year Ph.D. Students, University of Virginia, Charlottesville, Virginia. April 2019.

Asa W. Nichols. *Summer Research Opportunities and Graduate Program in Chemistry at the University of Virginia*. Oral presentation at Heritage University. Toppenish, Washington. April 2019.

Asa W. Nichols. *Gas Chromatography in an Ecology Setting*. Oral Presentation at Heritage University. Toppenish, Washington. April 2019.

2018

Asa W. Nichols, Diane A. Dickie, and Charles W. Machan. *Electrocatalytic CO_2 Reduction with Fe(III) Schiff Base-Type Complexes Containing Pendent Proton Sources*. Poster presentation at 2018 Annual Chemistry Department Retreat. Barboursville, Virginia. October 2018.

Asa W. Nichols, Michal Sabat, and Charles W. Machan. *Electrocatalytic Reduction of CO_2 to Formic Acid by an Fe(III) Schiff Base-Type Complex*. Poster presentation at 3rd International Conference on Proton-Coupled Electron Transfer. Blowing Rock, North Carolina. June 2018.

2015

Nicholas C. Anderson, Lance M. Wheeler, **Asa W. Nichols**, and Nathan R. Neale. *Connecting the Dots*. Oral presentation at Chemical Synthesis Symposium, Columbia University, New York City, New York. August 2015.

Lance M. Wheeler, Nicholas C. Anderson, **Asa W. Nichols**, and Nathan R. Neale. Inorganic Ligand Exchange on Germanium Nanocrystals. Oral presentation at 250th American Chemical Society National Meeting, Boston, Massachusetts. August 2015

Asa W. Nichols, Lance M. Wheeler, Nicholas C. Anderson, and Nathan R. Neale. *Nuclear magnetic resonance analysis of ligand exchanges on germanium nanocrystals*. Poster presentation at NREL Summer SULI Research Symposium, National Renewable Energy Laboratory, Golden, Colorado. August 2015.

Lance M. Wheeler, Boris Chernomordik, **Asa W. Nichols**, Nicholas C. Anderson, Matthew C. Beard, and Nathan R. Neale. *Ligand Exchange on Germanium Nanocrystals to Enable Photovoltaic Device Fabrication*. Oral presentation at Center for Advanced Solar Photophysics Teleconference, July 2015.

2014

Asa W. Nichols, Katharine C. Lambson, and Bjorn C. G. Soderberg. *Mechanistic investigation of reactions of aromatic nitro compounds with gold nanoparticle catalysts*. Poster presentation at Summer Undergraduate Research Symposium, West Virginia University, Morgantown, West Virginia. July 2014.

Conferences attended (4)

ACS Fall National Meeting & Exposition 2019
Conference on Proton-Coupled Electron Transfer 2018
University of Virginia Chemistry Department Retreat 2018, 2019

PROFESSIONAL AND ACADEMIC HONORS

2019	Department Retreat Poster Session: 3rd Place Poster
2018	Travel Award, 3rd International Conference on Proton Coupled Electron Transfer
2017	NSF-GRFP Honorable Mention
2016	Summa Cum Laude, West Virginia Wesleyan College
	Outstanding Chemist, Society of Analytical Chemists of Pittsburg
	Outstanding Senior Chemist, West Virginia Wesleyan College
	Pratt First Year Graduate Student Fellowship, University of Virginia
2015	Who's Who Among Students in American Universities and Colleges
	Nicholas Hyma Award, West Virginia Wesleyan College
	Outstanding Junior Chemist, West Virginia Wesleyan College
2014	Leadership Excellence and Applied Practice Bronze Level, West Virginia Wesleyan College
	Nicholas Hyma Award West Virginia Wesleyan College
2013	Outstanding Freshman Chemistry Student, West Virginia Wesleyan College
2012	Presidential Scholarship, West Virginia Wesleyan College (to 2016)
	WV 4-H All-Star
	Eagle Scout

TEACHING AND MENTORING

Heritage University; Toppenish, Washington

UVA Chemistry Department Representative
2018-2019
Shared my experience of graduate school at UVA and taught a course on mass spectrometry to ecology students with cultural backgrounds which are underrepresented in STEM fields.

University of Virginia, Charlottesville, Virginia
Graduate Teaching Assistant
August 2016-May 2017
General Chemistry Laboratory
January 2018
Structural Inorganic Chemistry

West Virginia Wesleyan College, Buckhannon, West Virginia
Walk-in Tutor Level I
8/2013-5/2016
100 Hours of In-person Tutoring

SERVICE, LEADERSHIP, AND OUTREACH

Service to Field
University of Virginia
Chemistry Department Representative; Graduate School of Arts and Sciences Council: 2019-2020
Steward; Synthetic Chemistry Colloquium: 2019
Student Invited Speaker Representative; Chemistry Graduate Student Council: 2018-2019
Tour guide for prospective students: 2017-present
Volunteer; Learning through Experiment and Demonstration: 2016-present

West Virginia Wesleyan College
President; Benzene Ring ACS Student Chapter: 2015-2016
Member; Benzene Ring ACS Student Chapter 2012-2016
Student Leader, BOOTCamp; college transition leader and outdoor recreation advisor: 2013-2015

Community
Board Member, The Wesley Foundation at UVA, Charlottesville, Virginia: 2019-present

SOCIETY MEMBERSHIPS

Student Member, American Chemical Society: 2013-present

REFERENCES

Charles W. Machan, PhD
Research Adviser
Assistant Professor, Department of Chemistry, University of Virginia
machan@virginia.edu

T. Brent Gunnoe, PhD
Dissertation Committee Chair
Commonwealth Professor of Chemistry, Department of Chemistry, University of Virginia
tbg7h@virginia.edu

A. Ian Harrison, PhD
Dissertation Committee Member
Professor of Chemistry, Department of Chemistry, University of Virginia
ah8t@virginia.edu

Lance M. Wheeler, PhD
Research Mentor
Researcher III, Materials Science, National Renewable Energy Laboratory
Lance.Wheeler@nrel.gov

Nathan R. Neale, PhD
Research Mentor
Senior Scientist and Group Manager, Interfacial Materials Scientist, National Renewable Energy Laboratory
Nathan.Neale@nrel.gov

Joanna M. Webb, PhD
Undergraduate Adviser
Department Chair and Associate Professor, Department of Chemistry, West Virginia Wesleyan College
webb_j@wvwc.edu